



Swansea University
Prifysgol Abertawe

DOCTORAL THESIS

**Synthesis and Characterisation of Novel
Phosphonate-based Linkers and Metal-Organic
Frameworks based on Tetravalent Metals**

Author

Stephen J. I. Shearan

Supervisors

Assoc. Prof. Enrico Andreoli

Asst. Prof. Marco Taddei

A thesis submitted in fulfillment of the requirements

for the degree of

Doctor of Philosophy

at the

Energy Safety Research Institute
Faculty of Science and Engineering
Swansea University


March 2022

Declaration of Authorship

I, Stephen J. I. Shearan, declare that this thesis titled, "Synthesis and Characterisation of Novel Phosphonate-based Linkers and Metal-Organic Frameworks based on Tetravalent Metals" and the work presented in it are my own. I confirm that:

- This work was done wholly or mainly while in candidature for a research degree at Swansea University.
- No part of this thesis has previously been submitted for a degree or any other qualification at this University or any other institution.
- Where I have consulted the published work of others, this is always clearly attributed.
- Where I have quoted from the work of others, the source is always given. With the exception of such quotations, this thesis is entirely my own work.
- Where the thesis is based on work done by myself jointly with others, I have made clear exactly what was done by others and what I have contributed myself.
- Where necessary, I have followed the ethical procedures and guidelines of the University.
- I hereby give my consent for my work, if relevant and accepted, to be available for photocopying and for inter-library loans after expiry of a bar on access approved by the University.

Signed:

A large black rectangular box redacting the signature of the author.

Date:

17/07/2022

"It is the struggle itself that is most important. We must strive to be more than we are. It does not matter that we will not reach our ultimate goal. The effort itself yields its own reward."

- Lt. Cmdr. Data, Star Trek: The Next Generation
(Written by Gene Roddenberry)

"Dyfal donc a dyr y garreg. - Tapping persistently breaks the stone."

- Welsh proverb

"La gatta frettolosa fece i gattini ciechi. - The hasty cat made blind kittens."

- Italian proverb



Swansea University
Prifysgol Abertawe

Abstract

Doctor of Philosophy

Synthesis and Characterisation of Novel Phosphonate-based Linkers and Metal-Organic Frameworks based on Tetravalent Metals

by Stephen J. I. Shearan

The interest in metal-organic frameworks (MOFs) has skyrocketed in the past two decades, owing mainly to their tunable structures and properties. The main approach for this thesis is to explore the synthesis of novel metal(IV) phosphonate frameworks, mainly based on zirconium(IV). Exploring the effect of linker geometry on the structure of MOFs, a series of non-linear linkers were synthesised and assessed on their effectiveness in forcing the structure away from the conventional pillared-layered structures observed in a large portion of metal phosphonate literature. The subsequent structures were then assessed for their suitability in applications such as carbon capture and photocatalysis. With the interest in crystallisation evident, an in-depth *in situ* XRD crystallisation study was also carried out on two existing Ce(IV)-based MOFs, one of which had been identified for its promising carbon capture properties, and was also subject to a scale-up study to assess the potential for commercial deployment.

Acknowledgements

I would first like to thank both Dr Marco Taddei and Dr Enrico Andreoli for allowing me the opportunity to undertake this journey and for their considerable support, guidance, and patience throughout. Marco's passion for MOFs and Enrico's profound ability to ask the right questions and guide the narrative have played vital roles in my success.

To all my friends and colleagues at the Energy Safety Research Institute (ESRI), past and present, I am deeply grateful for your support over the years, not only academically, but personally. A particular thank you to Dr Michael Warwick, Dr Kat Glover, Dr Dan Jones, Dr Daniel Stewart, Dr Donald Hill, Lucy Fisher, Odin Bain, Wafaa Al-Shatty, Henry Apsey, Max Newberry... the list undoubtedly goes on. I will truly cherish our time together and I hope to work with some of you again in the future. A second thank you to Dr Warwick for his guidance in the photocatalysis work.

Thank you to my friends for the amazing support you've given me over the years and for all of the well needed distractions you've provided during the tough times, you've truly helped in maintaining my sanity.

Last, but certainly not least, I would like to thank my family. Without your support and encouragement, particularly over the last few years, this would not have been possible. You have been my advocates my whole life and I hope I have made you proud.

Contents

Declaration of Authorship	iii
Abstract	vii
Acknowledgements	ix
List of Figures	xxxiv
List of Tables	xxxvii
List of Abbreviations	xxxix
1 Introduction	1
1.1 Thesis Scope	1
1.2 Thesis Structure	1
1.3 Metal-Organic Frameworks	3
1.3.1 An Introduction to Metal-Organic Frameworks	3
1.4 Metal Phosphonates	8
1.4.1 Synthesis and Characterisation	14
1.4.2 Applications	30
1.5 Copyright	47
1.6 References	47
2 Materials and Characterisation Techniques	61
2.1 Introduction	61
2.2 Materials	61

2.3	Analytical Methods and Theory	63
2.3.1	Nuclear Magnetic Resonance (NMR) Spectroscopy	63
2.3.2	Fourier-Transform Infrared (FT-IR) Spectroscopy	66
2.3.3	Ultraviolet–visible (UV-Vis) Absorption Spectroscopy	68
2.3.4	Mass Spectrometry	72
2.3.5	Powder X-ray Diffraction (PXRD) and Crystallography	77
2.3.6	Gas Adsorption Analysis	82
2.3.7	Scanning Electron Microscopy (SEM)	88
2.3.8	Thermogravimetric Analysis (TGA)	89
2.4	References	89
3	Synthesis and Characterisation of Novel Phosphonic Acid Linkers	91
3.1	Introduction	91
3.1.1	Phosphonate Esters and C-P Cross-Coupling Reactions	93
3.1.2	Hydrolysis of Phosphonate Esters to Phosphonic Acids	97
3.2	Experimental	99
3.2.1	C-P Coupling	99
3.2.2	Synthesis of Phosphonic Acids	103
3.3	Results and Discussion	106
3.4	Conclusions	150
3.5	References	151
4	Novel Metal Phosphonate Frameworks based on Tetravalent Metals	155
4.1	Introduction	155
4.1.1	An Overview of M ^{IV} –based Metal–Organic Frameworks	156
4.1.2	Scientific Motivation	162
4.2	Experimental	163
4.3	Results and Discussion	164
4.3.1	Structures Obtained using H ₄ BPA (1B)	164
4.3.2	Structures Obtained using H ₄ DPC (2B)	182

4.3.3	Structures Obtained using H ₄ DPPA (3B)	184
4.4	Conclusions	193
4.5	References	194
5	<i>In-situ</i> XRD Investigation of Perfluorinated Ce(IV)-MOFs	199
5.1	Introduction	199
5.2	Experimental	202
5.2.1	<i>In Situ</i> Experiments	202
5.2.2	Data Extraction using DAWN, the Data Analysis WorkbeNch	204
5.2.3	Modelling Crystallisation Kinetics	207
5.2.4	<i>Ex-situ</i> Experiments	209
5.3	Results and Discussion	211
5.3.1	Preliminary Screening	211
5.3.2	System 1 - Ce(IV)-TFBDC-HNO ₃	215
5.3.3	System 2 - Ce(IV)-TFBDC-HNO ₃ -AcOH	219
5.3.4	Optimising for the F4_UiO-66(Ce) Phase	232
5.3.5	<i>Ex situ</i> Optimisation of F4_MIL-140A(Ce) Synthesis	234
5.3.6	Scale-up of F4_MIL-140A(Ce)	238
5.4	Conclusions	243
5.5	References	245
5.6	Copyright and Authorship	249
6	Conclusions and Outlook	251
A	Metal Phosphonate Synthesis	257
B	Ce(IV)-MOF Synthesis and Crystallisation Kinetics	265

List of Figures

- 1.1 Crystal structure of copper(I) 4,4',4'',4'''-tetracyanotetraphenylmethane $[\text{Cu}^{\text{I}}(\text{C}(\text{C}_6\text{H}_4 \cdot \text{CN})_4)_n]^{n+}$ viewed (a) along the a -axis, (b) perpendicular to the c -axis, between the a - and b -axis, and (c) along the c -axis.⁷ © 1989, American Chemical Society. 4
- 1.2 (a) View of the interpenetrating adamantane-like units in $\text{Zn}(\text{CN})_2$ and $\text{Cd}(\text{CN})_2$, (b) View of $\text{Zn}(\text{CN})_2$ and $\text{Cd}(\text{CN})_2$ structures revealing multiple catenane associations.⁸ © 1990, American Chemical Society. 5
- 1.3 Crystal structure for $\text{CoC}_6\text{H}_3(\text{COOH}_{0.33})_3(\text{NC}_5\text{H}_5)_2 \cdot 0.66 \text{NC}_5\text{H}_5$, shown a) as a double layer along the z -axis, and b) looking between the layers perpendicular to the z -axis.⁹ © 1995, Nature Publishing Group. 6
- 1.4 (a) $\text{Zn}_4(\text{O})\text{O}_{12}\text{C}_6$ cluster shown as a ball-and-stick model. (b) $\text{Zn}_4(\text{O})\text{O}_{12}\text{C}_6$ cluster with ZnO_4 tetrahedra shown in blue. (c) A view of MOF-5 along the a -axis, with unit cell shown in black.³ © 1999, Nature Publishing Group. 8
- 1.5 Crystal structure of α -ZrP viewed along the b -axis (a) and perpendicular to the layer (b). Adapted with permission from ref. [21], © 1969 American Chemical Society. 9
- 1.6 Crystal structure of α -zirconium phenylphosphonate $[\text{Zr}(\text{C}_6\text{H}_5\text{PO}_3)_2]$ viewed a) along the a -axis, and b) along the b -axis. Remade using data from Ref [22], © 1978 Elsevier Ltd. 10

1.7	Structure of $\text{Mn}(\text{O}_3\text{PC}_6\text{H}_5) \cdot \text{H}_2\text{O}$ viewed along the <i>a</i> -axis. Reprinted with permission from ref. Reprinted with permission from reference [27] © 1988 American Chemical Society.	11
1.8	Crystal structure of $\text{Zr}(\text{C}_6\text{H}_5\text{PO}_3)_2$ viewed (a) along the <i>b</i> -axis, and (b) and perpendicular to the layer. Reprinted with permission from ref. Reprinted with permission from reference [30] © 1993 International Union of Crystallography.	11
1.9	Crystal structures of the open framework metal phosphonates (MPs): (a) $\beta\text{-Cu}(\text{CH}_3\text{PO}_3)$, (b) $\text{Zn}(\text{O}_3\text{PC}_2\text{H}_4\text{NH}_2)$, and (c) $\alpha\text{-Al}_2(\text{O}_3\text{PCH}_3)_2$. Colour code - light blue: copper, turquoise: zinc, light grey: aluminium, green: phosphorus, red: oxygen, blue: nitrogen, grey: carbon, white: hydrogen. ³¹⁻³⁵	12
1.10	Crystal structure of the $\text{Ga}_4\text{P}_4\text{O}_{12}$ core found in $[\text{}^t\text{BuGa}(\mu_3\text{-O}_3\text{PPh})]_4$. Reprinted with permission from reference [40] © 1998 Plenum Publishing Corporation.	13
1.11	Typical workflow for a high-throughput (HT) synthesis experiment. Reprinted with permission from reference [46] © 2009 Elsevier Inc.	14
1.12	Crystallization diagram of observed phases in the $\text{Zn}(\text{NO}_3)_2/\rho\text{-H}_2\text{O}_3\text{PCH}_2\text{C}_6\text{H}_4\text{COOH}/\text{NaOH}$ system and representative sections of the structures of $\text{Zn}(\text{HO}_3\text{PCH}_2\text{C}_6\text{H}_4\text{COOH})_2$ (1), $\text{Zn}(\text{O}_3\text{PCH}_2\text{C}_6\text{H}_4\text{COOH})$ (2), and $\text{Zn}_3(\text{HO}_3\text{PCH}_2\text{C}_6\text{H}_4\text{COO})_2 \cdot 4 \text{H}_2\text{O}$ (3). Colour code: white - zinc, black - carbon, dark grey - phosphorus, light grey - oxygen. Reprinted with permission from reference [48] © 2004 Wiley-VCH Verlag GmbH & Co.	16

- 1.13 Molecular structure and coordination polyhedra Cd^{2+} ions and hydrogen bonds (green dashed lines) of (a) $\text{Cd}(\text{O}_3\text{PPh}) \cdot \text{H}_2\text{O}$, (b) $\text{Cd}(\text{HO}_3\text{PPh})_2$, (c) $\text{Cd}(\text{HO}_3\text{PPh})_2(\text{H}_2\text{O}_3\text{PPh})$, and the crystal structures of $\text{Cd}(\text{O}_3\text{PPh}) \cdot \text{H}_2\text{O}$, (d) viewed along the *c*-axis, (e) $\text{Cd}(\text{HO}_3\text{PPh})_2$, viewed along the *c*-axis, and (f) $\text{Cd}(\text{HO}_3\text{PPh})_2(\text{H}_2\text{O}_3\text{PPh})$, viewed along the *a*-axis. Hydrogen atoms of the phenyl rings are omitted for clarity. Colour code: yellow - cadmium, orange - phosphorus, red - oxygen, grey - carbon, light grey - hydrogen. Reprinted with permission from reference [64] © 2016 Royal Society of Chemistry. 17
- 1.14 Crystal structure of $\text{Mn}(\text{HO}_3\text{PPh})_2 - (\text{H}_2\text{O}_3\text{PPh})_2(\text{H}_2\text{O})_2$. (a) Coordination sphere of the metal ion. (b) Structure of 1 shown along the *c*-axis. Hydrogen atoms are omitted for clarity. Colour code: purple - manganese, red - oxygen, orange - phosphorus, grey - carbon, light grey - hydrogen. Reprinted with permission from reference [65] © 2016 Royal Society of Chemistry. 18
- 1.15 Structure of $\text{Zn}(\text{O}_3\text{PCH}_2\text{NH}_2\text{CH}_2\text{CO}_2) \cdot \text{H}_2\text{O}$. (a) Coordination sphere of the Zn^{2+} ion. (b) Structure of the layer formed by the ZnO_4 -tetrahedra and the phosphono groups, shown along the *a*-axis. (c) Pillared structure of the framework shown along the *b*-axis. Hydrogen atoms are omitted for clarity. Colour code: Purple - zinc, red - oxygen, orange - phosphorus, blue - nitrogen, grey - carbon, white - hydrogen. Reprinted with permission from reference [66] © 2017 Springer Science Business Media. 19

1.16	Crystal structure of MIL-91 viewed (a) along the <i>c</i> -axis and (b) the <i>b</i> -axis. For clarity, only one set of the two symmetry-equivalent (but half-occupied) sets of diphosphonate ligands connecting octahedral chains along <i>c</i> are shown. (c) A corner-sharing chain of MO ₆ octahedra. Colour code: cyan - titanium, orange - phosphorus, red - oxygen, blue - nitrogen, purple - carbon. Reprinted with permission from reference [70] © 2006 American Chemical Society.	21
1.17	Crystal structures of STA-12 (left), based on N,N'-piperazinediphosphonic acid and STA-16 (right), based on N,N'-bispiperidinediphosphonic acid. Colour code: cobalt, nickel - purple, phosphorus - orange, oxygen - red, nitrogen - light blue, carbon - black, hydrogen - white. Reprinted with permission from reference [79] © 2011 American Chemical Society.	22
1.18	Crystal structures of (a) CAU-29 (Reprinted with permission from reference [54] © 2018, Royal Society of Chemistry), and (b) CAU-30 (Reprinted with permission from reference [55] © 2018, Royal Society of Chemistry). Colour code: green - nickel, light blue - zirconium, purple - phosphorus, red - oxygen, dark blue - nitrogen, grey - carbon, white - hydrogen.	23
1.19	Transmission electron micrographs of ICR-2 (left) (⁹⁰ © 2018, Wiley-VCH Verlag GmbH and Co.), and CAU-30. Reprinted with permission from reference [55] © 2018 Royal Society of Chemistry.	24
1.20	Surface energy-dispersive X-ray diffraction (EDXRD) plot of the transformation of the intermediate phase into Ln(O ₃ P-C ₄ H ₈ -SO ₃)·H ₂ O (bottom) and reaction progress ($\alpha(t)$) for both phases under conventional heating at 150 °C (top). Reprinted with permission from reference [100] © 2010 American Chemical Society.	26

- 1.21 Illustration of the reaction pathway leading to the formation of $[\text{Cu}_2(\text{O}_3\text{PC}_2\text{H}_4-\text{SO}_3)(\text{OH})(\text{H}_2\text{O})] \cdot 3 \text{H}_2\text{O}$ (1) through intermediates $\text{Cu}_2[(\text{O}_3\text{P}-\text{C}_2\text{H}_4-\text{SO}_3)(\text{H}_2\text{O})_2(\text{OH})] \cdot 4 \text{H}_2\text{O}$ (4) and $[\text{Cu}_2(\text{O}_3\text{P}-\text{C}_2\text{H}_4-\text{SO}_3)(\text{H}_2\text{O})_2(\text{OH})] \cdot 3 \text{H}_2\text{O}$ (6). The phase transformation at different temperatures is shown in the contour plot, and the correlated structural motifs of the copper oxygen chains are presented below. The gap in the contour plot at ≈ 30 mins is due to the stage at which the specimen was removed from the vessel. Reprinted with permission from reference [101] © 2012 American Chemical Society. 27
- 1.22 Crystallisation process of $\text{Co}(\text{PhPO}_3) \cdot \text{H}_2\text{O}$ followed *in situ* by (a) synchrotron X-ray diffraction (XRD) and (b) Raman spectroscopy. The first measurement of the Raman plot (grey) is the Raman spectrum of the empty Perspex jar, indicating the modes arising from the sample holder. Colour code: yellow: reactants, green: reactants and intermediate phases, blue: reactants, intermediate phases and product, purple: intermediate phases and product, red: product. Reprinted with permission from reference [102] © 2015 Wiley-VCH Verlag GmbH and Co. 29
- 1.23 Two-dimensional (2D) plots of (a) synchrotron X-ray diffraction (XRD) data with a description of the detected compounds and (b) *in situ* Raman spectroscopy measurements monitoring the synthesis of $\text{Mn}(\text{HO}_3\text{PPh})_2(\text{H}_2\text{O}_3\text{PPh})_2(\text{H}_2\text{O})_2$. Reprinted with permission from reference [65] © 2016 Royal Society of Chemistry. 30
- 1.24 Crystal structure of $\text{Zr}_2(\text{PO}_4)\text{H}_5[(\text{O}_3\text{PCH}_2)_2\text{NCH}_2\text{COO}]_2 \cdot \text{H}_2\text{O}$ viewed along the *c*-axis. Colour code: pink - zirconium, green - phosphorus, red - oxygen, blue - nitrogen, grey - carbon. Reprinted with permission from reference [112] © 2014 American Chemical Society. 31

1.25	Schematic representation of a mixed α -Zr phosphate aminoethylphosphonate. Adapted with permission from reference [116] © 2019 Royal Society of Chemistry.	33
1.26	Transmission electron micrograph of Au@ZP-AEP (left) and Au particle size distribution (right). Adapted with permission from reference [116] © 2019 Royal Society of Chemistry.	34
1.27	The epoxidation reaction of styrene (left) and (E)-stilbene (right) with the Co-based metal–organic framework material STA-12(Co). The graph on the left shows styrene conversion (black square), as well as the selectivity for styrene oxide (unfilled square), benzaldehyde (black circle), and benzoic acid (unfilled circle). The graph on the right shows (E)-stilbene conversion (black square), as well as the selectivity for trans-stilbene oxide (unfilled triangle) and benzaldehyde (black circle). Adapted with permission from reference [119] © 2012 Wiley-VCH Verlag GmbH & Co.	36
1.28	CO ₂ , CH ₄ , and N ₂ adsorption isotherms measured at 303 K on MIL-91(Al) up to 50 bar (a) and up to 1 bar (b). Adapted with permission from reference [78] © 2015 American Chemical Society.	37
1.29	Crystal structure of MIL-91(Al) before (left) and after (right) the adsorption of CO ₂ . The rotation of crystallographically independent linker units is highlighted within the white and blue circles. Reprinted with permission from reference [77] © 2015 American Chemical Society.	38
1.30	Breakthrough curves of the CO ₂ /CH ₄ /CO (70/15/15) mixture on (a) CPO-27-Co, (b) CPO-27-Zn, (c) CPO-27-Ni, and (d) STA-12-Ni at 303 K and 5 bar. Reprinted with permission from reference [79] © 2011 Elsevier Inc.	39
1.31	Schematic representations of a rechargeable lithium ion (Li-ion) battery (left) and a proton exchange membrane fuel cell (right). Adapted with permission from reference [133] © 2009 Elsevier Inc.	40

1.32 (a) Crystal structure of $\text{La}(\text{H}_5\text{DTMP}) \cdot 7\text{H}_2\text{O}$ and (b) the extended network of hydrogen-bonded water molecules along the a -axis, along with a detail of the hydrogen bonding distances. Colour code: lanthanum: purple, phosphorus: light blue, oxygen: red, nitrogen: dark blue, carbon: yellow. Adapted with permission from reference [140] © 2012 Royal Society of Chemistry.	42
1.33 (a) Illustration of the monoclinic unit cell of $\text{Li}_{1.4}\text{Fe}_{6.8}[\text{CH}_2(\text{PO}_3)_2]_3[\text{CH}_2(\text{PO}_3)(\text{PO}_3\text{H})] \cdot 4\text{H}_2\text{O}$ and the expanded crystal structure viewed along the c -axis. Colour code: octahedral iron: red, tetrahedral iron: orange, phosphorus: yellow, oxygen: blue, carbon: black, water: grey, and lithium: green. (b) Specific charge vs. cycle number plot of $\text{Li}_{1.4}\text{Fe}_{6.8}[\text{CH}_2(\text{PO}_3)_2]_3[\text{CH}_2(\text{PO}_3)(\text{PO}_3\text{H})] \cdot 4\text{H}_2\text{O}$ cycled at 20 mA/g with a 1-h potentiostatic step after each half-cycle. Adapted with permission from reference [145] © 2015 American Chemical Society.	44
1.34 Etidronic acid (ETID) release versus time for the control tablet (dark blue circles) and the Ca-ETID tablet (light blue triangles). The crystal structure of Ca-ETID is also displayed in the inset. Colour code: green - calcium, yellow - phosphorus, red - oxygen, black - carbon, pink - lattice water. Adapted with permission from reference [150] © 2018 Walter de Gruyter GmbH and Co. KG.	46
2.1 a) In the absence of an external magnetic field, nuclei are randomly oriented. b) When an external magnetic field is applied, the nuclei take up a specific orientation, either with (red) or against (blue) the external magnetic field.	63
2.2 Typical NMR spectrograph, displaying intensity of the y -axis and magnetic field strength, in ppm, on the x -axis.	64

2.3	Chemical shifts of halomethanes up the halogen group in order of increasing electronegativity, decreasing field strength, and decreased shielding.	65
2.4	A visual representation of the Beer-Lambert law, showing the absorption of radiation as dependent on the factors described in Equation 2.2. . . .	68
2.5	A simplified schematic diagram of a typical mass spectrometer.	73
2.6	A simplified schematic diagram for the electrospray ionisation process. Reprinted from reference [12] ©2002 John Wiley & Sons, Inc.	75
2.7	A simplified schematic diagram for a quadrupole mass analyser. ¹³	76
2.8	Visual representations of the fourteen Bravais lattices and corresponding crystal systems. Reproduced under a creative commons licence, CC BY-NC 4.0, from "Crystallography-Cristalografia", by Martin Martinez-Ripoll (Department of Crystallografy & Structural Biology). https://www.xtal.iqfr.csic.es/Cristalografia/	79
2.9	Examples of Miller indices, whereby a_1 , a_2 , and a_3 are the three vectors that define the unit cell. Reproduced under a creative commons licence, CC BY 3.0. https://en-academic.com/pictures/enwiki/77/Miller_Indices_Felix_Kling.svg	80
2.10	A representation of the diffraction process on the atomic scale.	82
2.11	Isotherm types as classified by IUPAC. ²⁰	85
3.1	A comparison between the bonding modes of a) carboxylates, and b) phosphonates, whereby, the latter has double the number of possible bonding modes. Adapted with permission from Ref. [15], © 2015 American Chemical Society.	92
3.2	Chemical structure of (1A) N,N-Bis(4-diisopropylphosphonophenyl)amine [iPr ₄ BPA].	100
3.3	Chemical structure of (2A) 3,6-bis(diisopropylphosphono)-9H-carbazole [iPr ₄ DPC].	101

3.4	Chemical structure of (3A) 4-diisopropylphosphono-N-(4-diisopropylphosphono-phenyl)-N-phenylaniline [iPr ₄ DPPA].	102
3.5	Chemical structure of (1B) N,N-Bis(4-phosphonophenyl)amine [H ₄ BPA].	103
3.6	Chemical structure of (2B) 3,6-diphosphono-9H-carbazole [H ₄ DPC]. . .	104
3.7	Chemical structure of (3B) 4-phosphono-N-(4-phosphonophenyl)-N-phenylaniline [H ₄ DPPA].	105
3.8	³¹ P NMR spectrum for iPr ₄ BPA (1A). (a) Full spectrum, (b) Zooming in on the single phosphorus signal. Solvent: Chloroform-d.	108
3.9	Chemical Structure of iPr ₄ BPA (1A), with proton environments labelled H _a to H _d , corresponding with A-D on the NMR spectrum.	109
3.10	Full ¹ H NMR spectrum for iPr ₄ BPA (1A). Solvent: Chloroform-d.	110
3.11	¹ H NMR spectrum for iPr ₄ BPA (1A). Solvent: Chloroform-d.	110
3.12	¹ H NMR spectrum for iPr ₄ BPA (1A). Solvent: Chloroform-d.	111
3.13	¹ H NMR spectrum for iPr ₄ BPA (1A). Solvent: Chloroform-d.	111
3.14	Chemical Structure of iPr ₄ BPA, with carbon environments labelled a to f , corresponding with A-F on the ¹³ C NMR spectrum.	113
3.15	Full ¹³ C NMR spectrum for iPr ₄ BPA (1A). Solvent: Chloroform-d.	113
3.16	Full HSQC NMR spectrum for iPr ₄ BPA (1A). Solvent: Chloroform-d. . .	114
3.17	Observed mass spectrum for iPr ₄ BPA.	115
3.18	Observed mass spectrum for iPr ₄ BPA and theoretical isotope pattern for the [M+H] ⁺ species.	115
3.19	³¹ P NMR spectrum for H ₄ BPA (1B). Solvent: 0.1M NaOH in D ₂ O.	116
3.20	Chemical Structure of H ₄ BPA, with proton environments labelled H _a to H _b , corresponding with A-B on the ¹ H NMR spectrum.	117
3.21	¹ H NMR spectrum for H ₄ BPA (1B). Solvent: 0.1M NaOH in D ₂ O.	117
3.22	¹ H NMR spectrum for H ₄ BPA (1B), focussing on the aromatic region. Solvent: 0.1M NaOH in D ₂ O.	118

3.23	Chemical Structure of H ₄ BPA, with carbon environments labelled a to d , corresponding with A-D on the ¹³ C NMR spectrum.	118
3.24	Full ¹³ C NMR spectrum for H ₄ BPA (1B). Solvent: 0.1M NaOH in D ₂ O.	119
3.25	HSQC NMR spectrum for H ₄ BPA (1B), . Solvent: 0.1M NaOH in D ₂ O.	120
3.26	Observed Mass spectrum for H ₄ BPA.	120
3.27	Observed Mass spectrum for H ₄ BPA and theoretical isotope pattern for the [M-2H] ²⁻ species.	121
3.28	³¹ P NMR spectrum for iPr ₄ DPC (2A). Solvent: Chloroform- <i>d</i>	122
3.29	Chemical Structure of iPr ₄ DPC (2A), with proton environments labelled H _a to H _e , corresponding with A-E on the NMR spectrum.	122
3.30	¹ H NMR spectrum for iPr ₄ DPC (2A). Solvent: Chloroform- <i>d</i>	123
3.31	¹ H NMR spectrum for iPr ₄ DPC (2A). Solvent: Chloroform- <i>d</i>	124
3.32	¹ H NMR spectrum for iPr ₄ DPC (2A). Solvent: Chloroform- <i>d</i>	125
3.33	¹ H NMR spectrum for iPr ₄ DPC (2A). Solvent: Chloroform- <i>d</i>	125
3.34	Chemical Structure of iPr ₄ DPC (2A), with carbon environments labelled a to h , corresponding with A-H on the ¹³ C NMR spectrum.	126
3.35	¹³ C NMR spectrum for iPr ₄ DPC (2A). Solvent: Chloroform- <i>d</i>	126
3.36	Full HSQC NMR spectrum for iPr ₄ DPC (2A). Solvent: Chloroform- <i>d</i>	127
3.37	Observed Mass spectrum for iPr ₄ DPC.	128
3.38	Observed Mass spectrum for iPr ₄ DPC and theoretical isotope pattern for the [M+H] ⁺ species.	128
3.39	³¹ P NMR spectrum for H ₄ DPC (2B). Solvent: Chloroform- <i>d</i>	129
3.40	Chemical Structure of H ₄ DPC (2B), with proton environments labelled H _a to H _c , corresponding with A-C on the NMR spectrum.	130
3.41	Full ¹ H NMR spectrum for H ₄ DPC (2B). Solvent: Chloroform- <i>d</i>	130
3.42	¹ H NMR spectrum for H ₄ DPC (2B). Solvent: 0.1M NaOH in D ₂ O.	131
3.43	Chemical Structure of H ₄ DPC (2B), with carbon environments labelled a to f	131
3.44	Full ¹³ C NMR spectrum for H ₄ DPC (2B). Solvent: 0.1M NaOH in D ₂ O.	132

3.45	Full HSQC NMR spectrum for H ₄ DPC (2B). Solvent: 0.1M NaOH in D ₂ O.	132
3.46	Observed Mass spectrum for H ₄ DPC.	133
3.47	Observed Mass spectrum for H ₄ DPC and theoretical isotope pattern for the [M-2H] ²⁻ species.	133
3.48	³¹ P NMR spectrum for iPr ₄ DPPA (3A). Solvent: Chloroform- <i>d</i>	134
3.49	Chemical Structure of iPr ₄ DPPA (3A), with proton environments labelled H _a to H _g , corresponding with A-G on the NMR spectrum. . . .	135
3.50	¹ H NMR spectrum for iPr ₄ DPPA (3A). Solvent: Chloroform- <i>d</i>	135
3.51	¹ H NMR spectrum for iPr ₄ DPPA (3A). Solvent: Chloroform- <i>d</i>	136
3.52	¹ H NMR spectrum for iPr ₄ DPPA (3A). Solvent: Chloroform- <i>d</i>	137
3.53	¹ H NMR spectrum for iPr ₄ DPPA (3A). Solvent: Chloroform- <i>d</i>	138
3.54	Chemical Structure of iPr ₄ DPPA (3A), with carbon environments labelled H _a to H _i , corresponding with A-I on the ¹³ C NMR spectrum. . .	138
3.55	Full ¹³ C NMR spectrum for iPr ₄ DPPA (3A). Solvent: Chloroform- <i>d</i>	139
3.56	HSQC NMR spectrum for iPr ₄ DPPA (3A). Solvent: Chloroform- <i>d</i>	140
3.57	Observed Mass spectrum for iPr ₄ DPPA.	140
3.58	Observed Mass spectrum for iPr ₄ DPPA and theoretical isotope pattern for the [M+H] ⁺ species.	141
3.59	³¹ P NMR spectrum for H ₄ DPPA (3B). Solvent: Solvent: 0.1M NaOH in D ₂ O.	142
3.60	Chemical Structure of H ₄ DPPA (3B), with proton environments labelled H _a to H _e , corresponding with A-E on the NMR spectrum.	142
3.61	Full ¹ H NMR spectrum for H ₄ DPPA (3B). Solvent: Solvent: 0.1M NaOH in D ₂ O.	143
3.62	¹ H NMR spectrum for H ₄ DPPA (3B). Solvent: 0.1M NaOH in D ₂ O. . . .	143
3.63	Chemical Structure of H ₄ DPPA (3B), with carbon environments labelled H _a to H _g , corresponding with A-G on the ¹³ C NMR spectrum.	144
3.64	Full ¹³ C NMR spectrum for H ₄ DPPA (3B). Solvent: 0.1M NaOH in D ₂ O.	145
3.65	HSQC NMR spectrum for H ₄ DPPA (3B). Solvent: 0.1M NaOH in D ₂ O. .	145

3.66	Observed Mass spectrum for H ₄ DPPA.	146
3.67	Observed Mass spectrum for H ₄ DPPA and theoretical isotope pattern for the [M-2H] ²⁻ species.	146
3.68	Experimental setup for the improved C-P cross coupling reaction.	148
4.1	a) Crystal structure of UiO-66, b) Structure of the Zr ₆ cluster. Colour code: Zirconium - Green, Oxygen - Red, Carbon - Black.	157
4.2	a) Crystal structure of MIL-140A viewed along the <i>c</i> -axis, b) Structure of the inorganic chain viewed along the <i>b</i> -axis. Colour code: Zirconium - Green, Oxygen - Red, Carbon - Black.	159
4.3	Crystal structure of Zrbtp-a showing a) one layer along the <i>c</i> -axis, and b) two layers along the <i>c</i> -axis, clearly showing the capping of the cavities by the SBU of the next layer. Colour code: green = zirconium, black = carbon, phosphorus = purple, oxygen = red.	160
4.4	Crystal structure of UPG-1, showing the unit cell and two channel types, along the <i>c</i> -axis. Colour code: green = zirconium, black = carbon, phosphorus = purple, oxygen = red, nitrogen = blue.	161
4.5	PXRD patterns of UPG-1 a1) as synthesised, a2) after a 3-day treatment in H ₂ O at 120 °C, a3) after a 2-day treatment in H ₂ O at 200 °C, a4) after a 3-day treatment in HCl at 80 °C, and a5) after a 3-day treatment in HCl at 120 °C. PXRD patterns of UiO-66 b1) as synthesised, b2) after a 3-day treatment in H ₂ O at 120 °C, b3) after a 2-day treatment in H ₂ O at 200 °C, b4) after a 3-day treatment in HCl at 80 °C, and b5) after a 3-day treatment in HCl at 120 °C. Starred peaks represent the hydrolysis product for UiO-66, terephthalic acid.	162
4.6	PXRD patterns obtained for materials 065 - 068. See Table A.1 for synthetic parameters.	165
4.7	PXRD pattern obtained for material 074. See Table A.1 for detailed synthetic parameters.	166

4.8	PXRD pattern obtained for material 085. See Table A.1 for detailed synthetic parameters.	167
4.9	Representative patterns for materials 088-117 where solvent effect was investigated. See Table A.1 for detailed synthetic parameters.	168
4.10	PXRD pattern obtained for material 127. See Table A.1 for detailed synthetic parameters.	168
4.11	Le Bail plots for the materials obtained in 085 (left - $R_p = 0.050$, $R_{wp} = 0.066$) and 127 (right - $R_p = 0.061$, $R_{wp} = 0.078$). $R_p = (\sum I_o - I_c / \sum I_o) \times 100$, $R_{wp} = [\sum w(I_o - I_c)^2 / \sum (wI_o)^2]^{1/2} \times 100$	169
4.12	Structural representation of the layer rotation in α -ZrPhPA which would facilitate the V-shaped linkers used in ZrBPA.	170
4.13	A comparison on the cells for ZrBPA and α -ZrPhPA, showing the switching of the b and c parameters.	171
4.14	A comparison between the linkers employed in the synthesis of (a) ZrBPA (bis(4-phosphonophenyl)amine) and (b) Zr-II-C (4-(4'-phosphonophenoxy) phenylphosphonic acid).	172
4.15	PXRD patterns for (a) a crystalline form of Zr-II-C, (b) a semi-crystalline form of Zr-II-C, and (c) ZrBPA.	173
4.16	TGA curve showing weight loss (black line) against temperature as well as the derivative weight loss (red line), indicating the inflection points for the change in mass.	174
4.17	Gas sorption analysis for 085, showing a) the N_2 isotherm (77 K), b) the N_2 pore size distribution, c) the CO_2 isotherm (273 K), and d) the CO_2 pore size distribution. N_2 BET S.A. = 583.1 m^2/g , CO_2 BET S.A. = 39.7 m^2/g	175
4.18	Measured diffuse reflectance spectrum for ZrBPA in the UV-Visible range (200-800 nm).	177

4.19	a) Tauc plot for each of the energy transitions: direct-allowed (black), direct-forbidden (red), indirect-allowed (blue), and indirect forbidden (pink). b) Tauc plot for the direct-allowed transition with extracted optical band gap energies, one in the range of 2.2-2.3 eV, and another at ~ 5.9 eV.	177
4.20	Photocatalytic degradation pathways for Rhodamine-B: a) N-dealkylation, b) chromophore cleavage, and c) mineralisation of chromophore cleavage products.	179
4.21	UV-Vis absorbance spectra for a) a dilute solution (0.1 mM) of Rhodamine-B, and the photocatalytic degradation of Rhodamine-B (0.8 mM), b) exposed to light source, with no photocatalyst present, c) not exposed to light source, with catalyst present, and d) exposed to light source, with catalyst present. Absorbance data for each plot has been normalised to λ_{max} in the relevant dataset.	180
4.22	PXRD patterns for crystalline/semi-crystalline materials obtained through the use of the H ₄ DPC (2B) linker and ZrOCl ₂ · 8 H ₂ O.	183
4.23	PXRD patterns for synthesis resulting in the formation of ZrDPPA through the use of H ₄ DPPA and ZrOCl ₂ · 8 H ₂ O.	185
4.24	Le Bail plot for the material obtained in 140 ($R_p = 3.9\%$, $R_{wp} = 5.2\%$). . .	187
4.25	TGA curve for ZrDPPA, showing %weight loss (black line) against temperature and the derivative weight loss (red line). Initial weight = 8.2760 mg.	188
4.26	Gas sorption analysis for 135, showing a) the N ₂ isotherm (77 K & 273 K), b) the N ₂ pore size distribution (77 K), c) the CO ₂ isotherm (273 K), and d) the CO ₂ pore size distribution. N ₂ BET S.A. = 228.1 m ² /g, CO ₂ BET S.A. = 132.7 m ² /g.	190
4.27	Measured diffuse reflectance spectrum for ZrDPPA in the UV-Visible range (200-800 nm).	192

4.28 a) Tauc plot for each of the energy transitions: direct-allowed (black), direct-forbidden (red), indirect-allowed (blue), and indirect forbidden (pink). b) Tauc plot for the direct-allowed transition with an extracted optical band gap energy in the range of 1.8-2.0 eV	192
5.1 Crystal structures of F4_UiO-66(Ce) and F4_MIL-140A(Ce)	201
5.2 Representative PXRD ring patterns recorded during <i>in situ</i> experiments	203
5.3 Representative PXRD ring patterns recorded during <i>in situ</i> experiments	205
5.4 Representative PXRD ring patterns recorded during <i>in situ</i> experiments	206
5.5 <i>In situ</i> PXRD patterns of the crystallisation of F4_UiO-66(Ce) (a) and F4_MIL-140A(Ce) (b) using the originally reported synthetic conditions.	207
5.6 SEM micrographs of phase pure F4_UiO-66(Ce) (a) and F4_MIL-140A(Ce) (b), showing the typical octahedral morphology for the former and a needle-like morphology for the latter.	209
5.7 PXRD patterns of the products of syntheses carried out in the presence of (a) 16 equivalents, and (b) 32 equivalents of HNO ₃ at 50 °C (black), 60 °C (red), 70 °C (green) and 80 °C (blue). The crystalline phase is F4_MIL-140A(Ce).	212

5.8 (a) PXRD patterns of the products of syntheses carried out in the presence of 98 equivalents (black), 147 equivalents (red), 196 equivalents (green) of AcOH and 6.4 equivalents of HNO₃ at 70 °C. The black pattern reveals the presence of both F4_MIL-140A(Ce) and F4_UiO-66(Ce), whereas the red and green pattern are phase-pure F4_UiO-66(Ce). The reflections of F4_MIL-140A(Ce) are indicated with the * symbol. (b) PXRD patterns of the products of syntheses carried out in the presence of 98 equivalents (black), 147 equivalents (red) of AcOH and 16 equivalents of HNO₃ at 70 °C. The products are mixtures of F4_MIL-140A(Ce) and F4_UiO-66(Ce). The reflections of F4_UiO-66(Ce) are indicated with the ‡ symbol. (c) PXRD patterns of the products of syntheses carried out in the presence of 28 equivalents (black), 49 equivalents (red) of AcOH and 32 equivalents of HNO₃ at 70 °C. The crystalline phase is F4_MIL-140A(Ce). 213

5.9 Three systems were chosen to investigate the parameter space for the synthesis of F4_MIL-140A(Ce) and F4_UiO-66(Ce). One equivalent corresponds to 0.25 mmol. The molar ratio Ce⁴⁺ to H₂TFBDC is fixed at a value of 1 to 1. 214

5.10 Plot of extent of crystallization (α , circles, left y-axis) and probability of nucleation (P_N , dashed lines, right y-axis) as a function of time for experiments performed at 50 °C (black), 60 °C (red) and 70 °C (green) in the presence of 32 equivalents of HNO₃. 215

5.11 Plot of $\ln(k_n)$ (red circles) and $\ln(k_g)$ (black circles) versus $1/T$ for experiments performed at 50 °C, 60 °C and 70 °C in the presence of 32 equivalents of HNO₃. The red line and the black line are the linear Arrhenius fittings for nucleation and crystal growth, respectively. . . . 217

5.12	Plot of extent of crystallization (α , circles, left y-axis) and probability of nucleation (P_N , dashed lines, right y-axis) as a function of time for experiments performed at 60 °C using 32 (black), 24 (red) and 16 (green) equivalents of HNO ₃	218
5.13	Plot of the extent of crystallisation (left) and absolute intensities (right) of the 110 reflection of the F4_MIL-140A(Ce) phase (black circles) and of the 111 reflection of the F4_UiO-66(Ce) phase (red circles) versus time for the experiment performed at 50 °C with 16 equivalents of HNO ₃ and 96 equivalents of AcOH.	220
5.14	Plot of the extent of crystallisation (left) and absolute intensities (right) of the 110 reflection of the F4_MIL-140A(Ce) phase (black circles) and of the 111 reflection of the F4_UiO-66(Ce) phase (red circles) versus time for the experiment performed at 60 °C with 16 equivalents of HNO ₃ and 96 equivalents of AcOH.	220
5.15	Plot of extent of crystallization (α , empty circles), Gualtieri fitting (solid lines) and probability of nucleation (P_N , dashed lines) as a function of time for experiments performed at 50 °C (a), 60 °C (b) and 70 °C (c) for the F4_UiO-66(Ce) (red) and F4_MIL-140A(Ce) (black) phases.	221
5.16	Plot of extent of crystallization (α , empty circles), Gualtieri fitting (solid lines) and probability of nucleation (P_N , dashed lines) as a function of time for experiments performed in the presence of 16 equivalents of HNO ₃ and 96 equivalents of AcOH at 50 °C (black), 60 °C (red) and 70 °C (green) for (a) the F4_MIL-140A(Ce) phase and (b) the F4_UiO-66(Ce) phase.	223

5.17	Plot of $\ln(k_N)$ (full red circles) and $\ln(k_g)$ (full black circles) for F4_MIL-140A(Ce) and $\ln(k_N)$ (open red circles) and $\ln(k_g)$ (open black circles) for F4_UiO-66(Ce) versus $1/T$ for experiments performed at 50 °C, 60 °C and 70 °C in the presence of 16 equivalents of HNO ₃ and 96 equivalents of AcOH. The red line and the black line are the linear Arrhenius fittings for nucleation and crystal growth, respectively. The value of $\ln(k_g)$ for F4_UiO-66(Ce) at 70 °C is not displayed because of the unreliable Gualtieri fitting for this experiment.	225
5.18	Plot of extent of crystallization (α , empty circles), Gualtieri fitting (solid lines) and probability of nucleation (P_N , dashed lines) as a function of time for experiments performed at 8 (top), 12 (middle) and 16 (bottom) equivalents of HNO ₃ at 60 °C for the F4_MIL-140A(Ce) (black) and the F4_UiO-66(Ce) (red) phases.	226
5.19	Plot of extent of crystallization (α , empty circles), Gualtieri fitting (solid lines) and probability of nucleation (P_N , dashed lines) as a function of time for experiments performed at 8 (green), 12 (red) and 16 (black) equivalents of HNO ₃ for (a) the F4_MIL-140A(Ce) phase and (b) the F4_UiO-66(Ce) phase.	228
5.20	Plot of $\ln(k_N)$ (full red circles) and $\ln(k_g)$ (full black circles) for F4_MIL-140A(Ce) and $\ln(k_N)$ (open red circles) and $\ln(k_g)$ (open black circles) for F4_UiO-66(Ce) versus the amount of HNO ₃ for experiments performed at 60 °C and 96 equivalents of AcOH in the presence of 8, 12 and 16 equivalents of HNO ₃	229
5.21	Plot of the absolute intensities of the 110 reflection of the F4_MIL-140A(Ce) phase (black circles) and of the 111 reflection of the F4_UiO-66(Ce) phase (red circles) versus time for the experiment performed at 60 °C with 16 equivalents of HNO ₃ and 149 equivalents of AcOH.	230

5.22	Plot of extent of crystallization (α , empty circles), Gualtieri fitting (solid lines) and probability of nucleation (P_N , dashed lines) as a function of time for experiments performed with 16 equivalents of HNO ₃ at 60 °C with (a) 0, 96, and 123 equivalents of AcOH for the F4_MIL-140A(Ce) phase and (b) with 96, 123, and 149 equivalents of AcOH for the F4_UiO-66(Ce) phase.	231
5.23	Plot of $\ln(k_N)$ (full red circles) and $\ln(k_g)$ (full black circles) for F4_MIL-140A(Ce) and $\ln(k_N)$ (open red circles) and $\ln(k_g)$ (open black circles) for F4_UiO-66(Ce) versus the amount of AcOH for experiments performed at 60 °C and 16 equivalents of HNO ₃ in the presence of 0, 96, 123 and 149 equivalents of AcOH.	232
5.24	Plot of extent of crystallization (α , empty circles), Gualtieri fitting (solid lines) and probability of nucleation (P_N , dashed lines) as a function of time for experiments performed at 60 °C (black), 70 °C (red) and 80 °C (green) in the presence of 8 equivalents of HNO ₃ and 149 equivalents of AcOH for the F4_UiO-66(Ce) phase.	233
5.25	Plot of $\ln(k_g)$ (open black circles) for F4_UiO-66(Ce) versus $1/T$ for experiments performed at 60 °C, 70 °C, and 80 °C in the presence of 8 equivalents of HNO ₃ and 149 equivalents of AcOH.	234
5.26	PXRD patterns of F4_MIL-140A(Ce) powders obtained from syntheses performed at 50 (black), 60 (red) and 70 °C (green) in the presence of 32 equivalents of HNO ₃	235
5.27	PXRD patterns of F4_MIL-140A(Ce) powders obtained from syntheses performed using CAN/HNO ₃ (black), CAN/H ₂ SO ₄ (red), Ce(SO ₄) ₂ /HNO ₃ (green) and Ce(SO ₄) ₂ /H ₂ SO ₄ (blue) as Ce(IV) source and protonation modulator, respectively, at 60 °C.	236

5.28	(Left) N ₂ adsorption-desorption isotherm of F4_MIL-140A(Ce) powder obtained from synthesis performed at 60 °C in the presence of 32 equivalents of HNO ₃ . BET S _A = 315 m ² g ⁻¹ . (Right) CO ₂ adsorption-desorption isotherms of F4_MIL-140A(Ce) powder obtained from synthesis performed at 60 °C in the presence of 32 equivalents of HNO ₃	238
5.29	PXRD patterns for Ce-004 (black), Ce-010 (red), and Ce-011 (green). . . .	241
5.30	CO ₂ adsorption isotherm for Ce-010 obtained at 273 K.	241
5.31	PXRD pattern and CO ₂ adsorption isotherm for Ce-020 obtained at 273 K.	242
5.32	Visual summary of the main outcomes of the <i>in situ</i> PXRD study. Arrows pointing up indicate an increase of a parameter, arrows pointing down indicate a decrease of a parameter.	243
B.1	SEM micrographs of F4_MIL-140A(Ce) powders obtained from syntheses performed at 50 (black), 60 (red) and 70 °C (green) in the presence of 32 equivalents of HNO ₃	266
B.2	SEM micrographs of F4_MIL-140A(Ce) powders obtained from syntheses performed using (a) CAN/H ₂ SO ₄ , (b) Ce(SO ₄) ₂ /HNO ₃ , and (c) Ce(SO ₄) ₂ /H ₂ SO ₄ as Ce(IV) source and protonation modulator, respectively, at 60 °C.	267

List of Tables

1.1	Results of catalytic tests for the Suzuki-Miyaura coupling displayed in scheme 1.1. Reprinted with permission from reference [113]. © 2015 Royal Society of Chemistry.	32
1.2	Representative results of Au@ZP-AEP catalyst in the switchable preparation of an azoxy derivative (2) and methoxyaniline (4 in Scheme 1.2) and their recovery and reuse. Reprinted with permission from reference [116] © 2019 Royal Society of Chemistry.	35
2.1	Typical IR absorptions of common functional groups. Adapted from [3].	67
2.2	The seven crystal systems and the fourteen corresponding Bravais lattices, and minimum symmetry requirements.	78
3.1	A comparison of conventional phosphonate synthesis with the improved method.	149
4.1	A comparison of the geometric properties of the linkers used in ZrBPA, Zr-II-C, and ZrBPDP.	172
5.1	Representative experiments carried out by combining CAN and H ₂ TFBDC (0.25 mmol each) in a total volume of 5 mL in the presence of different amounts of HNO ₃ and at different temperatures.	211
5.2	Representative experiments carried out by combining CAN and H ₂ TFBDC (0.25 mmol each) in a total volume of 5 mL in the presence of different amounts of HNO ₃ and at different temperatures.	212

5.3	Nucleation and growth rates for F4_MIL-140(Ce) in the presence of 32 equivalents (0.4 mL, 1.6 mol/L) of HNO ₃ at 50, 60, and 70 °C. The ratios shown for k_N and k_g are the ratio at each temperature vs 50 °C.	216
5.4	Nucleation and growth rates for F4_MIL-140(Ce) in the presence of 16 equivalents (0.2 mL, 0.8 mol/L), 24 equivalents (0.3 mL, 1.2 mol/L), and 32 equivalents (0.4 mL, 1.6 mol/L) of HNO ₃ at 60 °C. The ratios shown for k_N and k_g are the ratio at each equivalent of HNO ₃ vs 32 equivalents	218
5.5	Nucleation and growth rates for F4_MIL-140(Ce) and F4_UiO-66(Ce) in the presence of 16 equivalents (0.2 mL, 0.8 mol/L) of HNO ₃ , and 96 equivalents (1.1 mL, 4.8 mol/L) of AcOH at 50, 60, and 70 °C. The ratios shown for k_N and k_g are the ratio at each temperature vs 50 °C.	223
5.6	Nucleation and growth rates for F4_MIL-140(Ce) and F4_UiO-66(Ce) using 8 equivalents (0.1 mL, 0.4 mol/L), 12 equivalents (0.15 mL, 0.6 mol/L), and 16 equivalents (0.02 mL, 0.8 mol/L) of HNO ₃ in the presence of 96 equivalents (1.1 mL, 4.8 mol/L) of AcOH at 60 °C. The ratios shown for k_N and k_g are the ratio at each equivalent of HNO ₃ vs 8 equivalents.	228
5.7	Nucleation and growth rates for F4_MIL-140(Ce) and F4_UiO-66(Ce) using 0 equivalents, 96 equivalents (1.1 mL, 4.8 mol/L), and 123 equivalents (1.4 mL, 6.1 mol/L) of AcOH in the presence of 16 equivalents (0.2 mL, 0.8 mol/L) of HNO ₃ at 60 °C.	231
5.8	Nucleation and growth rates for F4_UiO-66(Ce) in the presence of 8 equivalents (0.1 mL, 0.4 mol/L) of HNO ₃ , and 149 equivalents (1.7 mL, 7.4 mol/L) of AcOH at 50, 60, and 70 °C.	234
A.1	Metal phosphonate synthesis based on the bis(4-phosphonophenyl)amine linker. Unless otherwise stated, all reactions were carried out in a total volume of 10 cm ⁻³	258

A.2	Metal phosphonate synthesis based on the 3,6-diphosphono-carbazole linker. Unless otherwise stated, all reactions were carried out in a total volume of 10 cm ⁻³	261
A.3	Metal phosphonate synthesis based on the 4-phosphono-N-(4-phosphonophenyl)-N-phenylaniline linker. Unless otherwise stated, all reactions were carried out in a total volume of 10 cm ⁻³	262
A.4	Structural and refinement details for ZrBPA, ZrDPPA, Zr-II-C, and UPG-1.	263
B.1	Reaction parameters and yield outcomes for the scale-up of F4_MIL-140A(Ce). TFBDC = Tetrafluorobenzene-dicarboxylic acid, CAN = Cerium(IV) ammonium nitrate, STY = Space time yield.	268

List of Abbreviations

BET	Brunauer-Emmett-Teller
CCSU	Carbon Capture, Storage, and Utilisation
DRS	Diffuse Reflectance Spectroscopy
EDX	Energy-Dispersive X-Ray Spectroscopy
MOF(s)	Metal-Organic Framework(s)
MP(s)	Metal Phosphonate(s)
NMR	Nuclear Magnetic Resonance Spectroscopy
PXRD	Powder X-Ray Diffraction
ppm	Parts Per Million
SCXRD	Single Crystal X-Ray Diffraction
SEM	Scanning Electron Microscopy
TGA	ThermoGravimetric Analysis
UV-Vis	UltraViolet Visible Spectroscopy
UPS	Ultraviolet Photoelectron Spectroscopy
XPS	X-Ray Photoelectron Spectroscopy
XRD	X-Ray Diffraction

I Dedicate this thesis to John 'Jack' Shearan, to me, Dad. Though you won't see the end of this journey, I will be forever grateful for your support in starting it. I also dedicate this to my Son, Lincoln Jack Shearan. Throughout this journey you've brightened up the darkest moments and brought me monumental joy. I love you!

Chapter 1

Introduction

1.1 Thesis Scope

The main aim of this thesis is to explore the chemistry of novel metal-organic frameworks (MOFs) based on tetravalent metals, specifically looking at the synthesis of novel metal phosphonates and the related phosphonate linkers, as well as looking at the crystallisation kinetics of Ce(IV)-based carboxylate MOFs. The main approach is taken from a synthetic point of view, exploring novel linker synthesis and as well as how different linkers can affect the resulting MOF structure. Secondary to this, a broad approach has been taken with regards to applications, examples of which are detailed here in Chapter 1, though we mainly considered carbon capture and photocatalysis for the experimental work.

1.2 Thesis Structure

Chapter 1 begins by giving general overviews of MOFs and the metal phosphonate sub-class, both of which should serve as a sufficient introduction for novices in the field and serve as the basis for understanding the data presented. Parts of this section, specifically the parts pertaining to metal phosphonates, have been adapted from a perspective article titled "New Directions in Metal Phosphonate and Phosphinate Chemistry", published in the peer-reviewed journal *Crystals* (MDPI) in May 2018.¹

The article itself not only explores the topics presented and discussed by some of the leading experts in the field at the *1st European Workshop on Metal Phosphonate and Phosphinate Chemistry*, hosted by Dr Marco Taddei at the Energy Safety Research Institute (Swansea University) in September 2018, but also gives a broad historical overview of the field. A more specific overview of metal(IV)-phosphonates and MOFs can be found later in Chapter 4.

Chapter 2 begins with a brief rundown on the materials used in each experimental chapter, including information such as supplier, purity, and CAS number. Following this, brief overviews have been given for each of the analytical techniques employed during this work, looking at the experimental setup and some of the theory behind these techniques.

Chapter 3 is the first experimental chapter and looks at the work done on the synthesis of organic linkers, specifically phosphonic acids. This begins with a brief literature review of the multi-step synthesis of phosphonic acids, whereby the different steps are considered separately. The first step is associated with the synthesis of the phosphonate ester, while the second is associated with the synthesis of the phosphonic acid.

Chapter 4 is the second experimental chapter and builds on the work from the previous chapter, looking at MOF synthesis carried out using the linkers synthesised in chapter 3 along with tetravalent metals. The primary metal considered for this chapter was zirconium(IV), but minor trials were also run using cerium(IV) and titanium(IV). In the introduction to this chapter, a brief overview of the use and motivation for the use of tetravalent metals in MOF synthesis is given.

Chapter 5 diverts slightly from the theme of the previous two chapters as it looks at two cerium(IV) MOFs which are based on carboxylate linkers, as opposed to phosphonates. Specifically, this chapter covers the crystallisation kinetics of two perfluorinated cerium-based MOFs, F4_MIL-140A(Ce) and F4_UiO-66(Ce), both of which have the equivalent zirconium analogues, namely, MIL-140A and UiO-66. The former of these

two is of particular interest due to its impressive carbon capture properties. This chapter was previously published in *Chemistry - A European Journal*, and has been adapted here to include the supporting information and additional discussion.

Chapter 6 looks at the final thoughts and conclusions for the work carried out, with some consideration given to future work and potential avenues that can and should be explored.

1.3 Metal-Organic Frameworks

1.3.1 An Introduction to Metal-Organic Frameworks

Metal-organic frameworks (MOFs) are a class of inorganic–organic hybrid polymeric materials built by the coordination of organic ligands to metal ions or metal oxide clusters, forming extended structures of various dimensionalities. Since their pioneering at the hands of Prof. Omar Yaghi in the mid 90s,^{2,3} MOFs have become some of the most studied materials not only due to their exceptionally interesting structures, but also for the multitude of potential applications for which they can be utilised. It should be noted, however, that while Prof. Yaghi was indeed one of, if not, the main proponent for the field of MOFs and MOF-type structures, there had already been reports in the literature as far back as 1897, when Hofmann and Küspert reported a layered ammonia-nickel cyanide complex with benzene $[\text{Ni}(\text{CN})_2(\text{NH}_3) \cdot \text{C}_6\text{H}_6]$ incorporated between the layers, though the crystal structure was not confirmed until 1952.^{4,5} Another notable example came along in 1959 when Kinoshita et al. reported the structure of bis(adiponitrile)copper(I) nitrate, which displayed three-dimensional networks of $[\text{Cu}(\text{NC}(\text{CH}_2)_4\text{CN})_2]_n^{n+}$ and nitrate ions.⁶

A few years before Yaghi's work, Hoskins and Robson were working on what they had termed 'infinite polymeric frameworks', or materials which are "afforded by linking together centres with either tetrahedral or an octahedral array of valencies by rod-like connecting units".⁷ Even at this early stage, they had realised the potential

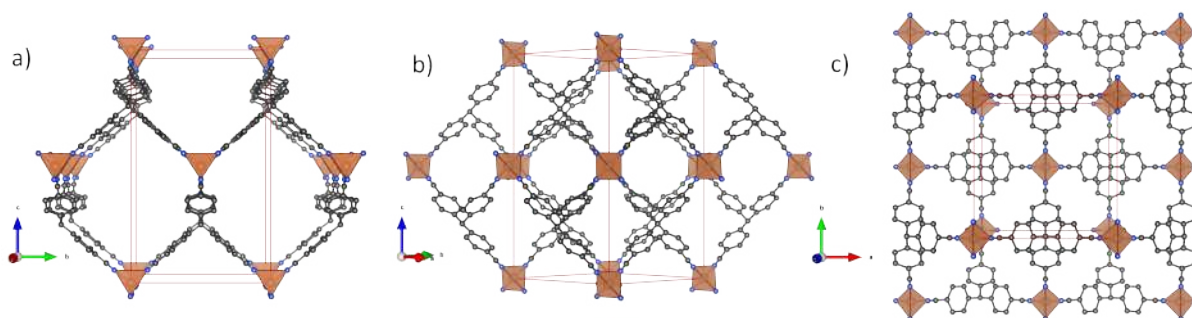


Figure 1.1: Crystal structure of copper(I) 4,4',4'',4'''-tetracyanotetraphenylmethane $[\text{Cu}^{\text{I}}(\text{C}_6\text{H}_4 \cdot \text{CN})_4]_n^{n+}$ viewed (a) along the a -axis, (b) perpendicular to the c -axis, between the a - and b -axis, and (c) along the c -axis.⁷ © 1989, American Chemical Society.

for these infinite polymeric materials for applications in molecular sieving, ion exchange, and heterogeneous catalysis, and they provided the first deliberate example of an infinite polymeric framework and speculated that it would be possible to improve the ease of this design process to produce materials that could be used in these various applications. In their first publication, they explored the structure of $[\text{Cu}^{\text{I}}(\text{C}(\text{C}_6\text{H}_4 \cdot \text{CN})_4)]_n^{n+}$, which was based on the substitution of acetonitrile ligands in $\text{Cu}^{\text{I}}(\text{CH}_3\text{CN})_4^+$ with 4,4',4'',4'''-tetracyanotetraphenylmethane, which allows for the formation of the infinite polymeric framework, see Figure 1.1. The crystal structure belongs to the tetragonal space group $I\bar{4}m2$, whereby the unit cell measures 13.620 Å along the a - and b -axes, and 22.642 Å along the c -axis, giving a total cell volume of 4200 Å³. Contained within the framework, i.e. in the interstitial space, are the BF_4^- ions and what can essentially be considered "liquid" nitrobenzene, although the specific positions could not be identified using crystallographic methods, indicating a random distribution of these species throughout the framework. The authors also note that the cavities are made up from two adamantane-like structures, one being Cu_4C_6 , and the other Cu_6C_4 , whereby the latter is slightly more positively charged and is thus where one would expect to find the anions, though, as mentioned, the authors found no evidence for this. They concluded this work with a positive outlook on the feasibility of deliberate construction of infinite three-dimensional frameworks.

Less than a year later, and building on this work, the author's second publication on this topic looked at a few different structures, but began by looking at zinc and

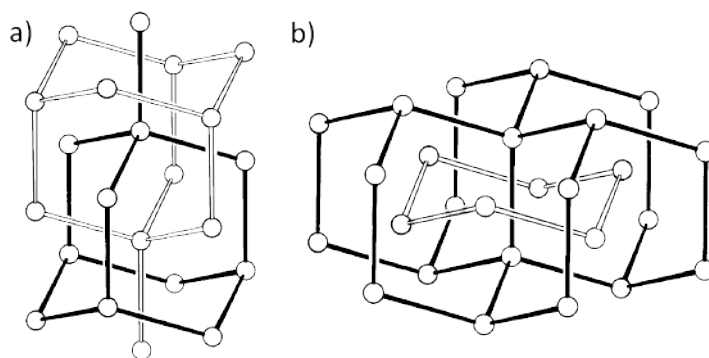


Figure 1.2: (a) View of the interpenetrating adamantane-like units in $\text{Zn}(\text{CN})_2$ and $\text{Cd}(\text{CN})_2$, (b) View of $\text{Zn}(\text{CN})_2$ and $\text{Cd}(\text{CN})_2$ structures revealing multiple catenane associations.⁸ © 1990, American Chemical Society.

cadmium cyanides, $\text{Zn}(\text{CN})_2$ and $\text{Cd}(\text{CN})_2$.⁸ These compounds, while not immediately obvious from the structural formula, do actually form large extended networks. It was already known, in fact, that these structures form similar adamantane-like cavities such as those the authors had previously reported for the $[\text{Cu}^{\text{I}}(\text{C}(\text{C}_6\text{H}_4 \cdot \text{CN})_4)]_n^{n+}$ framework. Unlike that compound, however, these metal cyanide structures tended to form two independent interpenetrating frameworks, as shown in Figure 1.2a. Here you can see that the cyanide moiety of one framework projects through the middle of a cyclohexane-like window of the other framework, and it should also be clear that at the centre of each adamantane-like cavity, you find the metal centre for the other framework. This also reveals the two types of metal centres present in the framework, i.e. one surrounded by carbon atoms, and a second surrounded by nitrogen atoms. From this then it is clear that there are also two types of adamantane-like units, 4C/6N and 6C/4N, both of which are present in equal number. Figure 1.2b also reveals the catenane-like structure of the frameworks, whereby catenanes, already well-studied themselves, consist of two or more macrocycles that are mechanically interlocked. In the case of $\text{Zn}(\text{CN})_2$ and $\text{Cd}(\text{CN})_2$, however, passing through each of the six-membered ring structures are six other rings which belong to the other framework, all sharing the central rod which protrudes through the "central" ring.

The authors then looked at producing just a single framework structure where there is no interpenetrating second structure. In order to do this, they could introduce a charge

to the framework, whereby the counter ions would prevent the interpenetration. In order to achieve this, copper(I) was used due to its known ability to form tetrahedral complexes such as $\text{Cu}(\text{CN})_4^{3-}$, with the intention being that this would replace every other zinc atom to form similar adamantane-like structures. Using $\text{N}(\text{CH}_3)_4^+$ as the countercation, the authors found that mixing the appropriate sources of Cu(I), Zn(II), and CN^- in a 1:1:4 ratio was enough to lead to spontaneous formation of $[\text{N}(\text{CH}_3)_4][\text{CuZn}(\text{CN})_4]$. The authors noted that the preferences of Cu(I) and Zn(II) for either end of the cyanide ion will have aided in the formation of the structure, and also found that the choice of countercation also had an effect on the structure, but did not speculate on the nature of this. Using single-crystal X-ray diffraction (SCXRD) analysis, they were not able to conclusively discriminate between either the two metal centres or the C and N atoms, but they were able to determine that the rods take the form Cu-cyanide-Zn. They also showed that each of the metal centres is surrounded by four of the same atom, and tentatively suggest that these metal centres would take the form of Cu-C and Zn-N.

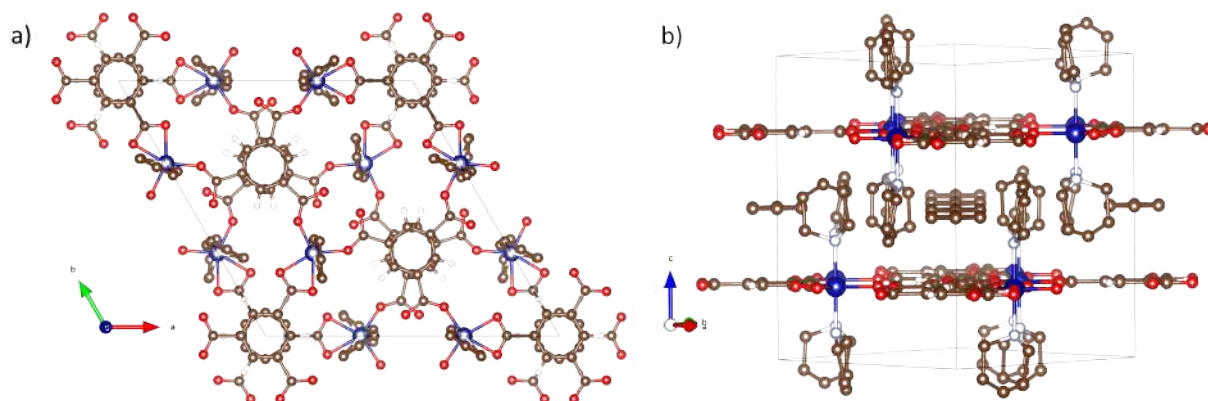


Figure 1.3: Crystal structure for $\text{CoC}_6\text{H}_3(\text{COOH}_{0.33})_3(\text{NC}_5\text{H}_5)_2 \cdot 0.66 \text{NC}_5\text{H}_5$, shown a) as a double layer along the z -axis, and b) looking between the layers perpendicular to the z -axis.⁹ © 1995, Nature Publishing Group.

Travelling forward four years, Yaghi et al., having already published similar work, released a paper looking at diamond-like open framework structures with adamantane cavities, such as those presented by Hoskins and Robson, who are, in fact, cited in the paper.¹⁰ This paper also contains the first mention of the term "metal-organic framework". The focus of the paper is on two classes of solids, namely

$M_xCo_{1-x}Ge_4S_{10} \cdot 2(CH_3)_4N$ ($x = 0.86$, $M = Mn$; $x = 1$, $M = Mn, Fe, Co,$ and Zn), and $Cu(4,4'-bpy)_2 \cdot PF_6$. In both cases the tetrahedral carbon in the diamond-like lattice are "replaced", by tetrahedral $Ge_4S_{10}^{4-}$ clusters and M^{II} in $M_xCo_{1-x}Ge_4S_{10} \cdot 2(CH_3)_4N$, and by tetrahedral Cu^I centres in $Cu(4,4'-bpy)_2 \cdot PF_6$. Further work on these $Cu[4,4'-bpy]$ type structures was published in the same year, and looked mainly at the replacement of the PF_6^- anion with nitrate and chloride anions.^{2,11} One of the first big breaks for MOFs came in the form of a *Nature* paper, which broke away from the previously discussed structures and more closely resembled what is now considered conventional, mainly in terms of the linker used.⁹ Here, the authors report the layered structure of $CoC_6H_3(COOH_{0.33})_3(NC_5H_5)_2 \cdot 0.66 NC_5H_5$, a compound consisting of layers of $Co(II)$ and 1,3,5-benzenetricarboxylate (BTC), with pyridine bonded to the open metal sites and projecting into the interlayer space.

These layers, which are separated by 7 Å, are held together by the π -stacking interactions of the bound pyridine groups. Between these layers one will find rectangular channels which are 7 x 10 Å, and in this case are holding guest pyridine molecules. The authors found that neither removal nor subsequent reintroduction of these guest molecules resulted in any alteration of the structure.

Over the next few years, a number of key papers were published on these types of open framework MOFs and looked at applications such as gas separation and storage, and catalysis.¹²⁻¹⁹ One of the most important papers was released in 1999, has since received over 5000 citations, and introduced one of the archetypal MOFs, namely, MOF-5.³ MOF-5 has a rigid structure made from 1,4-benzenedicarboxylate (BDC) and Zn^{2+} ions, the combination of which forms large $Zn_4(O)O_{12}C_6$ clusters, as can be seen in Figure 1.4a,b. Also seen here are the large cavities contained within each unit cell to form channels that are 18.5 Å in diameter, which the authors confirmed to contain guest DMF and chlorobenzene molecules. Figure 1.4c presents the view of MOF-5 along the a -axis, which represents the [100] layer, and shows the previously mentioned channels, which exist along all crystallographic axes.

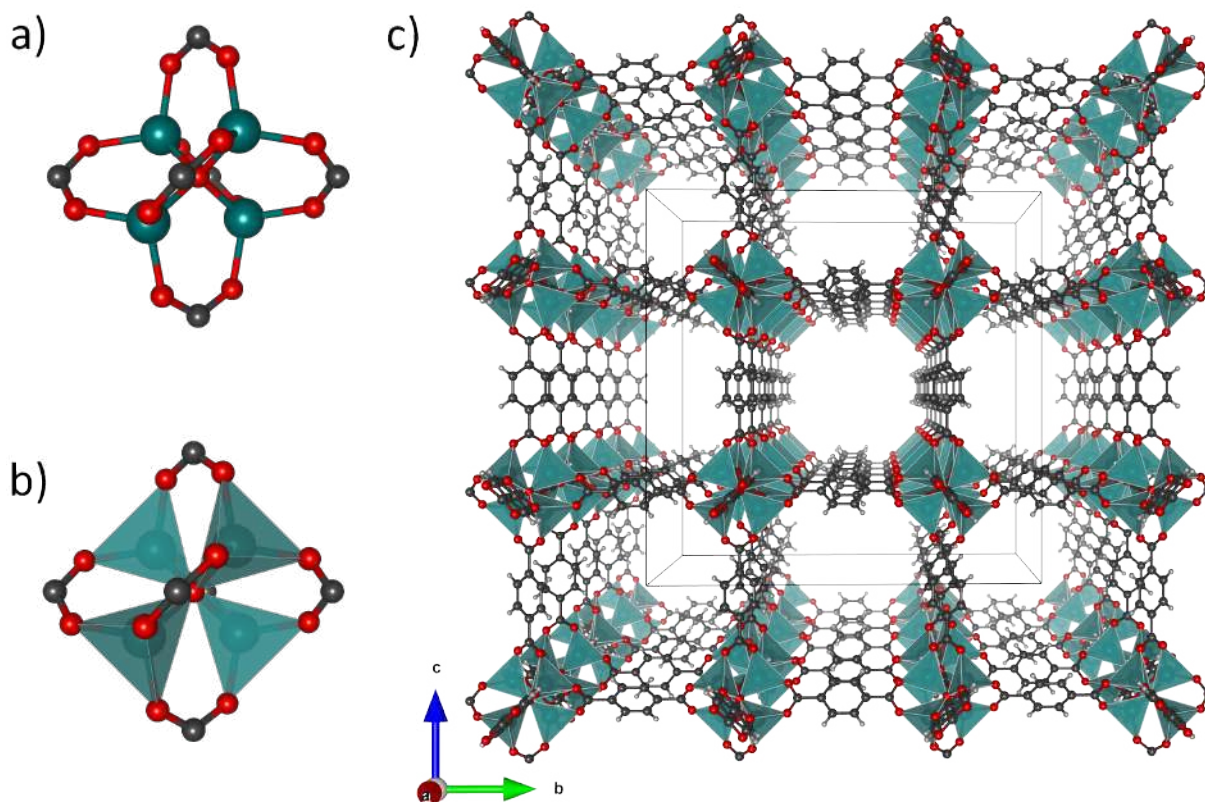


Figure 1.4: (a) $Zn_4(O)O_{12}C_6$ cluster shown as a ball-and-stick model. (b) $Zn_4(O)O_{12}C_6$ cluster with ZnO_4 tetrahedra shown in blue. (c) A view of MOF-5 along the a -axis, with unit cell shown in black.³ © 1999, Nature Publishing Group.

Since these early publications on the topic of MOFs, the number of publications has increased year-on-year, to the point that in 2020 over 10,000 papers were published in one year. It is also known that there is almost 100,000 MOF structures present on the CCDC database.²⁰ However, neither of these figures represent the sub-class of MOFs that will form part of the focus for this thesis, namely, metal phosphonates, which make up a very small portion of publications on metal-organic frameworks, despite having the potential to outperform conventional carboxylate MOFs in certain applications.

1.4 Metal Phosphonates

The initial interest in metal phosphonates (MPs) stemmed from the work by Clearfield et al. in the field of tetravalent metal phosphates, materials known for their exceptional ion exchange properties since the 1950s. The key step forward made by Clearfield

was the determination of the crystal structure of α -zirconium bis(monohydrogen orthophosphate) monohydrate $[\text{Zr}(\text{HPO}_4)_2 \cdot \text{H}_2\text{O}]$, hereafter α -ZrP (see Figure 1.5) from SCXRD data in 1969.²¹ α -ZrP has a layered structure constituted of Zr atoms octahedrally coordinated by tridentate monohydrogenphosphate groups, thus leaving free HO^- groups pointing towards the interlayer space and hydrogen bonding to water molecules accommodated between the layers. The atomic level understanding of the structure of α -ZrP triggered intense research that aimed at taking advantage of the acidic protons on the surface of the layers, especially for ion exchange and intercalation purposes.

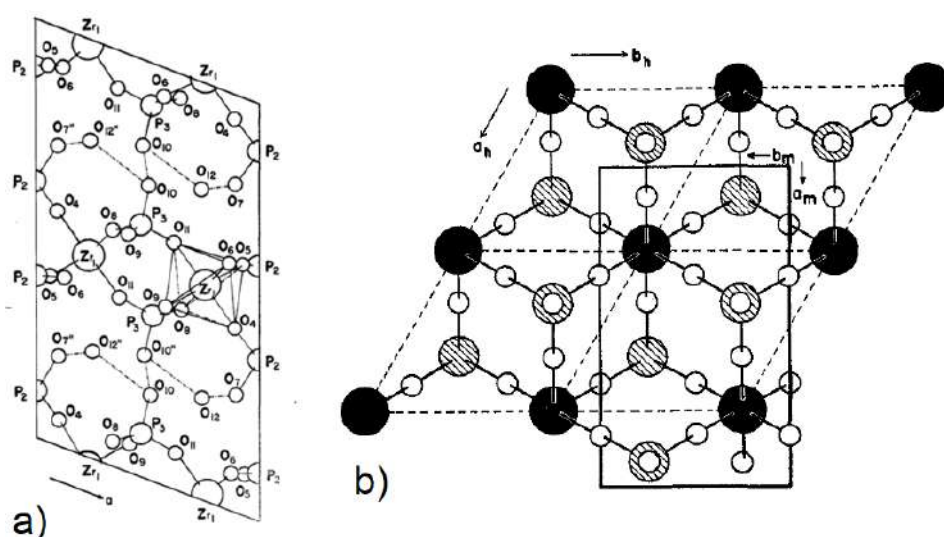


Figure 1.5: Crystal structure of α -ZrP viewed along the b -axis (a) and perpendicular to the layer (b). Adapted with permission from ref. [21], © 1969 American Chemical Society.

It was Alberti, Costantino et al. in 1978 that would inaugurate the field of MPs.²² They prepared three zirconium phosphonates: zirconium phenylphosphonate, $\text{Zr}(\text{C}_6\text{H}_5\text{PO}_3)_2$; hydroxymethylphosphonate, $\text{Zr}(\text{HOCH}_2\text{PO}_3)_2$; and ethylphosphate, $\text{Zr}(\text{C}_2\text{H}_5\text{OPO}_3)_2$. Due to the very high insolubility of these compounds, they were unable to obtain suitable single crystals for solving the structures by SCXRD. Given the similar method of preparation to that of α -ZrP and based on the powder X-ray diffraction (PXRD) patterns dominated by intense basal peaks at low angles, the authors hypothesised that these compounds would give comparable layered structures to α -ZrP, where the $-\text{OH}$ groups in the interlayer are substituted by the

organic moieties, which determine the interlayer distance, which is 14.8 Å (Figure 1.6). In the following years, a number of similar compounds were prepared, based on both monophosphonates and diphosphonates, obtaining analogous layered or pillared-layered structures, respectively.^{23,24}

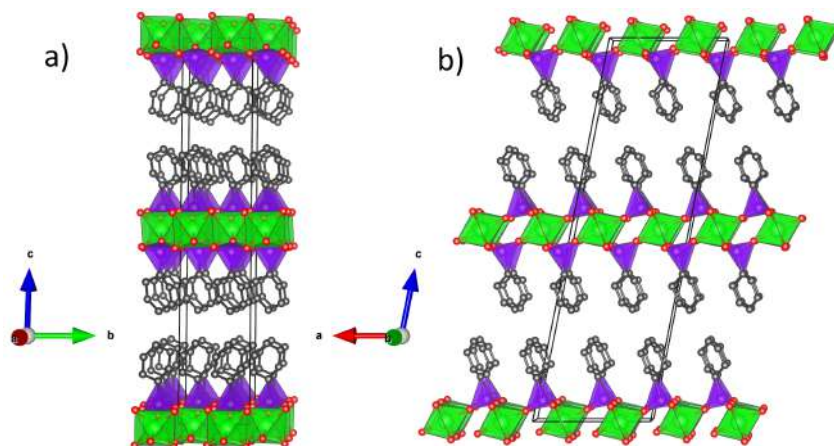


Figure 1.6: Crystal structure of α -zirconium phenylphosphonate $[\text{Zr}(\text{C}_6\text{H}_5\text{PO}_3)_2]$ viewed a) along the a -axis, and b) along the b -axis. Remade using data from Ref [22], © 1978 Elsevier Ltd.

The initial MP compounds were based on tetravalent metals, especially zirconium, but the late 1970s and 1980s brought about several structures based on divalent metal ions. Early work by Cunningham et al. looked at divalent metal phenylphosphonates and phenylarsonates, $\text{M}(\text{C}_6\text{H}_5\text{PO}_3)$ and $\text{M}(\text{C}_6\text{H}_5\text{AsO}_3)$, with $\text{M}^{2+} = \text{Mg}, \text{Mn}, \text{Fe}, \text{Co}, \text{Ni}, \text{Cu}, \text{Zn},$ and Cd .²⁵ They found that most of the synthetic processes were straightforward, and metal phenylphosphonates could be obtained by a simple reaction with the chloride or sulfate metal salts, with the exception of magnesium and iron. Thanks to the lower insolubility of these compounds, compared to tetravalent MPs, single crystals could be grown. Towards the end of the 1980s, a number of key papers detailing the crystal structures of various divalent MPs appeared.^{26–28} All of these compounds featured structures based on layers built by the connection of metal atoms and phosphonate groups, with the organic moiety accommodated in the interlayer space. Figure 1.7 shows the layered crystal structure of $\text{Mn}(\text{C}_6\text{H}_5\text{PO}_3) \cdot \text{H}_2\text{O}$, which is just one of the examples provided by Cao et al. (1988),²⁷ where a number of structures based on divalent metals were described, based on SCXRD data, including: Mn, Mg,

Ca, Cd, and Zn. Moving into the 1990s, MP structures expanded throughout the periodic table, covering a range of transition metals, all of the lanthanide series, and more than half of the s-block elements.²⁹

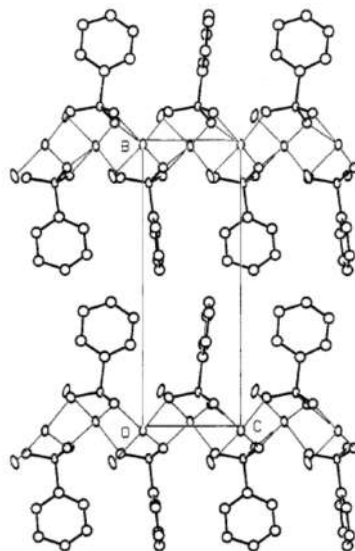


Figure 1.7: Structure of $\text{Mn}(\text{O}_3\text{PC}_6\text{H}_5) \cdot \text{H}_2\text{O}$ viewed along the a -axis. Reprinted with permission from ref. Reprinted with permission from reference [27] © 1988 American Chemical Society.

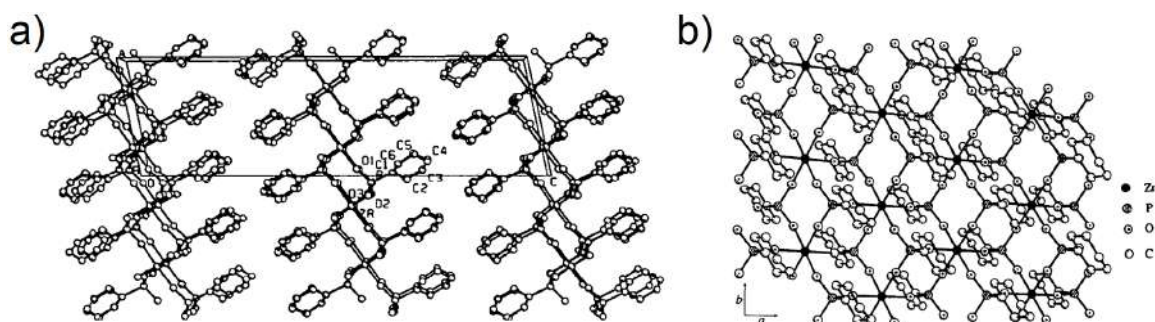


Figure 1.8: Crystal structure of $\text{Zr}(\text{C}_6\text{H}_5\text{PO}_3)_2$ viewed (a) along the b -axis, and (b) and perpendicular to the layer. Reprinted with permission from ref. Reprinted with permission from reference [30] © 1993 International Union of Crystallography.

While this expansion across the periodic table was taking place, there was also significant progress made with solving the crystal structures from PXRD data. This was of great importance for the field of MPs, since it has often proven difficult to obtain suitable single crystals for SCXRD, especially when metals with high oxidation states were involved. An example that has already been noted comes from the pioneering work of Alberti et al.,²² who were unable to obtain large crystals for

$\text{Zr}(\text{C}_6\text{H}_5\text{PO}_3)_2$. The structure was eventually solved by Poojary et al. in 1993 from PXRD data,³⁰ using a combination of modelling techniques and Patterson methods, and refined by Rietveld methods, confirming that the assumption made by Alberti et al. 15 years before was indeed correct and the structure of Zr phenylphosphonate was based on the same layered arrangement of α -ZrP (Figure 1.8a,b). With the development of more sophisticated laboratory powder X-ray diffractometers, the increased accessibility of synchrotron sources, and the availability of more powerful crystallographic software, structural solutions from PXRD have progressively become a workhorse for researchers working with MPs.

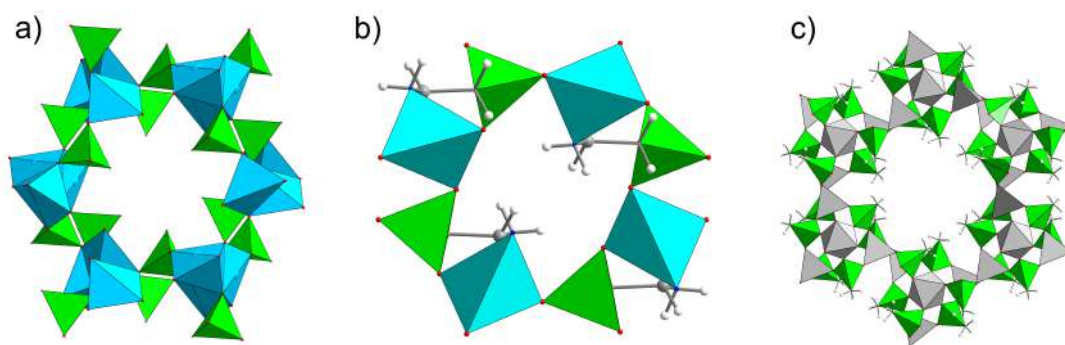


Figure 1.9: Crystal structures of the open framework metal phosphonates (MPs): (a) β - $\text{Cu}(\text{CH}_3\text{PO}_3)$, (b) $\text{Zn}(\text{O}_3\text{PC}_2\text{H}_4\text{NH}_2)$, and (c) α - $\text{Al}_2(\text{O}_3\text{PCH}_3)_2$. Colour code - light blue: copper, turquoise: zinc, light grey: aluminium, green: phosphorus, red: oxygen, blue: nitrogen, grey: carbon, white: hydrogen.³¹⁻³⁵

While the overwhelming majority of MPs described in the first 15 years of research displayed layered structures, the early to mid-1990s witnessed the discovery of several open framework MPs.³¹⁻³³ The first examples were all based on the small ligand methylphosphonic acid, which afforded structures with channel-like arrangement, which was reminiscent of some zeolite frameworks, when combined with Cu, Zn, and Al (Figure 1.9a-c).³¹⁻³⁵ The structural analogy with zeolites (and porous aluminium phosphates), which were at the time the most important class of crystalline and microporous materials, fuelled further investigation in the same direction.³⁶ This led to the discovery of more open framework materials, which were typically based on either monophosphonates or diphosphonates with short alkyl chains.^{37,38} Increasing the length of the alkyl chains almost exclusively produced layered or pillared-layered

structures, thus preventing the expansion of the channel size and generation of materials with higher porosity.

At the other end of the dimensionality scale, molecular MPs also started being the object of research in the second half of the 1990s, primarily for their potential as single molecule magnets and as model compounds for phosphate materials, especially those of group 13 elements (Figure 1.10).^{39–44} In order to overcome the strong tendency of MPs to polymerise, three strategies were devised to prevent the expansion of the structure: (1) using terminal ancillary ligands that can occupy coordination sites on the metal ions; (2) introducing sterically demanding groups on the phosphonic acids' backbone; (3) using a preformed cluster and performing controlled ligand exchange.³⁹

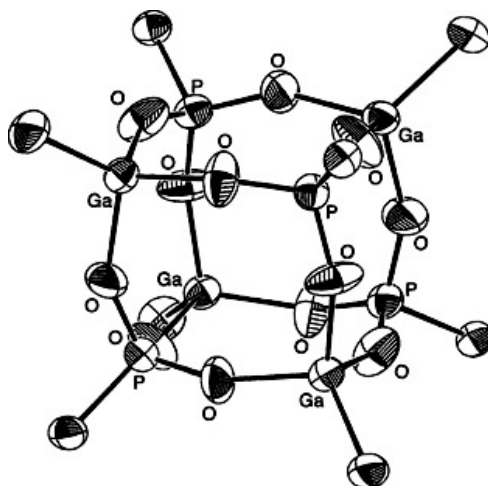


Figure 1.10: Crystal structure of the Ga₄P₄O₁₂ core found in [^tBuGa(μ₃-O₃PPh)]₄. Reprinted with permission from reference [40] © 1998 Plenum Publishing Corporation.

A more comprehensive account about the progress of the field until 2011 can be found in the book "Metal Phosphonate Chemistry: from Synthesis to Applications",²⁹ which includes a chapter on the early history of MPs chemistry, authored by Abraham Clearfield.⁴⁵

1.4.1 Synthesis and Characterisation

High-Throughput Methods

The synthesis of MPs is usually performed under hydrothermal or solvothermal conditions, with reaction times in the range of a few hours up to several days.⁴⁶ Identifying the proper conditions to obtain crystalline products involves the screening of reaction parameters such as pH, temperature, the concentration and molar ratios of reagents, and the amount of mineralisers or crystallisation modulators, which makes the discovery of novel MPs a time-consuming process. In addition, each “metal phosphonate” reaction system is unique, with its own idiosyncrasies. High-throughput (HT) methods have long been used to screen for ideal synthesis parameters, often leading to the accelerated discovery of novel compounds and further optimisation for increased yield (Figure 1.11).⁴⁷ This is also true for their application in MP synthesis, with the first reports of this approach falling in the early 2000s,^{48–52} and the methods are nowadays routinely used.^{53–55} The interest in HT methods stems from their high efficiency, allowing for the systematic investigation of reaction parameters.

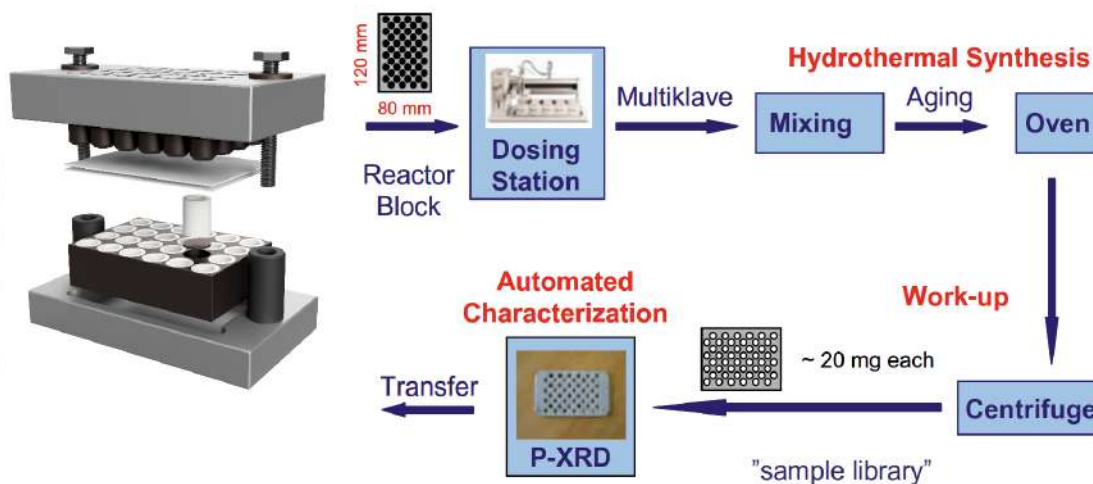


Figure 1.11: Typical workflow for a high-throughput (HT) synthesis experiment. Reprinted with permission from reference [46] © 2009 Elsevier Inc.

Some of the earliest work on HT methods applied to MPs was carried out in 2004, and looked at MPs based on the ligands $(\text{H}_2\text{O}_3\text{PCH}_2)_2\text{N}(\text{CH}_2)_4\text{N}(\text{CH}_2\text{PO}_3\text{H}_2)_2 \cdot 2\text{H}_2\text{O}$ ($\text{H}_8\text{L}_1 \cdot 2\text{H}_2\text{O}$), and $\rho\text{-H}_2\text{O}_3\text{PCH}_2\text{C}_6\text{H}_4\text{COOH}$ (H_3L_2).⁴⁸ The investigation began with

the design of two experiments to look at the system $\text{Zn}(\text{NO}_3)_2/\text{H}_3\text{L}_2/\text{NaOH}$. The first of the two varied the molar concentrations of the three starting materials while keeping the water content the same (Figure 1.12). This led to the discovery of three single crystalline compounds $\text{Zn}(\text{HO}_3\text{PCH}_2\text{C}_6\text{H}_4\text{COOH})_2$ (1), $\text{Zn}(\text{O}_3\text{PCH}_2\text{C}_6\text{H}_4\text{COOH})$ (2), and $\text{Zn}_3(\text{HO}_3\text{PCH}_2\text{C}_6\text{H}_4\text{COO})_2 \cdot 4\text{H}_2\text{O}$ (3). Throughout the experiment, pH measurements were taken periodically, allowing the researchers to correlate the pH measurements of the reaction mixture with the dimensionality of the MP structure. Thus $\text{Zn}_3(\text{HO}_3\text{PCH}_2\text{C}_6\text{H}_4\text{COO})_2 \cdot 4\text{H}_2\text{O}$ (3), featuring a three-dimensional (3D) framework structure based on highly condensed inorganic units, was favoured at $\text{pH} \approx 6$, whereas $\text{Zn}(\text{HO}_3\text{PCH}_2\text{C}_6\text{H}_4\text{COOH})_2$ (1) ($\text{pH} \approx 0$) and $\text{Zn}(\text{O}_3\text{PCH}_2\text{C}_6\text{H}_4\text{COOH})$ (2) ($\text{pH} \approx 1$) displayed isolated columns and layered structures, respectively. The second experiment began using a different variable to the first, with the molar ratio for $\text{Zn}(\text{NO}_3)_2/\text{H}_3\text{L}_2/\text{NaOH}$ kept constant while the water content was adjusted. This led to the discovery of a fourth phase, $\text{Zn}(\text{HO}_3\text{PCH}_2\text{C}_6\text{H}_4\text{COOH})_2 \cdot 4\text{H}_2\text{O}$ (4).

The researchers also carried out an investigation of the system $\text{M}^{2+}/\text{H}_8\text{L}_1 \cdot 2\text{H}_2\text{O}$ based on previous results [48].⁵⁶ In this case, various divalent ions were employed: $\text{M}^{2+} = \text{Mg}, \text{Ca}, \text{Sr}, \text{Ba}, \text{Mn}, \text{Fe}, \text{Co}, \text{Ni}, \text{Zn}, \text{Cd}, \text{Sn}, \text{and Pb}$. As with the Zn-phosphonates, the investigation was split between two experiments, with the first taking the form of a discovery library for which the molar ratios for the starting materials are adjusted (e.g., 1:1, 1:4, 4:1, 2:3), while the water content was kept constant. Results showed that the microcrystalline products had formed for $\text{M}^{2+} = \text{Mg}, \text{Ca}, \text{Mn}, \text{Fe}, \text{Co}, \text{Ni}, \text{Zn}, \text{and Cd}$, and that the compounds were isostructural. The second experiment showed that it was also possible to obtain single crystals, where $\text{M}^{2+} = \text{Mg}, \text{Mn}, \text{Co}, \text{Ni}, \text{Cd}, \text{and Zn}$, by keeping the $\text{M}^{2+}:\text{H}_8\text{L}_1$ molar ratio at 1:1 and adjusting the water content between 98–99.83 mol% in order to tune the concentration of the starting materials. In total, 48 individual reactions were carried out without direct manipulation of each sample, while also exploring a large parameter space.

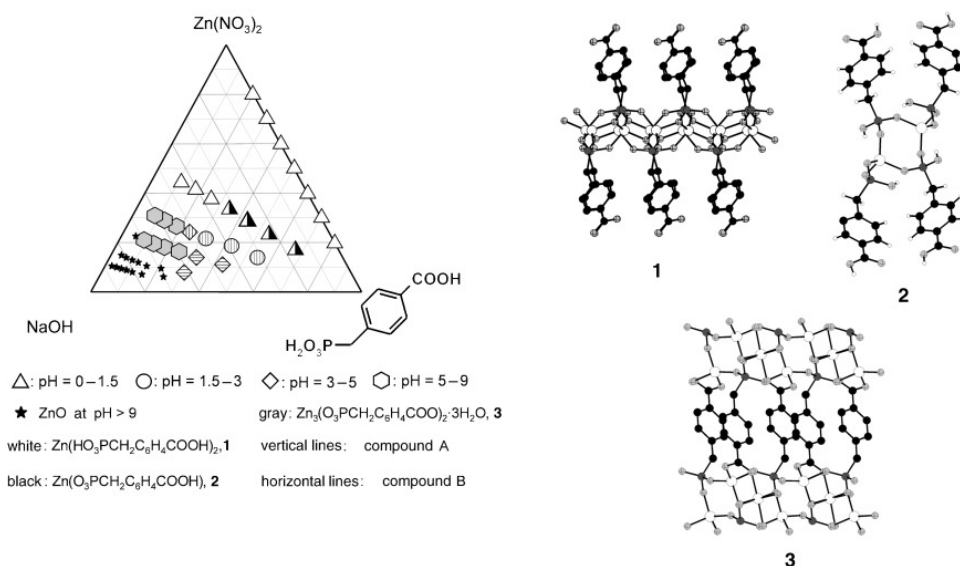


Figure 1.12: Crystallization diagram of observed phases in the $Zn(NO_3)_2/\rho$ - $H_2O_3PCH_2C_6H_4COOH/NaOH$ system and representative sections of the structures of $Zn(HO_3PCH_2C_6H_4COOH)_2$ (1), $Zn(O_3PCH_2C_6H_4COOH)$ (2), and $Zn_3(HO_3PCH_2C_6H_4COO)_2 \cdot 4H_2O$ (3). Colour code: white - zinc, black - carbon, dark grey - phosphorus, light grey - oxygen. Reprinted with permission from reference [48] © 2004 Wiley-VCH Verlag GmbH & Co.

Subsequent publications explored the multifunctional metal carboxyphosphonates via the method considered previously, successfully obtaining a range of structures based on Co and Mn.^{49,51} Over the years, several new MPs have been discovered thanks to the application of HT methods,^{53,57} whose efficacy was also proved for less conventional synthetic approaches, such as microwave-assisted synthesis and ultrasonic synthesis.^{58,59}

One of the initial drawbacks identified for HT methods has been the inability to control the temperature for each individual reaction. Since temperature has shown to play such a profound role in determining the product outcome and structures obtained, it would be worth having more control of this factor, allowing for a larger parameter space than is already available to be explored. The solution to the problem of temperature control was found in a thermocycler, or a polymerase chain reaction machine, which is usually found in the field of genetics.⁴⁷ This has allowed for the control of temperature for individual reaction chambers.

Mechanochemical Synthesis

Mechanochemistry has a long history extending back over 1000 years and had not, until recently, received mainstream attention as a viable tool in chemical synthesis.^{60,61} However, over the last two decades, there has been a massive push towards green and sustainable chemistry, which is perhaps one of the main reasons why mechanochemistry has since received a lot more attention in a range of specialised fields. While there are still a lot of details to be ironed out with regards to the specific mechanisms that drive mechanochemical synthesis, the basic principle is clear. The input of mechanical energy, i.e., through grinding/milling drives the reaction between two or more solids to form a desired product, which is often in the presence of little or no solvent.⁶² One of the key points that makes mechanochemistry more appealing is that it is possible for reactions to proceed via pathways that are not accessible through conventional methods.⁶³

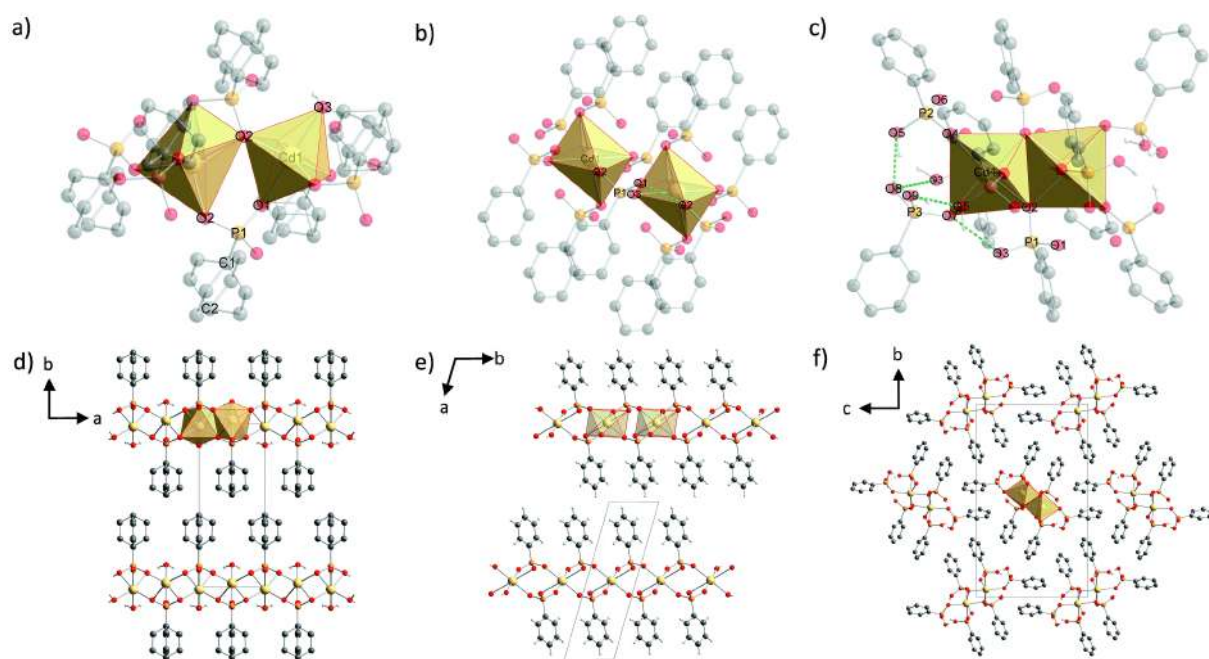


Figure 1.13: Molecular structure and coordination polyhedra Cd^{2+} ions and hydrogen bonds (green dashed lines) of (a) $\text{Cd}(\text{O}_3\text{PPh}) \cdot \text{H}_2\text{O}$, (b) $\text{Cd}(\text{HO}_3\text{PPh})_2$, (c) $\text{Cd}(\text{HO}_3\text{PPh})_2(\text{H}_2\text{O}_3\text{PPh})$, and the crystal structures of $\text{Cd}(\text{O}_3\text{PPh}) \cdot \text{H}_2\text{O}$, (d) viewed along the c -axis, (e) $\text{Cd}(\text{HO}_3\text{PPh})_2$, viewed along the c -axis, and (f) $\text{Cd}(\text{HO}_3\text{PPh})_2(\text{H}_2\text{O}_3\text{PPh})$, viewed along the a -axis. Hydrogen atoms of the phenyl rings are omitted for clarity. Colour code: yellow - cadmium, orange - phosphorus, red - oxygen, grey - carbon, light grey - hydrogen. Reprinted with permission from reference [64] © 2016 Royal Society of Chemistry.

Some of the most significant work on the mechanochemical synthesis of MPs has been carried out over the past few years. In 2016, a synthesis was reported using a vibration ball mill, in which cadmium acetate dihydrate and phenylphosphonic acid were combined inside a reaction vessel in various ratios (1:1, 1:2, and 1:4) and then milled for 15 minutes along with two 4.0 g stainless steel balls. One known and two novel cadmium phenylphosphonates were obtained: $\text{Cd}(\text{O}_3\text{PPh}) \cdot \text{H}_2\text{O}$ (Figure 1.13a,d), $\text{Cd}(\text{HO}_3\text{PPh})_2$ (Figure 1.13b,e), and $\text{Cd}(\text{HO}_3\text{PPh})_2(\text{H}_2\text{O}_3\text{PPh})$ (Figure 1.13c,f).⁶⁴ Each of the products obtained after milling were damp, which was caused by the release of water and acetic acid during the reaction, which in turn, means that each section of the synthesis was in fact liquid-assisted.

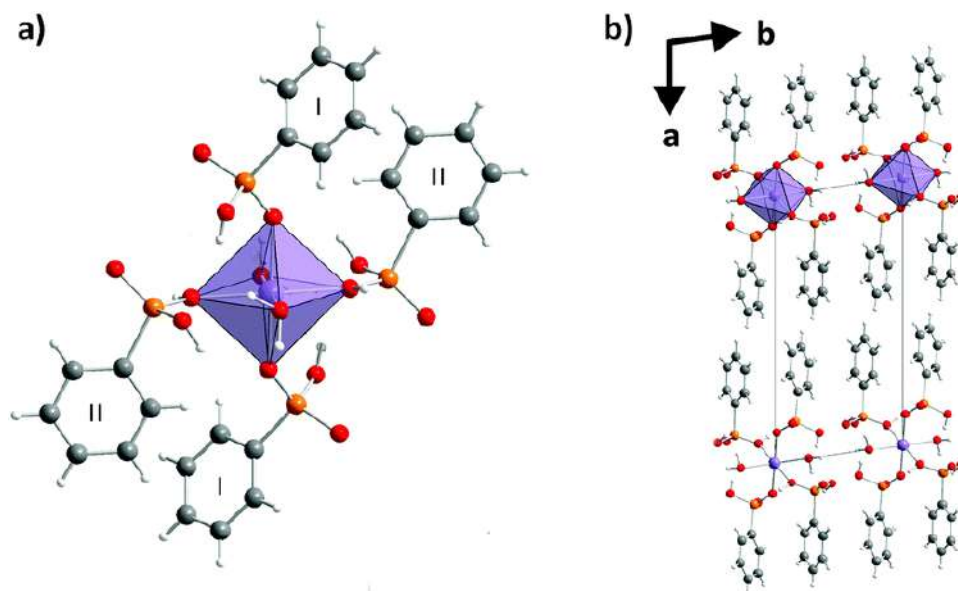


Figure 1.14: Crystal structure of $\text{Mn}(\text{HO}_3\text{PPh})_2-(\text{H}_2\text{O}_3\text{PPh})_2(\text{H}_2\text{O})_2$. (a) Coordination sphere of the metal ion. (b) Structure of 1 shown along the c -axis. Hydrogen atoms are omitted for clarity. Colour code: purple - manganese, red - oxygen, orange - phosphorus, grey - carbon, light grey - hydrogen. Reprinted with permission from reference [65] © 2016 Royal Society of Chemistry.

In the same year, further work was carried out which looked at substituting cadmium with various other metals. The authors state that this is the first work that explores the mechanochemical synthesis of molecular MPs.⁶⁵ They present isomorphous structures of molecular MPs, $\text{M}(\text{HO}_3\text{PPh})_2(\text{H}_2\text{O}_3\text{PPh})_2(\text{H}_2\text{O})_2$, where $\text{M} = \text{Mn}, \text{Co},$ and Ni (Figure 1.14a,b). Using the previously established procedure, the researchers were able to

successfully synthesise three pure compounds after neat grinding for 15 min. They also carried out a liquid-assisted grinding (LAG) run for each of the compounds, finding that it had no effect on the data obtained when compared to the “dry” run. The conclusion was that this approach could be applied to the synthesis of other molecular MPs and would bring great benefits in terms of its simplicity and speed. There would also be the opportunity for use in industrial applications due to the scalability, small environmental impact, and once again, the speed of synthesis.

More recent additions to the body of work looked at exploiting MPs with N-containing ligands. In 2017, the compound zinc N-(phosphonomethyl)glycinate $\text{Zn}(\text{O}_3\text{PCH}_2\text{NH}_2\text{CH}_2\text{CO}_2) \cdot \text{H}_2\text{O}$ was reported, displaying a 3D pillared-layered structure (Figure 1.15a-c).⁶⁶ This was achieved through the LAG of zinc acetate dihydrate and N-(phosphonomethyl)glycine in a 1:1 ratio in the presence of water over 15 min. Through PXRD, it was shown that after just 30 s, the starting materials were almost completely consumed, and were completely absent after three minutes. Rietveld refinement proved that a pure compound is obtained. Further work on N-containing phosphonate ligands was carried out on manganese phosphonates, namely manganese mono(nitrilotrimethylphosphonate) (MnNP_3) and manganese bis(N-(carboxymethyl)-iminodi(methylenephosphonate)) [$\text{Mn}(\text{NP}_2\text{AH})_2$].⁶⁷

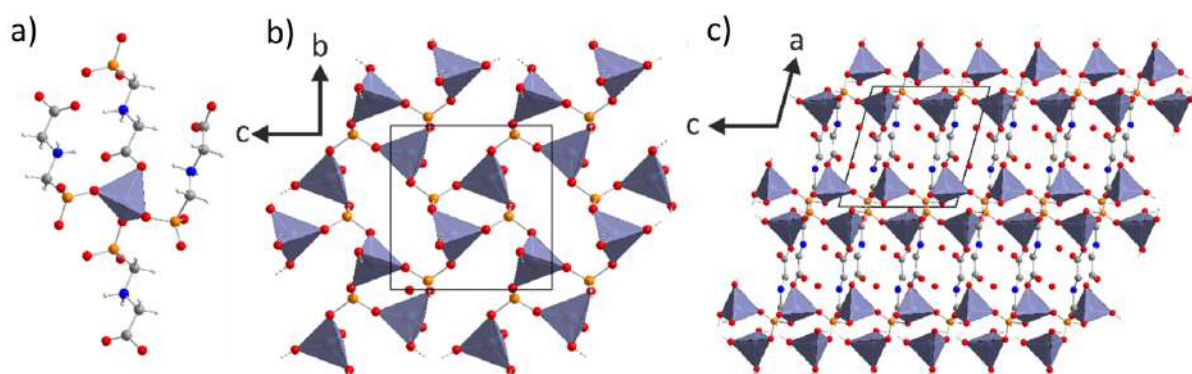


Figure 1.15: Structure of $\text{Zn}(\text{O}_3\text{PCH}_2\text{NH}_2\text{CH}_2\text{CO}_2) \cdot \text{H}_2\text{O}$. (a) Coordination sphere of the Zn^{2+} ion. (b) Structure of the layer formed by the ZnO_4 -tetrahedra and the phosphono groups, shown along the a -axis. (c) Pillared structure of the framework shown along the b -axis. Hydrogen atoms are omitted for clarity. Colour code: Purple - zinc, red - oxygen, orange - phosphorus, blue - nitrogen, grey - carbon, white - hydrogen. Reprinted with permission from reference [66] © 2017 Springer Science Business Media.

Numerous efforts have also been made to combine mechanochemical synthesis and *in situ* characterisation methods, which are discussed more in detail in a later section. It is worth reiterating that mechanochemical synthesis provides a range of advantages over more conventional methods. It is a facile technique that provides results in relatively short periods of time, e.g., 15 min, and full conversion is often achieved. It is also worth considering the green status of the technique, owing to the requirement for little to no solvent. Then, it is clear that mechanochemical synthesis is an invaluable tool on any scale requirement, and could provide researchers with an alternative to conventional synthesis methods, yielding products that may have previously been inaccessible.

Porous Materials

The structures of most of the early MPs were two-dimensionally (2D) layered, whereby organic molecules would coordinate to a central metal layer via the phosphonate group.^{21,22} Then, the organic functionalities would interlace with other metal–organic layers, creating a dense, multi-layered system. As discussed previously, some early examples of open framework MPs were reported in the 1990s which, with few exceptions,⁶⁸ displayed pores too small to accommodate guest species larger than water, and whose porosity could not be probed by the adsorption of N₂ at 77 K.³⁶ In an almost parallel arc to open framework MPs, another class of porous inorganic–organic materials, i.e., metal–organic frameworks (MOFs), which were discussed in the previous section, started attracting growing interest from 1999 onwards.^{3,69,70} Since then, MOFs have become one of the most intensely investigated classes of materials for applications such as gas separation and storage, catalysis, and drug delivery, owing to their large porosity, ease of functionalisation, and structural versatility.^{71,72} Phosphonate-based MOFs represent a rather small fraction of the thousands of MOF structures reported over the last 20 years. This is mainly due to the strong tendency of MPs to form extended inorganic layers, coupled with the tendency of the phosphonate moiety to bridge metal ions. This poses significant synthetic challenges when the aim is to generate open frameworks. However, some interesting advances have been

made recently in developing synthetic approaches that yield permanently porous MP materials.^{73–76}

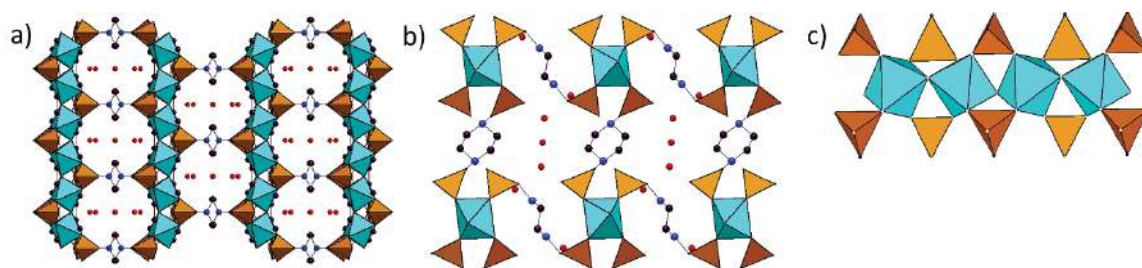


Figure 1.16: Crystal structure of MIL-91 viewed (a) along the *c*-axis and (b) the *b*-axis. For clarity, only one set of the two symmetry-equivalent (but half-occupied) sets of diphosphonate ligands connecting octahedral chains along *c* are shown. (c) A corner-sharing chain of MO₆ octahedra. Colour code: cyan - titanium, orange - phosphorus, red - oxygen, blue - nitrogen, purple - carbon. Reprinted with permission from reference [70] © 2006 American Chemical Society.

One of the first examples of permanently porous MPs is MIL-91,⁷⁰ this was based on the linker *N,N'*-piperazinediphosphonic acid, and was initially reported in 2006 by Serre et al. as two isorecticular analogues based on Al(III) and Ti(IV) (Figure 1.16a-c). The structures display monodimensional inorganic building units (IBUs) and channels running along the *b*-axis with an internal space of around $3.5 \times 3.5 \text{ \AA}$. A Langmuir surface area of around $500 \text{ m}^2 \cdot \text{g}^{-1}$, as well as a pore volume of $0.20 \text{ cm}^3 \cdot \text{g}^{-1}$, were measured by N₂ adsorption at 77 K. The compounds were also shown to be reasonably stable up to 550 K, after which there is a significant breakdown of the organic groups, causing the structure to become X-ray amorphous. The synthesis of both MIL-91(Al) and MIL-91(Ti) was successfully scaled up to the 100 g scale with milder procedures than those originally reported, i.e., using reflux instead of hydrothermal conditions, reducing the synthesis time and avoiding the use of hydrofluoric acid as a mineraliser.⁷⁷ A later study identified some unusual adsorption properties of the structure towards CO₂.⁷⁸

The same ligand was also employed to prepare a series of isorecticular compounds (named STA-12) based on divalent metals, namely Ni, Co, Fe, and Mn, and featuring large hexagonal channels running along the *c*-axis (Figure 1.17).⁸⁰ Interestingly, the STA-12 framework displays dehydration behaviour that is dependent on the metal

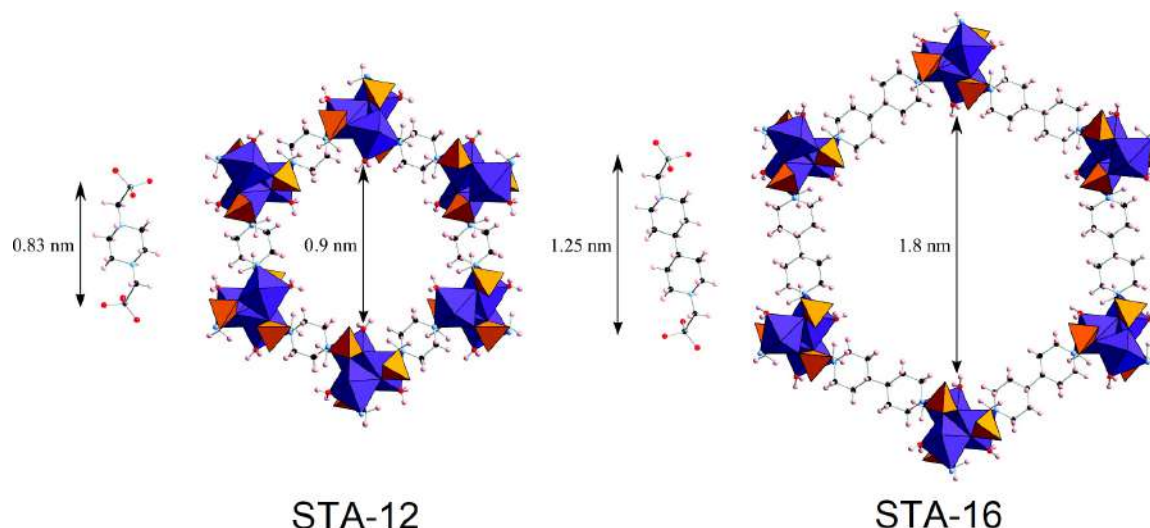


Figure 1.17: Crystal structures of STA-12 (**left**), based on *N,N'*-piperazinediphosphonic acid and STA-16 (**right**), based on *N,N'*-bispiperidinediphosphonic acid. Colour code: cobalt, nickel - purple, phosphorus - orange, oxygen - red, nitrogen - light blue, carbon - black, hydrogen - white. Reprinted with permission from reference [79] © 2011 American Chemical Society.

atom: while STA-12(Ni) and STA-12(Co) are porous to N_2 when coordinated water molecules are removed from the metal ions in the IBUs, the Mn and Fe analogues are not.⁸¹ This was attributed to the tilting of the piperazine rings and filling of the open coordination sites on Fe and Mn by the uncoordinated P–O group, which inhibits the uptake of N_2 probably by blocking access of the pores on the external surface. Using the linker *N,N'*-bispiperidinediphosphonic acid, an isorecticular analogue of STA-12, named STA-16, was obtained with Ni and Co as the metal atoms (Figure 1.17).⁷⁹ Thanks to the longer linker, STA-16 features pores with 1.8 nm diameter, approaching the mesoporous regime, and a large pore volume of $0.68 \text{ cm}^3 \cdot \text{g}^{-1}$. So far, this remains a unique example of isorecticular expansion for porous MPs.

More recently, the use of rigid linkers with non-linear geometries was proven to be a viable strategy to induce the formation of porous structures.⁷⁵ Among them, tritopic linkers have been particularly investigated by several groups, and a recent review on the topic has been published, to which the interested reader is directed.⁸² Besides tritopic linkers, tetratopic ones with either tetrahedral or square geometry have also proved successful in generating open framework compounds.^{83–86} A notable example

is the linker Ni-tetrakis(4-phosphonophenyl)porphyrin, which was combined with both divalent metals, namely Mn, Co, Ni, and Cd,^{54,87} and tetravalent metals, namely Zr and Hf,⁵⁵ to produce permanently porous compounds, termed CAU-29, CAU-36, and CAU-30, respectively (Figure 1.18a,b). HT methods were extensively employed to identify the best synthetic conditions to induce the formation of single crystals (in the case of divalent metals) and microcrystalline solids (in the case of tetravalent metals). Notably, the CAU-30 framework combines one of the most porous structures ever reported so far for MPs, featuring a specific surface area of almost $1000 \text{ m}^2 \cdot \text{g}^{-1}$ and a pore volume of $0.5 \text{ cm}^3 \cdot \text{g}^{-1}$, and exceptional stability, retaining its crystallinity up to $400 \text{ }^\circ\text{C}$ and pH 12.

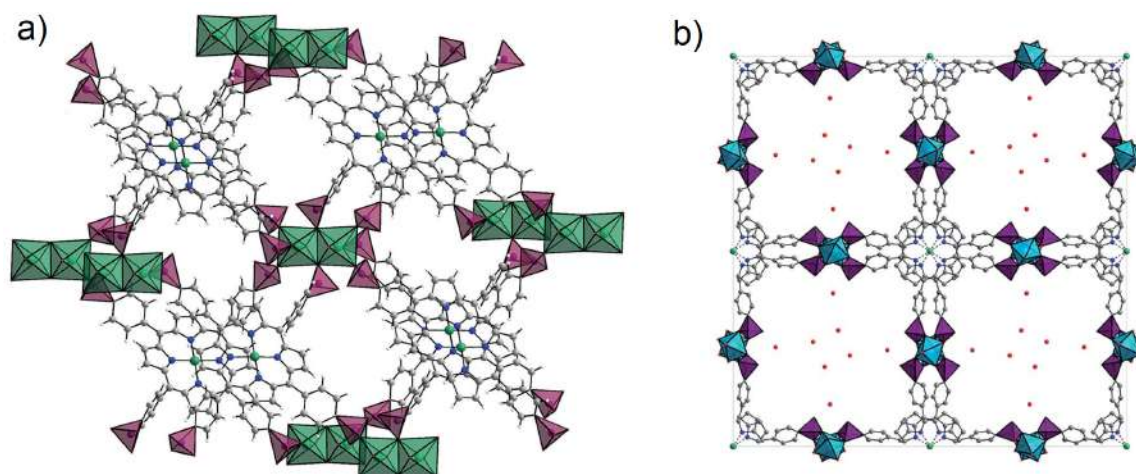


Figure 1.18: Crystal structures of (a) CAU-29 (Reprinted with permission from reference [54] © 2018, Royal Society of Chemistry), and (b) CAU-30 (Reprinted with permission from reference [55] © 2018, Royal Society of Chemistry). Colour code: green - nickel, light blue - zirconium, purple - phosphorus, red - oxygen, dark blue - nitrogen, grey - carbon, white - hydrogen.

While the field of carboxylate-based MOFs has moved beyond the initial phase—which was dominated by crystal engineering—towards practical applications and large-scale deployment, progress in phosphonate-based MOFs has been slower, and it still remains challenging to identify the right combination of linker, metal, and synthetic conditions to generate permanently porous structures. This section has shown that the recently renewed interest in microporous MPs has already produced some notable results, which hold promise for further advances in the near future.

Structure Determination by Electron Diffraction

2018 saw a major breakthrough for the structural characterisation of microcrystalline and nanocrystalline compounds, mostly thanks to two major papers reporting on the use of electron diffraction (ED) data to solve the crystal structures of small organic molecules.^{88,89} Using ED, it is possible to obtain diffraction patterns that are comparable to those usually observed when performing SCXRD experiments on sub-micrometre sized crystals. The method is particularly attractive because it does not require exotic instrumentation and, in principle, any transmission electron microscope could be adapted for such a task, holding promise for rapid deployment of the technique as a routine tool for structural characterisation.

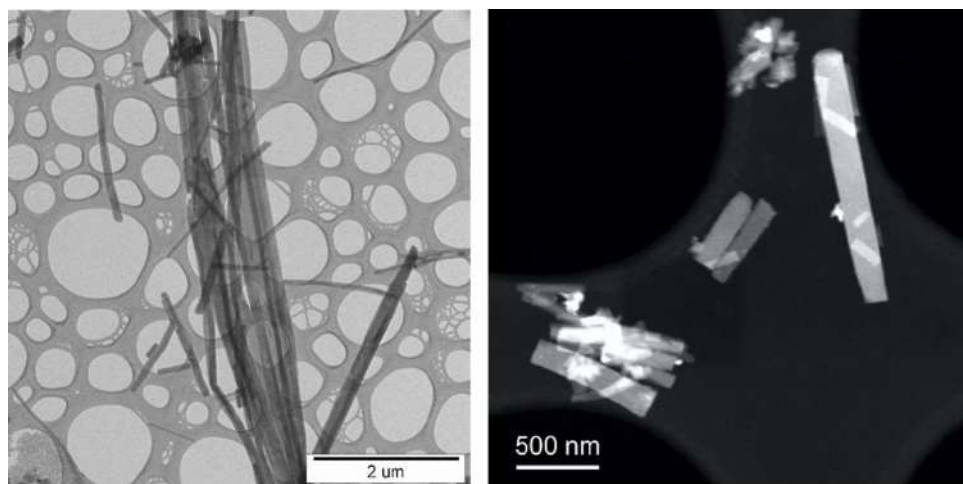


Figure 1.19: Transmission electron micrographs of ICR-2 (left) (⁹⁰ © 2018, Wiley-VCH Verlag GmbH and Co.), and CAU-30. Reprinted with permission from reference [55] © 2018 Royal Society of Chemistry.

Even before the two aforementioned papers appeared, ED had already been employed to determine the crystal structures of MOFs, covalent-organic frameworks (COFs), and Zeolites,⁹¹⁻⁹⁴ including some compounds mentioned earlier in this review: CAU-30, CAU-36.^{55,87} These compounds were obtained as microcrystalline powders, whose crystallite size was below the micrometre range and not sufficiently high to allow structure solution from PXRD data (Figure 1.19). In the case of CAU-30, the structural model was obtained from automated electron diffraction tomography.⁹⁵ In order to minimise beam damage, the samples were cooled to 95 K (CAU-30), and the beam was

shifted on the crystals. For all the compounds, the structural model was then validated by classical Rietveld refinement of the PXRD patterns. Another notable example of the use of ED in MP chemistry is represented by CAU-36,⁸⁷ which was a Co-based porous compound obtained using the same Ni-tetrakis(4-phosphonophenyl)porphyrin linker employed to prepare CAU-29 and CAU-30. In the case of CAU-29, continuous rotation electron diffraction was employed, allowing to precisely identify the location of the guest species (1,4-diazabicyclo[2,2,2]octane and solvent molecules) within the framework.⁹⁶

Given the difficulty in obtaining suitable crystals for SCXRD, especially when high oxidation state metals are employed, the structural determination of MPs has often been carried out from PXRD data. However, due to the limited amount of information contained in a PXRD pattern, some structures can require a large amount of time to be solved, if they can be solved at all. This is one of the main factors that have prevented the field of MPs from progressing at the pace of other classes of coordination polymers, such as carboxylate-based MOFs. The possibility of accessing ED as a tool for structural determination can be an absolute game changer in this sense.

***In situ* Characterisation**

In situ investigations have been widely used in materials chemistry to monitor synthetic processes, especially those involving the self-assembly of well-defined building blocks into crystalline compounds.⁹⁷ Besides simply following the products' formation, this approach is powerful in identifying the different phases and intermediates that form over the course of a reaction.⁹⁸ The application of *in situ* investigations can take many different forms and draw on a wide range of techniques, such as XRD, X-ray absorption spectroscopy, and vibrational spectroscopies.⁹⁹ The data obtained from *in situ* studies can be used to identify the different stages in a reaction and correlate this to the reaction parameters for further optimisation.

An early example of *in situ* investigations of MPs stems from Feyand et al. and the

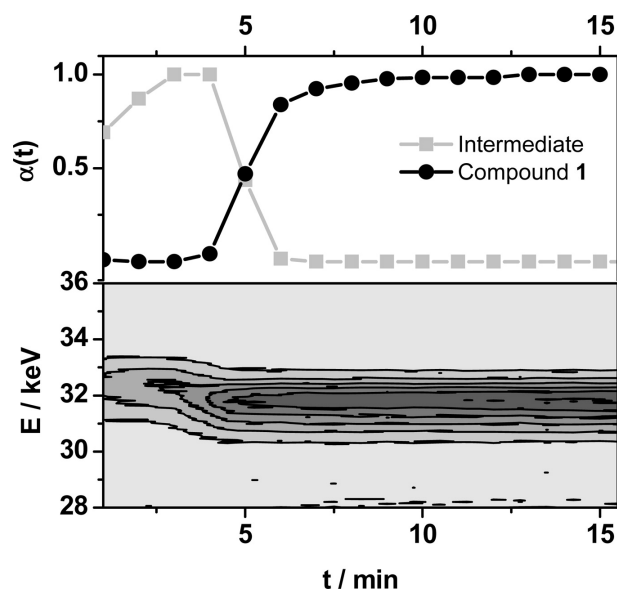


Figure 1.20: Surface energy-dispersive X-ray diffraction (EDXRD) plot of the transformation of the intermediate phase into $\text{Ln}(\text{O}_3\text{P}-\text{C}_4\text{H}_8-\text{SO}_3) \cdot \text{H}_2\text{O}$ (bottom) and reaction progress ($\alpha(t)$) for both phases under conventional heating at $150\text{ }^\circ\text{C}$ (top). Reprinted with permission from reference [100] © 2010 American Chemical Society.

work carried out on the HT synthesis of lanthanide phosphonatobutanesulfonates, $\text{Ln}(\text{O}_3\text{PC}_4\text{H}_8\text{SO}_3)(\text{H}_2\text{O})$, where $\text{Ln} = \text{La-Gd}$.¹⁰⁰ They managed to produce a series of isostructural compounds on which they carried out *in situ* analysis using energy-dispersive X-ray diffraction (EDXRD) during both conventional and microwave-assisted heating processes. A number of phases were identified before the formation of the final product (Figure 1.20). During the first five minutes, there was some background modulation, indicating that an amorphous side phase had formed in the initial part of the reaction, but after one minute, there was clear evidence for a crystalline intermediate. The formation of the product was observed at seven minutes, after which no significant events were identified in the diffraction pattern. The researchers concluded that the reaction takes place in two steps between $110\text{--}150\text{ }^\circ\text{C}$ for both conventional and microwave heating, with no observable difference in the phase change, but some in the ongoing crystallisation of the product.

The same group also carried out a temperature-dependent *in situ* EDXRD study for the formation and temperature-induced phase transition of previously described copper phosphonosulfonates.¹⁰¹ It was shown that at $90\text{ }^\circ\text{C}$, the formation of

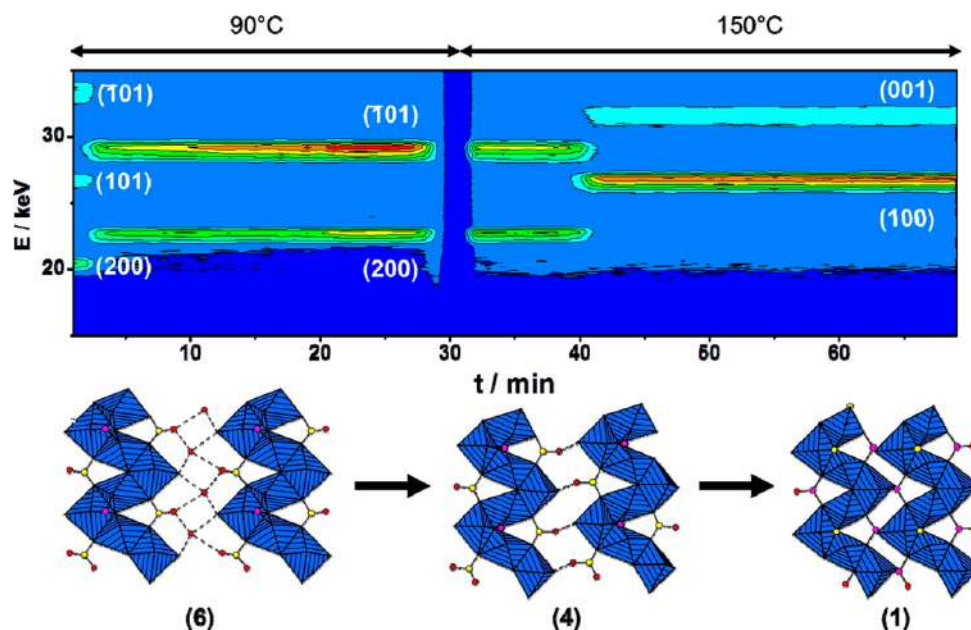


Figure 1.21: Illustration of the reaction pathway leading to the formation of $[\text{Cu}_2(\text{O}_3\text{PC}_2\text{H}_4-\text{SO}_3)(\text{OH})(\text{H}_2\text{O})] \cdot 3 \text{H}_2\text{O}$ (1) through intermediates $\text{Cu}_2[(\text{O}_3\text{P}-\text{C}_2\text{H}_4-\text{SO}_3)(\text{H}_2\text{O})_2(\text{OH})] \cdot 4 \text{H}_2\text{O}$ (4) and $[\text{Cu}_2(\text{O}_3\text{P}-\text{C}_2\text{H}_4-\text{SO}_3)(\text{H}_2\text{O})_2(\text{OH})] \cdot 3 \text{H}_2\text{O}$ (6). The phase transformation at different temperatures is shown in the contour plot, and the correlated structural motifs of the copper oxygen chains are presented below. The gap in the contour plot at ≈ 30 mins is due to the stage at which the specimen was removed from the vessel. Reprinted with permission from reference [101] © 2012 American Chemical Society.

$[\text{Cu}_2(\text{O}_3\text{PC}_2\text{H}_4-\text{SO}_3)(\text{OH})(\text{H}_2\text{O})] \cdot 3 \text{H}_2\text{O}$ is achieved after 5 min, but proceeds via a previously unknown phase, i.e., a tetrahydrate analogue of the previous compound, which they were able to obtain as a phase pure product by quenching the reaction mixture within the first few minutes. Alternatively, increasing the temperature from 90°C to 150°C saw the formation of the monohydrate analogue after 12 min, with full phase transformation at 15 min. This *in situ* EDXRD investigation allowed the researchers to propose the likely reaction pathway, shown in Figure 1.21.

In 2017, Heidenreich et al. published a detailed overview of a novel reaction cell with integrated stirring and heating systems (up to 200°C), which was named SynRAC, and used for *in situ* investigations of reactions under hydrothermal or solvothermal conditions using synchrotron radiation.⁹⁸ The setup and design of the cell is discussed in detail in the paper: the main advantage of the SynRAC is that it is designed to be as similar as possible to a common laboratory reaction vessel, which allows for the

extensive and reliable preliminary *ex situ* screening of reaction parameters before the actual *in situ* work, thus helping maximise the amount of information obtainable from the available synchrotron beamtime. A number of case studies are also presented to demonstrate the methods they use and the results that can be achieved. These do not include any MPs, but the SynRAC could easily find employment for this class of materials as well.

We have already suggested that *in situ* studies can be very informative for mechanochemical syntheses.^{64–67,102} The two techniques used in each of the *in situ* studies reported so far were XRD and Raman spectroscopy, which allow the reaction to be monitored at both molecular and crystalline levels.¹⁰² Traditionally, the vessel used in the milling/grinding process would be lined with an abrasion-resistant material, and would contain the grinding media, which is often constructed from steel, ceramic, and other suitable materials. However, for the *in situ* studies, the vessel needed to be adapted, which led to the grinding vessel to be made of Perspex. This allows radiation from both techniques to penetrate the vessel and reach the appropriate detector.

Combined XRD and Raman data on metal phenylphosphonates has allowed the researchers to identify various phases throughout reactions.⁶⁵ In 2015, Batzdorf et al. described the *in situ* investigation of the synthesis of cobalt(II) phenylphosphonates monohydrate ($\text{CoPhPO}_3 \cdot \text{H}_2\text{O}$), where equimolar amounts of cobalt(II) acetate and phenylphosphonic acid were ground together to form the product.¹⁰² The *in situ* XRD and Raman data confirmed that the product started forming after only 2.75 min of grinding, with completion of the reaction occurring at 27 min (Figure 1.22a,b). Different stages of the reaction were also identified, the main being where the product coexisted with intermediate phases.

An example where *in situ* analysis was able to provide unparalleled insight is the formation of $\text{Mn}(\text{HO}_3\text{PPh})_2(\text{H}_2\text{OPPh})_2(\text{H}_2\text{O})_2$. XRD data indicated that there were five phases during the reaction (Figure 1.23a,b).⁶⁵ The initial reflections represent the starting materials (phase 1), and it is not until 30 s into the reaction that

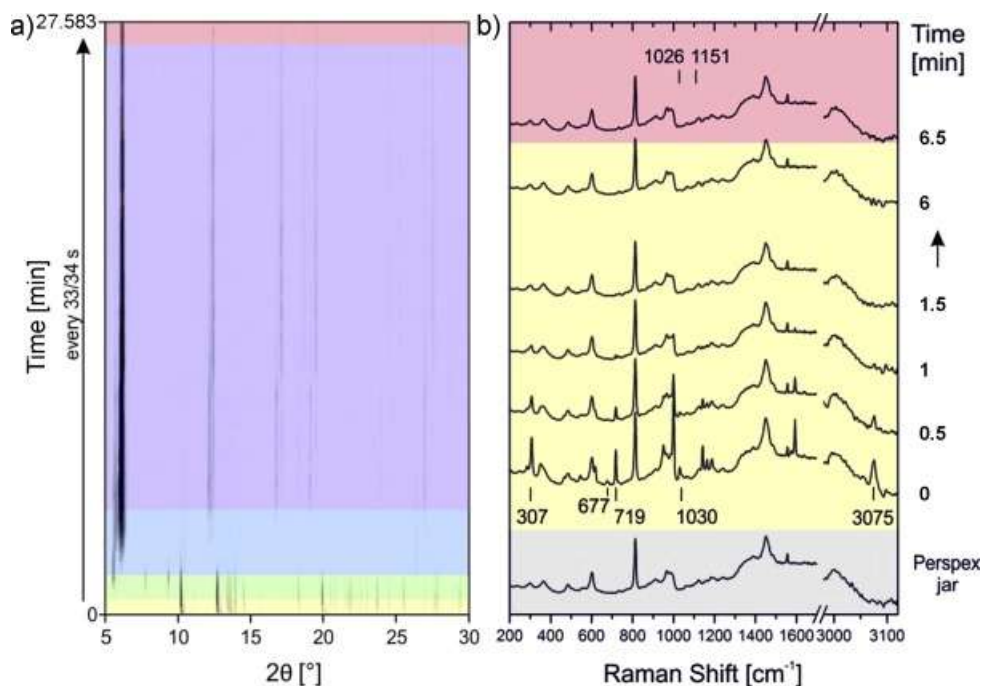


Figure 1.22: Crystallisation process of $\text{Co}(\text{PhPO}_3) \cdot \text{H}_2\text{O}$ followed *in situ* by (a) synchrotron X-ray diffraction (XRD) and (b) Raman spectroscopy. The first measurement of the Raman plot (**grey**) is the Raman spectrum of the empty Perspex jar, indicating the modes arising from the sample holder. Colour code: yellow: reactants, green: reactants and intermediate phases, blue: reactants, intermediate phases and product, purple: intermediate phases and product, red: product. Reprinted with permission from reference [102] © 2015 Wiley-VCH Verlag GmbH and Co.

additional reflections indicate the appearance of a new phase (phase 2), which itself lasts approximately 30 s. At this point, strong reflections for the final product can be observed alongside those of $\text{Mn}(\text{O}_3\text{PC}_6\text{H}_5) \cdot \text{H}_2\text{O}$ (phase 3). The reflections for both starting materials disappear at 1.15 min, after which the $\text{Mn}(\text{O}_3\text{PC}_6\text{H}_5) \cdot \text{H}_2\text{O}$ reflections start to decrease, while those of the final product intensify (phase 4). Then, at 6 min, the reflections for anything other than the product reach a minimum and go through no further changes (phase 5). Raman data, after 30 s of milling, shows bands exclusively for the uncoordinated phenylphosphonic acid. After an additional 30 s, bands assigned to the coordinated phenylphosphonic acid start to appear, followed by the disappearance of the uncoordinated phosphonic acid band. The final change is the increase in intensity for the coordinated phenylphosphonic acid band.

Based on the aforementioned examples, it is clear that the use of *in situ* investigations can provide invaluable information on the mechanism of a reaction as well as the

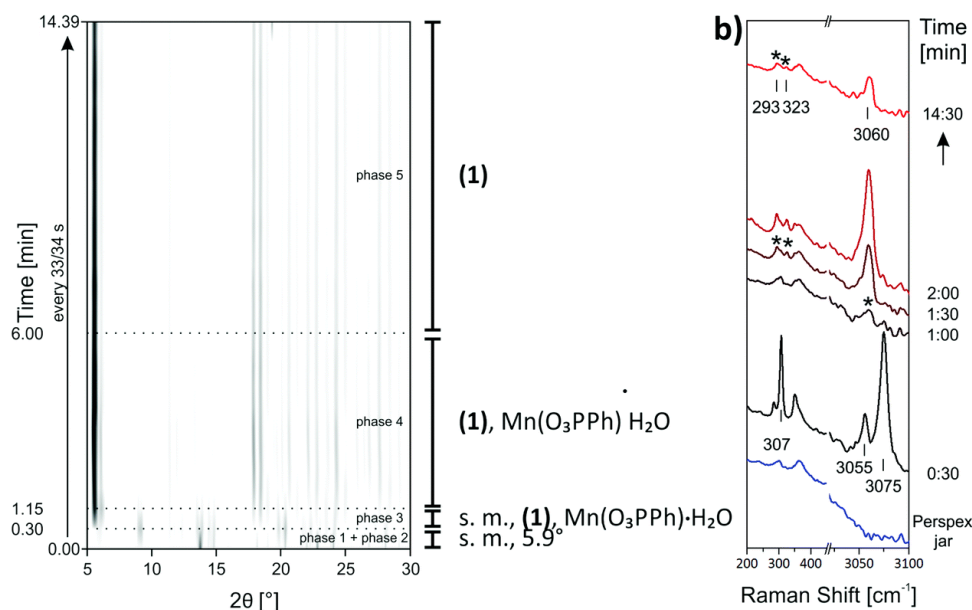


Figure 1.23: Two-dimensional (2D) plots of (a) synchrotron X-ray diffraction (XRD) data with a description of the detected compounds and (b) *in situ* Raman spectroscopy measurements monitoring the synthesis of $\text{Mn}(\text{HO}_3\text{PPh})_2(\text{H}_2\text{O}_3\text{PPh})_2(\text{H}_2\text{O})_2$. Reprinted with permission from reference [65] © 2016 Royal Society of Chemistry.

different crystalline phases appearing before reactions go to completion. Furthermore, they present opportunities to optimise conditions to isolate specific new materials that might exist as intermediate phases for products with previously known structures.

1.4.2 Applications

Catalysis

Catalysis has played a key role in enabling the huge progress of the chemical industry in the 20th century.¹⁰³ Most of the large-scale industrial processes producing essential commodities, such as ammonia, sulfuric acid, nitric acid, and polyolefins, are made possible by the use of heterogeneous catalysts.^{104,105} Typically employed catalysts in industrial settings consist of metal nanoparticles deposited on the surface of solid supports, such as metal oxides, carbon-based materials or zeolites.^{106,107} With the advent of MOFs and the precise atomic control that they allow, it has also become possible to introduce active sites, which are most often coordinatively unsaturated metal atoms, in the porous framework.^{108,109} Drawing inspiration from earlier work

on the use of zirconium and titanium phosphates as solid acid catalysts,¹¹⁰ initial applications of MPs in catalysis were focused on taking advantage of the Brønsted acidity of pendant sulfonic groups, which were successfully employed for cracking reactions in mild conditions.¹¹¹ This section presents recent examples of MPs employed both as supports for catalytically active species and as catalysts themselves.

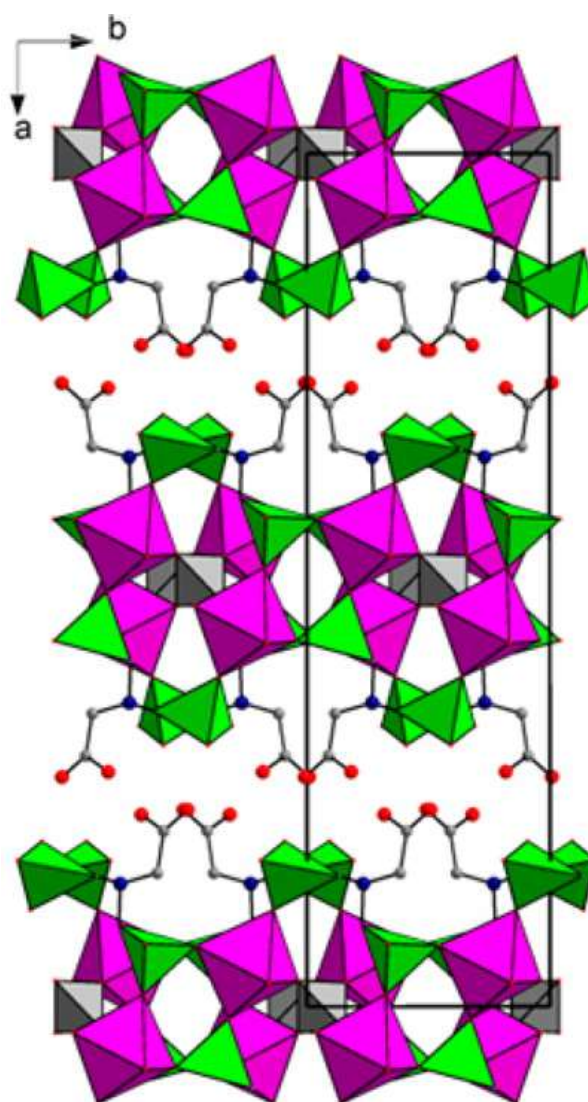
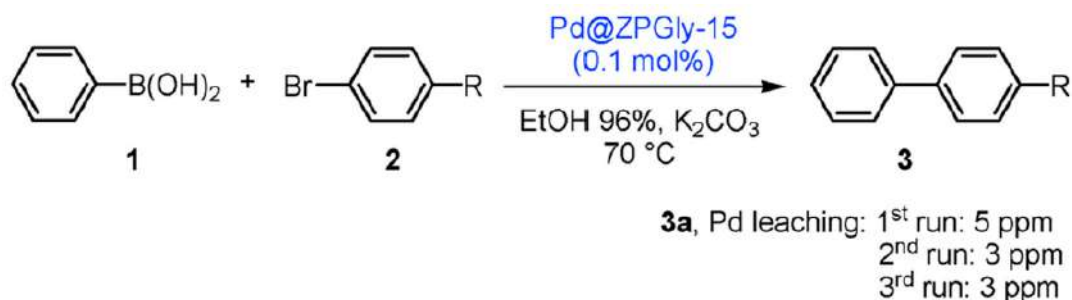


Figure 1.24: Crystal structure of $\text{Zr}_2(\text{PO}_4)\text{H}_5[(\text{O}_3\text{PCH}_2)_2\text{NCH}_2\text{COO}]_2 \cdot \text{H}_2\text{O}$ viewed along the c -axis. Colour code: pink - zirconium, green - phosphorus, red - oxygen, blue - nitrogen, grey - carbon. Reprinted with permission from reference [112] © 2014 American Chemical Society.

A crucial feature of effective catalyst supports is a large surface to make the active species easily accessible to reactants. This can be achieved by the use of porous supports or by the exfoliation of layered materials to generate



Scheme 1.1: Representative Suzuki-Miyaura coupling catalysed by Pd nanoparticles supported on $\text{Zr}_2(\text{PO}_4)\text{H}_5(\text{O}_3\text{PCH}_2)_2\text{NCH}_2\text{COO})_2 \cdot \text{H}_2\text{O}$ nanosheets (15 wt.% Pd). Reprinted with permission from reference [113] © 2015 Royal Society of Chemistry.

Table 1.1: Results of catalytic tests for the Suzuki-Miyaura coupling displayed in scheme 1.1. Reprinted with permission from reference [113]. © 2015 Royal Society of Chemistry.

Entry	Aryl Bromide	R	<i>t</i> (h)	Yield (%)
1	2a (1st)	Me	30	97
2	2a (2nd)	Me	30	97
3	2a (3rd)	Me	30	97
4	2b	H	30	96
5	2c	CHO	10	98
6	2d	NO_2	10	98

nanosheets consisting of single or few layers. A representative example of the latter strategy involves a mixed zirconium phosphate/phosphonate of formula $\text{Zr}_2(\text{PO}_4)\text{H}_5[(\text{O}_3\text{PCH}_2)_2\text{NCH}_2\text{COO}]_2 \cdot \text{H}_2\text{O}$ (Figure 1.24) containing *N,N*-bis[(phosphonomethyl)glycine] (glyphosine) as a ligand.¹¹² The interlayer region of this structure is characterised by the presence of both carboxylic and phosphonic acid groups, which make the layer surface highly polar and give rise to an extended network of hydrogen bonds. The presence of these groups makes the compound very prone to ion exchange and the intercalation of small organic amines, such as propylamine, yielding stable colloidal dispersions of hybrid nanosheets. The addition of palladium acetate to the dispersion led to the coordination of the metal to the non-coordinated carboxylic and phosphonic acid groups and enabled the deposition of palladium nanoparticles with size <2 nm onto the nanosheets with variable loadings, with the highest being reported at 19 wt.%.¹¹³ The catalyst loaded with 15 wt.% of Pd was tested for the Suzuki–Miyaura coupling between

phenylboronic acid and various aryl bromides, both in batch and continuous flow conditions, showing excellent performance and recyclability (Table 1.1 and Scheme 1.1). Importantly, the minimal leaching of Pd and no significant nanoparticle sintering were observed, suggesting the effectiveness of the support in binding the catalytically active species. The same catalyst was later successfully employed also for the hydrogenation in batch conditions of alkynes and nitroarenes and for the Heck reaction, proving its wide applicability.^{114,115}

More recently, a new strategy was adopted to obtain a zirconium phosphate–phosphonate decorated with very small gold nanoparticles on its surface.¹¹⁶ The procedure consisted of different steps: first, a nanosized zirconium phosphate was obtained using a synthesis from gel in propanol.¹¹⁷ Then, due to the small dimensions and high defectivity of the nanocrystals, this compound could be functionalised with amino groups through a topotactic anion exchange reaction of phosphates with incoming aminoethylphosphonate groups, and a compound with formula $\text{Zr}(\text{PO}_4)_{1.28}(\text{O}_3\text{PC}_2\text{H}_4\text{NH}_2)_{0.72}$ (hereafter ZP-AEP) was prepared (Figure 1.25). Finally, gold nanoparticles with dimensions less than 10 nm were produced by reduction, with NaBH_4 , of AuCl_4^- ions chemisorbed on the surface of nanocrystals (Figure 1.26).

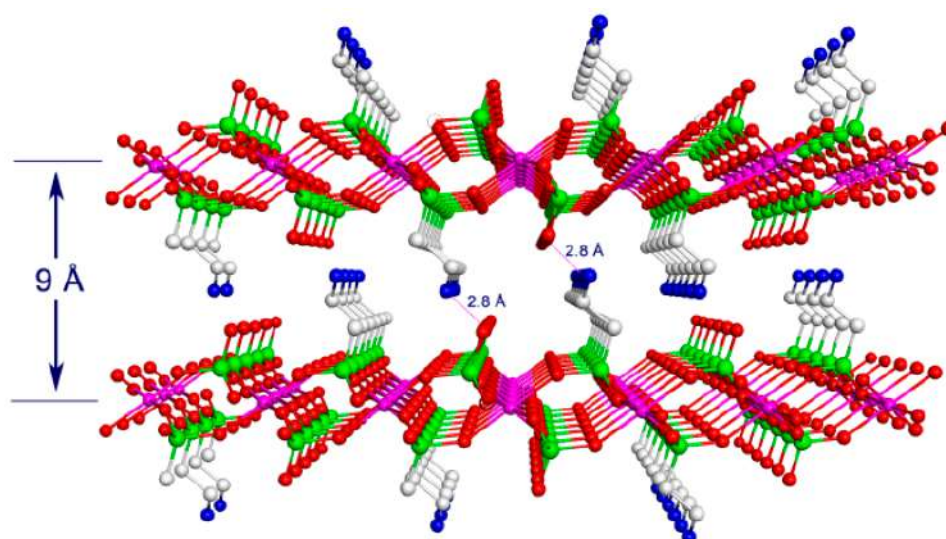


Figure 1.25: Schematic representation of a mixed α -Zr phosphate aminoethylphosphonate. Adapted with permission from reference [116] © 2019 Royal Society of Chemistry.

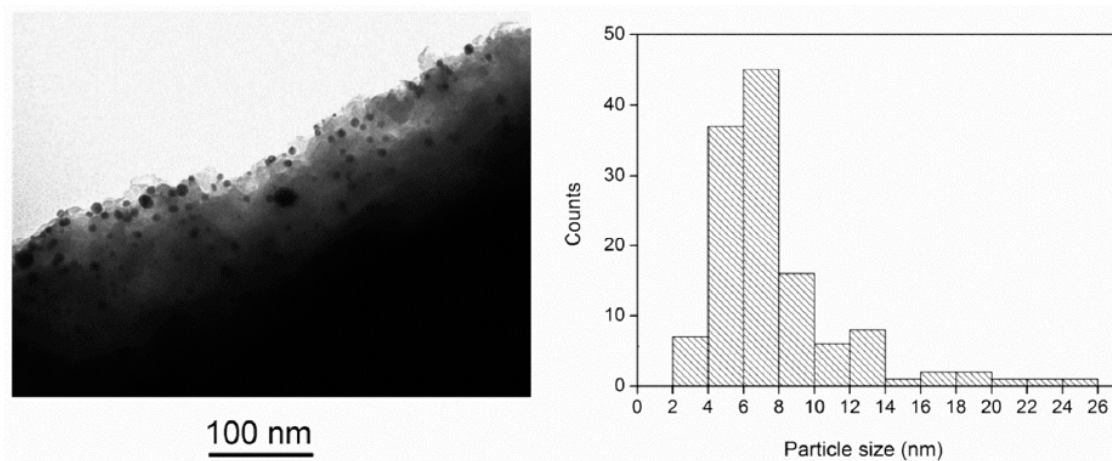
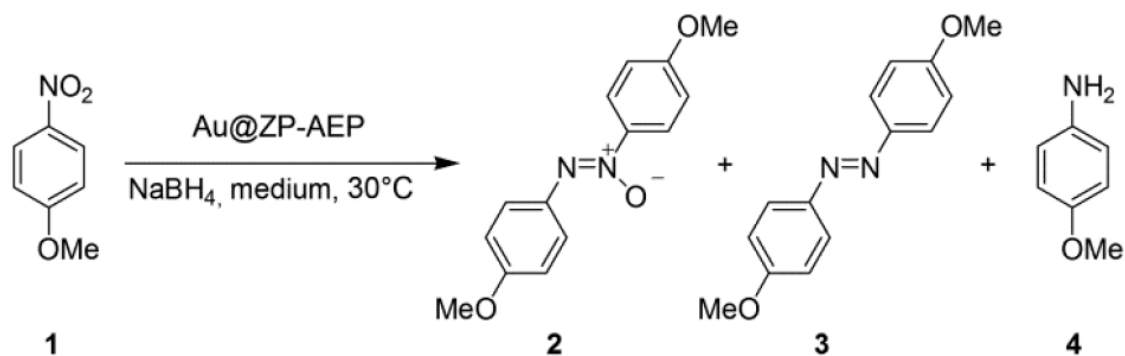


Figure 1.26: Transmission electron micrograph of Au@ZP-AEP (**left**) and Au particle size distribution (**right**). Adapted with permission from reference [116] © 2019 Royal Society of Chemistry.

A sample obtained with this procedure, and containing 1 wt.% Au, was found to be an efficient catalyst for the chemoselective reduction of a series of nitroarenes (Scheme 1.2); furthermore, the authors showed that it was possible to efficiently switch the reaction product between the corresponding azoxyarenes or anilines, simply by changing the solvent (96% EtOH or absolute EtOH, respectively). The recovery and reuse of the catalyst were also very efficient, as shown in Table 1.2.

A notable feature of both STA-12(Ni) and STA-12(Co) is their ability to be activated in order to create coordinatively unsaturated metal sites.¹¹⁸ This occurs due to the loss of chemisorbed water at around 85–109°C. Given the high density of these Lewis



Scheme 1.2: Representative reduction of nitroarenes using Au@ZP-AEP as the catalyst and NaBH₄ as the reducing agent. Reprinted with permission from reference [116] © 2019 Royal Society of Chemistry.

Table 1.2: Representative results of Au@ZP-AEP catalyst in the switchable preparation of an azoxy derivative (**2**) and methoxyaniline (**4** in Scheme 1.2) and their recovery and reuse. Reprinted with permission from reference [116] © 2019 Royal Society of Chemistry.

Entry ^a	Run	Medium	<i>t</i> (h)	<i>C</i> ^b (%)	2 : 3 : 4 Ratio ^b
1	Run 1	96% EtOH	98	97	96 : 4 : 0
2	Run 2	96% EtOH	96	97	97 : 3 : 0
3	Run 3	96% EtOH	94	97	97 : 3 : 0
4	Run 4	96% EtOH	93	96	96 : 4 : 0
5	Run 5	96% EtOH	87	98	98 : 2 : 0
6	Run 1	EtOH _{abs}	>99	98	0 : 0 : 100
7	Run 2	EtOH _{abs}	>99	97	0 : 0 : 100
8	Run 3	EtOH _{abs}	>99	97	0 : 0 : 100
9	Run 4	EtOH _{abs}	>99	97	0 : 0 : 100
10	Run 5	EtOH _{abs}	>99	96	0 : 0 : 100

^a Reaction conditions: **1** (0.1 mmol), Au@ZP-AEP (1 mol%), NaBH₄ (6 equivalents), reaction medium: 96% EtOH or EtOH_{abs} (1.8 mL), at 30 °C. ^b Conversion and product ratios determined by gas/liquid chromatography and ¹H-NMR analysis.

acidic metal sites, the STA-12 family of MPs has been investigated for a range of catalytic reactions. STA-12(Co) has been particularly notable for the catalysis of aerobic epoxidation of olefins, which are typically catalysed by Co-doped zeolites.¹¹⁹ The issue with zeolitic materials in this case is that in order to achieve the required isolated Co species, the loading of Co in the zeolite must be relatively low, which means that larger quantities of the catalyst will be required. The catalytic activity of STA-12(Co) was found to be comparable to the zeolite catalysts, obtaining similar results even when reducing the amount of catalyst by two orders of magnitude. It was also found that the substrate used could have a great effect on selectivity. With styrene, the selectivity to styrene oxide was low due to substrate oligomerization. Conversely, for (E)-stilbene, and (Z)-stilbene, the selectivities for the relative oxides were shown to be between 80–90%, with no considerable oligomerization of the substrate (Figure 1.27). It was also shown that the catalyst could be recycled, with little compromise on the activity. STA-12(Ni), similar to its Co analogue, has also shown reasonable catalytic activity. Both materials also showed little or no change in crystallinity when reused, with only a 1% difference in product formation after three cycles.

The combination of the high stability and structural versatility of MPs can be features

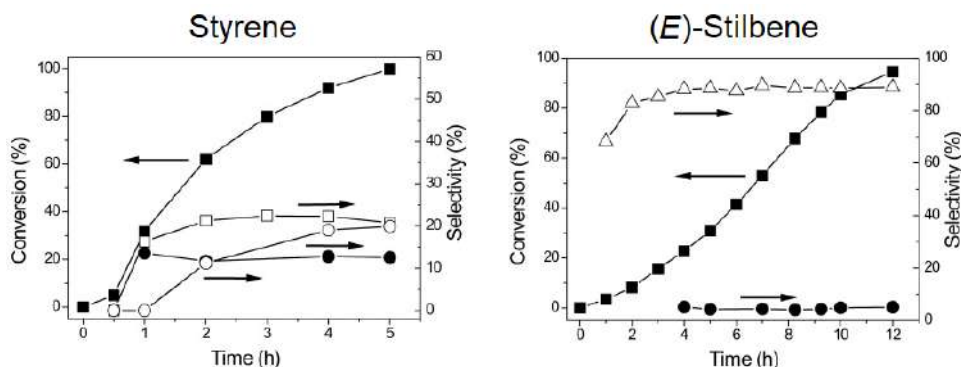


Figure 1.27: The epoxidation reaction of styrene (**left**) and (E)-stilbene (**right**) with the Co-based metal–organic framework material STA-12(Co). The graph on the left shows styrene conversion (black square), as well as the selectivity for styrene oxide (unfilled square), benzaldehyde (black circle), and benzoic acid (unfilled circle). The graph on the right shows (E)-stilbene conversion (black square), as well as the selectivity for trans-stilbene oxide (unfilled triangle) and benzaldehyde (black circle). Adapted with permission from reference [119] © 2012 Wiley-VCH Verlag GmbH & Co.

promoting their employment in heterogeneous catalysis. As for MOFs, the presence of organic groups prevents their employment in high-temperature processes similar to those that are typical of the heavy petrochemical industry. However, they could potentially find application in the production of fine chemicals and catalytic processes of importance for sustainability issues, such as the conversion of CO₂ into value-added feedstocks, methane oxidation to methanol, electrocatalytic or photocatalytic hydrogen production, and water oxidation, which generally involve milder conditions.^{120–124}

Gas Sorption and Separation

Microporous MPs have the potential to be ideal candidates for gas sorption due to their high stability, especially in humid conditions, which often exceeds that displayed by carboxylate-based MOFs.⁷³ Unfortunately, as already discussed previously, it has proved difficult for researchers to obtain porous MPs, since they are prone to forming densely packed layered structures, and only a small number have been reported to date.^{75,82} Microporous MPs usually feature relatively low surface areas and pore volumes, which limits their scope for gas storage. However, most of them display channel-like pores, with diameters often below 10 Å, which can in principle provide

favourable interaction between specific adsorbate species and the sorbent surface, which is a key requirement for the efficient separation of gaseous mixtures.^{125,126}

One of the most promising porous MPs identified for gas separation so far is MIL-91(Al/Ti), which features channels $3.5 \times 3.5 \text{ \AA}$ in size.^{70,127} On carrying out adsorption experiments with CO_2 , CH_4 , and N_2 at 303 K, a strong affinity of MIL-91(Al) for CO_2 was observed (Figure 1.28).⁷⁸ For both CH_4 and N_2 , the isotherms showed no significant uptake of the gases, and failed to show any saturation plateau, even at ~ 50 bar. On the other hand, the isotherm for CO_2 showed significant uptake, with the majority of the gas being adsorbed at pressures below 1 bar, and complete saturation reached at ~ 15 bar. Microcalorimetric experiments showed that the enthalpy of CO_2 adsorption is constant at about $40 \text{ kJ}\cdot\text{mol}^{-1}$ up to a loading of $4 \text{ mmol}\cdot\text{g}^{-1}$, suggesting a strong physisorptive character, which is likely induced by the close interaction of CO_2 with the surrounding pore walls.

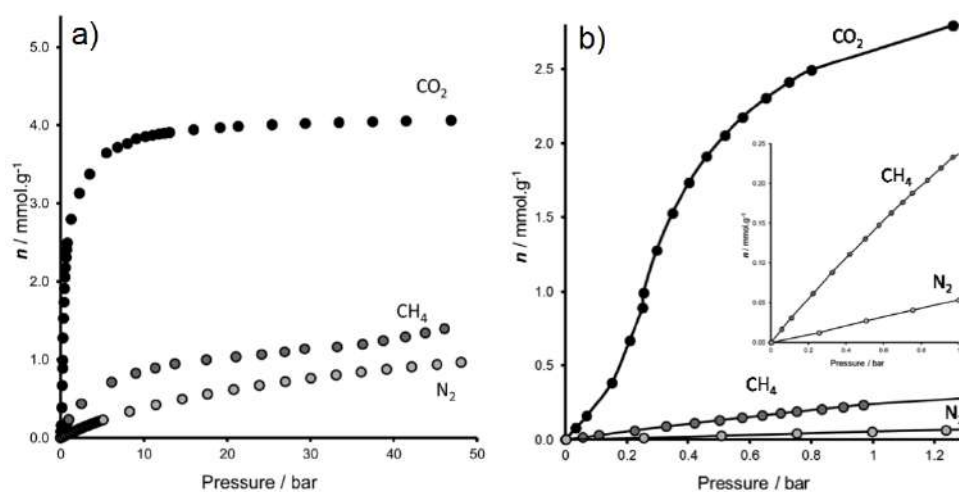


Figure 1.28: CO_2 , CH_4 , and N_2 adsorption isotherms measured at 303 K on MIL-91(Al) up to 50 bar (a) and up to 1 bar (b). Adapted with permission from reference [78] © 2015 American Chemical Society.

Furthermore, an inflection on the CO_2 adsorption isotherm was identified at low pressure (Figure 1.28), which is due to a cooperative phenomenon involving the twisting of the ligand when a threshold CO_2 pressure is reached (Figure 1.29). This “phase-change” behaviour is especially interesting for its potential to combine the high working capacity and low energy penalty for the regeneration of the sorbent. The

MIL-91(Ti) analogue showed a similar preference for CO₂ over the other gases, with a steep uptake at low pressure and saturation exceeding 4.0 mmol·g⁻¹.⁷⁷ However, unlike the Al analogue, no flexibility in the structure was observed, which was exemplified by the lack of inflection or S-character in the isotherm. Overall, MIL-91(Ti) was identified to be a viable material for CO₂ capture, owing to increased thermal stability when compared to other MOFs, its ability to selectively adsorb CO₂ over other gases, and the possibility to be produced in quantities beyond the laboratory scale.

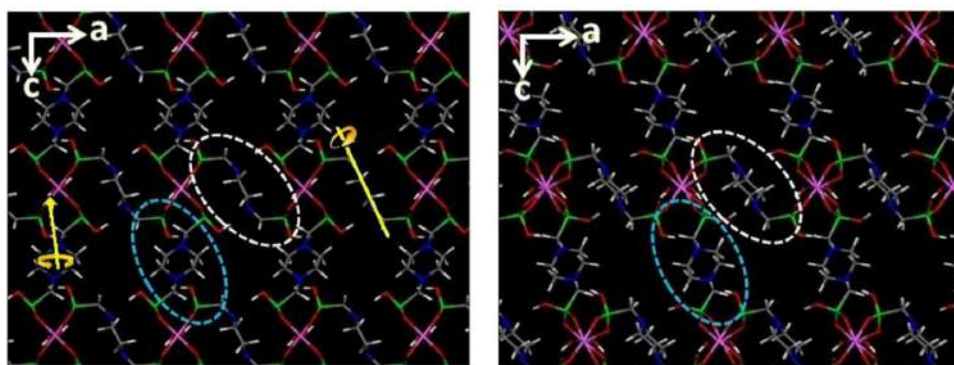


Figure 1.29: Crystal structure of MIL-91(Al) before (**left**) and after (**right**) the adsorption of CO₂. The rotation of crystallographically independent linker units is highlighted within the white and blue circles. Reprinted with permission from reference [77] © 2015 American Chemical Society.

The gas separation properties of the STA-12 framework were also thoroughly investigated for the analogues containing Ni, Co, and Mg.⁷⁹ IR experiments with CO and CO₂ as probes showed that despite the presence of coordinatively unsaturated metal sites, none of the STA-12 frameworks display a strong interaction of the adsorbates with these sites. By the adsorption of N₂ at 77 K and CO₂ at 195 K, it was found that STA-12(Ni) is the most porous compound of the series, and further characterisation demonstrated that it has a high selectivity for CO₂ over CH₄ at ambient temperature.¹²⁸ The separation performance of STA-12-Ni was compared with that of the CPO-27-M (M = Ni, Co, and Zn), which is a carboxylate-based MOF with a similar pore structure and a high density of open metal sites exposed on the channels.¹²⁹ The MOFs were tested for both binary 50:50 CO₂/CH₄ mixtures and ternary 70:15:15 CO₂/CO/CH₄ mixtures by means of single gas isotherms and

breakthrough analysis (Figure 1.30a-d). The CPO-27 frameworks outperformed STA-12 for the separation of the binary mixture, thanks to the strong interaction of CO₂ with the open metal sites. On the other hand, when exposed to the ternary mixture, CPO-27-Ni and CPO-27-Co displayed preferential adsorption of CO, whereas STA-12(Ni) and CPO-27-Zn maintained their selectivity for CO₂. STA-12(Ni) crystallises as submicron-size particles suitable for use as the stationary phase in a porous layer open tubular (PLOT) capillary column, which was used to separate alkanes according to boiling point, giving promising separation performance, even without optimization.⁷⁹ The stability and versatility of MOF structures suggest that they can find specialist application in this field.

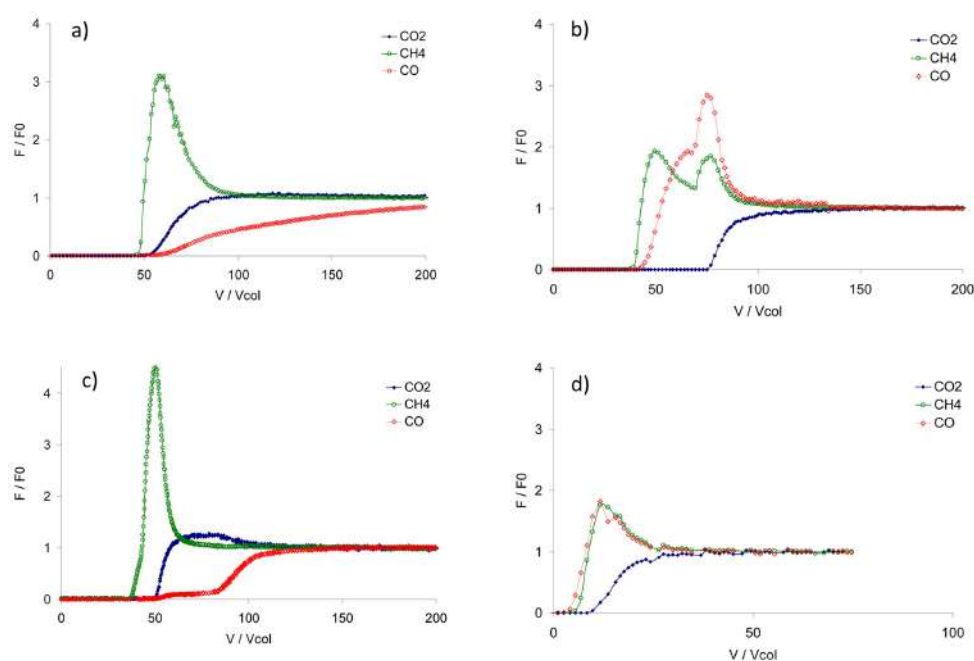


Figure 1.30: Breakthrough curves of the CO₂/CH₄/CO (70/15/15) mixture on (a) CPO-27-Co, (b) CPO-27-Zn, (c) CPO-27-Ni, and (d) STA-12-Ni at 303 K and 5 bar. Reprinted with permission from reference [79] © 2011 Elsevier Inc.

Given the recent progress made in synthesising porous MPs, more intensive investigation of their gas sorption and separation properties is likely to take place in the near future. Thanks to the enormous success of MOFs, gas sorption analysis has become a mainstream technique that can be readily employed for systematically assessing the potential of microporous MPs for a range of gas separations, especially

those where challenging conditions can limit the applicability of carboxylate-based MOFs.

Electrochemical Devices

While global energy demand grows year on year, with a projected 30% increase by the year 2040 there has been a lot of interest in finding new, more efficient, and cleaner ways of powering our future.¹³⁰ In this context, electrochemical devices such as rechargeable batteries and fuel cells are becoming increasingly important for energy storage and conversion, attracting considerable research efforts.^{131,132} Technically, a battery and a fuel cell are both electrochemical cells, consisting of an anodic and a cathodic compartment, which are connected through an electrical circuit that allows the exchange of electrons, while an electrolyte ensures the mobility of positive charge carriers (Figure 1.31).¹³³ The main difference between the two devices is that rechargeable batteries can reversibly store electricity in the form of chemical energy and release it on demand, whereas fuel cells convert the chemical energy contained in a fuel (typically hydrogen) into electricity. The interest in maximising the performance of these devices is currently a major drive in developing new materials that can serve as either electrodes or electrolyte components.¹³³

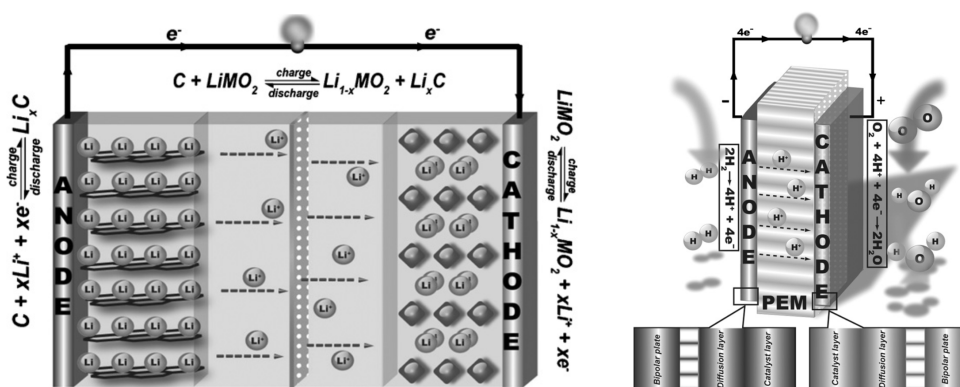


Figure 1.31: Schematic representations of a rechargeable lithium ion (Li-ion) battery (left) and a proton exchange membrane fuel cell (right). Adapted with permission from reference [133] © 2009 Elsevier Inc.

Solid-state Proton Conductors for Fuel Cells

The positive charge carriers in fuel cells are protons, which need to be efficiently transported via the electrolyte from the anode, where H_2 is oxidised, to the cathode, where they combine with oxygen to form water, in order to maximise the power generation. This makes the electrolyte a crucial component in determining the efficiency of a fuel cell, driving research into materials displaying high proton conductivity.^{134,135} The most common type of fuel cell is the proton exchange membrane fuel cells (PEMFC), where the electrolyte is typically a proton conductive polymer, such as Nafion, polybenzimidazole, and sulfonated polyether-ether ketones. In spite of their very high conductivity, these polymers often suffer from limited thermal and mechanical stability, which affects their long-term performance. As early as the 1990s, layered zirconium phosphonates were proposed as alternative proton conduction materials,^{136,137} owing to the ability to functionalise them with groups of variable acid strength. In particular, zirconium sulfophenylphosphonate was found to have excellent proton conductivity in humid conditions, reaching values as high as $1.6 \times 10^{-2} \text{ S cm}^{-1}$. The application of MPs as proton conductors has recently been extensively reviewed;^{138,139} therefore, we will only present some selected examples.

A recent example of a metal phosphonate with good proton conduction is that of $\text{La}(\text{H}_5\text{DTMP}) \cdot 7\text{H}_2\text{O}$, which is based on the hexamethylenediamine- $\text{N},\text{N},\text{N}',\text{N}'$ -tetrakis(methylenephosphonic acid) linker (Figure 1.32a).¹⁴⁰ Structural analysis of the compound showed that it is a three-dimensional (3D) framework featuring narrow one-dimensional (1D) channels where seven water molecules per formula unit are accommodated, forming a network of hydrogen bonds involving non-coordinated P–O groups that extend throughout the channels (Figure 1.32b). This allows for efficient proton conduction to take place, as proved by the conductivity value of $8 \times 10^{-3} \text{ S cm}^{-1}$ at 25°C and 98% relative humidity, as measured by impedance analysis. The activation energy was found to be 0.23 eV, which is typical of a Grotthuss-type mechanism, where well-ordered water molecules play a key role

in enabling efficient proton shuttling. Other MPs with similar “water channels” were subsequently reported, which displayed good proton conduction and activation energies consistent with the Grotthuss mechanism.^{141–144}

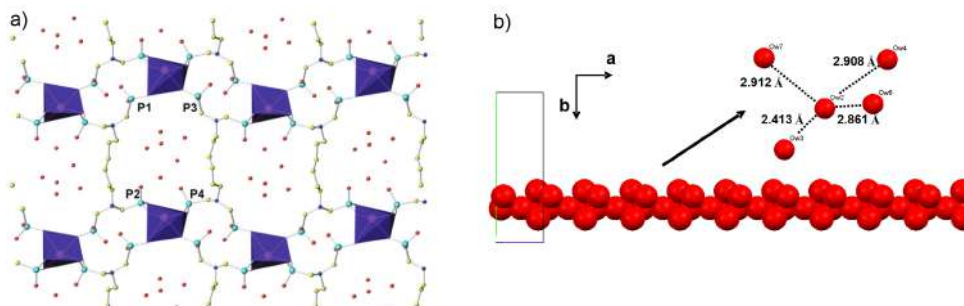


Figure 1.32: (a) Crystal structure of $\text{La}(\text{H}_5\text{DTMP}) \cdot 7\text{H}_2\text{O}$ and (b) the extended network of hydrogen-bonded water molecules along the a -axis, along with a detail of the hydrogen bonding distances. Colour code: lanthanum: purple, phosphorus: light blue, oxygen: red, nitrogen: dark blue, carbon: yellow. Adapted with permission from reference [140] © 2012 Royal Society of Chemistry.

These results highlight the importance of having well-defined pathways for the protons to hop between charge carriers to maximise conductivity. Clearly, knowledge of the crystal structure is essential to be able to identify such pathways in the first place. It is also worth emphasising that using polyphosphonic acids as linkers is crucial, since this increases the chances of having free P–OH groups that can facilitate the formation of extended hydrogen bond networks with water molecules. These characteristics can be enhanced by post-synthesis modifications, for instance by the adsorption of molecules, which contribute to generate robust proton transfer pathways.¹⁴¹

Electrodes for Rechargeable Batteries

Different from fuel cells, the efficiency of a rechargeable battery not only depends on the mobility of the charge carriers, but heavily relies on the ability of the electrodes to reversibly store and release these charge carriers during charging and discharging. Typical charge carriers are monovalent alkaline ions, with lithium element presently being the most employed, owing to its small size and low weight, which ensure high charge density. In order to maximise the performance, it is important that both electrodes possess high specific capacity and long-term stability. The state

of the art of the electrodes for lithium ion (Li-ion) batteries includes graphite as the anodic material (which is present in the negative electrode, theoretical specific capacity = $372 \text{ mAh}\cdot\text{g}^{-1}$) and LiCoO_2 as the cathodic material (which is present in the positive electrode, theoretical specific capacity = $137 \text{ mAh}\cdot\text{g}^{-1}$). They are both layered compounds where Li-ions are inserted and extracted by intercalation and deintercalation processes, respectively. The major limitation of the energy density of present Li-ion batteries is the relatively low specific capacity of the cathode. In addition, the latter is slowly decreasing during cycling due to the material instability (Co dissolution in the electrolyte) and other mechanisms.

Recently, a MP based on Fe(II) and methylenediphosphonic acid, of formula $\text{Li}_{1.4}\text{Fe}_{6.8}[\text{CH}_2(\text{PO}_3)_2]_3[\text{CH}_2(\text{PO}_3)(\text{PO}_3\text{H})] \cdot 4\text{H}_2\text{O}$, was extensively studied for its potential as a positive electrode for Li-ion batteries (Figure 1.33).¹⁴⁵ Structural characterisation was carried out combining synchrotron PXRD and neutron diffraction data, finding that the compound has a very similar structure to a previously reported Co methylenediphosphonate.³⁷ Three different crystallographic sites were identified for Fe(II) ions: two of them are octahedrally coordinated, while the other one is tetrahedrally coordinated. The compound was prepared in the presence of Li, which was retained within the crystal structure as an extra-framework species that was accommodated in the small 1D channels, thus rendering a pre-lithiated electrode. Electrochemical testing showed a specific charge of $85 \text{ mAh}\cdot\text{g}^{-1}$ until the 60th cycle, corresponding to 50% of the theoretical value of $168 \text{ mAh}\cdot\text{g}^{-1}$. The origin of this lower value was attributed to part of the Fe ions not undergoing any redox process, as evidenced by *in situ* near-edge X-ray absorption spectroscopy. Ex situ XRD analysis after the first electrochemical cycle showed that there was no significant loss of crystallinity, suggesting that activation did not proceed via decomposition of the compound. Successive studies focused on testing the same type of framework as a negative electrode, using both Fe and Co as the metal component,¹⁴⁶ and combining methylenediphosphonic acid with Ni, which leads to the formation of different crystal

structures.¹⁴⁷ In all cases, it was found that the structure irreversibly amorphises after the first cycle due to a conversion reaction mechanism involving the extrusion of the transition metal(II) as nanoparticles.

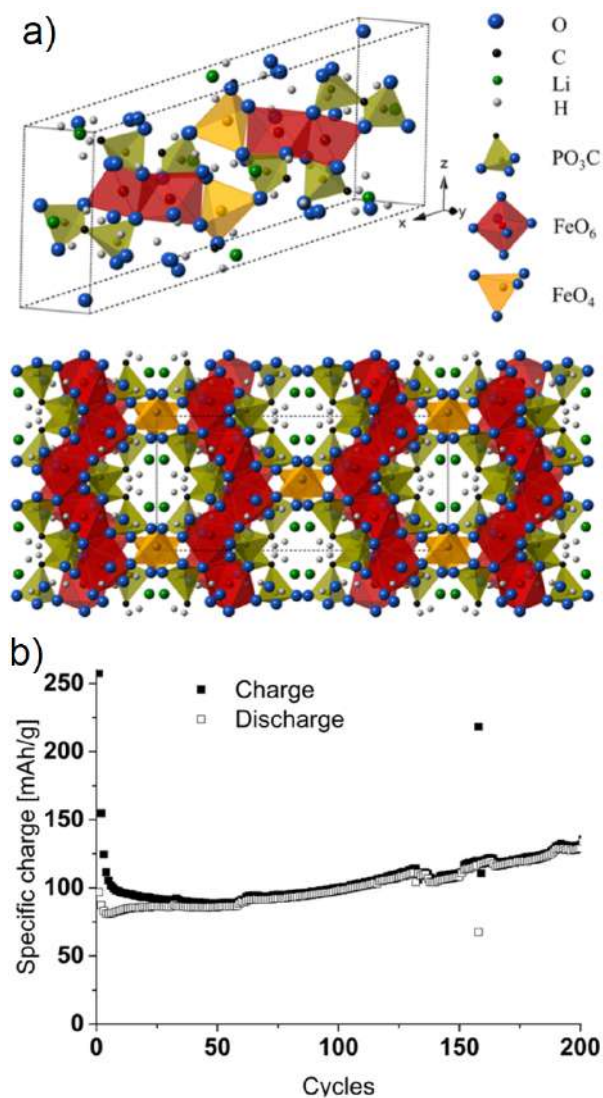


Figure 1.33: (a) Illustration of the monoclinic unit cell of $\text{Li}_{1.4}\text{Fe}_{6.8}[\text{CH}_2(\text{PO}_3)_2]_3[\text{CH}_2(\text{PO}_3)(\text{PO}_3\text{H})] \cdot 4\text{H}_2\text{O}$ and the expanded crystal structure viewed along the c -axis. Colour code: octahedral iron: red, tetrahedral iron: orange, phosphorus: yellow, oxygen: blue, carbon: black, water: grey, and lithium: green. (b) Specific charge vs. cycle number plot of $\text{Li}_{1.4}\text{Fe}_{6.8}[\text{CH}_2(\text{PO}_3)_2]_3[\text{CH}_2(\text{PO}_3)(\text{PO}_3\text{H})] \cdot 4\text{H}_2\text{O}$ cycled at 20 mA/g with a 1-h potentiostatic step after each half-cycle. Adapted with permission from reference [145] © 2015 American Chemical Society.

The compounds discussed above represent some of the first reported examples of MPs being applied as electrode materials for rechargeable batteries. There is a growing interest in employing hybrid organic–inorganic materials for this type of application,

mainly because of the possibility to tailor their structure, something that is not easily done when dealing with purely inorganic materials. Given the structural versatility of MPs and their high stability, there is great potential in this growing area of research.

Drug Delivery

Phosphonic acids (most often in their sodium phosphonate form) have featured in the treatment of bone-related conditions, e.g., osteoporosis and Paget's disease, for more than 30 years. Specifically, bisphosphonates (BPs) have been used as stable analogues of pyrophosphate, in which the P–O–P bonds are replaced with P–C–P bonds, making them more stable and less prone to enzymatic attack.¹⁴⁸ The way in which BPs can help in the treatment of bone-related conditions is through selective adsorption to the bone surface, leading to the interruption of bone resorption, whereby osteoclasts are prevented from resorbing bone tissue. There are two classes of BPs that can be used here: non-N-containing compounds, such as etidronate and clodronate, and N-containing compounds, such as pamidronate and alendronate. Perhaps one of the main drawbacks for the use of BPs for treating conditions such as osteoporosis is the limited bioavailability when delivered orally.¹⁴⁹ This means that in order to obtain the desired therapeutic effect, it is often the case that the drug dosage is increased. While this appears to overcome the bioavailability issue, it can also lead to an increase in other known side effects, i.e., hypocalcaemia, oesophageal cancer, and atrial fibrillation, etc. In order to overcome this issue, delayed release (DR) administration and other methods have been developed, helping to negate the need to increase the dosage. An example of one of the DR drugs is risedronate 35 mg. Unfortunately, these drugs still suffer in that they require long periods of fasting due to the complexing that can occur with food in the stomach.¹⁴⁹

In a paper published in 2019, Papathanasiou et al. explored various routes for the controlled release of bisphosphonates, one of which was based on self-sacrificial MOFs.¹⁵⁰ Using etidronic acid (ETID, one of the "early" BPs) as the linker, the

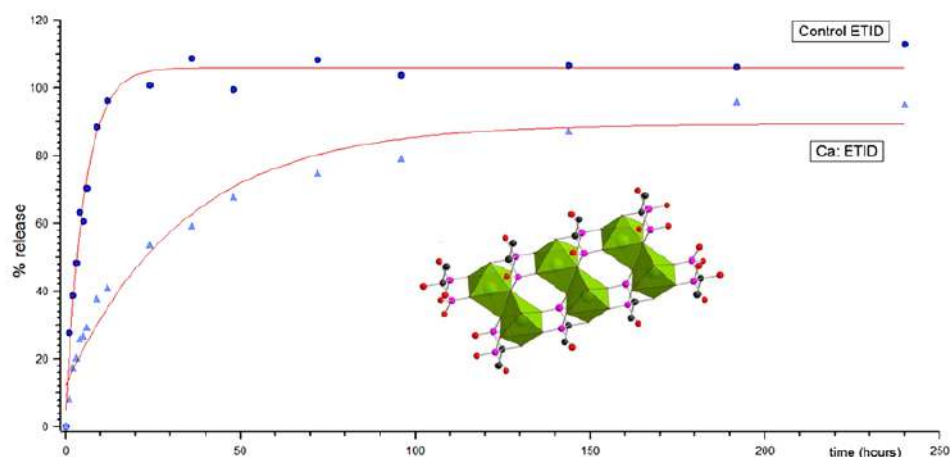


Figure 1.34: Etidronic acid (ETID) release versus time for the control tablet (dark blue circles) and the Ca-ETID tablet (light blue triangles). The crystal structure of Ca-ETID is also displayed in the inset. Colour code: green - calcium, yellow - phosphorus, red - oxygen, black - carbon, pink - lattice water. Adapted with permission from reference [150] © 2018 Walter de Gruyter GmbH and Co. KG.

researchers synthesised Ca-ETID and presented it in tablet form, comparing it to a control containing “free” ETID. The structure of Ca-ETID exists as a 1D chain, where each Ca^{2+} centre is coordinated to three ETID linkers, the -OH group, and water (Figure 1.34). Then, these single chains form ‘double chains’ held together by a network of hydrogen bonds between ETID linkers. The release rates of the control and Ca-ETID tablets upon soaking in an aqueous solution at pH 1.3 (representative of the environment in the stomach) were determined by NMR spectroscopy, finding that the control showed 100% release after just 10 h, whereas Ca-ETID showed only 30% release in the same time period, reaching a maximum of 90% after 150 h (Figure 1.34). The slower release rate of Ca-ETID tablets was ascribed to the slow rate of hydrolysis of the metal-phosphonate coordination bonds in the solvent medium.

These promising results are part of ongoing work that aims at systematically investigating the preparation and structural characterisation of a series of MPs based on various BP and biocompatible metals (e.g., Mg, Ca, Sr, and Ba), as well as their performance as matrices for controlled drug delivery. The final goal is to identify clear structure/activity relationships between specific structural features, such as the metal-phosphonate bond strength, the metal ion radius, the existence of

supramolecular interactions, and the drug delivery efficacy.

1.5 Copyright

Some of the material in Chapter 1 pertaining to metal phosphonates has been adapted from a perspective review published in *Crystals*, which operates under the MDPI trademark, and is available under a creative commons licence. Full citation:

S. J. I. Shearan, N. Stock, F. Emmerling, J. Demel, P. A. Wright, K. D. Demadis, M. Vassaki, F. Costantino, R. Vivani, S. Sallard, I. Ruiz Salcedo, Aurelio Cabeza, and M. Taddei, *Crystals*, 2019, 9, 270, DOI:10.3390/cryst9050270.

Conceptualisation: Stephen Shearan, Marco Taddei

Manuscript drafting: Stephen Shearan, Marco Taddei

Manuscript review and revisions: Stephen Shearan, Marco Taddei, Norbert Stock, Franziska Emmerling, Jan Demel, Paul Wright, Kostantinos Demadis, Maria Vassaki, Ferdinando Costantino, Ricardo Vivani, Sebastien Sallard, Ines Ruiz Salcedo, Aurelio Cabeza

1.6 References

1. S. J. I. Shearan, N. Stock, F. Emmerling, J. Demel, P. A. Wright, K. D. Demadis, M. Vassaki, F. Costantino, R. Vivani, S. Sallard, I. R. Salcedo, A. Cabeza and M. Taddei, "New Directions in Metal Phosphonate and Phosphinate Chemistry", *Crystals*, 2019, 9, 270, DOI: 10 . 3390 / cryst9050270.
2. O. M. Yaghi and H. Li, "Hydrothermal Synthesis of a Metal-Organic Framework Containing Large Rectangular Channels", *J. Am. Chem. Soc.*, 1995, 117, 10401–10402, DOI: 10 . 1021 / ja00146a033.
3. H. Li, M. Eddaoudi, M. O'Keeffe and O. M. Yaghi, "Design and synthesis of an exceptionally stable and highly porous metal-organic framework", *Nature*, 1999, 402, 276–279, DOI: 10 . 1038 / 46248.
4. K. A. Hofmann and F. Kuspert, "Verbindungen von Kohlenwasserstoffen mit Metallsalzen", *Z. Anorg. Chem.*, 1897, 15, 204–207, DOI: 10 . 1002 / zaac . 18970150118.

5. J. H. Rayner and H. M. Powell, "67. Structure of molecular compounds. Part X. Crystal structure of the compound of benzene with an ammonia-nickel cyanide complex", *J. Chem. Soc.*, 1952, **0**, 319–328, DOI: 10.1039/jr9520000319.
6. Y. Kinoshita, I. Matsubara, T. Higuchi and Y. Saito, "The Crystal Structure of Bis(adiponitrilo)copper(I) Nitrate", *Bull. Chem. Soc. Jpn.*, 1959, **32**, 1221–1226, DOI: 10.1246/bcsj.32.1221.
7. B. F. Hoskins and R. Robson, "Infinite polymeric frameworks consisting of three dimensionally linked rod-like segments", *J. Am. Chem. Soc.*, 1989, **111**, 5962–5964, DOI: 10.1021/ja00197a079.
8. B. F. Hoskins and R. Robson, "Design and construction of a new class of scaffolding-like materials comprising infinite polymeric frameworks of 3D-linked molecular rods. A reappraisal of the zinc cyanide and cadmium cyanide structures and the synthesis and structure of the diamond-related frameworks $[\text{N}(\text{CH}_3)_4][\text{Cu}^{\text{I}}\text{Zn}^{\text{II}}(\text{CN})_4]$ and $\text{Cu}^{\text{I}}[4,4',4'',4''']\text{-tetracyanotetraphenylmethane}[\text{BF}_4 \cdot x\text{C}_6\text{H}_5\text{NO}_2]$ ", *J. Am. Chem. Soc.*, 1990, **112**, 1546–1554, DOI: 10.1021/ja00160a038.
9. O. M. Yaghi, G. Li and H. Li, "Selective binding and removal of guests in a microporous metal-organic framework", *Nature*, 1995, **378**, 703–706, DOI: 10.1038/378703a0.
10. O. M. Yaghi, D. A. Richardson, G. Li, C. E. Davis and T. L. Groy, "Open-Framework Solids with Diamond-Like Structures Prepared from Clusters and Metal-Organic Building Blocks", *MRS Proceedings*, 1994, **371**, DOI: 10.1557/proc-371-15.
11. O. M. Yaghi and G. Li, "Mutually Interpenetrating Sheets and Channels in the Extended Structure of $[\text{Cu}(4,4'\text{-bpy})\text{Cl}]$ ", *Angew. Chem. Int. Ed.*, 1995, **34**, 207–209, DOI: 10.1002/anie.199502071.
12. T. E. Mallouk, "Crowns get organized", *Nature*, 1997, **387**, 350–351, DOI: 10.1038/387350a0.
13. J. Lu, T. Paliwala, S. C. Lim, C. Yu, T. Niu and A. J. Jacobson, "Coordination Polymers of $\text{Co}(\text{NCS})_2$ with Pyrazine and 4,4'-Bipyridine: Syntheses and Structures", *Inorg. Chem.*, 1997, **36**, 923–929, DOI: 10.1021/ic961158g.
14. T. P. Vaid, E. B. Lobkovsky and P. T. Wolczanski, "Covalent 3- and 2-Dimensional Titanium-Quinone Networks", *J. Am. Chem. Soc.*, 1997, **119**, 8742–8743, DOI: 10.1021/ja971658o.
15. L. R. MacGillivray, R. H. Groeneman and J. L. Atwood, "Design and Self-Assembly of Cavity-Containing Rectangular Grids", *J. Am. Chem. Soc.*, 1998, **120**, 2676–2677, DOI: 10.1021/ja973584m.
16. O. M. Yaghi, H. Li and T. L. Groy, "Construction of Porous Solids from Hydrogen-Bonded Metal Complexes of 1,3,5-Benzenetricarboxylic Acid", *J. Am. Chem. Soc.*, 1996, **118**, 9096–9101, DOI: 10.1021/ja960746q.

17. O. M. Yaghi, C. E. Davis, G. Li and H. Li, "Selective Guest Binding by Tailored Channels in a 3-D Porous Zinc(II)-Benzenetricarboxylate Network", *J. Am. Chem. Soc.*, 1997, **119**, 2861–2868, DOI: 10.1021/ja9639473.
18. O. M. Yaghi, H. Li, C. Davis, D. Richardson and T. L. Groy, "Synthetic Strategies, Structure Patterns, and Emerging Properties in the Chemistry of Modular Porous Solids", *Acc. Chem. Res.*, 1998, **31**, 474–484, DOI: 10.1021/ar970151f.
19. H. Li, M. Eddaoudi, T. L. Groy and O. M. Yaghi, "Establishing Microporosity in Open Metal-Organic Frameworks: Gas Sorption Isotherms for Zn(BDC) (BDC = 1,4-Benzenedicarboxylate)", *J. Am. Chem. Soc.*, 1998, **120**, 8571–8572, DOI: 10.1021/ja981669x.
20. P. Z. Moghadam, A. Li, X.-W. Liu, R. Bueno-Perez, S.-D. Wang, S. B. Wiggin, P. A. Wood and D. Fairen-Jimenez, "Targeted classification of metal–organic frameworks in the Cambridge structural database (CSD)", *Chem. Sci.*, 2020, **11**, 8373–8387, DOI: 10.1039/d0sc01297a.
21. A. Clearfield and G. D. Smith, "Crystallography and structure of α -zirconium bis(monohydrogen orthophosphate) monohydrate", *Inorg. Chem.*, 1969, **8**, 431–436, DOI: 10.1021/ic50073a005.
22. G. Alberti, U. Costantino, S. Allulli and N. Tomassini, "Crystalline $Zr[R-(PO)_3]_2$ and $Zr[R-(OPO)_3]_2$ compounds (R = organic radical). A new class of materials having layered structure of zirconium phosphonate type.", *J. Inorg. Nucl. Chem.*, 1978, **40**, 1113–1117, DOI: 10.1016/0022-1902(78)80520-x.
23. G. Alberti, M. Casciola, U. Costantino and R. Vivani, "Layered and pillared metal(IV) phosphates and phosphonates", *Adv. Mater.*, 1996, **8**, 291–303, DOI: 10.1002/adma.19960080405.
24. R. Vivani, F. Costantino and M. Taddei, in *Metal Phosphonate Chemistry*, ed. A. Clearfield and K. Demadis, Royal Society of Chemistry, 2011, ch. 2, pp. 45–86, DOI: 10.1039/9781849733571-00045.
25. D. Cunningham, P. J. D. Hennesly and T. Deeney, "Divalent metal phenylphosphonates and phenylarsonates", *Inorg. Chim. Acta*, 1979, **37**, 95–102, DOI: 10.1016/S0020-1693(00)95524-5.
26. G. Cao, H. Lee, V. M. Lynch and T. E. Mallouk, "Structural studies of some new lamellar magnesium, manganese and calcium phosphonates", *Solid State Ionics*, 1988, **26**, 63–69, DOI: 10.1016/0167-2738(88)90016-1.
27. G. Cao, H. Lee, V. M. Lynch and T. E. Mallouk, "Synthesis and structural characterization of a homologous series of divalent-metal phosphonates, $M^{II}(O_3PR) \cdot H_2O$ and $M^{II}(HO_3PR)_2$ ", *Inorg. Chem.*, 1988, **27**, 2781–2785, DOI: 10.1021/ic00289a008.
28. K. J. Martin, P. J. Squattrito and A. Clearfield, "The crystal and molecular structure of zinc phenylphosphonate", *Inorg. Chim. Acta*, 1989, **155**, 7–9, DOI: 10.1016/S0020-1693(00)89271-3.

29. *Metal Phosphonate Chemistry*, ed. A. Clearfield and K. Demadis, Royal Society of Chemistry, Cambridge, 2011, DOI: 10.1039/9781849733571.
30. M. D. Poojary, H.-L. Hu, F. L. Campbell and A. Clearfield, "Determination of crystal structures from limited powder data sets: crystal structure of zirconium phenylphosphonate", *Acta. Crystallogr. B. Struct. Sci. Cryst. Eng. Mater.*, 1993, **49**, 996–1001, DOI: 10.1107/S0108768193006937.
31. K. Maeda, Y. Kiyozumi and F. Mizukami, "Synthesis of the First Microporous Aluminum Phosphonate with Organic Groups Covalently Bonded to the Skeleton", *Angew. Chem. - Int. Ed.*, 1994, **33**, 2335–2337, DOI: 10.1002/anie.199423351.
32. J. L. Bideau, C. Payen, P. Palvadeau and B. Bujoli, "Preparation, Structure, and Magnetic Properties of Copper(II) Phosphonates. β -Cu^{II}(CH₃PO₃), an Original Three-Dimensional Structure with a Channel-Type Arrangement", *Inorg. Chem.*, 1994, **33**, 4885–4890, DOI: 10.1021/ic00100a011.
33. K. Maeda, J. Akimoto, Y. Kiyozumi and F. Mizukami, "AlMepO- α : A Novel Open-Framework Aluminum Methylphosphonate with Organo-Lined Unidimensional Channels", *Angew. Chem. - Int. Ed.*, 1995, **34**, 1199–1201, DOI: 10.1002/anie.199511991.
34. S. Drumel, P. Janvier, D. Deniaud and B. Bujoli, "Synthesis and crystal structure of Zn(O₃PC₂H₄NH₂), the first functionalized zeolite-like phosphonate", *J. Chem. Soc., Chem. Commun.*, 1995, 1051, DOI: 10.1039/c39950001051.
35. K. Maeda, J. Akimoto, Y. Kiyozumi and F. Mizukami, "Structure of aluminium methylphosphonate, AlMepO- β , with unidimensional channels formed from ladder-like organic-inorganic polymer chains", *J. Chem. Soc., Chem. Commun.*, 1995, 1033–1034, DOI: 10.1039/c39950001033.
36. K. Maeda, "Metal phosphonate open-framework materials", *Microporous Mesoporous Mater.*, 2004, **73**, 47–55, DOI: 10.1016/j.micromeso.2003.10.018.
37. D. L. Lohse and S. C. Sevov, "CO₂(O₃PCH₂PO₃)·H₂O: A Novel Microporous Diphosphonate with an Inorganic Framework and Hydrocarbon-Lined Hydrophobic Channels", *Angew. Chem. - Int. Ed.*, 1997, **36**, 1619–1621, DOI: 10.1002/anie.199716191.
38. G. B. Hix, B. M. Kariuki, S. Kitchin and M. Tremayne, "Synthesis and Structural Characterization of Zn(O₃PCH₂OH), a New Microporous Zinc Phosphonate", *Inorg. Chem.*, 2001, **40**, 1477–1481, DOI: 10.1021/ic000943x.
39. J. Goura and V. Chandrasekhar, "Molecular Metal Phosphonates", *Chem. Rev.*, 2015, **115**, 6854–6965, DOI: 10.1021/acs.chemrev.5b00107.
40. M. R. Mason, "Molecular Phosphates, Phosphonates, Phosphinates, and Arsonates of the Group 13 Elements", *J. Cluster Sci.*, 1998, **9**, 1–23, DOI: 10.1023/a:1022671821691.

41. M. G. Walawalkar, H. W. Roesky and R. Murugavel, "Molecular Phosphonate Cages: Model Compounds and Starting Materials for Phosphate Materials", *Acc. Chem. Res.*, 1998, **32**, 117–126, DOI: 10.1021/ar980040w.
42. K. Gopal, S. Ali and R. E. P. Winpenny, in *Metal Phosphonate Chemistry*, Royal Society of Chemistry, 2011, pp. 364–419, DOI: 10.1039/9781849733571-00364.
43. V. Chandrasekhar, T. Senapati, A. Dey and S. Hossain, "Molecular transition-metal phosphonates", *Dalton Trans.*, 2011, **40**, 5394, DOI: 10.1039/c0dt01069c.
44. M. R. Mason, M. S. Mashuta and J. F. Richardson, "Cyclic and Cubic Organophosphonates of Gallium and Their Relationship to Structural Motifs in Gallophosphate Molecular Sieves", *Angew. Chem. - Int. Ed.*, 1997, **36**, 239–241, DOI: 10.1002/anie.199702391.
45. A. Clearfield, in *Metal Phosphonate Chemistry*, Royal Society of Chemistry, 2011, pp. 1–44, DOI: 10.1039/9781849733571-00001.
46. N. Stock, "High-throughput investigations employing solvothermal syntheses", *Micropor. Mesopor. Mat.*, 2010, **129**, 287–295, DOI: 10.1016/j.micromeso.2009.06.007.
47. S. Bauer and N. Stock, "Implementation of a Temperature-Gradient Reactor System for High-Throughput Investigation of Phosphonate-Based Inorganic-Organic Hybrid Compounds", *Angew. Chem. Int. Ed.*, 2007, **46**, 6857–6860, DOI: 10.1002/anie.200701575.
48. N. Stock and T. Bein, "High-Throughput Synthesis of Phosphonate-Based Inorganic-Organic Hybrid Compounds under Hydrothermal Conditions", *Angew. Chem. Int. Ed.*, 2004, **43**, 749–752, DOI: 10.1002/anie.200351718.
49. S. Bauer, T. Bein and N. Stock, "High-Throughput Investigation and Characterization of Cobalt Carboxy Phosphonates", *Inorg. Chem.*, 2005, **44**, 5882–5889, DOI: 10.1021/ic0505089.
50. P. M. Forster, N. Stock and A. K. Cheetham, "A High-Throughput Investigation of the Role of pH, Temperature, Concentration, and Time on the Synthesis of Hybrid Inorganic-Organic Materials", *Angew. Chem. - Int. Ed.*, 2005, **44**, 7608–7611, DOI: 10.1002/anie.200501766.
51. N. Stock and T. Bein, "High-throughput investigation of metal carboxyarylphosphonate hybrid compounds", *J Mater Chem*, 2005, **15**, 1384, DOI: 10.1039/b413318h.
52. P. Maniam and N. Stock, in Royal Society of Chemistry, 2011, pp. 87–106, DOI: 10.1039/9781849733571-00087.
53. N. Hermer and N. Stock, "The new triazine-based porous copper phosphonate $\text{Cu}_3(\text{PPT})(\text{H}_2\text{O})_3 \cdot 10 \text{H}_2\text{O}$ ", *Dalton Trans.*, 2015, **44**, 3720–3723, DOI: 10.1039/c4dt03698k.
54. T. Rhauderwiek, K. Wolkersdörfer, S. Øien-Ødegaard, K.-P. Lillerud, M. Wark and N. Stock, "Crystalline and permanently porous porphyrin-based metal tetraphosphonates", *Chem. Commun.*, 2018, **54**, 389–392, DOI: 10.1039/c7cc07766a.

55. T. Rhauderwiek, H. Zhao, P. Hirschle, M. Döblinger, B. Bueken, H. Reinsch, D. D. Vos, S. Wuttke, U. Kolb and N. Stock, "Highly stable and porous porphyrin-based zirconium and hafnium phosphonates - electron crystallography as an important tool for structure elucidation", *Chem. Sci.*, 2018, **9**, 5467–5478, DOI: 10.1039/c8sc01533c.
56. N. Stock, M. Rauscher and T. Bein, "Inorganic-organic hybrid compounds: hydrothermal synthesis and characterization of a new three-dimensional metal tetraphosphate $\text{Mn}[(\text{HO}_3\text{PCH}_2)\text{N}(\text{H})(\text{CH}_2)_4(\text{H})\text{N}(\text{CH}_2\text{PO}_3\text{H})_2]$ ", *J. Solid State Chem.*, 2004, **177**, 642–647, DOI: 10.1016/j.jssc.2003.08.005.
57. N. Hermer, H. Reinsch, P. Mayer and N. Stock, "Synthesis and characterisation of the porous zinc phosphonate $[\text{Zn}_2(\text{H}_2\text{PPB})(\text{H}_2\text{O})_2] \cdot x\text{H}_2\text{O}$ ", *CrystEngComm*, 2016, **18**, 8147–8150, DOI: 10.1039/c6ce01580h.
58. M. Feyand, C. F. Seidler, C. Deiter, A. Rothkirch, A. Lieb, M. Wark and N. Stock, "High-throughput microwave-assisted discovery of new metal phosphonates", *Dalton Trans.*, 2013, **42**, 8761, DOI: 10.1039/c3dt50413a.
59. L.-H. Schilling and N. Stock, "High-throughput ultrasonic synthesis and in situ crystallisation investigation of metal phosphonocarboxylates", *Dalton Trans.*, 2014, **43**, 414–422, DOI: 10.1039/c3dt52576g.
60. V. V. Boldyrev and K. Tkáčová, "Mechanochemistry of solids: past, present, and prospects", *J. Mater. Synth. Process.*, 2000, **8**, 121–132, DOI: 10.1023/a:1011347706721.
61. L. Takacs, "The historical development of mechanochemistry", *Chem. Soc. Rev.*, 2013, **42**, 7649, DOI: 10.1039/c2cs35442j.
62. A. Bruckmann, A. Krebs and C. Bolm, "Organocatalytic reactions: effects of ball milling, microwave and ultrasound irradiation", *Green Chem.*, 2008, **10**, 1131, DOI: 10.1039/b812536h.
63. J. L. Howard, Q. Cao and D. L. Browne, "Mechanochemistry as an emerging tool for molecular synthesis: what can it offer?", *Chem. Sci.*, 2018, **9**, 3080–3094, DOI: 10.1039/c7sc05371a.
64. M. Wilke, L. Batzdorf, F. Fischer, K. Rademann and F. Emmerling, "Cadmium phenylphosphonates: preparation, characterisation and *in situ* investigation", *RSC Adv.*, 2016, **6**, 36011–36019, DOI: 10.1039/c6ra01080f.
65. M. Wilke, A. G. Buzanich, U. Reinholz, K. Rademann and F. Emmerling, "The structure and *in situ* synthesis investigation of isomorphic mononuclear molecular metal phenylphosphonates", *Dalton Trans.*, 2016, **45**, 9460–9467, DOI: 10.1039/c6dt00787b.
66. M. Wilke, A. Kabelitz, A. Zimathies, K. Rademann and F. Emmerling, "Crystal structure and *in situ* investigation of a mechanochemical synthesized 3D zinc N-(phosphonomethyl)glycinate", *J Mater Sci*, 2017, **52**, 12013–12020, DOI: 10.1007/s10853-017-1121-7.

67. I. Akhmetova, K. Schutjajew, M. Wilke, A. Buzanich, K. Rademann, C. Roth and F. Emmerling, "Synthesis, characterization and *in situ* monitoring of the mechanochemical reaction process of two manganese(II)-phosphonates with N-containing ligands", *J Mater Sci*, 2018, **53**, 13390–13399, DOI: 10.1007/s10853-018-2608-6.
68. K. Maeda, Y. Kiyozumi and F. Mizukami, "Characterization and Gas Adsorption Properties of Aluminum Methylphosphonates with Organically Lined Unidimensional Channels", *J Phys Chem B*, 1997, **101**, 4402–4412, DOI: 10.1021/jp962112b.
69. S. S. Chui, "A Chemically Functionalizable Nanoporous Material", *Science*, 1999, **283**, 1148–1150, DOI: 10.1126/science.283.5405.1148.
70. C. Serre, J. A. Groves, P. Lightfoot, A. M. Z. Slawin, P. A. Wright, N. Stock, T. Bein, M. Haouas, F. Taulelle and G. Férey, "Synthesis, Structure and Properties of Related Microporous N,N'-Piperazinebismethylenephosphonates of Aluminum and Titanium", *Chem. Mater.*, 2006, **18**, 1451–1457, DOI: 10.1021/cm0521491.
71. J. R. Long and O. M. Yaghi, "The pervasive chemistry of metal-organic frameworks", *Chem. Soc. Rev.*, 2009, **38**, 1213, DOI: 10.1039/b903811f.
72. H.-C. Zhou, J. R. Long and O. M. Yaghi, "Introduction to Metal-Organic Frameworks", *Chem. Rev.*, 2012, **112**, 673–674, DOI: 10.1021/cr300014x.
73. G. K. H. Shimizu, R. Vaidhyanathan and J. M. Taylor, "Phosphonate and sulfonate metal organic frameworks", *Chem. Soc. Rev.*, 2009, **38**, 1430–1449, DOI: 10.1039/b802423p.
74. K. J. Gagnon, H. P. Perry and A. Clearfield, "Conventional and Unconventional Metal-Organic Frameworks Based on Phosphonate Ligands: MOFs and UMOFs", *Chem. Rev.*, 2012, **112**, 1034–1054, DOI: 10.1021/cr2002257.
75. G. Yücesan, Y. Zorlu, M. Stricker and J. Beckmann, "Metal-organic solids derived from arylphosphonic acids", *Coord. Chem. Rev.*, 2018, **369**, 105–122, DOI: 10.1016/j.ccr.2018.05.002.
76. J. M. Rueff, G. B. Hix and P. A. Jaffres, in *Tailored organic-inorganic materials*, ed. E. Brunet, J. L. Colon and A. Clearfield, Wiley, Hoboken, New Jersey, 2014, ch. Rigid phosphonic acids as building blocks for crystalline hybrid materials, pp. 341–393.
77. V. Benoit, R. S. Pillai, A. Orsi, P. Normand, H. Jobic, F. Nouar, P. Billefont, E. Bloch, S. Bourrelly, T. Devic, P. A. Wright, G. de Weireld, C. Serre, G. Maurin and P. L. Llewellyn, "MIL-91(Ti), a small pore metal-organic framework which fulfils several criteria: an upscaled green synthesis, excellent water stability, high CO₂ selectivity and fast CO₂ transport", *J Mater Chem A*, 2016, **4**, 1383–1389, DOI: 10.1039/c5ta09349j.
78. P. L. Llewellyn, M. Garcia-Rates, L. Gaberová, S. R. Miller, T. Devic, J.-C. Lavalley, S. Bourrelly, E. Bloch, Y. Filinchuk, P. A. Wright, C. Serre, A. Vimont and G. Maurin, "Structural Origin of

- Unusual CO₂ Adsorption Behavior of a Small-Pore Aluminum Bisphosphonate MOF”, *J. Phys. Chem. C*, 2015, **119**, 4208–4216, DOI: 10.1021/jp512596u.
79. M. T. Wharmby, J. P. S. Mowat, S. P. Thompson and P. A. Wright, “Extending the Pore Size of Crystalline Metal Phosphonates toward the Mesoporous Regime by Isoreticular Synthesis”, *J. Am. Chem. Soc.*, 2011, **133**, 1266–1269, DOI: 10.1021/ja1097995.
80. J. A. Groves, S. R. Miller, S. J. Warrender, C. Mellot-Draznieks, P. Lightfoot and P. A. Wright, “The first route to large pore metal phosphonates”, *Chem. Commun.*, 2006, 3305, DOI: 10.1039/b605400e.
81. M. T. Wharmby, G. M. Pearce, J. P. Mowat, J. M. Griffin, S. E. Ashbrook, P. A. Wright, L.-H. Schilling, A. Lieb, N. Stock, S. Chavan, S. Bordiga, E. Garcia, G. D. Pirngruber, M. Vreeke and L. Gora, “Synthesis and crystal chemistry of the STA-12 family of metal N,N'-piperazinebis(methylenephosphonate) and applications of STA-12(Ni) in the separation of gases”, *Micropor. Mesopor. Mat.*, 2012, **157**, 3–17, DOI: 10.1016/j.micromeso.2011.12.003.
82. M. Taddei, F. Costantino and R. Vivani, “Robust Metal-Organic Frameworks Based on Tritopic Phosphonoaromatic Ligands”, *Eur. J. Inorg. Chem.*, 2016, **2016**, 4300–4309, DOI: 10.1002/ejic.201600207.
83. A. D. Firmino, F. Figueira, J. P. Tomé, F. A. A. Paz and J. Rocha, “Metal-Organic Frameworks assembled from tetraphosphonic ligands and lanthanides”, *Coord. Chem. Rev.*, 2018, **355**, 133–149, DOI: 10.1016/j.ccr.2017.08.001.
84. J. K. Zareba, “Tetraphenylmethane and tetraphenylsilane as building units of coordination polymers and supramolecular networks - A focus on tetraphosphonates”, *Inorg. Chem. Commun.*, 2017, **86**, 172–186, DOI: 10.1016/j.inoche.2017.10.013.
85. T. Zheng, Z. Yang, D. Gui, Z. Liu, X. Wang, X. Dai, S. Liu, L. Zhang, Y. Gao, L. Chen, D. Sheng, Y. Wang, J. Diwu, J. Wang, R. Zhou, Z. Chai, T. E. Albrecht-Schmitt and S. Wang, “Overcoming the crystallization and designability issues in the ultrastable zirconium phosphonate framework system”, *Nat Commun*, 2017, **8**, DOI: 10.1038/ncomms15369.
86. Y. Zorlu, D. Erbahar, A. Çetinkaya, A. Bulut, T. S. Erkal, A. O. Yazaydin, J. Beckmann and G. Yücesan, “A cobalt arylphosphonate MOF - superior stability, sorption and magnetism”, *Chem. Commun.*, 2019, **55**, 3053–3056, DOI: 10.1039/c8cc09655d.
87. B. Wang, T. Rhauderwiek, A. K. Inge, H. Xu, T. Yang, Z. Huang, N. Stock and X. Zou, “A Porous Cobalt Tetraphosphonate Metal-Organic Framework: Accurate Structure and Guest Molecule Location Determined by Continuous-Rotation Electron Diffraction”, *Chem. Eur. J.*, 2018, **24**, 17429–17433, DOI: 10.1002/chem.201804133.

88. C. G. Jones, M. W. Martynowycz, J. Hattne, T. J. Fulton, B. M. Stoltz, J. A. Rodriguez, H. M. Nelson and T. Gonen, "The CryoEM Method MicroED as a Powerful Tool for Small Molecule Structure Determination", *ACS Cent. Sci.*, 2018, **4**, 1587–1592, DOI: 10.1021/acscentsci.8b00760.
89. T. Gruene, J. T. C. Wennmacher, C. Zaubitzer, J. J. Holstein, J. Heidler, A. Fecteau-Lefebvre, S. D. Carlo, E. Müller, K. N. Goldie, I. Regeni, T. Li, G. Santiso-Quinones, G. Steinfeld, S. Handschin, E. van Genderen, J. A. van Bokhoven, G. H. Clever and R. Pantelic, "Rapid Structure Determination of Microcrystalline Molecular Compounds Using Electron Diffraction", *Angew. Chem. Int. Ed.*, 2018, **57**, 16313–16317, DOI: 10.1002/anie.201811318.
90. J. Hynek, P. Brázda, J. Rohlíček, M. G. S. Londesborough and J. Demel, "Phosphinic Acid Based Linkers: Building Blocks in Metal-Organic Framework Chemistry", *Angew. Chem. Int. Ed.*, 2018, **57**, 5016–5019, DOI: 10.1002/anie.201800884.
91. J. Sun, C. Bonneau, Á. Cantín, A. Corma, M. J. Diaz-Cabañas, M. Moliner, D. Zhang, M. Li and X. Zou, "The ITQ-37 mesoporous chiral zeolite", *Nature*, 2009, **458**, 1154–1157, DOI: 10.1038/nature07957.
92. T. Willhammar, J. Sun, W. Wan, P. Oleynikov, D. Zhang, X. Zou, M. Moliner, J. Gonzalez, C. Martinez, F. Rey and A. Corma, "Structure and catalytic properties of the most complex intergrown zeolite ITQ-39 determined by electron crystallography", *Nat Chem*, 2012, **4**, 188–194, DOI: 10.1038/nchem.1253.
93. M. Feyand, E. Mugnaioli, F. Vermoortele, B. Bueken, J. M. Dieterich, T. Reimer, U. Kolb, D. de Vos and N. Stock, "Automated Diffraction Tomography for the Structure Elucidation of Twinned, Sub-micrometer Crystals of a Highly Porous, Catalytically Active Bismuth Metal-Organic Framework", *Angew. Chem. Int. Ed.*, 2012, **51**, 10373–10376, DOI: 10.1002/anie.201204963.
94. Y.-B. Zhang, J. Su, H. Furukawa, Y. Yun, F. Gándara, A. Duong, X. Zou and O. M. Yaghi, "Single-Crystal Structure of a Covalent Organic Framework", *J. Am. Chem. Soc.*, 2013, **135**, 16336–16339, DOI: 10.1021/ja409033p.
95. U. Kolb, E. Mugnaioli and T. E. Gorelik, "Automated electron diffraction tomography - a new tool for nano crystal structure analysis", *Cryst. Res. Technol.*, 2011, **46**, 542–554, DOI: 10.1002/crat.201100036.
96. W. Wan, J. Sun, J. Su, S. Hovmöller and X. Zou, "Three-dimensional rotation electron diffraction: software RED for automated data collection and data processing", *J. Appl. Crystallogr.*, 2013, **46**, 1863–1873, DOI: 10.1107/S0021889813027714.
97. R. I. Walton and F. Millange, in *The Chemistry of Metal-Organic Frameworks: Synthesis, Characterization, and Applications*, ed. S. Kaskel, Wiley-VCH, 2016, ch. 24, pp. 729–764, DOI: 10.1002/9783527693078.ch24.

98. N. Heidenreich, U. Rutt, M. Koppen, A. K. Inge, S. Beier, A. C. Dippel, R. Suren and N. Stock, "A multi-purpose reaction cell for the investigation of reactions under solvothermal conditions", *Rev. Sci. Instrum.*, 2017, **88**, 104102, DOI: 10.1063/1.4999688.
99. M. J. Van Vleet, T. Weng, X. Li and J. R. Schmidt, "In Situ, Time-Resolved, and Mechanistic Studies of Metal-Organic Framework Nucleation and Growth", *Chem. Rev.*, 2018, **118**, 3681–3721, DOI: 10.1021/acs.chemrev.7b00582.
100. M. Feyand, C. Näther, A. Rothkirch and N. Stock, "Systematic and In Situ Energy Dispersive X-ray Diffraction Investigations on the Formation of Lanthanide Phosphonatobutanesulfonates: $\text{Ln}(\text{O}_3\text{P-C}_4\text{H}_8\text{-SO}_3)(\text{H}_2\text{O})$ ($\text{Ln} = \text{La-Gd}$)", *Inorg. Chem.*, 2010, **49**, 11158–11163, DOI: 10.1021/ic101786r.
101. M. Feyand, A. Hubner, A. Rothkirch, D. S. Wragg and N. Stock, "Copper phosphonatoethanesulfonates: temperature dependent in situ energy dispersive X-ray diffraction study and influence of the pH on the crystal structures", *Inorg. Chem.*, 2012, **51**, 12540–7, DOI: 10.1021/ic301976s.
102. L. Batzdorf, F. Fischer, M. Wilke, K.-J. Wenzel and F. Emmerling, "Direct *in situ* Investigation of Milling Reactions Using Combined X-ray Diffraction and Raman Spectroscopy", *Angew. Chem. Int. Ed.*, 2014, **54**, 1799–1802, DOI: 10.1002/anie.201409834.
103. G. Rothenberg, *Catalysis: concepts and green applications*, Wiley-VCH Verlag GmbH & Co. KGaA, Weinheim, Germany, 2017.
104. R. Schlögl, "Heterogeneous Catalysis", *Angew. Chem. - Int. Ed.*, 2015, **54**, 3465–3520, DOI: 10.1002/anie.201410738.
105. J. M. Thomas, *Principles and Practice of Heterogeneous Catalysis*, Wiley VCH Verlag GmbH, 2014.
106. R. J. White, R. Luque, V. L. Budarin, J. H. Clark and D. J. Macquarrie, "Supported metal nanoparticles on porous materials. Methods and applications", *Chem. Soc. Rev.*, 2009, **38**, 481–494, DOI: 10.1039/b802654h.
107. D. Astruc, *Nanoparticles and catalysis*, ed. D. Astruc, Wiley-VCH, Weinheim, 2008.
108. Z. Hu and D. Zhao, "Metal-organic frameworks with Lewis acidity: synthesis, characterization, and catalytic applications", *CrystEngComm*, 2017, **19**, 4066–4081, DOI: 10.1039/c6ce02660e.
109. M. Ranocchiari and J. A. van Bokhoven, "Catalysis by metal-organic frameworks: fundamentals and opportunities", *Phys. Chem. Chem. Phys.*, 2011, **13**, 6388, DOI: 10.1039/c0cp02394a.
110. A. Clearfield and D. S. Thakur, "Zirconium and titanium phosphates as catalysts: a review", *Appl Catal*, 1986, **26**, 1–26, DOI: 10.1016/s0166-9834(00)82538-5.
111. Z. Wang, J. M. Heising and A. Clearfield, "Sulfonated Microporous Organic-Inorganic Hybrids as Strong Bronsted Acids", *J. Am. Chem. Soc.*, 2003, **125**, 10375–10383, DOI: 10.1021/ja030226c.

112. A. Donnadio, M. Nocchetti, F. Costantino, M. Taddei, M. Casciola, F. da Silva Lisboa and R. Vivani, "A Layered Mixed Zirconium Phosphate-Phosphonate with Exposed Carboxylic and Phosphonic Groups: X-ray Powder Structure and Proton Conductivity Properties", *Inorg. Chem.*, 2014, **53**, 13220–13226, DOI: 10.1021/ic502473w.
113. F. Costantino, R. Vivani, M. Bastianini, L. Ortolani, O. Piermatti, M. Nocchetti and L. Vaccaro, "Accessing stable zirconium carboxy-aminophosphonate nanosheets as support for highly active Pd nanoparticles", *Chem. Commun.*, 2015, **51**, 15990–15993, DOI: 10.1039/c5cc06292f.
114. F. Costantino, M. Nocchetti, M. Bastianini, A. Lavacchi, M. Caporali and F. Liguori, "Robust Zirconium Phosphate-Phosphonate Nanosheets Containing Palladium Nanoparticles as Efficient Catalyst for Alkynes and Nitroarenes Hydrogenation Reactions", *ACS Appl. Nano Mater.*, 2018, **1**, 1750–1757, DOI: 10.1021/acsanm.8b00193.
115. V. Kozell, T. Giannoni, M. Nocchetti, R. Vivani, O. Piermatti and L. Vaccaro, "Immobilized Palladium Nanoparticles on Zirconium Carboxy-Aminophosphonates Nanosheets as an Efficient Recoverable Heterogeneous Catalyst for Suzuki-Miyaura and Heck Coupling", *Catalysts*, 2017, **7**, 186, DOI: 10.3390/catal7060186.
116. F. Ferlin, M. Cappelletti, R. Vivani, M. Pica, O. Piermatti and L. Vaccaro, "Au@zirconium-phosphonate nanoparticles as an effective catalytic system for the chemoselective and switchable reduction of nitroarenes", *Green Chem.*, 2019, **21**, 614–626, DOI: 10.1039/c8gc03513j.
117. M. Pica, A. Donnadio, D. Capitani, R. Vivani, E. Troni and M. Casciola, "Advances in the Chemistry of Nanosized Zirconium Phosphates: A New Mild and Quick Route to the Synthesis of Nanocrystals", *Inorg. Chem.*, 2011, **50**, 11623–11630, DOI: 10.1021/ic2015594.
118. L. Mitchell, B. Gonzalez-Santiago, J. P. S. Mowat, M. E. Gunn, P. Williamson, N. Acerbi, M. L. Clarke and P. A. Wright, "Remarkable Lewis acid catalytic performance of the scandium trimesate metal organic framework MIL-100(Sc) for C-C and C-N bond-forming reactions", *Catal. Sci. Technol.*, 2013, **3**, 606–617, DOI: 10.1039/c2cy20577g.
119. M. J. Beier, W. Kleist, M. T. Wharmby, R. Kissner, B. Kimmerle, P. A. Wright, J.-D. Grunwaldt and A. Baiker, "Aerobic Epoxidation of Olefins Catalyzed by the Cobalt-Based Metal-Organic Framework STA-12(Co)", *Chem. Eur. J.*, 2011, **18**, 887–898, DOI: 10.1002/chem.201101223.
120. D. Narváez-Celada and A. S. Varela, "CO₂ electrochemical reduction on metal-organic framework catalysts: current status and future directions", *J. Mater. Chem. A*, 2022, **10**, 5899–5917, DOI: 10.1039/d1ta10440c.
121. B. An, Z. Li, Z. Wang, X. Zeng, X. Han, Y. Cheng, A. M. Sheveleva, Z. Zhang, F. Tuna, E. J. L. McInnes, M. D. Frogley, A. J. Ramirez-Cuesta, L. S. Natrajan, C. Wang, W. Lin, S. Yang and M.

- Schröder, "Direct photo-oxidation of methane to methanol over a mono-iron hydroxyl site", *Nat. Mater.*, 2022, DOI: 10.1038/s41563-022-01279-1.
122. D. A. Reddy, Y. Kim, M. Gopannagari, D. P. Kumar and T. K. Kim, "Recent advances in metal-organic framework-based photocatalysts for hydrogen production", *Sustain. Energy Fuels*, 2021, **5**, 1597–1618, DOI: 10.1039/c9se00749k.
123. H. H. Do, T. H. C. Nguyen, T. V. Nguyen, C. Xia, D. L. T. Nguyen, P. Raizada, P. Singh, V.-H. Nguyen, S. H. Ahn, S. Y. Kim and Q. V. Le, "Metal-organic-framework based catalyst for hydrogen production: Progress and perspectives", *Int. J. Hydrog. Energy*, 2022, DOI: 10.1016/j.ijhydene.2022.01.080.
124. S. Mukhopadhyay, O. Basu, R. Nasani and S. K. Das, "Evolution of metal organic frameworks as electrocatalysts for water oxidation", *Chem. Commun.*, 2020, **56**, 11735–11748, DOI: 10.1039/d0cc03659e.
125. M. Oschatz and M. Antonietti, "A search for selectivity to enable CO₂ capture with porous adsorbents", *Energy Environ. Sci.*, 2018, **11**, 57–70, DOI: 10.1039/c7ee02110k.
126. B. Li and B. Chen, "Fine-Tuning Porous Metal-Organic Frameworks for Gas Separations at Will", *Chem*, 2016, **1**, 669–671, DOI: 10.1016/j.chempr.2016.10.011.
127. N. Hermer, M. T. Wharmby and N. Stock, "Re-Determination of the Crystal Structure of MIL-91(Al)", *Zeitschrift für anorganische und allgemeine Chemie*, 2016, **643**, 137–140, DOI: 10.1002/zaac.201600358.
128. S. R. Miller, G. M. Pearce, P. A. Wright, F. Bonino, S. Chavan, S. Bordiga, I. Margiolaki, N. Guillou, G. Férey, S. Bourrelly and P. L. Llewellyn, "Structural Transformations and Adsorption of Fuel-Related Gases of a Structurally Responsive Nickel Phosphonate Metal-Organic Framework, Ni-STA-12", *J. Am. Chem. Soc.*, 2008, **130**, 15967–15981, DOI: 10.1021/ja804936z.
129. E. J. García, J. P. S. Mowat, P. A. Wright, J. Pérez-Pellitero, C. Jallut and G. D. Pirngruber, "Role of Structure and Chemistry in Controlling Separations of CO₂/CH₄ and CO₂/CH₄/CO Mixtures over Honeycomb MOFs with Coordinatively Unsaturated Metal Sites", *J Phys Chem C*, 2012, **116**, 26636–26648, DOI: 10.1021/jp309526k.
130. *World Energy Outlook 2017 - Executive Summary*, tech. rep., International Energy Agency, France, 2017.
131. M. Winter and R. J. Brodd, "What Are Batteries, Fuel Cells, and Supercapacitors?", *Chem. Rev.*, 2004, **104**, 4245–4270, DOI: 10.1021/cr020730k.
132. V. S. Bagotskii, *Electrochemical power sources: batteries, fuel cells, and supercapacitors*, Wiley, Hoboken, New Jersey, 2014.

133. B. Peng and J. Chen, "Functional materials with high-efficiency energy storage and conversion for batteries and fuel cells", *Coord. Chem. Rev.*, 2009, **253**, 2805–2813, DOI: 10.1016/j.ccr.2009.04.008.
134. K.-D. Kreuer, "Proton Conductivity: Materials and Applications", *Chem. Mater.*, 1996, **8**, 610–641, DOI: 10.1021/cm950192a.
135. G. Alberti and M. Casciola, "Solid state protonic conductors, present main applications and future prospects", *Solid State Ion.*, 2001, **145**, 3–16, DOI: 10.1016/s0167-2738(01)00911-0.
136. G. Alberti, U. Costantino, M. Casciola, R. Vivani and A. Peraio, "Proton conductivity of zirconium carboxy n-alkyl phosphonates with an α -layered structure", *Solid State Ion.*, 1991, **46**, 61–68, DOI: 10.1016/0167-2738(91)90129-y.
137. G. Alberti, M. Casciola, R. Palombari and A. Peraio, "Protonic conductivity of layered zirconium phosphonates containing $-(\text{SO})_3\text{H}$ groups. I. Preparation and characterization of a mixed zirconium phosphonate of composition $\text{Zr}(\text{O}_3\text{PR}^1)_{0.73}(\text{O}_3\text{PR}^2)_{1.27} \cdot n\text{H}_2\text{O}$, with $\text{R}^1 = -\text{C}_6\text{H}_4-\text{SO}_3\text{H}$ and $\text{R}^2 = -\text{CH}_2-\text{OH}$ ", *Solid State Ion.*, 1992, **58**, 339–344, DOI: 10.1016/0167-2738(92)90138-f.
138. S. S. Bao, G. K. H. Shimizu and L. M. Zheng, "Proton conductive metal phosphonate frameworks", *Coord. Chem. Rev.*, 2019, **378**, 577–594, DOI: 10.1016/j.ccr.2017.11.029.
139. G. K. H. Shimizu, J. M. Taylor and K. W. Dawson, in *Metal Phosphonate Chemistry*, Royal Society of Chemistry, 2011, pp. 493–524, DOI: 10.1039/9781849733571-00493.
140. R. M. P. Colodrero, P. Olivera-Pastor, E. R. Losilla, M. A. G. Aranda, L. Leon-Reina, M. Papadaki, A. C. McKinlay, R. E. Morris, K. D. Demadis and A. Cabeza, "Multifunctional lanthanum tetraphosphonates: Flexible, ultramicroporous and proton-conducting hybrid frameworks", *Dalton Trans.*, 2012, **41**, 4045, DOI: 10.1039/c2dt11992g.
141. M. Bazaga-García, R. M. P. Colodrero, M. Papadaki, P. Garczarek, J. Zoń, P. Olivera-Pastor, E. R. Losilla, L. León-Reina, M. A. G. Aranda, D. Choquesillo-Lazarte, K. D. Demadis and A. Cabeza, "Guest Molecule-Responsive Functional Calcium Phosphonate Frameworks for Tuned Proton Conductivity", *J. Am. Chem. Soc.*, 2014, **136**, 5731–5739, DOI: 10.1021/ja500356z.
142. R. M. P. Colodrero, K. E. Papathanasiou, N. Stavgianoudaki, P. Olivera-Pastor, E. R. Losilla, M. A. G. Aranda, L. León-Reina, J. Sanz, I. Sobrados, D. Choquesillo-Lazarte, J. M. García-Ruiz, P. Atienzar, F. Rey, K. D. Demadis and A. Cabeza, "Multifunctional Luminescent and Proton-Conducting Lanthanide Carboxyphosphonate Open-Framework Hybrids Exhibiting Crystalline-to-Amorphous-to-Crystalline Transformations", *Chem. Mater.*, 2012, **24**, 3780–3792, DOI: 10.1021/cm302381k.
143. R. M. P. Colodrero, P. Olivera-Pastor, E. R. Losilla, D. Hernández-Alonso, M. A. G. Aranda, L. Leon-Reina, J. Rius, K. D. Demadis, B. Moreau, D. Villemin, M. Palomino, F. Rey and A.

- Cabeza, "High Proton Conductivity in a Flexible, Cross-Linked, Ultramicroporous Magnesium Tetraphosphate Hybrid Framework", *Inorg. Chem.*, 2012, **51**, 7689–7698, DOI: 10.1021/ic3007316.
144. M. Bazaga-García, M. Papadaki, R. M. P. Colodrero, P. Olivera-Pastor, E. R. Losilla, B. Nieto-Ortega, M. Á. G. Aranda, D. Choquesillo-Lazarte, A. Cabeza and K. D. Demadis, "Tuning Proton Conductivity in Alkali Metal Phosphonocarboxylates by Cation Size-Induced and Water-Facilitated Proton Transfer Pathways", *Chem. Mater.*, 2015, **27**, 424–435, DOI: 10.1021/cm502716e.
145. S. Schmidt, D. Sheptyakov, J.-C. Jumas, M. Medarde, P. Benedek, P. Novák, S. Sallard and C. Villevieille, "Lithium Iron Methylendiphosphonate: A Model Material for New Organic-Inorganic Hybrid Positive Electrode Materials for Li-Ion Batteries", *Chem. Mater.*, 2015, **27**, 7889–7895, DOI: 10.1021/acs.chemmater.5b02595.
146. S. Schmidt, S. Sallard, D. Sheptyakov, M. Nachtegaal, P. Novák and C. Villevieille, "Fe and Co methylene diphosphonates as conversion materials for Li-ion batteries", *J Power Sources*, 2017, **342**, 879–885, DOI: 10.1016/j.jpowsour.2016.12.090.
147. S. Schmidt, S. Sallard, D. Sheptyakov, P. Novák and C. Villevieille, "Ligand influence in Li-ion battery hybrid active materials: Ni methylendiphosphonate vs. Ni dimethylamino methylendiphosphonate", *Chem. Commun.*, 2017, **53**, 5420–5423, DOI: 10.1039/c7cc01982c.
148. J. Galezowska and E. Gumienna-Kontecka, "Phosphonates, their complexes and bio-applications: A spectrum of surprising diversity", *Coord. Chem. Rev.*, 2012, **256**, 105–124, DOI: 10.1016/j.ccr.2011.07.002.
149. M. Pazianas, B. Abrahamsen, S. Ferrari and R. G. Russell, "Eliminating the need for fasting with oral administration of bisphosphonates", *Ther. Clin. Risk Manag.*, 2013, 395, DOI: 10.2147/tcrm.s52291.
150. K. E. Papathanasiou, M. Vassaki, A. Spinthaki, F.-E. G. Alatzoglou, E. Tripodianos, P. Turhanen and K. D. Demadis, "Phosphorus chemistry: from small molecules, to polymers, to pharmaceutical and industrial applications", *Pure Appl. Chem.*, 2018, **91**, 421–441, DOI: 10.1515/pac-2018-1012.

Chapter 2

Materials and Characterisation Techniques

2.1 Introduction

The initial aim of this section is to provide relevant information on the materials used to carry out the experimental work for this thesis. It will also provide overviews for some of the main techniques employed in this work, giving descriptions of the equipment and setup used as well as brief overviews of the theory behind these techniques. The length of these descriptions is based on the importance of the technique to the work and the level of complexity involved.

2.2 Materials

The reagents listed below were used as received and were not subjected to further purification and were stored appropriately.

Materials used in Chapter 3

- Acetonitrile, anhydrous (75-05-8, 99.8%, CH₃CN, Sigma-Merck)
- Bis-(4-bromophenyl)amine (16292-17-4, 97%, C₁₂H₉Br₂N, Sigma-Merck)

- 4-Bromo-N-(4-bromophenyl)-N-phenylaniline (81090-53-1, 98%, $C_{18}H_{13}Br_2N$, Fluorochem)
- 3,6-Dibromo-9H-carbazole (6825-20-3, 97%, $C_{12}H_7Br_2N$, Fluorochem)
- Ethyl acetate (141-78-6, 99.7%, $CH_3CO_2C_2H_5$, Sigma-Merck)
- Hexane (110-54-3, 97%, $CH_3(CH_2)_4CH_3$, Sigma-Merck)
- Nickel(II) chloride, anhydrous (7718-54-9, 98%, $NiCl_2$, Alfa Aesar)
- Triisopropyl phosphite (116-17-6, 95%, $[(CH_3)_2CHO]_3P$, Sigma-Merck)
- Trimethylbromosilane (2857-97-8, 97%, $(CH_3)_3SiBr$, Sigma-Merck)

Materials used in Chapter 4

- Hydrofluoric acid (7664-39-3, 48-51%, HF, Alfa Aesar)
- Methanol (67-56-1, 99.8%, CH_3OH , Sigma-Merck)
- Ethanol (64-17-5, 99.9%, CH_3CH_2OH , Sigma-Merck)
- 2-Propanol (67-63-0, 99.5%, $(CH_3)_2CHOH$, Sigma-Merck)
- Zirconium(IV) oxide chloride octahydrate (13520-92-8, 99.0%, $ZrOCl_2 \cdot 8H_2O$, Supelco)

Materials used in Chapter 5

- Cerium(IV) ammonium nitrate (16774-21-3, 99%, $Ce(NH_4)_2(NO_3)_6$, Sigma-Merck)
- Cerium(IV) sulfate (10294-42-5, 98%, $Ce(SO_4)_2 \cdot 4H_2O$, Sigma-Merck)
- Glacial acetic acid (64-19-7, 99%, CH_3COOH , Sigma-Merck)
- Nitric acid (7697-37-2, 68%, HNO_3 , VWR)
- Sulfuric acid (7664-93-9, 95-97%, H_2SO_4 , Honeywell-Fluka)

- Tetrafluoroterephthalic acid (652-36-8, 97%, C₈H₂F₄O₄, Fluorochem)

2.3 Analytical Methods and Theory

2.3.1 Nuclear Magnetic Resonance (NMR) Spectroscopy

Equipment

¹H, ³¹P, ¹³C, and HSQC NMR spectra were recorded on a Bruker Avance III 500 MHz instrument. All chemical shifts are reported in ppm and coupling constants are reported in Hz.

Theory

It is not unreasonable to say that NMR spectroscopy is one of the most important tools available to organic chemists for the purpose of structure elucidation. Despite the power and broad applicability of the technique, it is most often used in tandem with other techniques, including Fourier-transform infrared (FT-IR) spectroscopy and mass spectrometry, in order to get a better understanding of the material being studied.

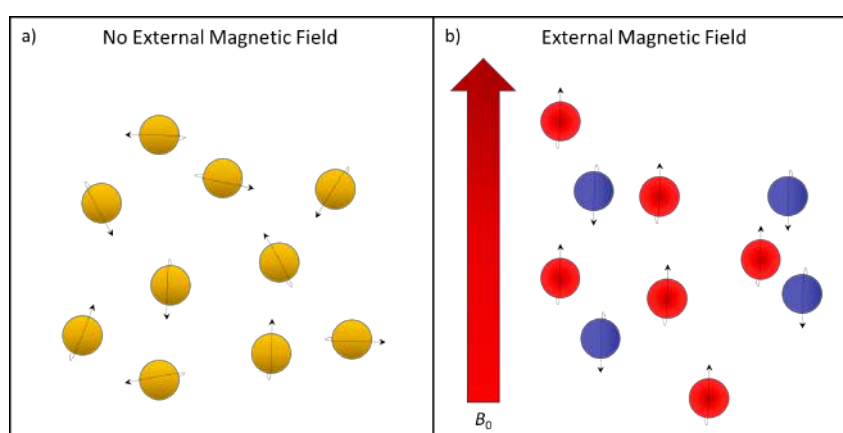


Figure 2.1: a) In the absence of an external magnetic field, nuclei are randomly oriented. b) When an external magnetic field is applied, the nuclei take up a specific orientation, either with (red) or against (blue) the external magnetic field.

The technique looks specifically at the interaction between electromagnetic radiation and the nuclei of atoms, examples of which are ¹H, ¹³C, ¹⁵N, ¹⁹F, and ³¹P, notably all

containing nuclei with an odd number of protons and/or neutrons. It is this possession of this kind of nuclei which is the origin of the quantum mechanical property known as *nuclear spin*, whereby a magnetic field is generated by the nuclei, and is more often referred to as the magnetic moment. In the absence of an external magnetic field (B_0), these nuclei adopt random orientations, but align when a magnetic field is applied (see Figure 2.1). The alignment of these nuclei will either be with the applied magnetic field, known as the alpha (α) spin state, or against it in the higher energy beta (β) spin state, the former of which is favourable as it has a lower energy. The energy gap between the two states is relatively small, and requires the use of a very strong magnetic field to increase the energy difference to a level that can be detected.¹⁻⁴

It is the absorption of electromagnetic radiation, most often in the radio wave region, which cause nuclei to flip from the α to the β state and is generally referred to as *resonance*, which is where the term *nuclear magnetic resonance* originates. The difference in energy between these states is entirely dependent on the nuclei and the strength of the magnetic field applied. In terms of the applied magnetic field, the stronger the magnetic field, the larger the energy difference between the two spin states and therefore, higher-frequency, or energy, radiation will be required to induce the resonance state.

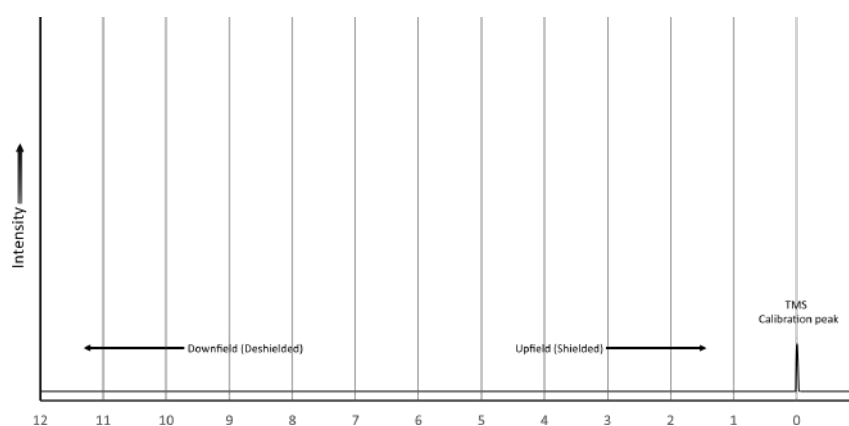


Figure 2.2: Typical NMR spectrograph, displaying intensity of the y-axis and magnetic field strength, in ppm, on the x-axis.

Another important effect to note here is *shielding*, which refers to the local (induced) magnetic fields generated by electrons in the presence of an external magnetic field,

whereby the induced field opposes the external field. This induced field effectively lowers the influence of the magnetic field on the nucleus by a relatively small degree, thus it is said that the nucleus is *shielded* from the external magnetic field. Since nuclei often occupy environments with differing electron densities, the shielding effect can vary. Environments with more electron density are said to be *shielded*, while environments with lower electron density are said to be *deshielded*, and typically exist when the neighbouring atom is more electronegative. This is something that arises from inductive effects, whereby electronegative atoms withdraw electron density.

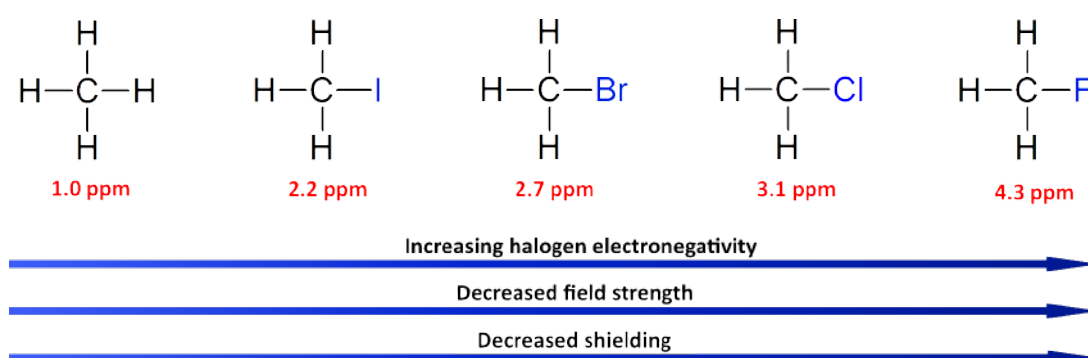


Figure 2.3: Chemical shifts of halomethanes up the halogen group in order of increasing electronegativity, decreasing field strength, and decreased shielding.

Typical NMR spectra are displayed as a chart which plots signal intensity against magnetic field strength (see Figure 2.2). Moving to the left of the chart is referred to as downfield; signals found here will represent nuclei which have less electron density and thus are less shielded, and require lower field strength to achieve resonance. Moving to the opposite side of the chart is referred to as upfield; signals found here represent nuclei that are more shielded as they have more electron density, and thus require higher field strength to achieve resonance. Typical information that can be obtained from an ¹H NMR spectrum is:

- **The number of different electronic environments** - determined by looking at the number of signals present, though it should not be confused for the total number of environments, since some may be chemically equivalent.

- **The type of electronic environment (i.e. the electron density)** - determined by looking at the location of the signals.
- **The number of neighbouring protons** - determined by looking at the shape, or number of peaks, and splitting patterns.
- **The number of contributing protons** - determined by integrating the area beneath the peak and comparing the relative peak integrals.

2.3.2 Fourier-Transform Infrared (FT-IR) Spectroscopy

Equipment

Thermo Scientific Nicolet iS10 FT-IR-ATR Spectrometer.

Theory

Infrared (IR) spectroscopy is another one of the most useful techniques in the organic chemist's toolbox, providing vital indicators for which functional groups are present on a molecule, and is often used in conjunction with other techniques like NMR and mass spectrometry. NMR for example, gives a lot of valuable information about the carbon skeleton, and can prove useful in elucidating the presence of some carbon-containing functional groups, such as carbonyl and alkene groups, both of which can be seen in ^{13}C NMR spectra. For other functional groups, NMR can only go so far as to indicate their presence in the way that these functional groups affect the chemical shifts of the H and C atoms around them.

The IR region of the electromagnetic spectrum runs from 0.7 μm to 1 mm, though the region considered for IR spectroscopy lies in the mid-IR region between 2500 nm and 25,000 nm, but is most often referred to in terms of wavenumbers ($\tilde{\nu}$), which translates to a range of 4000 - 400 cm^{-1} , and is simply the reciprocal of wavelength, $\tilde{\nu} = 1/\lambda$.

Unlike NMR, which looks at the electronic environments of nuclei, IR spectroscopy looks instead at the bending and stretching of bonds on absorption of infrared

radiation. IR spectroscopy takes advantage of the fact that molecules exist in quantised energy states, which is to say that the energy of a molecule is not a continuous variable. Take a C-H bond for example, which vibrates at a specific frequency, stretching and contracting like a spring. When this bond is irradiated with IR radiation, it will only absorb radiation that matches the frequency at which the bond is vibrating, and the result of this absorption is an increase in the amplitude of the vibration.¹⁻⁴

Table 2.1: Typical IR absorptions of common functional groups. Adapted from [3].

Functional Group	Absorption (cm ⁻¹)	Intensity	Functional Group	Absorption (cm ⁻¹)	Intensity
Alkane			Amine		
C-H	2850-2960	m	N-H	3300-3500	m
Alkene			C-N	1030-1230	m
=C-H	3020-3100	m	Carbonyl		
C=C	1640-1680	m	C=O	1670-1780	s
Alcohol			Carboxylic acid		
O-H	3400-3650	s, b	O-H	2500-3100	s, b
C-O	1050-1150	s	Nitrile		
Arene			C≡N	2210-2260	m
C-H	3030	w	Nitro	1540	s
Aromatic	1660-2000	w	NO ₂	1540	s
ring	1450-1600	m	Alkyl Halide		
Alkyne			C-Cl	600-800	s
≡C-H	3300	s	C-Br	500-600	s
C≡C	2100-2260	m			

Typical IR spectra can often appear quite complex, which can be both a blessing and a curse. The complexity of IR spectra can often mean that only pure samples can be analysed. Since organic molecules already have dozens of absorptions due to an equivalent number of vibrational modes, analysing non-pure samples would only increase this complexity, thus decreasing the ease with which the spectra can be interpreted. On the other hand, the complexity of these spectra make them quite unique to the corresponding molecule, and can thus be used as fingerprints for identification of said molecule, hence the name "fingerprint region", which refers to the 1500 to 400 cm⁻¹ region of the spectrum, which is the most complex region of the spectra.

2.3.3 Ultraviolet–visible (UV-Vis) Absorption Spectroscopy

The interaction of electromagnetic radiation with matter has long been used as a way to obtain information about the properties of said matter. Here, we discuss the radiation from the ultraviolet and visible ranges of the spectrum, which are approximately 200 - 400 nm and 400 - 750 nm, respectively. UV-Vis spectroscopy is a technique that exploits the electronic state of matter. Since all materials and their components contain discrete energy levels, which are said to be quantised, the promotion or excitation of an electron in the ground state to an excited energy state is also a quantifiable property. Another thing to be said here is that in order to achieve this excitation of the valence electron into an excited energy state, the wavelength or energy of the radiation/photon must directly translate to the energy gap between the ground and excited state of the electron, else the transition will not take place. The electrons don't stay in this state for very long, possibly as short as 10^{-16} s, with most of the energy being lost as heat and some emitted as lower energy radiation, a process known as fluorescence.⁵⁻⁷

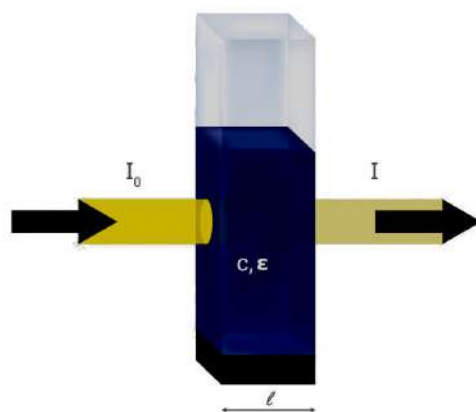


Figure 2.4: A visual representation of the Beer-Lambert law, showing the absorption of radiation as dependent on the factors described in Equation 2.2.

When considering the use of UV-Vis spectroscopy, what usually comes to mind are absorption and transmittance, whereby the former refers to the amount of radiation absorbed by the sample and the latter to the amount of radiation that successfully passes through. It is clear then that both measurements have some interrelation since they both consider light either passing or not passing through a sample, as shown in

Figure 2.4. The relationship between these measurements should be even more evident when you look at equations 2.1 and 2.2.

$$\text{Transmittance } (T) = \frac{I}{I_0} \quad (2.1)$$

$$\text{Absorbance } (A) = \varepsilon cl = \log_{10} \left(\frac{I_0}{I} \right) \quad (2.2)$$

I_0 = Intensity of incident light

I = Intensity of light leaving the sample cell

c = Molar concentration

l = Path length of the cell (cm)

ε = Molar absorptivity

Diffuse Reflectance Spectroscopy

A discussion of absorption and transmission measurements in UV-Vis spectroscopy has been presented above, though it omits a somewhat less commonly used measurement known as reflectance, specifically diffuse reflectance. This kind of measurement looks at the scattered radiation of powders and other samples with rough surfaces. Measurements here can be quite a bit more complex than for absorption and transmission, and require a few additions to the instrument in order to be obtained. What is being referred to here is what is known as an integrating sphere. The purpose of this sphere is to direct, through reflection, diffusely reflected light towards a detector, while blocking specular reflections, which are those that exit at the same angle as the incident ray. This can be achieved in two ways: a) the sample is attached via an external sample port which is tilted as if to aim at the detector, with

a blocking mechanism; or b) by placing the sample with no tilt so that the specular reflection leaves the sphere via the same port it entered.⁸

Band-gap Estimation using Kubelka-Munk Theory

The initial application for Kubelka-Munk theory, and the reason for its existence, was to be used in the modelling of paint film appearance.⁹ Since then, it has been applied in many areas for similar reasons. In this case, it has been used to estimate the band gap of powder samples which, in terms of this model, are considered to be infinitely thick layers.¹⁰

In order to estimate the band gap of a material the Tauc method is employed, though this requires absorption spectra. In order to achieve this, the Kubelka-Munk equation is employed to transform the reflectance data. An assumption made by the Tauc method is that the energy-dependent absorption coefficient (α) can be expressed by Equation 2.3.

$$(\alpha \cdot hv)^{1/n} = B(hv - E_g) \quad (2.3)$$

We see here the familiar terms h and v , which represent the Planck constant and frequency, respectively. We also see B which represents the proportionality constant and E_g which represents the band energy gap. The symbol n , which will be explored later, represents the different electronic transitions, with a different value for each. By applying the Kubelka-Munk function ($f(R_\infty)$), reflectance spectra can be transformed to obtain the absorption coefficient.

$$\alpha = f(R_\infty) = \frac{K}{S} = \frac{(1 - R_\infty)^2}{2R_\infty} \quad (2.4)$$

In this equation, the R_∞ component represents the ratio of the sample reflectance against a high reflectance reference sample ($R_\infty = R_{sample}/R_{reference}$), such as

polytetrafluoroethylene (PTFE). The symbols K and S represent the absorption and scattering coefficients, respectively. If we substitute this function into equation 2.3, we obtain the following:

$$[f(R_\infty) \cdot hv]^{1/n} = B(hv - E_g) \quad (2.5)$$

It should be noted here that n represents the same electronic transitions referred to previously for equation 2.3, which are:

- Direct-allowed, $n = 0.5$
- Direct-forbidden, $n = 1.5$
- Indirect-allowed, $n = 2$
- Indirect-forbidden, $n = 3$

Using the appropriate value for n , this new equation can then be plotted against photon energy (eV) to achieve the Kubelka-Munk absorbance plot (a.k.a. Tauc plot) for the sample. If the appropriate value for n is not initially known, the next step should make it clear. Having obtained the quasi-absorption curve for each of the electron transitions, for any which are present in the material, there will be a linear section of the curve in the negative direction. Extrapolating this linear section towards the x -axis allows for the approximation of the band gap at the point where the line intersects with the x -axis, giving a value in eV, which can be used as the approximation of the optical band gap energy. Further analysis using either X-ray photoelectron spectroscopy (XPS) and ultraviolet photoelectron spectroscopy (UPS), or a combination thereof, can also be used to directly measure the energy gap between the valence and conduction bands.

2.3.4 Mass Spectrometry

Equipment

All mass spectral analyses were carried out at the National Mass Spectrometry Facility (NMSF), Swansea University Medical School, and processed using vendor XCalibur software.

iPr₄BPA, iPr₄DPC, and iPr₄DPPA samples were prepared for analysis by solvation in 350 μ L MeOH and further 1:1000 dilution in MeOH with 30 mM ammonium acetate (NH₄OAc). 20 μ L was aliquoted into a 96 well plate and sprayed via an Advion NanoMate in positive ion mode at +1.5 kV into the API source of a Thermo LTQ Orbitrap XL. API source conditions were capillary temperature 200 °C, capillary voltage 41 V and tube lens voltage 150 V.

H₄BPA, H₄DPC, and H₄DPPA samples were prepared for analysis by solvation in 350 μ L MeOH and further 1:1000 dilution in MeOH with 1% diethylamine (DEA) to promote deprotonation. 20 μ L was aliquoted into a 96 well plate and sprayed via an Advion NanoMate in negative ion mode at -1.5 kV into the API source of a Thermo LTQ Orbitrap XL. API source conditions were capillary temperature 200 °C, capillary voltage -32 V and tube lens voltage -100 V.

Theory

Mass spectrometry, perhaps more so than some of the other techniques discussed in this chapter, is often used as a complementary technique, such as in organic synthesis to confirm the structure of compounds in conjunction with FT-IR, UV-Vis, and NMR; or as a combined technique, such as in LC-MS and GC-MS, whereby complex mixtures can be separated through chromatography and individual components can be assessed using mass spectroscopy without interference from other components in the parent mixture. Some of the ideas behind mass spectrometry date back to the late 1800s when the mass-to-charge ratio of the electron was determined. It was then in the early 1900s

that the existence of isotopes was confirmed when neon-22 was discovered in samples of neon-20. The first mass spectrometer was actually built in 1918, but did not become a mainstream technique until well into the second half of the century.^{6,11}

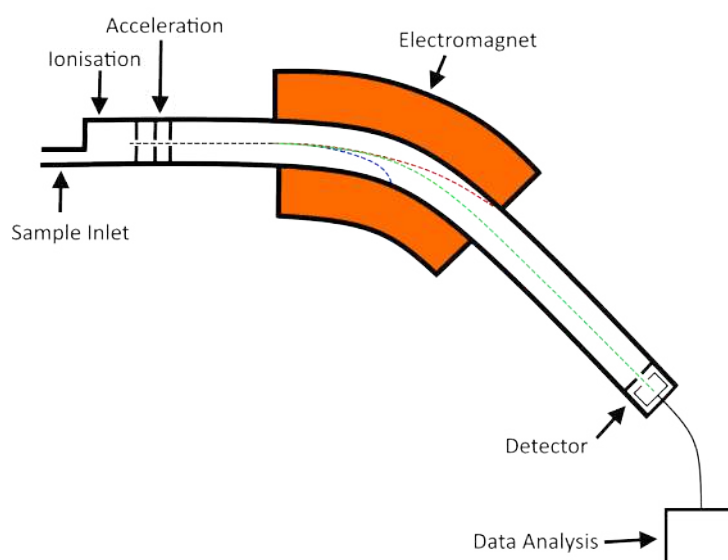


Figure 2.5: A simplified schematic diagram of a typical mass spectrometer.

In its basic form, a mass spectrometer can be split up into a small number of component parts or processes, as shown in Figure 2.5, though realistically, mass spectrometers are considerably complex than shown here. The first part of the process involves sample injection, which is most commonly achieved in one of two ways. The first is through direct injection of the sample into the instrument, for which solids, liquids, and gases can be used. Generally, gases and volatile liquids and solids require a relatively simple inlet system, while less volatile compounds will require the use of an oven to increase the vapour pressure. Regardless of the sample inlet used, once the sample is sufficiently volatilised, the sample vapour can pass through a small pin hole called the molecular leak, which directs the sample into the ionisation chamber as a steady stream. The second method involves coupling the technique with either gas chromatography (GC) or high-performance liquid chromatography (HPLC), whereby mass spectrometry essentially plays the role of detector. For the former, the coupling is relatively simple since the sample is already in the gas/vapour phase, and all that is necessary is that the gas stream is passed over the molecular leak.

Following injection, the volatilised sample is transferred through the molecular leak into the ionisation chamber where the sample is ionised by one of a series of techniques. The ionisation method used for the analysis presented in Chapter 3 of this thesis used electrospray ionisation, so the focus will be given here, though other ionisation techniques include:

- Electron ionisation - this technique employs an electron beam emitted from a filament heated to a few thousand degrees Celsius. This beam is directed towards the stream of molecules that are entering the chamber through the molecular slit, resulting in collisions that lead to the formation of cations. The positively charged species are then directed through a series of accelerating and focusing steps before arriving in the mass analyser (electromagnet) as a uniform stream of cationic species.
- Chemical ionisation - this technique employs a preionised gas which is combined in great excess with the sample molecules, resulting in the ionisation of the sample through mechanisms such as proton transfer, electron transfer, and adduct formation.
- Desorption ionisation - the previous two techniques are generally preferred for volatile compounds. For the analysis of larger non-volatile compounds, one of the following techniques can be used: secondary ion mass spectrometry (SIMS), first atom bombardment (FAB), and matrix-assisted laser desorption ionisation (MALDI). Generally, the sample is either suspended or dispersed in a matrix and subsequently exposed to a beam of high energy particles. The collision of these high energy particles with the sample molecules results in some of the sample molecules ejecting from the surface of the matrix.

ESI is another useful technique for the analysis of large non-volatile compounds. The technique works by dissolving the sample in an appropriate solvent, after which the resulting solution is sprayed from a fine capillary into a heated chamber, as shown in Figure 2.6. The capillary from which the solution is sprayed also has a high

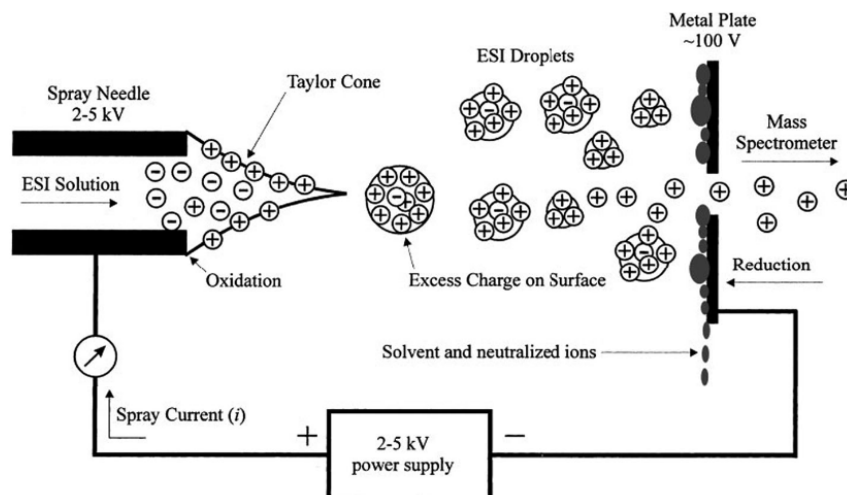


Figure 2.6: A simplified schematic diagram for the electrospray ionisation process. Reprinted from reference [12] ©2002 John Wiley & Sons, Inc.

voltage potential passed across its surface, which results in small charged droplets being sprayed into the chamber. Due to a counter flow of a drying gas (e.g. N_2), solvent molecules evaporate from the droplet and subsequently the charge density of the droplet increases. At a certain point, this charge density is too much and the larger droplets break up into smaller droplets in a process that continues until charged solvent-free sample molecules are left in the chamber. One of the main advantages of the technique is that it can be used in either positive or negative mode, whereby the sample ions can form either cations or anions, respectively, through the reversal of the high voltage potential applied across the capillary.

Following ionisation, the ionised sample passes through the mass analyser, and just as in the ionisation step, there are a few types to choose from. The analyser employed for the work in this thesis was the LTQ Orbitrap XL, which is simply a type of quadrupole mass analyser. The other three types of analysers are:

- Magnetic mass analyser - This is the most typical setup that most people think of with regards to mass analysers, and is what is shown in Figure 2.5. Using this technique, sample ions are passed through a magnetic field, following a curvature of a specific radius. The size of this radius is determined by the mass-to-charge (m/z) ratio, whereby the larger this ratio, the larger the radius

of curvature. Since only ions with specific m/z ratio are able to pass at one time, the strength of the magnetic field is also varied in order to scan the full range of m/z ratio.

- Double-focussing mass analyser - Incorporating all of the features described for the magnetic mass analyser, this type of analyser adds an additional step where the sample is also passed through an electric field to ensure all ions are travelling at the same velocity. This increases the resolution by more than a factor of 10, and it is generally the case that magnetic mass analysers in use today almost always include this additional step.
- Time of flight (TOF) mass analyser - Unlike the previous method, this one takes advantage of the idea that ions created using the same kinetic energy will have a velocity that varies depending on the mass of the ion, i.e. the lighter the ion, the higher its velocity, and the sooner it hits the detector relative to ions with larger masses.

Quadrupole mass analysers employ four rods which are parallel to the ion beam, as shown in Figure 2.7. The application of direct-current (DC) and a radiofrequency (RF) to the rods results in the generation of an oscillating electrostatic field between the rods.

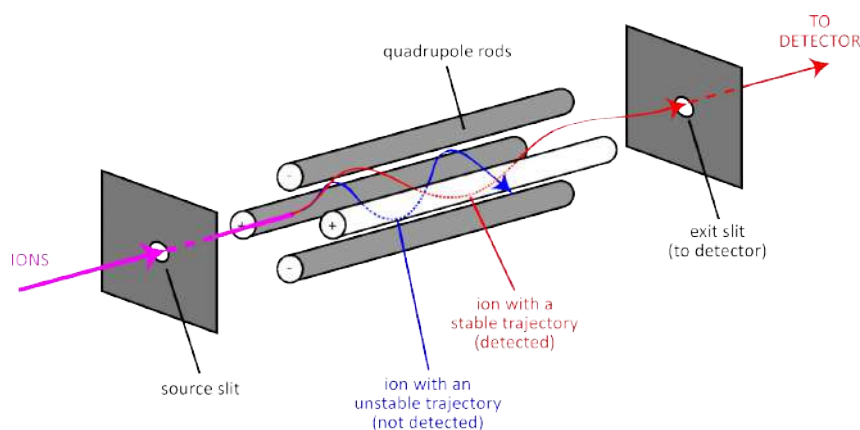


Figure 2.7: A simplified schematic diagram for a quadrupole mass analyser.¹³

Ions passing through this electrostatic field also develop an oscillation, depending on

their m/z ratio. Ions which have the correct m/z ratio develop a stable corkscrew-like oscillation, allowing them to pass through the analyser and into the detector, while those with an incorrect m/z ratio develop an unstable oscillation and are unable to pass through the analyser. Similarly to the magnetic mass analyser, it is necessary to scan the m/z ratio range. The analyser used for the work in this thesis is called a quadrupole ion trap analyser, which operates on the same basic principles described above, the difference being the layout of the quadrupoles. In this case, the sample inlet and the exit slit are themselves two of the poles, or endcap electrodes, between which we now have a doughnut shaped ring electrode, to which the RF frequency is applied. Using this setup negates the need to scan the m/z ratio range as all of the ions are present in the trap simultaneously. It is the sweeping of the RF that then results in the destabilisation of ion oscillations and subsequent ejection of the ion from the trap and towards the detector.

2.3.5 Powder X-ray Diffraction (PXRD) and Crystallography

Equipment

Qualitative PXRD patterns were collected in the $2\theta = 4 - 30$ range with a Bruker D8 Discover diffractometer working in reflection geometry and equipped with a LYNXEYE XE detector, using the Cu $K\alpha$ radiation. The X-ray tube was operated at 40 kV and 40 mA.

The *in situ* study described in Chapter 5 took place at beamline P23 (DESY, Hamburg) and was carried out with the recently developed **SynRAC** (Synchrotron-based Reaction cell for the Analysis of Chemical reactions) unit.¹⁴ The reaction vessel, a simple 11 mL Pyrex reaction vial, is accommodated inside an aluminium casing and is surrounded by a heating mantle made from copper-galvanised heating wires, which allows for fine control of the temperature up to 180 °C. An electromagnetic stirrer is also incorporated for sample agitation up to 1200 rpm.

Basic Crystallography

Before discussing the use of PXRD for structural analysis, presented here is an introduction to the basic principles of crystallography. A crystalline material can be reduced to a three dimensional lattice. Crystals, simply put, are made up of an array of repeating units which can be achieved simply through translation, a type of symmetry present in all crystalline materials. A common mistake made when first approaching this topic is the assumption that the lattice points describe the position of atoms within the crystal structure, which is not the case. In order to describe the actual atomic structure, we need to identify the repeating units, i.e. the unit cell. In three dimensions, this unit cell can be described in terms of the lengths (a , b , and c) and the angles (α , β , and γ) between these. Resulting from the different arrangement of these crystallographic properties that make up the unit cell, are the seven crystal systems, which can be subdivided into the 14 Bravais lattices, as shown in Table 2.2. A visual representation of these can be found in Figure 2.8.^{15,16}

Table 2.2: The seven crystal systems and the fourteen corresponding Bravais lattices, and minimum symmetry requirements.

Crystal System	Bravais Lattice	Lengths & Angles	Minimum Symmetry
Cubic	P, I, F	$a = b = c, \alpha = \beta = \gamma = 90^\circ$	4 threefold rotational axes
Tetragonal	P, I	$a = b \neq c, \alpha = \beta = \gamma = 90^\circ$	1 fourfold rotational axis
Orthorhombic	P, I, C, F	$a \neq b \neq c, \alpha = \beta = \gamma = 90^\circ$	3 twofold rotations and/or mirrors
Trigonal	P	$a = b \neq c, \alpha = \beta = 90^\circ, \gamma = 120^\circ$	1 threefold rotational axis
Hexagonal	P	$a = b \neq c, \alpha = \beta = 90^\circ, \gamma = 120^\circ$	1 sixfold rotational axis
Monoclinic	P, C	$a \neq b \neq c, \alpha = \gamma = 90^\circ \neq \beta \geq 90^\circ$	1 twofold rotation and/or mirror
Triclinic	P	$a \neq b \neq c, \alpha \neq \beta \neq \gamma \neq 90^\circ$	None

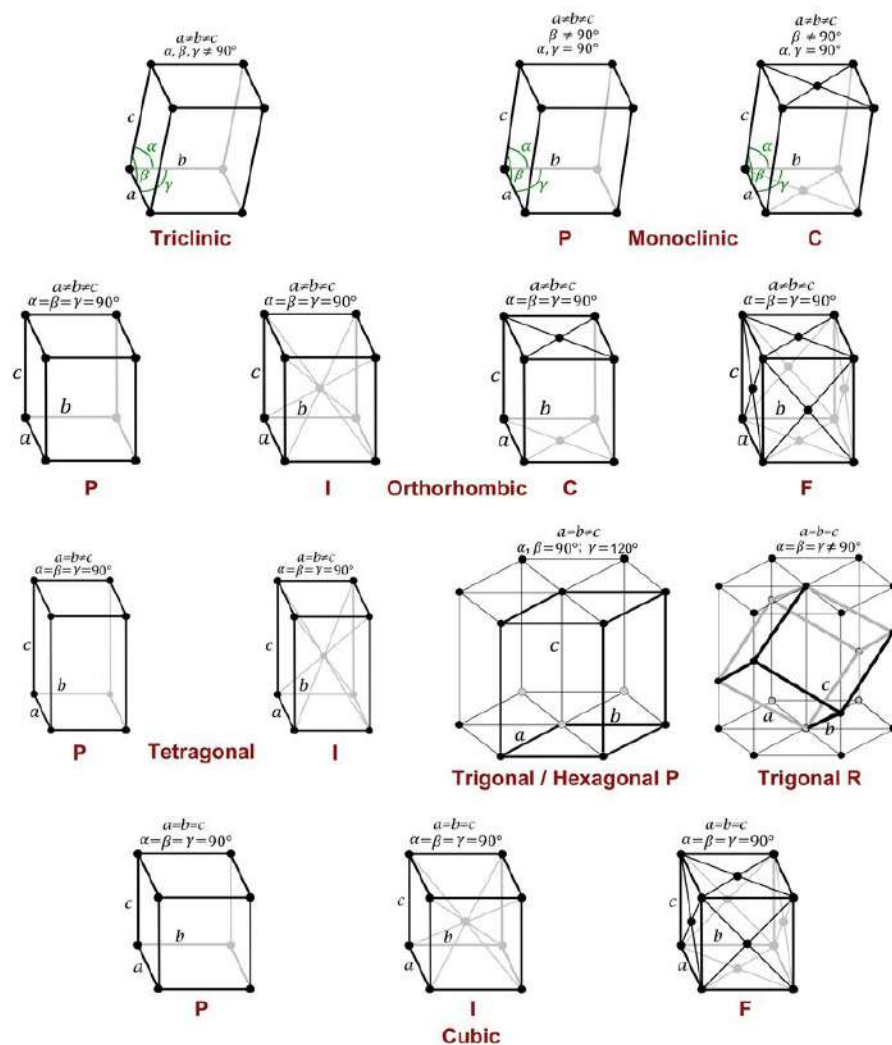


Figure 2.8: Visual representations of the fourteen Bravais lattices and corresponding crystal systems. Reproduced under a creative commons licence, CC BY-NC 4.0, from "Crystallography-Cristalografia", by Martin Martinez-Ripoll (Department of Crystallography & Structural Biology). <https://www.xtal.iqfr.csic.es/Cristalografia/>

These Bravais lattices can then be further subdivided in terms of the different symmetry elements present, of which there are 32 in total. The combination of these symmetry elements with the fourteen Bravais lattices gives the 230 space groups. Detailed descriptions of these space groups can be found in the *International Tables of Crystallography*.¹⁷ A further way to describe crystal lattices is in terms of their lattice planes and directions, often referred to as Miller indices. These are generally described by three parenthesised numbers, (hkl) , which refer to the axes that the plane intersects, i.e. a , b , and c , respectively. Figure 2.9 shows a few basic examples of these lattice

planes.

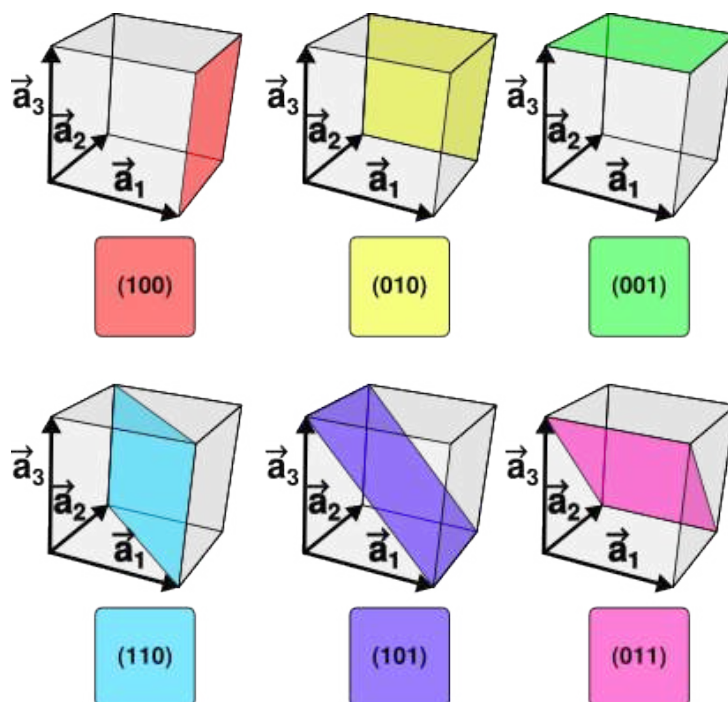


Figure 2.9: Examples of Miller indices, whereby a_1 , a_2 , and a_3 are the three vectors that define the unit cell. Reproduced under a creative commons licence, CC BY 3.0. https://en-academic.com/pictures/enwiki/77/Miller_Indices_Felix_Kling.svg

Powder X-Ray Diffraction

As with NMR spectroscopy in organic chemistry, X-ray diffraction (XRD) is one of the most powerful techniques in the toolkit of the materials chemist and is routinely used to perform structural analysis on crystalline materials, including phase analysis and structure solution. The discovery of X-ray diffraction took place in the early 20th Century under the supervision of Max Von Laue with help from Paul Peter Ewald, though his contributions went mostly uncredited. The development of the technique we know today took place a little later in the century in the hands of William Henry Bragg, and later his son William Lawrence Bragg, though it wasn't until the last few decades that the techniques became the workhorse that it is now considered.¹⁵ Generally, we can think of XRD as being two quite distinct techniques, which are powder XRD (PXRD) and single-crystal XRD (SCXRD). The main difference between

the two is that the former takes measurements on a bulk polycrystalline material, while the latter, as its name suggests, looks at a single crystal.

On a typical lab diffractometer, the process of generating X-rays begins with electrons, which are emitted when a suitable filament is heated through electromagnetic induction. These electrons are directed towards a metal target (Cu, Mo, Fe, Cr) at high velocity through an X-ray or cathode tube, at an electrical potential of between 20 - 60 kV. When the electron reaches the water cooled target, the majority of the energy is lost to heat, but a portion of it leads to the generation of X-rays. This X-ray generation occurs when the electron beam interacts with atoms on the target, causing the ejection of an electron from a lower energy orbital. This creates a vacancy that can be filled by an electron in a higher energy orbital, which causes radiation to emit at specific frequencies and wavelengths. Due to the multiple possible transitions, the emitted radiation often consists of an array of different wavelengths in the X-ray range, though this is not true for lighter elements which release lower energy radiation. It is also possible to select for specific wavelengths by passing these X-rays through a monochromator, causing the selected wavelengths to diffract while the other wavelengths will pass straight through. The X-ray beam is then directed at the target, i.e. a (micro)crystalline sample, whose periodic structure is responsible for the diffraction effect. The process is described by Bragg's Law (See Equation 2.6), which tells us that constructive interference of diffracted X-rays occurs when specific conditions are fulfilled.^{15,18}

$$n\lambda = 2d_{hkl} \sin \theta \quad (2.6)$$

In the Bragg equation, n is an integer, λ is the wavelength of the incident radiation beam, d is the spacing between the crystallographic planes, and θ represents the angle between the crystallographic planes and the incident radiation beam. Essentially, we say that in order for constructive interference to occur, the difference in path length

($2ab$ in Figure 2.10) between two waves diffracted by neighbouring crystallographic planes at distance $d(hkl)$, must be an integer (n) multiple of the wavelength (λ) of the incident radiation. Based on trigonometry, $2ab$ can be written as $2d_{hkl} \sin \theta$. It should be noted that this is a rather simplistic explanation of X-ray scattering, and what actually happens and the assumptions made are more complex, which is where you approach the different theories of diffraction, such as kinematical and dynamical. The former assumes that the diffracted beam will not undergo secondary or higher order scattering. The assumptions made to explain this refer to misalignment of the individual crystallites with a larger crystal and the small size of said crystallites, which simply means there is a negligible interaction between the X-ray and additional crystallites after the primary diffraction event. In general, this constructive interference is more prominent at lower scattering angles, and get weaker as this angle increases.

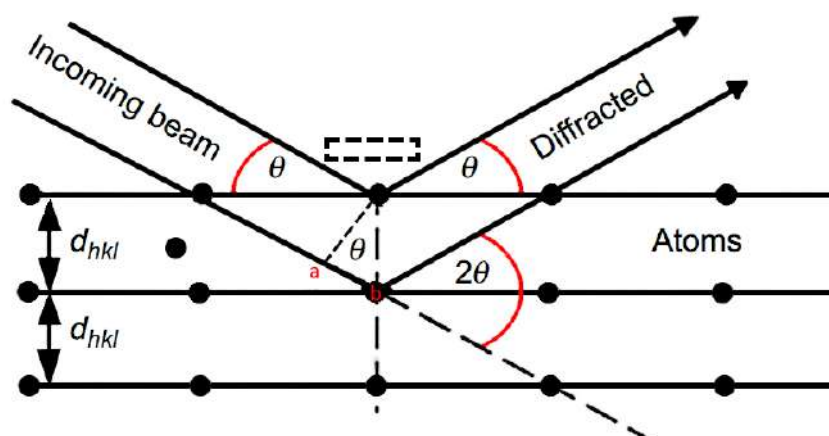


Figure 2.10: A representation of the diffraction process on the atomic scale.

2.3.6 Gas Adsorption Analysis

Equipment

Gas sorption analysis was performed using the Quantachrome NOVA 2000e Surface Area and Pore Size Analyser in helium mode at 77 K (N_2) and 273 K (CO_2 , N_2). Samples were activated under vacuum between 120 - 140 °C for four hours prior to analysis. All subsequent data treatment was carried out using the Quantachrome NovaWin

software. Pore size distributions were obtained using the non-local density functional theory (NLDFT) method with the calculation models based on N₂ at 77 K on carbon and CO₂ at 273 K on carbon.

Theory

Gas sorption analysis is a rather broad term but generally, and particularly in terms of this thesis, it refers to measurements which are used to obtain information such as surface area, pore size distribution, and the ability of materials to adsorb certain species, e.g. CO₂ and N₂. Generally, the material on which adsorption is taking place is called the adsorbent, while the gas to be adsorbed is the adsorptive in its gas state, and the adsorbate in its condensed state. To save confusion, the latter term, adsorbate, will be used from this point.

Nitrogen tends to be used as the standard adsorbate in most laboratories for these measurements which are carried out at 77 K, i.e. the boiling point of nitrogen, unless other adsorbates are required for specific applications, though argon is the adsorbate recommended by IUPAC for typical pore size and surface area measurements. It's easy to see why this is the case since argon, unlike nitrogen, is monoatomic, which means its orientation when packing into a material is consistent, and thus eliminates any uncertainty in the surface area measurements caused by ambiguous cross-sectional area. Argon also lacks any form of magnetic moment, e.g. dipole or quadrupole, which means there is little chance for interaction with functional groups or ions, which can be a risk with other adsorbates. Argon also has the advantage of shifting the filling of micropores to higher relative pressures, which will generally mean that analysis times are shorter, and also provides an improvement to the kinetics since analysis is generally carried out at slightly higher temperatures. Despite this, nitrogen is still very much the adsorbate of choice for these measurements due to the ease of access to liquid nitrogen in general laboratories.¹⁹

Adsorption processes can generally be defined as being either physisorption or

chemisorption. The latter of these, chemisorption, most often involves the formation of a chemical bond between the adsorbate and the adsorbent, which implies that an activation energy must be met in order for bond formation to occur. The formation of a chemical bond also means that the adsorbate has a very small chance to migrate about the surface of the adsorbent. Chemisorption will often occur when an adsorbent material has active sites present, whereby these active sites are the positions where chemical bond formation will take place. Physisorption on the other hand, as implied by the name, refers to a physical interaction between the adsorbent and adsorbate due to the Van der Waals forces, and does not lead to any bond formation. It can also be said that physisorption is a reversible process, which allows for the study of both adsorption and desorption, unlike chemisorption, whereby the formation of chemical bonds makes desorption very difficult to study.

Conveniently, the types of information that can be derived using gas sorption analysis can all be obtained from the same experiments by applying different mathematical treatments to the data. The output of gas sorption experiments is what is referred to as an isotherm, which in itself, can reveal a lot of useful information, since the shape of these isotherms is highly dependent on the properties of the material being studied and its porosity. Isotherms generally show the relationship between the pressure of the adsorbate and the amount adsorbed at certain temperatures, and can generally be subdivided into six types as classified by IUPAC,²⁰ see Figure 2.11.

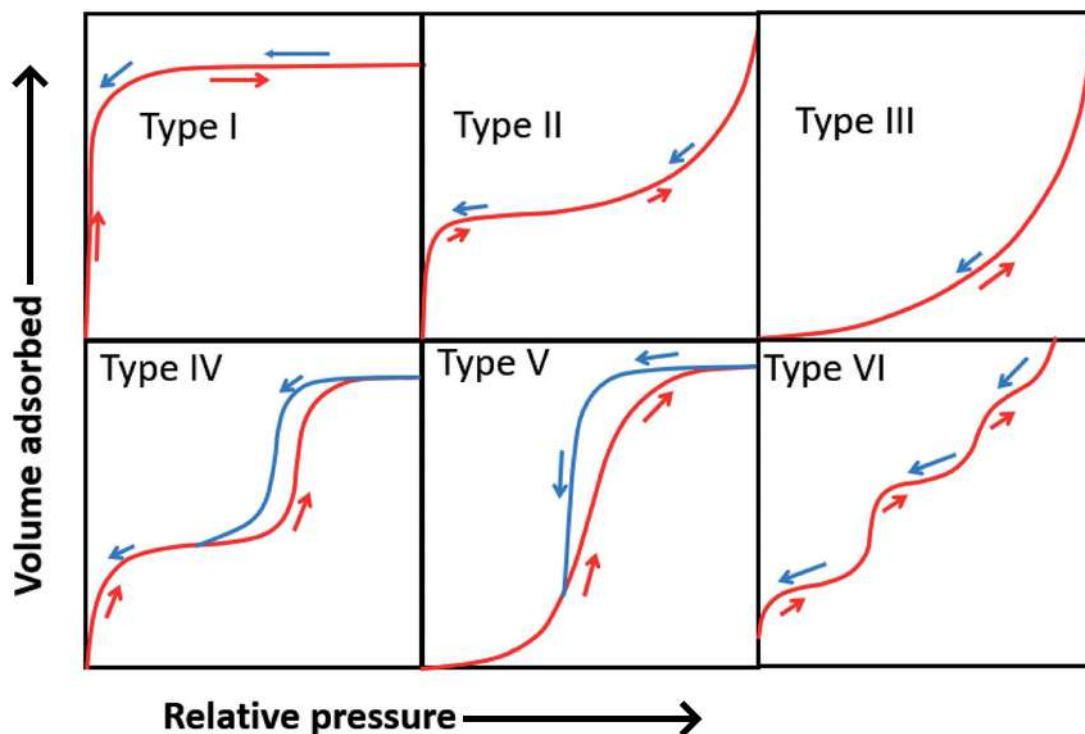


Figure 2.11: Isotherm types as classified by IUPAC.²⁰

By looking at the isotherm alone and determining which type it fits, you can already make a few predictions. A type I isotherm, for example, is indicative of a microporous material ($<20 \text{ \AA}$) and is concave to the x -axis. It is also common to see a saturation point or plateau, at which point no further adsorption takes place. The degree of concavity and the point where saturation occurs also gives us clues as to the pore size distribution, where more concave isotherms where saturation is reached early on indicating the presence of mainly small micropores, while less concave isotherms where saturation occurs at higher pressures indicating the presence of larger micropores and potentially small mesopores ($20\text{-}500 \text{ \AA}$). The type II isotherm is indicative of adsorption on non-porous or macroporous materials ($>500 \text{ \AA}$), whereby the initial sharp increase and levelling off in adsorption is due to the formation of the monolayer while the subsequent part of the curve is due to multilayer adsorption. The type III isotherm signifies no monolayer formation, instead suggesting that adsorbed species are clusters at preferential adsorption sites, though it still indicates the material is either non-porous or macroporous. A type IV isotherm suggests that

the adsorbent material is mesoporous. Looking at the isotherm, the first part is caused by monolayer-multilayer adsorption within the mesopore, while the second part of the isotherm is due to pore condensation, whereby the adsorbate gas condenses into a liquid state within the pore before reaching the saturation pressure of the liquid. The hysteresis loop seen here is most often caused when a pore exceeds a system and temperature-dependent critical width, which is generally anything over 40 Å when N₂ is the adsorbate. The type V isotherm shows a relatively similar pattern to a type III initially, and is caused by weak interaction between the adsorbent and the adsorbate. The subsequent plateau is caused by pore filling. The type VI isotherm is quite specific to stepwise layer-by-layer adsorption onto highly ordered, non-porous surfaces.

Once this isotherm has been obtained, it can be treated with various mathematical models to obtain the previously mentioned information.

Surface Area Analysis

Obtaining surface area measurements can be important for a number of reasons, and correlates with a number of properties of materials, e.g. reactivity, separation potential, dissolution, etc. A number of different models have been developed for the purpose of obtaining surface area, but there are two that stand out. The first of these is the Langmuir model, which was developed by Irvin Langmuir in 1918 and looked at the adsorption of gases onto different surfaces, i.e. glass, mica, and titanium. This theory makes the assumption that an adsorbate forms a monolayer when it is adsorbed, or condenses, onto the surface of an adsorbent.²¹ On the other hand, this isn't necessarily the case, as suggested by Brunauer et al. in 1938, when they proposed their model, aptly named the Brunauer, Emmett, Teller (BET) model.²² While this model was based on Langmuir's work, it made the assumption that adsorbates formed multilayers, though the resultant surface area is still based on the adsorbed monolayer. This is often the reason that the calculated BET surface area will be smaller than the Langmuir surface area for the same material, since the Langmuir model

assumes that the adsorbate forms a monolayer on the adsorbent surface, thus covers a larger surface area, while the BET model assumes the formation of multilayers, whereby the same volume of adsorbate forms a multilayer, and thus doesn't cover the same surface area assumed by Langmuir. Since this work uses BET surface area, further discussion will only consider this theory. One of the assumptions made in BET theory is that the surface of the adsorbent material is homogeneous, allowing adsorption to occur equally and without preference at different sites. It also assumes a local equilibrium between the adsorbed species and those in the gas/vapour phase, whereby the rate of adsorption and desorption are the same. A third assumption says that the adsorption process is not limited by diffusion, rather it is limited by kinetics, with surface adsorption requiring the same energy as the heat of adsorption, while additional layers require energy input equivalent to the heat of condensation. It is also assumed that adsorbed species can act as a single sorption site for an additional adsorbate molecule, though there is no consideration given to other interactions, such as those between adsorbed species, or between gas/vapour phase molecules. The final assumption made is that the sorbent material, once at saturation pressure, is completely surrounded by the condensed liquid-phase adsorbate.

With these assumptions, and through the application of the Arrhenius equation, it is possible to calculate the kinetic rates based on the surface coverage, giving the generalised BET equation as shown in Equation 2.7, whereby v = volume of gas adsorbed, v_m = volume of the adsorbed monolayer, p = equilibrium gas pressure, p_0 = saturation pressure, and c = BET constant.

$$v = \frac{v_m c p}{(p_0 - p) \left[1 + (c - 1) \left(\frac{p}{p_0} \right) \right]} \quad (2.7)$$

Equation 2.7 can then be rearranged to give the linear function of p/p_0 , as shown in Equation 2.8.

$$\frac{1}{v \left[\left(\frac{p}{p_0} \right) - 1 \right]} = \frac{c - 1}{v_m c} \left(\frac{p}{p_0} \right) + \frac{1}{v_m c} \quad (2.8)$$

It is then possible to solve for the constants c and v_m , whereby c (= slope / intercept + 1) and v_m (= 1 / (slope + intercept)). Using the latter of these constants, we can then obtain the specific BET surface area (S) as follows:

$$S = \frac{v_m N A}{V m} \quad (2.9)$$

Here, in Equation 2.9 N = Avogadro's number, A = cross-sectional surface area of a single gas molecule (gas dependent), V = molar volume of gas at standard temperature and pressure (generally given as 22,400 cm³), and m = the mass of sample used for analysis. Removing the latter term for the mass of sample used, m , gives the total surface area.

2.3.7 Scanning Electron Microscopy (SEM)

Equipment

SEM micrographs were collected using a Hitachi TM3030Plus Tabletop Microscope with an acceleration voltage of 5 kV. The samples were deposited on conductive copper tape on an aluminium support and required no sputtering process.

Theory

SEM is a surface analysis technique which allows for two-dimensional topological visualisation of a sample. This is achieved through irradiation of the sample surface with an electron beam which results in the emission of secondary electrons which originate from the sample. These secondary electrons are then then picked up by the detector and eventually converted to an electrical signal which then allows for the visualisation of sample surface. As with optical microscopy, the magnification can be

adjusted as necessary, though it is done slightly differently. With an optical microscope, the magnification is adjusted by either swapping out the lens, or by adjusting the distance of the lens from the sample. With an SEM, the magnification is adjusted by changing the scan width of the electron beam, whereby, decreasing the scan width increases the magnification, which increasing the scan width decreases it.

2.3.8 Thermogravimetric Analysis (TGA)

Equipment

TGA was performed using the TA Instruments Q600 SDT Thermogravimetric Analyser under an argon flow of 100 mL/min at a heating rate of 5 °C per minute up to 1000 °C for ZrBPA and 1500 °C for ZrDPPA.

Theory

TGA is a thermal analysis technique whereby the mass of a sample is continuously measured over a range of temperature within a controlled environment, allowing for the extraction of information such as the fraction of volatile components, the thermal stability of the sample, as well as a range of more complex information.

2.4 References

1. J. Clayden, N. Greeves, S. Warren and N. Greeves, *Organic Chemistry*, Oxford University Press, Oxford New York, Second, 2012.
2. T. W. G. Solomons, C. B. Fryhle and S. A. Snyder, *Organic Chemistry*, Wiley, Hoboken, NJ, Eleventh, 2014.
3. J. McMurry, *Organic Chemistry*, Brooks/Cole, Cengage Learning, Belmont, CA, 2012.
4. D. R. Klein, *Organic Chemistry*, Wiley, Hoboken, NJ, Second, 2013.
5. S. Higson, *Analytical chemistry*, Oxford University Press, 2003.
6. D. L. Pavia, G. M. Lampman, G. S. Kriz and J. R. Vyvyan, *Introduction to spectroscopy*, Cengage Learning, Fifth, 2015.

7. M. Picollo, M. Aceto and T. Vitorino, "UV-Vis spectroscopy", *Phys. Sci. Rev.*, 2018, **4**, DOI: 10.1515/psr-2018-0008.
8. J. P. Blitz, in ed. F. M. Mirabella, John Wiley & Sons, 1998, ch. 1: Diffuse Reflectance Spectroscopy, pp. 185–219.
9. P. Kubelka and F. Munk, "An Article of Optics of Paint Layers", *Z. Tech. Phys.*, 1931, **12**, 593–601.
10. P. Makuła, M. Pacia and W. Macyk, "How To Correctly Determine the Band Gap Energy of Modified Semiconductor Photocatalysts Based on UV-Vis Spectra", *J. Phys. Chem. Lett.*, 2018, **9**, 6814–6817, DOI: 10.1021/acs.jpcclett.8b02892.
11. J. Thompson, *Mass spectrometry*, Pan Stanford Publishing, Milton, 2017.
12. N. B. Cech and C. G. Enke, "Practical implications of some recent studies in electrospray ionization fundamentals", *Mass Spectrom. Rev.*, 2001, **20**, 362–387, DOI: 10.1002/mas.10008.
13. P. J. Gates, "Quadrupole Mass Analysis", Online, 2014.
14. N. Heidenreich, U. Rutt, M. Koppen, A. K. Inge, S. Beier, A. C. Dippel, R. Suren and N. Stock, "A multi-purpose reaction cell for the investigation of reactions under solvothermal conditions", *Rev. Sci. Instrum.*, 2017, **88**, 104102, DOI: 10.1063/1.4999688.
15. C. Hammond, *The Basics of Crystallography and Diffraction*, Oxford University Press, Fourth, 2015, 528 pp.
16. W. Clegg, *X-Ray Crystallography*, Oxford University Press, 2015.
17. C. P. Brock, T. Hahn, H. Wondratschek, U. Müller, U. Shmueli, E. Prince, A. Authier, V. Kopský, D. B. Litvin, E. Arnold, D. M. Himmel, M. G. Rossmann, S. Hall, B. McMahon, M. I. Aroyo, C. J. Gilmore, J. A. Kaduk, H. Schenk, C. T. Chantler, F. Boscherini, B. Bunker and T. R. Welberry, eds., *International Tables for Crystallography*, DOI: 10.1107/97809553602060000001.
18. V. Pecharsky and P. Zavalij, *Fundamentals of powder diffraction and structural characterization of materials*, Springer, 2005.
19. S. Lowell, J. E. Shields, M. A. Thomas and M. Thommes, *Characterization of Porous Solids and Powders: Surface Area, Pore Size and Density*, Springer Netherlands, 2004, DOI: 10.1007/978-1-4020-2303-3.
20. M. Thommes, K. Kaneko, A. V. Neimark, J. P. Olivier, F. Rodriguez-Reinoso, J. Rouquerol and K. S. Sing, "Physisorption of gases, with special reference to the evaluation of surface area and pore size distribution (IUPAC Technical Report)", *Pure Appl. Chem.*, 2015, **87**, 1051–1069, DOI: 10.1515/pac-2014-1117.
21. I. Langmuir, "The Adsorption of Gases on Plane Surfaces of Glass, Mica, and Platinum", *J. Am. Chem. Soc.*, 1918, **40**, 1361–1403, DOI: 10.1021/ja02242a004.
22. S. Brunauer, P. H. Emmett and E. Teller, "Adsorption of Gases in Multimolecular Layers", *J. Am. Chem. Soc.*, 1938, **60**, 309–319, DOI: 10.1021/ja01269a023.

Chapter 3

Synthesis and Characterisation of Novel Phosphonic Acid Linkers

3.1 Introduction

Phosphonates and phosphonic acids are a very interesting class of materials and examples of their use can be found in a number of different areas, including pharmaceuticals,¹⁻⁶ metal chelation,⁷⁻⁹ anti-corrosion coatings,¹⁰⁻¹² fertilizers,^{13,14} amongst others. The interest for phosphonates in this work however, as should have been made clear, is in their use as organic linkers in metal-organic frameworks, or more aptly, metal phosphonate frameworks. Conventionally, MOFs are most often synthesised using carboxylates as the primary coordinating group, though other functionalities have been employed, including sulfonates, amines, and heterocycles. The carboxylate ligand has proven to be one of the most versatile and ubiquitous groups in coordination chemistry, and the bonding modes it presents are relatively simple in comparison to phosphonates, which makes it more predictable and much easier to work with. In fact, as is shown in Figure 3.1, phosphonates have double the number of bonding modes at 18, versus 9 for carboxylates.¹⁵

The phosphonate group exists in an almost tetrahedral geometry due to the sp^3 hybridisation of the central phosphorus atom, and has a general formula of

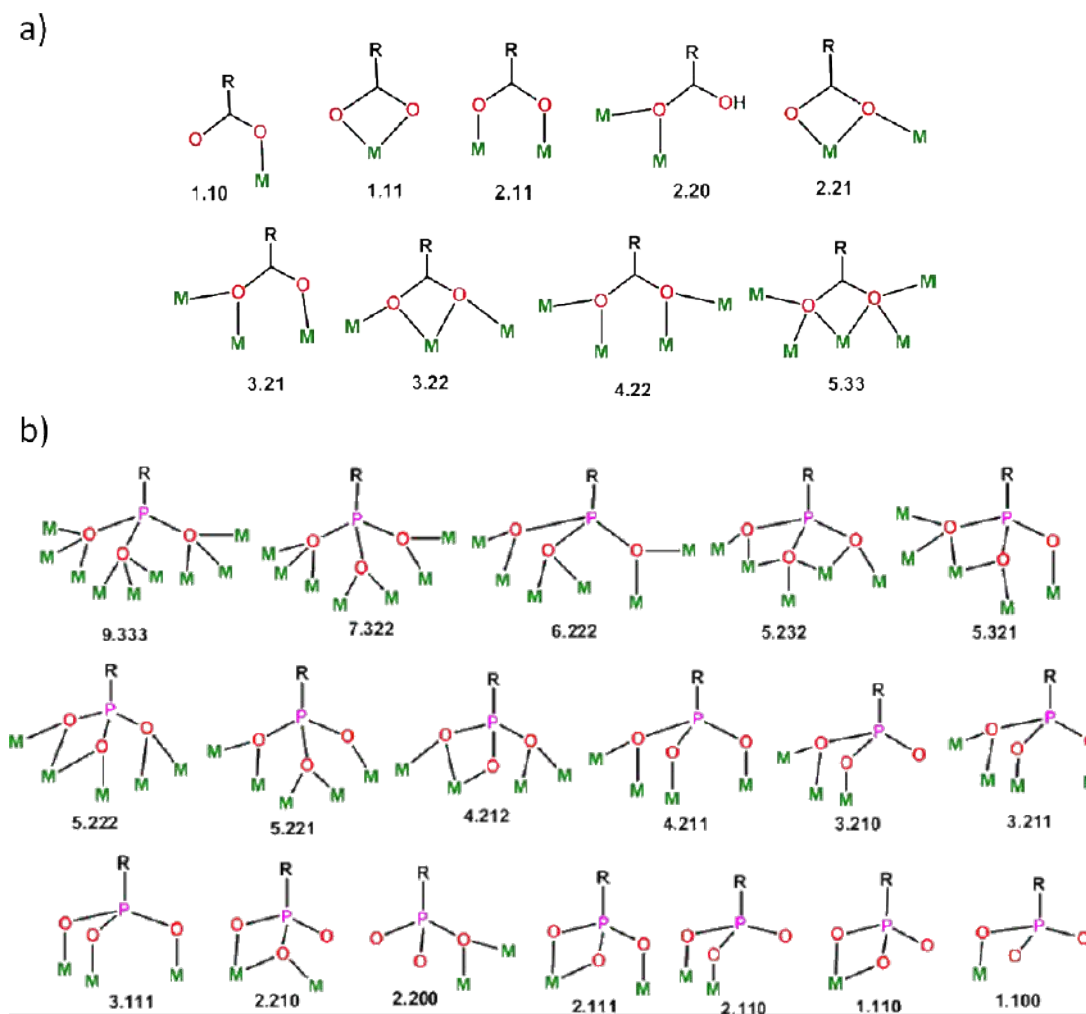


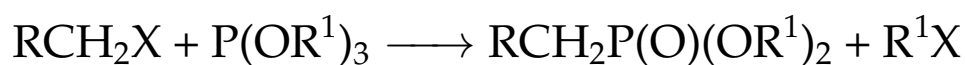
Figure 3.1: A comparison between the bonding modes of a) carboxylates, and b) phosphonates, whereby, the latter has double the number of possible bonding modes. Adapted with permission from Ref. [15], © 2015 American Chemical Society.

$R^1P(O)(OR^2)_2$.¹⁶ In terms of acidity for the acid form, where $R^2=H$, the pK_a of the first proton is often in the range between 0.5 to 3.0, while the second is in the range between 5.0 to 9.0, with these ranges depending highly on the presence of electron-withdrawing and electron-donating groups on the molecule, for which the former increases acidity, while the latter decreases it. When directly bonded to a phenyl group, this pK_a range narrows to between 1.1 and 2.3 for the first acidic proton and between 5.3 and 7.2 for the second acid proton.¹⁷ When compared to carboxylic acids, which have a pK_a value between 3.2 and 4.5, we see that phosphonic acids are the more acidic of the two species.

3.1.1 Phosphonate Esters and C-P Cross-Coupling Reactions

One of the main challenges in the synthesis metal phosphonates is that the linkers can often be difficult to prepare, and here we shall explore several routes. The challenge is, in fact, not in the synthesis of the phosphonic acid itself, but in that of the phosphonic ester precursor. Various routes for obtaining these compounds have been explored, with a large majority involving a reaction between a primary alkyl halide and a trialkyl phosphite.

Perhaps the most well-known C-P coupling procedure is the Michaelis-Arbuzov rearrangement, first reported in the late 1890s, the general scheme for which can be seen in Scheme 3.1.¹⁸ This reaction proceeds in two steps, initiating when the α -carbon of the primary alkyl halide undergoes a nucleophilic attack from the phosphorus lone pair of the trialkyl phosphite, leading to the formation of a quasi-phosphonium salt. In the second step, the α -carbon on one of the three alkoxy groups undergoes nucleophilic attack by the free halide ion generated in the first step, resulting in the formation of a new C-X bond and the cleavage of the C-O bond. Recent advances in the reaction have included a decrease in reaction time when microwave-assisted heating is applied, resulting in almost stoichiometric yields with no requirement for the use of solvents. It should be noted that this reaction is not suitable for use with aryl halide substrates due to the poor reactivity between aryl halides and trialkyl phosphites.¹⁶

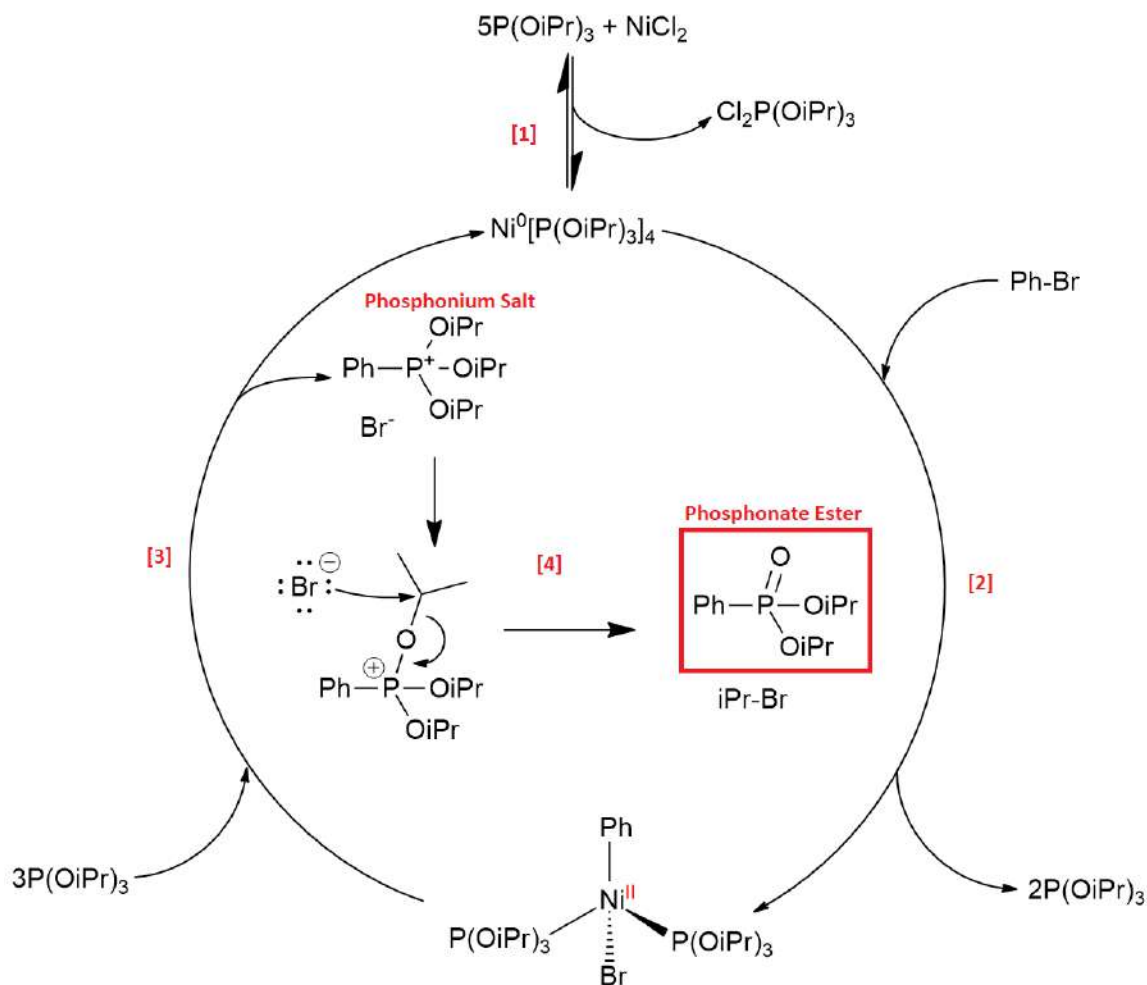


Scheme 3.1: A general scheme for the Michaelis-Arbuzov reaction.

Some of the most studied C-P coupling reactions involving aryl substrates are those employing catalysts, which are required in order to lower the energy barrier of the reaction and overcome the poor reactivity between aryl halides and trialkyl phosphites.¹⁹⁻²¹ These catalytic cross-coupling reactions tend to follow similar pathways to the Michaelis-Arbuzov reaction, with inclusion of a catalytic intermediate step. A number of suitable catalysts have been identified, ranging from nickel(II)

bromide and nickel(II) chloride, to palladium(II) acetate and palladium(II) chloride. Reactions involving these catalysts are most often carried out at high temperatures, usually in excess of 160 °C, and involves slow dropwise addition of the trialkyl phosphite to the substrate.¹⁶ In the search for milder reaction conditions, a new catalyst, tetrakis(triphenylphosphine)palladium(0), was introduced, which allowed for the lowering of the reaction temperature to approximately 90 °C.²²⁻²⁴ Although new to this kind of cross-coupling reaction, it has been commonly used in the Suzuki-Miyaura cross-coupling reaction, where new C-C bonds form between boronic acids and aryl halides.²⁵ In this work, a nickel(II) chloride pre-catalyst was chosen due to its relatively low cost in comparison to the palladium catalysts. Despite the harsher conditions, the nickel catalysts are still widely used, but the mechanism for the reaction has proven difficult to pin down. However, a mechanism put forward shows the full catalytic cycle for the reaction, as shown in Scheme 3.2.^{16,26}

The cycle begins with the reduction of the nickel(II) chloride pre-catalyst by the trialkyl phosphite (shown here as triisopropyl phosphite) to form the catalyst, tetrakis(triisopropyl phosphite)nickel(0) [**Step 1**]. The aryl halide then undergoes oxidative addition to the nickel complex, forming a new nickel(II) complex [**Step 2**]. We then see the formation of the arylphosphonium salt and the regeneration of the nickel(0) catalyst [**Step 3**]. The final step in the cycle is identical to the Michaelis-Arbuzov reaction, whereby diisopropyl phosphonate and isopropyl bromide are formed through a nucleophilic substitution of the halide anion [**Step 4**]. Conventionally, the reaction described is carried out by placing the aryl halide and the pre-catalyst into a round-bottom flask in the presence of a suitable solvent, most often 1,3-diisopropylbenzene, and setting to reflux. The advantage of using such solvents lies in their high boiling points, which allows for reactions to be run at much higher temperatures, thus increasing the rate of the reaction. While the reaction mixture is refluxing, the alkyl phosphite is added in several small portions. At this point, the reaction can be monitored using thin layer chromatography (TLC) in order to

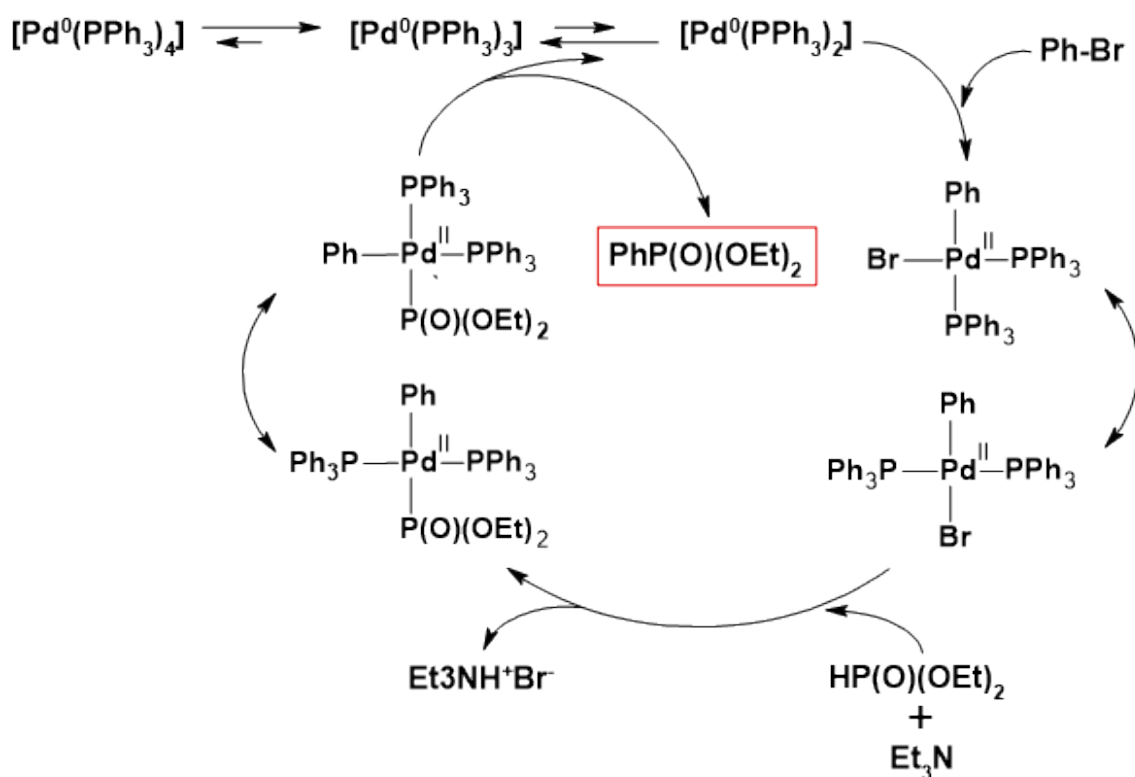


Scheme 3.2: The catalytic cycle for the nickel-catalysed cross coupling reaction of aryl halides with triisopropyl phosphite.

determine when the next portion should be added, i.e. when little to no intermediates or starting materials are present.

Another form of cross-coupling reaction, known as the Hirao method, makes use of an alternative catalyst to that of nickel(II) salts, namely tetrakis(triphenylphosphine)palladium(0), $\text{Pd(PPh}_3)_4$, for the synthesis of arylphosphonates and vinylphosphonates, and unlike both the nickel cross-coupling and the Michaelis-Arbozov methods, requires the use of a dialkyl phosphite as opposed to the trialkyl phosphites.²²⁻²⁴ Another important feature of the reaction is the use of a base, e.g. triethyl amine, which acts as a proton scavenger when the substitution of the halide for the phosphite occurs. This reaction is particularly noted for its allowance of milder reaction conditions in terms of temperature, which

in this case is 90 °C, as opposed to that used for the nickel(II) cross-coupling reaction, which is often well in excess of 160 °C. Additionally, a microwave-assisted modification to the reaction allows for an even more rapid reaction, but at the cost of higher temperatures, which not only required more energy input, but also risks potential degradation of the product.²⁷ Another development to the method, namely the change of the catalyst in the form of a mixture of palladium(II) acetate and 1,10-bis(diphenylphosphino)ferrocene, meant the amount of palladium could be decreased.²⁸



Scheme 3.3: The mechanism for the palladium catalysed cross coupling reaction of aryl halides with dialkyl phosphite. Reproduced with permission from ref. [16], © 2011 Royal Society of Chemistry.

As with the nickel catalysed reaction, the mechanism for the palladium catalysed reaction also presents some difficulty and the rate can be greatly affected by several factors. The catalytic cycle is presented in Scheme 3.3 The first step involves the formation of an active palladium(0) complex, which in this case is $\text{Pd}^0(\text{PPh}_3)_2$. Next, the oxidative addition of the aryl halide occurs, thereby forming a new palladium(II)

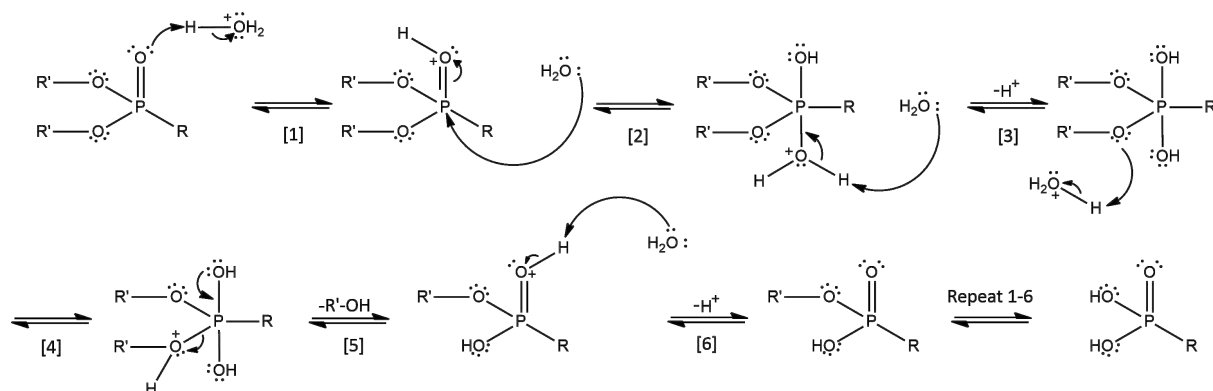
complex which includes both the aryl and halide moieties. The third step involves the ligand exchange of the halide for a deprotonated dialkyl phosphite. The final stage involves reductive elimination of the aryl and phosphonate moieties from the complex, thus regenerating the palladium(0) complex and leading to the formation of a new C-P bond, i.e. the aryl phosphonate product.

Another C-P coupling route, known as either the Moedritzer-Irani reaction or the Mannich-type condensation, has been used for the synthesis of *N,N*-disubstituted aminomethylphosphonic acids and *N*-substituted iminobis(methylphosphonic acids).²⁹ Unlike the previous reaction, the use of phosphorous acid means that the final product is a phosphonic acid, as opposed to a dialkyl phosphonate. Despite the inherent simplicity of the method, there are some drawbacks which can limit its use over other methods, mostly in the formation of undesirable by-products. The possible oxidation of phosphorous acid to phosphoric acid can also impart issues in terms of affecting the stoichiometry. In terms of the work presented in this thesis, this method is limited in that it requires the use of aliphatic amine precursors, which do not necessarily lend themselves to the formation of rigid structures when considering MOFs.^{5,30,31} Despite this, the method has been used in the synthesis of one of the more successful linkers used for open-framework metal phosphonates, *N,N'*-bis(phosphonomethyl)-piperazine.³²⁻³⁴

3.1.2 Hydrolysis of Phosphonate Esters to Phosphonic Acids

Once the aryl-phosphonates have been obtained, they need to undergo hydrolysis to reach the final aryl-phosphonic acid target. The most common route for the hydrolysis of phosphonates in general is through reflux with concentrated HCl (~37%) in a 1:1 mixture (6 M) with water for up to 12 hours, often followed by a relatively simple workup.³⁵⁻³⁸ This will usually just require the removal of HCl, water, and the R-OH byproduct by distillation, resulting in the pure phosphonic acid, though

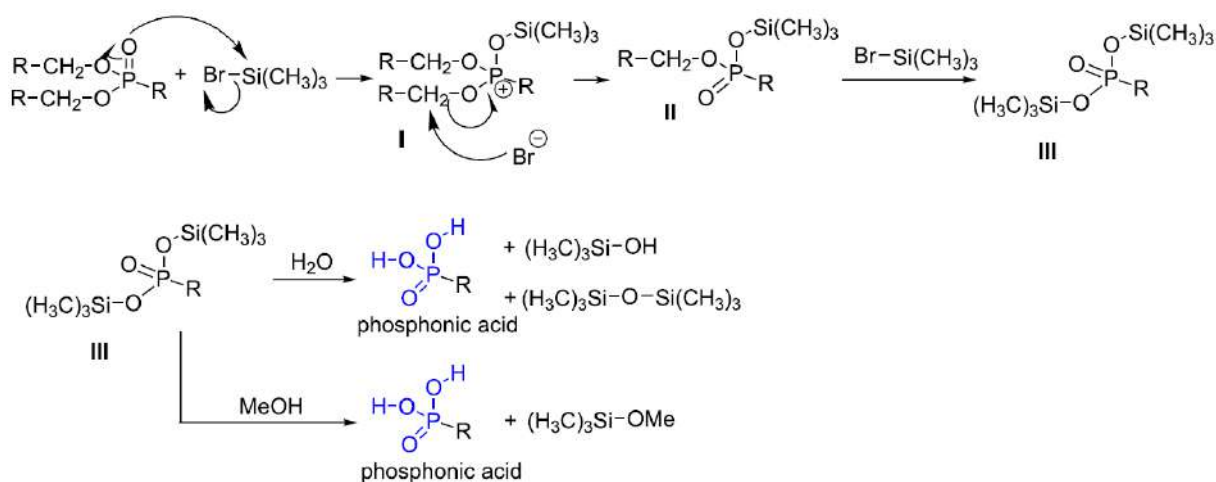
recrystallisation in polar solvents, such as acetonitrile, is sometimes required to further purify the product.



Scheme 3.4: A potential mechanism for the hydrolysis of phosphonate esters using HCl.

With regards to the mechanism for the reaction, as shown in Scheme 3.4, step 1 begins with the protonation of the double bonded oxygen, which is followed by a nucleophilic attack by water on the phosphorus atom in step 2. In step 3, deprotonation on the newly added positively charged oxygen leads to the formation of a hydronium ion. Step 4 then sees the protonation of the oxygen on one of the ester groups. In a concerted step, the oxygen on the P-OH group then reforms a double bond with phosphorus, resulting in an acyl cleavage-like elimination of an aliphatic alcohol. A deprotonation of the P=OH group then occurs in step 6 to form the phosphonate monoester and a hydronium ion. The repeat of this process then gives the phosphonic acid.³⁹

This HCl method described above requires quite harsh conditions in order to obtain the desired product, which can be an issue when sensitive functional groups are present. An alternative method, put forward by McKenna et al. (1977), involves the use of trimethylbromosilane (TMSiBr) in a transesterification of the dialkyl phosphonate to bis(trimethylsilyl) phosphonate, followed by treatment in water or short-chain alcohols to obtain a phosphonic acid, as shown in Scheme 3.5.⁴⁰ The initial step in this mechanism proceeds via an oxophilic substitution on the silicon of TMSiBr, whereby bromide acts as the leaving group, resulting in the formation of intermediate I. A nucleophilic attack by the bromide on the electrophilic carbon then leads to the



Scheme 3.5: The suggested mechanism for the hydrolysis of dialkyl phosphonates using trimethylbromosilane. Adapted from ref. [17] under a creative commons licence (CC BY 4.0).

formation of intermediate II, and then intermediate III through repetition of the same process. From here, there are two possible routes for obtaining a phosphonic acid. The first route is hydrolysis and leads to the formation of the phosphonic acid and two volatile side products, trimethylsilanol and hexamethyldisiloxane. The second, more favourable route, is methanolysis and leads to the formation of the phosphonic acid and methoxytrimethylsilane, a side product that is inherently more volatile than those formed during hydrolysis.

3.2 Experimental

3.2.1 C-P Coupling

(1A) N,N-Bis(4-diisopropylphosphonophenyl)amine [iPr₄BPA]

Bis(4-bromophenyl)amine (5.0 g, 15.3 mmol) was placed into a screw powder addition funnel and attached to a 100 mL round-bottom flask. Triisopropyl phosphite (52.5 mL, 214 mmol, 7 equivalents) and anhydrous nickel chloride (13 mol%) were then added to the round-bottom flask and the temperature set to 160 °C under argon. Once the mixture had reached temperature, the bis(4-bromophenyl)amine was added

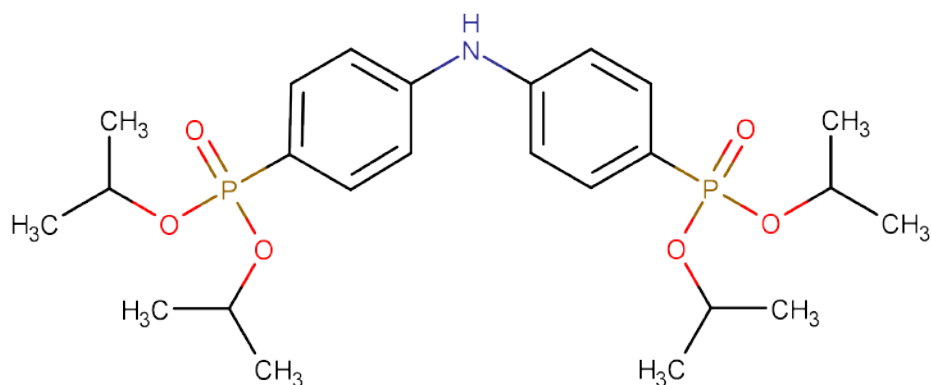


Figure 3.2: Chemical structure of (1A) N,N-Bis(4-diisopropylphosphonophenyl)amine [iPr₄BPA].

slowly over 2 hours and the reaction monitored via TLC using an acetone:ethyl acetate mixture in a 1:9 ratio. Once the addition was complete, the reaction mixture was left for a further 3.5 hours and again monitored by TLC to identify when the reaction had gone to completion. After 3.5 hours, the gas flow rate was increased in order to remove excess phosphite and remaining byproducts, resulting in a dark treacle-like substance. This was left to cool and subsequently washed overnight in hexane, resulting in the formation of a fine grey powder (5.57 g). This powder was then placed in an acetone:ethyl acetate mixture (1:9), whereby partial dissolution of the powder resulted in an off-yellow solution and a dark black solid. After filtering to remove the dark solid, the solvent mixture was removed by vacuum rotary evaporation, resulting in 5.36 g of the expected product, which is a fine white powder. (Yield = 85.3%)

³¹P NMR (202 MHz, CDCl₃): δ 17.31 (m, J ≈ 4.4 Hz, 2P)

¹H NMR (500 MHz, CDCl₃): δ 7.71 (dd, J = 12.6, 8.4 Hz, 4H, aromatic), δ 7.19 (dd, J = 8.5, 3.1 Hz, 4H, aromatic), δ 4.68 (dp, J = 7.9, 6.1 Hz, 4H, O-C(H)-CH₃), δ 1.37 (d, J = 6.23 Hz, 12H, O-C-CH₃), δ 1.25 (d, J = 6.23 Hz, 12H, O-C-CH₃)

¹³C NMR (500 MHz, CDCl₃): δ 145.13 (s, 2C), δ 133.50 (d, J = 10.95 Hz, 4C), δ 122.65 (s, 2C), δ 116.97 (s, 4C), δ 70.50 (d, J = 5.54 Hz, 4C), δ 24.00 (dd, J = 25.6, 4.4 Hz, 8C)

m/z: 498.22 ([M+H]⁺), 995.43 ([2M+H]⁺)

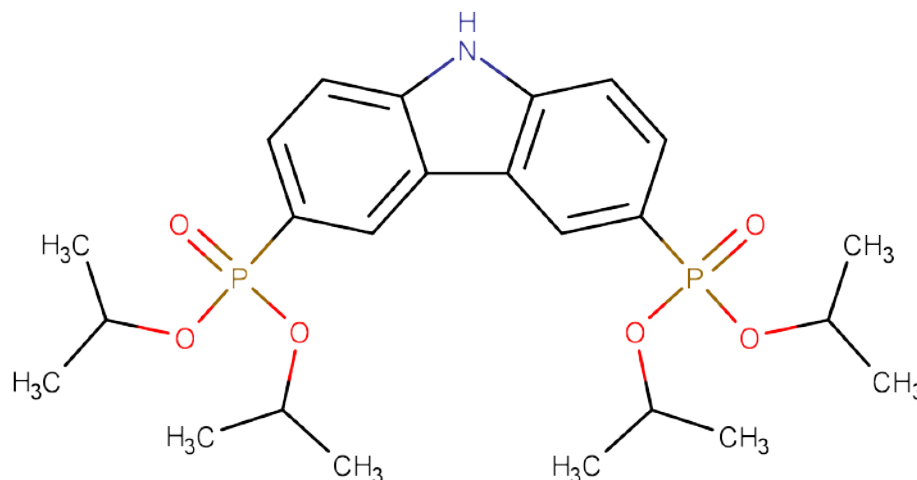
(2A) 3,6-bis(diisopropylphosphono)-9H-carbazole [iPr₄DPC]

Figure 3.3: Chemical structure of (2A) 3,6-bis(diisopropylphosphono)-9H-carbazole [iPr₄DPC].

3,6-dibromo-9H-carbazole (5.0 g, 15.4 mmol) was placed into a screw powder addition funnel and attached to a 100 mL round-bottom flask. Triisopropyl phosphite (52.5 mL, 214 mmol, 7 equivalents) and anhydrous nickel chloride (13 mol%) were then added to the round-bottom flask and the temperature set to 160 °C under argon. Once the mixture in the round-bottom had reached temperature, the 3,6-dibromo-9H-carbazole was added slowly over 1.5 hours and monitored via TLC. Once the addition was complete, the reaction mixture was left for a further 2.5 hours and monitored by TLC to identify when the reaction had gone to completion. After 2.5 hours, the flow of argon had already removed the bulk of the excess phosphite, resulting in a pink-brown sticky mixture. This was washed overnight in hexane, resulting in the formation of a pale pink / off-white powder. This was isolated by vacuum filtration and washed in acetone. This resulted in 6.26 g of the target product, an off-white powder. (Yield = 86.1%)

³¹P NMR (202 MHz, CDCl₃): δ 18.63 (s, 2P)

¹H NMR (500 MHz, CDCl₃): δ 8.95 (s, 1H, N-H), δ 8.66 (d, J = 15.1 Hz, 2H, aromatic), δ 7.91 (ddd, J = 12.4, 8.3, 1.4 Hz, 2H, aromatic), δ 7.55 (dd, J = 8.4, 3.1 Hz, 2H, aromatic),

δ 4.75 (dp, $J = 8.0, 6.2$ Hz, 4H, CH), δ 1.43 (d, $J = 6.2$ Hz, 12H, O-C-CH₃), δ 1.26 (d, $J = 6.2$ Hz, 12H, O-C-CH₃)

¹³C NMR (500 MHz, CDCl₃): δ 141.98 (s, 2C), δ 129.68 (d, $J = 11.76$ Hz, 2C), δ 125.40 (s, $J = 10.87$ Hz, 2C), δ 122.84 (s, 2C), δ 121.40 (s, 2C), δ 110.96 (d, $J = 16.55$ Hz, 2C), δ 70.66 (d, $J = 5.36$ Hz, 4C), δ 24.04 (dd, $J = 25.9, 4.1$ Hz, 8C)

m/z: 496.2 ([M+H]⁺), 991.39 ([2M+H]⁺)

(3A) 4-diisopropylphosphono-N-(4-diisopropylphosphophenyl)-N-phenylaniline
[iPr₄DPPA]

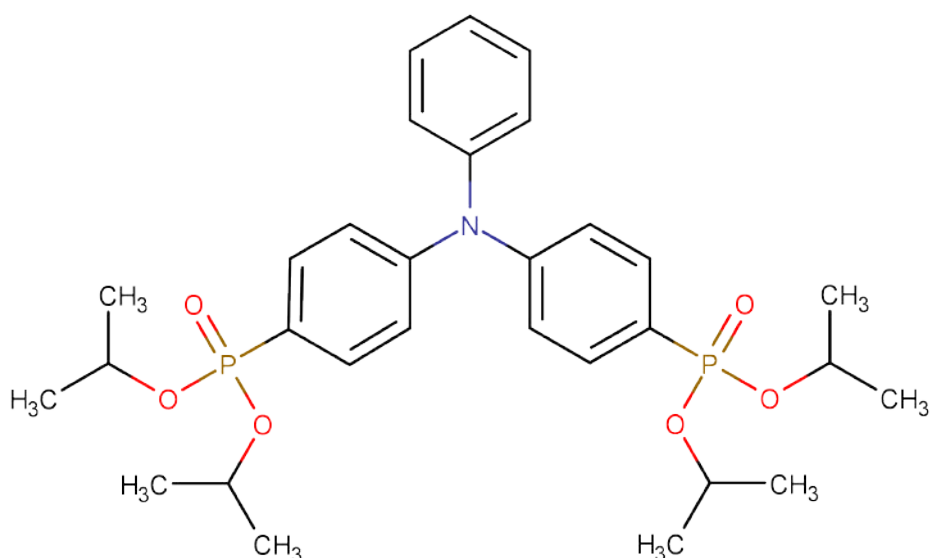


Figure 3.4: Chemical structure of (3A) 4-diisopropylphosphono-N-(4-diisopropylphosphophenyl)-N-phenylaniline [iPr₄DPPA].

4-bromo-N-(4-bromophenyl)-N-phenylaniline (3.0 g, 7.4 mmol) was placed into a screw powder addition funnel and attached to a 100 mL round-bottom flask. Triisopropyl phosphite (25.7 mL, 104.2 mmol, 7 equivalents) and anhydrous nickel chloride (13 mol%) were then added to the round-bottom flask and the temperature set to 160 °C under argon. Once the mixture in the round-bottom had reached temperature, the 4-bromo-N-(4-bromophenyl)-N-phenylaniline was added slowly over 2.5 hours and monitored via TLC. Once the addition was complete, the reaction mixture was left for a further 3 hours and monitored by TLC to identify when the

reaction had gone to completion. After 3 hours, the gas flow rate was increased in order to remove excess phosphite and remaining byproducts. The mixture was then left to cool and became a sticky, treacle-like substance, and was subsequently washed overnight in hexane, resulting in the formation of a fine white solid. The hexane was decanted and the powder again washed in hexane. (Yield = 93.2%)

^{31}P NMR (202 MHz, CDCl_3): δ 17.02 (m, 2P)

^1H NMR (500 MHz, CDCl_3): δ 7.68 (dd, $J = 12.8, 8.2$ Hz, 4H, Aromatic), δ 7.36 (t, $J = 7.8$ Hz, 2H, Aromatic), δ 7.20 (t, $J = 7.5$ Hz, 1H, Aromatic), δ 7.15 (d, $J = 8.1$ Hz, 2H, Aromatic), δ 7.12 (dd, 4H, Aromatic), δ 4.73 (h, $J = 6.6$ Hz, 4H), δ 1.39 (d, $J = 6.2$ Hz, 12H, O-C- CH_3), δ 1.28 (d, $J = 6.2$ Hz, 12H, O-C- CH_3)

^{13}C NMR (500 MHz, CDCl_3): δ 150.25 (s, 2C), δ 146.08 (s, 1C), δ 133.03 (d, $J = 10.80$ Hz, 4C), δ 129.84 (s, 2C), δ 126.54 (s, 2C), δ 125.27 (s, 2C), δ 123.95 (s, 1C), δ 122.46 (d, $J = 15.5$ Hz, 4C), δ 70.63 (d, $J = 5.7$ Hz, 4C), δ 70.63 (dd, $J = 21.3, 4.4$ Hz, 8C)

m/z: 574.2 ($[\text{M}+\text{H}]^+$)

3.2.2 Synthesis of Phosphonic Acids

(1B) N,N-Bis(4-phosphonophenyl)amine [H_4BPA]

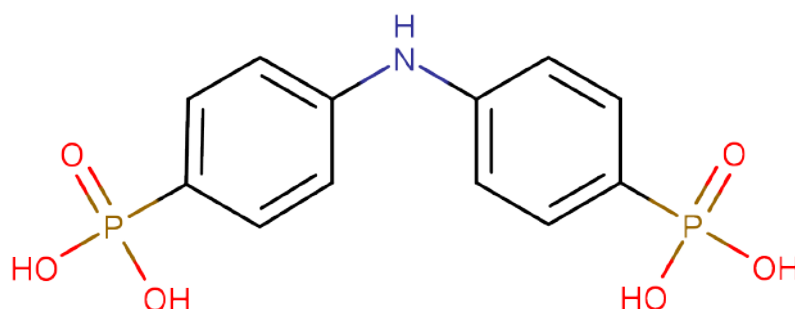


Figure 3.5: Chemical structure of (1B) N,N-Bis(4-phosphonophenyl)amine [H_4BPA].

$i\text{Pr}_4\text{BPA}$ (2.0 g, 4.02 mmol) was dissolved in approximately 50 mL of acetonitrile inside a 100 mL round bottom flask and flushed with argon. The temperature of the vessel was then set to 65 °C. Trimethylbromosilane (3.7 mL, 28.14 mmol) was then added

to the flask, resulting in a colour change of the solution to a blue colour. After one and a half hours, TLC showed that the starting material had already been consumed, thus the heating was turned off and the solution allowed to cool. Once sufficiently cooled, rotary evaporation was used to remove the solvent, acetonitrile, resulting in a blue oil. On treatment of this oil with water, a white solid began forming. Water was then progressively added until no oil remained. The white solid was then washed with water and acetone. (Yield = 82.6%)

^{31}P NMR (202 MHz, 0.1M NaOH in D_2O): δ 12.39 (s, 2P)

^1H NMR (500 MHz, 0.1M NaOH in D_2O): δ 7.50 (dd, $J = 11.6, 8.1$ Hz, 4H, aromatic), δ 7.05 (d, $J = 8.6$ Hz, 4H, aromatic)

^{13}C NMR (500 MHz, 0.1M NaOH in D_2O): δ 143.43 (s, 2C), δ 133.70 (s, 2C), δ 131.53 (d, $J = 9.8$ Hz, 4C), δ 116.81 (d, $J = 13.3$ Hz, 4C)

m/z: 163.5 ($[\text{M}-2\text{H}]^{2-}$), 328.01 ($[\text{M}-\text{H}]^{-}$)

(2B) 3,6-diphosphono-9H-carbazole [H_4DPC]

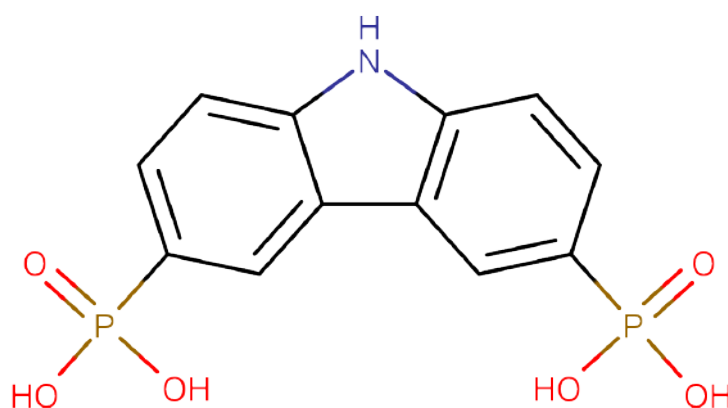


Figure 3.6: Chemical structure of (2B) 3,6-diphosphono-9H-carbazole [H_4DPC].

iPr_4DPC (3.0 g, 6.05 mmol) was partially dissolved in approximately 100 mL of acetonitrile inside a 250 mL round bottom flask and flushed with argon. Trimethylbromosilane (5.6 mL, 42.4 mmol) was then added to the flask, resulting in a colour change of the solution to a blue colour. The temperature was then set to

65 °C and left to react for five and a half hours, and monitored via TLC. Once the starting material was consumed, the heating was turned off and the solution allowed to cool. Once sufficiently cooled, rotary evaporation was used to remove the solvent, acetonitrile, resulting in a blue oil. On treatment of this oil with water, a white solid began forming. Water was then progressively added until no oil remained. The white solid was then washed with water and acetone. (Yield = 93.0%)

^{31}P NMR (202 MHz, 0.1M NaOH in D_2O): δ 12.91 (t, J = 11.7 Hz, 2P)

^1H NMR (500 MHz, 0.1M NaOH in D_2O): δ 8.41 (d, J = 12.2 Hz, 2H, aromatic), δ 7.72 (dd, J = 10.9, 8.3 Hz, 2H, aromatic), δ 7.46 (dd, J = 8.2, 2.3 Hz, 2H, aromatic)

^{13}C NMR (500 MHz, 0.1M NaOH in D_2O): δ 140.15 (s, 2C), δ 128.38 (s, 2C), δ 122.18 (s, 4C), δ 110.22 (s, 4C) - Intensity not great enough for full characterisation.

m/z : 162.5 ($[\text{M}-2\text{H}]^{2-}$), 325.99 ($[\text{M}-\text{H}]^{-}$)

(3B) 4-phosphono-N-(4-phosphonophenyl)-N-phenylaniline [H_4DPPA]

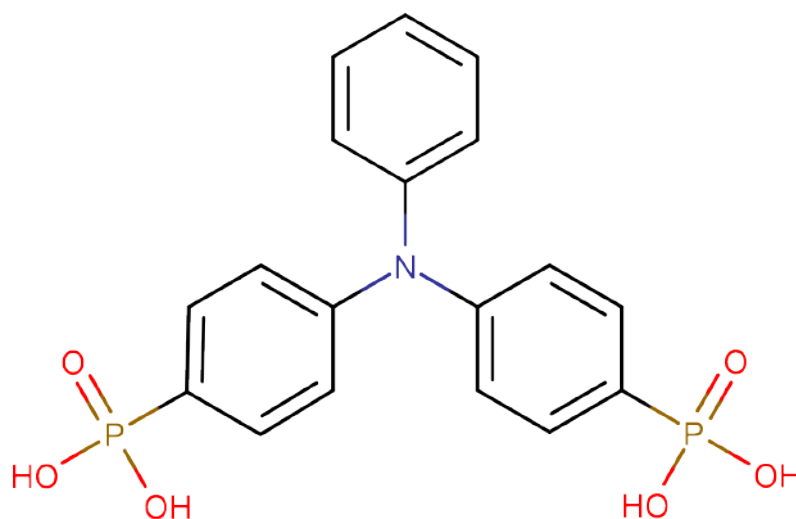


Figure 3.7: Chemical structure of (3B) 4-phosphono-N-(4-phosphonophenyl)-N-phenylaniline [H_4DPPA].

iPr_4DPPA (2.5 g, 3.46 mmol) was dissolved in approximately 10 mL of acetonitrile inside a 100 mL round bottom flask, resulting in a clear light green solution, and was

then flushed with argon. Trimethylbromosilane (2.8 mL, 30.5 mmol) was then added to the flask, resulting in a colour change of the solution to a blue colour. The temperature was then set to 65 °C and left to react for four hours, and monitored via TLC. Once the starting material was consumed, the heating was turned off and the solution allowed to cool. Once sufficiently cooled, rotary evaporation was used to remove the solvent, acetonitrile, resulting in a blue oil. On treatment of this oil with water, a white solid began forming. Water was then progressively added until no oil remained. The white solid was then washed with water and acetone. (Yield = 94.2%)

^{31}P NMR (202 MHz, 0.1M NaOH in D_2O): δ 11.32 (t, J = 11.2 Hz, 2P)

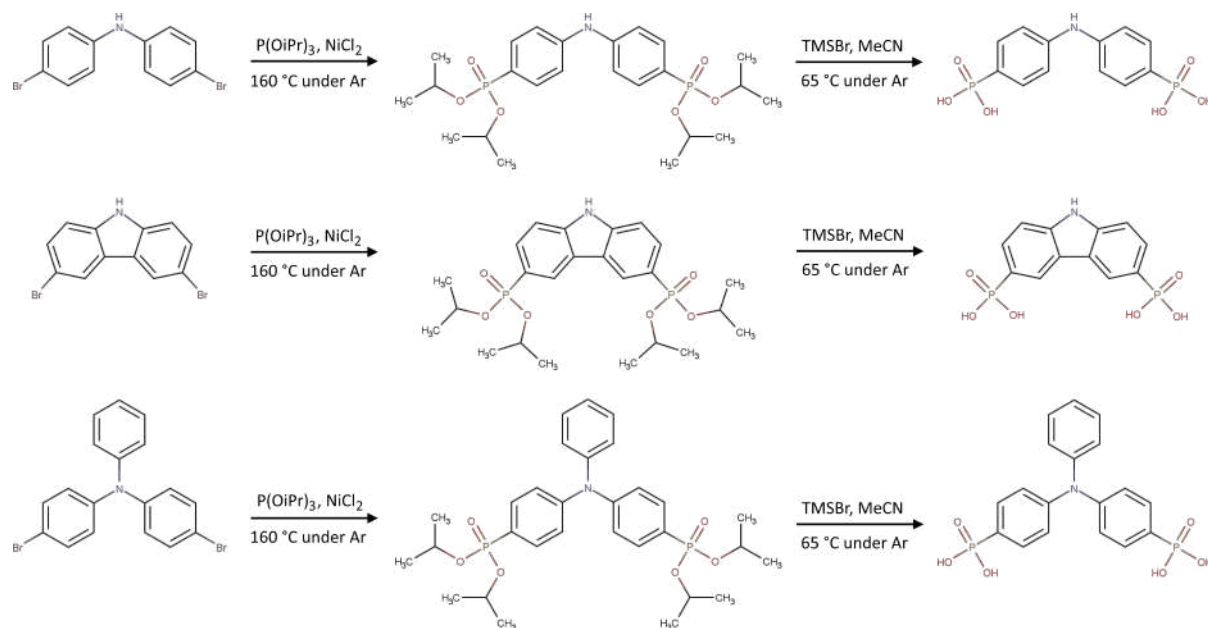
^1H NMR (500 MHz, 0.1M NaOH in D_2O): δ 7.52 (dd, J = 11.2, 8.0 Hz, 4H, Aromatic), δ 7.29 (t, J = 7.7 Hz, 2H, Aromatic), δ 7.13 (d, J = 7.9 Hz, 2H), δ 7.07 (t, J = 7.5 Hz, 1H, Aromatic), δ 7.03 (d, J = 6.1 Hz, 4H)

^{13}C NMR (500 MHz, 0.1M NaOH in D_2O): δ 133.97 (d, 4C), δ 132.11 (s, 2C), - Intensity not great enough for full characterisation.

m/z : 201.52 ($[\text{M}-2\text{H}]^{2-}$), 404.05 ($[\text{M}-\text{H}]^-$)

3.3 Results and Discussion

The main driver for this work has been to produce a series of non-linear polyarylphosphonic acids to be used as linkers in open framework metal phosphonates, which have been of great interest in various fields of research, as was discussed in Chapter 1. Since the substrates of focus are unlikely to proceed via the Michaelis-Arbuzov reaction and other C-P coupling reactions discussed present other issues, e.g. cost of reagents, we focus here on the nickel-catalysed cross-coupling reaction. Specifically, we are looking at the phosphorylation of the bromo-substituted N-aryl precursors bis(4-bromophenyl)amine (Br_2BPA), 3,6-dibromocarbazole (Br_2DPC), 4-bromo-N-(4-bromophenyl)-N-phenylaniline (Br_2DPPA) (see 3.6). Two other linkers were also explored, but limitations in yield



Scheme 3.6: Scheme showing the transformation of the Br-substrates to phosphonate esters and then to phosphonic acids.

and purity along with expense of starting materials prevented these from being taken further. Two of the main considerations made when selecting these linkers were rigidity and geometry. In the compounds considered here, rigidity is ensured by the network of sp^2 hybridised carbon atoms, or aromatic rings, and is important to ensure a stability can be obtained in potential MOF structures. The geometry of these linkers, what has now been termed V-shaped, was selected to try and move away from the pillared-layered structures that are obtained when using linear diphosphonate linkers, which are often either non-porous or have low porosity, and have little to no long range order. These types of structures were discussed as part of the main introduction to metal phosphonates in Chapter 1, and will be approached again in Chapter 4. The idea here was that the V-shaped linkers, as well as substituents attached to nitrogen, could potentially force a non-layered porous structure, as seen in CAU-8, which is a carboxylate-based geometric analogue of some of the linkers considered in this work, though the presence of the carboxylate coordinating group prevents direct comparisons.⁴¹

N,N-Bis(4-diisopropylphosphonophenyl)amine (iPr₄BPA) (1A)

The first synthetic target obtained was N,N-Bis(4-diisopropylphosphonophenyl)amine, known herein as iPr₄BPA (1A). The procedure to obtain this compound was relatively simple and reproducible, whereby the product could be obtained consistently at yields above 80%. Before the workup of the crude reaction product, which took the form of a dark brown treacle-like mixture, TLC analysis often showed that some starting material was still present, alongside what is reasoned to be the mono-substituted intermediate, N-(4-diisopropylphosphonophenyl)-N-phenylamine. This is easily removed by employing flash chromatography, using a mixture of acetone and ethyl acetate in a 1:9 ratio. The first product to elute off the column is the starting material, followed by the mono-substituted intermediate. This leaves a pure iPr₄BPA (1A) product in the final vials of eluate. The pure product could then be obtained quickly by rotary evaporation to remove the solvent, resulting in a white solid in yields most often between 80 to 90%. The phase purity of this was then confirmed by ¹H, ³¹P, 2D HSQC NMR spectra, and mass spectrometry.

Looking at the full ³¹P spectrum in Figure 3.8a, we see a single signal at δ 17.3 ppm which corresponds to the phosphonate ester product, suggesting that no other phosphorus-containing impurities are present. A closer look at this signal, as shown in Figure 3.8b, reveals a complex multiplet splitting pattern with coupling constants of

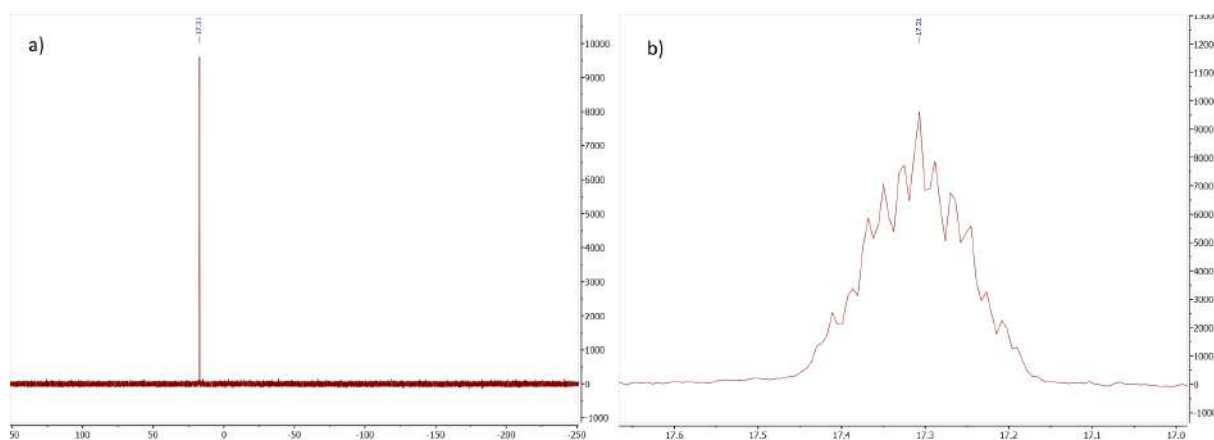


Figure 3.8: ³¹P NMR spectrum for iPr₄BPA (1A). (a) Full spectrum, (b) Zooming in on the single phosphorus signal. Solvent: Chloroform-d.

between 4.4 and 50 Hz. Coupling constants at the lower end of this range indicate that three- and four-bond couplings are present, suggesting that phosphorus is coupling with the protons present on the methyl groups on the isopropyl moieties as well as the aromatic protons furthest away from phosphorus on the corresponding rings and those of the methine groups. At the upper end of this range, it is expected that phosphorus is coupling with the protons closest to it on the aromatic ring.

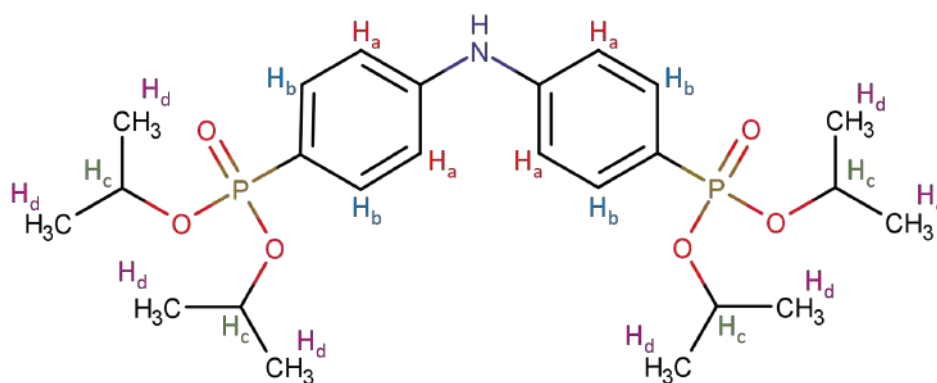


Figure 3.9: Chemical Structure of iPr₄BPA (1A), with proton environments labelled H_a to H_d, corresponding with A-D on the NMR spectrum.

With the positive result demonstrated on the ³¹P spectrum, ¹H NMR provides a similar story. A quick investigation of the full spectrum, as shown in Figure 3.10, immediately reveals the correct number of proton environments for the molecule, there are no significant impurities, and we see that each of the signals integrate to give the correct number of protons in each environment.

Looking specifically at the aromatic region (Figure 3.11) we see three peaks, including a singlet at δ 7.28 ppm, which is due to the deuterated solvent (chloroform-*d*), and two doublet of doublets at δ 7.71 ppm and δ 7.19 ppm which correspond to the protons on the phenyl rings. On first viewing of these signals, it was tempting to assign the more downfield of the two (δ 7.71 ppm) to the protons nearest to nitrogen, represented as H_a in Figure 3.9, though examination of the coupling constants reveals that the downfield signal has a larger coupling constant. This implies that the signal actually represents the protons closest to the phosphonate group (H_b), since phosphorus, like a proton,

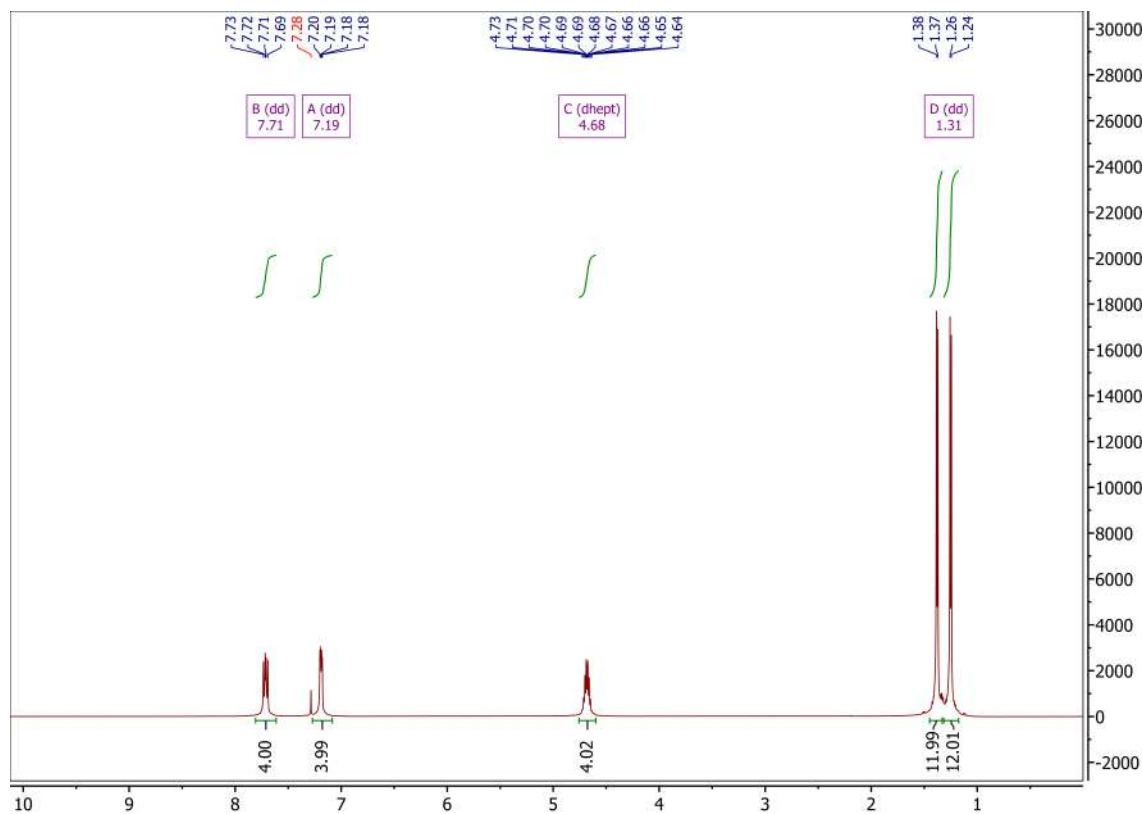


Figure 3.10: Full ^1H NMR spectrum for $i\text{Pr}_4\text{BPA}$ (**1A**). Solvent: Chloroform-d.

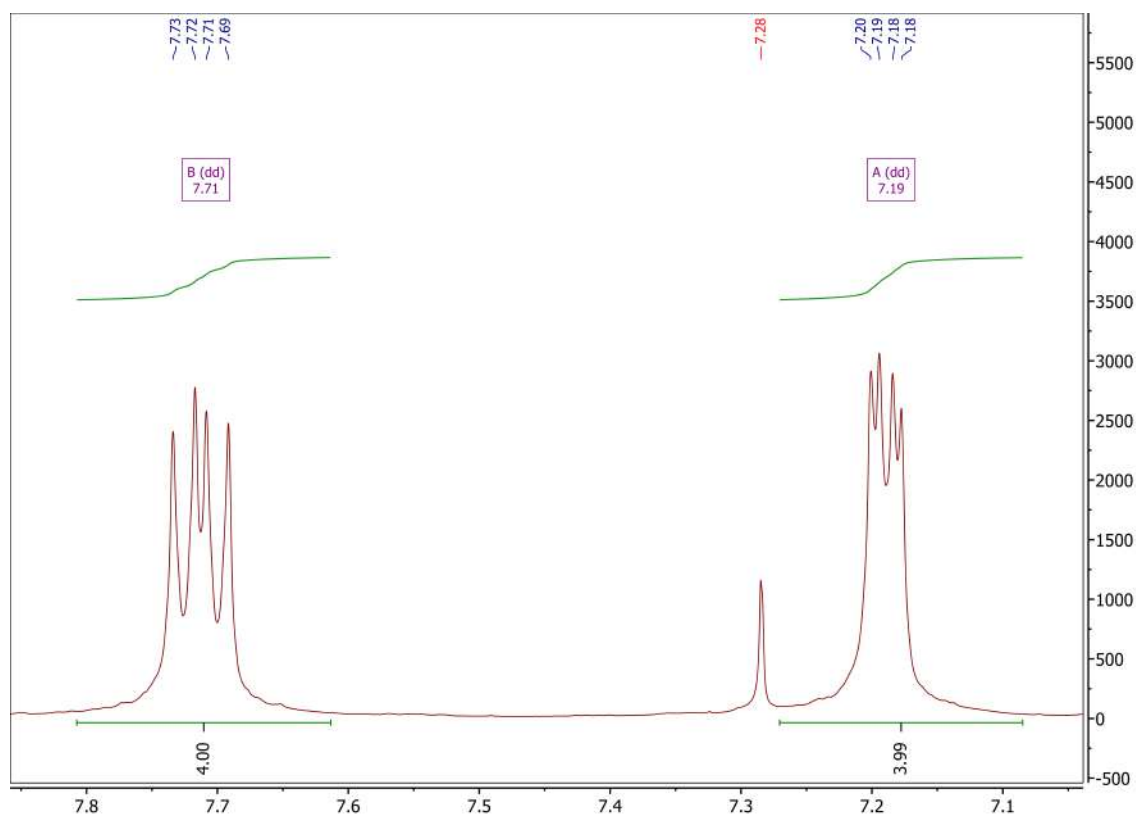
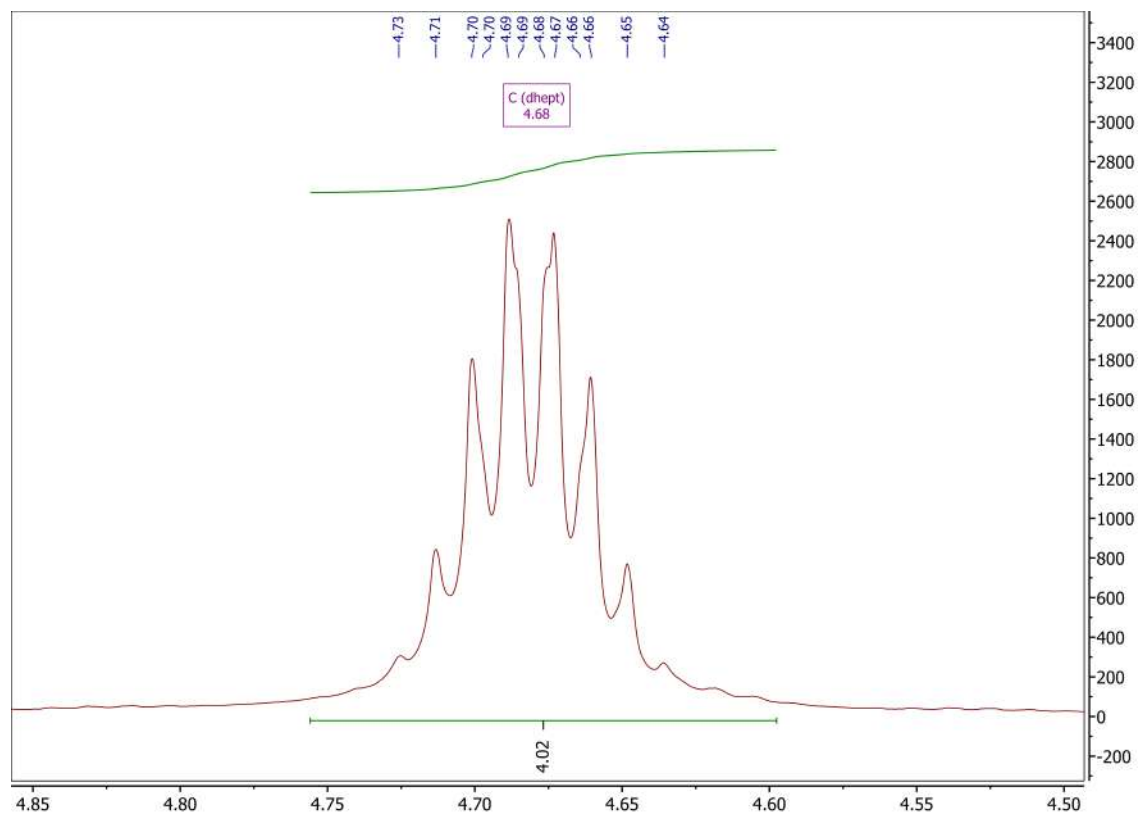
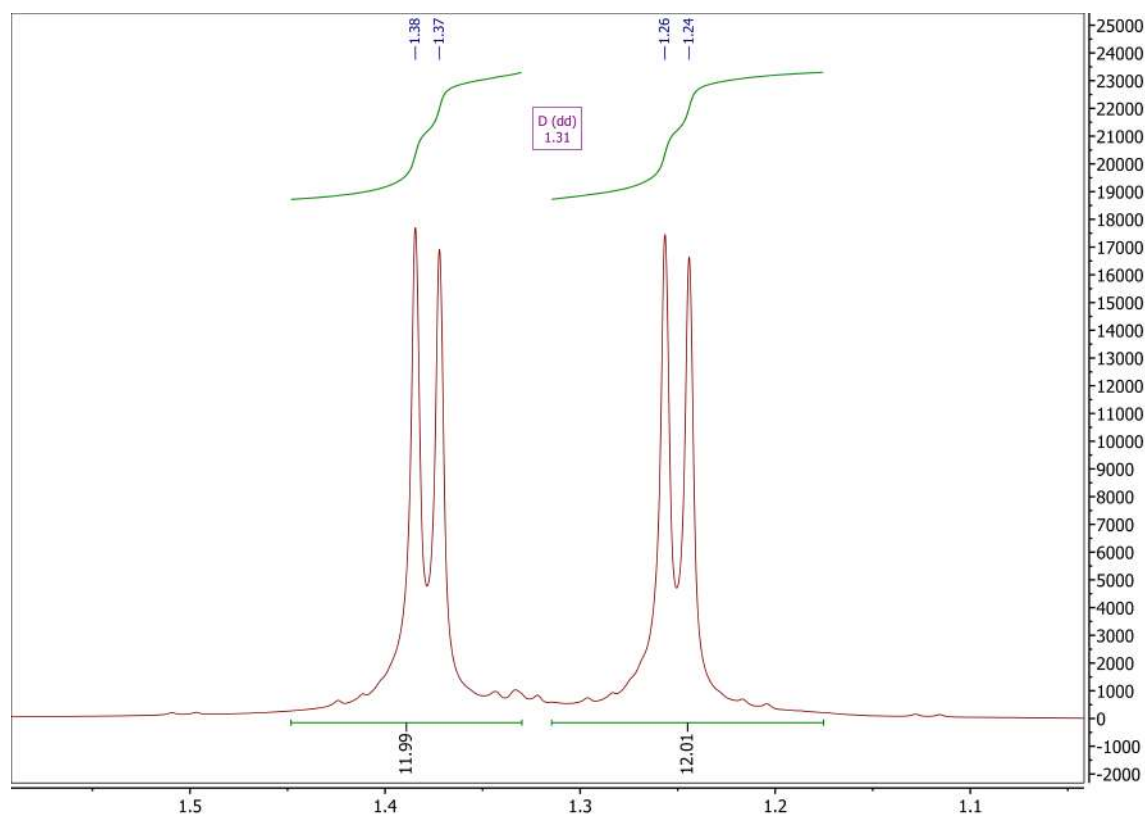


Figure 3.11: ^1H NMR spectrum for $i\text{Pr}_4\text{BPA}$ (**1A**). Solvent: Chloroform-d.

Figure 3.12: ^1H NMR spectrum for $i\text{Pr}_4\text{BPA}$ (1A). Solvent: Chloroform-d.Figure 3.13: ^1H NMR spectrum for $i\text{Pr}_4\text{BPA}$ (1A). Solvent: Chloroform-d.

has a quantum spin number of $1/2$, and will thus be involved in coupling with protons. This means that the upfield signal at δ 7.19 ppm can be assigned to the protons nearest to nitrogen (**H_b**). Moving further upfield (Figure 3.12), there is a signal at δ 4.68 ppm which is easily attributed to the methine group (**H_c**) of the isopropyl moiety. Initially, you might expect to see a septuplet here arising from the six aliphatic protons on each isopropyl moiety, though it appears to be a sextet. Closer analysis would appear to suggest that, in fact, the signal is a pair of overlapping sextets, since there are clear shoulders on some of the peaks. In this sense however, multiplet analysis appears to miss two shoulders that would in fact make this a doublet of "leaning" septets. This analysis appears to be confirmed in the ^1H NMR spectrum for iPr_4DPC (**2A**), as seen in Figure 3.32, whereby a multiplet analysis appears to identify the previously hidden shoulders. The complicated nature of this signal is likely brought about by the coupling of ^{31}P and ^1H nuclei, as was mentioned in the discussion for the aromatic signals. Most importantly, the signal integrates to give the correct number of protons for the methine groups on the molecule. The final signals on this spectrum, as seen in Figure 3.13, were originally thought to be a well-resolved doublet of doublets that corresponds to the terminal methyl groups (**H_d**) on the phosphonate ester. However, due to the relatively large coupling constant and the need to integrate the peaks separately, it was determined that the signals are actually two doublets, indicating that there are two types of chemically inequivalent isopropyl groups present on the molecule. Working on this basis, the signal integrates to a total of 24 protons, as expected. Each of the doublets arises from the coupling with the methine proton.

Moving to the ^{13}C NMR spectrum, as shown in Figure 3.15, we can immediately see the number of signals expected, with perhaps a few minor signals indicating minor impurities. Starting downfield, the signal at δ 145.13 ppm is the result of the carbons bonded to nitrogen, labelled A. Moving upfield, we see the peak at δ 133.50 ppm corresponding to the four carbons labelled C. Next is the peak at δ 122.65 ppm, which corresponds to the two carbons bonded to phosphorus, labelled D. The final peak for

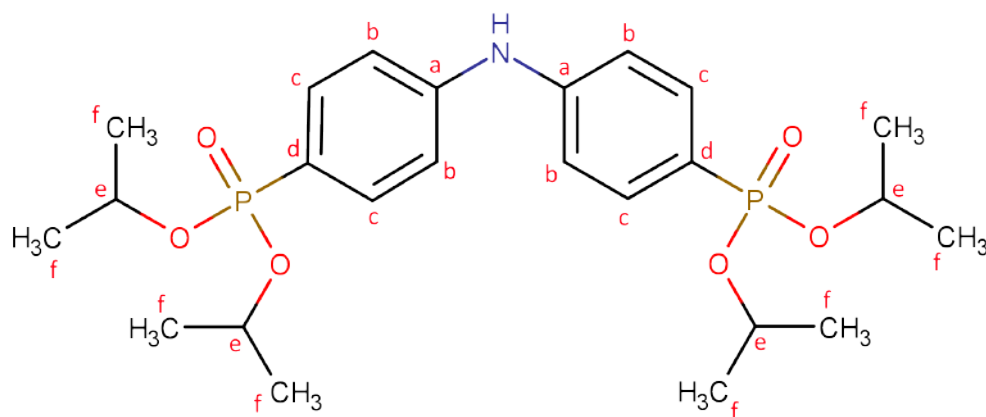


Figure 3.14: Chemical Structure of iPr_4BPA , with carbon environments labelled **a** to **f**, corresponding with A-F on the ^{13}C NMR spectrum.

the aromatic region is the one labelled B at δ 116.97 ppm, which corresponds to four carbons in the β positions relative to nitrogen. We then see a large peak at δ 76.0 ppm which goes off the scale which belongs to the solvent, $CDCl_3$. Next to this, at δ 70.55 ppm, is the peak attributed to methine carbon on the isopropyl groups. The final peak, at δ 24.00 ppm, corresponds to the terminal methyl carbons on the isopropyl groups.

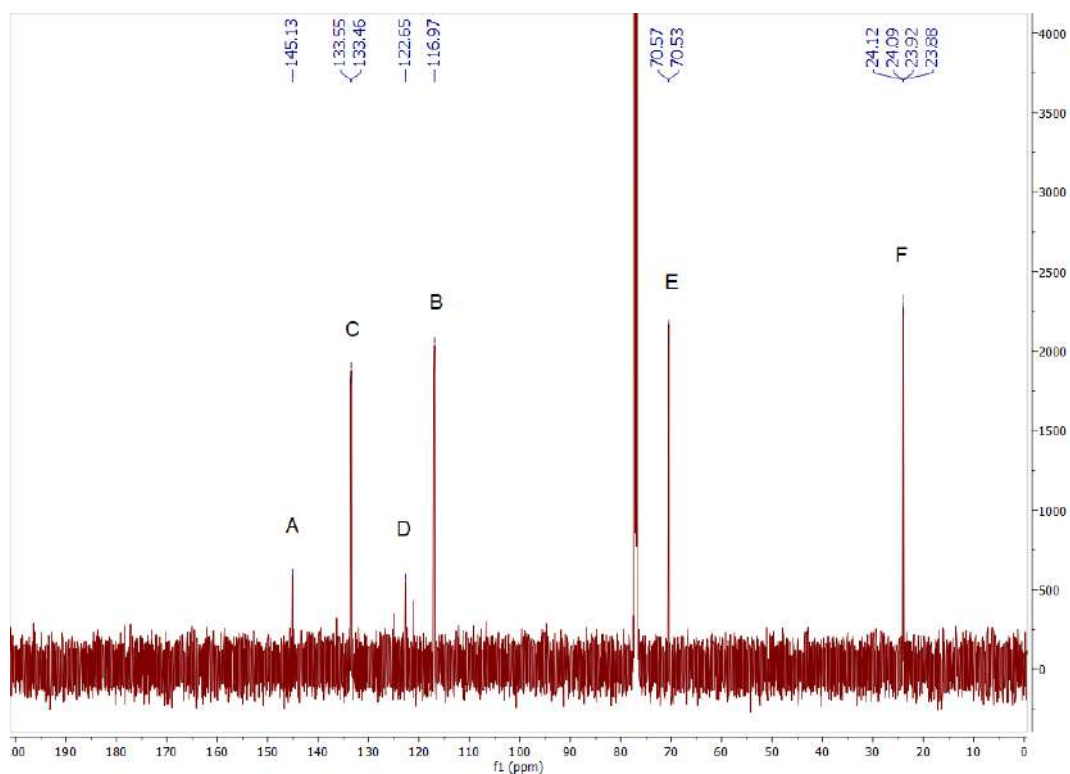


Figure 3.15: Full ^{13}C NMR spectrum for iPr_4BPA (**1A**). Solvent: Chloroform-d.

In order to obtain further confirmation of the NMR results, 2D H-C coupled NMR (HSQC) was carried out, which at least allows the assignment of carbon signals based on those for the proton signals. Looking at Figure 3.16, we can immediately see that the furthest downfield signals on both spectra, at δ 133.50 ppm, correlate to B and C on the proton and carbon NMR spectra, respectively. The other correlation in the aromatic region, at δ 116.97 ppm, is shown between B on the proton NMR spectrum and C on the carbon NMR spectrum. The next two signals, at δ 70.55 ppm and δ 24.00 ppm correctly show the H-C correlations for the methine and methyl groups.

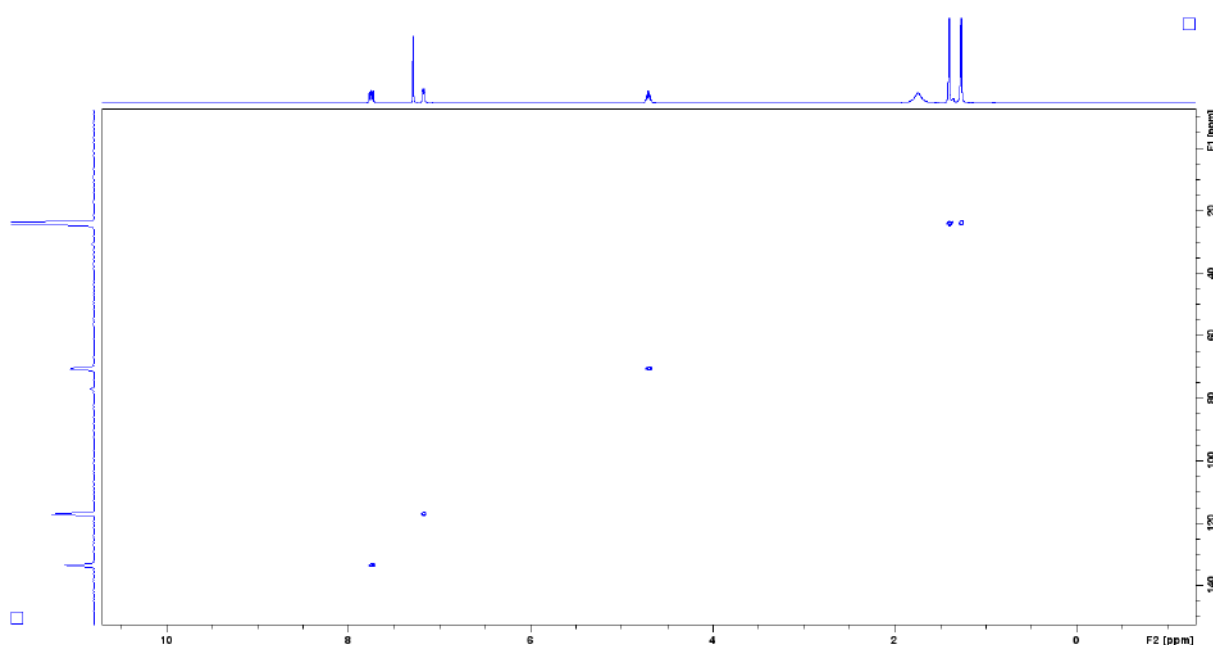
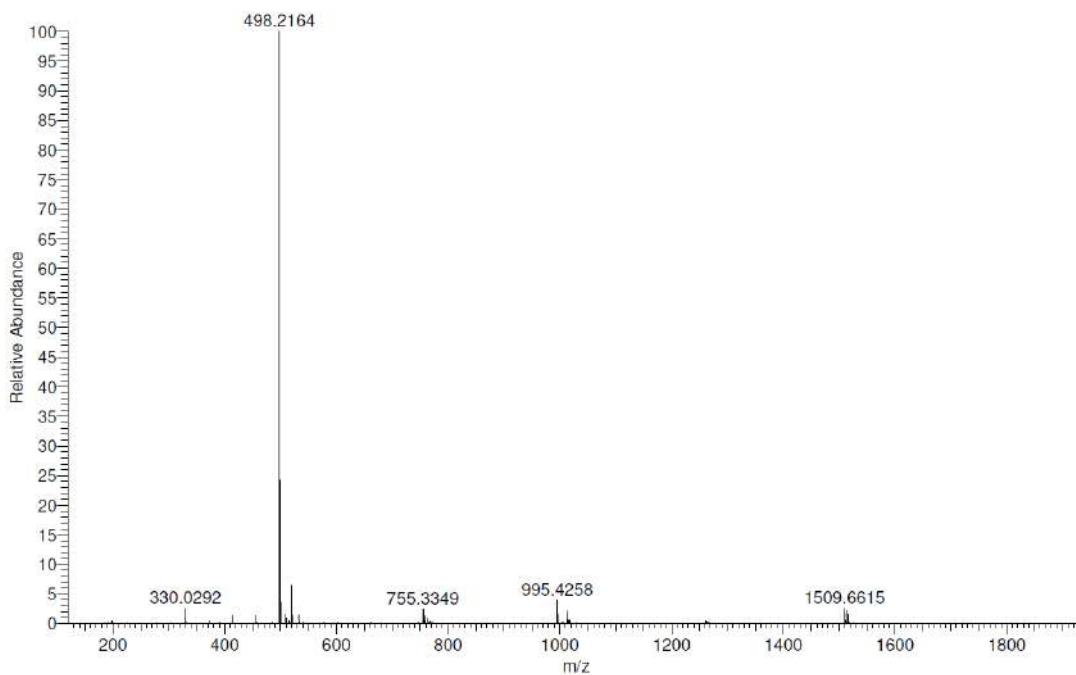
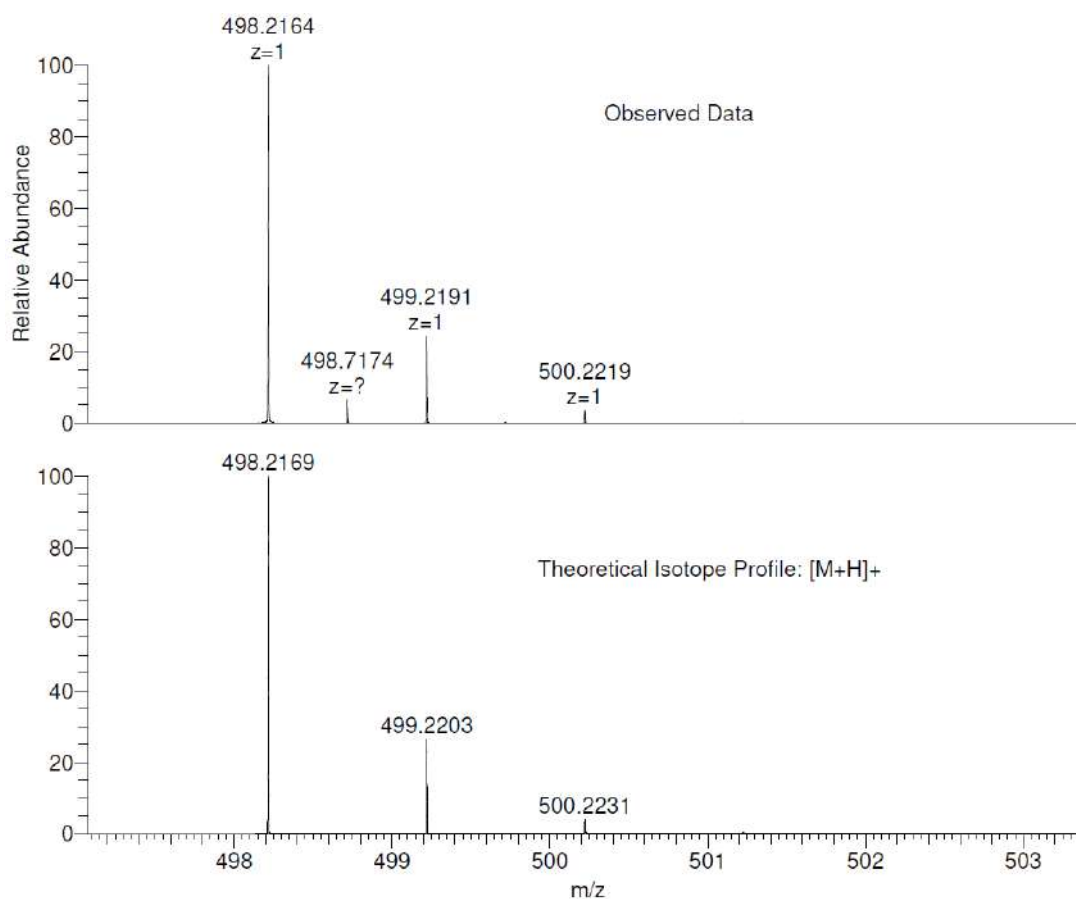


Figure 3.16: Full HSQC NMR spectrum for iPr_4BPA (**1A**). Solvent: Chloroform-d.

With NMR data clearly showing successful synthesis of iPr_4BPA , mass spectral analysis was carried out to provide further support. Figure 3.17 shows the full mass spectrum, where the base peak can be seen with an m/z of 498.22, and is shown in more detail in Figure 3.18. Here we see the theoretical isotope profile for $[M+H]^+$ and the observed experimental data, with an almost exact match between the two. Moving back to the full spectrum, the peak at m/z 995.43 corresponds a dimer species, $[2M+H]^+$, of the target molecule. The peak at m/z 330 has a clear relation to those at m/z 755.33 and 1509.66, whereby the former is likely a degradation product of the target

Figure 3.17: Observed mass spectrum for iPr_4BPA .Figure 3.18: Observed mass spectrum for iPr_4BPA and theoretical isotope pattern for the $[M+H]^+$ species.

molecule, likely corresponding to the acid form, $[\text{N}(\text{C}_6\text{H}_4)_2+\text{H}]^+$, and the latter two corresponding to the dimer and trimer species respectively.

N,N-Bis(4-phosphonophenyl)amine (H₄BPA) (1B)

With a clean product obtained for *i*Pr₄BPA (**1A**), the attention shifted to obtaining the corresponding phosphonic acid, N,N-Bis(4-phosphonophenyl)amine H₄BPA (**1B**). The initial method considered for this was hydrolysis using 6M hydrochloric acid. The results here were quite hit and miss, as it was found that this route sometimes led to the cleavage of the C-P bond, which was confirmed by the absence of signals on the ³¹P NMR spectrum. As an alternative to these harsh conditions, a different route which involved silylation using trimethylsilyl bromide (TMSiBr) and subsequent hydrolysis using water was chosen. Overall, this method proved very simple and required very little work up, often just requiring separate washes with water and acetone, and leading to yields between 65 to 91%.

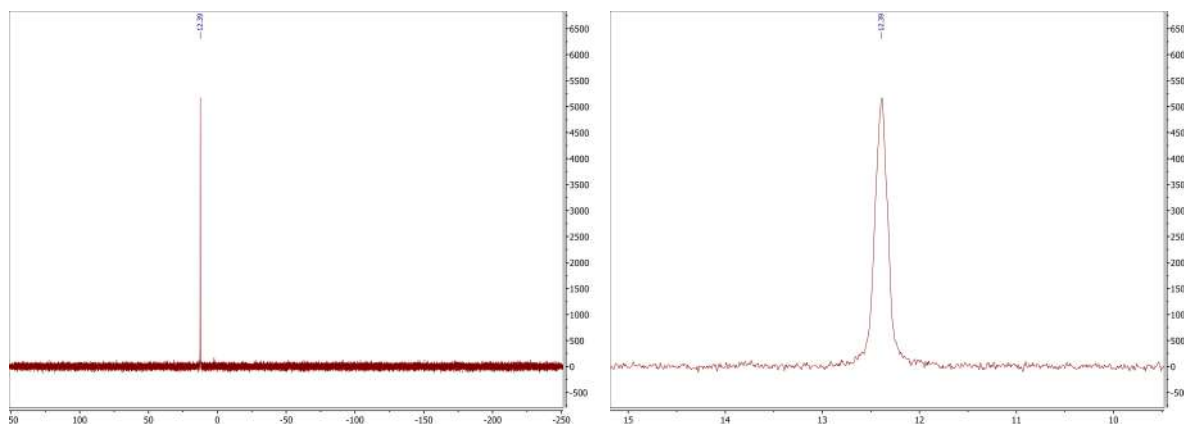


Figure 3.19: ³¹P NMR spectrum for H₄BPA (**1B**). Solvent: 0.1M NaOH in D₂O.

As with the ester, purity is confirmed with both ³¹P and ¹H NMR. Looking first at the ³¹P spectrum (Figure 3.19), it initially seems like the splitting pattern has changed, though the breadth of the peak remains similar to that of the ester, so it is likely here that the signals are unresolved. It should be noted, however, that there is now less coupling taking place due to the loss of the isopropyl group, leaving only the aromatic

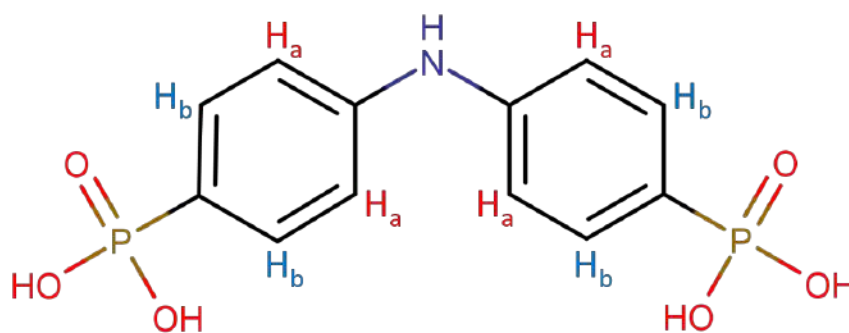


Figure 3.20: Chemical Structure of H₄BPA, with proton environments labelled H_a to H_b, corresponding with A-B on the ¹H NMR spectrum.

protons for coupling. It is also clear that no phosphorus-containing impurities are present, and thus the washing protocol used is satisfactory.

Moving next to the ¹H NMR spectrum, as shown in Figure 3.21, it is clear that the isopropyl groups are no longer present, since the signals for the methyl (-CH₃) and methine (-CH-) groups have disappeared. Taking a closer look at the aromatic region, as shown in Figure 3.22, the signals can be assigned as they were for iPr₄BPA (1A),

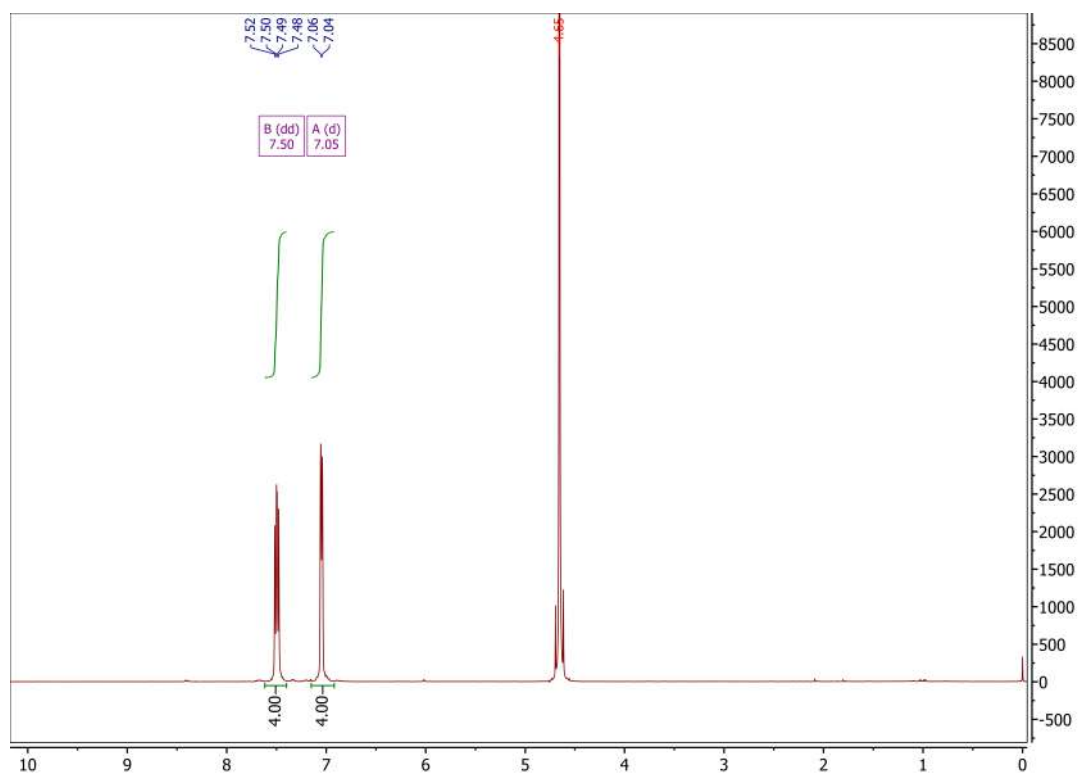


Figure 3.21: ¹H NMR spectrum for H₄BPA (1B). Solvent: 0.1M NaOH in D₂O.

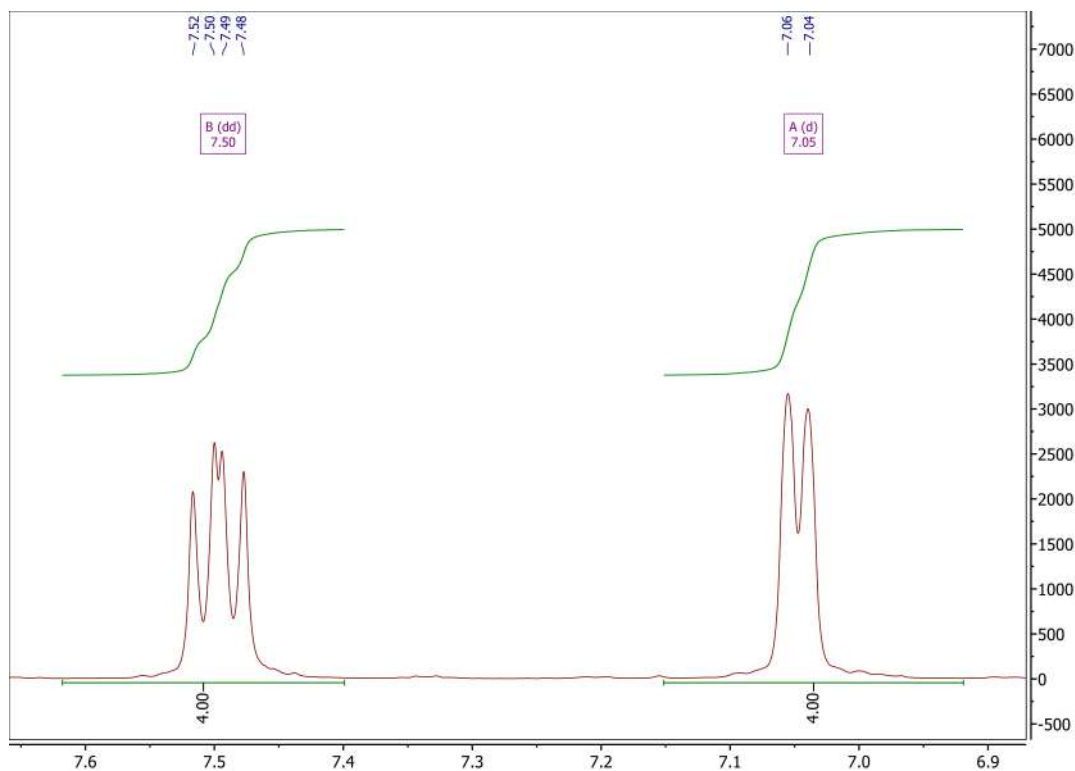


Figure 3.22: ^1H NMR spectrum for H_4BPA (**1B**), focussing on the aromatic region. Solvent: 0.1M NaOH in D_2O .

whereby the downfield signal at δ 7.50 ppm (**B**) can be assigned to the protons nearest to phosphorus on the phenyl ring, represented by H_b , since it has a larger coupling constant. The signal at δ 7.05 ppm (**A**) can be assigned to the protons nearest to nitrogen on the phenyl ring, represented by H_a . This signal, while appearing as a single doublet, is more likely to be an unresolved doublet of doublets, as was seen in Figure 3.11 for iPr_4BPA (**1A**).

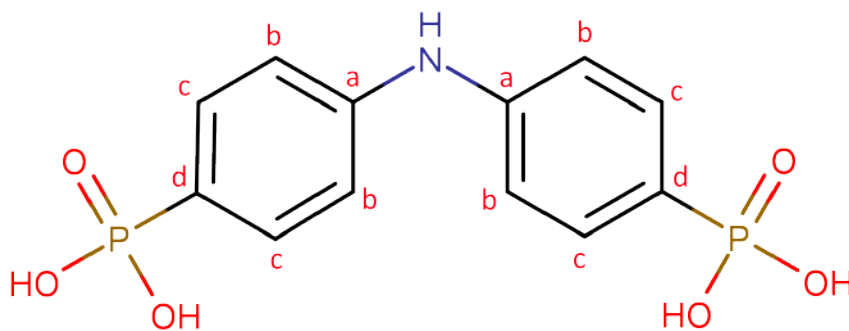


Figure 3.23: Chemical Structure of H_4BPA , with carbon environments labelled **a** to **d**, corresponding with A-D on the ^{13}C NMR spectrum.

Moving to the ^{13}C NMR spectrum, as shown in Figure 3.24, we can immediately confirm the lack of signal for the methine and methyl groups. Starting downfield, we see the peak, labelled A on the spectrum, which has been assigned to the two carbon atoms bonded to nitrogen, as was the case for iPr_4BPA . The next signal, labelled D, has been assigned to the two carbons bonded to phosphorus, which has actually shifted when compared with the spectrum for iPr_4BPA . The next two signals then are assigned to the carbons with bonded protons, labelled C and B respectively, with the latter of these being the more downfield. It was unfortunate here, in fact, that the acid is relatively insoluble and thus obtaining a spectrum with reasonable intensities was not possible, even though the signals were able to be assigned.

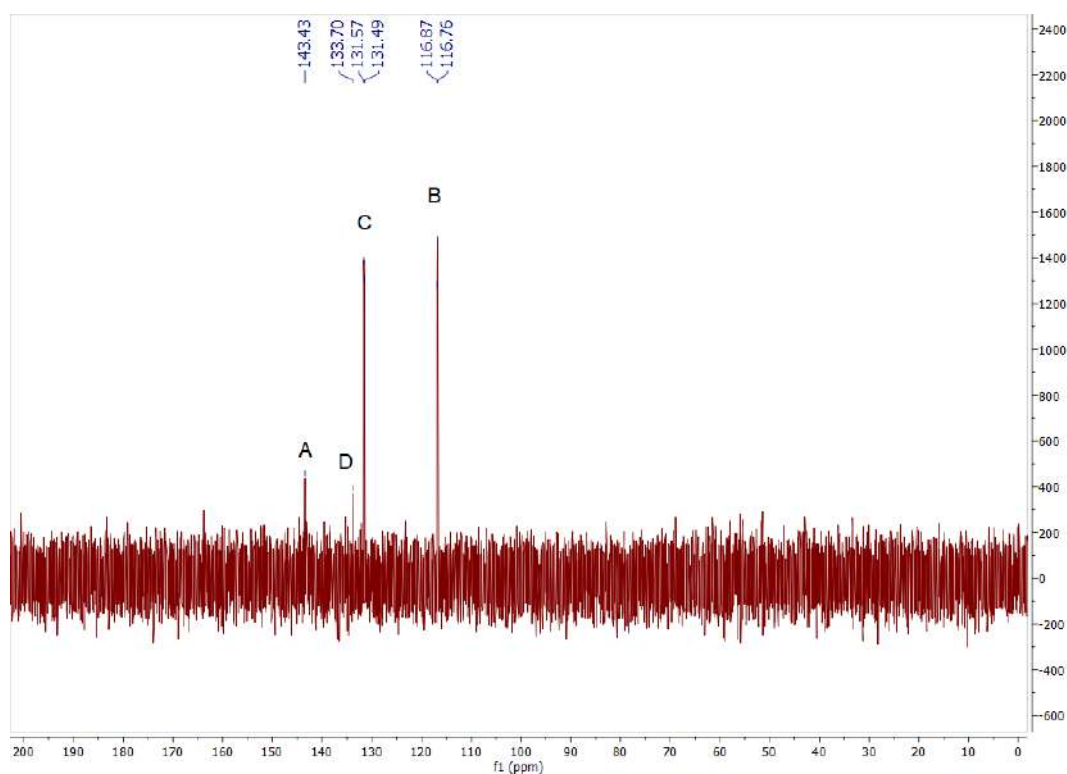


Figure 3.24: Full ^{13}C NMR spectrum for H_4BPA (**1B**). Solvent: 0.1M NaOH in D_2O .

As was done for iPr_4BPA , we again use coupled C-H NMR (HSQC) to lend support for the assignments for H_4BPA NMR spectra. Looking at the spectra in Figure 3.25, we can again see the lack of signals associated with the isopropyl groups. We can, however, see the two expected signals for the two sets of aromatic carbons with associated protons.

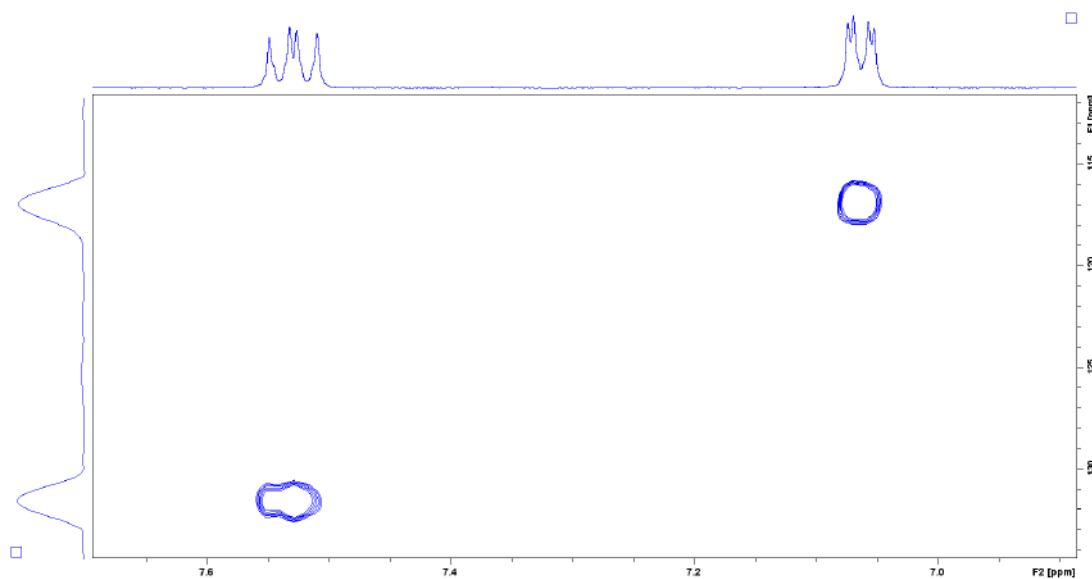


Figure 3.25: HSQC NMR spectrum for H₄BPA (**1B**), . Solvent: 0.1M NaOH in D₂O.

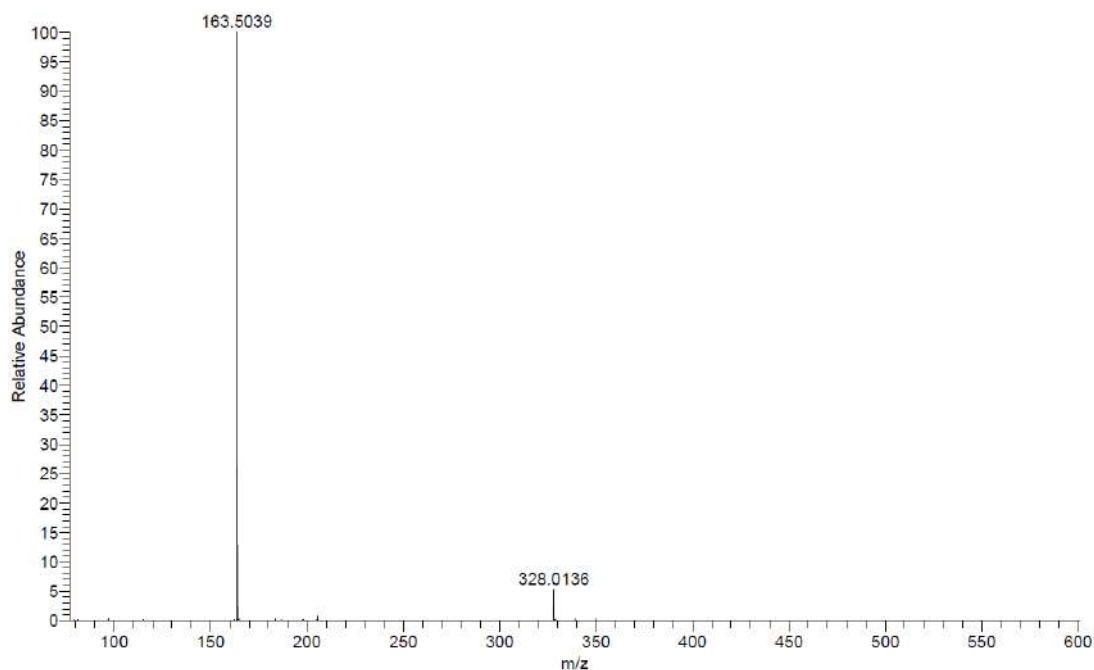


Figure 3.26: Observed Mass spectrum for H₄BPA.

As with the ester precursor, mass spectral analysis was carried out to confirm the results of the NMR analysis. Looking at Figure 3.26, the base peak is clear at a m/z of 163.50, which corresponds to the $[M+2H]^{2+}$ species. Figure 3.27 takes a closer look at this peak, showing a close match to the theoretical isotope profile. A second peak is located with a m/z of 328.01, and corresponds to the $[M+H]^+$ species.

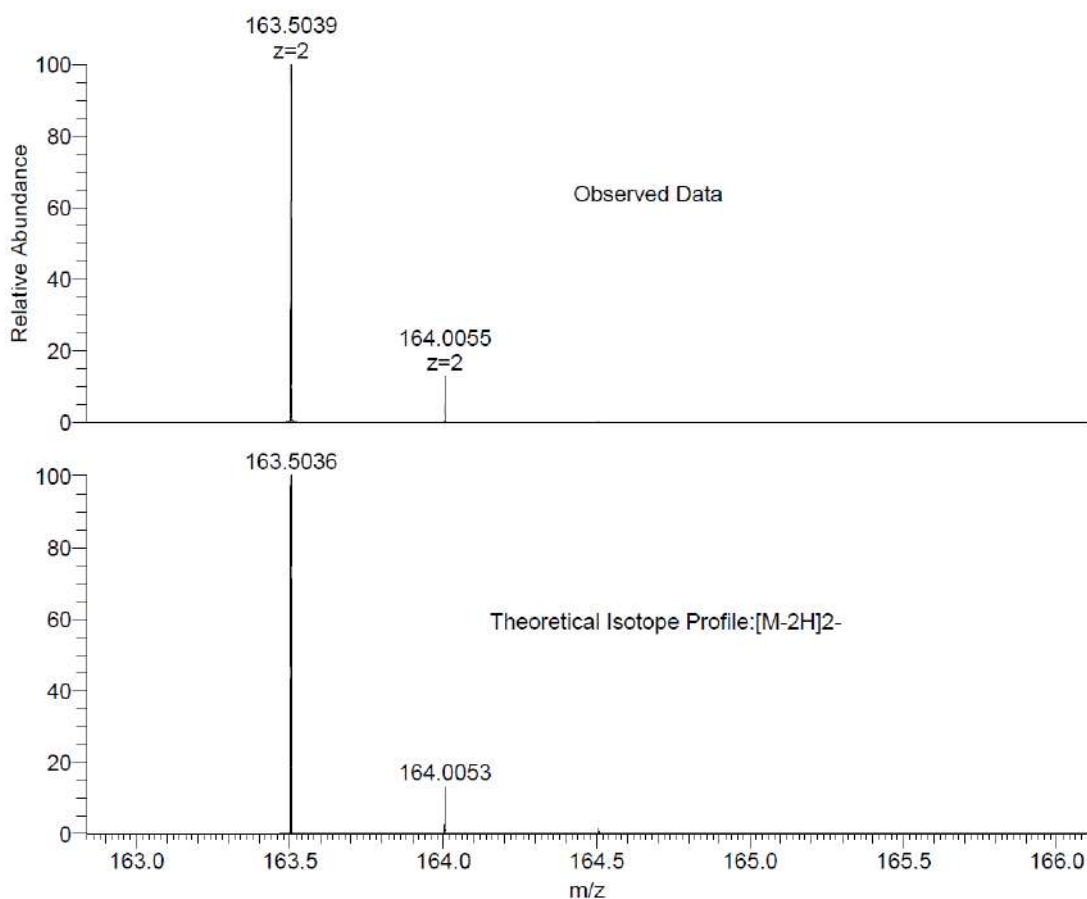


Figure 3.27: Observed Mass spectrum for H₄BPA and theoretical isotope pattern for the [M-2H]²⁻ species.

3,6-bis(diisopropylphosphono)-9H-carbazole (iPr₄DPC) (2A)

The second synthetic target, building upon the success of the first linker, was 3,6-bis(diisopropylphosphono)-9H-carbazole (iPr₄DPC) (**2A**). As with the previous linker, this was also a simple and reproducible procedure from which relatively high yields could be obtained. As with the amine linker, the crude reaction product was most often obtained as a dark brown treacle-like mixture, containing the target product alongside the monosubstituted side-product, some starting material, and some triisopropyl phosphite. Washing this in hexane then yielded a pinky/off-white solid, which could then be purified by flash chromatography. The yields here were often higher on average than for the previous linker, with synthetic yields obtained in the range of 82-97%.

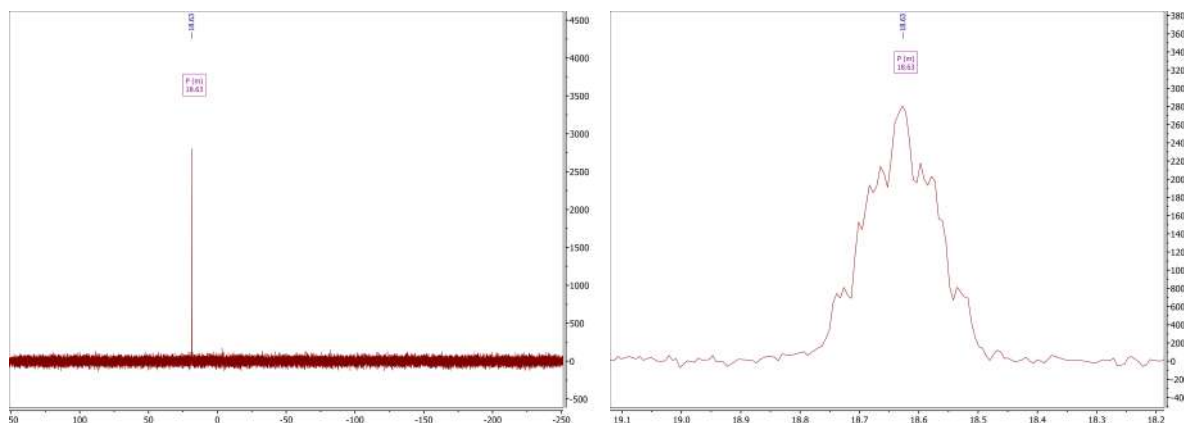


Figure 3.28: ^{31}P NMR spectrum for $i\text{Pr}_4\text{DPC}$ (**2A**). Solvent: Chloroform-*d*.

The ^{31}P NMR spectrum again reveals a significant signal corresponding to the target product, which shows a less resolved splitting pattern than was observed for $i\text{Pr}_4\text{BPA}$ (**2A**), though it still indicates higher order coupling with both the methine (H_d) and methyl (H_e) groups on the isopropyl moiety, as well as the aryl protons H_{a-b} .

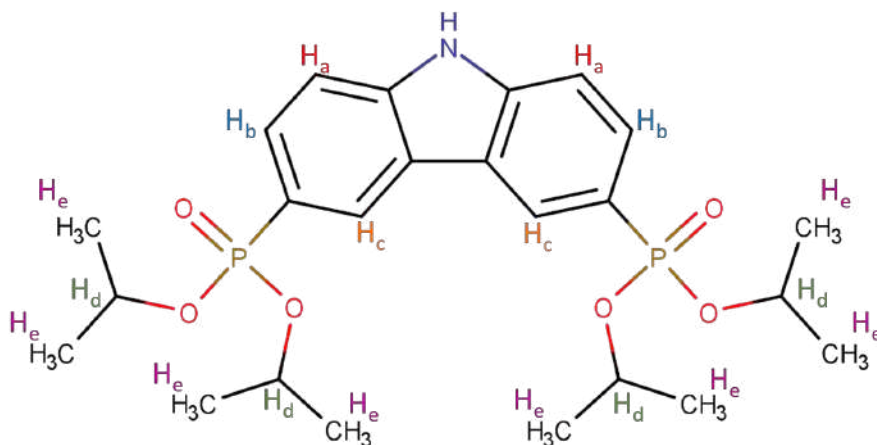


Figure 3.29: Chemical Structure of $i\text{Pr}_4\text{DPC}$ (**2A**), with proton environments labelled H_a to H_e , corresponding with A-E on the NMR spectrum.

Moving to the ^1H spectrum, in Figure 3.30 we see that there are some unexpected signals amongst those attributed to the product. Firstly, at δ 1.76 ppm we see a slightly broadened singlet, which is likely to be water, though the chemical shift is slightly higher than you would usually expect for water, δ 1.56 ppm.⁴² It is also possible that this belongs to the methyl group of either triisopropyl phosphite [$\text{P}(\text{O}i\text{Pr})_3$] and/or isopropyl bromide [$\text{BrCH}(\text{CH}_3)_2$]. This is also the case for the peaks at δ 4.64 ppm and

δ 1.35 ppm. Despite the difficulty in identifying this component, it should be noted that this did not seem to have an effect on the synthesis of the corresponding phosphonic acid, and is therefore not too much of a concern.

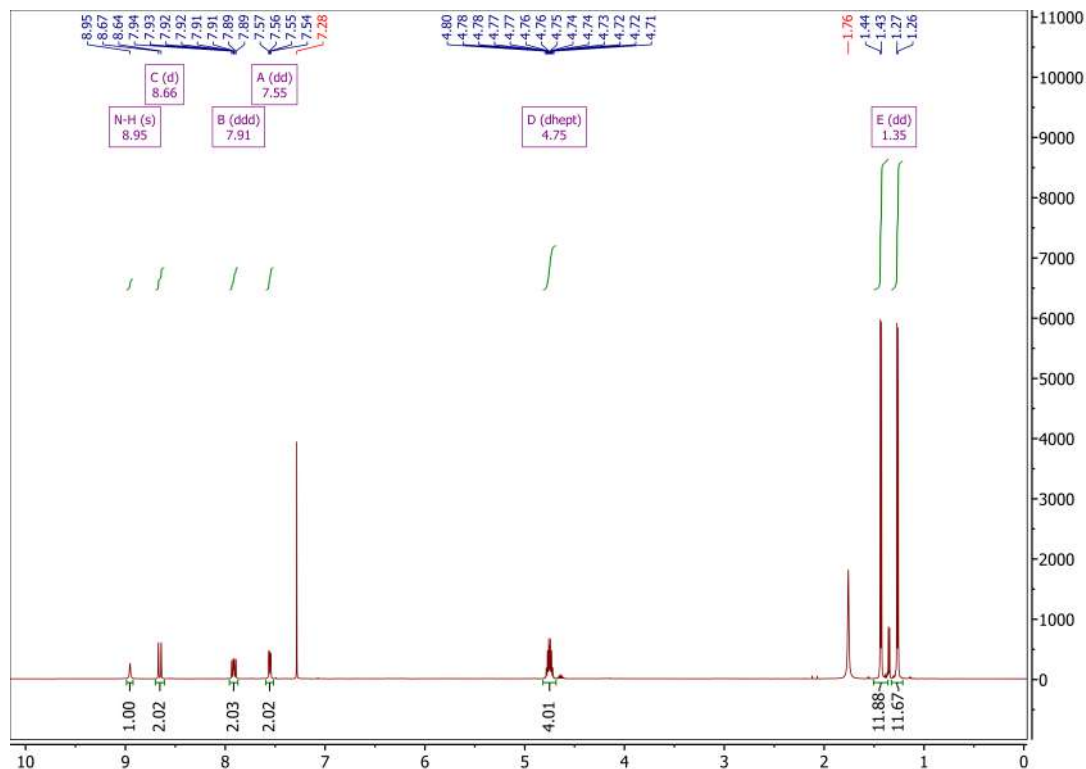


Figure 3.30: ^1H NMR spectrum for iPr_4DPC (**2A**). Solvent: Chloroform- d .

Moving to Figure 3.31 to focus on the aromatic region, we see four signals, three of which are to be attributed to the aryl protons and one to the proton bound to nitrogen. The latter of these has been attributed to the broadened signal at δ 8.95 ppm and integrates to 1 proton. Though you might not usually expect to see a signal for these protons, the solvent used, chloroform- d , is both apolar and aprotic, so there is no considerable exchange with the N-H proton. What we are left with then are the three signals associated with the aryl protons. The first of these signals (**C**), a doublet at δ 8.66 ppm, has been attributed to the proton labelled H_c in Figure 3.29. The splitting here is likely due to higher order coupling with phosphorus, causing the signal to display higher coupling constant than the other signals, which also display splitting patterns that indicate neighbouring protons, which H_c does not have. The next signal (**B**), at δ 7.91 ppm, has been attributed to the aryl proton labelled H_b in Figure 3.29.

Here we see a doublet of doublets of doublets (ddd), which is the result of the multiple opportunities for coupling. You would initially expect to see just a doublet caused by coupling with the aryl proton H_a , but this splits further due to coupling with both the aryl proton H_c and phosphorus, resulting in the ddd splitting pattern observed. This leaves the final signal (A) in this region, a doublet of doublets (dd) at δ 7.55 ppm, which has been attributed the proton labelled H_a . Coupling the adjacent aryl proton causes the initial splitting into a doublet, while further coupling with phosphorus causes further splitting, resulting in the observed doublet of doublets. This is again supported by the smaller coupling constants observed as you move to smaller δ shifts.

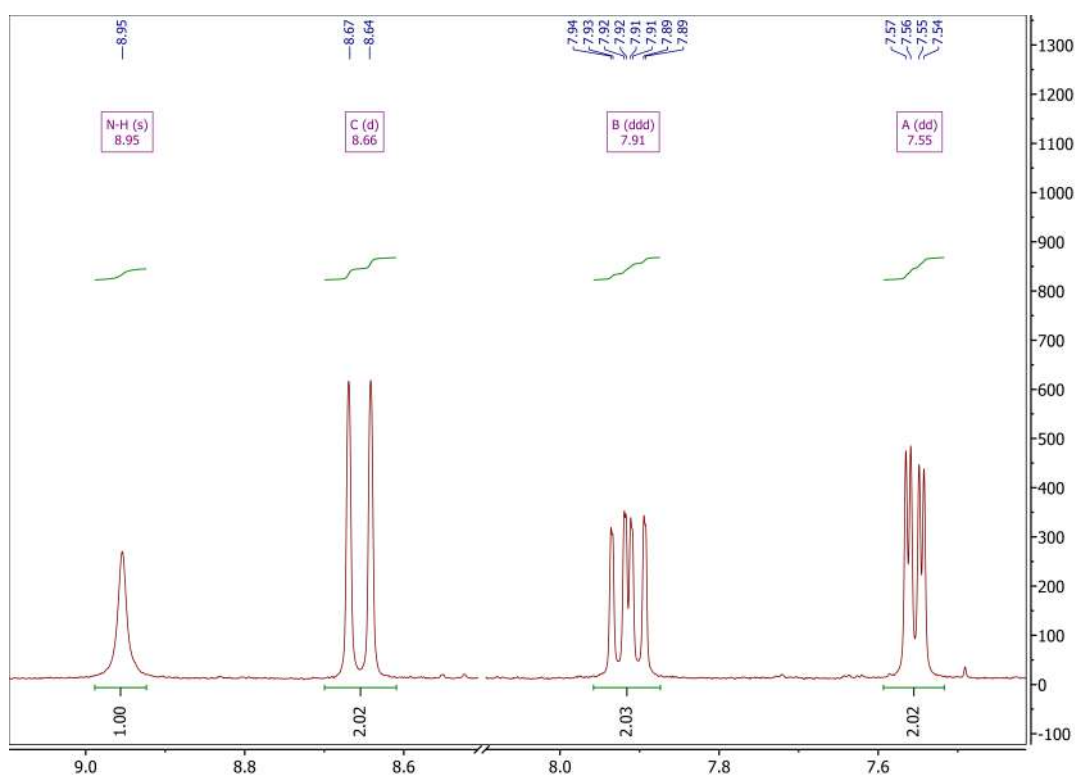


Figure 3.31: ^1H NMR spectrum for $i\text{Pr}_4\text{DPC}$ (**2A**). Solvent: Chloroform- d .

The final signal of concern in these spectrum, which again, was initially thought to be a doublet of doublets, can be seen at δ 1.35 ppm in Figure 3.33. As was established for $i\text{Pr}_4\text{BPA}$, however, this is in fact more likely to be two doublets which are the result of two chemically distinct methyl groups, and the splitting in each of the doublets arises through coupling with the methine proton. There is also a small impurity present

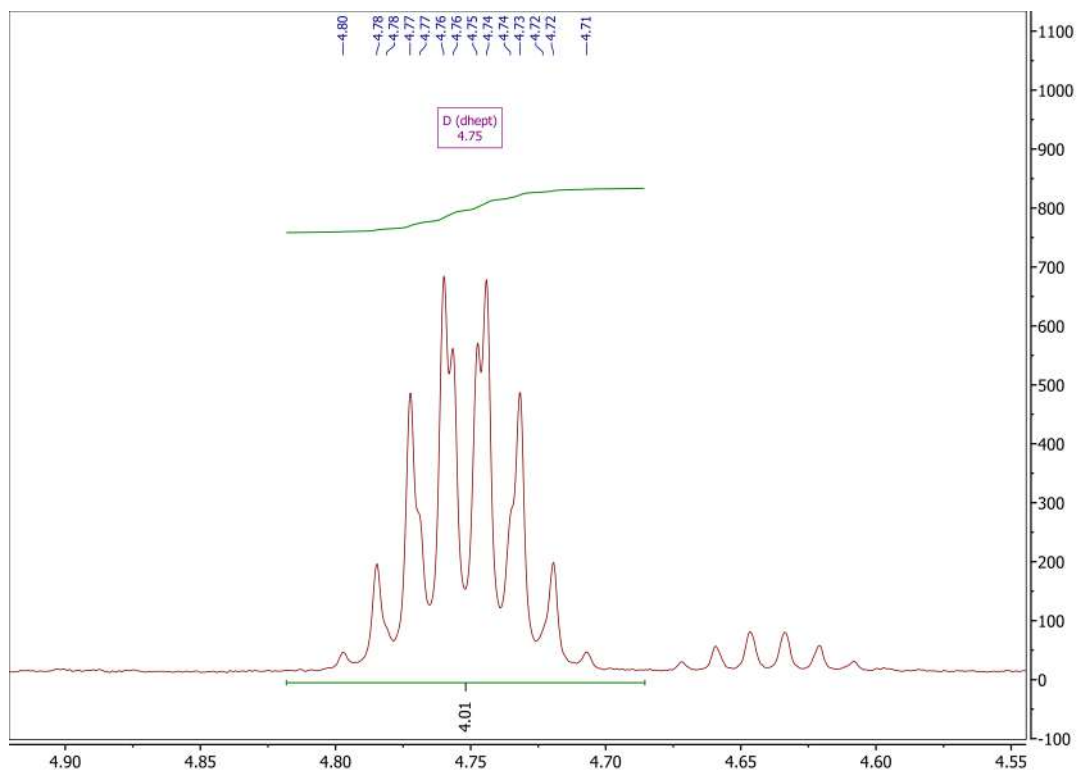


Figure 3.32: ^1H NMR spectrum for $i\text{Pr}_4\text{DPC}$ (2A). Solvent: $\text{Chloroform-}d$.

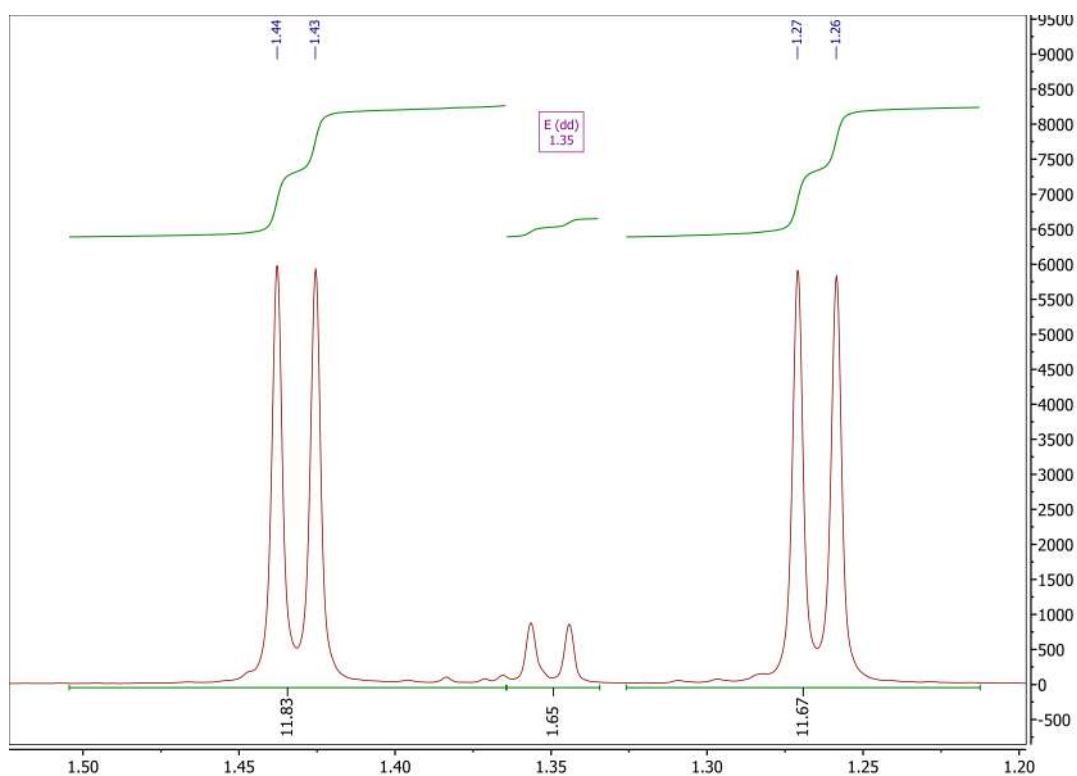


Figure 3.33: ^1H NMR spectrum for $i\text{Pr}_4\text{DPC}$ (2A). Solvent: $\text{Chloroform-}d$.

between the dd peaks, which, as mentioned previously, is suspected either isopropyl bromide or triisopropyl phosphite.

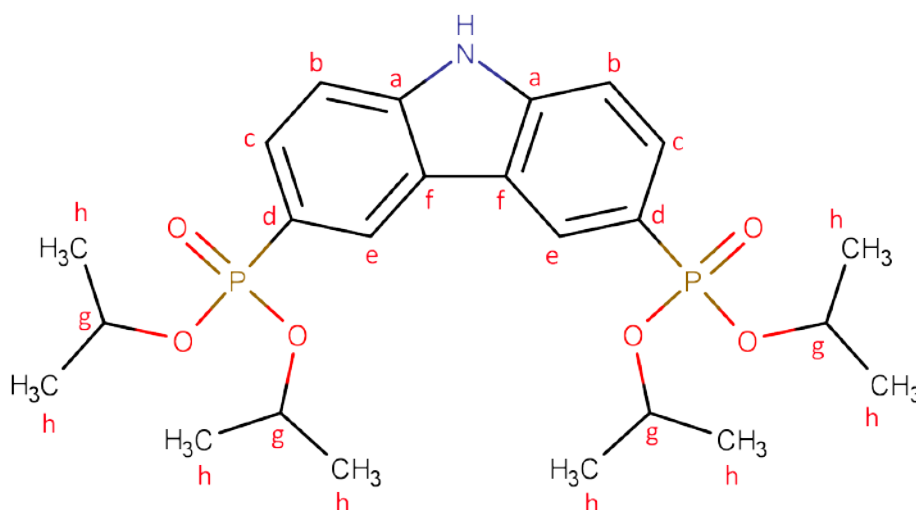


Figure 3.34: Chemical Structure of iPr_4DPC (**2A**), with carbon environments labelled **a** to **h**, corresponding with A-H on the ^{13}C NMR spectrum.

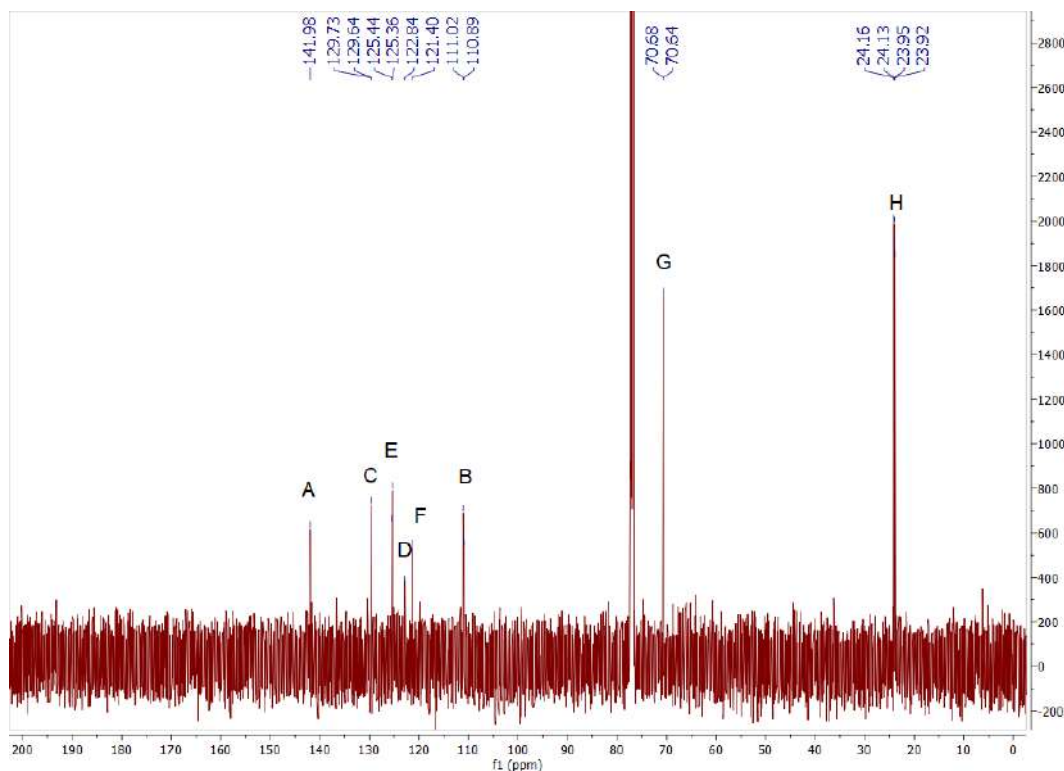


Figure 3.35: ^{13}C NMR spectrum for iPr_4DPC (**2A**). Solvent: Chloroform-*d*.

Looking to the ^{13}C NMR spectrum shown in Figure for iPr_4DPC , we can immediately see it is slightly more complicated than that of iPr_4BPA . Starting downfield, the first signal we see is the one at δ 141.98 ppm, which has been assigned to the carbons bonded to nitrogen, labelled A. Next we see two signals, labelled C (δ 129.69 ppm)

and E (δ 125.40 ppm), have been assigned to the aromatic carbons bearing protons, labelled accordingly, with the third of these aromatic signals (δ 110.96 ppm) labelled B. Then we have the peak labelled D at δ 122.84 ppm, assigned to the carbon bonded to phosphorus, followed by the peak at δ 121.40 ppm which is assigned to carbon in the β position, relative to nitrogen on the pyrrole-like ring. The final two peaks of interest labelled G (δ 70.66 ppm) and H (δ 24.04 ppm) are assigned to the carbons on the isopropyl groups.

Looking to the HSQC NMR spectra for clarification, we can confirm that the peaks labelled C, E, and B on the ^{13}C NMR spectrum, are indeed correlated with those labelled B, C, and A on the ^1H NMR spectrum. We also see the expected correlations for the methine and methyl groups.

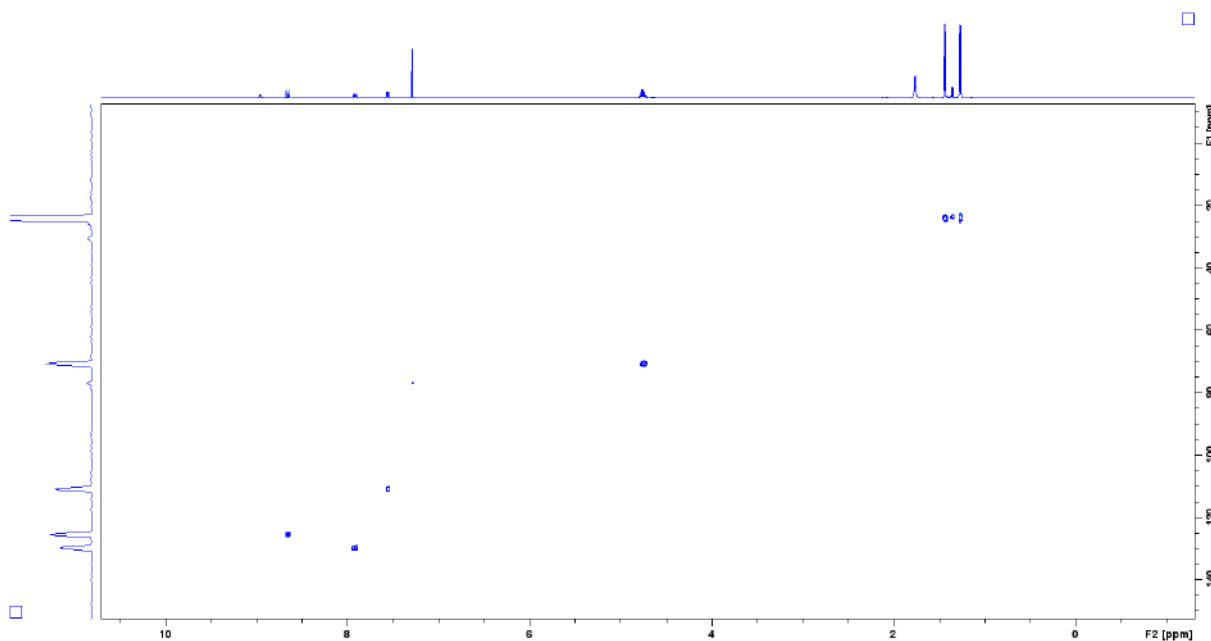
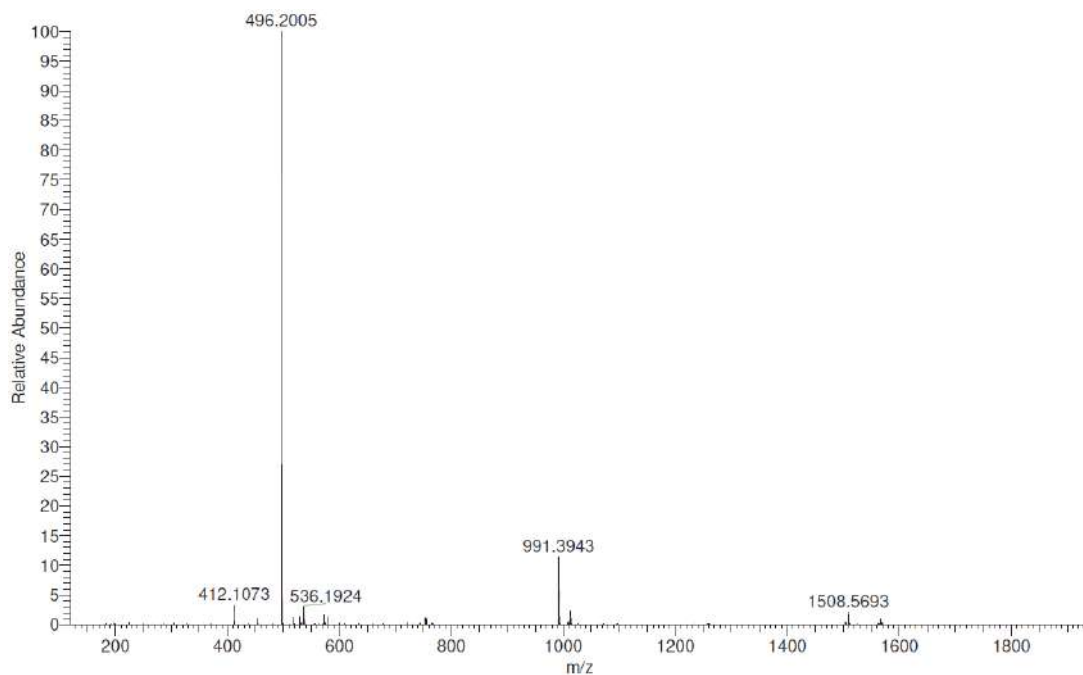
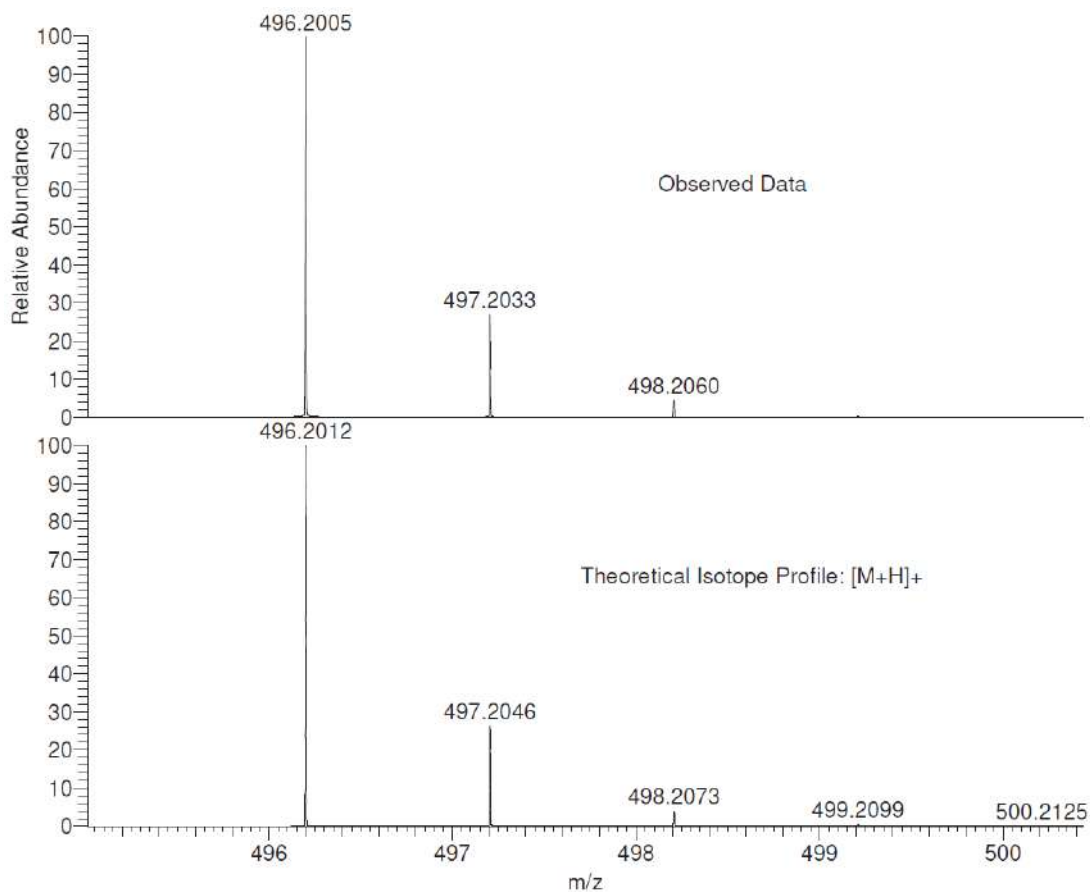


Figure 3.36: Full HSQC NMR spectrum for $i\text{Pr}_4\text{DPC}$ (**2A**). Solvent: Chloroform-*d*.

Moving the mass spectroscopy data, Figure 3.37 clearly shows the base peak at m/z 496.20 which corresponds to the $[\text{M}+\text{H}]^+$ species, as confirmed in Figure 3.38. A second major peak can be seen at 991.39, which corresponds to the $[\text{2M}+\text{H}]^+$ dimer species.

Figure 3.37: Observed Mass spectrum for iPr_4DPC .Figure 3.38: Observed Mass spectrum for iPr_4DPC and theoretical isotope pattern for the $[M+H]^+$ species.

3,6-diphosphono-9H-carbazole (H_4DPC) (**2B**)

Having successfully obtained iPr_4DPC , attention again shifted to obtaining the corresponding phosphonic acid, 3,6-diphosphono-9H-carbazole (H_4DPC). As with the amine, this was a relatively simple procedure and the product was often obtained in yields between 87-98% when using the silylation and hydrolysis using $TMSiBr$, since hydrolysis using HCl again seemed to cleave the P-C bond.

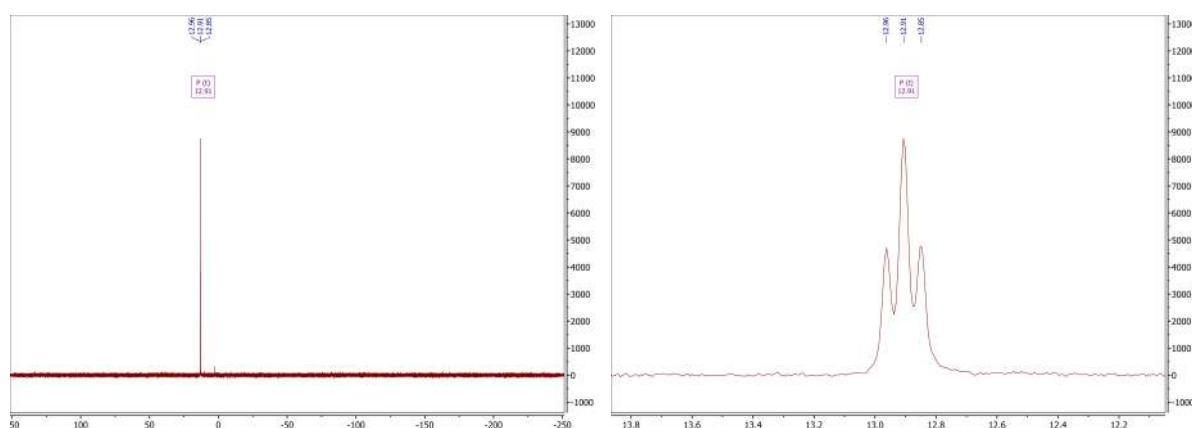


Figure 3.39: ^{31}P NMR spectrum for H_4DPC (**2B**). Solvent: Chloroform-*d*.

Looking first at the ^{31}P NMR spectrum, as seen in Figure 3.39, there is a major signal at δ 12.91 ppm, which corresponds to the target product, H_4DPC . There is also a clear change in splitting pattern here, whereby a triplet is observed, though this can be attributed to coupling with the two nonequivalent aryl protons (H_b & H_c). There is also a minor signal upfield at δ 2.6 ppm which may correspond with hydrolysis of leftover triisopropyl phosphite, though this signal is relatively weak in comparison and can be ignored.

Moving next to the 1H NMR spectrum as shown in Figure 3.41, it is clear that there are no signals corresponding to the isopropyl groups, thus the hydrolysis has been successful, and there seem to be no signals that indicate other impurities. It is also clear that the signal observed previously for N-H has now disappeared, since a protic solvent is now being used.

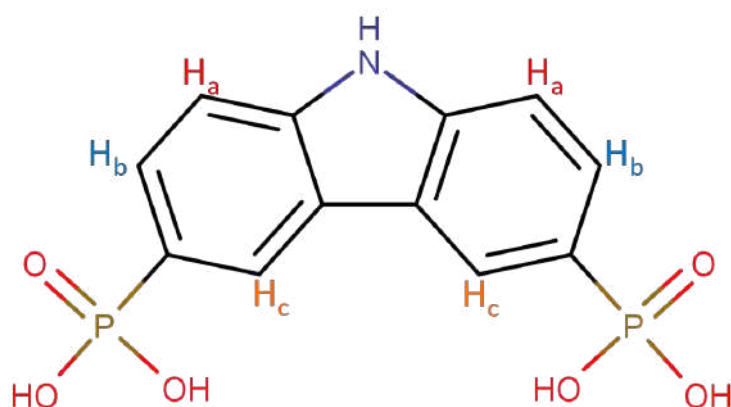


Figure 3.40: Chemical Structure of H₄DPC (**2B**), with proton environments labelled H_a to H_c, corresponding with A-C on the NMR spectrum.

Taking a closer look at the aromatic region, as seen in Figure 3.42, the signals present can be assigned exactly as they were for iPr₄DPC, whereby protons labelled H_{a-c} correspond to signals A-C respectively. One clear difference however, is the less resolved nature of the spectrum, which causes overlap of signals.

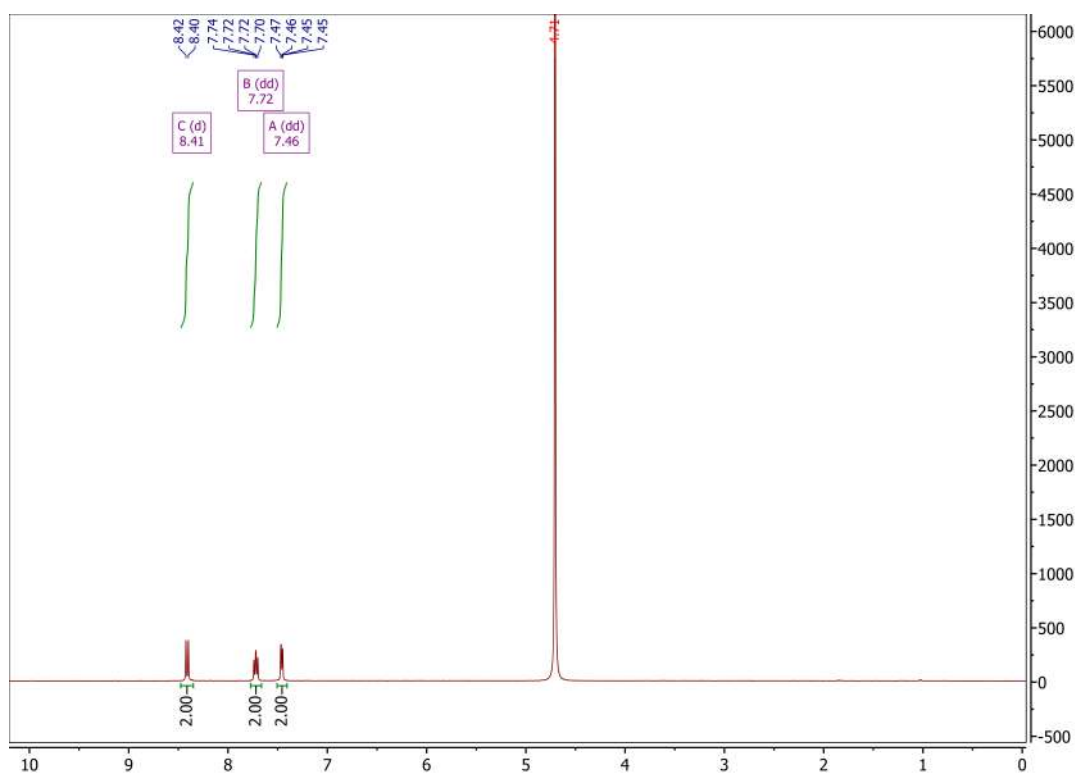


Figure 3.41: Full ¹H NMR spectrum for H₄DPC (**2B**). Solvent: Chloroform-*d*.

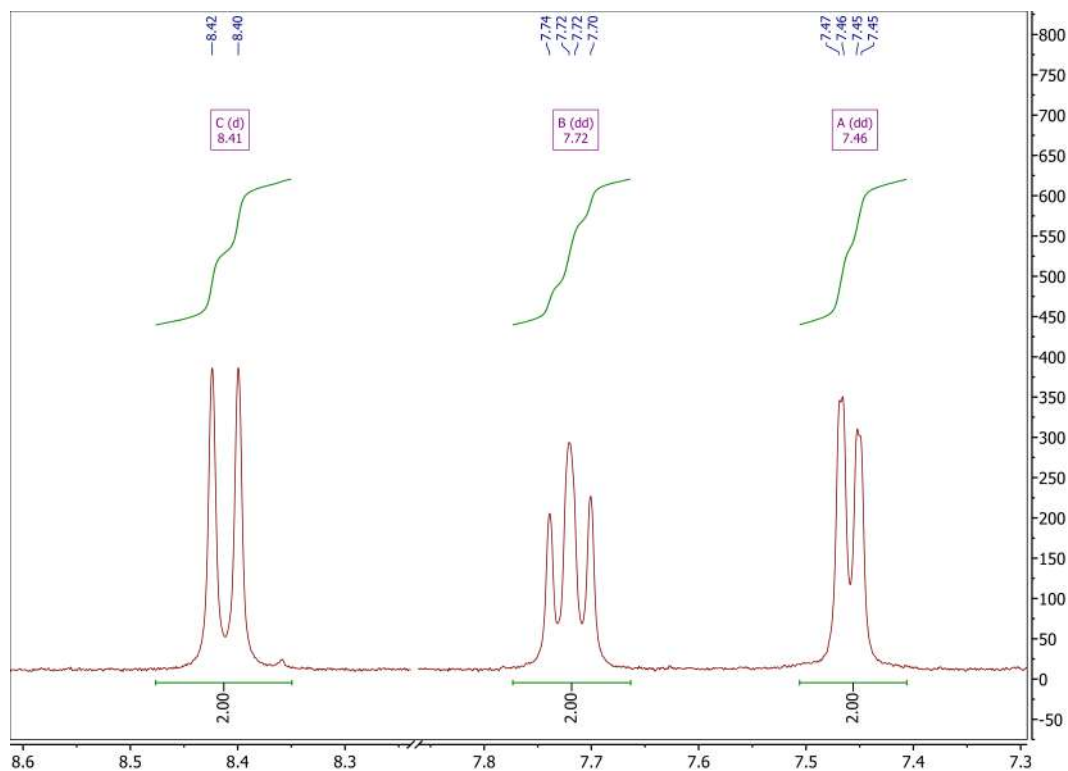


Figure 3.42: ^1H NMR spectrum for H_4DPC (**2B**). Solvent: 0.1M NaOH in D_2O .

This is immediately clear for the signal at δ 7.72 ppm, which was previously classified as a doublet of doublets of doublets (ddd), though now seems to be a triplet. This increased intensity of the central peak is caused by the overlap of multiple peaks which, when resolved, would represent the expected ddd splitting pattern as caused by coupling to the other aryl protons and phosphorus.

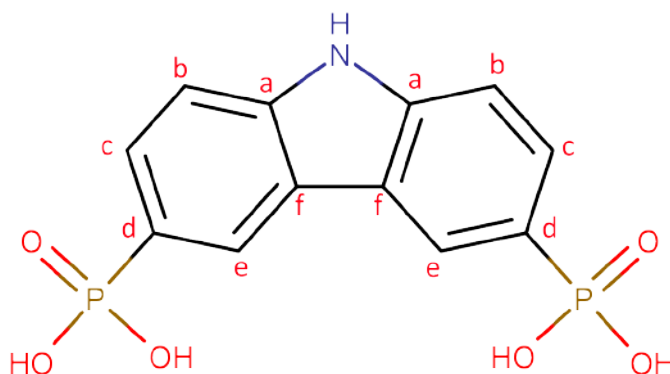


Figure 3.43: Chemical Structure of H_4DPC (**2B**), with carbon environments labelled **a** to **f**.

Further characterisation using ^{13}C NMR was less successful, most likely due to the insolubility of H_4DPC and the subsequent inability to obtain an spectrum with sufficient peak intensities to accurately assign peaks, at least fully. Looking at Figure 3.44, it is clear that some of the potential signals in the area of interest are barely above the rather noisy background. Referring to the HSQC NMR spectra, however,

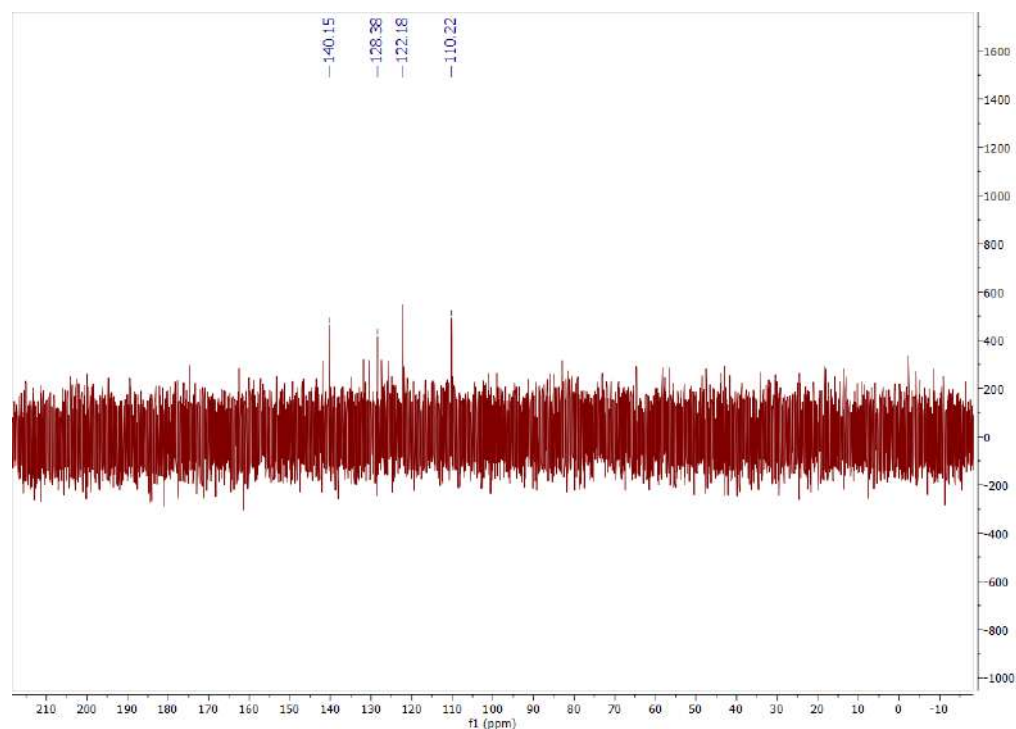


Figure 3.44: Full ^{13}C NMR spectrum for H_4DPC (**2B**). Solvent: 0.1M NaOH in D_2O .

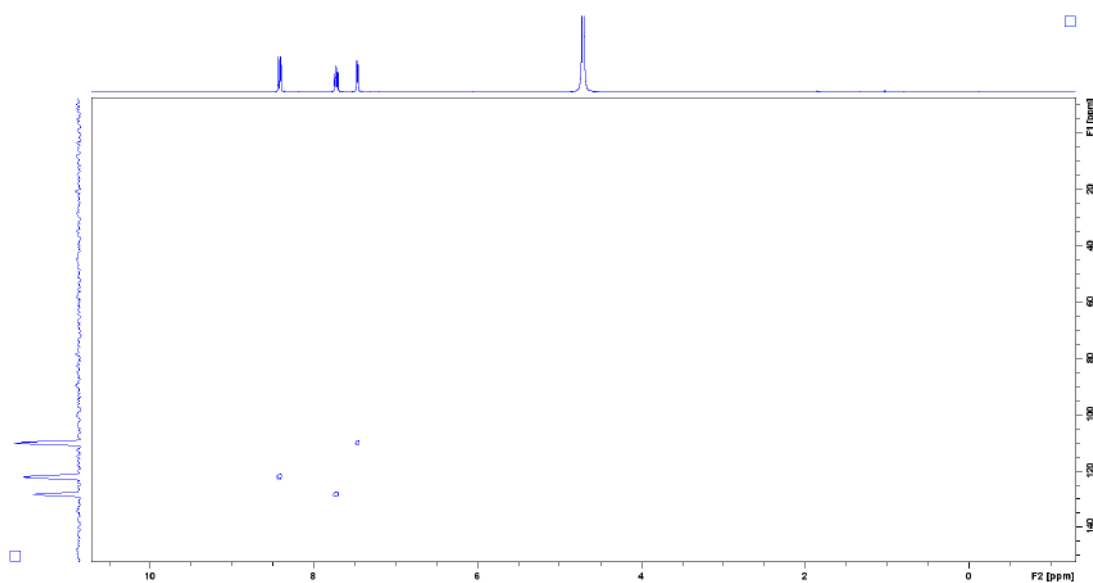


Figure 3.45: Full HSQC NMR spectrum for H_4DPC (**2B**). Solvent: 0.1M NaOH in D_2O .

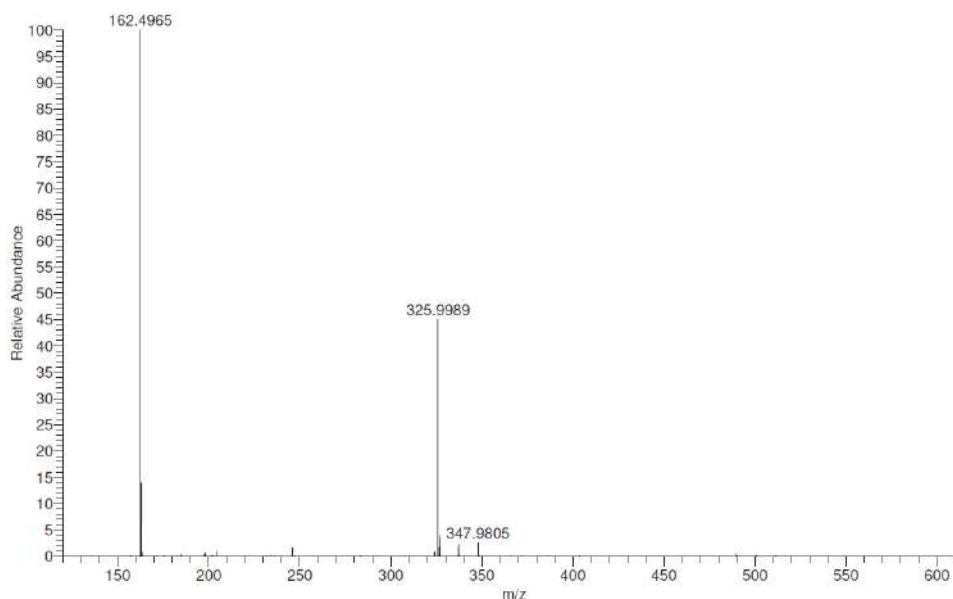


Figure 3.46: Observed Mass spectrum for H₄DPC.

it is possible to at least assign the peaks for carbons with bonded protons. With this in mind, it is clear that the ¹³C peaks at δ 128.38, δ 122.18, and δ 110.22 ppm can be assigned to the carbons labelled E, C, and B, respectively.

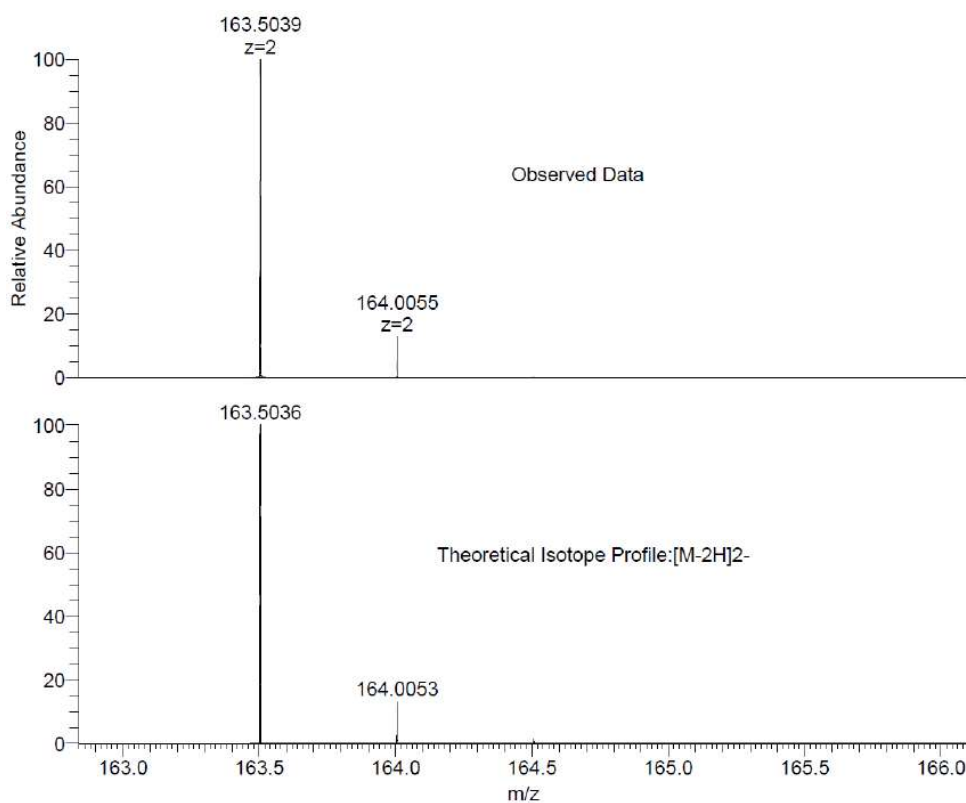


Figure 3.47: Observed Mass spectrum for H₄DPC and theoretical isotope pattern for the [M-2H]²⁻ species.

Looking at the mass spectral data, Figure 3.46 clearly shows the base peak at m/z 162.50 corresponding to the $[M-2H]^{2-}$ species, and can be seen in more detail in Figure 3.47. Another peak is shown at m/z 325.99, corresponding to the $[M-H]^{-}$ species.

4-diisopropylphosphono-N-(4-diisopropylphosphonophenyl)-N-phenylaniline [iPr₄DPPA] (3A)

The third synthetic target obtained was 4-diisopropylphosphono-N-(4-diisopropylphosphonophenyl)-N-phenylaniline (iPr₄DPPA) (3A), with the idea behind this linker being the replacement of the N-H proton on iPr₄BPA with a phenyl group to see if and how this might affect the formation of potential metal phosphonate frameworks, though this will be explored in Chapter 4. As with the two previous linkers, this synthesis was also straightforward and could be achieved in yields above 80%. The procedure itself was essentially identical, with a simple workup in hexane to obtain the linker.

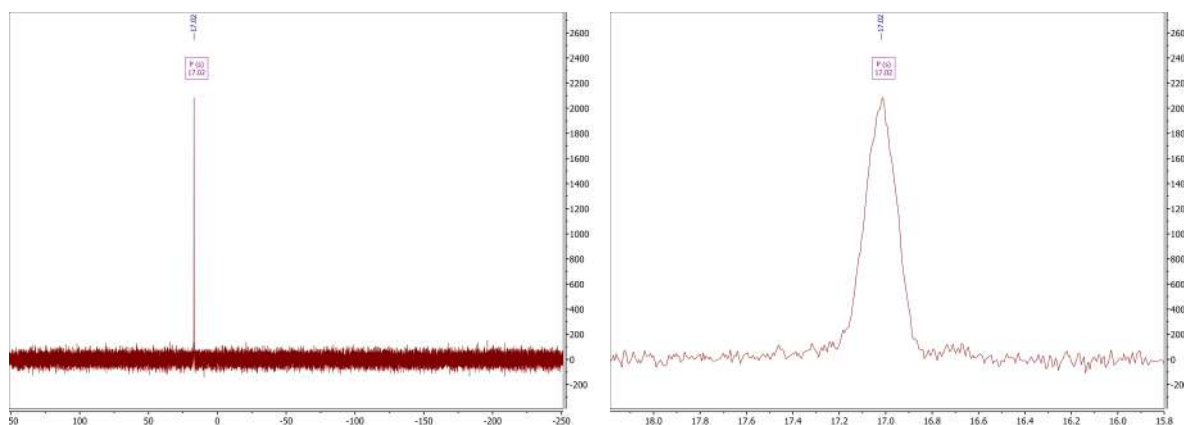


Figure 3.48: ³¹P NMR spectrum for iPr₄DPPA (3A). Solvent: Chloroform-*d*.

Looking first at the ³¹P NMR spectrum, see Figure 3.48, we see just a single signal which can be attributed to the target product, iPr₄DPPA. Taking a closer look at the signal, it seems that the splitting observed for the two previous linkers is not present, though this is most likely due to low resolution.

Moving to the ¹H NMR spectrum, as shown in Figure 3.50, we again see the impurities suspected to be either triisopropyl phosphite and/or isopropyl bromide, as was

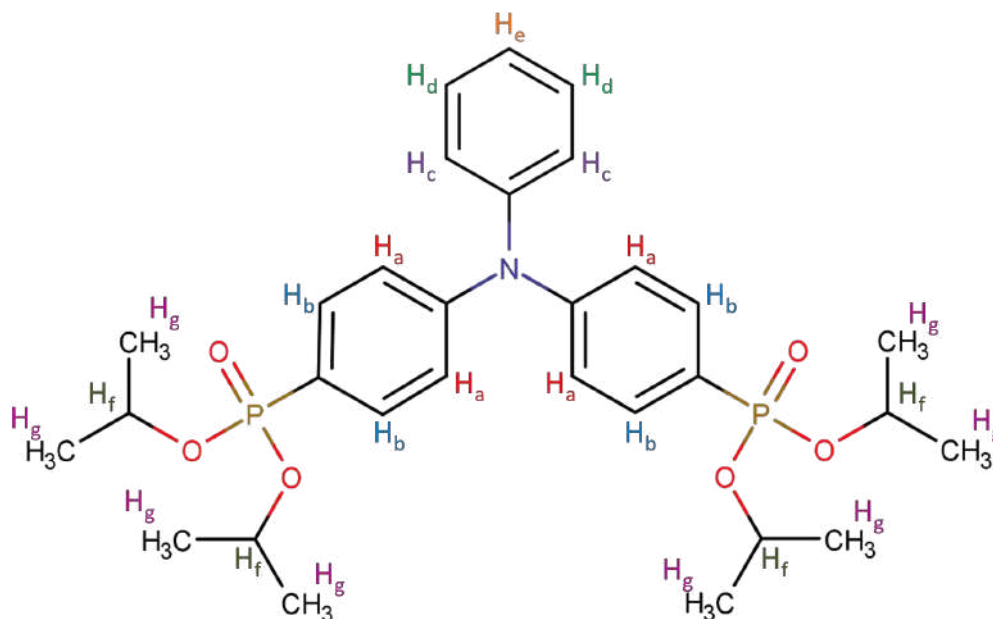


Figure 3.49: Chemical Structure of *iPr*₄DPPA (3A), with proton environments labelled H_a to H_g, corresponding with A-G on the NMR spectrum.

indicated for *iPr*₄DPC. Beyond this there are no other unexpected signals, and the only other features of note are the slightly unresolved signals in the aromatic region.

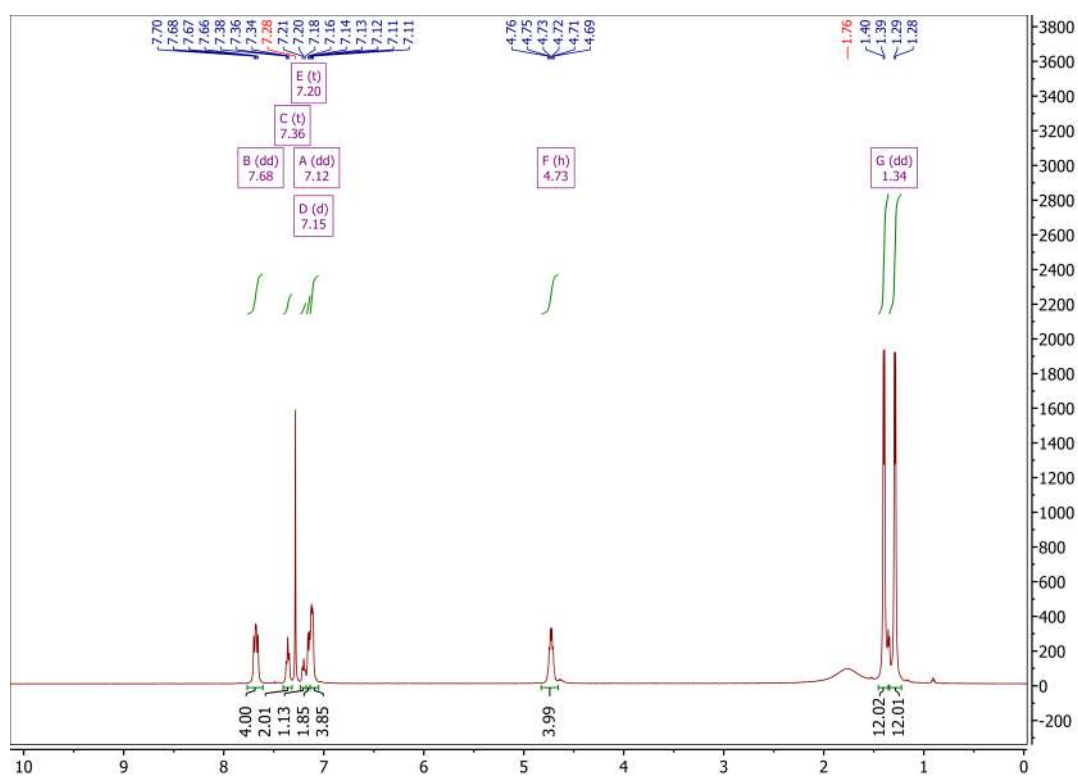


Figure 3.50: ¹H NMR spectrum for *iPr*₄DPPA (3A). Solvent: Chloroform-*d*.

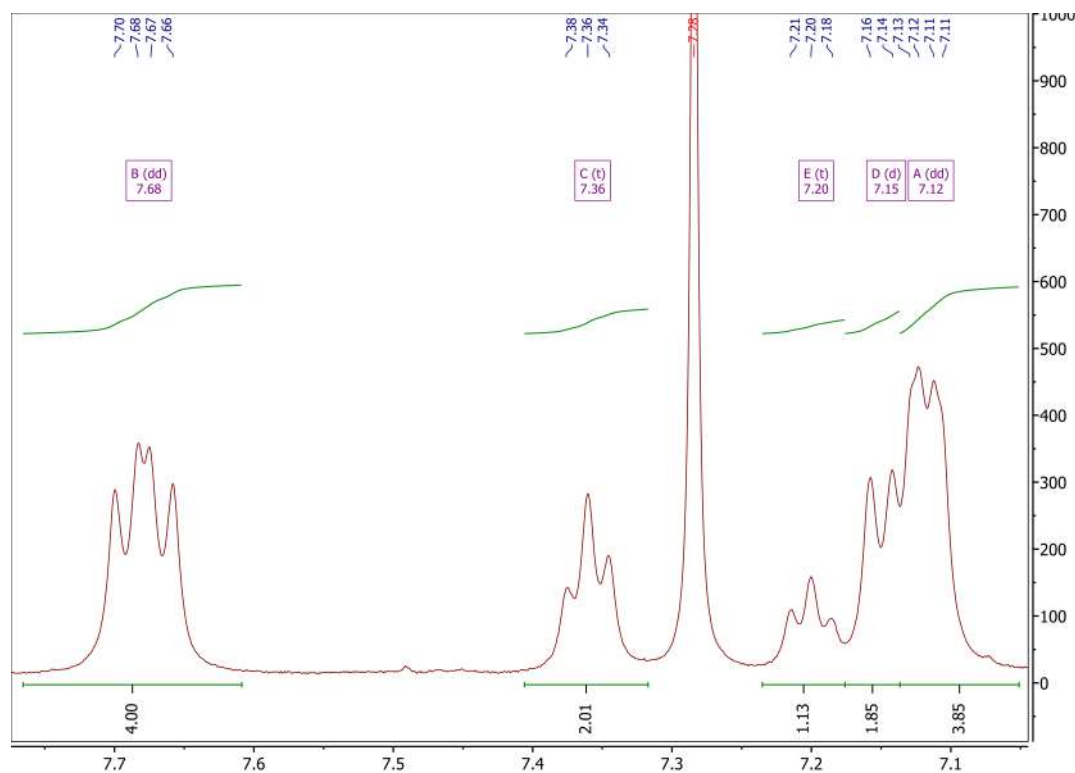


Figure 3.51: ^1H NMR spectrum for $i\text{Pr}_4\text{DPPA}$ (**3A**). Solvent: Chloroform- d .

Zooming in on the aromatic region, as seen in Figure 3.51, it is possible to identify five signals in total. The first of these signals has a δ -shift of 7.86 ppm, which can be assigned similarly to the $i\text{Pr}_4\text{BPA}$ linker, whereby the peak corresponds to protons nearest to phosphorus on the phenyl rings, labelled H_b in Figure 3.49, again indicated by the large coupling constants. The integration also indicates that it at least belongs to the rings containing phosphonate groups. The next signal, at δ 7.36 ppm, has been assigned to the protons labelled H_c on the phenyl ring with no phosphonate group. The splitting on the spectrum shows a triplet, though you might expect a doublet of doublets for the associated proton, therefore it is likely that this is what we are seeing, simply unresolved. Next we see the solvent peak at δ 7.28 ppm. Moving upfield, we see a relatively easy to assign signal at δ 7.20 ppm, and in this case has been attributed to the proton labelled H_e , and is supported by the 1.13 integration value. The final two signals in the aromatic region, while not fully resolved, can be assigned and the splitting can also be identified. The first one, at δ 7.15 ppm, appears to be a simple doublet, and integrates approximately to two, and should therefore be assigned to the

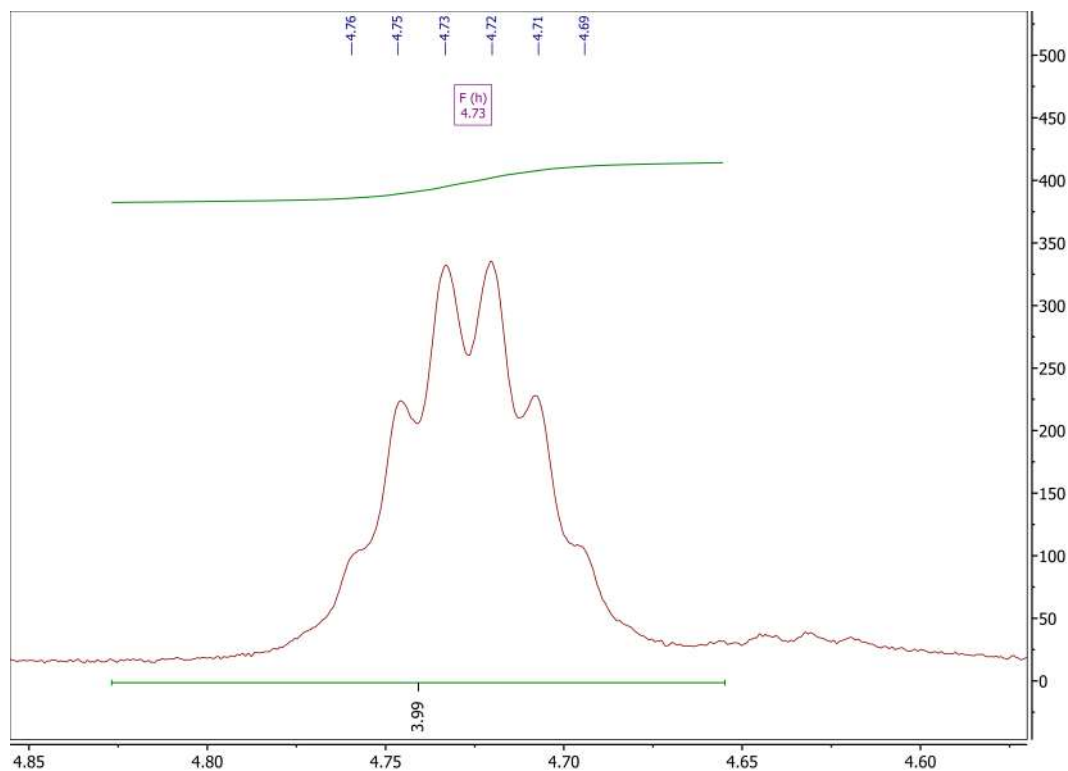


Figure 3.52: ^1H NMR spectrum for iPr_4DPPA (**3A**). Solvent: Chloroform-*d*.

remaining protons on the non-phosphonate-containing ring labelled H_d . By process of elimination, this leaves the final aromatic signal at δ 7.12 ppm to be assigned to the protons labelled H_a , though this assignment is supported by the doublet of doublet splitting pattern as well as the integration of approximately four.

Moving to the signal at δ 4.73 ppm, as shown in Figure 3.52, we see what initially looked like a sextet, though as we have previously explored, is most likely an unresolved doublet of heptets, as you would expect for the methine moiety on the isopropyl groups, labelled H_f in Figure 3.49. The integration of four is also in favour of this assignment.

The final signal, as shown in Figure 3.53, appears at δ 1.34 ppm as a pair of doublets, as was established for iPr_4BPA and iPr_4DPC . The integration for each of the doublets is 12, together totalling 24, as expected.

Moving on to the ^{13}C NMR spectra, as shown in Figure 3.55, we see a series of signals that initially seems to be one too many for what you might expect. Straight away, we

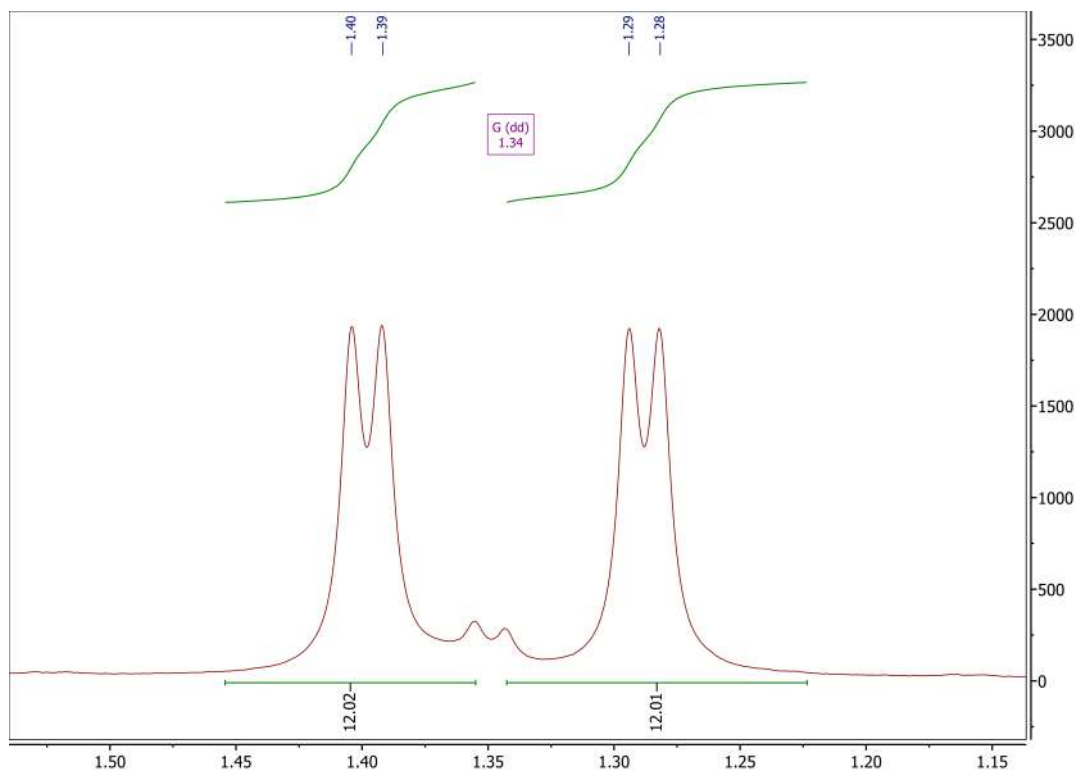


Figure 3.53: ^1H NMR spectrum for $i\text{Pr}_4\text{DPPA}$ (**3A**). Solvent: Chloroform- d .

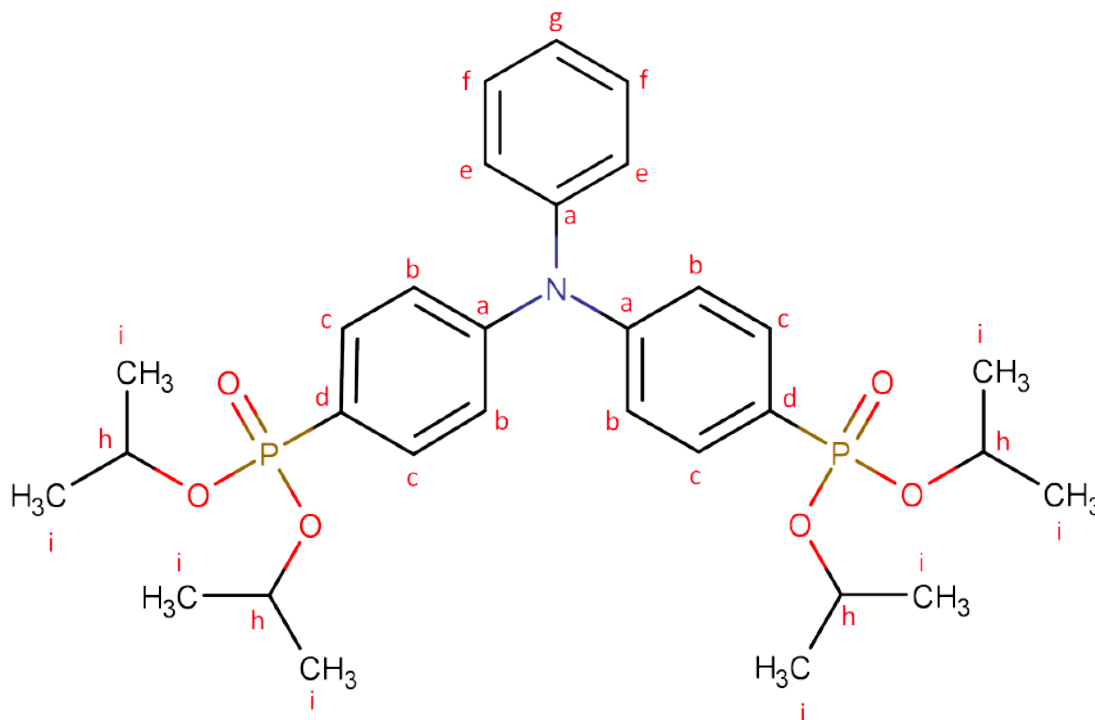


Figure 3.54: Chemical Structure of $i\text{Pr}_4\text{DPPA}$ (**3A**), with carbon environments labelled H_a to H_i , corresponding with A-I on the ^{13}C NMR spectrum.

can assign the methyl (i) and methine (h) carbons to the signals at δ 24.02 ppm and δ 70.63 ppm, respectively.

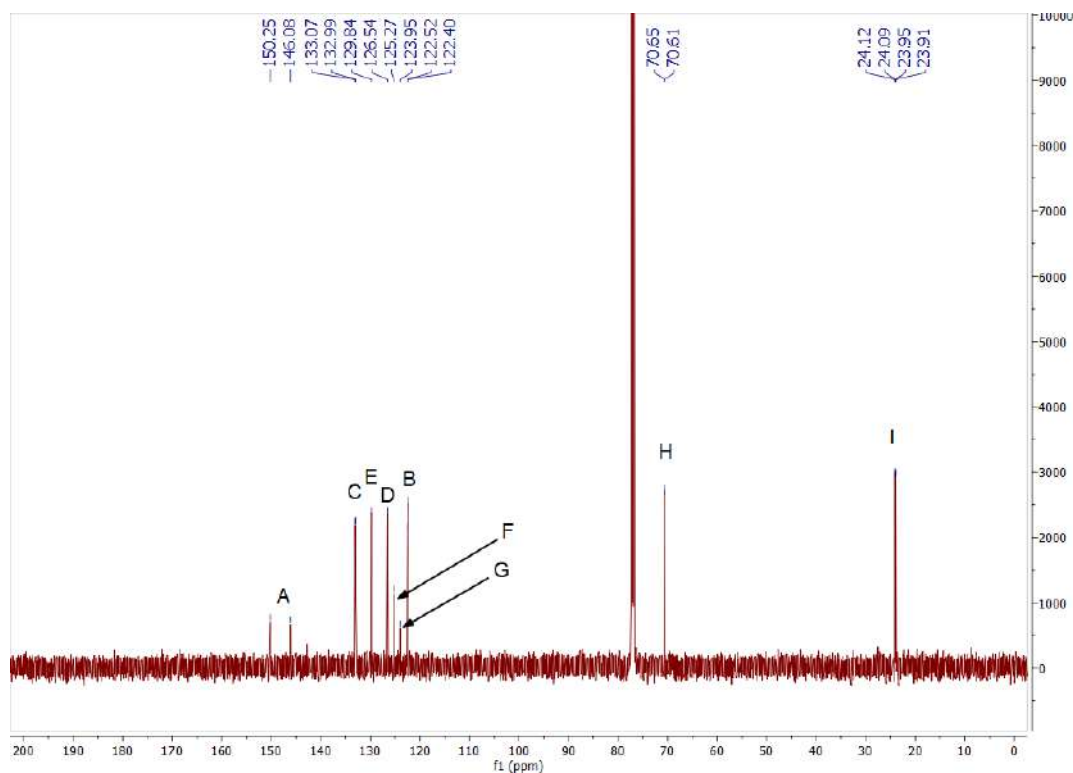


Figure 3.55: Full ^{13}C NMR spectrum for $i\text{Pr}_4\text{DPPA}$ (**3A**). Solvent: Chloroform-*d*.

Moving downfield, things start to get slightly more complicated. The first two signals at δ 150.25 ppm and δ 145.08 ppm have both been assigned to the carbon atoms bonded to nitrogen, labelled (**a**) in Figure 3.54, with one representing the rings containing phosphonate groups and the other representing the ring with no phosphonate group. Following this we have the signal at δ 133.03 ppm, which has been assigned to the carbons labelled (**c**). Next is the signal at δ 129.84 ppm, which has been assigned to the carbons on the non-phosphonate-containing ring, labelled (**e**). The next signal, at δ 126.54 ppm, has been assigned to the carbons directly bonded to phosphorus, labelled (**d**). The next two signals at δ 125.27 ppm and δ 123.95 ppm, which are of slightly lower intensity, have been assigned to the carbons on the non-phosphonate-containing ring, labelled (**f**) and (**g**), respectively. The final signal on the spectrum, δ 122.46 ppm, has been assigned to the carbons in the β positions, relative to nitrogen, on the phosphonate containing rings, labelled (**b**). Lending support for these assignments as well as those for the proton NMR, is the HSQC NMR spectrum shown in Figure 3.56, in which the signals have been labelled 1-5 for clarity. The signals show the correlations

between C_c-H_b (1), C_e-H_c (2), C_g-H_e (3), C_f-H_d (4), and C_b-H_a (5).

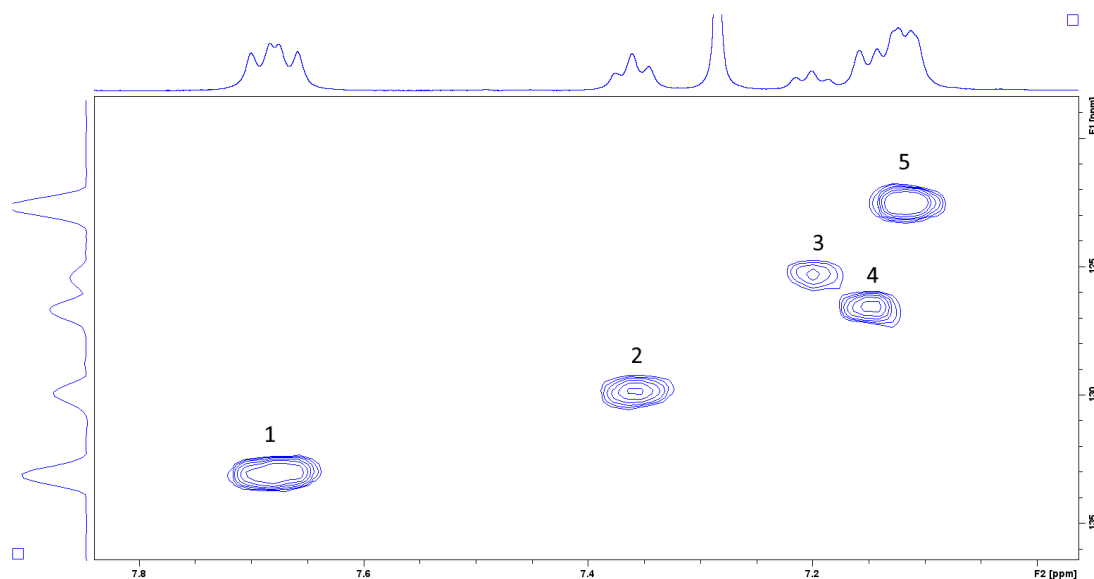


Figure 3.56: HSQC NMR spectrum for iPr_4DPPA (3A). Solvent: Chloroform- d .

Mass spectral analysis was carried out, and Figure 3.57 clearly shows the base peak at m/z 574/25, which corresponds to the $[M+H]^+$ species. This can be seen in greater detail in Figure 3.58, which compares the theoretical isotope profile with observed data, shown a good match between the two.

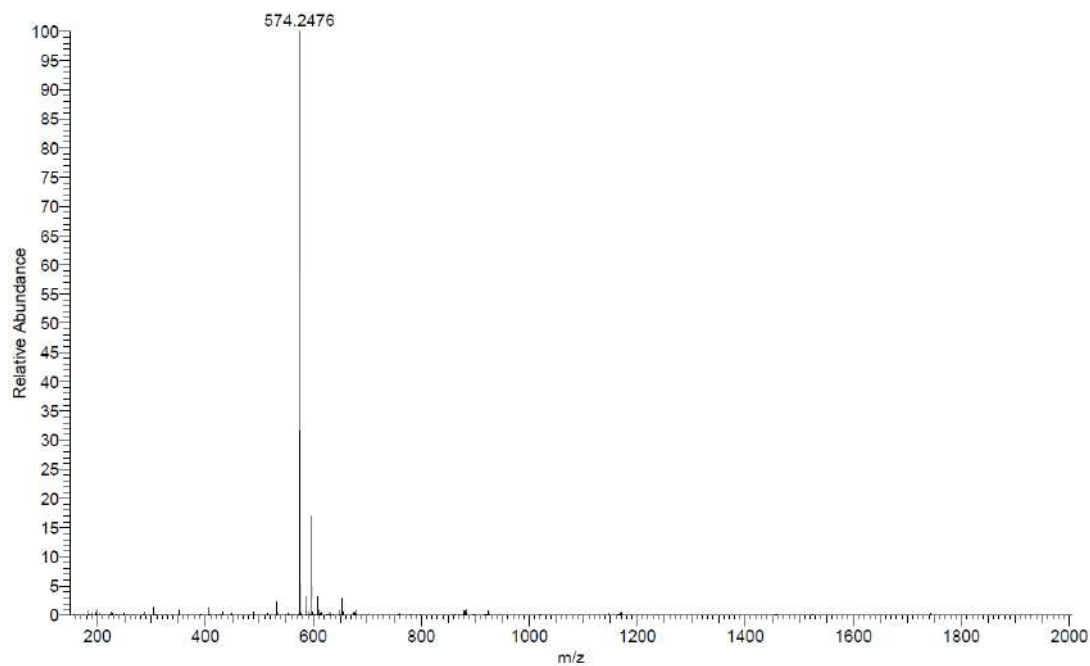


Figure 3.57: Observed Mass spectrum for iPr_4DPPA .

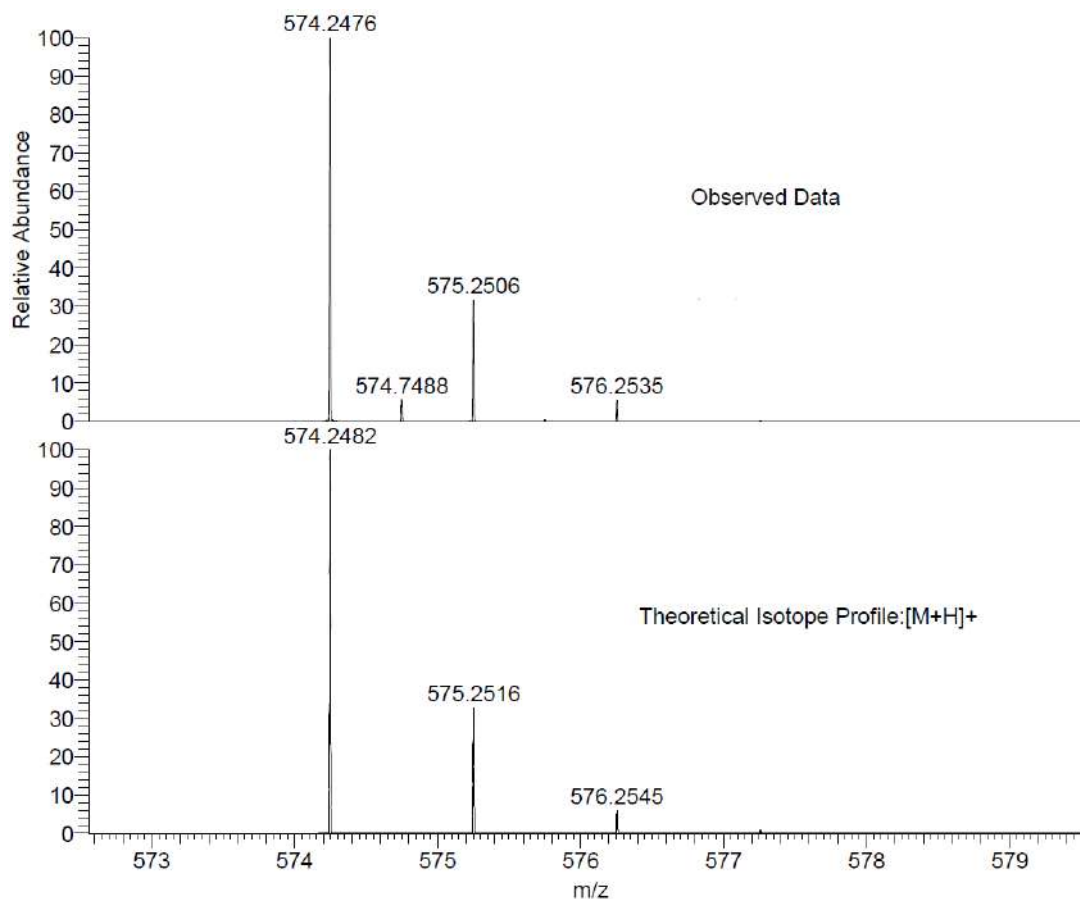


Figure 3.58: Observed Mass spectrum for iPr_4DPPA and theoretical isotope pattern for the $[M+H]^+$ species.

4-phosphono-N-(4-phosphophenyl)-N-phenylaniline [H₄DPPA] (3B)

Although a rather repetitive statement at this point, the hydrolysis of iPr_4DPPA to obtain H_4DPPA was, as was the case for the other two linkers, a relatively simple procedure, and pretty reasonable yields of between 70-95% could be achieved. Unlike the previous two, this linker was not assessed for its suitability for hydrolysis using HCl, instead opting to go straight for the less harsh procedure involving silylation through the use of TMSiBr.

Starting with the ^{31}P NMR spectrum, we can immediately see the presence of only one signal, indicating relative purity with regards to phosphorus-containing compounds. We can already observe the loss of the isopropyl groups here from the huge change

in the splitting pattern. Here, we see only a triplet, likely caused by coupling with the aromatic protons, whereas the pattern for the ester presented a much more complicated and much less resolved pattern due to the amount of coupling taking place.

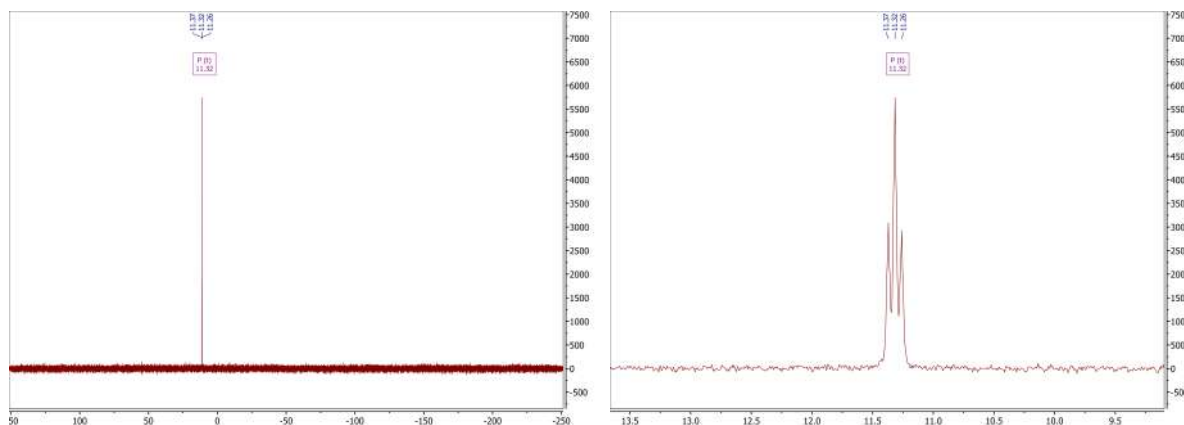


Figure 3.59: ^{31}P NMR spectrum for H_4DPPA (**3B**). Solvent: Solvent: 0.1M NaOH in D_2O .

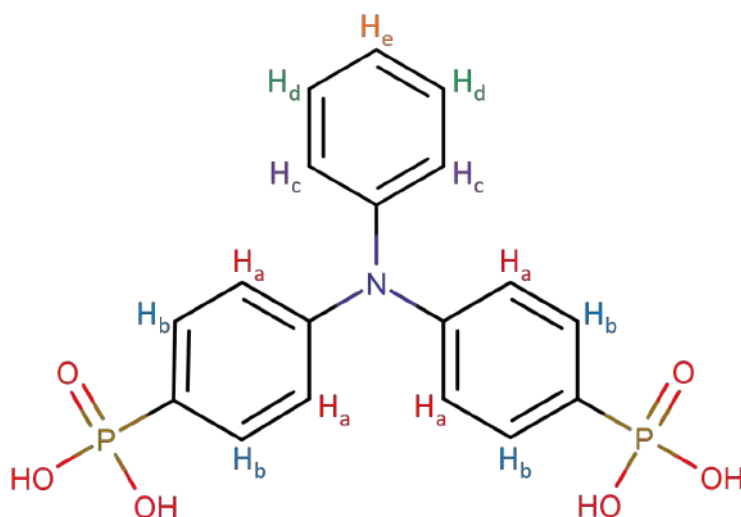


Figure 3.60: Chemical Structure of H_4DPPA (**3B**), with proton environments labelled H_a to H_e , corresponding with A-E on the NMR spectrum.

Moving to the ^1H NMR spectrum as shown in Figure 3.61, we can immediately confirm the loss of the isopropyl groups through the lack of methine and methyl signals upfield. Beyond this, the only potential impurity shown at δ 0.0 ppm, which can be attributed to phosphorus acid (H_3PO_3), though the amount present must be quite small as it is not seen in ^{31}P NMR spectrum, and could easily be removed through further washing in small amounts of water or ethanol.

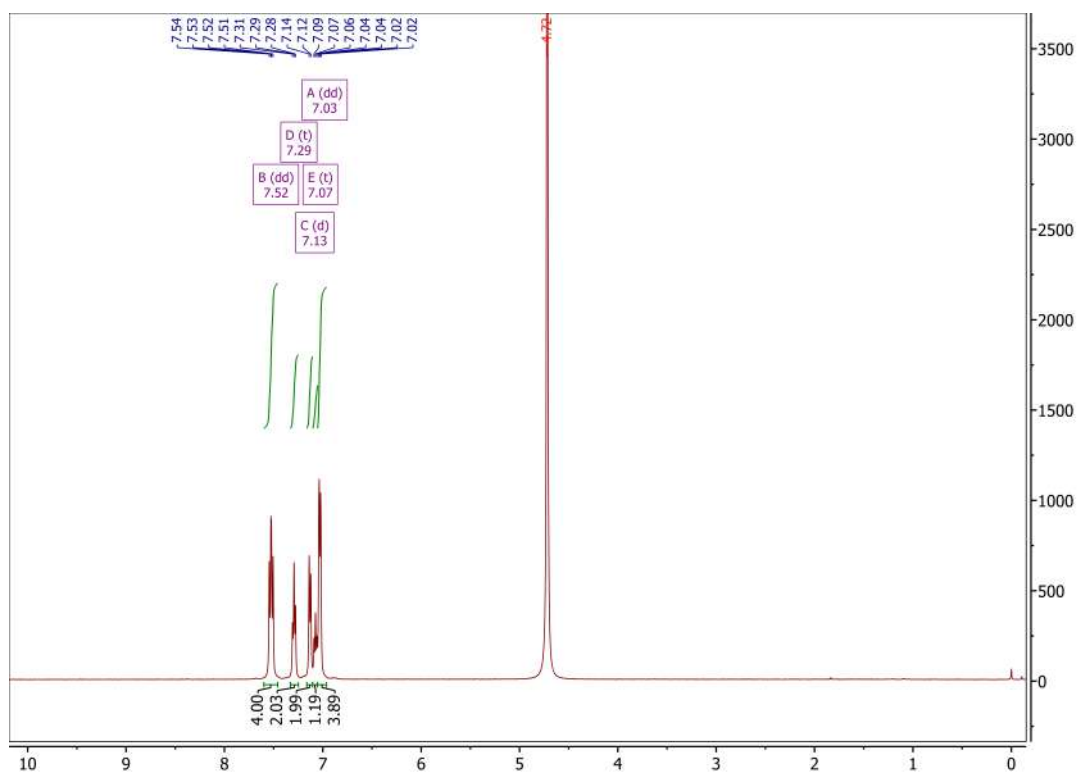


Figure 3.61: Full ^1H NMR spectrum for H_4DPPA (**3B**). Solvent: Solvent: 0.1M NaOH in D_2O .

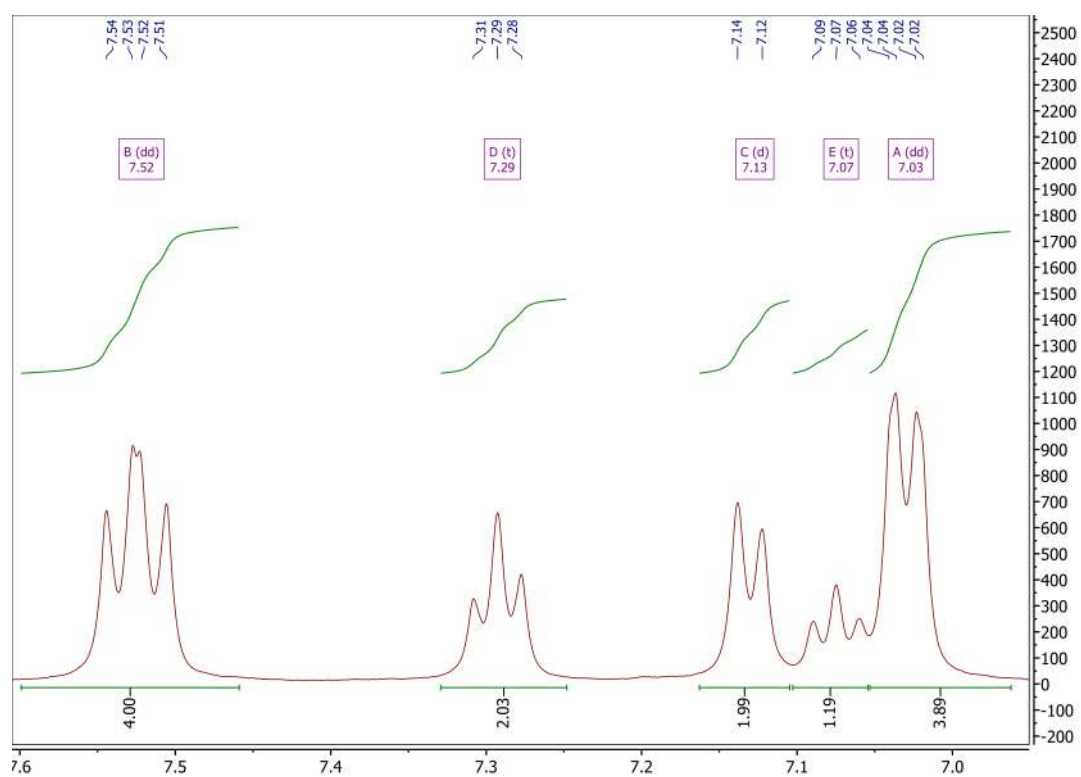


Figure 3.62: ^1H NMR spectrum for H_4DPPA (**3B**). Solvent: 0.1M NaOH in D_2O .

Focussing on the aromatic region, as shown in Figure 3.62, and comparing it to that of the ester in Figure 3.51, the assignment of the signals is clear, though there is one striking difference, which is that two of the signals, C and E, have switched places on the spectrum. Turning back to the assignment of the signals, as was the case for the ester, the signal at δ 7.52 ppm has been assigned to the protons nearest to phosphorus, labelled H_b. The next signal, at δ 7.29 ppm, has been assigned to the protons labelled H_d on the non-phosphonate-containing ring. The signal at δ 7.13 ppm has been assigned to the protons nearest nitrogen on the non-phosphonate-containing ring, labelled H_c. The next signal, and generally the easiest to assign due to the integration, has been assigned to the proton labelled H_e on the non-phosphonate-containing ring. This leaves the final signal at δ 7.13 ppm, which through process of elimination, supported by splitting pattern and integration, be attributed to the protons labelled H_a.

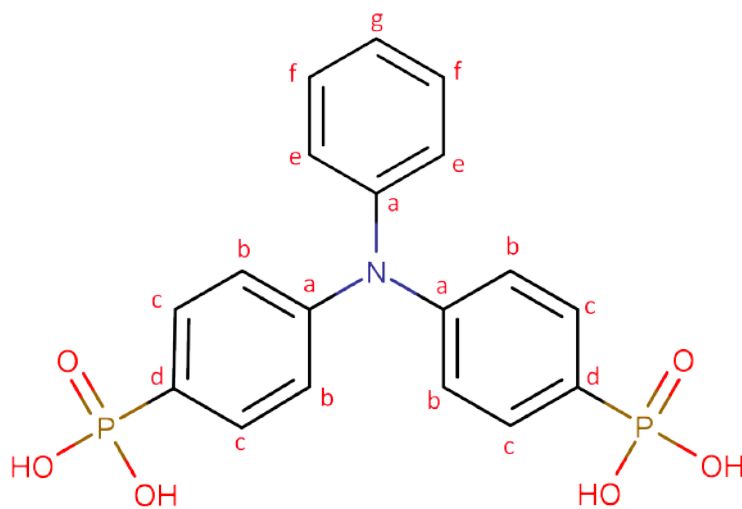


Figure 3.63: Chemical Structure of H₄DPPA (**3B**), with carbon environments labelled H_a to H_g, corresponding with A-G on the ¹³C NMR spectrum.

As was the case for the ester, ¹³C NMR, as shown in Figure 3.64, has proven insufficient in aiding full characterisation of the linker. This is mostly due to the insolubility of the product, which has resulted in a poor signal-to-noise ratio. With this in mind, HSQC should help with assigning some of the ¹³C NMR peaks. It should be noted here that the ¹³C NMR spectrum clearly shows the lack of isopropyl group peaks.

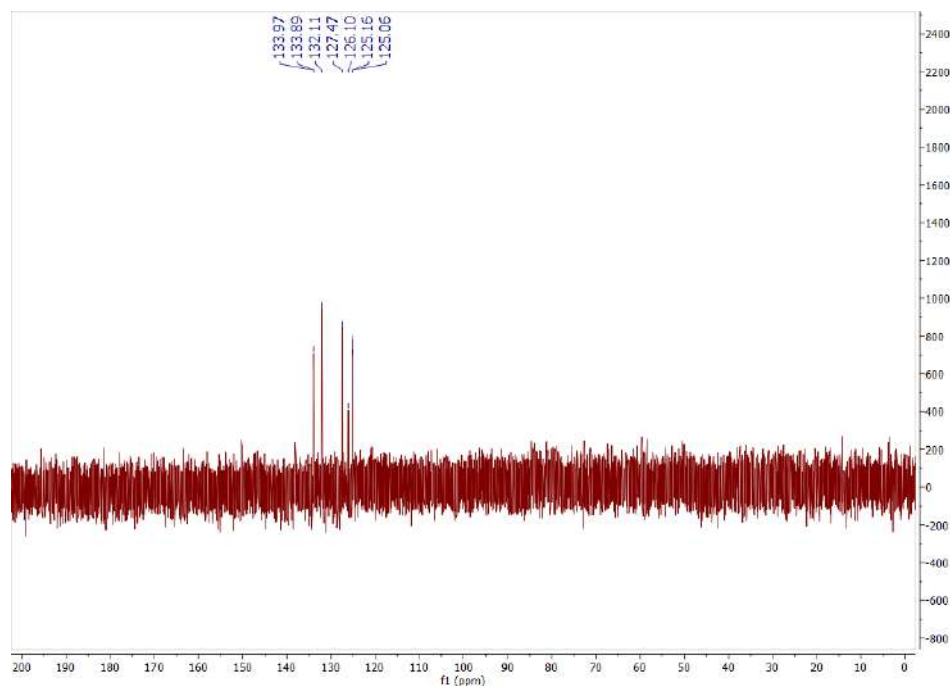


Figure 3.64: Full ^{13}C NMR spectrum for H_4DPPA (**3B**). Solvent: 0.1M NaOH in D_2O .

Looking at the HSQC NMR spectra in Figure 3.65, we can indeed see the switching of signals 3 and 4 when comparing with that of the ester in Figure 3.56. Beyond that, the assignments are identical, with the signals showing correlations between $\text{C}_c\text{-H}_b$ (1), $\text{C}_e\text{-H}_c$ (2), $\text{C}_g\text{-H}_e$ (3), $\text{C}_f\text{-H}_d$ (4), and $\text{C}_b\text{-H}_a$ (5).

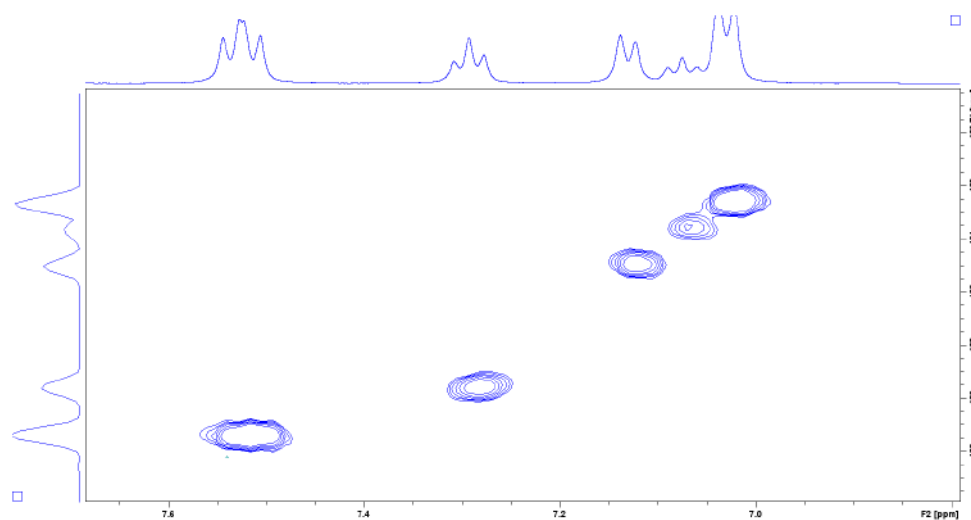


Figure 3.65: HSQC NMR spectrum for H_4DPPA (**3B**). Solvent: 0.1M NaOH in D_2O .

Mass spectral analysis was carried out, and Figure 3.66 clearly shows the base peak at m/z 201.52, which corresponds to the $[\text{M}+2\text{H}]^{2+}$ species. This can be seen in greater

detail in Figure 3.67, which compares the theoretical isotope profile with observed data, shown a good match between the two.

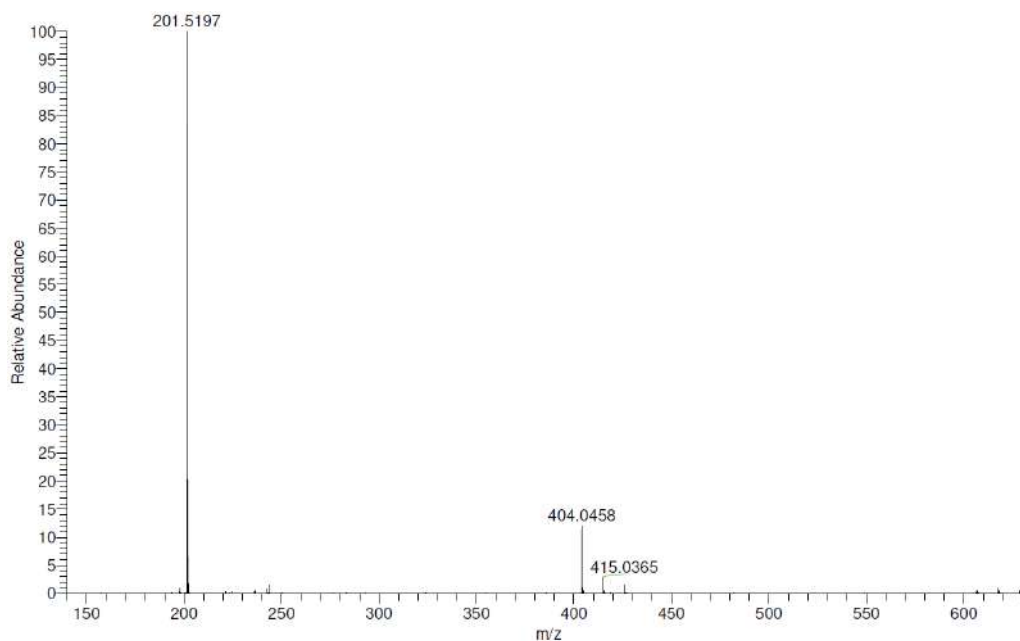


Figure 3.66: Observed Mass spectrum for H₄DPPA.

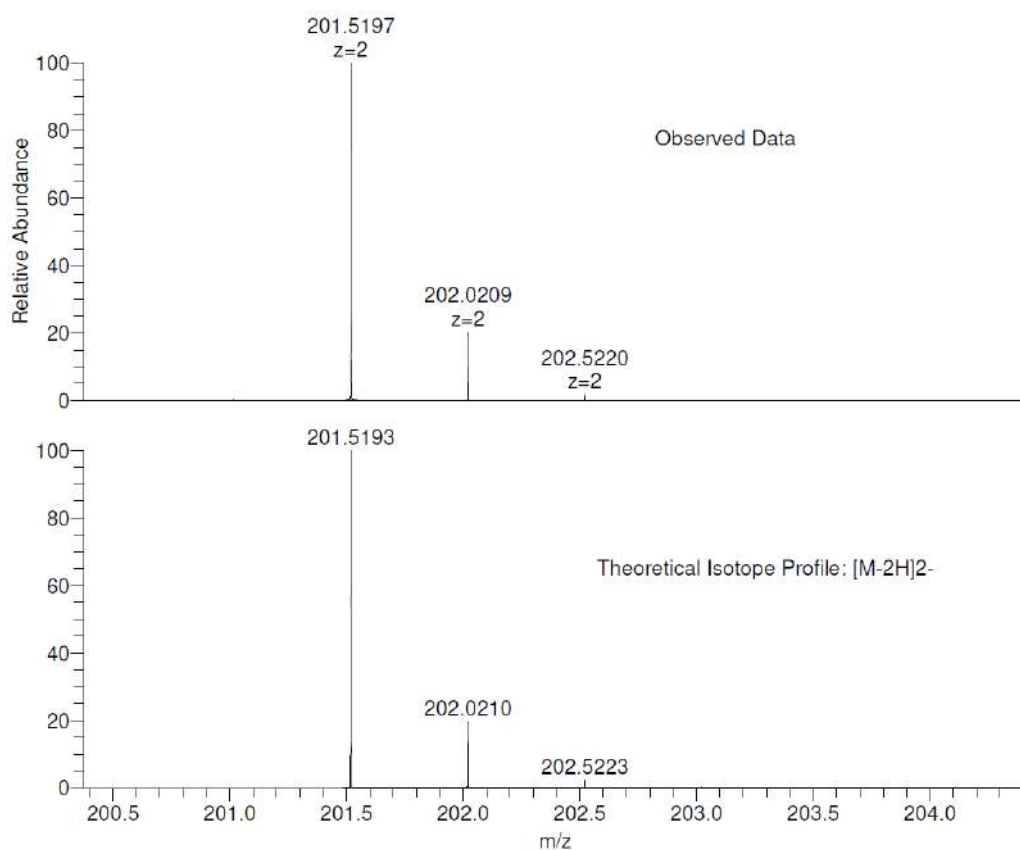


Figure 3.67: Observed Mass spectrum for H₄DPPA and theoretical isotope pattern for the [M-2H]²⁻ species.

Discussion

Where the work presented differs from the conventional nickel-catalysed cross-coupling reaction can be found in the different order of addition of the reactants, but also in that we use no solvent. This absence of solvent, in particular, presents a few advantages over the original method. First of all, the removal of said solvent is no longer required and thus there is a simplification of the work-up procedure. Second, there is no dilution of the reaction mixture, which obviously lends itself to an increased reaction rate, something we have observed in our results. The choice of phosphite is also important, partially due to the boiling point and the potential for running reactions at higher temperatures, and also the formation of an alkyl halide by-product. It is the reactivity of this by-product which determines which phosphite is chosen. In this case, triisopropyl phosphite has been chosen over others such as triethyl phosphite since the latter results in a more reactive alkyl halide (e.g. ethyl bromide), which would react with triethyl phosphite to produce diethyl ethylphosphonate, thus consuming the triisopropyl phosphite in a competing reaction and introducing undesired side-products.

As described previously, the conventional procedure involves the addition of the aryl halide and the pre-catalyst (NiCl_2) into a round-bottom flask in the presence of a suitable solvent. The alkyl phosphite is then added dropwise over a relatively long time period until no more remains. In this improved method, however, we have discovered that the use of a solvent can be eliminated, and the reaction time greatly decreased when the aryl halide (in solid form) is added to an alkyl phosphite and catalyst mixture.

Contrary to the conventional method, this improved method starts with the nickel(II) pre-catalyst and the alkyl phosphite, triisopropyl phosphite in our case, being added to a round-bottom flask and set to approximately 160 °C, leading to the formation of the nickel(0) catalyst, more accurately representing the catalytic cycle presented in Figure 3.2. The solid aryl bromide is then added to the mixture via a powder

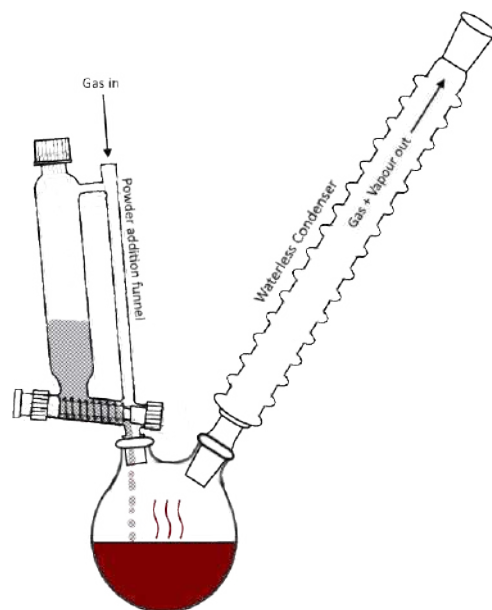


Figure 3.68: Experimental setup for the improved C-P cross coupling reaction.

addition funnel over a 2-4 hour period, depending on the substrate, and then left to react for an additional 1 hour. Figure 3.68 shows the set-up for the reaction, with the solid aryl bromide in grey and the pre-catalyst/triisopropyl phosphite mixture in red. It is important to note here that the system is kept under a constant flow of either argon or nitrogen, mainly to avoid reactions with components in the air (humidity, oxygen), but also to prevent the solid in the addition funnel from contacting any vapour and turning soggy before it is added to the round-bottom flask. As can be seen in Figure 3.68, this is achieved by flowing the gas through the powder addition funnel via a gas inlet. This also allowed for the quick removal of residual triisopropyl phosphite by simply increasing the gas flow, preventing the equilibrium between the gas and liquid phases, and thus eliminating the further step which would have involved removing these components by vacuum distillation. Although not shown in Figure 3.68, the addition of a second condenser and collection flask perpendicular to the first column also allows for the collection of unreacted phosphite, and by-product such isopropyl bromide. Firstly, this prevents any release of toxic compounds and facilitates appropriate disposal procedures. Secondly, it is likely that the majority of what remains in the flask at the end is simply unreacted phosphite, which would

ideally need to be investigated to assess its recyclability, and lead to a process with greener attributes. In this sense, the phosphite is likely to be the last product coming over via distillation, and should be relatively pure, but further investigation is required in order to confirm this.

Table 3.1: A comparison of conventional phosphonate synthesis with the improved method.

	Improved Method	Conventional A [43]	Conventional B [44]	Conventional C [45]	Microwave Assisted [46]
Time	3-4 h	20 h	20 h	20 h	45 min
Scale	2-5 g	30 g	8 g	10 g	0.5 g
Temperature	160 °C	180 °C	180 °C	170 °C	225 °C
Solvent	No Solvent	1,3-di-isopropyl benzene	1,3-di-isopropyl benzene	1,3-di-isopropyl benzene	No Solvent
P(Oi-Pr)₃/ Br Ratio	7	1.5	3	2.5	5
Mol%/Br NiX₂	13% X=Cl	17% X=Cl	39% X=Br	16% X=Br	15% X=Cl
Isolated Yield	70-90%	60%	89%	61%	82%
Procedure	Addition of Br-substrate	Addition of Phosphite	Addition of Phosphite	Addition of Phosphite	One-pot Synthesis

In Table 3.1, we see a range of different methods based on cross-coupling reactions compared to the improved method proposed in this work. The first, and one of the most important comparisons, is time. The upper range for our method is around the 4-hour mark, whereas the conventional routes, excluding the microwave-assisted reaction, often run for 20 hours or more. This, in part, can be attributed to the absence of solvent, which we cited previously as an advantage in that we are not diluting the reaction mixture and thus not slowing down the reaction. This in turn explains the high phosphite:bromine ratio, which in our case is higher than all the other routes, since the phosphite itself acts as the solvent as well as being a reactant. If this ratio was lower, there would be a considerable drop in the reaction rate towards the end and would likely lead to generally lower yields. This issue could be further minimised upon exploration of recycling the phosphite distillate. We also manage to use less catalyst than some of the other methods, again, except for the microwave-assisted reaction. In keeping with the mild conditions, the temperature we use is most often 160 °C, which

is lower than that of the other reactions. Notably, the yield we achieve, which varies between substrates, is generally comparable to those of conventional routes, which means that the improvements we have made to the method are, in the end, worthwhile.

3.4 Conclusions

Presented in this chapter is the synthesis of three novel phosphonate esters and their corresponding phosphonic acids. While the phosphonic acids are indeed the target products, the progress made here is mainly focused on the improvement of the cross-coupling reaction used to obtain the phosphonate esters. Oftentimes, these reactions take up to 24 hours to reach completion, sometimes more, while here we have presented a simple yet effective change that can be made to the order of addition of reactants which affords a reaction time that is at least five times faster than most conventional methods with no considerable effect on the yield or the purity of the product. This has also completely removed the requirement of a solvent, since triisopropylphosphite acts as the solvent once the reaction mixture has reached at least reaction temperature. In making savings for both cost of reagents and in total reaction time, and with no detriment to the yield, it is clear that this method presents a considerable advantage over the conventional route, both in terms of cost and efficient use of time.

Referring specifically to the linkers presented in this chapter, we have obtained three structurally related linkers on which we can now move forward with synthesising metal phosphonates in order to determine the effects of the geometry and of different substituents on the formation of metal phosphonate frameworks and indeed whether they form at all. Each of the linkers were obtained in good yields and with no considerable impurities identified during characterisation.

3.5 References

1. K. D. Demadis, M. Paspalaki and J. Theodorou, "Controlled Release of Bis(phosphonate) Pharmaceuticals from Cationic Biodegradable Polymeric Matrices", *Ind. Eng. Chem. Res.*, 2011, **50**, 5873–5876, DOI: 10.1021/ie102546g.
2. J. Galezowska and E. Gumienna-Kontecka, "Phosphonates, their complexes and bio-applications: A spectrum of surprising diversity", *Coord. Chem. Rev.*, 2012, **256**, 105–124, DOI: 10.1016/j.ccr.2011.07.002.
3. M. Pazianas, B. Abrahamsen, S. Ferrari and R. G. Russell, "Eliminating the need for fasting with oral administration of bisphosphonates", *Ther. Clin. Risk Manag.*, 2013, 395, DOI: 10.2147/tcrm.s52291.
4. R. Lange, R. ter Heine, R. (Knapp, J. M. de Klerk, H. J. Bloemendal and N. H. Hendrikse, "Pharmaceutical and clinical development of phosphonate-based radiopharmaceuticals for the targeted treatment of bone metastases", *Bone*, 2016, **91**, 159–179, DOI: 10.1016/j.bone.2016.08.002.
5. K. E. Papathanasiou, M. Vassaki, A. Spinthaki, F-E. G. Alatzoglou, E. Tripodianos, P. Turhanen and K. D. Demadis, "Phosphorus chemistry: from small molecules, to polymers, to pharmaceutical and industrial applications", *Pure Appl. Chem.*, 2018, **91**, 421–441, DOI: 10.1515/pac-2018-1012.
6. P. A. Turhanen, K. D. Demadis and P. Kafarski, "Editorial: Phosphonate Chemistry in Drug Design and Development", *Front. Chem.*, 2021, **9**, DOI: 10.3389/fchem.2021.695128.
7. B. Nowack and J. M. VanBriesen, in *Biogeochemistry of Chelating Agents*, American Chemical Society, 2005, pp. 1–18, DOI: 10.1021/bk-2005-0910.ch001.
8. Y. Wang and A. T. Stone, "Phosphonate- and Carboxylate-Based Chelating Agents that Solubilize (Hydr)oxide-Bound Mn^{III}", *Environ. Sci. Technol.*, 2008, **42**, 4397–4403, DOI: 10.1021/es7032668.
9. S. M. Bhosle, S. Ponrathnam, S. S. Tambe and N. N. Chavan, "Adsorption of strontium (II) metal ions using phosphonate-functionalized polymer", *Bull. Mater. Sci.*, 2016, **39**, 1541–1556, DOI: 10.1007/s12034-016-1295-7.
10. T. Du, J. Chen and D. Cao, "N,N-Dipropoxy methyl amine trimethyl phosphonate as corrosion inhibitor for iron in sulfuric acid", *J. Mater. Sci.*, 2001, **36**, 3903–3907, DOI: 10.1023/a:1017909919388.
11. R. Tourir, N. Dkhireche, M. E. Touhami, M. Sfaira, O. Senhaji, J. Robin, B. Boutevin and M. Cherkaoui, "Study of phosphonate addition and hydrodynamic conditions on ordinary steel

- corrosion inhibition in simulated cooling water”, *Mater. Chem. Phys.*, 2010, **122**, 1–9, DOI: 10.1016/j.matchemphys.2010.02.063.
12. C. M. Fernandes, L. V. Faro, V. G. Pina, M. C. B. de Souza, F. C. Boechat, M. C. de Souza, M. Briganti, F. Totti and E. A. Ponzio, “Study of three new halogenated oxoquinolinecarbohydrazide N-phosphonate derivatives as corrosion inhibitor for mild steel in acid environment”, *Surf. Interfaces*, 2020, **21**, 100773, DOI: 10.1016/j.surfin.2020.100773.
 13. S. Habash and L. Al-Banna, “Phosphonate fertilizers suppressed root knot nematodes *Meloidogyne javanica* and *M. incognita*.”, *J. Nematol.*, 2011, **43**, 95–100.
 14. M. C. Manghi, M. Masiol, R. Calzavara, P. L. Graziano, E. Peruzzi and B. Pavoni, “The use of phosphonates in agriculture. Chemical, biological properties and legislative issues”, *Chemosphere*, 2021, **283**, 131187, DOI: 10.1016/j.chemosphere.2021.131187.
 15. J. Goura and V. Chandrasekhar, “Molecular Metal Phosphonates”, *Chem. Rev.*, 2015, **115**, 6854–6965, DOI: 10.1021/acs.chemrev.5b00107.
 16. J. Zon, P. Garczarek and M. BiaLek, in *Metal Phosphonate Chemistry*, Royal Society of Chemistry, 2011, pp. 170–191, DOI: 10.1039/9781849733571-00170.
 17. C. M. Sevrain, M. Berchel, H. Couthon and P.-A. Jaffrès, “Phosphonic acid: preparation and applications”, *Beilstein J. Org. Chem.*, 2017, **13**, 2186–2213, DOI: 10.3762/bjoc.13.219.
 18. A. K. Bhattacharya and G. Thyagarajan, “Michaelis-Arbuzov rearrangement”, *Chem. Rev.*, 1981, **81**, 415–430, DOI: 10.1021/cr00044a004.
 19. P. Tavs and F. Korte, “Zur herstellung aromatischer phosphonsaureester aus arylhalogeniden und trialkylphosphiten”, *Tetrahedron*, 1967, **23**, 4677–4679, DOI: 10.1016/s0040-4020(01)92565-7.
 20. P. Tavs and H. Weitkamp, “Herstellung und KMR-spektren einiger α,β -ungesättigter phosphonsaureester”, *Tetrahedron*, 1970, **26**, 5529–5534, DOI: 10.1016/s0040-4020(01)98763-0.
 21. J. Heinicke, B. R. Aluri, M. S. Adam and P. G. Jones, “Novel Benzo-and Pyrido-Anellated 1, 3-Azaphospholes”, *Phosphorus, Sulfur, and Silicon and the Related Elements*, 2008, **183**, 779–782, DOI: 10.1080/10426500701807905.
 22. T. Hirao, T. Masunaga, Y. Ohshiro and T. Agawa, “Stereoselective synthesis of vinylphosphonate”, *Tetrahedron Lett.*, 1980, **21**, 3595–3598, DOI: 10.1016/0040-4039(80)80245-0.
 23. T. Hirao, T. Masunaga, Y. Ohshiro and T. Agawa, “A Novel Synthesis of Dialkyl Arenephosphonates”, *Synthesis*, 1981, **1981**, 56–57, DOI: 10.1055/s-1981-29335.

24. T. Hirao, T. Masunaga, N. Yamada, Y. Ohshiro and T. Agawa, "Palladium-catalyzed New Carbon-Phosphorus Bond Formation", *Bull. Chem. Soc. Jpn.*, 1982, **55**, 909–913, DOI: 10.1246/bcsj.55.909.
25. N. Miyaura and A. Suzuki, "Palladium-Catalyzed Cross-Coupling Reactions of Organoboron Compounds", *Chem. Rev.*, 1995, **95**, 2457–2483, DOI: 10.1021/cr00039a007.
26. T. M. Balthazor and R. C. Grabiak, "Nickel-catalyzed Arbuzov reaction: mechanistic observations", *J. Org. Chem.*, 1980, **45**, 5425–5426, DOI: 10.1021/jo01314a059.
27. M. Kalek, A. Ziadi and J. Stawinski, "Microwave-Assisted Palladium-Catalyzed Cross-Coupling of Aryl and Vinyl Halides with H-Phosphonate Diesters", *Org. Lett.*, 2008, **10**, 4637–4640, DOI: 10.1021/ol1801935r.
28. Y. Belabassi, S. Alzghari and J.-L. Montchamp, "Revisiting the Hirao cross-coupling: improved synthesis of aryl and heteroaryl phosphonates", *J. Organomet. Chem.*, 2008, **693**, 3171–3178, DOI: 10.1016/j.jorganchem.2008.07.020.
29. K. Moedritzer and R. R. Irani, "The Direct Synthesis of α -Aminomethylphosphonic Acids. Mannich-Type Reactions with Orthophosphorous Acid", *The Journal of Organic Chemistry*, 1966, **31**, 1603–1607, DOI: 10.1021/jo01343a067.
30. K. D. Demadis and N. Stavgiannoudaki, in *Metal Phosphonate Chemistry*, Royal Society of Chemistry, 2011, pp. 438–492, DOI: 10.1039/9781849733571-00438.
31. M. Taddei, P. Sassi, F. Costantino and R. Vivani, "Amino-Functionalized Layered Crystalline Zirconium Phosphonates: Synthesis, Crystal Structure, and Spectroscopic Characterization", *Inorg. Chem.*, 2016, **55**, 6278–6285, DOI: 10.1021/acs.inorgchem.6b00943.
32. M. Taddei, F. Costantino and R. Vivani, "Synthesis and Crystal Structure from X-ray Powder Diffraction Data of Two Zirconium Diphosphonates Containing Piperazine Groups", *Inorg. Chem.*, 2010, **49**, 9664–9670, DOI: 10.1021/ic1014048.
33. M. Taddei, F. Costantino, V. Manuali and R. Vivani, "New Hybrid Zirconium Aminophosphonates Containing Piperidine and Bipiperidine Groups", *Inorg. Chem.*, 2011, **50**, 10835–10843, DOI: 10.1021/ic201381t.
34. F. Steinke and N. Stock, "Systematic investigation of new alkaline earth phosphonates based on the linker molecule N,N'-4,4'-bipiperidine-bis(methylenephosphonic acid)", *Zeitschrift für anorganische und allgemeine Chemie*, 2021, **647**, 1046–1051, DOI: 10.1002/zaac.202000390.
35. G. Will, G. Boschloo, S. N. Rao and D. Fitzmaurice, "Potentiostatic Modulation of the Lifetime of Light-Induced Charge Separation in a Heterosupermolecule", *J. Phys. Chem.*, 1999, **103**, 8067–8079, DOI: 10.1021/jp990414i.

36. A. Charmot, A. Solovyov, A. G. DiPasquale and A. Katz, "Silica-Supported Phosphonic Acids as Thermally and Oxidatively Stable Organic Acid Sites", *Chem. Mater.*, 2016, **28**, 6166–6177, DOI: 10.1021/acs.chemmater.6b02027.
37. N. Hugot, M. Roger, J.-M. Rueff, J. Cardin, O. Perez, V. Caignaert, B. Raveau, G. Rogez and P.-A. Jaffrès, "Copper–Fluorenephosphonate $\text{Cu-PO}_3\text{-C}_{13}\text{H}_9\text{)}\cdot\text{H}_2\text{O}$: A Layered Antiferromagnetic Hybrid", *Eur. J. Inorg. Chem.*, 2015, **2016**, 266–271, DOI: 10.1002/ejic.201501041.
38. E. Chauveau, C. Marestin, R. Mercier, A. Brunaux, V. Martin, R. P. Nogueira, A. Percheron, V. Roche and H. Waton, "Phosphonic acid-containing polysulfones as anticorrosive layers", *J. Appl. Polym. Sci.*, 2015, **132**, DOI: 10.1002/app.41890.
39. N. Harsági and G. Keglevich, "The Hydrolysis of Phosphinates and Phosphonates: A Review", *Molecules*, 2021, **26**, 2840, DOI: 10.3390/molecules26102840.
40. M. S. Marma, L. A. Khawli, V. Harutunian, B. A. Kashemirov and C. E. McKenna, "Synthesis of α -fluorinated phosphonoacetate derivatives using electrophilic fluorine reagents: Perchloryl fluoride versus 1-chloromethyl-4-fluoro-1,4-diazoniabicyclo[2.2.2]octane bis(tetrafluoroborate) (Selectfluor®)", *J. Fluorine Chem.*, 2005, **126**, 1467–1475, DOI: 10.1016/j.jfluchem.2005.04.002.
41. H. Reinsch, M. Krüger, J. Marrot and N. Stock, "First Keto-Functionalized Microporous Al-Based Metal–Organic Framework: $[\text{Al}(\text{OH})(\text{O}_2\text{C}-\text{C}_6\text{H}_4-\text{CO}-\text{C}_6\text{H}_4-\text{CO}_2)]$ ", *Inorg. Chem.*, 2013, **52**, 1854–1859, DOI: 10.1021/ic301961q.
42. G. R. Fulmer, A. J. M. Miller, N. H. Sherden, H. E. Gottlieb, A. Nudelman, B. M. Stoltz, J. E. Bercaw and K. I. Goldberg, "NMR Chemical Shifts of Trace Impurities: Common Laboratory Solvents, Organics, and Gases in Deuterated Solvents Relevant to the Organometallic Chemist", *Organometallics*, 2010, **29**, 2176–2179, DOI: 10.1021/om100106e.
43. R. K. Mah, M. W. Lui and G. K. H. Shimizu, "Enhancing Order and Porosity in a Highly Robust Tin(IV) Triphosphonate Framework", *Inorg. Chem.*, 2013, **52**, 7311–7313, DOI: 10.1021/ic400274e.
44. N. Hermer and N. Stock, "The new triazine-based porous copper phosphonate $\text{Cu}_3(\text{PPT})(\text{H}_2\text{O})_3\cdot 10\text{H}_2\text{O}$ ", *Dalton Trans.*, 2015, **44**, 3720–3723, DOI: 10.1039/c4dt03698k.
45. J. K. Zareba, M. J. Bialek, J. Janczak, J. Zoń and A. Dobosz, "Extending the Family of Tetrahedral Tectons: Phenyl Embraces in Supramolecular Polymers of Tetraphenylmethane-based Tetraphosphonic Acid Templated by Organic Bases", *Cryst. Growth Des.*, 2014, **14**, 6143–6153, DOI: 10.1021/cg501348g.
46. M. Taddei, F. Costantino, R. Vivani, S. Sabatini, S.-H. Lim and S. M. Cohen, "The use of a rigid tritopic phosphonic ligand for the synthesis of a robust honeycomb-like layered zirconium phosphonate framework", *Chem. Commun.*, 2014, **50**, 5737–5740, DOI: 10.1039/c4cc01253d.

Chapter 4

Synthesis and Characterisation of Novel Metal Phosphonate Frameworks based on Tetravalent Metals

4.1 Introduction

With the successful synthesis of three novel linkers shown in Chapter 3, the focus of experimental work shifted to the synthesis of metal phosphonates, specifically looking at zirconium(IV) phosphonates, though other metals were considered. Part of the history of zirconium(IV) phosphonates has been explored in Chapter 1, where we discussed the work published by the groups of Clearfield and Alberti. We noted here that the work on zirconium phosphonates began with the work of Clearfield et al. (1969) on solving the structure of α -ZrP, which was achieved using SCXRD.¹ We then looked at the work of Alberti and Costantino, which came later in the decade, where we discussed the preparation of three zirconium phosphonates, which were determined to have layered structures analogous to that of α -ZrP, though this was not confirmed experimentally until 1993 when Poojary et al. used various modelling and refinement techniques to solve the structure.^{2,3} A lot of the work that followed after this looked only at mono- and diphosphonates which had analogous layered and

pillared-layered structures. It has long been an aim of the field, however, to develop highly crystalline microporous metal phosphonates, which show more promise in fields such as gas sorption and catalysis. Before jumping straight into a discussion about metal phosphonates that employ tetravalent metals, it is important to first explore the use of tetravalent metals in MOF construction as well as the motivation behind it. After this, we will also think about linker geometry and the effect it can have on MOF structures, particularly those including the aforementioned tetravalent metals.

4.1.1 An Overview of M^{IV} –based Metal –Organic Frameworks

Up until this point, only a very general overview of both MOFs and the metal phosphonate sub-class has been given. The experimental work from this point, however, will focus on structures constructed using tetravalent metals, mainly zirconium(IV) and cerium(IV). As has already been pointed out, though, it is well known that despite their huge potential in many applications, not all MOFs present sufficient stability, whether thermal, chemical, or hydrolytic, etc., to be considered optimal for these applications, as evidenced by the continued efforts to produce new stable MOFs or to increase the stability of existing materials.⁴⁻⁷ One method to enhance the stability of potential MOFs is through the use of high-valency metals, particularly those in group 4, i.e. titanium(IV), zirconium(IV), and hafnium(IV), though this can be extended to include other tetravalent metals, such as cerium(IV) and tin(IV).^{8,9} The question here then, is, why use tetravalent metals? One of the main reasons for the use of high-valency metals is due to their classification as hard acids, which, when combined with a carboxylate ligand, i.e. a hard base, leads to the formation of strong metal-ligand bonds, as predicted by hard-soft acid-base (HSAB) theory.^{10,11} The higher charge on the metal can also lead to higher connectivity around the metal node or secondary building unit (SBU), since more ligands are required to balance the charge. It can also be argued that this increased connectivity provides somewhat of a barrier

against attack from guest molecules, a typical example of which would be water.

The interest in using these tetravalent metals for MOF synthesis began in 2008 with the reporting of UiO-66, which has since become one of the most well-studied MOFs.¹² It was obtained by combining the 1,4-benzene-dicarboxylic acid (BDC) linker with the $Zr_6O_4(OH)_4^{12+}$ cluster (Figure 4.1b), with the resulting structure shown in Figure 4.1a. As with most MOFs, UiO-66 possesses inherent porosity, containing two types of micropores and a measured BET surface area of $1200 \text{ m}^2 \cdot \text{g}^{-1}$. When you consider the arrangement of the clusters, the crystal structure can be classified as cubic close packed.

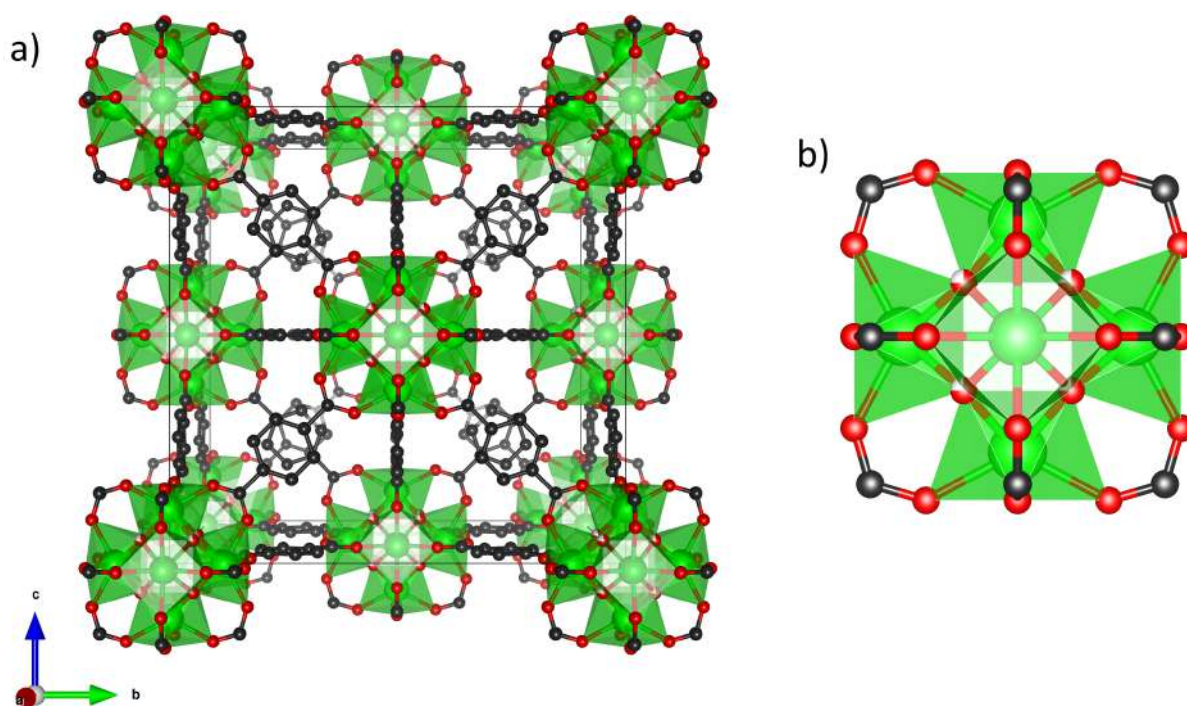


Figure 4.1: a) Crystal structure of UiO-66, b) Structure of the Zr_6 cluster. Colour code: Zirconium - Green, Oxygen - Red, Carbon - Black.

The authors also explored the isoreticular expansion of the linker in the same paper, with UiO-67 and UiO-68 also reported. The former of these was built using the 4,4'-biphenyl-dicarboxylate (BPDC) linker, while the latter was constructed using the terphenyl-dicarboxylate (TPDC) linker. With regards to thermal stability, the authors found that UiO-66 and UiO-67 behaved quite similarly, with a decomposition temperature of approximately $540 \text{ }^\circ\text{C}$. Mass spectrum analysis of the breakdown of

the materials showed that benzene was present in the gas phase, which suggested the weak links in the structure are the bonds between benzene and the carboxylate groups as well as those between the two benzene rings, rather than the linker-metal bond. From this, the authors concluded that this represented the ultimate thermal stability possible for hybrid frameworks using organic linkers. The stability of the materials in different solvents was also found to be high, with 24 hours stirring in water, DMF, benzene, and acetone, respectively, having no effect on the structure. Further testing of the material showed that the structure was again unaffected when placed under increased pressure (10 kg/cm²).

Moving beyond this initial leap into the field of Zr-MOFs, much of the work thereafter explored the functionalisation and applications for UiO-66 and the UiO-family of materials, work which is still very much carried out quite commonly today, a testament to UiO-66 and the UiO family of MOFs.¹³ In the initial years, this focus on the UiO family of MOFs could mostly be attributed to the difficulties in the crystallisation process whereby the fast crystallisation rate most often led to powders of low crystallinity, making characterisation and structure solution significantly more challenging.¹⁴ This issue was overcome through the use of modulated synthesis, whereby so-called modulators, such as acetic acid and benzoic acid, can be used to slow down the crystallisation process, and thus produce a more crystalline product.¹⁴

Shortly after this work on overcoming some of the crystallinity issues associated with Zr-MOFs, another notable family structures, closely related to UiO-66, were first reported in the literature. In 2012, Guillerm et al. published their work on the MIL-140 family of MOFs, ranging from A to D.¹⁵ The most notable of these, MIL-140A, is built using the 1,4-benzenedicarboxylic acid (BDC), as in UiO-66, though the inorganic building unit is different. In MIL-140, the inorganic unit consists of infinite zirconium oxide chains along the *c*-axis, with each of these connected along the *ab* plane to six other chains through the organic linker, as shown in Figure 4.2.

The other materials in the MIL-140 family were based on isorecticular expansion

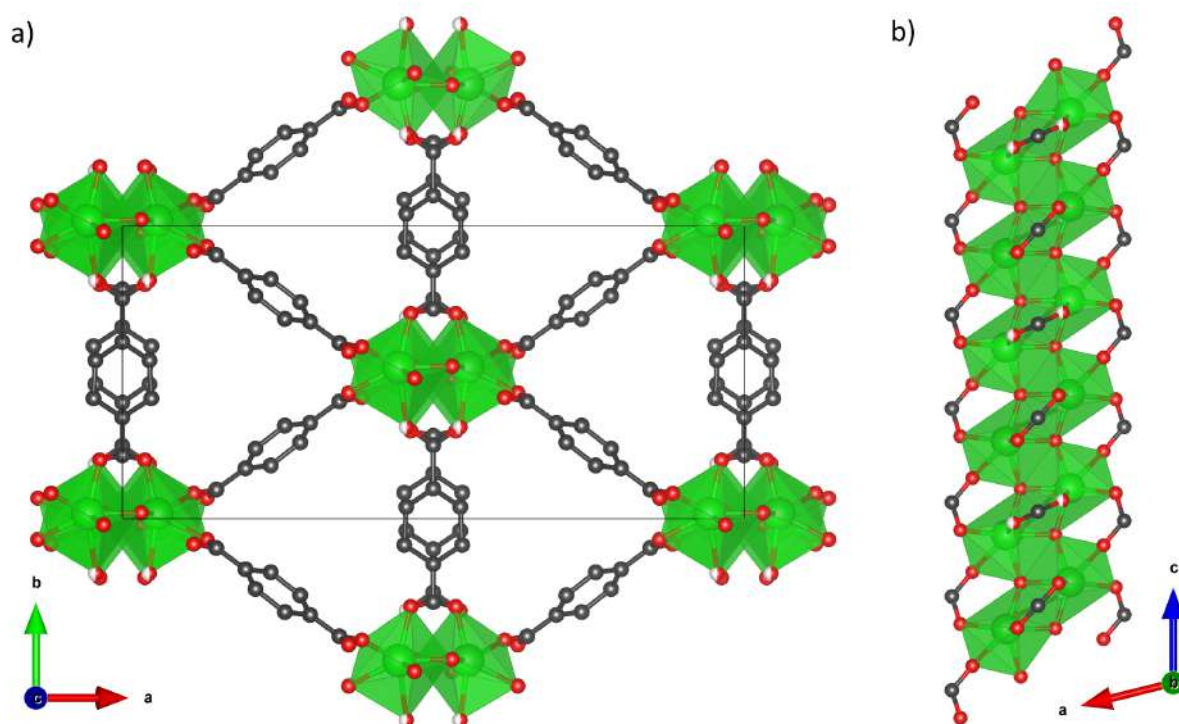


Figure 4.2: a) Crystal structure of MIL-140A viewed along the *c*-axis, b) Structure of the inorganic chain viewed along the *b*-axis. Colour code: Zirconium - Green, Oxygen - Red, Carbon - Black.

of the organic linker, whereby the BDC linker in MIL-140A was replaced with 2,6-naphthalenedicarboxylic acid (NDC), 4,4'-biphenylcarboxylic acid (BPDC), and 3,3'-dichloro-4,4'-azobenzenedicarboxylic acid (ABDC), for MIL-140B-D respectively. With respect to surface area, MIL-140A has a measured BET surface area of $415 \text{ m}^2 \cdot \text{g}^{-1}$, which is considerably smaller than that of UiO-66. TGA studies also show that, in an oxidative environment, MIL-140A is stable up to around $420 \text{ }^\circ\text{C}$.

Something important to note here, which is explored further in Chapter 5 with their perfluorinated Ce(IV)-analogues, is that MIL-140A and UiO-66 are quasi-polymorphs, and can be obtained in similar synthetic conditions by changing certain variables, such as temperature, reagent concentration, or the addition of certain protonation modulators. In this light, we can determine that MIL-140A is the more stable of the two, since it can be synthesised at $220 \text{ }^\circ\text{C}$ versus UiO-66, which is obtained at $150 \text{ }^\circ\text{C}$, making them the thermodynamic and kinetic products, respectively.¹⁵

With these initial developments leading to more MOFs based on tetravalent metals

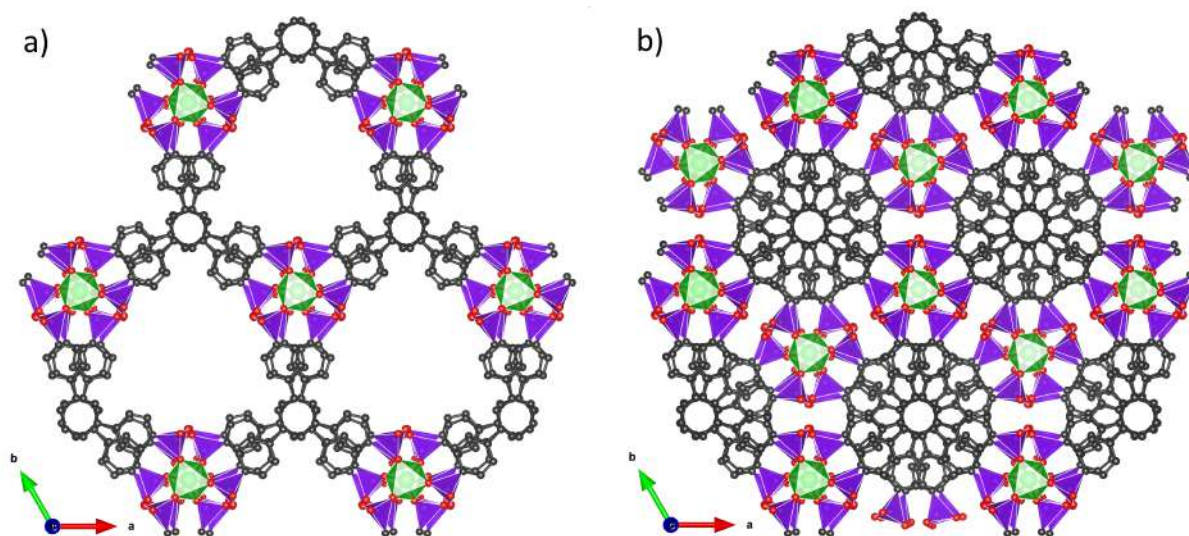


Figure 4.3: Crystal structure of Zrbtbp-a showing a) one layer along the c -axis, and b) two layers along the c -axis, clearly showing the capping of the cavities by the SBU of the next layer. Colour code: green = zirconium, black = carbon, phosphorus = purple, oxygen = red.

in combination with carboxylate linkers, a gap was left for M^{IV} -MOFs based on phosphonate linkers which have permanent microporosity. In 2014, Taddei et al. reported the synthesis of Zrbtbp, formula: $Zr_3(H_3btbp)_4 \cdot 15 H_2O$, which employed the 1,3,5-tris(4-phosphonophenyl)benzene (H_6btbp) linker, resulting in a "honeycomb-like structure displaying remarkable thermal stability and hydrolysis resistance".¹⁶ While overcoming the stability issues of a lot of carboxylate-based MOFs, it still presented the issue of low porosity, at least to certain adsorbents. N_2 adsorption was quite low, with a measured N_2 BET surface area of $5.2 \text{ m}^2 \cdot \text{g}^{-1}$ (77 K), and low CO_2 adsorption at $33.2 \text{ cm}^3 \cdot \text{g}^{-1}$, or 1.5 mmol/g (196 K, 1 atm). This low porosity is due to the stacking of the layers along the c -axis, whereby the channel or cavity found in each layer is capped by the SBU of another layer, as can be seen in Figure 4.3b. Each SBU consists of three ZrO_6 octahedra which are connected by phosphonate groups. Within each layer, each of the SBUs is connected via the H_6btbp linker, with each linker bridging between three separate SBUs, Figure 4.3a. In terms of stability, the material is stable up to 400°C , after which point the framework begins to break down. While this was a positive step in achieving stable open-framework metal^{IV} phosphonates, it still suffered from the lack of porosity due to the capping of the cavities.

This was until Taddei et al. reported "the first crystalline microporous zirconium phosphonate metal-organic framework", which they termed UPG-1, where UPG stands for the University of Perugia.¹⁷ The MOF itself is made up of 1D ZrO_6 chains which are linked together by the 2,4,6-tris(4-(phosphonomethyl)phenyl)-1,3,5-triazine (H_6 tbbmp) linker, forming a structure with two types of channels, one of which is lined by uncoordinated phosphonate groups, and the other lined by phosphonate groups and aromatic rings, as can be seen in Figure 4.4. As mentioned above, the

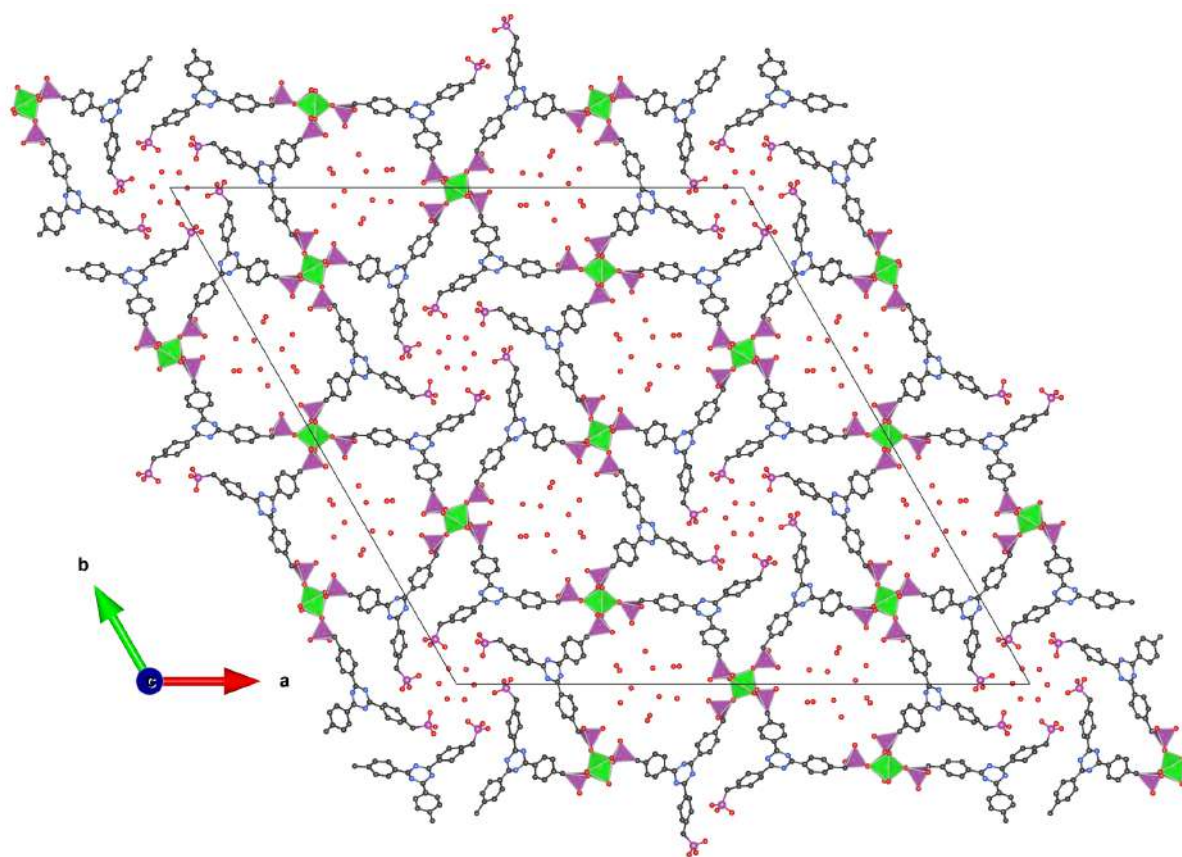


Figure 4.4: Crystal structure of UPG-1, showing the unit cell and two channel types, along the c -axis. Colour code: green = zirconium, black = carbon, phosphorus = purple, oxygen = red, nitrogen = blue.

inorganic chains are composed of a central zirconium atom coordinated by six oxygen atoms, each of which belong to distinct phosphonate groups. Of these six phosphonate groups, two are monodentate, bridging between different ZrO_6 chains on the ab -plane, while the remaining four are bidentate, and connect between the ZrO_6 clusters on the same chain. The existence of the infinite channels between these chains also meant that

the material is porous to CO₂, adsorbing approximately 112 cm³·g⁻¹, or 5.0 mmol/g (195 K, 1 atm), and having a measured BET surface area of 410 m²·g⁻¹ (77 K). Following TGA analysis, the authors found that the material is stable up to 430 °C, after which the framework collapses, though a phase change occurs before this between 350 - 400 °C, making it comparable to the previously discussed UiO-66 and MIL-140A. The authors also tested the material's resistance towards hydrolysis, which was measured in both water and HCl, and found to be comparable, if not better than, UiO-66, which experienced partial hydrolysis in similar conditions, see Figure 4.5.

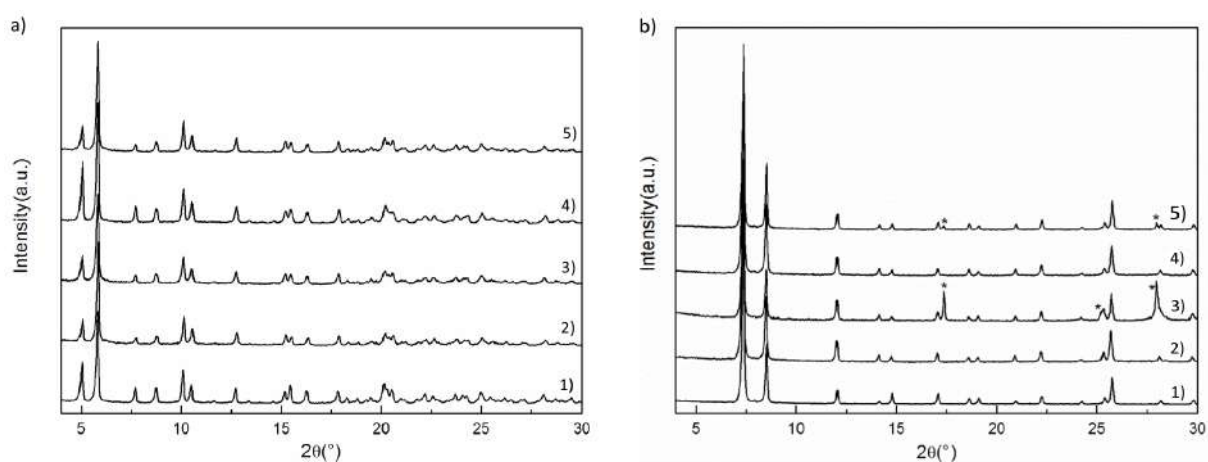


Figure 4.5: PXRD patterns of UPG-1 a1) as synthesised, a2) after a 3-day treatment in H₂O at 120 °C, a3) after a 2-day treatment in H₂O at 200 °C, a4) after a 3-day treatment in HCl at 80 °C, and a5) after a 3-day treatment in HCl at 120 °C. PXRD patterns of UiO-66 b1) as synthesised, b2) after a 3-day treatment in H₂O at 120 °C, b3) after a 2-day treatment in H₂O at 200 °C, b4) after a 3-day treatment in HCl at 80 °C, and b5) after a 3-day treatment in HCl at 120 °C. Starred peaks represent the hydrolysis product for UiO-66, terephthalic acid.

4.1.2 Scientific Motivation

The linkers synthesised in the previous chapter exist in a V-shaped geometry with regards to the phosphonic groups, though H₄DPPA (**3B**) does have the extra phenyl group protruding from the elbow of the V-shape. In the literature, there is a distinct lack of phosphonate-based linkers based on this geometry, though there are some examples of carboxylates. Direct comparisons, however, can be quite difficult to make due to the increased number of bonding modes possessed by phosphonates.

In terms of metal phosphonates, the literature is filled with examples of linear linkers which most often produce non-porous layered and pillared-layered structures. In fact, almost all of the metal phosphonates in the literature possess these kinds of structures, some of which have already been discussed. Again, thinking back to the work of both Clearfield and Alberti, we see a lot of layered and pillared-layered structures which, for the most part, are analogues of α -ZrP. The aim here then is to see how these novel linkers affect the structure of potential MOFs relative to α -ZrP or similar analogues, and to see if changing the relative geometry can push structures away from the non-porous pillared-layered arrangements to something different that may have more potential for applications such as gas sorption and catalysis.

4.2 Experimental

General procedure for the synthesis of metal phosphonates: Zirconium oxide chloride (0.3 mmol) was added to an HF-resistant plastic reaction vessel and dissolved in 1.0 mL of 2.9 M hydrofluoric acid. Water and methanol were then added to the solution along with the linker (0.3 mmol). The plastic reaction vessel was then placed into an oven at 80 °C and left to react for 3-7 days. The bottle was then removed from the oven and left to cool for a few minutes. The solid and solution were then poured into centrifuge tubes and centrifuged for 5 minutes. The solution was then poured off, leaving just the solid. Clean water was then added to the tube, sealed, and then agitated for 5 minutes. The tube was again centrifuged for 5 minutes, after which the water was poured off, leaving just the solid. This process was repeated again with water, and then acetone. After the acetone wash, the acetone was poured off and the solid was allowed to air dry overnight.

**All results have been tabulated in Appendix A according to linker selection.*

4.3 Results and Discussion

4.3.1 Structures Obtained using H₄BPA (1B)

Synthetic Screening

The initial synthetic parameters used in this work were constructed while taking some inspiration from the procedures for two previously discussed materials, that of Zr₂btbp and UPG-1.^{16,17} The synthesis of these materials was quite simple and involved very few variables and led to stable framework structures, and in the case of UPG-1, an open-framework structure. As is almost always the case in the synthesis of zirconium-based MOFs, hydrofluoric acid (HF) is used as a mineraliser, helping to slow the crystallisation process by keeping zirconium in solution as hexafluorozirconate,⁹ and in some cases helping with selectivity for specific crystalline phases. It is also important to note here that the use of alternative and less harmful mineralisers such as hydroxides and oxalates have been reported in the literature, though HF remains the best mineraliser for use in the synthesis of metal phosphonates. Since the aim of this work is to look at the synthesis of novel metal phosphonates with the highest possible crystallinity, HF was the preferred route in this case. Alongside HF, the main reaction medium used was water, though some exploration of alternative solvents and solvent mixtures was also carried out, looking at methanol, ethanol, isopropanol, dimethylformamide (DMF), and dimethylsulfoxide (DMSO). There was also some exploration for the use of hydrochloric acid (HCl) as a protonation modulator with the aim of slowing down the crystallisation by keeping the linker protonated.

Starting with N,N-Bis(4-phosphonophenyl)amine (H₄BPA), the initial screening employed this linker in a 1:1 molar ratio at 0.3 mmol with zirconium oxide chloride octahydrate (ZrOCl₂ · 8 H₂O) in water at 80 °C. The amount of HF (2.9 M) was then varied between 1.0, 2.0, and 3.0 mL and made up to 10 mL with water, though none of the three yielded any considerable product, at least not enough to characterise (059-061 in Table A.1). Moving forward, it was assumed that the lack of product

was most likely due to the concentration of HF in the solution, thus the volume of HF was lowered to 0.8, and 0.6 mL respectively while keeping all other parameters the same, both of which resulted in green crystalline solids in yields of 28.0 mg and 51.2 mg respectively (065 and 066 in Table A.1). The number of moles for the linker was then doubled to give a 2:1 ratio for L:M, and repeating the parameters of the previous two syntheses, resulting in an approximately two-fold increase in yield for both (067 and 068 in Table A.1). The PXRD patterns obtained for these four syntheses are shown in Figure 4.6, and it is immediately clear that the products all represent the same phase, henceforth known as **ZrBPA**, though they are not very crystalline and display what is considered a typical pattern for layered compounds. Looking at the PXRD patterns, we see the peak at $6.2^\circ 2\theta$, which represents a d -spacing of approximately 1.45 nm, or 14.5 Å. Given that the linker measures approximately 13.1 Å in width from the widest edges of each of the phosphonate groups (oxygen to oxygen), we can postulate that this peak represents the distance between the layers in the structure. The broad peaks seen on the diffraction pattern can be partially attributed to the heterogeneous distribution of the linker throughout the layers, as well as the small crystallite sizes. In an attempt to improve the crystallinity of the material, methanol was used, with all other parameters remaining the same as 065,

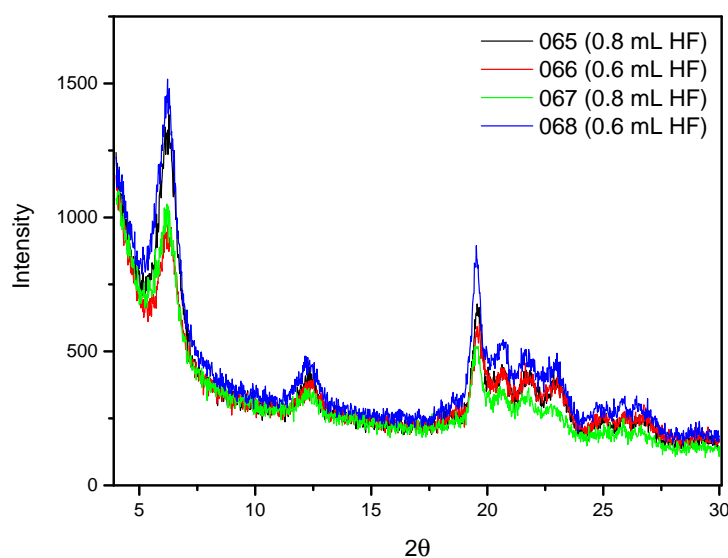


Figure 4.6: PXRD patterns obtained for materials 065 - 068. See Table A.1 for synthetic parameters.

to try and increase the solubility of the linker and keep it in solution for longer, thus slowing down crystallisation (074-075). It is here that there was a clear change in the product with the material now being blue in colour. The PXRD pattern also showed a slight increase in crystallinity, though an amorphous bump had now appeared in the 7-11° 2θ range, which might suggest some linker was still present. This was repeated using linker/metal ratio of 0.6, again resulting in a blue solid and a similar PXRD pattern, though slightly lower in intensity. Repeating the parameters of 075 at lower

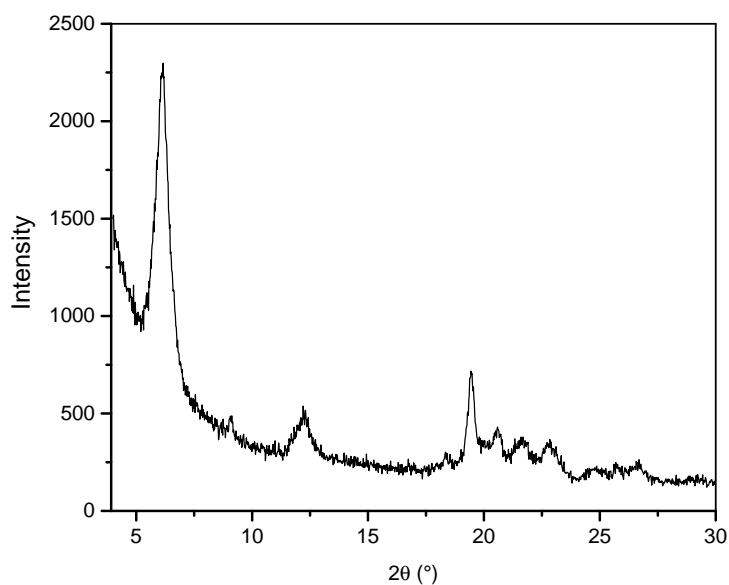


Figure 4.7: PXRD pattern obtained for material 074. See Table A.1 for detailed synthetic parameters.

temperature (70 °C) and increasing HF volume (0.8, 1.0, 1.2 mL) led to low intensity PXRD patterns with broad peaks (078-080). This is likely due to the small crystallite size caused by the changes in HF concentration and temperature, both of which act to slow down crystallisation. It should be noted here that the reaction time was also longer than the previously mentioned syntheses, the longest of which was 144 hours, while these syntheses were left for 167 hours. If only to prove the inherent difficulties involved in metal phosphonate synthesis, repeating 078 led to a similar pattern to before (084), but on increasing the HF volume and keeping all other parameters the same, the resultant pattern represented what was perhaps the most crystalline phase yet observed (085), herein known as ZrBPA (see Figure 4.8). Since the product phase

here was still not very crystalline, at least not crystalline enough to successfully solve the structure and perform Rietveld refinement, the decision was made to introduce a protonation modulator, in this case HCl, which should keep the linker protonated and further contribute in slowing down the crystallisation process. What was actually observed was that this led to very little difference in the observed PXRD pattern, save for the intensity. With this in mind, I attempted to see if changing the co-solvent would make any difference, comparing methanol, ethanol, isopropanol, butanol, dimethyl formamide, and dimethyl sulfoxide. Unfortunately, the result of these experiments was more often than not, a less crystalline phase or no crystalline phase whatsoever (088-117), as shown in Figure 4.9. Within these, the lack of solvent was also assessed via mechanochemical synthesis, though we again are unable to obtain crystalline phases. Shifting back to the original solvent and working with the parameters of 085 as a base, the quantity of HF was assessed again as well as a lower temperature of 70 °C, in the last set of syntheses based on this material. From here, the volume of HF (2.9 M) in the reaction was adjusted between 1.5 mL to 5.0 mL. Within the range of 1.5 mL to 3.0 mL (122-124, 126), the same phase that has been observed previously is present, though it is clear that the increase in HF has a considerable effect on the crystallinity. It is

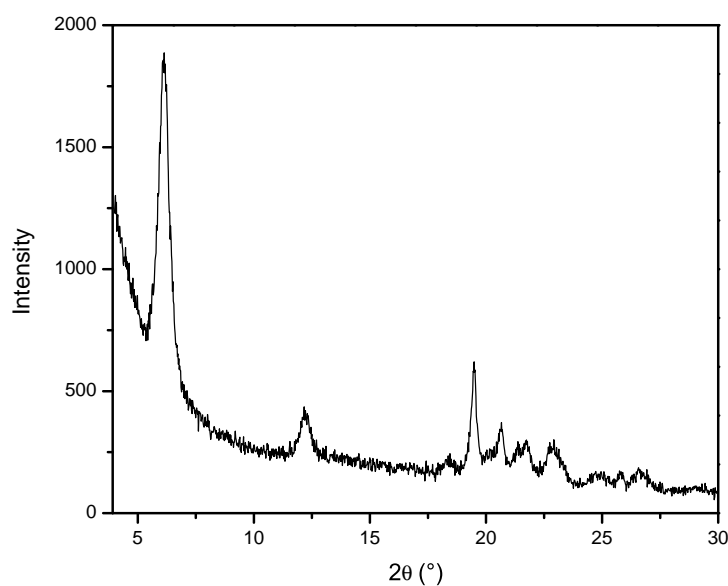


Figure 4.8: PXRD pattern obtained for material 085. See Table A.1 for detailed synthetic parameters.

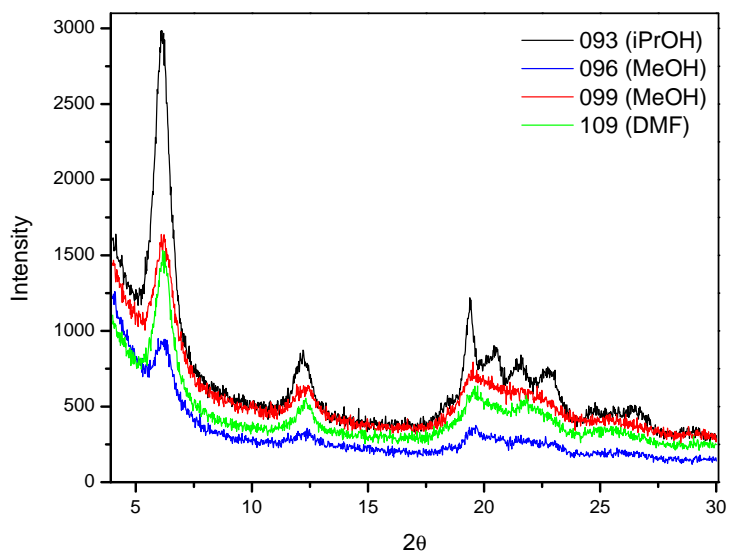


Figure 4.9: Representative patterns for materials 088-117 where solvent effect was investigated. See Table A.1 for detailed synthetic parameters.

also important to note here that the reaction time was greatly decreased from previous runs, though similar yields were obtained. On the other end of the scale, using 5.0 mL of HF meant that nothing crystallised whatsoever (128), though this might not be true with longer reaction times. In between these two sets (127), however, was actually something rather surprising. The PXRD pattern obtained for this run actually yielded a phase with what seems like greatly improved crystallinity compared to all previous

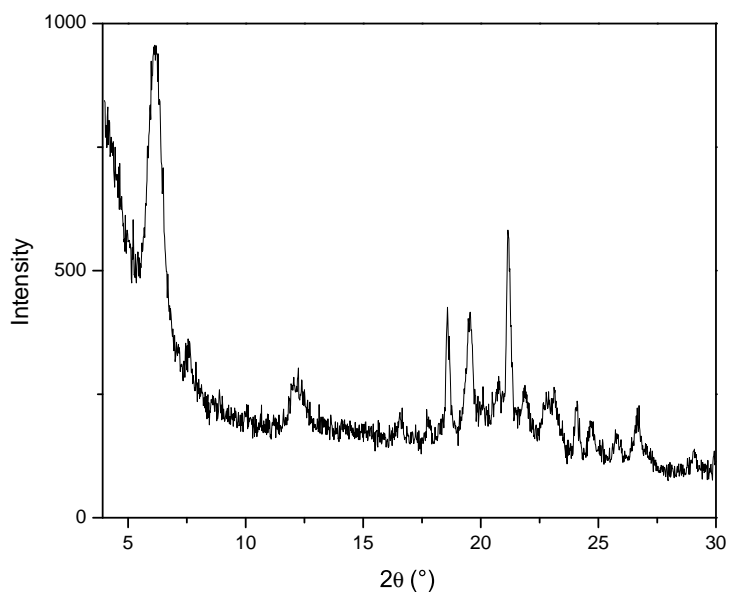


Figure 4.10: PXRD pattern obtained for material 127. See Table A.1 for detailed synthetic parameters.

patterns in the range of 15-30° 2θ , though overall, the intensity of the pattern is much less, see Figure 4.10.

Structural Analysis

With this in mind, crystallographic analysis was performed on the PXRD patterns for both 085 and 127 using the EXPO2014 (see Chapter 2 for further details) software and N-TREOR09 for indexing.^{18,19} Through indexing and Le Bail refinement of the pattern of 085, the following cell parameters were obtained: $a = 9.22 \text{ \AA}$, $b = 29.64 \text{ \AA}$, $c = 4.70 \text{ \AA}$, $\alpha = \gamma = 90.0^\circ$, $\beta = 94.5^\circ$, and $V = 1280.5 \text{ \AA}^3$. The space group was determined to be monoclinic, specifically $P2_1/a$. The Le Bail plot for this is shown in Figure 4.11. Here we see unweighted (R_p) and weighted (R_{wp}) R-values of 0.050 and 0.066, respectively, suggesting a good fit for the data. Repeating the process for the pattern obtained from

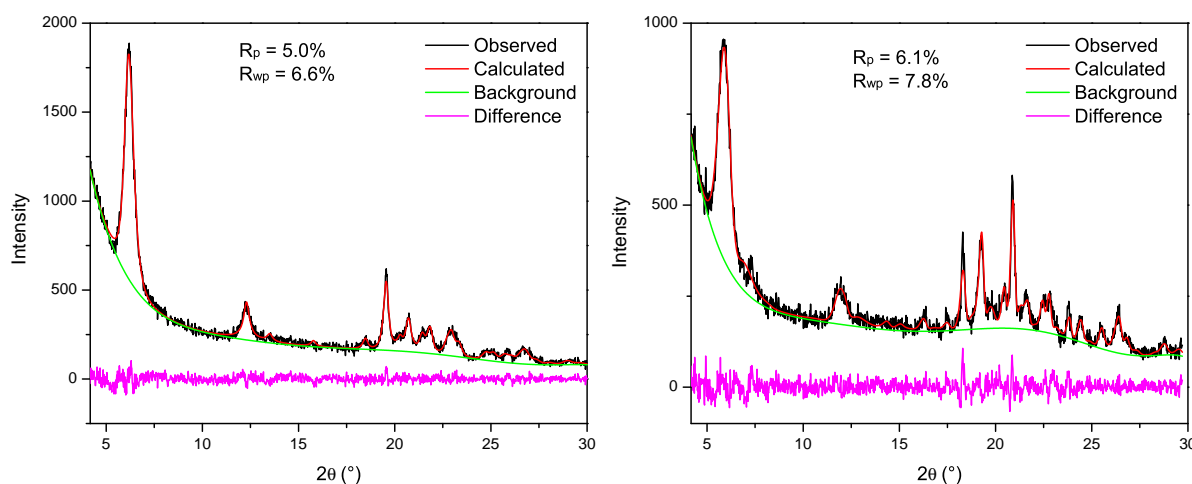


Figure 4.11: Le Bail plots for the materials obtained in 085 (left - $R_p = 0.050$, $R_{wp} = 0.066$) and 127 (right - $R_p = 0.061$, $R_{wp} = 0.078$). $R_p = (\sum |I_o - I_c| / \sum I_o) \times 100$, $R_{wp} = [\sum w(I_o - I_c)^2 / \sum (wI_o)^2]^{1/2} \times 100$.

material 127 yields relatively similar results, again obtaining a monoclinic space group, $P2_1/n$, and the following cell parameters: $a = 11.86 \text{ \AA}$, $b = 28.91 \text{ \AA}$, $c = 6.09 \text{ \AA}$, $\alpha = \gamma = 90.0^\circ$, $\beta = 103.3^\circ$, and $V = 2032.1 \text{ \AA}^3$. Again, there seems to be a good fit for the data, with R_p and R_{wp} values of 0.06 and 0.08 respectively. The Le Bail plot for this is shown in Figure 4.11.

Looking realistically at the two refinements, they seem to be very similar and in good agreement with one another, both having monoclinic space groups, as well as having fairly good unweighted (R_p) and weighted (R_{wp}) R-values for the fittings. Unfortunately, further attempts to solve the structure have been unsuccessful, as has been the case for the large majority of metal(IV) phosphonate structures in the literature. On the other hand, based on past structure solutions, it is possible to speculate as to the structure since it gives a typical PXRD pattern for a layered structure. Both in Chapter 1 and earlier in this chapter, we briefly mentioned the work presented by Alberti et al. on the synthesis of α -zirconium phenylphosphonate (α -ZrPhPA), as well as two other structures, which we would consider, at least for the purposes of this work, to be the archetypal structures for layered metal phosphonates, which we should not forget are somewhat related to the structure of α -zirconium phosphate (α -ZrP). The structure of α -ZrPhPA, like the structure reported here, ZrBPA, is reported to have a monoclinic space group ($C2/c$), with the cell parameters: $a = 9.09 \text{ \AA}$, $b = 5.42 \text{ \AA}$, $c = 30.24 \text{ \AA}$, $\alpha = \gamma = 90.0^\circ$, $\beta = 101.3^\circ$, and $V = 1461.0 \text{ \AA}^3$. One difference that is strikingly clear is that the long axis swaps from c in α -ZrPhPA to b in ZrBPA. As can be seen in Figure 1.6 and Figure 4.12, the inorganic units within the layers of α -ZrPhPA exist in the same orientation, with the phenyl rings pointing towards one another. This configuration however, does not support the inclusion of

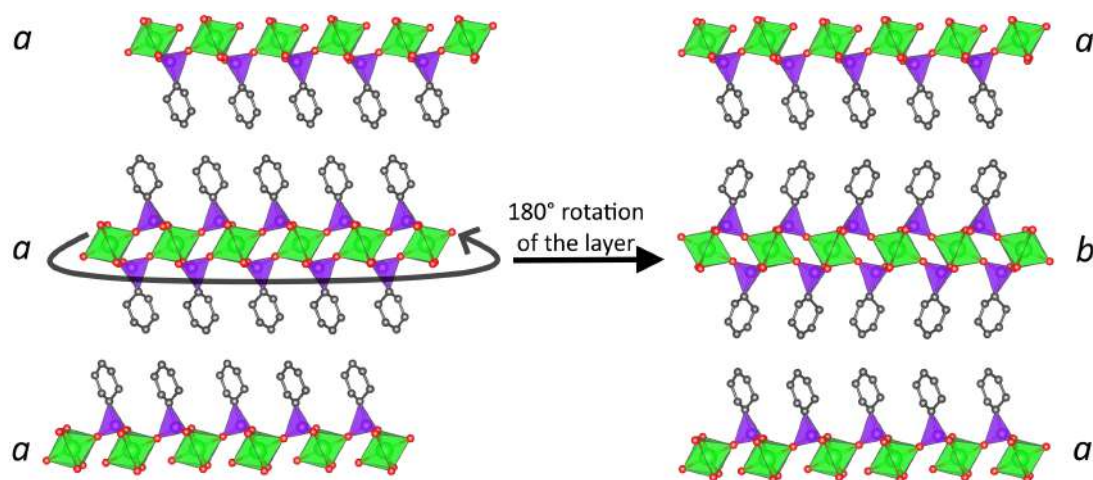


Figure 4.12: Structural representation of the layer rotation in α -ZrPhPA which would facilitate the V-shaped linkers used in ZrBPA.

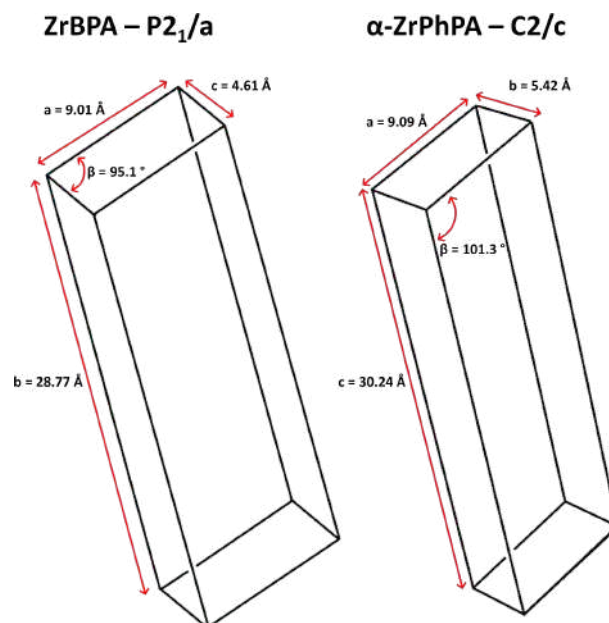


Figure 4.13: A comparison on the cells for ZrBPA and α -ZrPhPA, showing the switching of the b and c parameters.

the V-shaped linkers synthesised in the previous chapter, therefore it is necessary to consider how these linkers would fit into these α -type layers. One likely scenario is shown in Figure 4.12, whereby one of the inorganic layers is rotated 180° , which causes the reorientation of the phenyl rings and makes the inclusion of the V-shaped linkers possible. Realistically, what we're actually describing here is the reorientation of the zirconium oxide octahedra. Looking more closely at the structure of α -ZrPhPA, we can see that the layers exist in an a-a-a stacking arrangement, which becomes an a-b-a stacking arrangement in the proposed structure for ZrBPA. This change in stacking arrangement has a reasonably significant effect on the cell parameters, as we've already seen with the difference in space group between ZrBPA ($P2_1/a$) and α -ZrPhPA ($C2/c$) and cell parameters. The most obvious difference, as has already been pointed out, is the switching of the b and c parameters, whereby b describes the long axis in ZrBPA, while c describes the long axis in α -ZrPhPA. This can be seen in Figure 4.13, where we also see the β parameter switch from the largest plane to the smallest. This is something that could perhaps have already been predicted by looking at Figure 4.12, where it is clear that the reorientation of the inorganic units and the shifting of layers to accommodate the linker causes what was the β angle in α -ZrPhPA, becomes the γ

Table 4.1: A comparison of the geometric properties of the linkers used in ZrBPA, Zr-II-C, and ZrBPDP.

	ZrBPA	Zr-II-C	ZrBPDP
C-N-C Angle (°)	132.0	-	-
C-O-C Angle (°)	-	117.3	-
Dihedral Angle* (°)	24.8	48.6	53.5
P-P Distance (Å)	11.03	10.39	10.65
OP-PO Distance (Å)	13.16	12.68	11.91

*The dihedral angle here refers to the offset angle of the phenyl rings.

angle in ZrBPA, the latter of which we know will be 90° since the unit cell is monoclinic.

Having looked at the relationship of ZrBPA with that of historically layered metal phosphonates, there is a more recent comparison to be made with a material, which is that of Zr(IV) ether-bisphosphonate ($\text{Zr}[\text{O}_3\text{PC}_6\text{H}_4-\text{O}-\text{C}_6\text{H}_4\text{PO}_3] \cdot 0.5\text{H}_2\text{O}$, **Zr-II-C**).²⁰ In this case, the authors were unable to solve the structure but did manage to index the reflections to give a monoclinic unit cell with the following parameters: $a = 9.21 \text{ \AA}$, $b = 28.49 \text{ \AA}$, $c = 5.28 \text{ \AA}$, $\alpha = \gamma = 90.0^\circ$, $\beta = 91.85^\circ$, and $V = 1384.7 \text{ \AA}^3$. It should be immediately clear that these parameters are very similar to those of ZrBPA, whereby the b and c parameters are swapped relative to α -ZrPhPA. What makes this material an interesting comparison for ZrBPA is that it employs a linker with quite similar V-shaped geometry, as can be seen in Figure 4.14 and Table 4.1. Further, looking at the PXRD pattern, we also see striking similarities here, as can be seen in Figure 4.15. The presence of the low angle peak at $\sim 6^\circ 2\theta$ persists in all cases, as well as the peak at $\sim 12^\circ 2\theta$. The major difference in the patterns is in the range above $18^\circ 2\theta$, where we

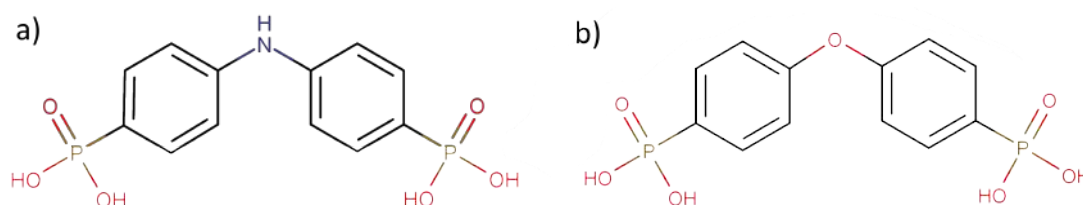


Figure 4.14: A comparison between the linkers employed in the synthesis of (a) ZrBPA (bis(4-phosphonophenyl)amine) and (b) Zr-II-C (4-(4'-phosphonophenoxy)phenylphosphonic acid).

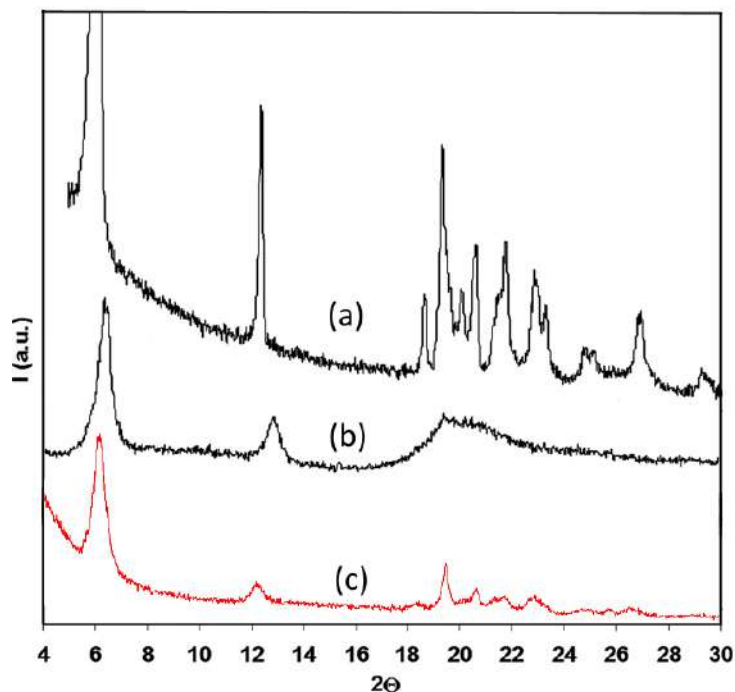


Figure 4.15: PXRD patterns for (a) a crystalline form of Zr-II-C, (b) a semi-crystalline form of Zr-II-C, and (c) ZrBPA.

see that the pattern for (a) Zr-II-C is well resolved due to its high crystallinity, while (c) ZrBPA is much less crystalline and thus the pattern is less resolved.

Thermogravimetric Analysis

Despite being unable to solve the structure through crystallographic methods, the authors were able to use thermogravimetric analysis (TGA) to obtain the structural formula, which they calculated to be $\text{Zr}[\text{O}(\text{C}_6\text{H}_4\text{PO}_3)_2] \cdot 0.5\text{H}_2\text{O}$. Doing this for ZrBPA gave a very similar result, with the calculated structural formula being $\text{Zr}[\text{NH}(\text{C}_6\text{H}_4\text{PO}_3)_2] \cdot \text{H}_2\text{O}$. The TGA plot for ZrBPA can be seen in Figure 4.16. Looking at the black and red lines on the TGA curve, we see four independent loss events, the first three of which account for a 5.99% loss from the starting sample (8.0980 mg) and have been attributed to the loss of methanol and water, both of which are used as co-solvents in the reaction mixture. Minus the weight of the solvents, we are now left with 7.6129 mg of sample. This means then that the fourth weight loss event, which is attributed to the degradation of the sample, i.e. loss of diphenylamine

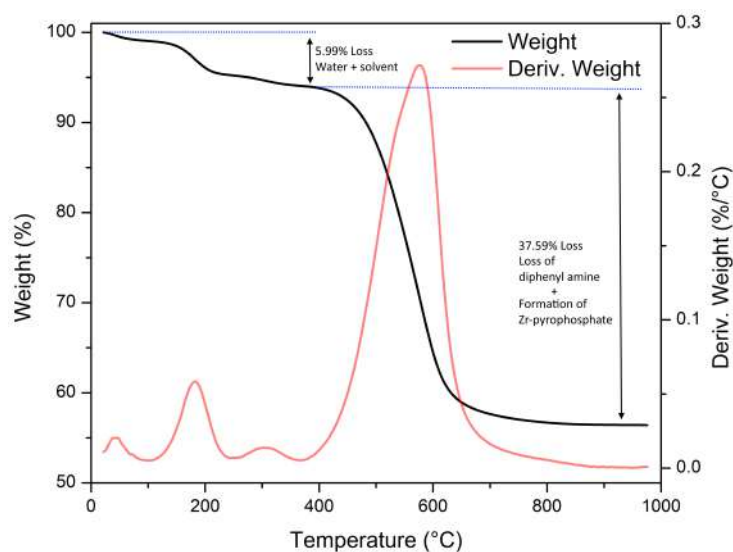


Figure 4.16: TGA curve showing weight loss (black line) against temperature as well as the derivative weight loss (red line), indicating the inflection points for the change in mass.

($\text{NH}(\text{C}_6\text{H}_4)_2$), now accounts for a 39.98% (3.0436 mg) loss due to decomposition of the sample, leaving 4.5692 mg zirconium pyrophosphate (ZrP_2O_7) accounts for 60.02% of the sample. Looking back to the previously mentioned structural formula, $\text{Zr}[\text{NH}(\text{C}_6\text{H}_4\text{PO}_3)_2] \cdot \text{H}_2\text{O}$, we can see indeed that ZrP_2O_7 does indeed make up 61.04% while $\text{NH}(\text{C}_6\text{H}_4)_2$ makes up 38.50%, which are both extremely close to the experimental values which are, of course, subject to human error with regards to where the mass loss is measured on the TGA curve. Based on this, it is reasonable to say that the structural formula for ZrBPA is $\text{Zr}[\text{NH}(\text{C}_6\text{H}_4\text{PO}_3)_2] \cdot \text{H}_2\text{O}$, with the potential to have more water of crystallisation, likely from the third mass loss event, if at all. We can also extract the thermal stability of ZrBPA by looking at the local minima on the red line between the third and fourth mass loss events, which indicates that the material is thermally stable up to $\sim 365^\circ\text{C}$, after which it starts to degrade to ZrP_2O_7 .

Gas Sorption Analysis

Due to the pillared-layered nature of ZrBPA it was expected that, like its historical counterparts, it would not exhibit any significant surface area or gas sorption properties. Rather unexpectedly, however, it was determined to have a measured BET N_2 surface area of $583.06 \text{ m}^2 \cdot \text{g}^{-1}$, and did exhibit significant N_2 sorption and

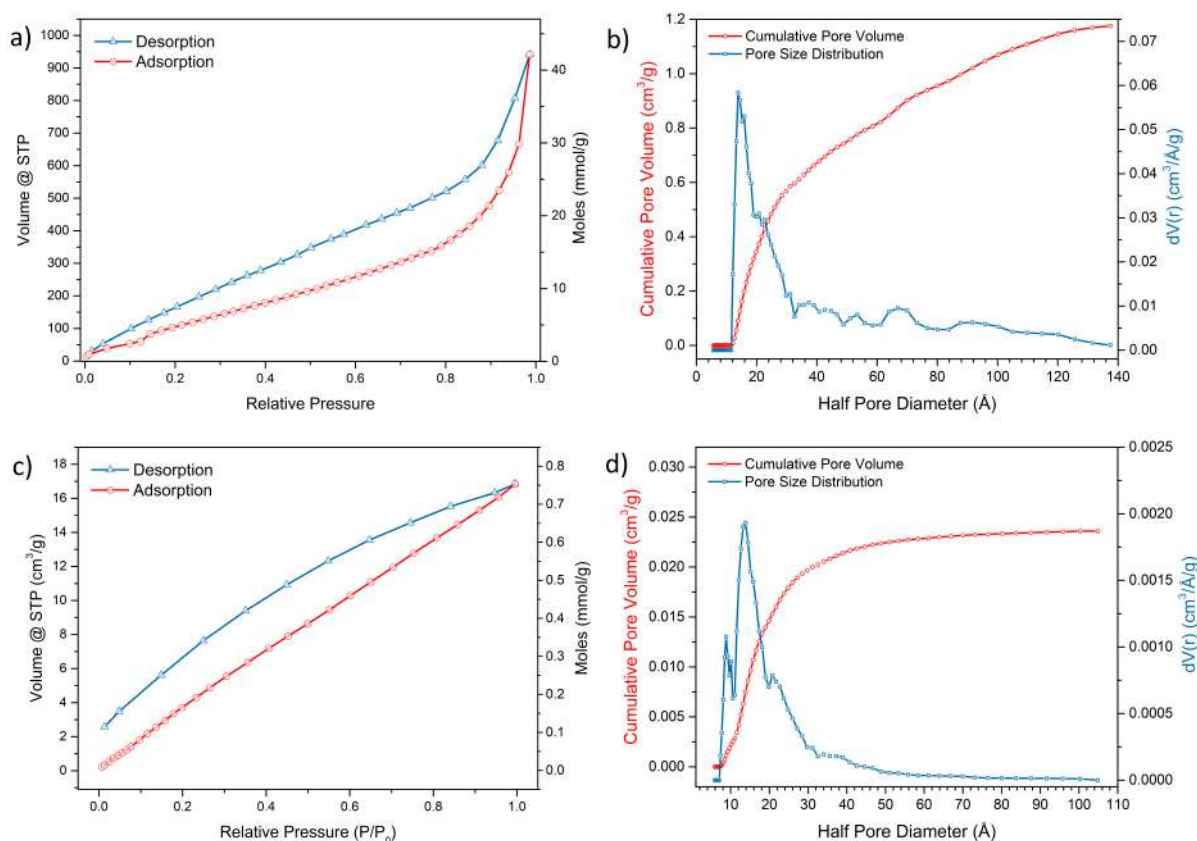


Figure 4.17: Gas sorption analysis for 085, showing a) the N_2 isotherm (77 K), b) the N_2 pore size distribution, c) the CO_2 isotherm (273 K), and d) the CO_2 pore size distribution. N_2 BET S.A. = $583.1 \text{ m}^2/\text{g}$, CO_2 BET S.A. = $39.7 \text{ m}^2/\text{g}$.

some minor CO_2 sorption properties, for which the adsorption-desorption isotherms are shown in Figure 4.17. Here, we see that the nitrogen uptake at 1 bar is quite considerable at $941.5 \text{ cm}^3/\text{g}$ or $42.0 \text{ mmol}/\text{g}$, though there is considerable hysteresis, see Figure 4.17a-b. Considering the shape of the isotherm, it falls somewhere between a type III and a type V, the latter of which is somewhat of a variation on the former. Looking again at the isotherm, it never reaches saturation, which indicates that unrestricted multi-layer formation is taking place, which in turn suggests the presence of large pores. This notion is supported by the pore size distribution, where we see the large majority of the pores have diameters that are 27.7 \AA or higher (note that the graph displays this in half pore diameter). This is not unexpected, since layered materials tend not to possess microporosity unless mixed linker synthesis has been utilised, whereby one of the linkers is shorter and introducing pores into the structure, or where there are defects present.⁸ This lack of microporosity is suggestive that the

adsorption is taking place on either the outer surface or within mesopores formed by structural defects, or both. We do also see some CO₂ uptake at 16.8 cm³/g or 0.75 mmol/g 273 K, 1 atm), see Figure 4.17c-d. The shape of the isotherm, despite looking quite linear, is slightly concave with regards to the *x*-axis, suggesting that it falls into the type I isotherm category, though it clearly does not fit the typical Langmuir or Freundlich-types. The shape of the curve shows that the rate of adsorption stays relatively constant across the whole pressure range, which is more in line with a Nernst-type isotherm. That the isotherm fits the type I classification suggests that there is indeed some microporosity within the structure. This is indeed supported by the pore size distribution, which shows that there are pores accessible to CO₂ which are 17.6 Å in diameter, though the majority of the pores accessible to CO₂ exist above 26.4 Å in diameter, as was also shown for N₂.

Photocatalytic Testing

Due to the blue colour of the material, which in itself is relatively odd for metal phosphonates (they are usually white), as well as previous work carried out on diphenylamine detailing its ability to form a radical cation,^{21,22} it was assumed that it might have some interesting photoactive properties. With this in mind, UV-Vis diffuse reflectance spectroscopy (DRS) and some photocatalytic testing, in the form of a dye degradation study, were carried out in order to assess this hypothesis. Looking at the UV-Vis DRS spectra in Figure 4.18, we can immediately see significant reflectance at 440 nm, which accounts for the blue colour of the material. We also see significant absorbance at 600 nm, which is well into the visible range, as well as further absorbance in the UV region at around 300nm. The absorbance at 600 nm is particularly interesting as this means solar radiation in the form of visible light can be utilised for photocatalytic reactions, and was the basis behind subsequent preliminary experiments using solar simulators as the light source. On the other hand, it should also be noted that transitions involving UV radiation in the UVA and potentially the UVB range would also be interesting since they are also emitted by the Sun, though

they only account for less than 5% of the solar spectrum. UVC, however, while emitted from the Sun, does not make it through the atmosphere and thus transitions in this energy range are not of much interest for photocatalysis using solar radiation. Prior to further experiments, the initial DRS spectrum was used to extract and estimate of the optical band gap of the material using the method described in Chapter 2, resulting the Tauc plots shown in Figure 4.19. Here, in Figure 4.19a, we see Tauc plots for

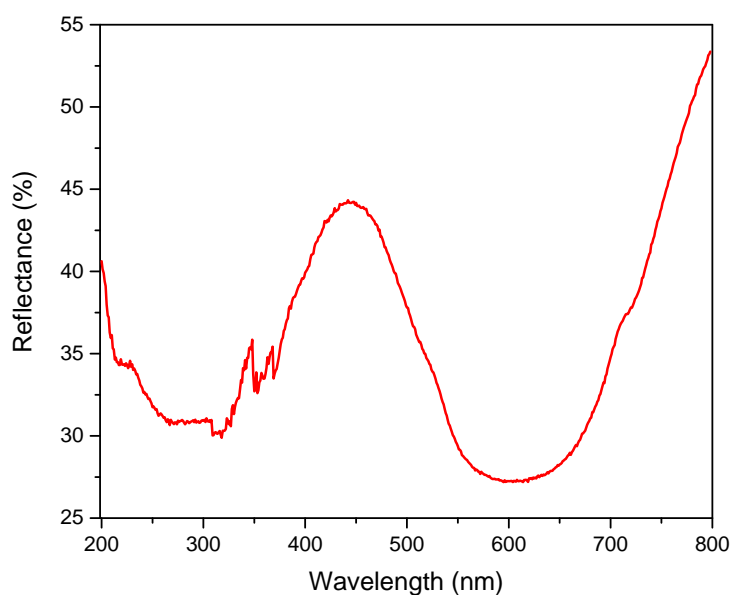


Figure 4.18: Measured diffuse reflectance spectrum for ZrBPA in the UV-Visible range (200-800 nm).

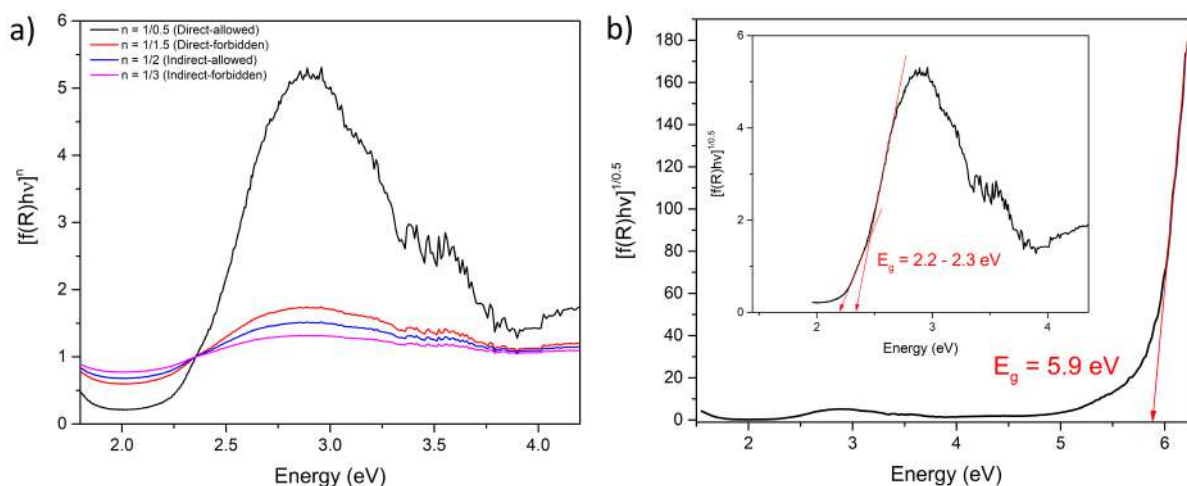


Figure 4.19: a) Tauc plot for each of the energy transitions: direct-allowed (black), direct-forbidden (red), indirect-allowed (blue), and indirect forbidden (pink). b) Tauc plot for the direct-allowed transition with extracted optical band gap energies, one in the range of 2.2-2.3 eV, and another at ~ 5.9 eV.

each of the energy transitions. It is clear that the direct-allowed transition is the most prominent of these, and thus the optical band-gap energy was extracted using this. Figure 4.19b shows the extrapolation of the optical band-gap energy from the Tauc plot using the line-of-best-fit method, whereby we see two transitions. One of these transitions has an optical band-gap energy of 5.9 eV, and is almost in the middle of the UVC region, which, as previously suggested, makes this transition less interesting with regards to using solar radiation as the energy source for photocatalysis. We also see one or possibly two (reported here as a range) energy transitions within the visible light region, with optical band-gaps between 2.2 - 2.3 eV. It is important to note here that an effective photocatalyst should possess a maximum optical band-gap energy below 3.0 eV to keep it in the visible range of the electromagnetic spectrum, but should not descend too far into the IR range since this form of radiation does not provide sufficient energy to facilitate photocatalytic activity, at least not on convenient time-scales. It is commonly stated that the minimum band-gap energy for photocatalytic water splitting is 1.23 eV, though efficient photocatalysts have been found with larger band-gap energies.^{23,24}

The next step in the process of assessing the photocatalytic activity of the material was to carry out a photocatalytic dye degradation study on Rhodamine-B. Before discussing the experiment, we should first briefly consider why this is important. The total production of synthetic dye totals approximately 700,000 tons annually, a large portion of which, estimated to be around 15%, is thought to be lost in the wastewater stream.^{25,26} Unfortunately, synthetic dyes are already known to possess significant chemical stability and are not prone to degradation through biological methods. It is clear that this poses a huge environmental threat, with huge implications to aquatic life as well as land dwellers and humans, particularly in areas where access to clean drinking water is already limited.²⁷⁻³¹ Looking specifically at the degradation of Rhodamine-B, this most often occurs via two pathways.³² The first of these is the N-dealkylation pathway, whereby the ethyl groups on the amine moieties are

sequentially removed, transforming the tertiary amine to a primary amine, as shown in Figure 4.20a. The second pathway is chromophore cleavage, and refers to the breakdown of the Rhodamine-B structure into smaller molecules, as can be seen in Figure 4.20b. The third pathway, mineralisation, refers to the transformation of these small molecules into simpler ones such as water, carbon dioxide, and various ring opening products. The mineralisation pathway is one that tends to occur after the first two, and such, is not too important in the context of this work. What we are looking at here, is which of the two pathways, N-dealkylation or chromophore cleavage, is the most dominant. There is a simple qualitative way to do this which involves looking at the shape of the absorption spectra. Figure 4.21a shows the typical absorption spectra for Rhodamine-B. If the dye were to degrade via the N-dealkylation process, you would expect to see what is known as a hypsochromic shift, whereby the

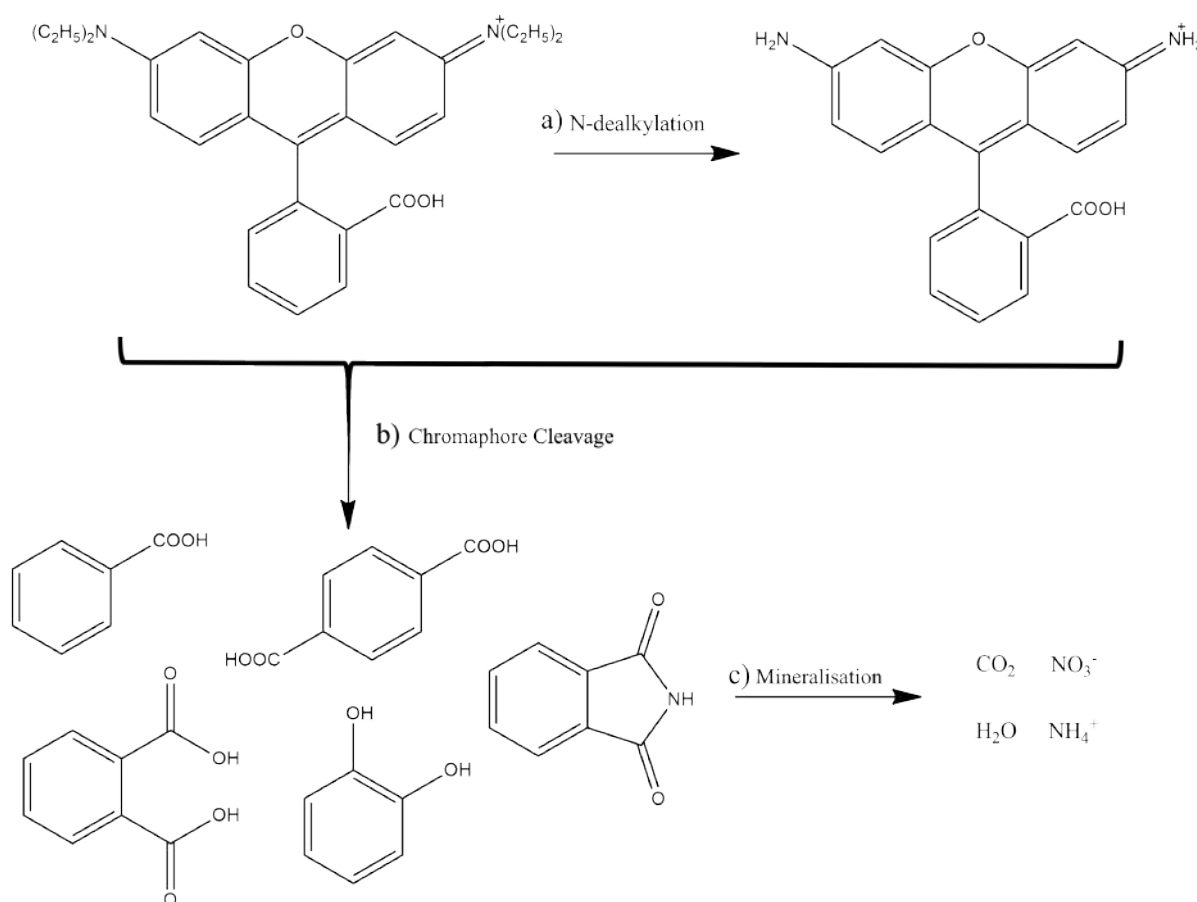


Figure 4.20: Photocatalytic degradation pathways for Rhodamine-B: a) N-dealkylation, b) chromophore cleavage, and c) mineralisation of chromophore cleavage products.

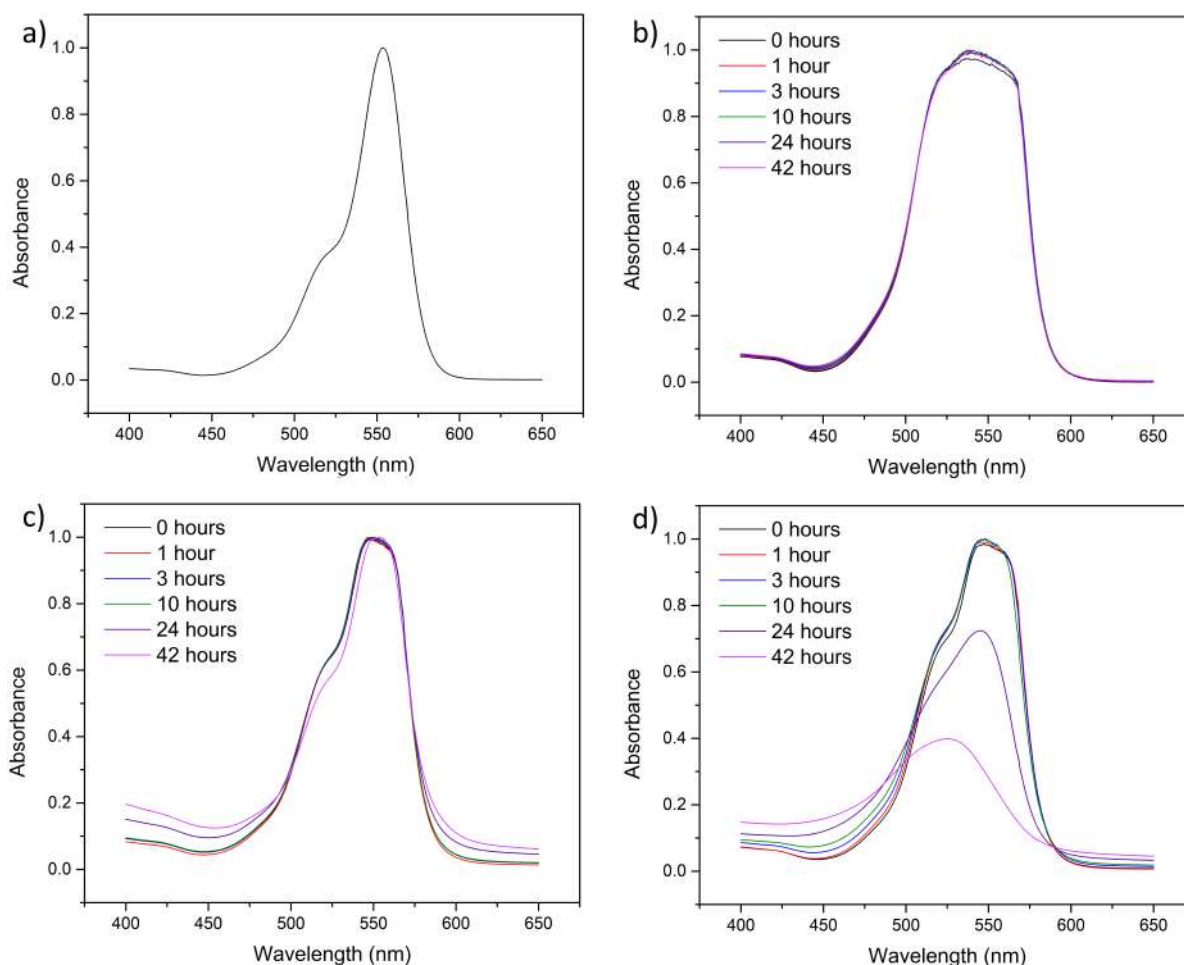


Figure 4.21: UV-Vis absorbance spectra for a) a dilute solution (0.1 mM) of Rhodamine-B, and the photocatalytic degradation of Rhodamine-B (0.8 mM), b) exposed to light source, with no photocatalyst present, c) not exposed to light source, with catalyst present, and d) exposed to light source, with catalyst present. Absorbance data for each plot has been normalised to λ_{max} in the relevant dataset.

position λ_{max} literally shifts with the successive removal of the ethyl groups, equating to approximately 15 nm per ethyl group.³² Proceeding via the chromophore cleavage pathway would cause no wavelength shift in λ_{max} , but a gradual drop in intensity to zero.

In this preliminary setup, a class ABB small area solar simulator was used as the radiation source, specifically the LCS-100. The letters in the class rating refer to three specific properties, which are spectral match (how far the lamp deviates from the ideal spectral range), spacial uniformity of irradiance (higher standards minimise the impact of hotspots on experimental results), and temporal stability (ensures the stability of

light output over time to ensure that fluctuations don't affect experimental results), respectively. To carry out these experiments, a 0.2 mM stock solution of Rhodamine-B was diluted and decanted into three separate sample tubes: a control containing just the Rhodamine-B solution, and two containing 10 mg of the photocatalyst (ZrBPA) additional to the Rhodamine-B solution, one of which is used as an additional control and kept in the dark. These were then left to stir in the dark overnight to ensure sufficient mixing, after which UV-Vis measurements were taken to establish a baseline. The samples, except the dark control, were then exposed to the solar simulator in a custom made light box, ensuring no outside interference affected results. Further UV-Vis measurements were taken after 1, 3, 10, 24, and 42 hours, with each measurement preceded by centrifugation of the sample to ensure no photocatalyst was present.

Initially, the concentration of the diluted Rhodamine-B solution was 0.01 mM, though we observed that the colour of the solution, which begins as a very vibrant pink, becomes almost colourless after being left to stir in the dark overnight in the presence of ZrBPA. This is most likely due to the adsorption of the dye in the defect-derived mesopores observed in the pore size distribution plot in Figure 4.17b & d. Moving forward, this meant that the concentration of Rhodamine-B needed to be increased until the material was saturated and no further adsorption could take place, which in this case was determined to be 0.08 mM. This adsorption of the dye is actually something that is clearly visible in Figure 4.21, whereby comparing 4.21a with 4.21b and 4.21c/d shows a clear oversaturation of the detector, causing some of the absorption spectra to be cut off, while the introduction of the photocatalyst leads to a clear drop in the concentration of Rhodamine-B.

Looking closely at the control in Figure 4.21b, which was exposed to visible light irradiation, we can see that Rhodamine-B did not appear undergo any degradation over the 42 hour experiment. Looking at 4.21c, which had the photocatalyst present but was kept in the dark, we see some change in the UV-Vis spectrum. It is possible

that this is caused by some adsorption of the dye into the material, as observed at lower concentrations, but also by exposure to light during the centrifugation process and transport of the sample to and from instruments. Moving to 4.21d, we see considerable degradation of the dye. Looking carefully at the shape of the curve you will notice the hypsochromic shift of λ_{max} from 552 nm to 525 nm, which approximately equates to a 30 nm shift, which indicates the removal of two ethyl groups.³² As well as this, there is a clear reduction in the absorption intensity after 24 hours under irradiation, which indicates that chromophore cleavage is occurring in a competitive process with dealkylation. While it is true that we can only see this after 24 hours when comparing λ_{max} , looking either side of λ_{max} at the tails of the curve, we are clearly already seeing changes after three hours, changes which indicate the formation of degradation products. Since the true λ_{max} is not visible due to the concentration of Rhodamine-B, it's impossible to give absolute values on the latter concentrations.

4.3.2 Structures Obtained using H₄DPC (2B)

Although the N,N-Bis(4-phosphonophenyl)amine (H₄BPA) provided some rather interesting data, it was unfortunate that it was a pillared-layered structure analogous to those already discussed in the literature. Moving forward with the idea of trying to avoid these kinds of structures due to their intrinsic lack of microporosity, it was theorised that a linker with a smaller C-N-C angle might better encourage this than the previous linker. Rather favourably, one of the linkers prepared in the previous chapter does, in fact, possess this trait. The 3,6-diphosphono-9H-carbazole (H₄DPC) linker is relatively similar to the diphenylamine-based linker, with the addition of a single bond to form a five-membered heterocycle, i.e. a carbazole. With the point on comparison clear, the synthetic screening of this linker, with ZrOCl₂ · 8 H₂O as the metal source, went ahead with a 1:1 molar ratio (0.3 mmol) between the two in 0.8 mL of HF (2.9 M) and water in a total volume of 10 mL and heated to 80 °C, with the procedure being identical to that stated for the diphenylamine screening. This first

attempt resulted in a blue powder from which the PXRD pattern labelled **076** in Figure 4.22 was obtained. It is unfortunate, however, that this pattern indicates that the crystal structure is again likely to be a pillared-layered structure. On this basis, and due to time constraints, interest in investigating this linker further was limited, but a few more trials were carried out, exploring the L:M ratio, co-solvents, HF concentration, and the addition of HCl as a protonation modulator (see Table A.2 for detailed synthetic parameters). This most often led to X-ray amorphous materials or to materials with PXRD patterns similar to those labelled **086**, **133**, and **137** in Figure 4.22. Again, these patterns were indicative of pillared-layered structures, making the material(s) much less attractive for further exploration with regards to open-frameworks structures and their applications. Like ZrBPA, however, these materials might present some

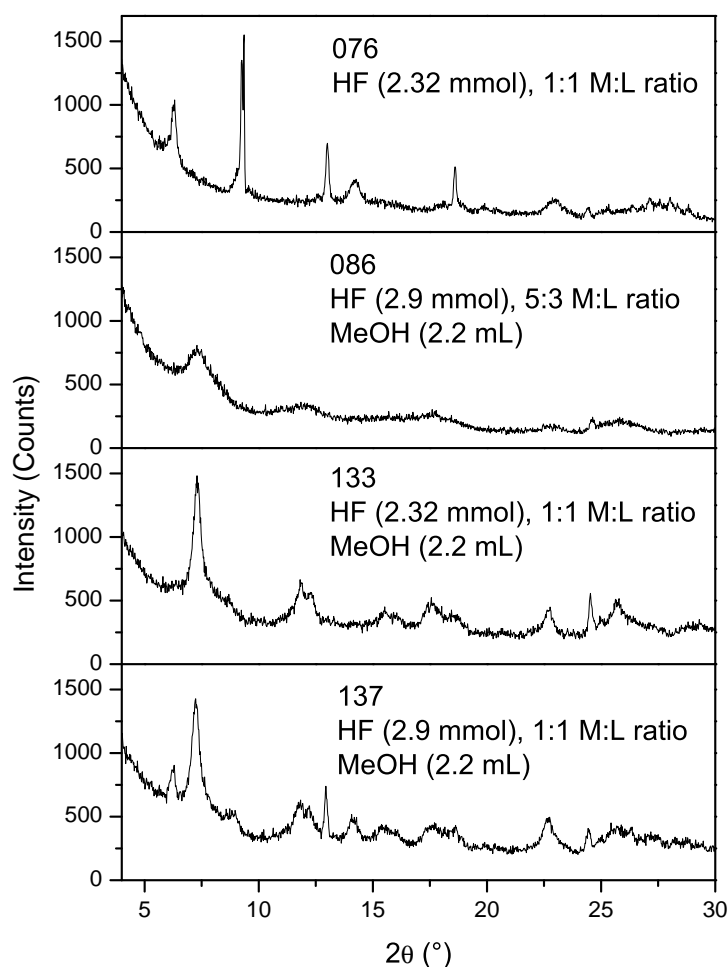


Figure 4.22: PXRD patterns for crystalline/semi-crystalline materials obtained through the use of the H₄DPC (**2B**) linker and ZrOCl₂ · 8 H₂O.

interesting photocatalytic activity, and should be subject to further study in this direction.

4.3.3 Structures Obtained using H₄DPPA (3B)

Synthetic Screening

With the initial idea of using smaller C-N-C angles not yielding the desired result, another idea to cross the table involved adding substituents to the nitrogen atom, with the thought here being that adding substituents would sterically prevent the pillaring between layers and should therefore prevent the formation of pillared-layered structures completely. Again, this was already a consideration before the synthetic screening, with the 4-phosphono-N-(4-phosphonophenyl)-N-phenylaniline (H₄DPPA) linker serving as the representation of this idea, which should be referred to more as a Y-shaped linker. Despite having a relatively short time to work with this linker in terms of MOF screening, it was actually a relatively easy process. In fact, almost every synthesis performed, regardless of changes in parameters, resulted in materials with almost identical PXRD patterns with differing intensities, as shown in Figure 4.23.

With regards to the synthesis, this began using the same 1:1 ratio for the metal source and the linker at 0.3 mmol with 0.8 mL of HF (2.9 M), 2.2 mL of methanol, and 7.0 mL of water, making a total volume of 10 mL. The reaction mixture was heated to 80 °C in a furnace for a total of 138 hours (5.75 days), resulting in a blue solid with a yield of 71.6 mg, the PXRD pattern for which is labelled **134** in Figure 4.23. Increasing the volume of HF (2.9 M) to 1 mL, whereby the HF/Zr ratio increases from 27.3 to 34.1, and dropping the reaction time down to 96 hours (4 days), gave the pattern labelled **135** and a yield of 80.6 mg. The major observation here is that the reaction is likely complete well before the 4-day mark, as we see no additional peaks to indicate there is any unreacted precursor present, regardless of the presence of more HF. Run alongside this was a reaction where the concentration of both the linker and the metal were doubled, while the HF volume was kept at the original 0.8 mL, resulting in a PXRD

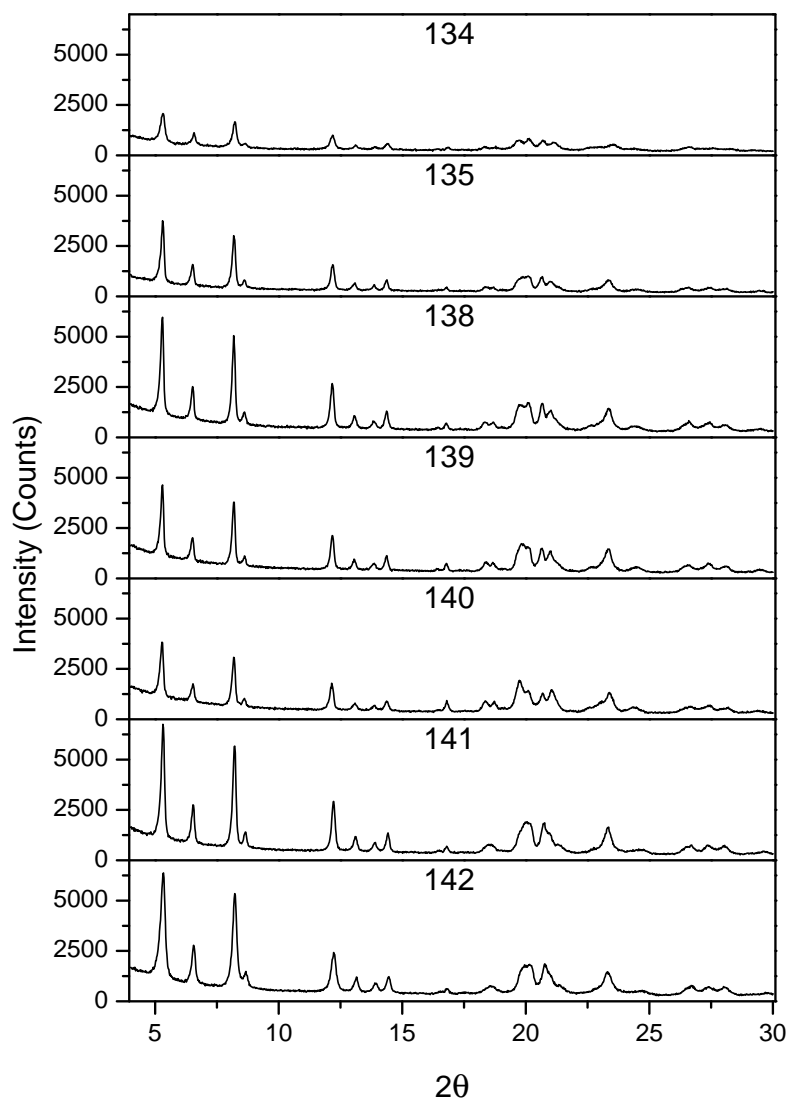


Figure 4.23: PXRD patterns for synthesis resulting in the formation of ZrDPPA through the use of H_4DPPA and $\text{ZrOCl}_2 \cdot 8\text{H}_2\text{O}$.

pattern which showed only amorphous bumps which is likely caused by the massive drop in the HF/Zr ratio to 13.7. Reverting back to the original reagent concentrations, the next two runs explored the effect of increasing the volume of HF in the added mixture, going to 1.2 and 1.4 mL (**139** and **140**), which equate to HF/Zr ratios of 41.0 and 47.8, respectively. Both produced relatively crystalline products, though there was a notable increase in crystallinity when using 1.4 mL of HF. Conversely to this, though not unexpected, the final product yield decreased in the presence of more HF, going from 80% at 1.0 mL to 70% at 1.4 mL of HF. With this in mind, the volume of HF was reduced back to 1.0 mL in order to compromise with crystallinity and yield, and the

next two runs looked at assessing the effect of changing the volume of methanol used, with the idea being that increasing the methanol would slow the synthesis by keeping the linker in solution for longer, potentially leading to a more crystalline product. The volumes of methanol went from 2.2 mL (as was used for all previous runs), to 4.4 mL (**141**) and 6.6 mL (**142**). This resulted in an increase in the yield to 81.1% and 85.3%, respectively, though there was not noticeable increase in the crystallinity.

Structural Analysis

What is initially clear when looking at the PXRD patterns obtained for ZrDPPA, is that they do not present as typical for a pillared-layered structure, as was the case for ZrBPA. As was done previously for ZrBPA, crystallographic analysis was also carried out here in order to obtain vital information about the structure of the material. As before, this was done using the EXPO2014 software package with integrated N-TREOR09 for indexing. Through indexing and Le Bail refinement, the following cell parameters were obtained: $a = 16.99 \text{ \AA}$, $b = 13.72 \text{ \AA}$, $c = 7.75 \text{ \AA}$, $\alpha = 98.9^\circ$, $\beta = 97.8^\circ$, $\gamma = 85.9^\circ$, and $V = 1767.1 \text{ \AA}^3$. The space group was determined to be triclinic, specifically $P - 1$. The Le Bail plot for this is shown in Figure 4.24. Here we see unweighted (R_p) and weighted (R_{wp}) R-values of 3.9% and 5.2%, respectively, suggesting a good fit for the data.

Looking realistically at the Le Bail refinement, it has very good unweighted (R_p) and weighted (R_{wp}) R-values for the fittings, suggesting that the pattern shows a good fit for the $P - 1$ space group. Unfortunately, further attempts to solve the structure have been unsuccessful, as was the case for ZrBPA and the large majority of metal(IV) phosphonate structures in the literature. With the structure proving very difficult to solve, it has been necessary to draw some comparisons with other materials. This also proved to be rather difficult, though a comparison was indeed drawn with UPG-1, which has already been discussed in the introduction to this chapter.¹⁷ Comparing the linkers, it is clear that the one employed in UPG-1,

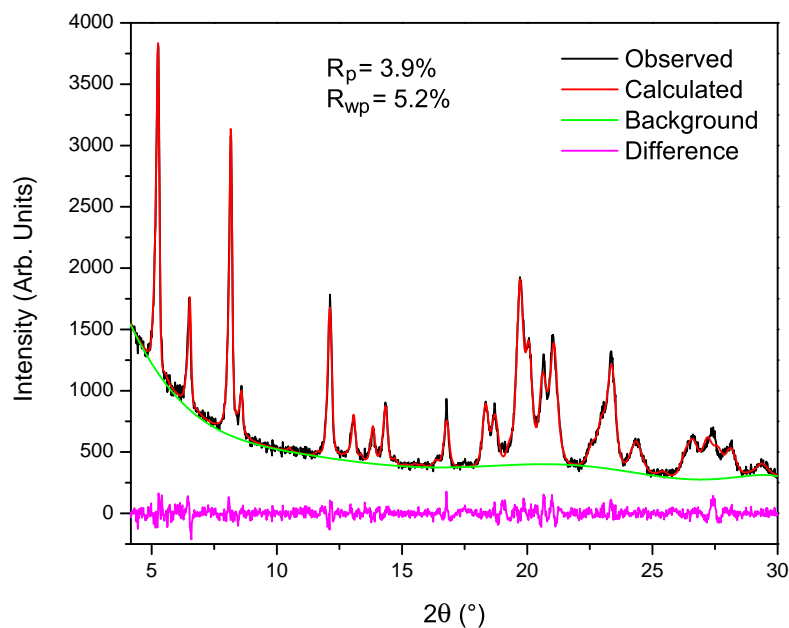


Figure 4.24: Le Bail plot for the material obtained in 140 ($R_p = 3.9\%$, $R_{wp} = 5.2\%$).

2,4,6-tris(4-(phosphonomethyl)phenyl)-1,3,5-triazine (H_4 ttbmp), has a few differences to H_4 DPPA. First of all, the central ring present in H_4 ttbmp is simply a nitrogen atom in H_4 DPPA. Second, the H_4 ttbmp linker contains three phosphonate coordinating groups, as opposed to the two in H_4 DPPA, though only two are coordinated, which is why somewhat of a comparison can be made. The third and final difference is that the phosphonate groups in H_4 ttbmp are connected to the ring via a methyl group, while those in H_4 DPPA are connected straight to the rings. The fact that only two of the phosphonate groups in H_4 ttbmp are involved in the coordination to make UPG-1 is actually the main point of comparison. The idea here is that uncoordinated phenyl ring on H_4 DPPA might play a similar role in the structure of ZrDPPA as the uncoordinated phosphonate groups in UPG-1. This would likely give a similar structure, wherein there are two types of channels, one where the uncoordinated phenyl rings point into the pore, and another where diameter of the circumference of the pore is populated with the phosphonate groups, aromatic rings and the zirconium coordination sphere, which in UPG-1 took the form of ZrO_6 chains bridged via the H_4 ttbmp linker. Looking at the PXRD patterns presented in Figure 4.23, we can obtain the d-spacings for the first few reflections and attempt to reason what might be causing them. The d-spacings are

as follows: $5.26^\circ 2\theta = 16.8 \text{ \AA}$, $6.52^\circ 2\theta = 13.6 \text{ \AA}$, $8.17^\circ 2\theta = 10.8 \text{ \AA}$, and $12.13^\circ 2\theta = 7.3 \text{ \AA}$. The stand out figure here is that one at $8.17^\circ 2\theta$, as the d-spacing is almost equal to the distance between the phosphorus atoms on the opposite sides of the linker, which is 10.5 \AA when measured after geometry optimisation (MMFF94s) using Avogadro. With that in mind, it is likely that the first reflection at $5.26^\circ 2\theta$, which has a larger d-spacing at 16.8 \AA , is likely related to the distance between zirconium atoms, which may very well exist as ZrO_6 chains, as in UPG-1. Beyond UPG-1, there was no clear comparison to be found in the literature, and it seems that there are no Y-shaped linkers like H_4DPPA , whereby one of the three protrusions does not have a coordinating group present.

Thermogravimetric Analysis

With the inability to solve the structure through crystallographic methods, TGA was again employed in an attempt to obtain an empirical formula, from which the structural formula can be implied. Looking at the TGA curve shown in Figure 4.25, it is clear that there are six independent mass loss events. The first two of these

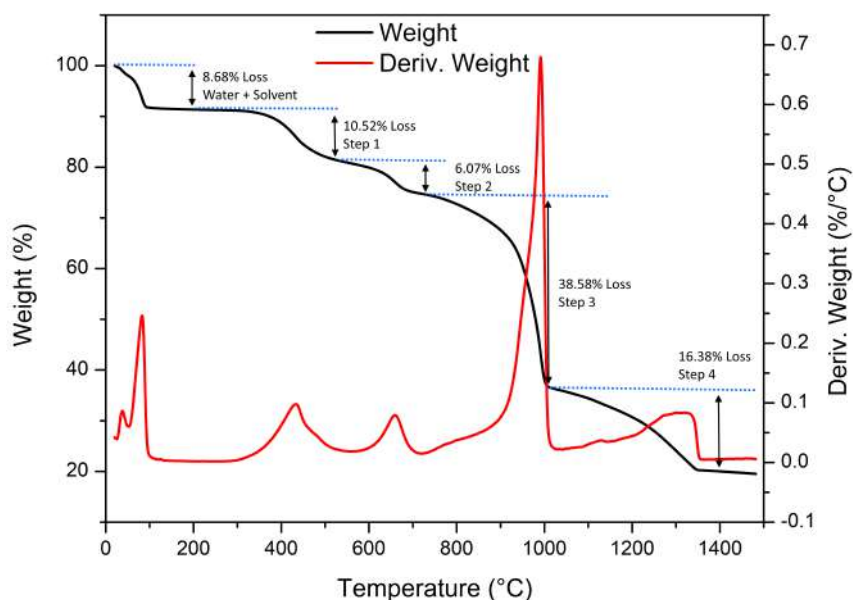


Figure 4.25: TGA curve for ZrDPPA, showing %weight loss (black line) against temperature and the derivative weight loss (red line). Initial weight = 8.2760 mg.

account for a weight loss of 8.68%, and have been attributed to the loss of methanol

and water respectively. With this in mind, the weight of ZrDPPA in the sample can be estimated to be 7.5578 mg in total, based on the 8.2760 mg starting weight (moving forward, all %weight loss is based on this starting weight). From here, the material goes through a rather complicated degradation pathway involving multiple mass loss events. Without further in-depth analysis it is difficult to say what these individual events represent, though, working on the basis that the final mass should just be zirconium pyrophosphate (ZrP_2O_7), we can attempt to work backwards from there to obtain the structural formula.^{33,34} So going from the point after the loss of water and solvent (7.5578 mg), to the final mass (1.6368 mg), we see a total loss of 5.9210 mg, or 78.54%, which means that the components of ZrP_2O_7 make up 21.46% of the material, i.e. 1.6368 mg, of which Zr makes up 34.40% of the mass at 0.5565 mg which is 7.36% of the total sample. This comes pretty close to the potential formula of $\text{Zr}[\text{N}(\text{C}_6\text{H}_5)(\text{C}_6\text{H}_4\text{PO}_3)_2]_3$, where Zr makes up 7.04% of the mass. The difference here is most likely due to the selection of points where the mass losses were measured. Looking at the other mass loss events, step 1 and step 2 together would approximately account for the loss of the non-phosphonate containing phenyl ring, which makes up approximately 18.16% of the material, though why this would occur in two steps is unclear. This is interesting, however, as it means there is possible scope to increase the free volume within the material by annealing the material at a maximum of 700 °C. By default, the remaining mass loss events must account for further degradation of the linker, which is now likely to be in the form of diphenylamine.

Gas Sorption Analysis

With the PXRD pattern suggesting that the material has indeed moved away from the pillared layered motif, the expectation here was that it should indeed possess some microporosity. When you consider this alongside the comparison with UPG-1, you would expect there to be slightly less accessible space simply due to the size difference in the linker, almost as if they were part of the same analogous series, wherein H_4ttbmp is the larger version of H_4DPPA . Looking first at the N_2 isotherms in Figure 4.26a, we

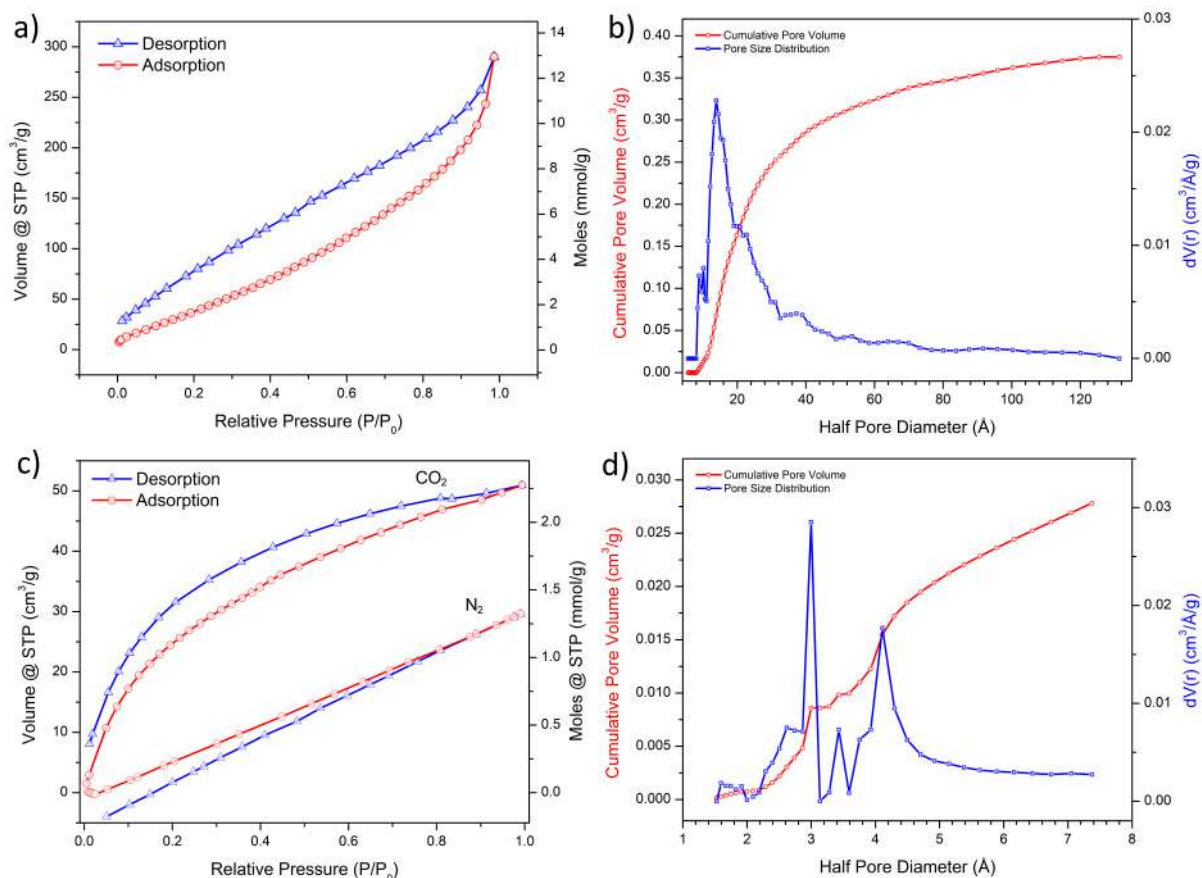


Figure 4.26: Gas sorption analysis for 135, showing a) the N₂ isotherm (77 K & 273 K), b) the N₂ pore size distribution (77 K), c) the CO₂ isotherm (273 K), and d) the CO₂ pore size distribution. N₂ BET S.A. = 228.1 m²/g, CO₂ BET S.A. = 132.7 m²/g.

see the one obtained at 77 K takes up quite a lot of N₂ at just below 300 cm³/g or 13.0 mmol/g (at 1 atm), and exhibits considerable hysteresis. Looking at the shape of the isotherm, it clearly fits the type III motif, which indicates the presence of mesopores, which is supported by the pore size distribution in Figure 4.26b, whereby it is clear that most of the accessible space to N₂ exists in pores that are around 28 Å in diameter. Due to thermodynamic limitations, this decreases drastically for the isotherm collected at 273 K, where the total uptake drops 10-fold to just under 30 cm³/g or 1.3 mmol/g.

Moving to Figure 4.26c, we see what should be a reasonable CO₂ uptake of 51 cm³/g or 2.3 mmol/g at 1 atm, though it does have a relatively low IAST CO₂/N₂ selectivity of around 8. The shape of the isotherm clearly fits the type I motif, which immediately suggests that there is significant microporosity within the structure accessible to CO₂. The presence of microporosity is also supported by the pore size distribution shown

in Figure 4.26d, where we see two or three significant pore types with diameters measuring 6.0 Å, 6.8 Å, and 8.2 Å, all of which are on the lower end of the microporous range. Jumping back to the comparison with UPG-1, which had two significant pore types, it would also be reasonable in this case to suggest the ZrDPPA pore with a diameter of 6.8 Å, is likely a variation of the pore with a diameter of 6.0 Å, wherein there may be a slight variation in the pore structure or other potential defects. Comparing the CO₂ uptake of ZrDPPA with UPG-1, we see that despite the larger pore sizes of UPG-1, it takes up 1/5 the amount, at approximately 10 cm³/g or 0.45 mmol/g at 1 atm.

Photocatalytic Properties

As was done for ZrBPA, the photocatalytic properties of ZrDPPA were also explored, though not in as much detail due to an unfortunate lack of time. Like ZrBPA, ZrDPPA was also a blue colour, pretty much the same shades in fact. Due to the similarities in the linkers, with H₄DPPA being a more conjugated system than H₄BPA, it was assumed that ZrDPPA might have even better photocatalytic properties than those observed in ZrDPA.

Looking first at the UV-Vis DRS spectra in Figure 4.27, there is a clear and significant reflectance between 400-600 nm, whereby the highest value is at 448 nm, which again accounts for the blue colour of the material. There is also significant absorbance in both the visible and the UV regions at around 640 nm and 325 nm, respectively. As was mentioned previously, the absorption at 650 nm would be of particular interest for photocatalytic reactions employing solar energy. This is also true to a smaller extent with the absorption at around 325 nm, which overlaps the UVA and UVB regions of the EM spectrum.

Following the same procedure as before, the DRS spectrum was used to extract an estimate of the optical band gap energy of ZrDPPA, with the resulting Tauc plot for each of the energy transitions being shown in Figure 4.28a. Here, we see that the

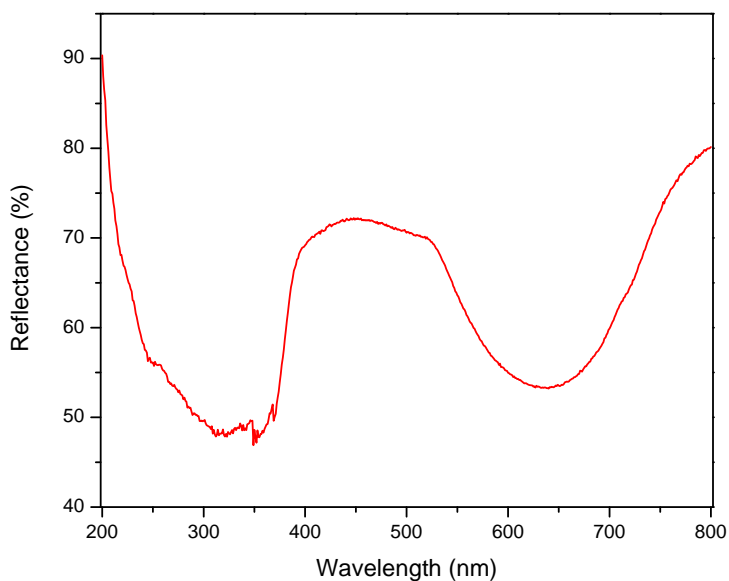


Figure 4.27: Measured diffuse reflectance spectrum for ZrDPPA in the UV-Visible range (200-800 nm).

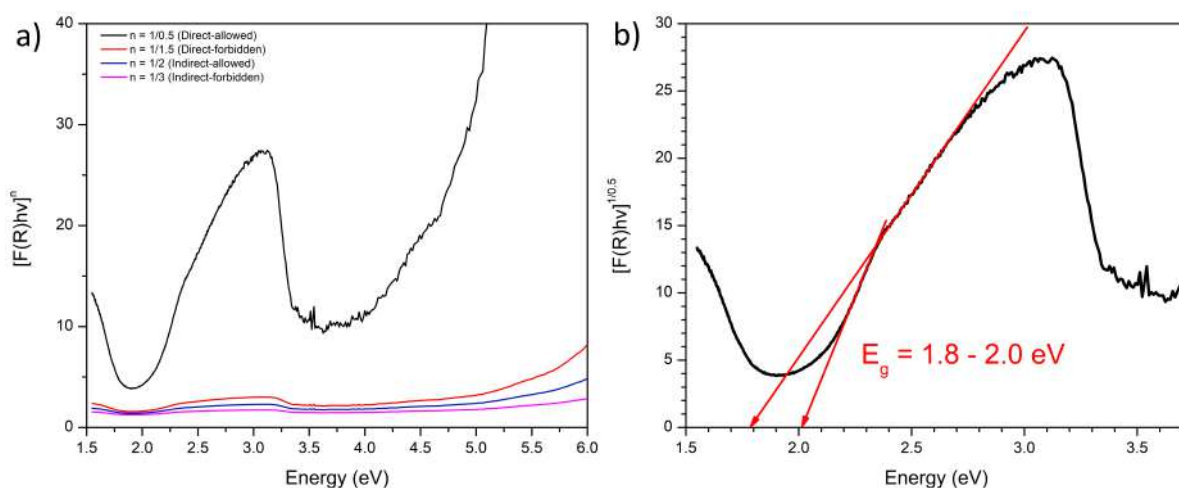


Figure 4.28: a) Tauc plot for each of the energy transitions: direct-allowed (black), direct-forbidden (red), indirect-allowed (blue), and indirect forbidden (pink). b) Tauc plot for the direct-allowed transition with an extracted optical band gap energy in the range of 1.8-2.0 eV

direct-allowed transition is by far the dominant transition, so it was from this that the estimate of the optical band gap energy was extracted. The extrapolation of this can be seen in Figure 4.28b, whereby the band gap energy was extracted using the line-of-best-fit method. As was the case with ZrBPA, we again see two potential transitions, though they are slightly lower here at 1.8 and 2.0 eV, which is likely due to the presence of an extra phenyl ring, this increasing the charge delocalisation and closing the gap between the valence and conduction bands. As was noted previously,

this ideally placed for an effective photocatalyst, which should be above the infrared range, but below the UV range. Due to time constraints, photocatalytic testing could not be carried out on this material.

4.4 Conclusions

The main goal for the experimental work in this chapter was to use the linkers obtained from previous work (discussed in Chapter 3), and use them in the synthesis of potentially microporous MOF materials, with the idea being that the different linkers would have differing effects on the resulting crystal structures. Both H₄BPA and H₄DPC, when combined with Zr(IV), led to the formation of pillared-layered structures, which we were ideally trying to avoid due to their almost inherent lack of microporosity. Despite this, ZrBPA was found to have a measured N₂ BET surface area of 583 m² g⁻¹ and did actually prove to have pores that were on the higher end of the micropore range. It also displayed a CO₂ uptake of 16.8 cm³ g⁻¹ or 0.75 mmol/g (273 K, 1 atm), which is well below the best performing MOFs and metal phosphonates, an example of which is MIL-91 (Al/Ti), which has a CO₂ uptake of 67.2 cm³ g⁻¹ or 3.0 mmol/g (273 K, 1 atm).^{35,36} ZrBPA was also found to have some interesting photocatalytic properties, with an optical band gap energy between 2.0-2.2 eV. It was also found to be reasonably adept as a photocatalyst in the degradation of Rhodamine-B, though not necessarily outperforming alternative photocatalysts. In terms of structure, the formula was obtained through TGA analysis and found to be ZrNH(C₆H₄PO₃)₂ · H₂O through comparison with Zr-II-C.²⁰

Since the ZrDPC system produced a series of different materials which all succumb to the pillared-layered motif and lack of time to do in-depth characterisation, it was passed over in favour of pursuing the H₄DPPA linker. This turned out to be the right move, as the H₄DPPA linker in combination with Zr(IV) gave a structure which moved away from the pillared layered motif, actually showing significant microporosity, with a total CO₂ uptake of 51 cm³ g⁻¹ or 2.3 mmol/g (273 K, 1 atm) and some selectivity for

CO₂ over N₂, making it comparable with materials such as MIL-91.^{35,36} On the other hand, the low IAST CO₂/N₂ selectivity suggests that this material might not be suitable as a CO₂ sorbent when nitrogen is present, e.g. direct-air capture. As with ZrBPA, the optical band gap energy was also extracted for ZrDPPA, and found to be in the range of 1.8-2.0 eV. Again, the structural formula was obtained through TGA analysis and found to be Zr[N(C₆H₅)(C₆H₄PO₃)₂]₃, whereby the metal:linker ratio is 1:3.

From these results, it is clear that further work should be done in the direction of these V-shaped and Y-shaped linkers, specifically the latter since there is scope to try a range of different non-coordinating substituents to assess how these affect the final structure. It is also clear that these N-containing linkers, which form part of a larger conjugated system, should also be subject to further photocatalytic study.

4.5 References

1. A. Clearfield and G. D. Smith, "Crystallography and structure of α -zirconium bis(monohydrogen orthophosphate) monohydrate", *Inorg. Chem.*, 1969, **8**, 431–436, DOI: 10.1021/ic50073a005.
2. G. Alberti, U. Costantino, S. Allulli and N. Tomassini, "Crystalline Zr[R-(PO)₃]₂ and Zr[R-(OPO)₃]₂ compounds (R = organic radical). A new class of materials having layered structure of zirconium phosphonate type.", *J. Inorg. Nucl. Chem.*, 1978, **40**, 1113–1117, DOI: 10.1016/0022-1902(78)80520-x.
3. M. D. Poojary, H.-L. Hu, F. L. Campbell and A. Clearfield, "Determination of crystal structures from limited powder data sets: crystal structure of zirconium phenylphosphonate", *Acta. Crystallogr. B. Struct. Sci. Cryst. Eng. Mater.*, 1993, **49**, 996–1001, DOI: 10.1107/S0108768193006937.
4. M. Ding, X. Cai and H.-L. Jiang, "Improving MOF stability: approaches and applications", *Chem Sci*, 2019, **10**, 10209–10230, DOI: 10.1039/c9sc03916c.
5. C. Healy, K. M. Patil, B. H. Wilson, L. Hermanspahn, N. C. Harvey-Reid, B. I. Howard, C. Kleinjan, J. Koliën, F. Payet, S. G. Telfer, P. E. Kruger and T. D. Bennett, "The thermal stability of metal-organic frameworks", *Coord. Chem. Rev.*, 2020, **419**, 213388, DOI: 10.1016/j.ccr.2020.213388.
6. X. Liu, X. Wang and F. Kapteijn, "Water and Metal–Organic Frameworks: From Interaction toward Utilization", *Chem. Rev.*, 2020, **120**, 8303–8377, DOI: 10.1021/acs.chemrev.9b00746.

7. H. Bunzen, "Chemical Stability of Metal-organic Frameworks for Applications in Drug Delivery", *ChemNanoMat*, 2021, **7**, 998–1007, DOI: 10.1002/cnma.202100226.
8. A. Clearfield and Z. Wang, "Organically pillared microporous zirconium phosphonates", *Dalton Trans.*, 2002, 2937–2947, DOI: 10.1039/b202371g.
9. A. Clearfield, "Unconventional metal organic frameworks: porous cross-linked phosphonates", *Dalton Trans.*, 2008, 6089, DOI: 10.1039/b807676f.
10. S. Yuan, L. Feng, K. Wang, J. Pang, M. Bosch, C. Lollar, Y. Sun, J. Qin, X. Yang, P. Zhang, Q. Wang, L. Zou, Y. Zhang, L. Zhang, Y. Fang, J. Li and H.-C. Zhou, "Stable Metal-Organic Frameworks: Design, Synthesis, and Applications", *Adv. Mater.*, 2018, **30**, 1704303, DOI: 10.1002/adma.201704303.
11. S. Yuan, J.-S. Qin, C. T. Lollar and H.-C. Zhou, "Stable Metal-Organic Frameworks with Group 4 Metals: Current Status and Trends", *ACS Cent. Sci.*, 2018, **4**, 440–450, DOI: 10.1021/acscentsci.8b00073.
12. J. H. Cavka, S. Jakobsen, U. Olsbye, N. Guillou, C. Lamberti, S. Bordiga and K. P. Lillerud, "A New Zirconium Inorganic Building Brick Forming Metal Organic Frameworks with Exceptional Stability", *J. Am. Chem. Soc.*, 2008, **130**, 13850–13851, DOI: 10.1021/ja8057953.
13. J. Winarta, B. Shan, S. M. McIntyre, L. Ye, C. Wang, J. Liu and B. Mu, "A Decade of UiO-66 Research: A Historic Review of Dynamic Structure, Synthesis Mechanisms, and Characterization Techniques of an Archetypal Metal–Organic Framework", *Cryst. Growth Des.*, 2019, **20**, 1347–1362, DOI: 10.1021/acs.cgd.9b00955.
14. A. Schaate, P. Roy, A. Godt, J. Lippke, F. Waltz, M. Wiebcke and P. Behrens, "Modulated Synthesis of Zr-Based Metal-Organic Frameworks: From Nano to Single Crystals", *Chem. Eur. J.*, 2011, **17**, 6643–6651, DOI: 10.1002/chem.201003211.
15. V. Guillerm, F. Ragon, M. Dan-Hardi, T. Devic, M. Vishnuvarthan, B. Campo, A. Vimont, G. Clet, Q. Yang, G. Maurin, G. Ferey, A. Vittadini, S. Gross and C. Serre, "A series of isoreticular, highly stable, porous zirconium oxide based metal-organic frameworks", *Angew. Chem. Int. Ed.*, 2012, **51**, 9267–71, DOI: 10.1002/anie.201204806.
16. M. Taddei, F. Costantino, R. Vivani, S. Sabatini, S.-H. Lim and S. M. Cohen, "The use of a rigid tritopic phosphonic ligand for the synthesis of a robust honeycomb-like layered zirconium phosphonate framework", *Chem. Commun.*, 2014, **50**, 5737–5740, DOI: 10.1039/c4cc01253d.
17. M. Taddei, F. Costantino, F. Marmottini, A. Comotti, P. Sozzani and R. Vivani, "The first route to highly stable crystalline microporous zirconium phosphonate metal-organic frameworks", *Chem. Commun.*, 2014, **50**, 14831–14834, DOI: 10.1039/c4cc06223j.

18. A. Altomare, G. Campi, C. Cuocci, L. Eriksson, C. Giacobazzo, A. Moliterni, R. Rizzi and P.-E. Werner, "Advances in powder diffraction pattern indexing:N-TREOR09", *J. Appl. Crystallogr.*, 2009, **42**, 768–775, DOI: 10.1107/s0021889809025503.
19. A. Altomare, C. Cuocci, C. Giacobazzo, A. Moliterni, R. Rizzi, N. Corriero and A. Falcicchio, "EXPO2013: a kit of tools for phasing crystal structures from powder data", *J. Appl. Crystallogr.*, 2013, **46**, 1231–1235, DOI: 10.1107/s0021889813013113.
20. A. Cabeza, M. del Mar Gómez-Alcántara, P. Olivera-Pastor, I. Sobrados, J. Sanz, B. Xiao, R. E. Morris, A. Clearfield and M. A. Aranda, "From non-porous crystalline to amorphous microporous metal(IV) bisphosphonates", *Micropor. Mesopor. Mat.*, 2008, **114**, 322–336, DOI: 10.1016/j.micromeso.2008.01.018.
21. R. Nehru, R. C. Murugesan, S.-M. Chen and R. Sankar, "Electrochemical sensing of free radical antioxidant diphenylamine cations (DPAH^{•+}) with carbon interlaced nanoflake-assembled Mg_xNi_{9-x}S₈ microspheres", *CrystEngComm*, 2019, **21**, 724–735, DOI: 10.1039/c8ce02004c.
22. K. Y. Hwa, A. Santhan, A. Ganguly and T. S. K. Sharma, "Synthesis of Nickel Vanadate Anchored on Reduced Graphene Oxide for Electrochemical Determination of Antioxidant Radical Cations of Diphenylamine H^{•+}", *ACS Appl. Electron. Mater.*, 2021, **3**, 2247–2260, DOI: 10.1021/acsaelm.1c00183.
23. I. Dincer and C. Zamfirescu, in *Sustainable Hydrogen Production*, Elsevier, 2016, pp. 309–391, DOI: 10.1016/b978-0-12-801563-6.00005-4.
24. J. Wu, Y. Huang, W. Ye and Y. Li, "CO₂ Reduction: From the Electrochemical to Photochemical Approach", *Adv. Sci.*, 2017, **4**, 1700194, DOI: 10.1002/advs.201700194.
25. H. Park and W. Choi, "Visible light and Fe(III)-mediated degradation of Acid Orange 7 in the absence of H₂O₂", *J. Photochem. Photobiol.*, 2003, **159**, 241–247, DOI: 10.1016/s1010-6030(03)00141-2.
26. A. Ajmal, I. Majeed, R. N. Malik, H. Idriss and M. A. Nadeem, "Principles and mechanisms of photocatalytic dye degradation on TiO₂ based photocatalysts: a comparative overview", *RSC Adv.*, 2014, **4**, 37003–37026, DOI: 10.1039/c4ra06658h.
27. J.-S. Bae, H. S. Freeman and S. D. Kim, "Influences of new azo dyes to the aquatic ecosystem", *Fiber Polym*, 2006, **7**, 30–35, DOI: 10.1007/bf02933599.
28. J.-S. Bae and H. S. Freeman, "Aquatic toxicity evaluation of new direct dyes to the *Daphnia magna*", *Dyes Pigment.*, 2007, **73**, 81–85, DOI: 10.1016/j.dyepig.2005.10.015.
29. A. Ahmad, S. H. Mohd-Setapar, C. S. Chuong, A. Khatoon, W. A. Wani, R. Kumar and M. Rafatullah, "Recent advances in new generation dye removal technologies: novel search for approaches to reprocess wastewater", *RSC Adv.*, 2015, **5**, 30801–30818, DOI: 10.1039/c4ra16959j.

30. G. A. R. de Oliveira, J. de Lapuente, E. Teixidó, C. Porredón, M. Borràs and D. P. de Oliveira, "Textile dyes induce toxicity on zebrafish early life stages", *Environ. Toxicol. Chem.*, 2015, **35**, 429–434, DOI: 10.1002/etc.3202.
31. R. Al-Tohamy, S. S. Ali, F. Li, K. M. Okasha, Y. A.-G. Mahmoud, T. Elsamahy, H. Jiao, Y. Fu and J. Sun, "A critical review on the treatment of dye-containing wastewater: Ecotoxicological and health concerns of textile dyes and possible remediation approaches for environmental safety", *Ecotoxicol. Environ. Saf.*, 2022, **231**, 113160, DOI: 10.1016/j.ecoenv.2021.113160.
32. O. Merka, V. Yarovyi, D. W. Bahnemann and M. Wark, "pH-Control of the Photocatalytic Degradation Mechanism of Rhodamine B over $Pb_3Nb_4O_{13}$ ", *J. Phys. Chem.*, 2011, **115**, 8014–8023, DOI: 10.1021/jp108637r.
33. S. L. Burkett, N. Ko, N. D. Stern, J. A. Caissie and D. Sengupta, "Covalently Linked Nanocomposites: Poly(methyl methacrylate) Brushes Grafted from Zirconium Phosphonate", *Chem. Mater.*, 2006, **18**, 5137–5143, DOI: 10.1021/cm0614517.
34. R. Silbernagel, C. H. Martin and A. Clearfield, "Zirconium(IV) Phosphonate–Phosphates as Efficient Ion-Exchange Materials", *Inorganic Chemistry*, 2016, **55**, 1651–1656, DOI: 10.1021/acs.inorgchem.5b02555.
35. C. Serre, J. A. Groves, P. Lightfoot, A. M. Z. Slawin, P. A. Wright, N. Stock, T. Bein, M. Haouas, F. Taulelle and G. Férey, "Synthesis, Structure and Properties of Related Microporous N,N' -Piperazinebismethylenephosphonates of Aluminum and Titanium", *Chem. Mater.*, 2006, **18**, 1451–1457, DOI: 10.1021/cm0521491.
36. V. Benoit, R. S. Pillai, A. Orsi, P. Normand, H. Jobic, F. Nouar, P. Billefont, E. Bloch, S. Bourrelly, T. Devic, P. A. Wright, G. de Weireld, C. Serre, G. Maurin and P. L. Llewellyn, "MIL-91(Ti), a small pore metal-organic framework which fulfils several criteria: an upscaled green synthesis, excellent water stability, high CO_2 selectivity and fast CO_2 transport", *J Mater Chem A*, 2016, **4**, 1383–1389, DOI: 10.1039/c5ta09349j.

Chapter 5

***In-situ* X-ray Diffraction Investigation of the Crystallisation of Perfluorinated Ce(IV)-based Metal-Organic Frameworks with MIL-140A and UiO-66 Architectures**

5.1 Introduction

Investigating the influence of reaction conditions on the thermodynamics and kinetics of crystallisation of metal-organic frameworks (MOFs) is extremely beneficial to gather information on the relationship between crystal structure and synthetic parameters, to optimise the reaction conditions for up-scaling of synthetic protocols and to aid the design of new materials.¹⁻³ Since the majority of MOF syntheses is carried out starting from liquid reaction mixtures, the formation of the solid product can be followed *in situ* employing scattering techniques such as X-ray diffraction (XRD),⁴⁻⁸ small angle X-ray scattering (SAXS),⁹⁻¹¹ static/dynamic light scattering (SLS/DLS),^{12,13} NMR spectroscopy,¹⁴ and turbidity measurements.^{15,16} SAXS and DLS are especially

suited to study the earliest stages of crystallisation because they can detect particles with subnanometric size, but they provide no information about the crystal structure of the scattering objects.¹ On the other hand, XRD is limited to crystallites having size at least in the nanometre range and is blind to amorphous matter, making it not suitable for studying the earliest stages of crystallisation. However, it provides precious information about the crystalline phases present in the system, allowing to study the evolution of multiphase systems and even to identify possible transient, metastable phases.¹⁷ Thanks to its ability to provide insight on both kinetics and thermodynamics, XRD is the most widespread tool for *in situ*, time-resolved monitoring of MOF crystallisation.

Over the past few years, Ce(IV)-MOFs have appeared consistently in the literature, most often based on the connection of hexanuclear $[\text{Ce}_6(\text{O})_4(\text{OH})_4]^{12+}$ clusters with polycarboxylic linkers of various geometries and symmetries.¹⁸ These MOFs have attracted interest mainly thanks to their redox properties, which distinguish them from their Zr(IV)-based counterparts and can be exploited for various catalytic processes.^{19–21} In addition, they also display interesting photocatalytic properties.^{22–25} A review on Ce-MOFs has recently been published that summarises the synthetic and structural aspects as well as potential applications.²⁶ The synthesis of these MOFs is typically carried out in N,N-dimethylformamide (DMF) as a reaction medium and *in situ* studies have been key in revealing that the desired product is often quick to form.^{26,27} However, this phase is metastable and, if left in the reaction environment, undergoes dissolution to form Ce(III)-formate, having formula $\text{Ce}(\text{O}_2\text{CH})_3$. Formation of Ce(III)-formate was attributed to the reaction between Ce(III), derived from reduction of Ce(IV) in solution, and formate generated by hydrolysis of DMF. Dissolution of the Ce(IV)-based MOF is driven by the decrease of Ce(IV) concentration in solution due to its reduction to Ce(III), which is continuously withdrawn from the reaction environment as Ce(III)-formate.²⁷

A recent article reported on the water-based synthesis of two perfluorinated

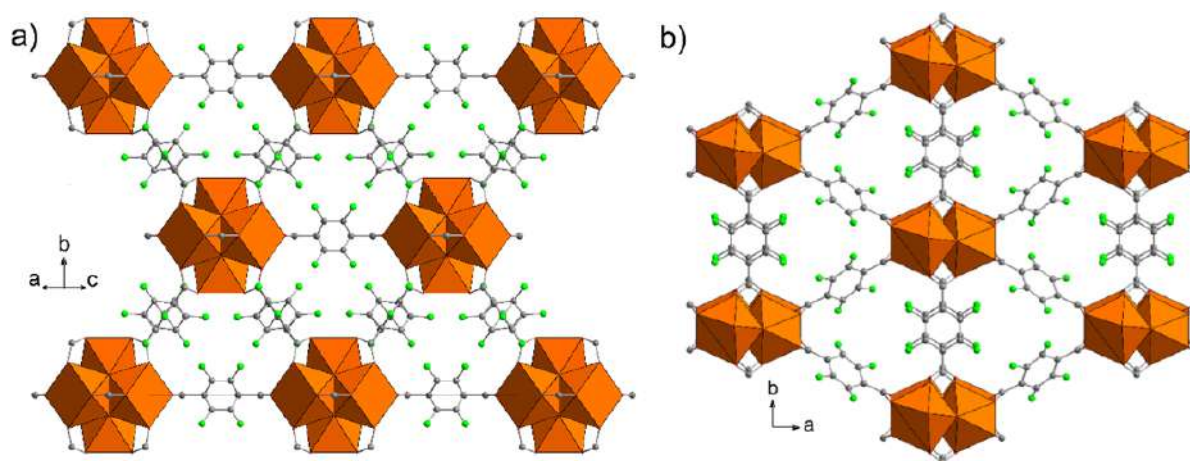


Figure 5.1: Crystal structures of F4_UiO-66(Ce) (a) and F4_MIL-140A(Ce) (b). Colour code: Ce, orange; F, green; O, red, C, grey. Reprinted with permission from reference [[27]]. Copyright 2019 American Chemical Society.

Ce(IV)-based analogues of the already well investigated Zr(IV)-MOFs UiO-66 and MIL-140A (Figure 5.1).²⁸ The pure MIL-140A phase, having formula $[\text{CeO}(\text{TFBDC}) \cdot \text{H}_2\text{O}]$ (where TFBDC^{2-} is tetrafluoroterephthalate) and named F4_MIL-140A(Ce), was obtained reacting stoichiometric amounts of cerium ammonium nitrate (CAN) and tetrafluoroterephthalic acid (H_2TFBDC) in water at 110 °C for 24 h, whereas the pure UiO-66 phase, having formula $[\text{Ce}_6\text{O}_4(\text{OH})_4(\text{TFBDC})_6]$ and named F4_UiO-66(Ce), was obtained in the same conditions, with addition of 100 equivalents of acetic acid (AcOH). In this case, no significant dissolution of the products was observed upon prolonged reaction time (up to 24 h), most likely because of the different reaction medium than the classical DMF-based synthesis. Addition of AcOH in amounts smaller than 100 equivalents produced phase mixtures with varying ratios between the two phases. The coexistence of the two crystalline phases had also been previously observed in the Zr-terephthalate system in DMF, in which UiO-66(Zr) is assumed to be the kinetic phase and MIL-140A(Zr) the thermodynamic phase, based on the observation that the former is preferentially obtained at lower temperatures than the latter, starting from reaction mixtures having the same composition.²⁹

In the original report on Ce(IV)-based perfluorinated MOFs, the authors speculated that in the Ce-TFBDC system in water the situation could be inverted, i.e.

F4_UiO-66(Ce) is the thermodynamic phase and F4_MIL-140A(Ce) is the kinetic one, on the basis that a large amount of AcOH modulator was needed to obtain F4_UiO-66(Ce) in pure form in otherwise identical reaction conditions.²⁸ In the case of polymorphs based on the same metal cluster, modulators have been seen to promote formation of thermodynamic products.^{30,31} However, UiO-66 is based on hexanuclear inorganic clusters, while MIL-140 contains infinite inorganic chains. It was recently shown that addition of 10 equivalents of AcOH to a DMF-based reaction mixture otherwise affording pure MIL-140A(Zr), a mixed MIL-140A/UiO-66 product is formed.³² Further increasing the amount of acetic acid up to 30 equivalents appears to increase the MIL-140/UiO-66 ratio. These results may suggest that, at least in DMF solvent, the coordination modulator can in fact favour the thermodynamic product in the MIL-140/UiO-66 system.

We therefore set out to employ *in situ* synchrotron PXRD to further understand how various reaction parameters influence the crystallisation process, both in terms of kinetics and thermodynamics, and to identify the range of parameters affording the two different F4_MIL-140A(Ce) and F4_UiO-66(Ce) single phases. In addition, since the MIL-140A analogue displayed promising CO₂ capture properties - thanks to its non-hysteretic S-shaped isotherm and high CO₂/N₂ selectivity - we aimed at applying the knowledge deriving from the *in situ* investigation to identify an optimised synthesis protocol for the prospective production of this MOF on a multigram scale.

5.2 Experimental

5.2.1 *In Situ* Experiments

The *in situ* study described hereafter took place at beamline P23 (DESY, Hamburg) and was carried out with the recently developed **SynRAC** (**S**ynchrotron-based **R**eaction cell for the **A**nalysis of **C**hemical reactions) unit, was specifically developed for *in situ* monitoring of solvothermal reactions using synchrotron X-ray-based techniques.³³

Figure 5.2 shows the unit in detail. The unit was designed to be simple, while incorporating a number of features that make it very versatile in its application. The reaction vessel, a simple 11 mL Pyrex test tube, is accommodated inside an aluminium casing and is surrounded by a heating mantle made from copper-galvanised heating wires which allow for fine control of the temperature up to 180 °C. An electromagnetic stirrer is also incorporated for sample agitation up to 1200 rpm.

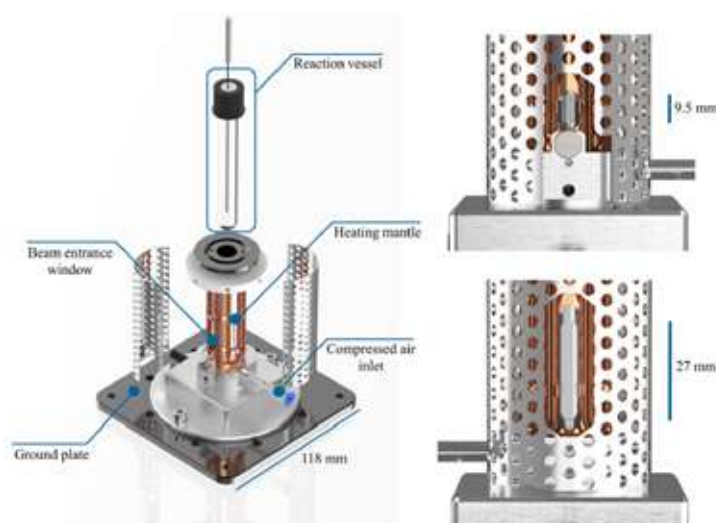


Figure 5.2: Schematic of the SynRAC *in situ* cell (left) and close-up view of the entrance (top right) and exit (bottom right) windows. Reprinted from DOI: 10.1063/1.4999688.

As part of this investigation, two different systems were investigated. The first system involved only HNO_3 as a protonation modulator and the effect of the following two parameters was evaluated: temperature, and amount of HNO_3 . The second system involved the combined use of HNO_3 and AcOH as protonation and coordination modulators, respectively, and the effect of the following three parameters was evaluated: temperature, amount of HNO_3 , amount of AcOH . For each reaction, H_2TFBDC was first dissolved in water, HNO_3 and - where applicable - AcOH , before heating the solution to the appropriate temperature under stirring inside the reaction chamber. The volume of this solution was 3.2 mL and the concentration of H_2TFBDC was $0.0625 \text{ mol L}^{-1}$. On reaching the appropriate temperature, 0.8 mL of a 0.25 mol L^{-1} solution of cerium ammonium nitrate (CAN) in water was injected, thus starting the reaction. Initially, there is a small drop in the temperature on addition of CAN, but

this returns to the specified temperature within 1 minute. The final concentration of H₂TFBDC and CAN in the reaction mixture was 0.05 mol L⁻¹.

XRD patterns were collected using 18.7 keV (0.663 Å) radiation. The beamline was equipped with an X-Spectrum Lambda 750K 2D detector with GaAs sensor. The detector has an area of 512x1528 pixels, with each pixel having size 55 x 55 μm. The detector was positioned at 4 °2θ from the incident beam direction, allowing us to span the angular region comprised between 0.47 and 7.37 °2θ. The acquisition time for each PXRD pattern was 2 s, with an unavoidable delay time between successive measurements of 0.43 s, hence providing a 2.43 s time resolution.

5.2.2 Data Extraction using DAWN, the Data Analysis WorkbeNch

In order to extract any meaningful information from the raw data obtained from the *in situ* experiments, we used the DAWN software, an open source software funded primarily by Diamond Light Source, used for the visualisation and processing of scientific data, but not necessarily just XRD-type data.^{34,35}

The first step in this process was the visualisation of the raw data, which simply involved importing the raw data file into the data visualisation tool. This allowed us to look at each individual frame measured and visualise a portion of the diffraction rings, as shown in Figure 5.3, which meant we could identify when crystallisation started for each experiment. This is also representative of the live view you see throughout the experiment.

The ring patterns can then be processed by first importing the detector calibration, which in our case was done by self-referencing to the expected 2θ values for the MIL-140A phase. This was necessary because the lowest angle reflections of the LaB₆ standard available at the beamline necessitated the detector to be moved to higher 2θ angle. Given that the main information we were seeking to extract is the intensity of the Bragg reflections for the two crystalline phases involved in the process, we could accept to compromise on the reflection positions having a small error. The command

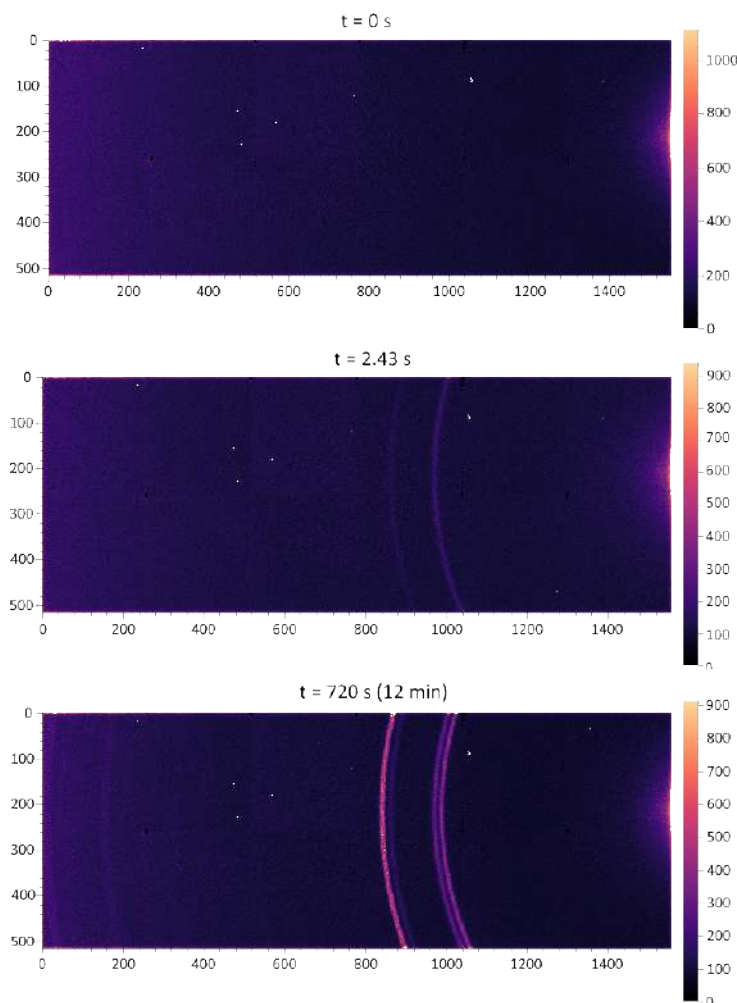


Figure 5.3: Representative PXRD patterns recorded at different times during the experiment performed at 50 °C in the presence of 16 equivalents of HNO₃ and 96 equivalents of AcOH: t = 0 s is the pattern collected when the CAN solution is added to the reaction vessel; t = 2.43 s is the first diffraction pattern collected after the addition; t = 720 s is the time when both products are fully crystallised. The x- and y-axis represent the number of pixels of the detector, whereas diffracted intensity is colour coded according to scale on the right-hand side.

“Threshold masking” is then used in order to eliminate bright/dark spots from the image, thus excluding any ‘outlier’ values. The intensities are then extracted using the command “Azimuthal integration”, whereby Cartesian coordinates are converted to polar space, initially providing the PXRD pattern (i.e. intensity versus 2 θ angle) corresponding to each frame. The command “Processing” provides a plot of the intensities over the number of frames.

It is then from this plot that we obtain the plot for the degree of crystallisation versus time (Figure 5.5). This is obtained by applying the command ‘box profile’ on the

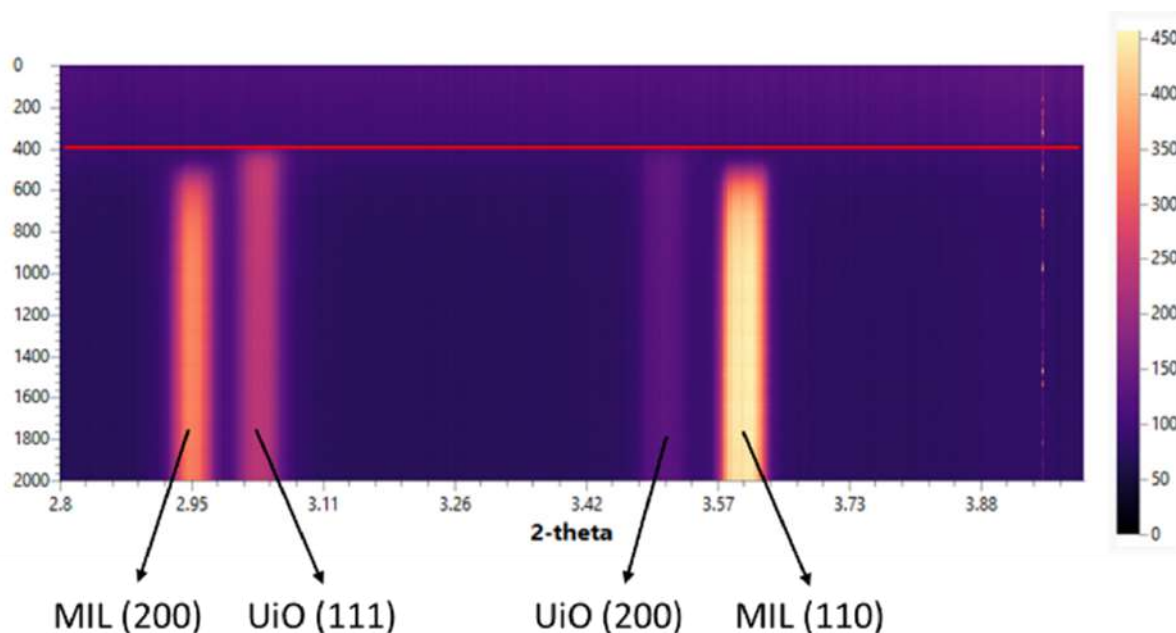


Figure 5.4: PXRD patterns recorded during the experiment performed at 50 °C in the presence of 16 equivalents of HNO₃ and 96 equivalents of AcOH. The *y*-axis is the frame number, whereas diffracted intensity is colour coded according to scale on the right-hand side. The horizontal red line marks the time at which the CAN solution is added to the reaction vessel.

intensity plot. This operation takes an average of the data in the 2D image in order to produce a 1D plot containing two profiles, *x* and *y*. The *x*-profile represents integrated intensity as a function of the 2θ angle and was used to ensure that the integrated range spanned over a single specific reflection. The *y*-profile represents intensity as a function of time. It is the latter *y*-profile which is of interest in terms of obtaining time dependent information such as the rapidity of the onset of crystallisation, how long it takes to reach its maximum, and whether or not any degradation of the product takes place.

The value of the extent of crystallisation, α , was then obtained from the absolute intensities using the following formula:

$$\alpha = \frac{I_t - I_0}{I_{max} - I_0} \quad (5.1)$$

Where I_t is the integrated intensity of the Bragg reflection of interest at time *t* after the

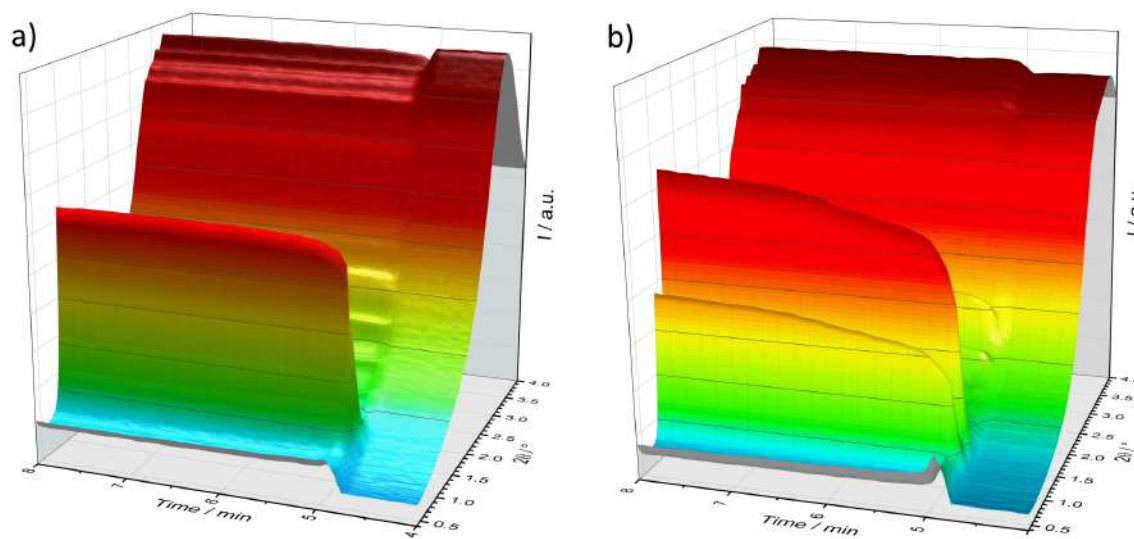


Figure 5.5: *In situ* PXRD patterns of the crystallisation of F4_UiO-66(Ce) (a) and F4_MIL-140A(Ce) (b) using the originally reported synthetic conditions.

addition of the CAN solution, I_0 is the intensity of the same reflection at time zero, i.e. when the addition of CAN takes place, I_{max} is the intensity when the crystallisation curve plateaus, indicating that the process has reached completion.

The data from this plot can then be used to obtain useful information about the kinetics of crystallisation, which can be done using various models. These models can be useful in obtaining information such as the degree of crystallisation, nucleation rate, and growth rate.

5.2.3 Modelling Crystallisation Kinetics

Using the data obtained during these *in situ* experiments, it is possible to extract the intensities of the Bragg peaks, which can be plotted as a function of time, thus showing the degree of crystallisation as the reaction proceeds. One can then apply specific models to this data in order to make inferences about the kinetics of the reaction. The two most common models used in the context of MOFs are the Avrami–Erofe’ev model (equation 5.2), and the Gualtieri model (equation 5.3). The first of these models, the Avrami–Erofe’ev, is a general model which does not correspond to a particular type of reaction, but its origins lie in the field of metallurgy.²

$$\alpha = 1 - \exp\{-(kt)^n\} \quad (5.2)$$

Here we see the extent of crystallisation, α , as a function of time, t , and the rate constant, k . The Avrami exponent, n , is used to obtain information on the mechanism of crystallisation, of which various situations have been tabulated. An example of this can be found in a paper by De Bruijn et al. (1981) where at a constant nucleation rate, $n = 2$ (one-dimensional growth), $n = 3$ (two-dimensional growth), and $n = 4$ (three-dimensional growth). Conversely, where the nucleation rate is zero i.e. the number of nuclei is constant, $n = 1$ (one-dimensional growth), $n = 2$ (two-dimensional growth), and $n = 3$ (three-dimensional growth).^{2,36}

A more appropriate model for crystallisation that takes place under solvothermal conditions is the Gualtieri model (Equation 5.3).^{2,6,37} Unlike the Avrami–Erofe’ev model, the Gualtieri model is a physically derived model which stemmed from experimental studies of the hydrothermal crystallisation of silicate zeolites. This makes it an attractive model for crystallisation of MOFs under hydro- or solvothermal conditions. The reason this model is preferred over most others stems from two main factors. Firstly, the model is one based somewhat in reality on the way it was developed, i.e. looking at solvent-mediated reactions of solid reagents. Secondly, crystallisation is separated into two functions: nucleation and growth. This adds a new dimension to the understanding of the crystallisation process that cannot be obtained by other models.

$$\alpha = \frac{1}{1 + \exp\left\{-\left(\frac{t-a}{b}\right)\right\}} \cdot \{1 - \exp[-(k_g t)^n]\} \quad (5.3)$$

As with the Avrami–Erofe’ev equation, we again look at the extent of crystallisation, α , as a function of time, t . In the equation, n represents the dimensionality of crystal growth, and is thus fixed depending on the crystal morphology of the material undergoing analysis. In this case, we are looking at F4_MIL-140A(Ce) and

F4_UiO-66(Ce), the former of which forms rod-like crystals ($n = 1$), and the latter forms crystals with octahedral geometry ($n = 3$), as evidenced by SEM micrographs. The rate constant for crystal growth is represented by k_g . The constant, a , is the reciprocal of the nucleation rate: and b , the rate constant (equation 5.4):

$$k_N = 1/a \quad (5.4)$$

The constant b describes the variance of the nucleation probability distribution. Using a and b , the probability of nucleation (equation 5.5), P_N , which can be calculated as follows:

$$P_N = \exp \left\{ -\frac{(t - a)^2}{2b^2} \right\} \quad (5.5)$$

Comparison of the terms k_g and k_n allow for the inference as to which of the two factors, nucleation or growth, is the rate determining process.

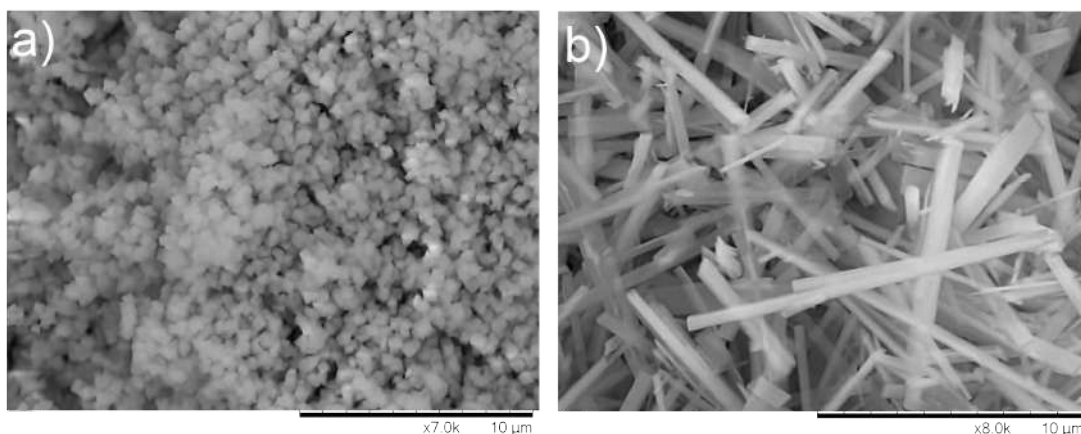


Figure 5.6: SEM micrographs of phase pure F4_UiO-66(Ce) (a) and F4_MIL-140A(Ce) (b), showing the typical octahedral morphology for the former and a needle-like morphology for the latter.

5.2.4 *Ex-situ* Experiments

Optimised Synthetic Protocol for F4_MIL-140A(Ce)

H₂TFBDC (179 mg, 0.75 mmol) was dissolved in water (10.5 mL) and 16 mol L⁻¹ HNO₃

(1.5 mL, 24 mmol) in a 20 mL scintillation vial, which was kept at 60 °C under stirring either in an aluminium heating block or in an oil bath. After 10 minutes, a solution of CAN (411 mg, 0.75 mmol) in water (3 mL) was added to the vial and the mixture was left to react for 1 h. At the end of the reaction, the yellow solid was centrifuged, washed twice with water (15 mL each time) and finally washed with acetone (15 mL). The solid was dried in an oven at 80 °C. Yield: 177 mg (60%).

Ex situ Analysis

PXRD patterns were collected in the 4-30 °2 θ range with a Bruker D8 Avance diffractometer working in reflection geometry and equipped with a LYNXEYE XE detector, using the Cu K α radiation. The X-ray tube was operated at 40 kV and 40 mA.

Scanning electron microscopy (SEM) micrographs were collected using a Hitachi TM3030Plus Tabletop Microscope using an acceleration voltage of 5 kV. The samples were deposited on conductive copper tape on an aluminium support, without any sputtering process.

N₂ sorption analysis at 77 K was performed on a Micromeritics ASAP 2020 gas sorption analyser. The sample (about 50 mg) was activated for 16 h at 120 °C under dynamic vacuum prior to analysis. The BET equation was fitted in the 0.007-0.07 P/P₀ range.

High pressure CO₂ adsorption isotherms up to 5 bar were measured with a Quantachrome iSorb High Pressure Gas Analyser at 25, 40, 55 and 70 °C. About 200 mg of sample was used for the adsorption studies. The sample was degassed at 120 °C under dynamic vacuum for 12 h prior to analysis and at 120 °C for 1 h in between subsequent measurements.

5.3 Results and Discussion

5.3.1 Preliminary Screening

We started our investigation performing preliminary *in situ* PXRD experiments employing analogous conditions to those reported in the original paper describing the synthesis of F4_MIL-140A(Ce) and F4_UiO-66(Ce): for the former, we dissolved 0.21 mmol H₂TFBDC in 2 mL of water, heated the mixture up to 110 °C, then added 0.21 mmol of CAN dissolved in 0.4 mL of water; for the latter, 1 mL water was replaced by 1 mL glacial AcOH, keeping the same total volume. These experiments clearly showed that crystallisation was complete within a few seconds from introduction of Ce(IV) in the reaction vessel, too fast to be followed with satisfactory time resolution (Figure 5.5). This pushed us to investigate options to gain control of the crystallisation kinetics, with the primary aim of slowing the process down and make it occur within a time-frame in the range of a few minutes, compatible with *in situ* monitoring using XRD. In order to ensure full reproducibility, the *ex situ* experiments discussed in this section were performed using the same types of reaction vessels and stir bars to be used for the *in situ* study. We chose to test HNO₃ as a protonation modulator, under the hypothesis that, being a strong acid, it should inhibit deprotonation of H₂TFBDC, making it less available for coordination to the metal, while releasing nitrate ions in

Table 5.1: Representative experiments carried out by combining CAN and H₂TFBDC (0.25 mmol each) in a total volume of 5 mL in the presence of different amounts of HNO₃ and at different temperatures.

Equiv HNO ₃	Temp (°C)	Time (min)	Yield	Product
64	32 - 80	30 - 120	No Solid	-
48	80	120	No Solid	-
32	50	60	39 mg	MIL
32	60	60	65 mg	MIL
32	70	60	34 mg	MIL
32	80	60	36 mg	MIL
16	50	60	81 mg	MIL
16	60	60	76 mg	MIL
16	70	60	72 mg	MIL
16	80	30	83 mg	MIL

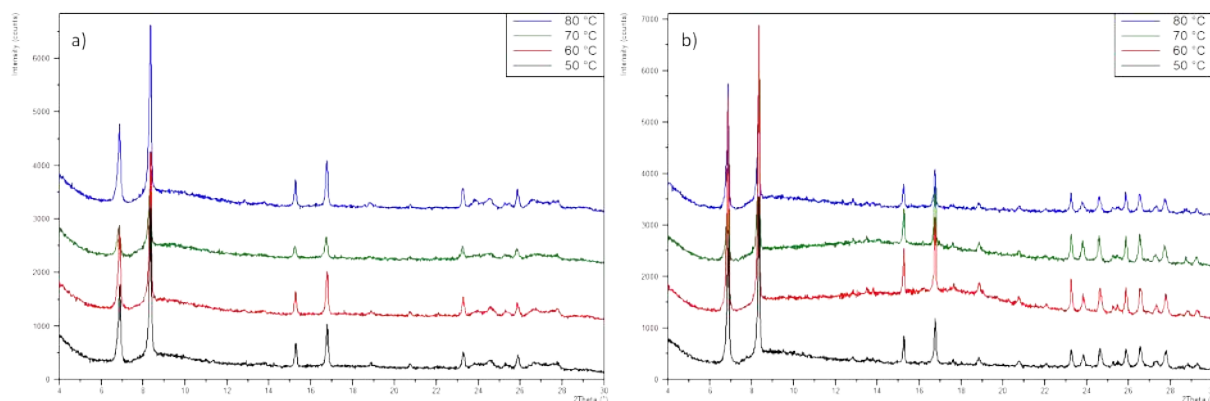


Figure 5.7: PXRD patterns of the products of syntheses carried out in the presence of (a) 16 equivalents, and (b) 32 equivalents of HNO₃ at 50 °C (black), 60 °C (red), 70 °C (green) and 80 °C (blue). The crystalline phase is F4_MIL-140A(Ce).

solution, i.e. the same anion present in the metal precursor CAN, thus not introducing a new species in the reaction environment. Addition of 1 mL of 16 mol L⁻¹ HNO₃ (64 equivalents) to an equimolar mixture of H₂TFBDC and CAN (0.25 mmol each) in 4 mL of H₂O completely prevented crystallisation at 32 °C, suggesting that the desired modulating effect was taking place. Notably, even upon heating the solution to 80 °C no solid formed, whereas the solution changed from a dark yellow to colourless within 2 hours. This suggests that, when crystallisation is inhibited, reduction of Ce(IV) to Ce(III) becomes the dominant process occurring in the reaction mixture.³⁸ These observations were the starting point for an extensive synthetic screening aimed at determining a range of conditions to be investigated *in situ*.

Table 5.2: Representative experiments carried out by combining CAN and H₂TFBDC (0.25 mmol each) in a total volume of 5 mL in the presence of different amounts of HNO₃ and at different temperatures.

Equiv HNO ₃	Equiv AcOH	Time (min)	Yield	Product
6.4	98	60	75 mg	MIL-UiO
6.4	147	60	86 mg	UiO
6.4	196	60	82 mg	UiO
16	98	60	85 mg	MIL-UiO
16	147	60	67 mg	MIL-UiO
16	196	180	No solid	-
32	28	60	67 mg	MIL
32	49	60	60 mg	MIL
32	98	240	No solid	-

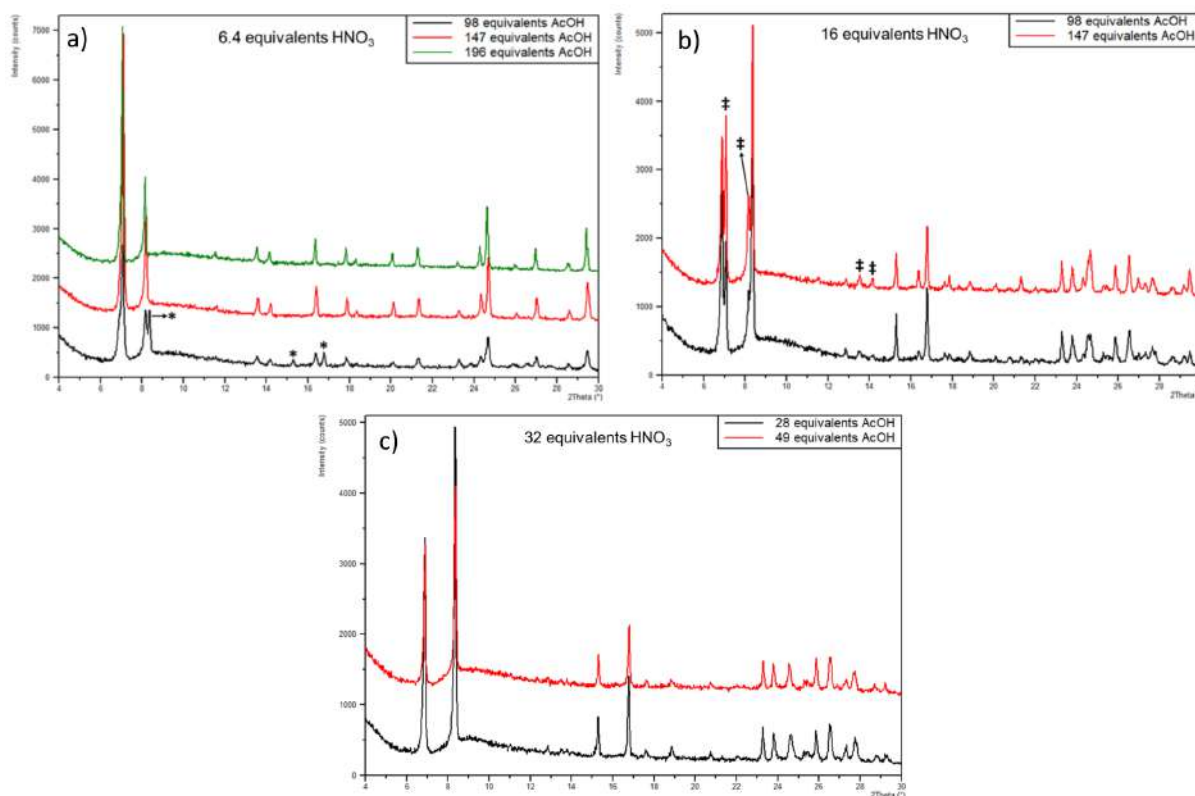


Figure 5.8: (a) PXR D patterns of the products of syntheses carried out in the presence of 98 equivalents (black), 147 equivalents (red), 196 equivalents (green) of AcOH and 6.4 equivalents of HNO₃ at 70 °C. The black pattern reveals the presence of both F4_MIL-140A(Ce) and F4_UiO-66(Ce), whereas the red and green pattern are phase-pure F4_UiO-66(Ce). The reflections of F4_MIL-140A(Ce) are indicated with the * symbol. (b) PXR D patterns of the products of syntheses carried out in the presence of 98 equivalents (black), 147 equivalents (red) of AcOH and 16 equivalents of HNO₃ at 70 °C. The products are mixtures of F4_MIL-140A(Ce) and F4_UiO-66(Ce). The reflections of F4_UiO-66(Ce) are indicated with the ‡ symbol. (c) PXR D patterns of the products of syntheses carried out in the presence of 28 equivalents (black), 49 equivalents (red) of AcOH and 32 equivalents of HNO₃ at 70 °C. The crystalline phase is F4_MIL-140A(Ce).

This initial screening provided a lot of useful information which guided a lot of the decisions when developing a plan for the *in situ* experiments. Below is a list of the most important observations made during this preliminary screening.

- F4_MIL-140A(Ce) was the sole crystalline phase obtained when only HNO₃ was added to the reaction mixture as a modulator.
- Keeping the concentration of H₂TFBDC and CAN fixed at 0.05 mol L⁻¹ and varying the amount of HNO₃ added, we found that, above 32 equivalents of HNO₃, precipitation of the MOF was inhibited and the solution lost colour within

2 hours of heating at both 80 and 100 °C, indicating reduction of Ce(IV) to Ce(III).

- Keeping the amount of HNO₃ fixed at 32 equivalents and varying the temperature between 50 and 80 °C, we observed that appearance of the solid occurred progressively earlier as the temperature increased, suggesting that temperature has a significant effect on the crystallisation kinetics.
- The F4_UiO-66(Ce) phase was only accessible when AcOH was also present in the reaction environment and could be obtained in pure form in the presence of 6.4 equivalents of HNO₃ and at least 147 equivalents of AcOH.
- Increasing the amount of HNO₃ to 16 equivalents or lowering the AcOH amount to 96 equivalents or less yielded mixed-phase products, with varying phase ratios depending on the HNO₃/AcOH ratio.
- No solid formation was observed when reactions were carried out in the presence of 32 equivalents of HNO₃ and 98 equivalents of AcOH at 70 °C, as well as in the presence of 16 equivalents of HNO₃ and 196 equivalents of AcOH at 70 °C.

Based on these observations, the parameter space displayed in Figure 5.9 was investigated in the *in situ* PXRD study.

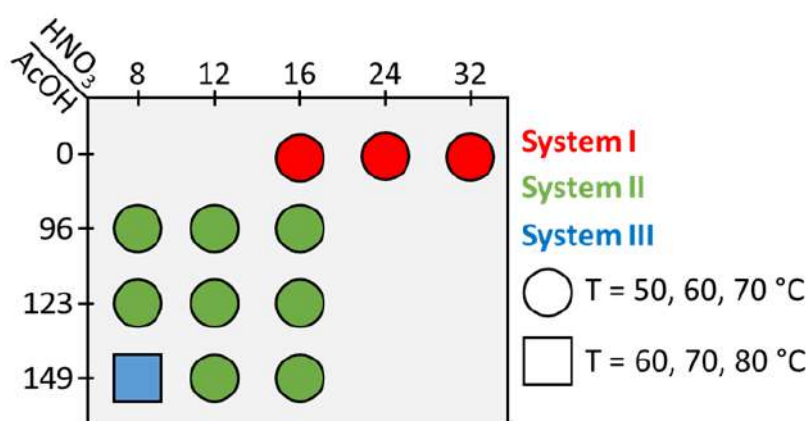


Figure 5.9: Three systems were chosen to investigate the parameter space for the synthesis of F4_MIL-140A(Ce) and F4_UiO-66(Ce). One equivalent corresponds to 0.25 mmol. The molar ratio Ce⁴⁺ to H₂TFBDC is fixed at a value of 1 to 1.

5.3.2 System 1 - Ce(IV)-TFBDC-HNO₃

Effect of Temperature

In assessing the effect of temperature, we varied between 50, 60, and 70 °C, while keeping the amount of HNO₃ fixed at 32 equivalents. We observed that the increase in temperature greatly amplified the rate of crystallisation (Figure 5.10). The probability of nucleation (P_N), displayed in the form of the dashed lines in Figure 5.10, peaks in correspondence of progressively lower α values as the temperature increases ($\alpha = 0.50$ when P_N peaks at 50 °C, $\alpha = 0.25$ when P_N peaks at 60 °C, $\alpha = 0.12$ when P_N peaks at 70 °C), suggesting that nucleation is more sensitive than crystal growth to changes in temperature. Fitting the Gualtieri equation to each set of data, as shown in Figure 5.10, the results reported in Table 5.3 were extracted. These results show in fact that the nucleation rate at 70 °C is 33 times greater than at 50 °C, whereas the crystal growth rate only increases by a factor of 4 in the same range. Nucleation is rate determining at 50 °C ($k_N < k_g$), but already at 60 °C the situation is inverted, and crystal growth becomes rate determining. The k_N/k_g ratio increases from 0.46 to 1.66 to 3.66 at 50, 60 and 70 °C, respectively (Table 5.3).

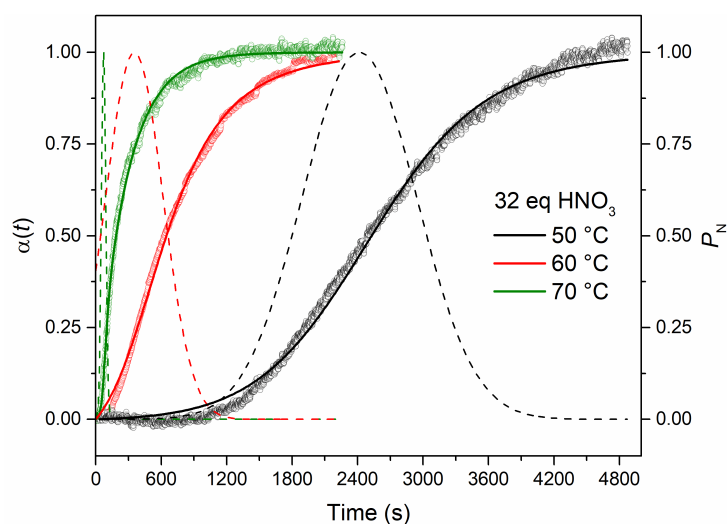


Figure 5.10: Plot of extent of crystallization (α , circles, left y-axis) and probability of nucleation (P_N , dashed lines, right y-axis) as a function of time for experiments performed at 50 °C (black), 60 °C (red) and 70 °C (green) in the presence of 32 equivalents of HNO₃.

Table 5.3: Nucleation and growth rates for F4_MIL-140(Ce) in the presence of 32 equivalents (0.4 mL, 1.6 mol/L) of HNO₃ at 50, 60, and 70 °C. The ratios shown for k_N and k_g are the ratio at each temperature vs 50 °C.

Temp (°C)	a (s)	b (s)	k_g (s ⁻¹)	k_N (s ⁻¹)	Ratio k_g	Ratio k_N	Ratio k_N/k_g	R ²
70	72	20	0.0038	0.0139	4.0	33.5	3.66	0.9879
60	353	263	0.0017	0.0028	1.8	6.8	1.66	0.9974
50	2415	525	0.0009	0.0004	1.0	1.0	0.46	0.9961

By plotting the natural logarithm of k_N and k_g versus $1/T$, the activation energy for nucleation and crystal growth can be extracted by simple linear fitting, according to the logarithmic form of the Arrhenius equation:

$$\ln k_r = \ln A - \frac{E_a}{RT} \quad (5.6)$$

By plotting the natural logarithm of k_N and k_g versus $1/T$, the activation energy for nucleation and crystal growth can be extracted by simple linear fitting, according to the logarithmic form of the Arrhenius equation. Figure 5.11 shows the fits for both nucleation and crystal growth. The two lines cross over at a value of $1/T$ corresponding to about 57 °C: below this temperature nucleation is the rate determining step, whereas above this temperature crystal growth becomes rate determining. The extracted activation energies are $154 \pm 4 \text{ kJmol}^{-1}$ for nucleation ($E_{a,N}$) and $63 \pm 6 \text{ kJmol}^{-1}$ for crystal growth ($E_{a,g}$). These values are in line with those of MOFs such as MOF-14 ($E_{a,N} = 114 \text{ kJmol}^{-1}$, $E_{a,g} = 83 \text{ kJmol}^{-1}$),⁸ and Mn-MIL-100 ($E_{a,N} = 127 \text{ kJmol}^{-1}$, $E_{a,g} = 99 \text{ kJmol}^{-1}$), whereby nucleation has a considerably higher activation energy than growth.³⁹ However, neither MOF-14 nor Mn-MIL-140 show any crossing of the lines in the range of temperatures investigated, which means that nucleation is always the rate determining step. There are also examples of MOFs where the activation energies for nucleation and growth are relatively similar, which include ZIF-8 ($E_{a,N} = 69 \text{ kJmol}^{-1}$,

$E_{a,g} = 72 \text{ kJmol}^{-1}$),⁷ HKUST-1 ($E_{a,N} = 72 \text{ kJmol}^{-1}$, $E_{a,g} = 64 \text{ kJmol}^{-1}$),⁸ and Zr-fumarate ($E_{a,N} = 71 \text{ kJmol}^{-1}$, $E_{a,g} = 66 \text{ kJmol}^{-1}$).⁶ Given the very similar slopes of the lines, the rate determining step for these systems is always the same (i.e. nucleation in the case of both HKUST-1 and Zr-Fumarate, growth for ZIF-8) over a wide range of temperatures. Rather interestingly, the activation energies for Zr-UiO-66 seem to be much lower with growth as the limiting factor ($E_{a,N} = 11\text{-}39 \text{ kJmol}^{-1}$, $E_{a,g} = 19\text{-}46 \text{ kJmol}^{-1}$), depending on both the amount of HCl present and the source of Zr used.⁴⁰

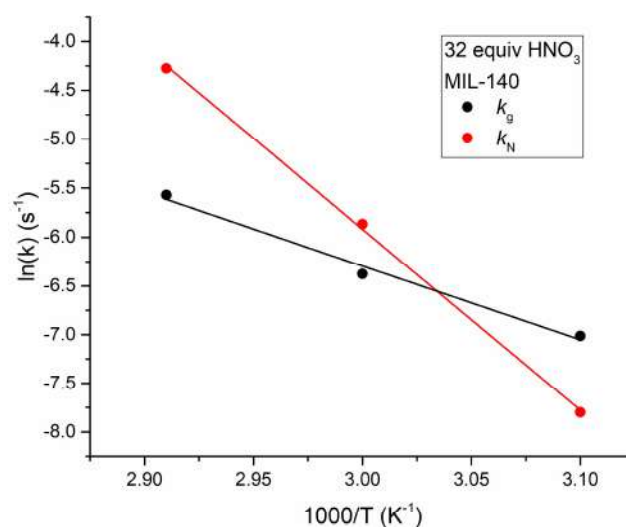


Figure 5.11: Plot of $\ln(k_n)$ (red circles) and $\ln(k_g)$ (black circles) versus $1/T$ for experiments performed at 50 °C, 60 °C and 70 °C in the presence of 32 equivalents of HNO₃. The red line and the black line are the linear Arrhenius fittings for nucleation and crystal growth, respectively.

Effect of HNO₃ Equivalents

The second parameter we explored in this system was the amount of HNO₃, whose number of equivalents was varied in the order of 32-24-16, keeping the temperature at 60 °C throughout. We observed that decreasing the amount of HNO₃ led to a large increase in the rate of crystallisation (Figure 5.12). While P_N for 32 equivalents of HNO₃ peaks after 350 s, for 24 and 16 equivalents this drops to 18 and 5 s, respectively (Figure 5.12). However, P_N peaks at about 0.25 α in all cases, suggesting that nucleation and crystal growth rates evolve in a similar manner. As a matter of fact, Gualtieri fitting showed that the effect of HNO₃ on both the rate of nucleation and growth

was relatively similar, with both being about 68 times greater at 16 equivalents of HNO₃ than they were at 32 equivalents (Table 5.4, Figure S14). Crystal growth is rate determining at each amount of HNO₃ added. The k_N/k_g ratio changes from 1.66 (32 equivalents) to 2.10 (24 equivalents) to 1.69 (16 equivalents), confirming that HNO₃ affects nucleation and growth basically to the same extent (Table 5.4). This is also evident from the plot of $\ln(k_N)$ and $\ln(k_g)$ versus the amount of HNO₃ (Figure ??).

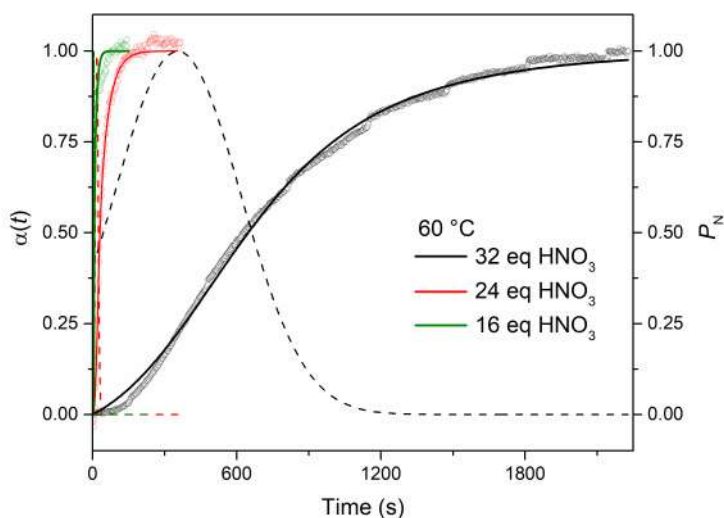


Figure 5.12: Plot of extent of crystallization (α , circles, left y-axis) and probability of nucleation (P_N , dashed lines, right y-axis) as a function of time for experiments performed at 60 °C using 32 (black), 24 (red) and 16 (green) equivalents of HNO₃.

Table 5.4: Nucleation and growth rates for F4_MIL-140(Ce) in the presence of 16 equivalents (0.2 mL, 0.8 mol/L), 24 equivalents (0.3 mL, 1.2 mol/L), and 32 equivalents (0.4 mL, 1.6 mol/L) of HNO₃ at 60 °C. The ratios shown for k_N and k_g are the ratio at each equivalent of HNO₃ vs 32 equivalents

HNO ₃ (eq)	a (s)	b (s)	k_g (s ⁻¹)	k_N (s ⁻¹)	Ratio k_g	Ratio k_N	Ratio k_N/k_g	R ²
16	5.2	0.6	0.1140	0.1923	67.9	67.9	1.69	0.9664
24	17.8	5.9	0.0267	0.0562	15.9	19.8	2.10	0.9984
32	353	263	0.0017	0.0028	1.0	1.0	1.66	0.9974

5.3.3 System 2 - Ce(IV)-TFBDC-HNO₃-AcOH

The second system we explored involved the addition of AcOH, which was used as a coordination modulator, besides HNO₃. In the exploration of this system, we kept the concentration of CAN and H₂TFBDC fixed at 0.05 mol L⁻¹ and looked independently at three parameters - temperature, amount of HNO₃ and amount of AcOH - in order to assess their effect on the rates of nucleation and crystal growth of the two crystalline phases [F4_MIL-140A(Ce) and F4_UiO-66(Ce)] formed during these experiments.

Effect of Temperature

As with the first system, the first parameter we looked at was the effect of temperature on crystallisation, varying in the range 50, 60 and 70 °C, while HNO₃ and AcOH were kept fixed at 16 equivalents and 96 equivalents, respectively. Comparing the plots of α vs t for the two phases at each temperature (Figure 5.15), it is evident that the F4_UiO-66(Ce) phase is formed first at each temperature. This provides experimental evidence that F4_UiO-66(Ce) is in fact the kinetically favoured phase, in line with what originally suggested for the Zr-terephthalate system in DMF, when AcOH is present in the reaction environment for the Ce-TFBDC water-based synthesis.²⁹ It is plausible that AcOH plays a role in promoting solution templation of discrete clusters, which are essential to enable the formation of the F4_UiO-66(Ce) framework in aqueous environment through a ligand exchange process whereby TFBDC²⁻ replaces acetate.

At both 50 and 60 °C (Figures 5.13, 5.14), we observe some drop in the intensity for the F4_UiO-66(Ce) phase upon prolonged reaction, which might suggest either some degradation or consumption of this phase due to interconversion into F4_MIL-140A(Ce). However, the drop in intensity of F4_UiO-66(Ce) starts after most of F4_MIL-140A(Ce) has already formed and, looking at the plots reporting absolute intensities for both experiments, it is clear that the small drop in intensity of F4_UiO-66(Ce) cannot account for the large increase seen in the intensity of F4_MIL-140A(Ce). This suggests that the two phases form independently and there

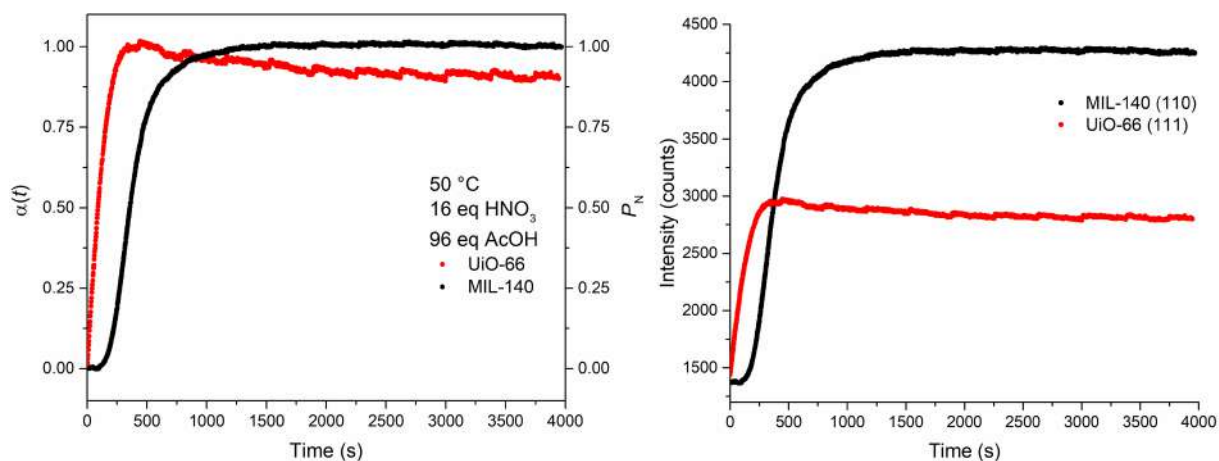


Figure 5.13: Plot of the extent of crystallisation (left) and absolute intensities (right) of the 110 reflection of the F4_MIL-140A(Ce) phase (black circles) and of the 111 reflection of the F4_UiO-66(Ce) phase (red circles) versus time for the experiment performed at 50 °C with 16 equivalents of HNO₃ and 96 equivalents of AcOH.

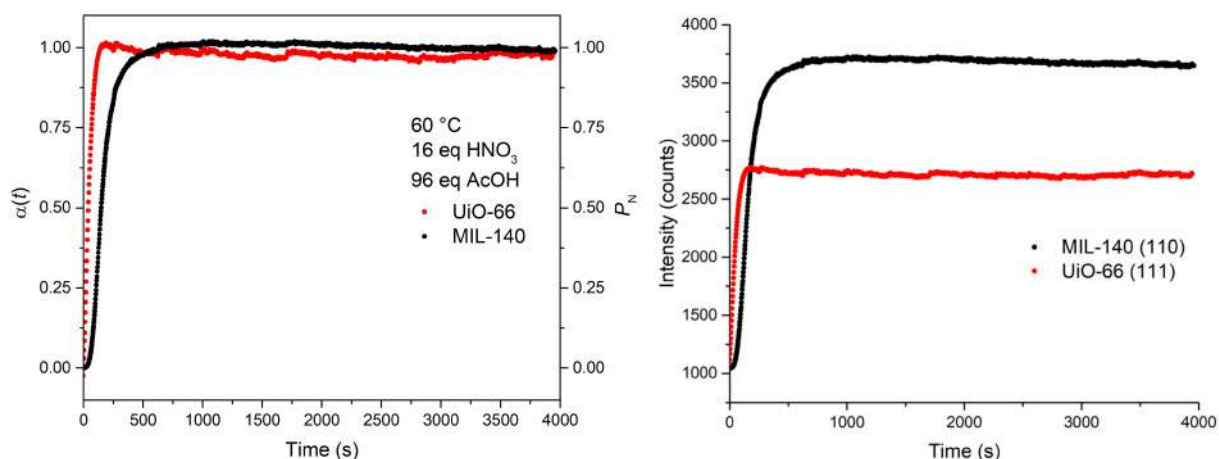


Figure 5.14: Plot of the extent of crystallisation (left) and absolute intensities (right) of the 110 reflection of the F4_MIL-140A(Ce) phase (black circles) and of the 111 reflection of the F4_UiO-66(Ce) phase (red circles) versus time for the experiment performed at 60 °C with 16 equivalents of HNO₃ and 96 equivalents of AcOH.

is no significant interconversion between them. Rather, the two phases compete for reagents present in solution. Furthermore, the intensity of F4_UiO-66(Ce) plateaus after some time, suggesting that decomposition of this MOF does not continue until complete disappearance.

In the experiments performed at 50 and 60 °C (Figure 5.15a,b), PN for F4_MIL-140A(Ce) peaks when F4_UiO-66(Ce) is already completely crystallised. The experiment performed at 70 °C (Figure 5.15c) shows instead that the curve for F4_UiO-66(Ce) experiences a sudden change in slope after about 30 s, when it has

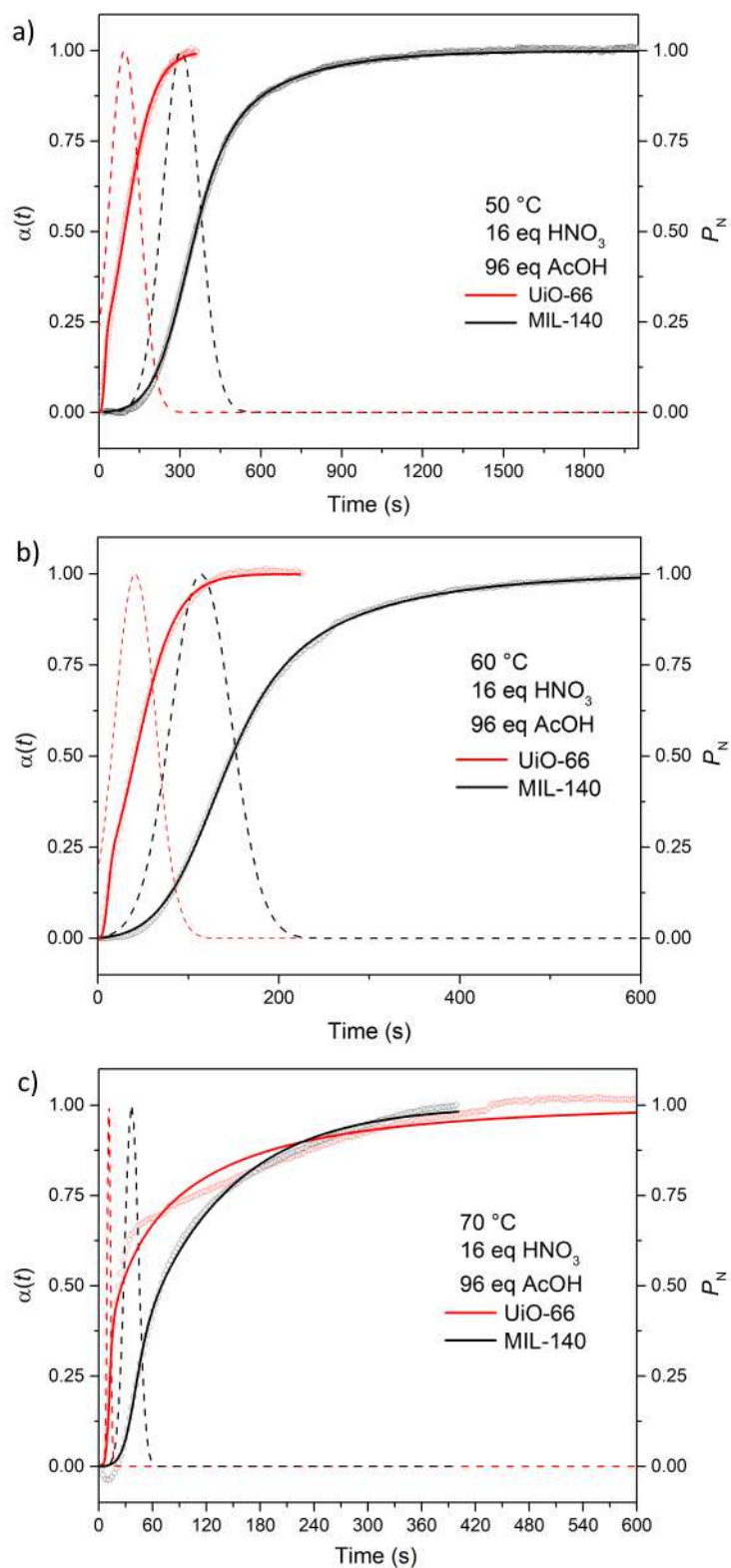


Figure 5.15: Plot of extent of crystallization (α , empty circles), Gualtieri fitting (solid lines) and probability of nucleation (P_N , dashed lines) as a function of time for experiments performed at 50 °C (a), 60 °C (b) and 70 °C (c) for the F4_UiO-66(Ce) (red) and F4_MIL-140A(Ce) (black) phases.

reached α of about 0.63 and its P_N is at zero, substantially decreasing its rate of crystal growth.

Interestingly, this event occurs when the P_N for F4_MIL-140A(Ce) reaches its peak, suggesting that growth of F4_UiO-66(Ce) in these conditions could be inhibited by competition with F4_MIL-140A(Ce) for reagents. Looking at the evolution of the intensity ratio between the two phases at full crystallisation, we can have a proxy of the effect of a parameter on the relative yield of each phase. We used the intensity of the 110 reflection for the F4_MIL-140A(Ce) phase and the intensity of the 111 reflection for the F4_UiO-66(Ce) phase at full crystallisation to extract MIL/UiO ratios of 1.5 at 50 °C, 1.3 at 60 °C and 1.7 at 70 °C, thus observing no obvious trend due to the temperature increase. It is to be noted, though, that the intensity ratio at 70 °C is probably affected by the deceleration of F4_UiO-66(Ce) crystallisation, which is likely to lead to a lower amount of this phase being formed at the end of the reaction than if there was no competition with F4_MIL-140A(Ce).

Focusing on the crystallisation kinetics of the F4_MIL-140A(Ce) phase, it is clear that temperature increases the rate of crystallisation (Figure 9a), and, as already observed in the absence of AcOH, this is affected more by the rate of nucleation than growth (Table 5.5). One thing that is also clear is that the addition of AcOH has dampened the $E_{a,N}$ when compared with the first system, with this one having a k_N ratio between 50 and 70 °C of 1:8, compared with 1:34 for the first system.

The k_N/k_g ratio changes from 0.92 (50 °C) to 1.14 (60 °C) to 2.73 (70 °C), suggesting that, also in this system, temperature accelerates nucleation preferentially over crystal growth, with the latter becoming increasingly rate determining as the temperature increases. This can also be seen from the plot of P_N (Figure 5.16a), which peaks in correspondence of progressively lower α as the temperature increases. Comparing the values of k_N and k_g for the experiments conducted at 60 °C in the presence of 16 equivalents of HNO₃, the effect of the addition of AcOH on nucleation and growth can be assessed. In the presence of 96 equivalents of AcOH, k_N is 0.00877 s⁻¹ and k_g

Table 5.5: Nucleation and growth rates for F4_MIL-140(Ce) and F4_UiO-66(Ce) in the presence of 16 equivalents (0.2 mL, 0.8 mol/L) of HNO₃, and 96 equivalents (1.1 mL, 4.8 mol/L) of AcOH at 50, 60, and 70 °C. The ratios shown for k_N and k_g are the ratio at each temperature vs 50 °C.

	Temp (°C)	a (s)	b (s)	k_g (s ⁻¹)	k_N (s ⁻¹)	Ratio k_g	Ratio k_N	Ratio k_N/k_g	R ²
MIL-140A	70	36.6	7.6	0.01	0.0273	2.8	8.3	2.73	0.9990
	60	114	33	0.0077	0.0088	2.1	2.7	1.14	0.9991
	50	304	68	0.0036	0.0033	1.0	1.0	0.92	0.9992
UiO-66	70*	11	1.8	0.02	0.0909	0.5**	8.6	4.55	0.9651
	60	41.3	22.5	0.0862	0.0242	2.0	2.3	0.28	0.9978
	50	94.3	55.1	0.044	0.0106	1.0	1.0	0.24	0.9977

*n had to be left free to refine to have a reasonable fitting, returning a value of 0.55 ± 0.01 ; **Value not reliable due to the change in rate during crystallisation.

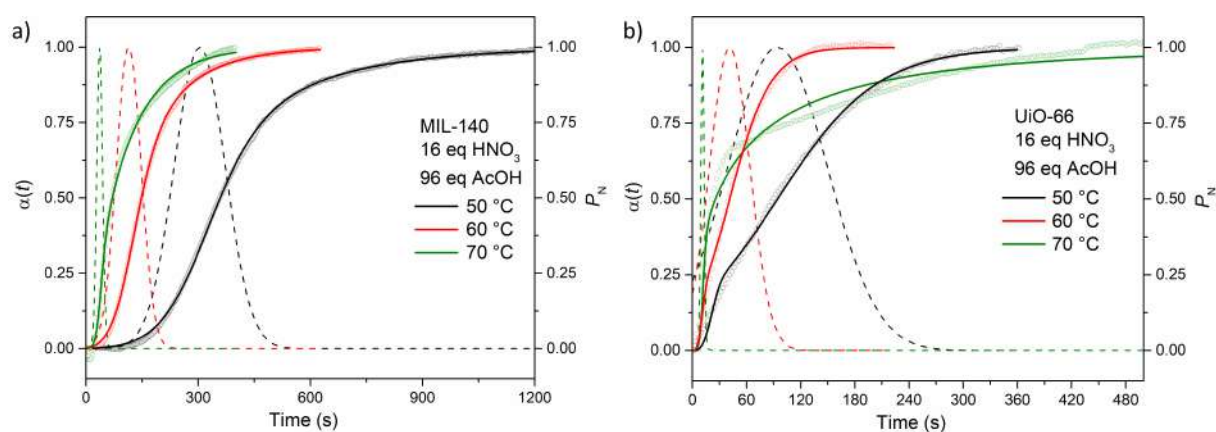


Figure 5.16: Plot of extent of crystallization (α , empty circles), Gualtieri fitting (solid lines) and probability of nucleation (P_N , dashed lines) as a function of time for experiments performed in the presence of 16 equivalents of HNO₃ and 96 equivalents of AcOH at 50 °C (black), 60 °C (red) and 70 °C (green) for (a) the F4_MIL-140A(Ce) phase and (b) the F4_UiO-66(Ce) phase.

is 0.00769 s^{-1} , whereas in the absence of AcOH k_N is 0.19231 s^{-1} and k_g is 0.1140 s^{-1} , indicating that AcOH dampens both nucleation and crystal growth rates, but the first is more affected, decreasing by a factor of 22, versus growth, decreasing by a factor of 15, when AcOH is added into the reaction environment.

The F4_UiO-66(Ce) phase also shows a similar trend to F4_MIL-140A(Ce), in that the k_N ratio between 50 and 70 °C is 1:9, and again has a larger contribution to the overall rate of crystallisation than the rate of growth (Figure 5.16b, Table 5.5). Both at 50 and 60 °C, nucleation is rate determining. Due to the change in slope of the curve at 70 °C, a reliable value for k_g at this temperature could not be extracted. The k_N/k_g ratio changes

from 0.24 (50 °C) to 0.28 (60 °C), suggesting that temperature accelerates nucleation and growth of F4_UiO-66(Ce) to the same extent (Table 5.5). The fitting of the Gualtieri model in this case seemed to present some issues, whereby the model does not reliably reproduce the experimental data, especially in the initial stages of crystallisation. This can be identified in Figure 5.16b, where the lines representing the Gualtieri fit deviate from the experimental points at the start of the curve. A similar behaviour was reported when modelling the crystallisation kinetics of formate-modulated ZIF-8.⁷ We believe that the most likely reason for this effect is the lack of induction time for F4_UiO-66(Ce), whose crystallisation starts immediately when Ce(IV) is introduced to the system. Nonetheless, R^2 values above 0.997 are obtained for the curves relative to the experiments performed at 50 and 60 °C. A better fit for these experiments ($R^2 > 0.999$) can be achieved by freeing the value for n in the Gualtieri model, which refines to 1.19 and 1.23 for the experiment at 50 °C and 60 °C, respectively, with similar values for a , b and k_g to those obtained when n was fixed to 3. However, these values of n are much less meaningful in physical terms, given that the F4_UiO-66(Ce) phase grows in octahedral shape (Figure 5.6). Therefore, we preferred to have a slightly worse fit, while preserving a physically sound value of n .

Comparing the values of k_N and k_g for F4_MIL-140A(Ce) and F4_UiO-66(Ce) at the same temperatures, we see that F4_UiO-66(Ce) formation is faster both in nucleation and in crystal growth (Table 5.5). Temperature does not seem to have an influence on the relative rates, which stay basically unchanged. Arrhenius analysis for the F4_MIL-140A(Ce) phase shows a similar trend to the one already seen when only HNO₃ is present in the reaction environment, with the two fitting lines for nucleation and growth crossing at a $1/T$ value corresponding to about 54 °C (Figure 5.17). The extracted activation energies are 92 ± 7 kJ mol⁻¹ for nucleation and 45 ± 11 kJ mol⁻¹ for crystal growth. These values are lower than those found when only HNO₃ is present in the reaction environment, but they cannot be straightforwardly compared, due to the presence of a lower amount of HNO₃. For the F4_UiO-66(Ce) phase, only the

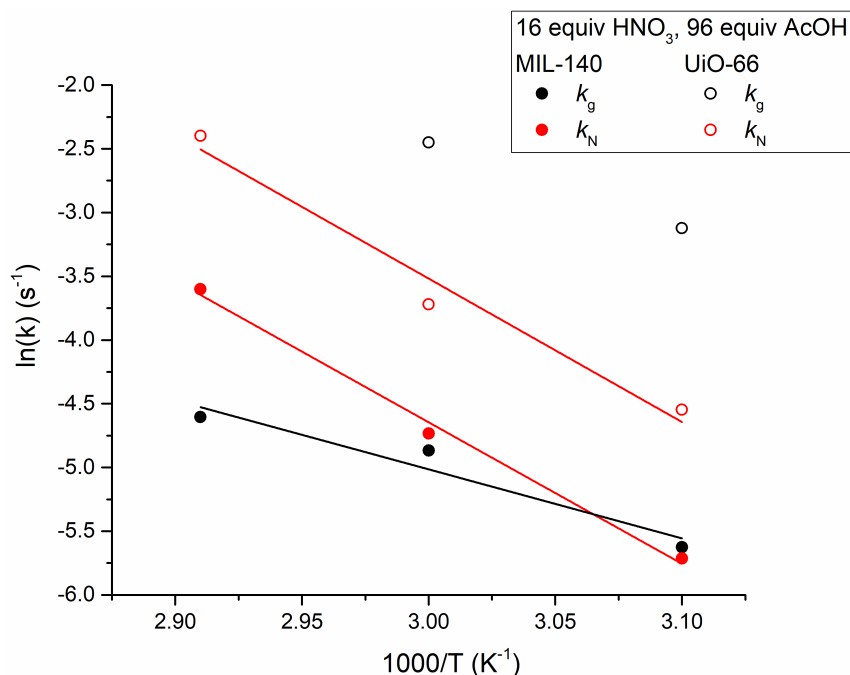


Figure 5.17: Plot of $\ln(k_N)$ (full red circles) and $\ln(k_g)$ (full black circles) for F4_MIL-140A(Ce) and $\ln(k_N)$ (open red circles) and $\ln(k_g)$ (open black circles) for F4_UiO-66(Ce) versus $1/T$ for experiments performed at 50 °C, 60 °C and 70 °C in the presence of 16 equivalents of HNO₃ and 96 equivalents of AcOH. The red line and the black line are the linear Arrhenius fittings for nucleation and crystal growth, respectively. The value of $\ln(k_g)$ for F4_UiO-66(Ce) at 70 °C is not displayed because of the unreliable Gualtieri fitting for this experiment.

nucleation part could be fitted, finding an activation energy of 94 ± 15 kJ mol⁻¹, very similar to that of the F4_MIL-140A(Ce) phase. In the absence of a reliable value of k_g at 70 °C, no conclusions could be drawn for the growth of the F4_UiO-66(Ce) phase.

Effect of HNO₃ Equivalents

The second parameter we investigated, as with the first system, was the equivalents of HNO₃ used in the reaction. In this case, the amount of HNO₃ was varied between 8, 12, and 16 equivalents, whereas temperature was kept constant at 60 °C and the amount of AcOH was kept constant at 96 equivalents. In drawing a comparison between the two phases (Figure 5.18), one can see that the F4_UiO-66(Ce) phase is again kinetically favoured in each experiment. P_N for F4_MIL-140A(Ce) always peaks when crystallisation of F4_UiO-66(Ce) is almost complete, resulting in the two phases not competing for reagents. Again, we can also see some drop in the intensity

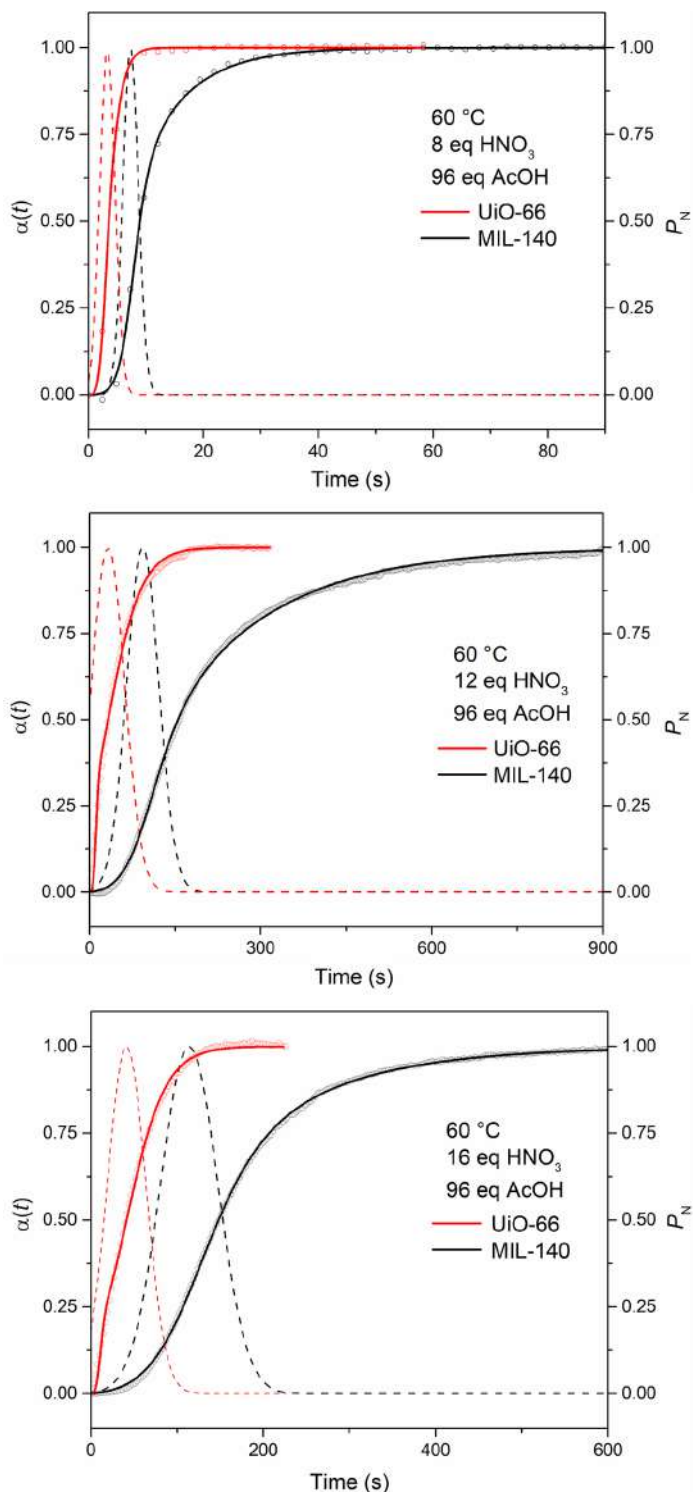


Figure 5.18: Plot of extent of crystallization (α , empty circles), Gaultieri fitting (solid lines) and probability of nucleation (P_N , dashed lines) as a function of time for experiments performed at 8 (top), 12 (middle) and 16 (bottom) equivalents of HNO₃ at 60 °C for the F4_MIL-140A(Ce) (black) and the F4_UiO-66(Ce) (red) phases.

for the F4_UiO-66(Ce) phase, which suggests that some degradation of this phase takes place over time. Looking at the intensity ratio between the 110 reflection of

the F4_MIL-140A(Ce) phase and the 111 reflection of the F4_UiO-66(Ce) phase at the end of crystallisation, we can see that this increases from 0.6 to 0.8 to 1.3 when HNO₃ is increased from 8 to 12 to 16 equivalents, respectively, indicating that a larger amount of HNO₃ favours the formation of more F4_MIL-140A(Ce). It is to be noted that the largest change in intensity ratio occurs between 12 and 16 equivalents of HNO₃, where an almost negligible change in rate constants is observed (vide infra), suggesting that variation of the HNO₃ amount within said range mainly has an effect on the equilibrium composition. This could be due to the role of HNO₃ in inhibiting deprotonation of AcOH and its coordination to Ce(IV) to form the hexanuclear [Ce₆O₄(OH)₄(-COO)₁₂] clusters needed for the F4_UiO-66(Ce) phase.

Another possibility could be that lowering the pH increases the possibility of linker protonation on the formed MOFs themselves, adding additional reversibility to the process and allowing the thermodynamic product F4_MIL-140A(Ce) to be formed, as suggested in a recent paper reporting a systematic investigation of the influence of several parameters on the crystallisation of phase pure MIL-140 type MOFs in DMF solvent.³² However, the evidence in our hands does not indicate that a more acidic environment promotes such a dissolution-recrystallisation process.

For the F4_MIL-140A(Ce) phase, lowering the equivalents of HNO₃ used in the reaction increases the rate of nucleation, with the ratio between 16 and 8 equivalents of 1:15.5 (Figure 5.19a, Table 5.6). Crystal growth is affected to a similar degree, with a k_g ratio of 1:15.2 in the same equivalents range. Growth is rate determining at each amount of HNO₃ added, as already observed in the absence of AcOH. The k_N/k_g ratio changes from 1.16 (8 equivalents) to 2.06 (12 equivalents) to 1.14 (16 equivalents), suggesting that the amount of HNO₃ does not have a significant effect on the relative rates.

Compared with the F4_MIL-140A(Ce) phase, the effect of lowering the amount of HNO₃ in the system is similar on nucleation of the F4_UiO-66(Ce) phase, with a 1:13 k_N ratio between 16 and 8 equivalents (Figure 5.19b, Table 5.6). The effect on growth

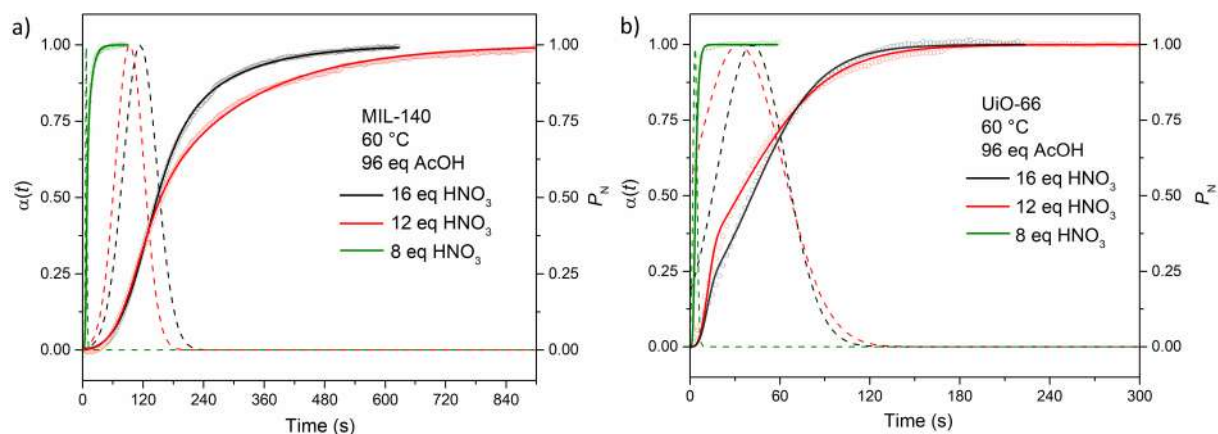


Figure 5.19: Plot of extent of crystallization (α , empty circles), Gualtieri fitting (solid lines) and probability of nucleation (P_N , dashed lines) as a function of time for experiments performed at 8 (green), 12 (red) and 16 (black) equivalents of HNO_3 for (a) the F4_MIL-140A(Ce) phase and (b) the F4_UiO-66(Ce) phase.

Table 5.6: Nucleation and growth rates for F4_MIL-140(Ce) and F4_UiO-66(Ce) using 8 equivalents (0.1 mL, 0.4 mol/L), 12 equivalents (0.15 mL, 0.6 mol/L), and 16 equivalents (0.0.2 mL, 0.8 mol/L) of HNO_3 in the presence of 96 equivalents (1.1 mL, 4.8 mol/L) of AcOH at 60 °C. The ratios shown for k_N and k_g are the ratio at each equivalent of HNO_3 vs 8 equivalents.

	HNO_3 (eq)	a (s)	b (s)	k_g (s^{-1})	k_N (s^{-1})	Ratio k_g	Ratio k_N	Ratio k_N/k_g	R^2
MIL-140A	8	7.34	1.35	0.1170	0.1362	15.2	15.5	1.16	0.9991
	12	93.2	28.2	0.0052	0.0107	0.7	1.2	2.06	0.9993
	16	114	33	0.0077	0.0088	1.0	1.0	1.14	0.9991
UiO-66	8	3.3	1.3	0.38	0.3030	4.4	12.5	0.80	0.9997
	12	32.4	29.2	0.08	0.0309	0.9	1.3	0.39	0.9958
	16	41.3	22.5	0.0862	0.0242	1.0	1.0	0.28	0.9978

is relatively small in comparison, with k_g growing by a factor of 4 in the same HNO_3 range. Nucleation is consistently rate determining at each amount of HNO_3 added. The k_N/k_g ratio changes from 0.80 (8 equivalents of HNO_3) to 0.39 (12 equivalents of HNO_3) to 0.28 (16 equivalents of HNO_3), suggesting that larger amounts of HNO_3 do in fact inhibit nucleation to a larger extent than growth (Table 5.8). It is to be noted that both k_N and k_g stay basically unchanged for both the F4_MIL-140A(Ce) and the F4_UiO-66(Ce) phase when decreasing the amount of HNO_3 from 16 to 12 equivalents, suggesting that there is little kinetic effect of HNO_3 in this range of parameters, as previously noted. Comparing the values of k_N and k_g for F4_MIL-140A(Ce) and F4_UiO-66(Ce) at the same HNO_3 amounts, we see that F4_UiO-66(Ce) formation is

consistently faster both in nucleation and in crystal growth (Figure 5.20, Table 5.6).

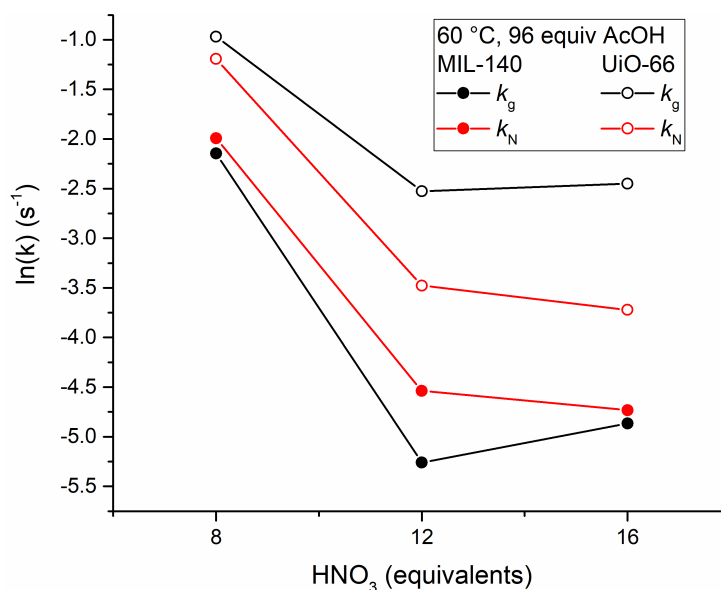


Figure 5.20: Plot of $\ln(k_N)$ (full red circles) and $\ln(k_g)$ (full black circles) for F4_MIL-140A(Ce) and $\ln(k_N)$ (open red circles) and $\ln(k_g)$ (open black circles) for F4_UiO-66(Ce) versus the amount of HNO₃ for experiments performed at 60 °C and 96 equivalents of AcOH in the presence of 8, 12 and 16 equivalents of HNO₃.

Effect of AcOH Equivalents

The third parameter investigated for this system is the amount of AcOH used, which was varied between 96, 123 and 149 equivalents, while keeping HNO₃ fixed at 16 equivalents and temperature fixed at 60 °C. At 149 equivalents of AcOH, the formation F4_MIL-140A(Ce) is very slow and this phase does not reach full crystallisation within the investigated timeframe of 2700 s (Figure 5.21). For this reason, we include the result of the experiment performed with 0 equivalents of AcOH for comparison to identify trends in k_N and k_g for the F4_MIL-140A(Ce) phase. Comparing the results of the experiments performed using 96 and 123 equivalents of AcOH, we note that increasing the amount of AcOH leads to slowing down the crystallisation rate for both phases (Figure 5.22). Once again, the F4_UiO-66(Ce) phase is clearly kinetically favoured and P_N for F4_MIL-140A(Ce) peaks when crystallisation of F4_UiO-66(Ce) is almost complete, resulting in the two phases not competing for reagents (Figure 5.22). We can also see slow degradation of the F4_UiO-66(Ce) phase over time. A

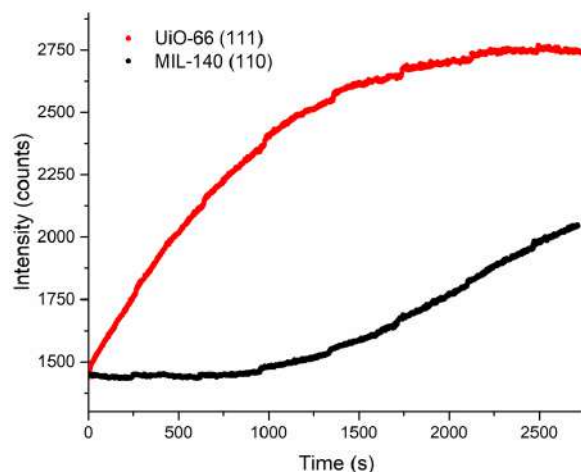


Figure 5.21: Plot of the absolute intensities of the 110 reflection of the F4_MIL-140A(Ce) phase (black circles) and of the 111 reflection of the F4_UiO-66(Ce) phase (red circles) versus time for the experiment performed at 60 °C with 16 equivalents of HNO₃ and 149 equivalents of AcOH.

decrease in the ratio between the intensity of the F4_MIL-140A(Ce) 110 reflection and the F4_UiO-66(Ce) 111 reflection from 1.3 to 0.9 is found when AcOH increases from 96 to 123 equivalents. This suggests that AcOH shifts the equilibrium in favour of the formation of F4_UiO-66(Ce) over F4_MIL-140A(Ce) and that the coordination modulator favours indeed the kinetic product. This is probably due to the role of AcOH in promoting the formation of the hexanuclear $[\text{Ce}_6\text{O}_4(\text{OH})_4(-\text{COO})_{12}]$ clusters needed for the F4_UiO-66(Ce) phase, thus reducing the availability of isolated metal ions that can react with TFBDC²⁻ in solution to form the extended inorganic building units at the basis of F4_MIL-140A(Ce).

We see here that decreasing the amount of AcOH present in the system has a relatively similar effect on nucleation and crystal growth of the F4_MIL-140A(Ce) phase, which increase by a factor of 38.7 and 27.8, respectively, when AcOH goes from 123 to 0 equivalents (Figure 5.22a, Table 5.7). Crystal growth is rate determining in all the range investigated. The k_N/k_g ratio changes from 1.68 (0 equivalents) to 1.14 (96 equivalents) to 1.21 (123 equivalents), suggesting that the amount of AcOH has a similar effect on the nucleation and crystal growth stages.

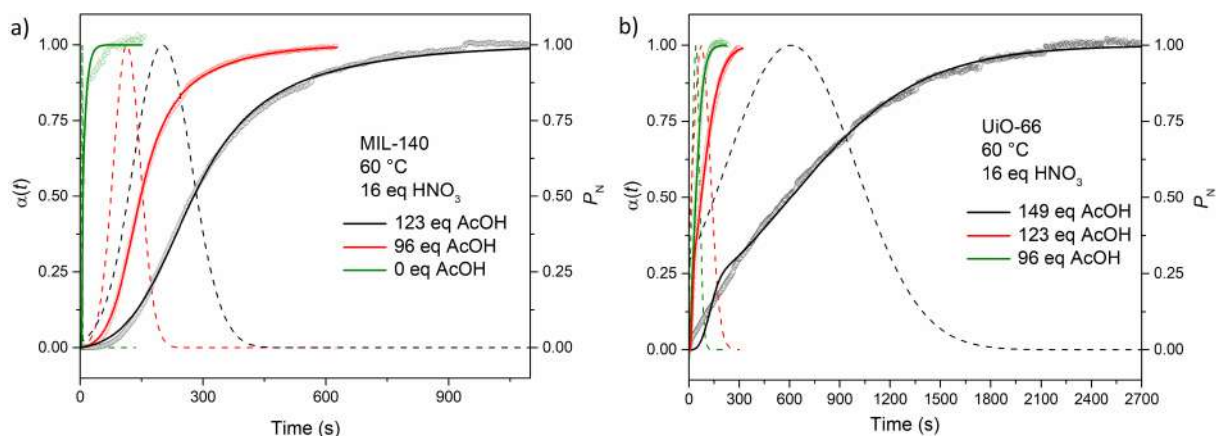


Figure 5.22: Plot of extent of crystallization (α , empty circles), Gualtieri fitting (solid lines) and probability of nucleation (P_N , dashed lines) as a function of time for experiments performed with 16 equivalents of HNO_3 at 60°C with (a) 0, 96, and 123 equivalents of AcOH for the F4_MIL-140A(Ce) phase and (b) with 96, 123, and 149 equivalents of AcOH for the F4_UiO-66(Ce) phase.

Table 5.7: Nucleation and growth rates for F4_MIL-140(Ce) and F4_UiO-66(Ce) using 0 equivalents, 96 equivalents (1.1 mL, 4.8 mol/L), and 123 equivalents (1.4 mL, 6.1 mol/L) of AcOH in the presence of 16 equivalents (0.2 mL, 0.8 mol/L) of HNO_3 at 60°C .

	AcOH (eq)	a (s)	b (s)	k_g (s^{-1})	k_N (s^{-1})	Ratio k_g	Ratio k_N	Ratio k_N/k_g	R^2
MIL-140A	0	5.2	0.57	0.1140	0.1923	27.8	38.7	1.7	0.9663
	96	114	33	0.0077	0.0088	1.9	1.8	1.1	0.9991
	123	201	71	0.0041	0.0050	1.0	1.0	1.2	0.9984
UiO-66	96	41.3	22.5	0.0862	0.0242	11.5	14.7	0.28	0.9978
	123	74	53.5	0.0470	0.0135	6.3	8.2	0.29	0.9964
	149	607	386	0.0075	0.0016	1.0	1.0	0.22	0.9961

Regarding the effect of decreasing AcOH on the crystallisation of F4_UiO-66(Ce), there is a similar increase in the rates of nucleation and crystal growth, which grow by a factor of 14.7 and 11.5, respectively, between 149 and 96 equivalents of AcOH (Figure 5.22b, Table 5.7). Nucleation is consistently rate determining at each amount of AcOH added. The k_N/k_g ratio changes from 0.28 (96 equivalents of AcOH) to 0.29 (123 equivalents of AcOH) to 0.22 (149 equivalents of AcOH), suggesting that AcOH affects nucleation and growth to the same extent. Comparing the values of k_N and k_g for F4_MIL-140A(Ce) and F4_UiO-66(Ce) at the same AcOH amounts, we see that F4_UiO-66(Ce) formation is faster both in nucleation and in growth (Figure 5.23).

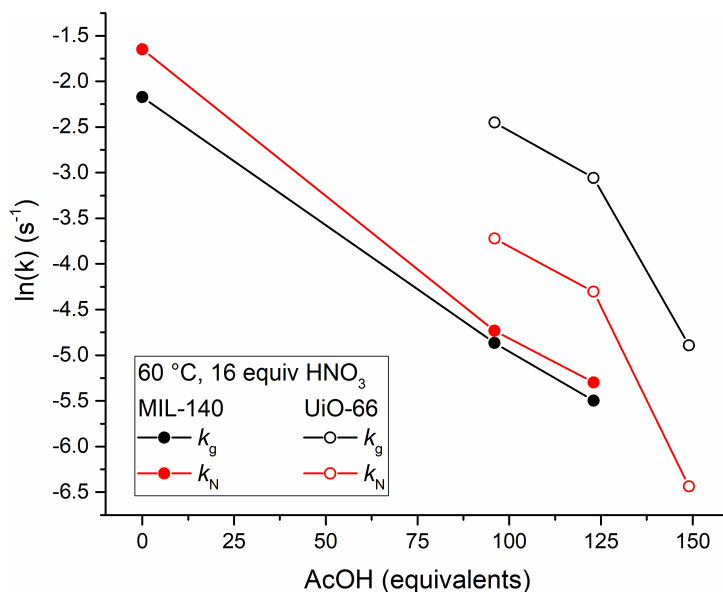


Figure 5.23: Plot of $\ln(k_N)$ (full red circles) and $\ln(k_g)$ (full black circles) for F4_MIL-140A(Ce) and $\ln(k_N)$ (open red circles) and $\ln(k_g)$ (open black circles) for F4_UiO-66(Ce) versus the amount of AcOH for experiments performed at 60 °C and 16 equivalents of HNO_3 in the presence of 0, 96, 123 and 149 equivalents of AcOH.

5.3.4 Optimising for the F4_UiO-66(Ce) Phase

In order to achieve the pure F4_UiO-66(Ce) phase, the conditions require the largest amount of AcOH investigated so far (149 equivalents), with some HNO_3 (8 equivalents) present in order to slow down the kinetics, which allows for crystallisation to be followed *in situ*. We kept the concentration of CAN and H_2TFBDC fixed at 0.05 mol L and investigated the effect of temperature on this pure F4_UiO-66(Ce) phase, running the reactions at 60, 70, and 80 °C. Full crystallisation is achieved in less than five minutes in all experiments, with the rate increasing when moving from 60 to 70 to 80 °C (Figure 5.24).

It should be noted that, in all the experiments discussed here, the n parameter in the Gualtieri equation had to be left free to refine, because the fit did not converge when its value was constrained to 3. All the fittings ended up with a similar refined value of n (≈ 0.5). Since n defines the dimensionality of crystal growth in the Gualtieri model, a value lower than 1 has no physical meaning. Further investigation would therefore be required to gain a better insight into the kinetics of crystallisation and test the

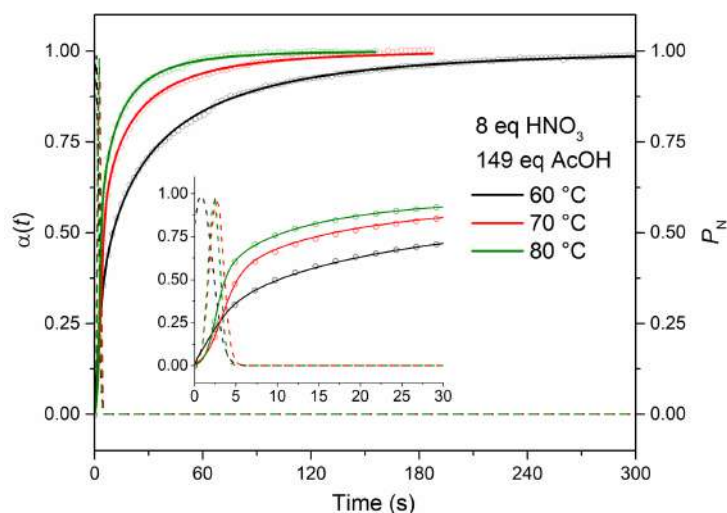


Figure 5.24: Plot of extent of crystallization (α , empty circles), Gualtieri fitting (solid lines) and probability of nucleation (P_N , dashed lines) as a function of time for experiments performed at 60 °C (black), 70 °C (red) and 80 °C (green) in the presence of 8 equivalents of HNO_3 and 149 equivalents of AcOH for the F4_UiO-66(Ce) phase.

limitations of the model, something that goes beyond the scope of this work. However, the similar values of n obtained at different temperatures can still allow us to make comparisons within this dataset and, in turn, draw some conclusions on the kinetics. Contrary to what has been seen in previous experiments for the F4_UiO-66(Ce) phase, crystal growth seems to be rate determining in this case (Table 5.8). Nucleation is practically instantaneous and P_N peaks within 5 s in each experiment (Figure 5.25). Quite surprisingly, k_N decreases when the temperature is increased above 60 °C. However, given the extremely fast nucleation process, we have a small number of observables in the timeframe where nucleation occurs, introducing significant errors in the fitting. This might also be the reason behind the impossibility to fit the Gualtieri equation when n is fixed to 3. Furthermore, we suspect that the temperature drop following addition of the CAN solution (held at RT) might affect the experiments performed at higher temperature to a larger extent, which could also explain the counterintuitive results obtained for k_N . Arrhenius analysis of the crystal growth stage gives an activation energy of $67 \pm 4 \text{ kJmol}^{-1}$ (Figure 5.25), a value similar to the one extracted for the F4_MIL-140A(Ce) phase in a similar temperature range and in the presence of 32 equivalents of HNO_3 (Figure 5.11).

Table 5.8: Nucleation and growth rates for F4_UiO-66(Ce) in the presence of 8 equivalents (0.1 mL, 0.4 mol/L) of HNO₃, and 149 equivalents (1.7 mL, 7.4 mol/L) of AcOH at 50, 60, and 70 °C.

Temp (°C)	<i>a</i> (s)	<i>b</i> (s)	<i>k_g</i> (s ⁻¹)	<i>k_N</i> (s ⁻¹)	Ratio <i>k_g</i>	Ratio <i>k_N</i>	Ratio <i>k_N/k_g</i>	R ²
80	2.37	0.68	0.1940	0.4219	3.9	0.4	2.17	0.9995
70	2.66	0.83	0.1120	0.3759	2.2	0.3	3.36	0.9793
60	0.83	1.32	0.0500	1.2050	1.0	1.0	24.10	0.9993

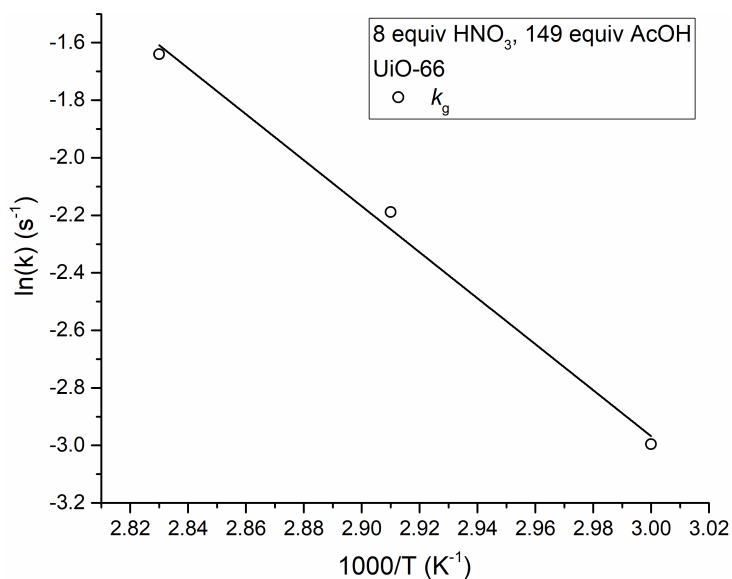


Figure 5.25: Plot of $\ln(k_g)$ (open black circles) for F4_UiO-66(Ce) versus $1/T$ for experiments performed at 60 °C, 70 °C, and 80 °C in the presence of 8 equivalents of HNO₃ and 149 equivalents of AcOH.

5.3.5 *Ex situ* Optimisation of F4_MIL-140A(Ce) Synthesis

Having gathered precious information about the kinetics of crystallisation and how these are affected by various reaction parameters during the *in situ* study, we carried out further synthetic work to investigate the possibility to expand the range of different Ce(IV) precursors as well as alternative inorganic acid modulators, with the aim of identifying different optimised protocols for the prospective production of F4_MIL-140A(Ce) on a larger scale.

Effect of Temperature

We first performed a series of experiments to look at the effect of temperature on the system Ce(IV)-H₂TFBDC – HNO₃, when HNO₃ was kept at 32 equivalents (1.5 mL; 24

mmol) in a total volume of 15 mL. The temperature range was the same as that used in the in-situ experiments for this system, i.e. 50 °C, 60 °C, and 70 °C. The synthetic procedure was also kept consistent with the *in situ* experiments: H₂TFBDC was first dissolved in 12 mL of a HNO₃/H₂O mixture at the desired temperature and under stirring in a scintillation vial, then 3 mL of a 0.25 M aqueous solution of CAN was added.

At 70 °C, the solid formed almost immediately after addition of CAN and the reaction was stopped after 30 min, yielding 0.155 g of the F4_MIL-140A(Ce) product. At 60 °C, the solution stayed clear upon addition of CAN and the solid appeared after about five min. The total reaction time was increased to 60 min to ensure completion of reaction, yielding 0.177 g of product. At 50 °C, the onset of crystallisation was delayed to 25 min and the reaction time was further prolonged to 120 min, obtaining 0.177 g of product. The quality of the product obtained was constant, as indicated by the FWHM of the 200 reflection (comprised between 0.1° and 0.11°) and the SEM micrographs, regardless of the temperature (Figures 5.26, B.1).

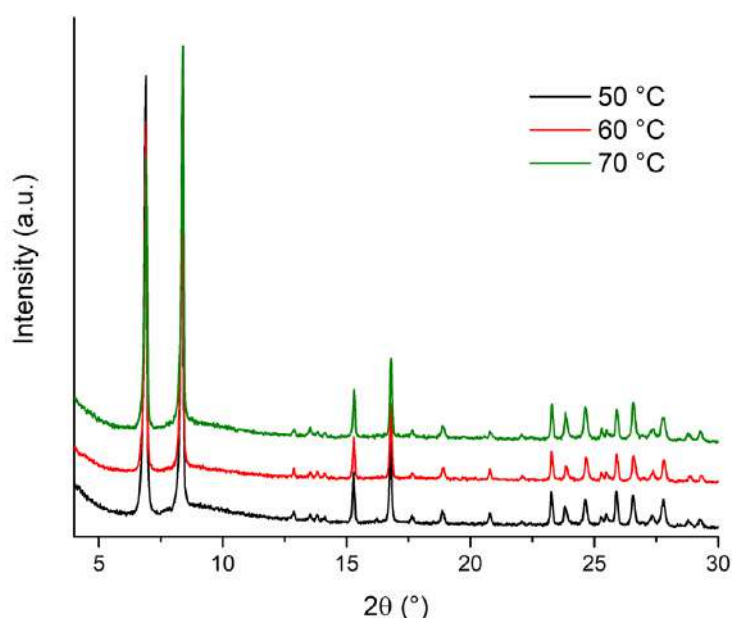


Figure 5.26: PXRD patterns of F4_MIL-140A(Ce) powders obtained from syntheses performed at 50 (black), 60 (red) and 70 °C (green) in the presence of 32 equivalents of HNO₃.

Effect of a Different Protonation Modulator

The use of concentrated HCl is not possible for the synthesis Ce(IV)-based MOFs, due to the oxidation of chloride by Ce(IV), which consumes all the Ce(IV) in solution as soon as HCl is added. We therefore tested concentrated H₂SO₄ (18 M) as an alternative to HNO₃. We note here that the two pK_a values of H₂SO₄ are -3 and 1.99, with the latter falling in between those of H₂TFBDC (1.18 and 2.49) so we can reasonably consider H₂SO₄ as a monoprotic modulator in the context of our system. Upon addition of 32 equivalents (1.3 mL, 1.6 mol/L) of H₂SO₄ to a 0.05 M solution of CAN and H₂TFBDC in water, no crystallisation was observed after 20 h at 60 °C. No evident loss of colour was observed for the solution in this case, suggesting that the presence of H₂SO₄ might prevent significant reduction of Ce(IV) to Ce(III), even over a long period of time. This was also observed at 16 equivalents (0.65 mL, 0.8 mol/L) of H₂SO₄ in the same timeframe. It was at 7.2 equivalents (0.3 mL, 0.4 mol/L) of H₂SO₄, that the first evidence of F4_MIL-140A(Ce) formation could be seen, with onset of crystallisation after about 2 h and a low yield of 0.091 g after 6.5 h. The best compromise was obtained

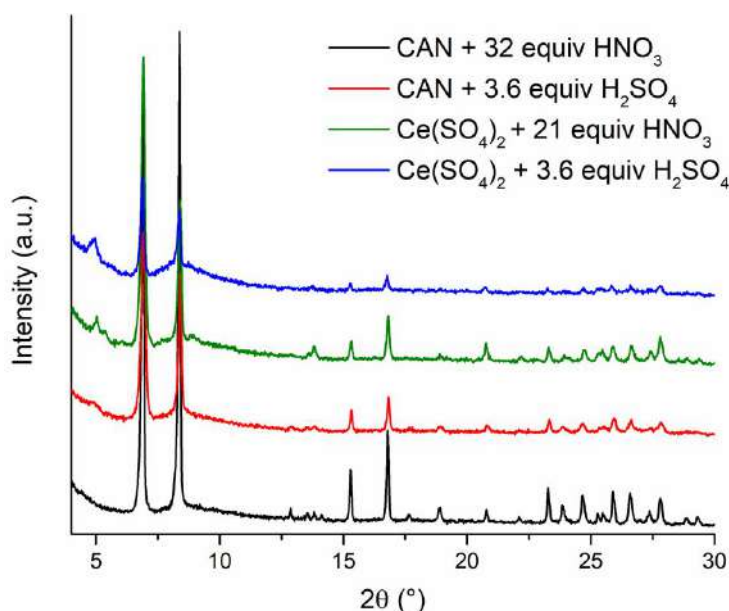


Figure 5.27: PXRD patterns of F4_MIL-140A(Ce) powders obtained from syntheses performed using CAN/HNO₃ (black), CAN/H₂SO₄ (red), Ce(SO₄)₂/HNO₃ (green) and Ce(SO₄)₂/H₂SO₄ (blue) as Ce(IV) source and protonation modulator, respectively, at 60 °C.

using 3.6 equivalents (0.15 mL, 0.2 mol/L) of H₂SO₄, which resulted in a total yield of 0.192 g of a product with FWHM of the 200 reflection of 0.20° and a total synthesis time of 120 min (Figure 5.27). The reason for the different modulation effect observed between H₂SO₄ and HNO₃ can be a combination of higher acidity of the former (pK_a -3 vs -1.4, respectively) and the stronger coordination character of sulfate versus nitrate towards Ce(IV), which might shelter the metal from attack by the linker. H₂SO₄ affords a lower quality product than HNO₃, as also evidenced by SEM, which displays the presence of conglomerates of a second phase (Figure B.2a), but it significantly reduces the impact of the parallel redox process.

Effect of a different metal precursor

In order to shed more light on the role of sulfate ions, we used cerium(IV) sulfate, Ce(SO₄)₂, as a metal precursor, in the presence of either HNO₃ or H₂SO₄ as protonation modulator. The experiments were carried out at 60 °C in a total volume of 15.0 mL and the concentration of CAN and H₂TFBDC kept constant at 0.05 M. In the presence of 32 equivalents of HNO₃, we only obtained 28 mg of product after 5 h. The amount of HNO₃ had to be decreased to 21 equivalents (1.0 mL, 1.1 mol/L), in order to achieve a yield of 0.161 g in just under 3 h. The FWHM of the 200 reflection was 0.18°, but a broad peak at about 5° suggested formation of an undesired, low crystallinity impurity (Figure 5.27). SEM displays less defined crystallites than when CAN is used as a metal precursor (Figure B.2b). This suggests that sulfate probably does exert a modulation effect by coordinating to Ce(IV), requiring a lower amount of HNO₃ modulator, but also that it can lead to formation of side products. In the presence of 3.6 equivalents (0.15 mL, 0.2 mol/L) of H₂SO₄, instead, a total yield of 0.264 g was achieved in 4.5 h, but the quality of the product was evidently much lower than the previous ones, with the additional reflection at about 5° again visible and evidence of diffuse scattering between 7 and 11°, most likely due to the presence of amorphous matter, which is also supported by SEM (Figure 5.27 and B.2c).

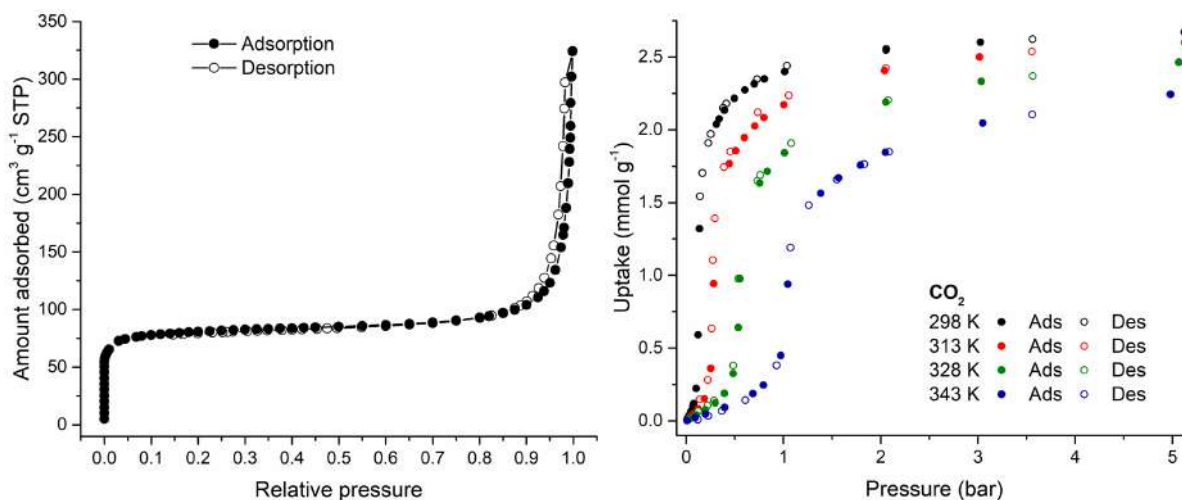


Figure 5.28: (Left) N_2 adsorption-desorption isotherm of F4_MIL-140A(Ce) powder obtained from synthesis performed at 60°C in the presence of 32 equivalents of HNO_3 . $\text{BET } S_A = 315 \text{ m}^2 \text{ g}^{-1}$. (Right) CO_2 adsorption-desorption isotherms of F4_MIL-140A(Ce) powder obtained from synthesis performed at 60°C in the presence of 32 equivalents of HNO_3 .

These experiments demonstrate that the combination of CAN as the Ce(IV) precursor and HNO_3 as the protonation modulator provides the best compromise in terms of reaction time, yield and quality of the F4_MIL-140A(Ce) product. This material displays the characteristic phase-change behaviour expected for F4_MIL-140A(Ce) and even higher CO_2 uptake at saturation (about 2.6 mmol g^{-1} , Figure 5.28) than that previously observed for the MOF obtained with the original synthesis conditions (about 2.0 mmol g^{-1}). Therefore, future efforts will be aimed at upscaling the synthetic protocol using CAN and HNO_3 . The fact that the reaction temperature (60°C) is well below the normal boiling point of water is a great advantage for upscaling, because there is no need for sophisticated, pressure resistant vessels.

5.3.6 Scale-up of F4_MIL-140A(Ce)

With the current need for cost-effective, robust, and environmentally deployment of CO_2 capture technologies, synthetic optimisation and scale-up of promising CO_2 sorbents will be an essential piece to the puzzle.⁴¹ Current CO_2 capture technologies primarily employ liquid-based amine scrubbing processes hampered by chemical stability, corrosion, and volatility issues, as well as high energy of regeneration.⁴²

Solid-based sorbents promise to be more stable, less energy intensive, and easier to operate in both temperature and pressure swing adsorption conditions, or a combination thereof. MOFs are often touted for their exceptional CO₂ adsorption properties, owing to their pore size and pore chemistry tunability.⁴³ MOFs with outstanding CO₂ capture performance are consistently reported in the literature and continue to be screened physically and computationally, though large scale production at a competitive cost has yet to be achieved.⁴⁴⁻⁴⁷ The ideal MOF should be made from cheap commercial reagents, non-toxic and readily available solvents (e.g. water), and employ reaction conditions that do not require expensive, special equipment. Furthermore, the process should entail high atom economy and space-time yield (STY).

The promising CO₂ capture properties of F4_MIL-140A(Ce) were already established in the previous section, noting a total uptake at saturation of 2.5 mmol g⁻¹ (1 Bar, 298 K), an IAST CO₂/N₂ selectivity of 1962, which is amongst the highest reported for solid sorbents, and high working capacity to achieve 90% recovery and 95% purity of CO₂. As shown in Figure 5.28, the material has a non-hysteretic S-shaped CO₂ adsorption isotherm where saturation of the pores occurs over a narrow range of pressure, achieving a large working capacity with low regeneration energy penalty. The density of the material is 2.2 g cm⁻³, which is desirable in terms of high volumetric CO₂ capacity, reduced footprint, capital, and operational cost.

With these requirements in mind, the synthetic optimisation and scale-up of F4_MIL-140A(Ce) was the next logical step in assessing its commercial promise. As can be seen in the *in situ* and *ex situ* work discussed in previous sections, the synthesis already occurs in relatively mild conditions (60 °C, 1 hour), though on a very small scale (15 mL volume, 0.2 g yield). The STY here is already 282 kg m⁻³ d⁻¹, which is not undesirable for large scale production, though one of the aims for this work was to increase this to over 400 kg m⁻³ d⁻¹. On achieving this, the synthesis could then be scaled up to achieve a yield over 100 g per batch. To further increase the commercial prospects of the scale up, being able to run the synthesis at room temperature was also

included as one of the main objectives. On achieving these objectives, the material would need to retain its purity, crystallinity, and CO₂ capture properties.

The starting point for the optimisation process began with the model synthesis obtained for the *ex situ* optimisation, labelled **SS-031** in Table B.1 Appendix B, which only aimed to slow down the crystallisation process. Taking the model synthesis (15 mL total volume, 60 °C), the temperature was lowered to 50 °C and run using both the same reagent concentrations (**Ce-001** - 0.050 mol dm⁻³) as well as increasing by 50% (**Ce-002** - 0.075 mol dm⁻³). This resulted in a drop in the overall yield for both runs, though the STY increased for **Ce-002** due to the higher reagent concentration. Attempting to increase the yield and STY, the volume of nitric acid was dropped from 1.5 mL to 1.2 mL, using the same concentrations as previous. The result here was an increase in the yield and the STY to above the initial starting points for both runs (**Ce-003** and **Ce-004**). Further dropping the volume of nitric acid, from 1.2 mL to 1.0 mL, led to a large increase in the yield and STY for **Ce-005**, but only a slight increase for **Ce-006**. Runs **Ce-003** - **Ce-006** were then repeated at room temperature, as opposed to 60 °C. This resulted in a decrease in yield of 20% and 2% for **Ce-007** and **Ce-009**, respectively, both of which were the runs with reagent concentrations of 0.050 mol dm⁻³. For the runs which had a reagent concentration of 0.075 mol dm⁻³, **Ce-008** and **Ce-010**, the drop to room temperature resulted in a 14% and 43% increase, respectively. Note that the larger increase occurred when less nitric acid was present. It should be noted that up until this point, crystallinity has been preserved in all syntheses, for which a representative PXRD pattern can be found in Figure 5.29 when looking at **Ce-004**. Something that this figure also shows in the pattern for **Ce-010**, there are now two phases, of which the second is F4_UiO-66(Ce), and this is also the case for **Ce-011**, which was a repetition of **Ce-010**. While this second phase was present, the material obtained in **Ce-110** maintained the CO₂ sorption properties expected, as shown in Figure 5.30, suggesting that there is not enough of the second phase to make much of a difference.

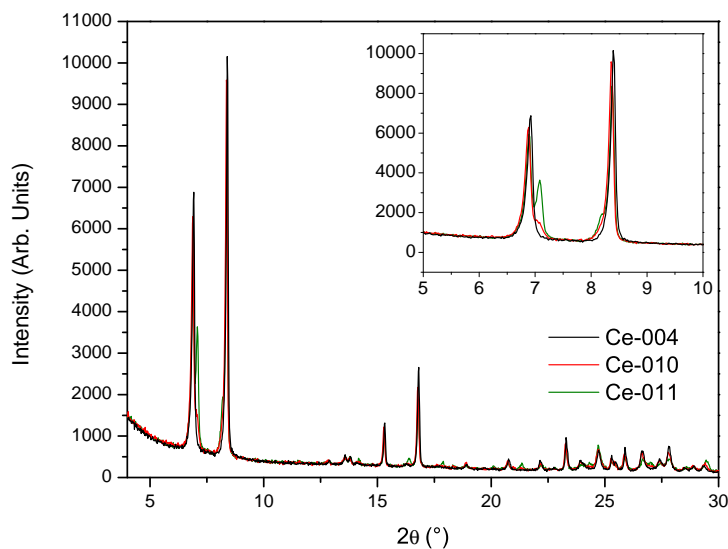


Figure 5.29: PXRD patterns for **Ce-004** (black), **Ce-010** (red), and **Ce-011** (green).

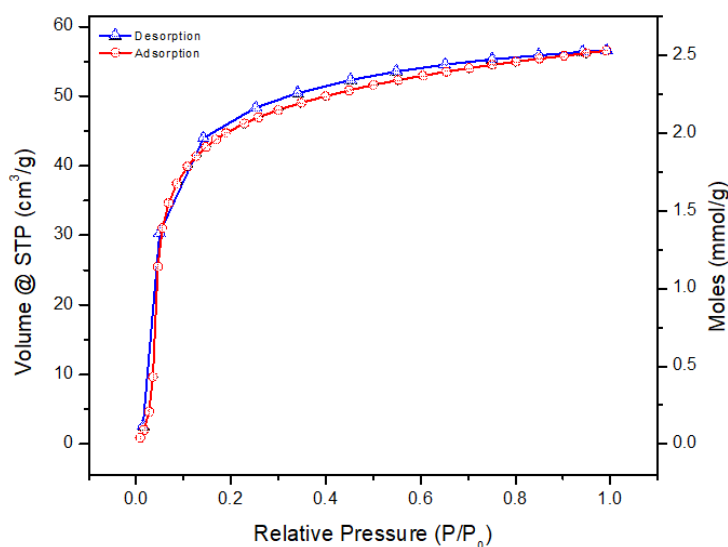


Figure 5.30: CO_2 adsorption isotherm for **Ce-010** obtained at 273 K.

Alongside these syntheses, simultaneous runs were carried out where the nitric acid volume was reduced to 0.8 (**Ce-012**), 0.6 (**Ce-013**), 0.4 (**Ce-014**), and 0.2 mL (**Ce-015**). While F4-UiO-66(Ce) still appeared to be present in **Ce-012**, it was either gone or barely present in the others, all of which had STYs of $674 \text{ kg m}^{-3} \text{ d}^{-1}$ or more and yields above 90%. Moving to the scale up, the next synthesis, **Ce-016**, was carried out in a total volume of 150 mL using 11.2 molar equivalents of nitric acid and reagent concentrations of $0.075 \text{ mol dm}^{-3}$. This resulted in the highest STY and yield for the process so far, reported at $726 \text{ kg m}^{-3} \text{ d}^{-1}$ and 98.4% respectively. Unfortunately, the

PXRD pattern showed a small amount of the F4_UiO-66(Ce) phase to be present, though CO₂ uptake saturation at 1 bar was still in the region of 2.36 mmol/g. On this basis, the scale up was carried out again in a total volume of 300 mL (**Ce-017**). Curiously, the PXRD pattern showed little to no trace of the F4_UiO-66(Ce) phase, and the CO₂ uptake saturation at 1 bar was again within the ideal region at 2.36 mmol/g. The yield and STY here were also promising when compared to where they started, which were above 80% and 600 kg m⁻³ d⁻¹ for the STY.

Spurred on, the synthesis was then scaled up 10-fold to 3.0 L, though it resulted in a slight drop in intensity in the PXRD pattern and a slight drop in CO₂ uptake, which was now 2.14 mmol/g. Unfortunately, it was impossible to obtain an accurate STY or yield for this run due to human error. Despite this, most of the sample was recovered and the STY and yield were still recorded as being 553 kg m⁻³ d⁻¹ and 75%. It is expected that at least 5-10 g more of sample could have been recovered, taking the yield up to between 81-86%. The final synthesis was subject to further scale up, taking the total volume to 4.5 L, and gave a yield of 98.1 % and an STY of 724 kg m⁻³ d⁻¹. The PXRD pattern also showed no sign of the F4_UiO-66(Ce) phase and showed reasonable crystallinity. With regards to CO₂ sorption properties, however, there was a drop in the total uptake, which is not shown to be in the region of 1.9 mmol/g, which constitutes just over a 20% drop in total CO₂ capacity.

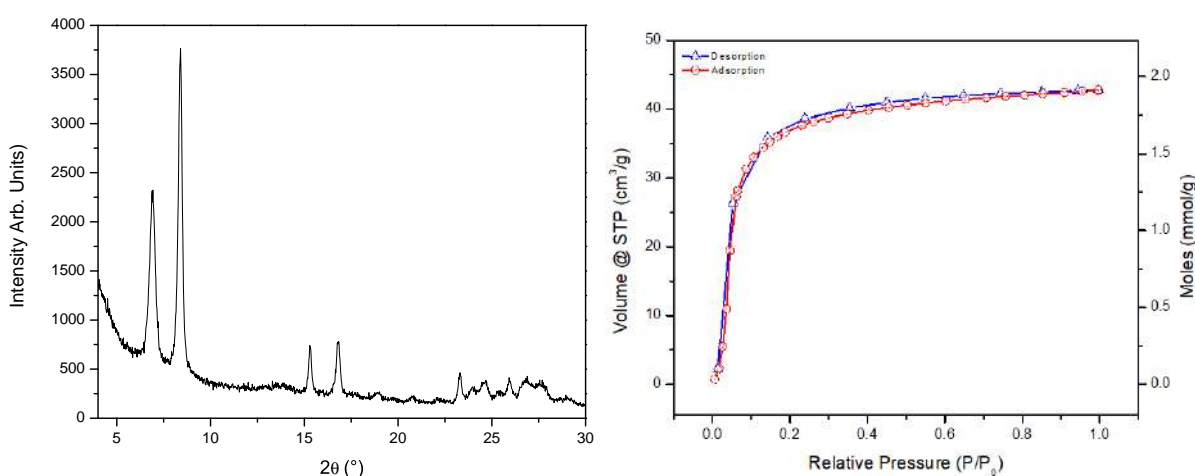


Figure 5.31: PXRD pattern and CO₂ adsorption isotherm for **Ce-020** obtained at 273 K.

5.4 Conclusions

In this work, we have performed a systematic *in situ* PXRD investigation of the influence of various reaction parameters on the thermodynamics and kinetics of crystallisation of the recently discovered perfluorinated Ce(IV)-based MOFs F4_MIL-140A(Ce) and F4_UiO-66(Ce) in aqueous medium. We introduced the use of HNO₃ as a protonation modulator, which allowed us to finely control the kinetics of crystallisation. The main outcomes of this investigation are visually summarised in Figure 5.32. In the presence of just HNO₃, phase pure F4_MIL-140A(Ce) was observed (System I in Figure 5.32). The effect of temperature and amount of HNO₃ was assessed for this system, finding that heating mainly accelerates nucleation,

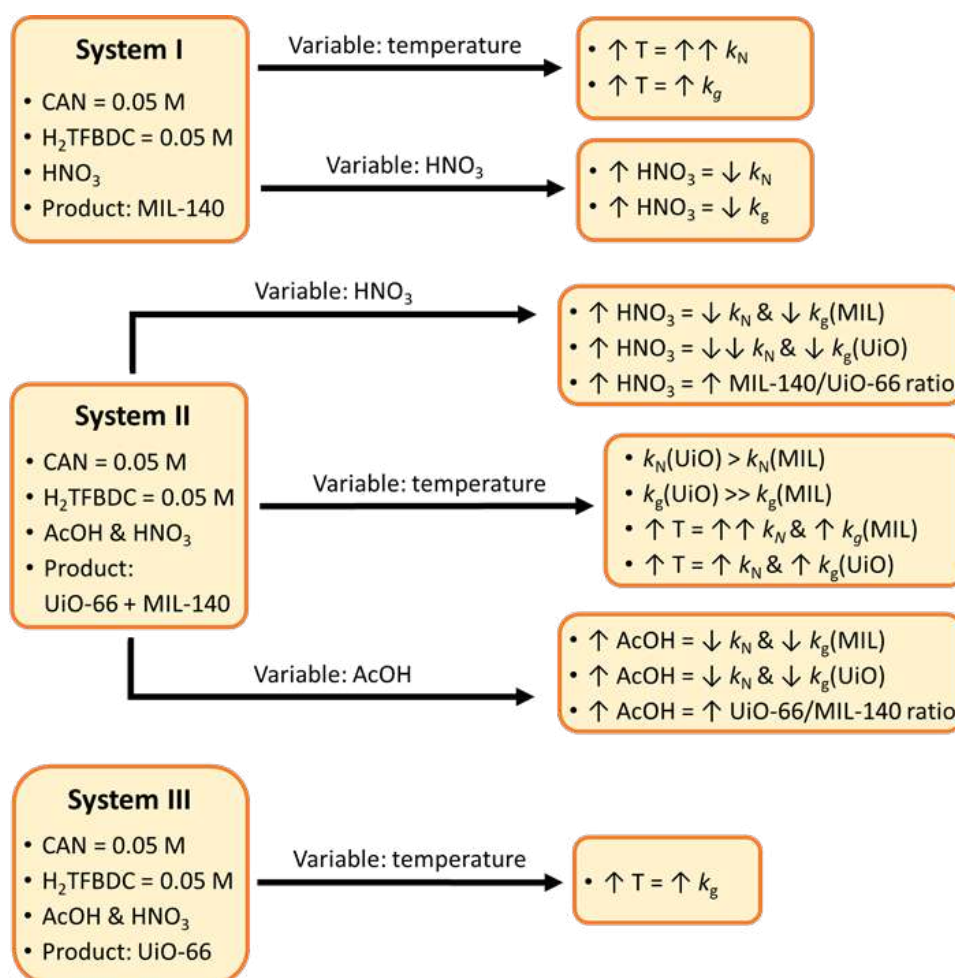


Figure 5.32: Visual summary of the main outcomes of the *in situ* PXRD study. Arrows pointing up indicate an increase of a parameter, arrows pointing down indicate a decrease of a parameter.

whereas the modulator influences nucleation and crystal growth to a similar extent. At temperatures above 57 °C, crystal growth becomes the rate determining process. Upon addition of AcOH to the system, alongside HNO₃, mixed-phased products, consisting of F4_MIL-140A(Ce) and F4_UiO-66(Ce), were obtained (System II in Figure 5.32). This makes it clear that AcOH is essential for the formation of the F4_UiO-66(Ce) phase. In all experiments with AcOH, the F4_UiO-66(Ce) phase formed earlier and faster than the F4_MIL-140A(Ce) phase, but we did not observe any significant degree of interconversion between the two phases in the investigated reaction conditions, suggesting that the two phases form independently and compete for the reagents in solution. Different from F4_MIL-140A(Ce), crystal growth is the rate determining step for the F4_UiO-66(Ce) phase. Comparing the two modulators in the mixed-phase system, we see that a decrease in the amount of HNO₃ present results in the preferential acceleration of nucleation for the F4_UiO-66(Ce) phase, whereas the F4_MIL-140A(Ce) phase experiences similar effect on nucleation and crystal growth. For AcOH, a decrease in the amount used leads to the acceleration of both nucleation and growth to a similar extent for both phases. Looking at the intensity ratios of the fully crystallised products alone, it is clear that HNO₃ favours the formation of the F4_MIL-140A(Ce) phase, while AcOH favours the formation of the F4_UiO-66(Ce) phase, which can be obtained in pure form in the presence of a large amount of AcOH (149 equivalents) and a little HNO₃ (8 equivalents). Thus, the coordination modulator appears to favour the kinetic product, probably by promoting the formation of the inorganic clusters necessary to construct the framework of F4_UiO-66(Ce), which grows upon exchange of acetate by TFBDC²⁻. This process reduces the concentration of isolated Ce(IV) ions from the solution, preventing them from reacting with TFBDC²⁻ to form F4_MIL-140A(Ce). Finally, we screened different combinations of Ce(IV) source and protonation modulator for the synthesis of F4_MIL-140A(Ce) *ex situ*, finding that the best results are obtained when CAN is the metal source and HNO₃ is the modulator. Based on these results, an optimised route to achieving F4_MIL-140A(Ce) in mild conditions (60 °C, 1 h) at the small scale was identified. The fundamental

understanding of the crystallisation process of perfluorinated Ce(IV)-based MOFs led to the development of the protocols for the scale up of their synthesis, in particular for F4_MIL-140A(Ce), given its interesting CO₂ capture properties. The result of this was this scale up was a 770-fold increase in the yield from 150 mg to 135 g, an increase in the %yield from 55% to over 95%, and a 2.5-fold increase of the STY to 724 kg m⁻³ d⁻¹. Unfortunately, there was also a slight drop in the crystallinity as well as a 25% drop in the CO₂ sorption capacity. Despite this, the material should still be considered promising for further commercialisation, of which would likely lead to a more crystalline material with higher CO₂ sorption capacity.

5.5 References

1. M. J. Van Vleet, T. Weng, X. Li and J. R. Schmidt, "In Situ, Time-Resolved, and Mechanistic Studies of Metal-Organic Framework Nucleation and Growth", *Chem. Rev.*, 2018, **118**, 3681–3721, DOI: 10.1021/acs.chemrev.7b00582.
2. R. I. Walton and F. Millange, in *The Chemistry of Metal-Organic Frameworks: Synthesis, Characterization, and Applications*, ed. S. Kaskel, Wiley-VCH, 2016, ch. 24, pp. 729–764, DOI: 10.1002/9783527693078.ch24.
3. N. Pienack and W. Bensch, "In situ monitoring of the formation of crystalline solids", *Angew. Chem. Int. Ed.*, 2011, **50**, 2014–34, DOI: 10.1002/anie.201001180.
4. H. H. Yeung, A. F. Sapnik, F. Massingberd-Mundy, M. W. Gaultois, Y. Wu, D. A. X. Fraser, S. Henke, R. Pallach, N. Heidenreich, O. V. Magdysyuk, N. T. Vo and A. L. Goodwin, "Control of Metal-Organic Framework Crystallization by Metastable Intermediate Pre-equilibrium Species", *Angew. Chem. Int. Ed.*, 2019, **58**, 566–571, DOI: 10.1002/anie.201810039.
5. Y. Wu, M. I. Breeze, G. J. Clarkson, F. Millange, D. O'Hare and R. I. Walton, "Exchange of Coordinated Solvent During Crystallization of a Metal-Organic Framework Observed by In Situ High-Energy X-ray Diffraction", *Angew. Chem. Int. Ed.*, 2016, **55**, 4992–6, DOI: 10.1002/anie.201600896.
6. G. Zahn, P. Zerner, J. Lippke, F. L. Kempf, S. Lilienthal, C. A. Schröder, A. M. Schneider and P. Behrens, "Insight into the mechanism of modulated syntheses: in situ synchrotron diffraction studies on the formation of Zr-fumarate MOF", *CrystEngComm*, 2014, **16**, 9198–9207, DOI: 10.1039/c4ce01095g.

7. J. Cravillon, C. A. Schröder, H. Bux, A. Rothkirch, J. Caro and M. Wiebcke, "Formate modulated solvothermal synthesis of ZIF-8 investigated using time-resolved *in situ* X-ray diffraction and scanning electron microscopy", *CrystEngComm*, 2012, **14**, 492–498, DOI: 10.1039/c1ce06002c.
8. F. Millange, R. El Osta, M. E. Medina and R. I. Walton, "A time-resolved diffraction study of a window of stability in the synthesis of a copper carboxylate metal-organic framework", *CrystEngComm*, 2011, **13**, 103–108, DOI: 10.1039/c0ce00530d.
9. X. Sang, J. Zhang, J. Xiang, J. Cui, L. Zheng, J. Zhang, Z. Wu, Z. Li, G. Mo, Y. Xu, J. Song, C. Liu, X. Tan, T. Luo, B. Zhang and B. Han, "Ionic liquid accelerates the crystallization of Zr-based metal-organic frameworks", *Nat. Commun.*, 2017, **8**, 175, DOI: 10.1038/s41467-017-00226-y.
10. M. G. Goesten, E. Stavitski, J. Juan-Alcañiz, A. Martínez-Joaristi, A. V. Petukhov, F. Kapteijn and J. Gascon, "Small-angle X-ray scattering documents the growth of metal-organic frameworks", *Catal. Today*, 2013, **205**, 120–127, DOI: 10.1016/j.cattod.2012.08.044.
11. E. Stavitski, M. Goesten, J. Juan-Alcañiz, A. Martínez-Joaristi, P. Serra-Crespo, A. V. Petukhov, J. Gascon and F. Kapteijn, "Kinetic control of metal-organic framework crystallization investigated by time-resolved *in situ* X-ray scattering", *Angew. Chem. Int. Ed.*, 2011, **50**, 9624–8, DOI: 10.1002/anie.201101757.
12. S. Van Cleuvenbergen, Z. J. Smith, O. Deschaume, C. Bartic, S. Wachsmann-Hogiu, T. Verbiest and M. A. van der Veen, "Morphology and structure of ZIF-8 during crystallisation measured by dynamic angle-resolved second harmonic scattering", *Nat. Commun.*, 2018, **9**, 3418, DOI: 10.1038/s41467-018-05713-4.
13. J. Cravillon, R. Nayuk, S. Springer, A. Feldhoff, K. Huber and M. Wiebcke, "Controlling Zeolitic Imidazolate Framework Nano- and Microcrystal Formation: Insight into Crystal Growth by Time-Resolved *In Situ* Static Light Scattering", *Chem. Mater.*, 2011, **23**, 2130–2141, DOI: 10.1021/cm103571y.
14. C. L. Jones, C. E. Hughes, H. H.-M. Yeung, A. Paul, K. D. M. Harris and T. L. Easun, "Exploiting *in situ* NMR to monitor the formation of a metal-organic framework", *Chem Sci*, 2021, **12**, 1486–1494, DOI: 10.1039/D0SC04892E.
15. S. L. Griffin, M. L. Briuglia, J. H. Ter Horst and R. S. Forgan, "Assessing Crystallisation Kinetics of Zr Metal-Organic Frameworks through Turbidity Measurements to Inform Rapid Microwave-Assisted Synthesis", *Chem. Eur. J.*, 2020, **26**, 6910–6918, DOI: 10.1002/chem.202000993.
16. F. Massingberd-Mundy, S. Poulston, S. Bennett, H. H. Yeung and T. Johnson, "Use of open source monitoring hardware to improve the production of MOFs: using STA-16(Ni) as a case study", *Sci. Rep.*, 2020, **10**, 17355, DOI: 10.1038/s41598-020-73780-z.

17. B. Bueken, H. Reinsch, N. Heidenreich, A. Vandekerckhove, F. Vermoortele, C. E. A. Kirschhock, N. Stock, D. De Vos and R. Ameloot, "An in situ investigation of the water-induced phase transformation of UTSA-74 to MOF-74(Zn)", *CrystEngComm*, 2017, **19**, 4152–4156, DOI: 10.1039/c7ce00094d.
18. Y. F. Zhang, Q. Wang, D. X. Xue and J. Bai, "Single-Crystal Synthesis and Diverse Topologies of Hexanuclear Ce(IV)-Based Metal-Organic Frameworks", *Inorg. Chem.*, 2020, **59**, 11233–11237, DOI: 10.1021/acs.inorgchem.0c01646.
19. M. Lammert, M. T. Wharmby, S. Smolders, B. Bueken, A. Lieb, K. A. Lomachenko, D. D. Vos and N. Stock, "Cerium-based metal organic frameworks with UiO-66 architecture: synthesis, properties and redox catalytic activity", *Chem. Commun.*, 2015, **51**, 12578–81, DOI: 10.1039/c5cc02606g.
20. S. Smolders, K. A. Lomachenko, B. Bueken, A. Struyf, A. L. Bugaev, C. Atzori, N. Stock, C. Lamberti, M. B. J. Roeffaers and D. E. De Vos, "Unravelling the Redox-catalytic Behavior of Ce⁴⁺ Metal-Organic Frameworks by X-ray Absorption Spectroscopy", *ChemPhysChem*, 2018, **19**, 373–378, DOI: 10.1002/cphc.201700967.
21. T. Islamoglu, A. Atilgan, S.-Y. Moon, G. W. Peterson, J. B. DeCoste, M. Hall, J. T. Hupp and O. K. Farha, "Cerium(IV) vs Zirconium(IV) Based Metal-Organic Frameworks for Detoxification of a Nerve Agent", *Chem. Mater.*, 2017, **29**, 2672–2675, DOI: 10.1021/acs.chemmater.6b04835.
22. Y. Song, Y. Pi, X. Feng, K. Ni, Z. Xu, J. S. Chen, Z. Li and W. Lin, "Cerium-Based Metal-Organic Layers Catalyze Hydrogen Evolution Reaction through Dual Photoexcitation", *J. Am. Chem. Soc.*, 2020, **142**, 6866–6871, DOI: 10.1021/jacs.0c00679.
23. M. Campanelli, T. Del Giacco, F. De Angelis, E. Mosconi, M. Taddei, F. Marmottini, R. D'Amato and F. Costantino, "Solvent-Free Synthetic Route for Cerium(IV) Metal-Organic Frameworks with UiO-66 Architecture and Their Photocatalytic Applications", *ACS Appl. Mater. Interfaces*, 2019, **11**, 45031–45037, DOI: 10.1021/acsami.9b13730.
24. X. Qiu, Y. Zhu, X. Zhang, Y. Zhang, L. T. Menisa, C. Xia, S. Liu and Z. Tang, "Cerium-Based Metal-Organic Frameworks with UiO Architecture for Visible Light-Induced Aerobic Oxidation of Benzyl Alcohol", *Sol. RRL*, 2019, **4**, DOI: 10.1002/solr.201900449.
25. X. P. Wu, L. Gagliardi and D. G. Truhlar, "Cerium Metal-Organic Framework for Photocatalysis", *J. Am. Chem. Soc.*, 2018, **140**, 7904–7912, DOI: 10.1021/jacs.8b03613.
26. J. Jacobsen, A. Ienco, R. D'Amato, F. Costantino and N. Stock, "The chemistry of Ce-based metal-organic frameworks", *Dalton Trans.*, 2020, DOI: 10.1039/d0dt02813d.
27. N. Heidenreich, S. Waitschat and H. Reinsch, "Investigation of the Kinetic Stabilization of a Ce⁴⁺-based MOF by *in situ* Powder X-ray Diffraction", *Zeitschrift für anorganische und allgemeine Chemie*, 2018, **644**, 1826–1831, DOI: 10.1002/zaac.201800354.

28. R. D'Amato, A. Donnadio, M. Carta, C. Sangregorio, D. Tiana, R. Vivani, M. Taddei and F. Costantino, "Water-Based Synthesis and Enhanced CO₂ Capture Performance of Perfluorinated Cerium-Based Metal-Organic Frameworks with UiO-66 and MIL-140 Topology", *ACS Sustainable Chem. Eng.*, 2018, **7**, 394–402, DOI: 10.1021/acssuschemeng.8b03765.
29. V. Guillermin, F. Ragon, M. Dan-Hardi, T. Devic, M. Vishnuvarthan, B. Campo, A. Vimont, G. Clet, Q. Yang, G. Maurin, G. Férey, A. Vittadini, S. Gross and C. Serre, "A series of isorecticular, highly stable, porous zirconium oxide based metal-organic frameworks", *Angew. Chem. Int. Ed.*, 2012, **51**, 9267–71, DOI: 10.1002/anie.201204806.
30. D. Bara, C. Wilson, M. Mörtel, M. M. Khusniyarov, S. Ling, B. Slater, S. Sproules and R. S. Forgan, "Kinetic Control of Interpenetration in Fe-Biphenyl-4,4'-dicarboxylate Metal-Organic Frameworks by Coordination and Oxidation Modulation", *J. Am. Chem. Soc.*, 2019, **141**, 8346–8357, DOI: 10.1021/jacs.9b03269.
31. L. Yang, T. Zhao, I. Boldog, C. Janiak, X.-Y. Yang, Q. Li, Y.-J. Zhou, Y. Xia, D.-W. Lai and Y.-J. Liu, "Benzoic acid as a selector-modulator in the synthesis of MIL-88B(Cr) and nano-MIL-101(Cr)", *Dalton Trans.*, 2019, **48**, 989–996, DOI: 10.1039/c8dt04186e.
32. M. Schulz, N. Marquardt, M. Schäfer, D. P. Warwas, S. Zailskas and A. Schaate, "A Low-Temperature Approach for the Phase-Pure Synthesis of MIL-140 Structured Metal-Organic Frameworks", *Chem. Eur. J.*, 2019, **25**, 13598–13608, DOI: 10.1002/chem.201902981.
33. N. Heidenreich, U. Rutt, M. Koppen, A. K. Inge, S. Beier, A. C. Dippel, R. Suren and N. Stock, "A multi-purpose reaction cell for the investigation of reactions under solvothermal conditions", *Rev. Sci. Instrum.*, 2017, **88**, 104102, DOI: 10.1063/1.4999688.
34. M. Basham, J. Filik, M. T. Wharmby, P. C. Chang, B. El Kassaby, M. Gerring, J. Aishima, K. Levik, B. C. Pulford, I. Sikharulidze, D. Sneddon, M. Webber, S. S. Dhesi, F. Maccherozzi, O. Svensson, S. Brockhauser, G. Naray and A. W. Ashton, "Data Analysis WorkbeNch (DAWN)", *J. Synchrotron Radiat.*, 2015, **22**, 853–8, DOI: 10.1107/S1600577515002283.
35. J. Filik, A. W. Ashton, P. C. Y. Chang, P. A. Chater, S. J. Day, M. Drakopoulos, M. W. Gerring, M. L. Hart, O. V. Magdysyuk, S. Michalik, A. Smith, C. C. Tang, N. J. Terrill, M. T. Wharmby and H. Wilhelm, "Processing two-dimensional X-ray diffraction and small-angle scattering data in DAWN 2", *J. Appl. Crystallogr.*, 2017, **50**, 959–966, DOI: 10.1107/S1600576717004708.
36. T. De Bruijn, W. De Jong and P. Van Den Berg, "Kinetic parameters in Avrami-Erofeev type reactions from isothermal and non-isothermal experiments", *Thermochim. Acta*, 1981, **45**, 315–325, DOI: 10.1016/0040-6031(81)85091-5.
37. A. F. Gualtieri, "Synthesis of sodium zeolites from a natural halloysite", *Phys. Chem. Miner.*, 2001, **28**, 719–728, DOI: 10.1007/s002690100197.

38. J.-X. Gu, H. Chen, Y. Ren, Z.-G. Gu, G. Li, W.-J. Xu, X.-Y. Yang, J.-X. Wen, J.-T. Wu and H.-G. Jin, "A Novel Cerium(IV)-Based Metal-Organic Framework for CO₂/sub Chemical Fixation and Photocatalytic Overall Water Splitting", *ChemSusChem*, 2021, **15**, DOI: 10.1002/cssc.202102368.
39. H. Reinsch and N. Stock, "Formation and characterisation of Mn-MIL-100", *CrystEngComm*, 2013, **15**, 544–550, DOI: 10.1039/c2ce26436f.
40. F. Ragon, P. Horcajada, H. Chevreau, Y. K. Hwang, U. H. Lee, S. R. Miller, T. Devic, J. S. Chang and C. Serre, "In situ energy-dispersive X-ray diffraction for the synthesis optimization and scale-up of the porous zirconium terephthalate UiO-66", *Inorg. Chem.*, 2014, **53**, 2491–500, DOI: 10.1021/ic402514n.
41. *Energy white paper: Powering our net zero future*, Department for Business, Energy & Industrial Strategy, UK Government, 2020.
42. K. Veltman, B. Singh and E. G. Hertwich, "Human and Environmental Impact Assessment of Postcombustion CO₂ Capture Focusing on Emissions from Amine-Based Scrubbing Solvents to Air", *Environ. Sci. Technol.*, 2010, **44**, 1496–1502, DOI: 10.1021/es902116r.
43. J. A. Mason, K. Sumida, Z. R. Herm, R. Krishna and J. R. Long, "Evaluating metal-organic frameworks for post-combustion carbon dioxide capture via temperature swing adsorption", *Energy Environ. Sci.*, 2011, **4**, 3030, DOI: 10.1039/c1ee01720a.
44. J. M. Simmons, H. Wu, W. Zhou and T. Yildirim, "Carbon capture in metal-organic frameworks - a comparative study", *Energy Environ. Sci.*, 2011, **4**, 2177, DOI: 10.1039/c0ee00700e.
45. R. Aniruddha, I. Sreedhar and B. M. Reddy, "MOFs in carbon capture-past, present and future", *Journal of CO₂ Utilization*, 2020, **42**, 101297, DOI: 10.1016/j.jcou.2020.101297.
46. G. Avci, I. Erucar and S. Keskin, "Do New MOFs Perform Better for CO₂ Capture and H₂ Purification? Computational Screening of the Updated MOF Database", *ACS Appl. Mater. Interfaces*, 2020, **12**, 41567–41579, DOI: 10.1021/acsami.0c12330.
47. M. Younas, M. Rezakazemi, M. Daud, M. B. Wazir, S. Ahmad, N. Ullah, Inamuddin and S. Ramakrishna, "Recent progress and remaining challenges in post-combustion CO₂ capture using metal-organic frameworks (MOFs)", *Prog. Energy Combust. Sci.*, 2020, **80**, 100849, DOI: 10.1016/j.pecs.2020.100849.

5.6 Copyright and Authorship

This chapter was published in *Chemistry - A European Journal*, which operates under the Wiley trademark, and has been adapted with permission of the copyright holder.

Adaptions have been made to include the supporting information into the main body of work. Full citation:

Shearan, S.J.I., Jacobsen, J., Costantino, F., D'Amato, R., Novikov, D., Stock, N., Andreoli, E. and Taddei, M. (2021), In situ X-ray Diffraction Investigation of the Crystallisation of Perfluorinated Ce(IV)-based Metal-Organic Frameworks with UiO-66 and MIL-140 architectures. Chem. Eur. J. 2021, 27, 6579. DOI: 10.1002/chem.202005085

Conceptualisation: Marco Taddei

Ex-situ work: Stephen Shearan, Marco Taddei

In-situ work: Stephen Shearan, Jannick Jacobsen, Ferdinando Costantino, Marco Taddei

Data Analysis: Stephen Shearan, Marco Taddei

Manuscript drafting: Stephen Shearan, Marco Taddei

Manuscript review and revisions: Stephen Shearan, Jannick Jacobsen, Ferdinando Costantino, Norbert Stock, Enrico Anddreoli, Marco Taddei

Other work: Dmitri Novikov (Beamline scientist), Roberto D'Amato

Chapter 6

Conclusions and Outlook

From the beginning, this thesis has three main goals in mind. Firstly, to explore the synthesis of novel N-polyaryl phosphonic acid-based linkers. Second, employing these linkers in the synthesis of metal phosphonate MOFs based on tetravalent metals and assessing how linker geometry affects the subsequent crystal structure. And finally, to explore the crystallisation kinetics of two newly discovered Ce-MOFs which are analogues to the well known MIL-140A and UiO-66. A simplified all encompassing aim would be to explore synthesis, optimisation, and crystallisation kinetics of novel and recently discovered materials for CO₂ capture and other applications.

With regards to the first of these goals, Chapter 3 explores the synthesis of novel N-polyaryl phosphonic acid linkers with V-shape and Y-shape geometries. The aim here was to produce a series of linkers which would later be employed in the synthesis of potentially microporous metal phosphonates frameworks. The novel factor here, however, lies not only with the synthesis of the linkers, but in the synthetic procedure itself. The conventional synthetic procedure for obtaining the phosphonate ester is, in fact, where these improvements were made, where reaction times are often in excess of 24 hours and employ temperatures well in excess of 160 °C. The main reason of the long reaction times was mostly a result of the large volumes of solvent used relative to the reactants. Referring to Figure 3.2, there was also a point to be made about the order of addition for the reactants. Traditionally, the aryl-bromide substrate

was dissolved in a suitable solvent, and the NiCl_2 pre-catalyst was added straight into this solution. The trialkyl phosphite would then be added drop-wise. Referring to the catalytic cycle, we realised that it might speed up the process if the phosphite (in full) and the pre-catalyst were added to the reaction vessel with no additional solvent present, since the phosphite actually acts as the solvent itself at high temperatures and is already used in excess. This means that the catalyst for the reaction is pre-formed before the substrate is added. We then added the aryl-bromide substrate via a powder addition funnel through which a flow of inert gas was maintained to prevent vapour from entering the funnel. Using this method, the reaction times were cut from 24+ hours down to 4-6 hours with no negative effects seen in purity or the final yield. This is obviously a great cost saving in terms of not needing to buy potentially expensive solvents, and clearly saves a great amount of time which could in fact be used to run additional syntheses. With this development, three novel linkers were obtained in good yields, generally above 80%, after silylation and subsequent hydrolysis.

Looking at the second goal, Chapter 4 looks at the use of the three novel N-polyaryl phosphonic acid linkers in the synthesis of metal phosphonate frameworks, specifically assessing the effect of linker geometry on the final structure. Phosphonic acid-based linkers are considered for use in MOF synthesis mainly due to their increased chemical, thermal, and hydrolytic stability compared with the more conventional carboxylate linkers. Where these linkers often fall, however, is that they often produce layered or pillared-layered structures, usually brought about by the linear geometry of the linker. Early on, structures such as Zr-phenylphosphonate presented layered structures whereby the phenyl group would point into the interlayer space. We would also see structures based on phenyldiphosphonates which cross-linked these layers, forming the so-called pillared-layered structure. The idea behind the work present in Chapter 3 was that moving away from these linear linkers would force the structure of subsequent metal phosphonates out of the pillared-layered motif. This was first achieved in 2014 when Taddei et al. published their work on

UPG-1, a MOF made up of 1D $[\text{ZrO}_6]_n$ chains and connected via the H_6ttbmp linker. Going ahead with the use of the novel linkers in MOF synthesis, we found that both H_4BPA and H_4DPC produced pillared-layered materials which were not really in the scope of the research. Despite this, ZrBPA did, in fact, display some microporosity and had a CO_2 uptake of $16.6 \text{ cm}^3 \text{ g}^{-1}$ or 0.75 mmol/g (273 K, 1 atm). As well as this, the blue colour of the material suggested that it might also prove to have interesting photochemical properties, which did indeed turn out to be the case, with an optical band gap energy 2.0-2.2 eV and a reasonable performance in the degradation of Rhodamine-B dye under a solar energy source. Skipping over H_4DPC due to time issues, the focus shifted to H_4DPPA . This linker turned out to be the best performing in terms of producing a microporous MOF, showing multiple pore types below 10 \AA in diameter which were accessible to CO_2 , for which the total uptake was $51 \text{ cm}^3 \text{ g}^{-1}$ or 2.3 mmol/g (273 K, 1 atm). This is comparable with F4_MIL-140A(Ce) , which was explored in Chapter 5 due to its promising CO_2 capture properties, where the total uptake was $56 \text{ cm}^3 \text{ g}^{-1}$ or 2.5 mmol/g (273 K, 1 atm).

Moving to the final goal, Chapter 5 reports the results of an *in situ* XRD study which looked at the crystallisation kinetics of F4_MIL-140A(Ce) and F4_UiO-66(Ce) , and how crystallisation was affected when different reaction parameters were changed. We initially explored the use of HNO_3 as a protonation modulator, which was vital in obtaining fine control of the crystallisation kinetics. The result of using HNO_3 was that phase pure F4_MIL-140A(Ce) was obtained, later becoming the basis of a scale-up study due to the previously mentioned CO_2 capture properties. We also found increasing or decreasing the temperature would, respectively, accelerate or decelerate the nucleation rate. The addition of AcOH as a coordination modulator was also assessed, and when used alongside HNO_3 , it resulted in mixed-phase products containing F4_MIL-140A(Ce) and F4_UiO-66(Ce) . In these reactions, it was generally observed that the F4_UiO-66(Ce) phase formed earlier and faster than F4_MIL-140A(Ce) , suggesting that the former is the kinetic product and the latter is

the thermodynamic product. A phase pure F4_UiO-66(Ce) product is obtained when using larger amount of AcOH and smaller amounts of HNO₃, which is likely due to the lower concentration of Ce(IV) ions in solution since they are coordinated to form Ce(IV) acetate. A screening of alternative metals sources and modulators showed that CAN and HNO₃ were in fact already the best options. Following the *in situ* work, we carried out synthetic optimisation and scale up studies on F4_MIL-140A(Ce) due to the interest in deploying it for CO₂ capture at a larger scale, which obviously necessitates the need to scale up and optimise the synthesis. Achieving some success in this, we were able to increase the yield 700-fold to 135 g. While there were drops in both crystallinity and the CO₂ capacity, this could still be considered viable for testing on a larger scale and could even undergo further optimisation.

Future Work

As is clear to all of us, the past two years have been fraught with immense difficulties due to the ongoing COVID-19 pandemic. For those of us working on laboratory-based projects, these difficulties might be even clearer in the sense that we have suffered a lack of access to these facilities for at least six months, though considerably more if you include subsequent restrictions since the initial lockdown ended. With regards to the work presented in this thesis, these difficulties, both direct and indirect, have meant that there is a lot of work that has not been carried out, whether due to a lack of time, or lack of access to equipment. To this end, I will detail all of the work I would like to see carried out in the future in order to fully round-off this work.

Starting with the synthesis of the linkers, further exploration, in terms of isorecticular expansion and synthesis of further analogues with V-shape and Y-shape geometries, should ideally lead to materials which display significant microporosity and potentially favourable CO₂ capture properties. It would also be interesting to carry out photocatalytic studies on the linkers themselves, and this was in fact suggested at the *2nd European Workshop on Metal Phosphonates and Phosphinates* by Prof. Dr. Jens

Beckmann, who had previously carried out such work on similar linkers. Another potential avenue for the linkers might involve retrosynthesis, mainly due to the high cost of the Br-precursors. Lowering the cost here would be of great benefit to the potential of these linkers and any subsequent materials they produce.

In terms of the metal phosphonate materials, I would have liked to have carried out water splitting experiments where ZrBPA and ZrDPPA were employed as the photocatalysts, since both have optical band gap energies that are considered to be in the optimal range for effective water splitting. On this, it would also have been ideal to have carried out the dye degradation studies with ZrDPPA. Further characterisation of the the phases employing H₄DPC as the linker would also provide some very valuable information for this work.

Moving finally to the Ce(IV)-MOFs, particularly that of F4_MIL-140A(Ce), it would be ideal for testing under dynamic conditions, such as breakthrough analysis, in order to further assess its capability as a CO₂ capture sorbent. With regards to this, shaping of the material is also important for this purpose, and this was already crudely attempted in this work through slow evaporation of the wash solvent (MeOH) in a mold, which led to the formation of relatively mechanically strong pellets. There is also an ongoing discussion with the Cambridge University spinout company, Immaterial Ltd, with regards to shaping the material through monolith formation.

Appendix A

Metal Phosphonate Synthesis

The tables in this section show the synthetic parameters used in the synthesis of metal phosphonates. These tables have been split according to the linker used, giving three tables in total, as shown below:

Table A.1: Synthesis using the bis(4-phosphonophenyl)amine (H_4 BPA) linker.

Table A.2: Synthesis using the 3,6-diphosphono-carbazole (H_4 DPC) linker.

Table A.3: Synthesis using the 4-phosphono-N-(4-phosphonophenyl)-N-phenyl-aniline (H_4 DPPA) linker.

Table A.1: Metal phosphonate synthesis based on the bis(4-phosphonophenyl)amine linker. Unless otherwise stated, all reactions were carried out in a total volume of 10 cm⁻³.

Ref.	Organic Linker		L/M N-ratio	Metal Source			HF		HCl 12 M (mL)	Solvent	V (mL)	H ₂ O (mL)	Yield (mg)	Time (h)	Temp (°C)
	N (mmol)	Mass (mg)		Metal Source	N (mmol)	Mass (mg)	V (mL)	N (mmol)							
059	0.3	91.1349	1.00	ZrOCl ₂ · 8 H ₂ O	0.3	93.0954	0.0010	2.9	N/A	N/A	0.0	9.0	0.0000	93	80
060	0.3	91.1349	1.00	ZrOCl ₂ · 8 H ₂ O	0.3	93.0954	0.0020	5.8	N/A	N/A	0.0	8.0	0.0000	93	80
061	0.3	91.1349	1.00	ZrOCl ₂ · 8 H ₂ O	0.3	93.0954	0.0030	8.7	N/A	N/A	0.0	7.0	0.0000	93	80
065	0.3	91.1349	1.00	ZrOCl ₂ · 8 H ₂ O	0.3	93.0954	0.0008	2.32	N/A	N/A	0.0	9.2	0.0280	144	80
066	0.3	91.1349	1.00	ZrOCl ₂ · 8 H ₂ O	0.3	93.0954	0.0006	1.74	N/A	N/A	0.0	9.4	0.0512	144	80
067	0.6	182.2699	2.00	ZrOCl ₂ · 8 H ₂ O	0.3	93.0954	0.0008	2.32	N/A	N/A	0.0	9.2	0.0591	144	80
068	0.6	182.2699	2.00	ZrOCl ₂ · 8 H ₂ O	0.3	93.0954	0.0006	1.74	N/A	N/A	0.0	9.4	0.0900	144	80
074	0.3	91.1349	1.00	ZrOCl ₂ · 8 H ₂ O	0.3	93.0954	0.0008	2.32	N/A	MeOH	2.2	7.0	0.0530	96	80
075	0.3	91.1349	0.60	ZrOCl ₂ · 8 H ₂ O	0.5	155.1590	0.0008	2.32	N/A	MeOH	2.2	7.0	0.0720	96	80
078	0.3	91.1349	0.60	ZrOCl ₂ · 8 H ₂ O	0.5	155.1590	0.0008	2.32	N/A	MeOH	2.2	7.0	0.0953	167	70
079	0.3	91.1349	0.60	ZrOCl ₂ · 8 H ₂ O	0.5	155.1590	0.0010	2.9	N/A	MeOH	2.2	6.8	0.1075	167	70
080	0.3	91.1349	0.60	ZrOCl ₂ · 8 H ₂ O	0.5	155.1590	0.0012	3.48	N/A	MeOH	2.2	6.6	0.1083	167	70
084	0.3	91.1349	0.60	ZrOCl ₂ · 8 H ₂ O	0.5	155.1590	0.0010	2.9	N/A	MeOH	2.2	6.8	0.0820	121	70
085	0.3	91.1349	0.60	ZrOCl ₂ · 8 H ₂ O	0.5	155.1590	0.0015	4.35	N/A	MeOH	2.2	6.3	0.0500	121	70
088	0.3	91.1349	1.00	ZrOCl ₂ · 8 H ₂ O	0.3	93.0954	0.0008	2.32	0.50	MeOH	2.2	6.5	0.0605	139	80
089	0.3	91.1349	1.00	ZrOCl ₂ · 8 H ₂ O	0.3	93.0954	0.0008	2.32	0.50	EtOH	2.2	6.5	0.0608	139	80
090	0.3	91.1349	1.00	ZrOCl ₂ · 8 H ₂ O	0.3	93.0954	0.0008	2.32	0.50	iPrOH	2.2	6.5	0.0255	139	80
091	0.3	91.1349	1.00	ZrOCl ₂ · 8 H ₂ O	0.3	93.0954	0.0008	2.32	0.50	MeOH	2.2	6.5	0.0826	120	80
092	0.3	91.1349	1.00	ZrOCl ₂ · 8 H ₂ O	0.3	93.0954	0.0008	2.32	0.50	EtOH	2.2	6.5	0.0877	120	80
093	0.3	91.1349	1.00	ZrOCl ₂ · 8 H ₂ O	0.3	93.0954	0.0008	2.32	0.50	iPrOH	2.2	6.5	0.0868	120	80
094	0.3	91.1349	1.00	ZrOCl ₂ · 8 H ₂ O	0.3	93.0954	0.0008	2.32	0.50	Butan-1-ol	2.2	6.5	0.0662	120	80
095	0.3	91.1349	1.00	ZrOCl ₂ · 8 H ₂ O	0.3	93.0954	0.0008	2.32	0.50	DMF	2.2	6.5	0.0000	120	80
096	0.3	91.1349	1.00	ZrOCl ₂ · 8 H ₂ O	0.3	93.0954	0.0008	2.32	0.00	MeOH	7.0	2.2	0.0694	120	80
097	0.3	91.1349	1.00	ZrOCl ₂ · 8 H ₂ O	0.3	93.0954	0.0008	2.32	0.00	MeOH	4.6	4.6	0.0599	120	80
099	0.3	91.1349	1.00	ZrOCl ₂ · 8 H ₂ O	0.3	93.0954	0.0008	2.32	0.50	MeOH	7.0	1.7	0.1079	24	80

Ref.	Organic Linker		L/M N-ratio	Metal Source			HF		HCl 12 M (mL)	Solvent	V (mL)	H ₂ O (mL)	Yield (mg)	Time (h)	Temp (°C)
	N (mmol)	Mass (mg)		Metal Source	N (mmol)	Mass (mg)	V (mL)	N (mmol)							
100	0.3	91.1349	1.00	ZrOCl ₂ · 8 H ₂ O	0.3	93.0954	0.0010	2.90	0.00	MeOH	7.0	2.0	0.0936	24	80
101	0.3	91.1349	1.00	ZrOCl ₂ · 8 H ₂ O	0.3	93.0954	0.0010	2.90	0.50	MeOH	7.0	1.5	0.0997	24	80
102	0.3	91.1349	1.00	ZrOCl ₂ · 8 H ₂ O	0.3	93.0954	0.0004	1.16	0.00	DMF	4.8	4.8	0.0965	48	80
103	0.3	91.1349	1.00	ZrOCl ₂ · 8 H ₂ O	0.3	93.0954	-	-	-	-	-	-	0.1295	0.25	RT
104	0.3	91.1349	1.00	ZrOCl ₂ · 8 H ₂ O	0.3	93.0954	-	-	-	-	-	-	0.0891	0.25	RT
105	0.3	91.1349	1.00	ZrOCl ₂ · 8 H ₂ O	0.3	93.0954	0.0008	2.32	0.00	DMF	4.8	4.4	0.0000	43	80
106	0.3	91.1349	1.00	ZrOCl ₂ · 8 H ₂ O	0.3	93.0954	0.0004	1.16	0.50	DMF	4.8	4.3	0.1025	43	80
107	0.3	91.1349	1.00	ZrOCl ₂ · 8 H ₂ O	0.3	93.0954	0.0004	1.16	0.50	DMF	9.1	0.0	0.1099	43	80
109	0.3	91.1349	1.00	ZrOCl ₂ · 8 H ₂ O	0.3	93.0954	0.0004	1.16	1.00	DMF	8.6	0.0	0.0000	55	100
110	0.6	182.2699	2.00	ZrOCl ₂ · 8 H ₂ O	0.3	93.0954	0.0004	1.16	1.00	DMF	8.6	0.0	0.1469	55	100
113	1.2	364.5398	2.00	ZrOCl ₂ · 8 H ₂ O	0.6	186.1908	N/A	N/A	N/A	N/A	0.0	N/A	0.4223	0.25	100
115	0.3	91.1349	1.00	ZrOCl ₂ · 8 H ₂ O	0.3	93.0954	0.0004	1.16	0.00	DMSO	9.6	0.0	0.1036	97	N/A
116	0.3	91.1349	1.00	ZrOCl ₂ · 8 H ₂ O	0.3	93.0954	0.0004	1.16	0.00	DMSO	4.8	4.8	0.0947	97	100
117	0.3	91.1349	1.00	ZrOCl ₂ · 8 H ₂ O	0.3	93.0954	0.0004	1.16	0.00	DMSO	2.0	7.6	0.1031	97	100
118	0.3	91.1349	1.00	(NH ₄) ₂ Ce(NO ₃) ₆	0.3	54.7186	0.0000	0	0.50	DMF	6.3	3.2	0.0399	N/A	100
119	0.3	91.1349	1.00	(NH ₄) ₂ Ce(NO ₃) ₆	0.3	54.7186	0.0000	0	0.50	DMF	4.7	4.8	0.0519	N/A	60
120	0.3	91.1349	1.00	(NH ₄) ₂ Ce(NO ₃) ₆	0.3	54.7186	0.0000	0	0.50	DMF	2.0	7.5	0.0000	1	60
122	0.3	91.1349	0.60	ZrOCl ₂ · 8 H ₂ O	0.5	155.1590	0.0015	4.35	N/A	MeOH	2.2	6.3	0.0989	26	60
123	0.3	91.1349	0.60	ZrOCl ₂ · 8 H ₂ O	0.5	155.1590	0.0015	4.35	N/A	MeOH	2.2	6.3	0.0948	26	70
124	0.3	91.1349	0.60	ZrOCl ₂ · 8 H ₂ O	0.5	155.1590	0.0020	5.8	N/A	MeOH	2.2	5.8	0.0926	26	70
125	0.3	91.1349	1.00	TiO ₂	0.3	375.6292	0.0001	0.29	0.00	N/A	0.0	2.7	0.0000	118	70
126	0.3	91.1349	0.60	ZrOCl ₂ · 8 H ₂ O	0.5	155.1590	0.0030	8.7	N/A	MeOH	2.2	4.8	0.0514	20	80
127	0.3	91.1349	0.60	ZrOCl ₂ · 8 H ₂ O	0.5	155.1590	0.0040	11.6	N/A	MeOH	2.2	3.8	0.0000	20	80
128	0.3	91.1349	1.00	ZrOCl ₂ · 8 H ₂ O	0.3	93.0954	0.0050	14.5	N/A	MeOH	2.2	2.8	0.0000	20	80
129	0.45	136.7024	0.60	ZrOCl ₂ · 8 H ₂ O	0.75	232.7386	0.0060	17.4	N/A	MeOH	3.3	5.7	0.0000	168	80

Ref.	Organic Linker		L/M N-ratio	Metal Source			HF		HCl 12 M (mL)	Solvent	V (mL)	H ₂ O (mL)	Yield (mg)	Time (h)	Temp (°C)
	N (mmol)	Mass (mg)		Metal Source	N (mmol)	Mass (mg)	V (mL)	N (mmol)							
130	0.3	91.1349	1.00	K ₂ TiF ₆	0.3	124.9740	0.0000	0	N/A	MeOH	2.2	7.8	0.0286	138	80
131	0.3	91.1349	1.00	K ₂ TiF ₆	0.3	124.9740	0.0000	0	0.50	MeOH	2.2	7.8	0.0414	138	80
132	0.3	91.1349	1.00	K ₂ TiF ₆	0.3	124.9740	0.0000	0	1.00	MeOH	2.2	7.8	0.0479	138	80

Table A.2: Metal phosphonate synthesis based on the 3,6-diphosphono-carbazole linker.
Unless otherwise stated, all reactions were carried out in a total volume of 10 cm⁻³.

Ref.	Organic Linker		L/M N-ratio	Metal Source			HF		HCl 12 M (mL)	Solvent	V (mL)	H ₂ O (mL)	Yield (mg)	Time (h)	Temp (°C)
	N (mmol)	Mass (mg)		Metal Source	N (mmol)	Mass (mg)	V (mL)	N (mmol)							
076	0.3	91.6966	1.00	ZrOCl ₂ ·8H ₂ O	0.3	93.0954	0.0008	2.32	N/A	N/A	0.0	9.2	0.0360	96	80
077	0.3	91.6966	0.60	ZrOCl ₂ ·8H ₂ O	0.5	155.1590	0.0008	2.32	N/A	N/A	0.0	9.2	0.0750	96	80
081	0.3	91.6966	0.60	ZrOCl ₂ ·8H ₂ O	0.5	155.1590	0.0008	2.32	N/A	MeOH	2.2	7.0	0.0963	167	70
082	0.3	91.6966	0.60	ZrOCl ₂ ·8H ₂ O	0.5	155.1590	0.0010	2.9	N/A	MeOH	2.2	6.8	0.1099	167	70
083	0.3	91.6966	0.60	ZrOCl ₂ ·8H ₂ O	0.5	155.1590	0.0012	3.48	N/A	MeOH	2.2	6.6	0.1040	167	70
086	0.3	91.6966	0.60	ZrOCl ₂ ·8H ₂ O	0.5	155.1590	0.0010	2.9	N/A	MeOH	4.0	5.0	0.0700	121	70
087	0.3	91.6966	0.60	ZrOCl ₂ ·8H ₂ O	0.5	155.1590	0.0015	4.35	N/A	MeOH	4.0	4.5	0.0000	121	70
108	0.3	91.6966	1.00	ZrOCl ₂ ·8H ₂ O	0.3	93.0954	0.0008	2.32	0.00	DMF	4.8	4.4	0.0000	43	80
111	0.3	91.6966	1.00	ZrOCl ₂ ·8H ₂ O	0.3	93.0954	0.0004	1.16	1.00	DMF	8.6	0.0	0.056	55	100
112	0.6	183.3931	2.00	ZrOCl ₂ ·8H ₂ O	0.3	93.0954	0.0004	1.16	1.00	DMF	8.6	0.0	0.072	55	100
114	1.2	366.7863	2.00	ZrOCl ₂ ·8H ₂ O	0.6	186.1908	N/A	N/A	N/A	N/A	0.0	N/A	0.0000	0.25	N/A
133	0.3	91.7105	1.00	ZrOCl ₂ ·8H ₂ O	0.3	93.0954	0.0008	2.32	0.00	MeOH	2.2	7.0	0.0930	138	80
137	0.3	91.7105	1.00	ZrOCl ₂ ·8H ₂ O	0.3	93.0954	0.0010	2.9	0.00	MeOH	2.2	6.8	0.0881	96	80

Table A.3: Metal phosphonate synthesis based on the 4-phosphono-N-(4-phosphonophenyl)-N-phenylaniline linker. Unless otherwise stated, all reactions were carried out in a total volume of 10 cm^{-3} .

Ref.	Organic Linker		L/M N-ratio	Metal Source			HF		HCl 12 M (mL)	Solvent	V (mL)	H ₂ O (mL)	Yield (mg)	Time (h)	Temp (°C)
	N (mmol)	Mass (mg)		Metal Source	N (mmol)	Mass (mg)	V (mL)	N (mmol)							
134	0.3	74.0232	1.00	ZrOCl ₂ ·8H ₂ O	0.3	93.0954	0.0008	2.32	0.00	MeOH	2.2	7.0	0.0716	138	80
135	0.3	74.0232	1.00	ZrOCl ₂ ·8H ₂ O	0.3	93.0954	0.0010	2.9	0.00	MeOH	2.2	6.8	0.0806	96	80
136	0.6	148.0465	1.00	ZrOCl ₂ ·8H ₂ O	0.6	186.1908	0.0008	2.32	0.00	MeOH	2.2	17.0	0.1389	96	80
138	0.3	74.0232	1.00	ZrOCl ₂ ·8H ₂ O	0.3	93.0954	0.0010	2.9	0.00	MeOH	2.2	6.8	0.0759	138	80
139	0.3	74.0232	1.00	ZrOCl ₂ ·8H ₂ O	0.3	93.0954	0.0012	3.48	0.00	MeOH	2.2	6.6	0.0752	138	80
140	0.3	74.0232	1.00	ZrOCl ₂ ·8H ₂ O	0.3	93.0954	0.0014	4.06	0.00	MeOH	2.2	6.4	0.0702	138	80
141	0.3	74.0232	1.00	ZrOCl ₂ ·8H ₂ O	0.3	93.0954	0.0010	2.9	0.00	MeOH	4.4	4.6	0.0811	138	80
142	0.3	74.0232	1.00	ZrOCl ₂ ·8H ₂ O	0.3	93.0954	0.0010	2.9	0.00	MeOH	6.6	2.4	0.0853	138	80

Table A.4: Structural and refinement details for ZrBPA, ZrDPPA, Zr-II-C, and UPG-1.

	ZrBPA	ZrDPPA	Zr-II-C	UPG-1
Empirical formula	C ₁₂ H ₁₂ NO _{7.5} P ₂ Zr	C ₅₄ H ₃₉ N ₃ O ₁₈ P ₆ Zr	C ₁₂ H ₉ O _{7.5} P ₂ Zr	C ₄₈ H ₆₄ N ₆ O ₂₈ P ₆ Zr
Structural formula	Zr[NH(C ₆ H ₄ PO ₃) ₂] · 1.5H ₂ O	Zr[N(C ₆ H ₅)(C ₆ H ₄ PO ₃) ₂] ₃	Zr[O(C ₆ H ₄ PO ₃) ₂] · 0.5H ₂ O	Zr[(C ₃ N ₃)(C ₆ H ₄ CH ₂ PO ₃) ₃] ₂ · 10 H ₂ O
Formula weight (g/mol)	443.40	1294.96	426.37	1442.05
Crystal system	Monoclinic	Triclinic	Monoclinic	Trigonal
Space group	<i>P</i> 2 ₁ / <i>a</i>	<i>P</i> – 1	-	<i>R</i> – 3
<i>a</i> (Å)	9.22	16.99	9.20	60.67
<i>b</i> (Å)	29.64	13.72	28.49	-
<i>c</i> (Å)	4.70	7.75	5.28	5.13
<i>α</i> (°)	90.0	98.9	90	-
<i>β</i> (°)	94.5	97.8	91.8	-
<i>γ</i> (°)	90.0	85.9	90	-
Volume (Å³)	1284.4	1767.1	1383	16348
Data range (° 2θ)	4 - 30	4 - 30	4 - 30	3.5 - 70
Wavelength	1.54056	1.54056	-	1.54056
<i>R_p</i>	0.050	0.039	-	0.057
<i>R_{wp}</i>	0.066	0.052	-	0.075
BET N₂ S.A. (m² g⁻¹)	583.1	228.1	< 20*	410.0

*less crystalline derivatives have higher BET S.A. in the range of 300 - 440 m² g⁻¹.

Appendix B

Ce(IV)-MOF Synthesis and Crystallisation Kinetics

The tables in this section show the synthetic parameters used in the synthesis of metal phosphonates. These tables have been split according to the linker used, giving three tables in total, as shown below:

Figure B.1: SEM micrographs of F4_MIL-140A(Ce) powders obtained from syntheses employing different temperatures.

Figure B.2: SEM micrographs of F4_MIL-140A(Ce) powders obtained from syntheses employing alternative metal sources and protonation modulators.

Table B.1: Reaction parameters and yield outcomes for the scale-up of F4_MIL-140A(Ce).

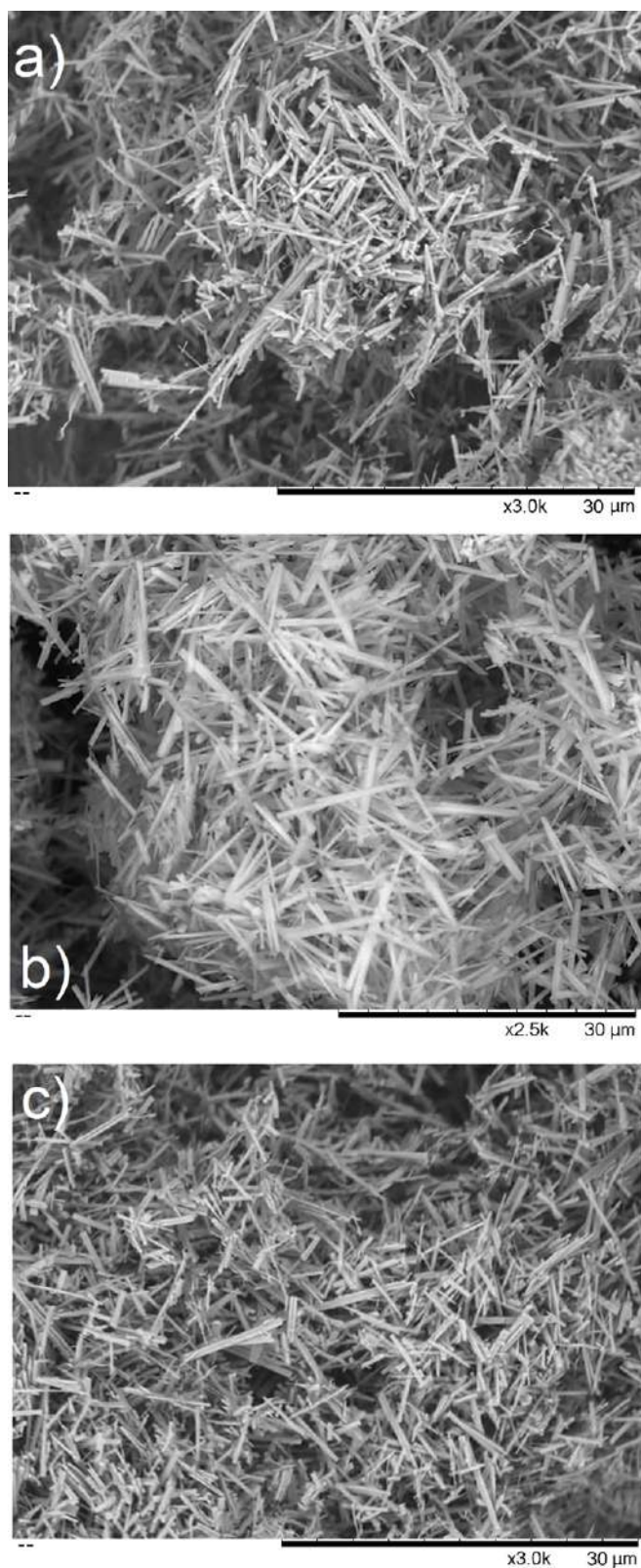


Figure B.1: SEM micrographs of F4_MIL-140A(Ce) powders obtained from syntheses performed at 50 (black), 60 (red) and 70 °C (green) in the presence of 32 equivalents of HNO₃.

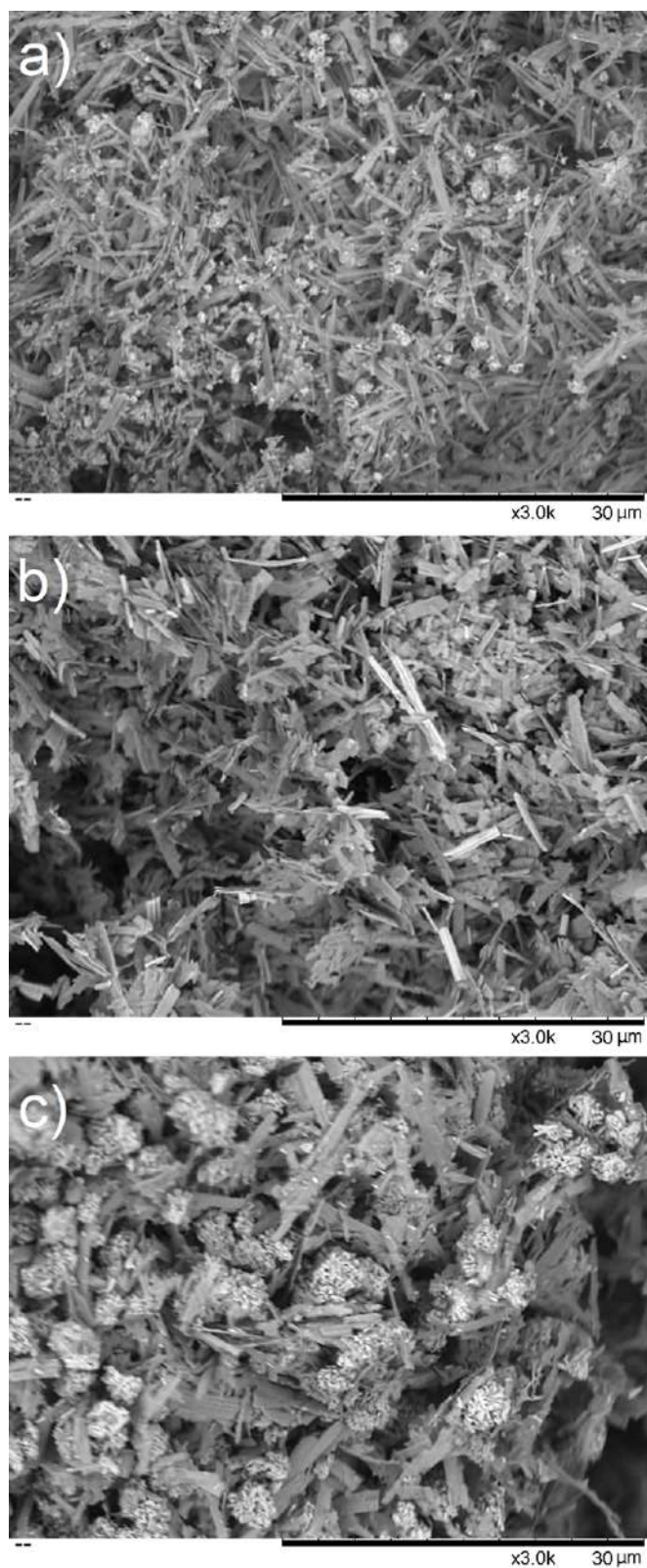


Figure B.2: SEM micrographs of F4_MIL-140A(Ce) powders obtained from syntheses performed using (a) $\text{CAN}/\text{H}_2\text{SO}_4$, (b) $\text{Ce}(\text{SO}_4)_2/\text{HNO}_3$, and (c) $\text{Ce}(\text{SO}_4)_2/\text{H}_2\text{SO}_4$ as Ce(IV) source and protonation modulator, respectively, at 60 °C.

Table B.1: Reaction parameters and yield outcomes for the scale-up of F4_MIL-140A(Ce).
 TFBDC = Tetrafluorobenzene-dicarboxylic acid, CAN = Cerium(IV) ammonium nitrate,
 STY = Space time yield.

Ref.	Vol. (mL)	Conc. (mol dm ⁻³)	TFBDC		CAN		Nitric Acid			Temp (°C)	Time (min)	Yield (mg)	Yield (%)	STY kg m ⁻³ d ⁻¹
			Mass (mg)	Mol. (mmol)	Mass (mg)	Mol. (mmol)	Vol. (mL)	Mol. (mmol)	Conc. (mol.dm ⁻³)					
SS-031	15	0.050	178.6	0.750	411.2	0.750	1.5	24.00	1.60	60	60	177.0	57.5	283.2
Ce-001	15	0.050	178.6	0.750	411.2	0.750	1.5	23.70	1.58	50	60	150.6	48.9	241.0
Ce-002	15	0.075	267.9	1.125	616.7	1.125	1.5	23.70	1.58	50	60	210.4	45.6	336.6
Ce-003	15	0.050	178.6	0.750	411.2	0.750	1.2	18.96	1.26	50	60	216.6	70.4	346.6
Ce-004	15	0.075	267.9	1.125	616.7	1.125	1.2	18.96	1.26	50	60	270.1	58.5	432.2
Ce-005	15	0.050	178.6	0.750	411.2	0.750	1.0	15.80	1.05	50	60	246.9	80.2	395.0
Ce-006	15	0.075	267.9	1.125	616.7	1.125	1.0	15.80	1.05	50	60	274.2	59.4	438.7
Ce-007	15	0.050	178.6	0.750	411.2	0.750	1.2	18.96	1.26	RT	180	173.2	56.3	92.4
Ce-008	15	0.075	267.9	1.125	616.7	1.125	1.2	18.96	1.26	RT	180	307.0	66.5	163.7
Ce-009	15	0.050	178.6	0.750	411.2	0.750	1.0	15.80	1.05	RT	180	242.4	78.8	129.3
Ce-010	15	0.075	267.9	1.125	616.7	1.125	1.0	15.80	1.05	RT	180	392.2	85.0	209.2
Ce-011	15	0.075	267.9	1.125	616.7	1.125	1.0	15.80	1.05	RT	60	362.4	78.5	579.8
Ce-012	15	0.075	267.9	1.125	616.7	1.125	0.8	12.64	0.84	RT	60	416.3	90.2	666.1
Ce-013	15	0.075	267.9	1.125	616.7	1.125	0.6	9.48	0.63	RT	60	421.4	91.3	674.2
Ce-014	15	0.075	267.9	1.125	616.7	1.125	0.4	6.32	0.42	RT	60	426.4	92.4	682.2
Ce-015	15	0.075	267.9	1.125	616.7	1.125	0.2	3.16	0.21	RT	60	428.3	92.8	685.3
Ce-016	150	0.075	2678.5	11.250	6167.5	11.250	8.0	126.40	0.84	RT	60	4540.0	98.4	726.4
Ce-017	300	0.075	5357.0	22.500	12334.9	22.500	16.0	252.80	0.84	RT	60	7579.6	82.1	606.4
Ce-018	300	0.075	5357.0	22.500	12334.9	22.500	16.0	252.80	0.84	RT	60	8002.1	86.7	640.2
Ce-019	3000	0.075	53570.3	225.000	123349.1	225.000	120.0	1896.00	0.63	RT	60	69199.6	75.0	553.6
Ce-020	4500	0.075	80355.4	337.500	185023.6	337.500	240.0	3792.00	0.84	RT	60	135784.0	98.1	724.2